Applications of Nonlinear Fiber Optics

OPTICS AND PHOTONICS

(Formerly Quantum Electronics)

Series Editors

PAUL L. KELLEY
Tufts University
Medford, Massachusetts

IVAN P. KAMINOW
Lucent Technologies
Holmdel, New Jersey

GOVIND P. AGRAWAL
University of Rochester
Rochester, New York

Recently Published Books in the Series:

Jean-Claude Diels and Wolfgang Rudolph, *Ultrashort Laser Pulse Phenomena: Fundamentals, Techniques, and Applications on a Femtosecond Time Scale*
Eli Kapon, editor, *Semiconductor Lasers I: Fundamentals*
Eli Kapon, editor, *Semiconductor Lasers II: Materials and Structures*
P. C. Becker, N. A. Olsson, and J. R. Simpson, *Erbium-Doped Fiber Amplifiers: Fundamentals and Technology*
Raman Kashyap, *Fiber Bragg Gratings*
Katsunari Okamoto, *Fundamentals of Optical Waveguides*
Govind P. Agrawal, *Nonlinear Fiber Optics, Third Edition*

A complete list of titles in this series appears at the end of this volume.

Applications of Nonlinear Fiber Optics

GOVIND P. AGRAWAL
The Institute of Optics
University of Rochester

OPTICS AND PHOTONICS

ACADEMIC PRESS
A Harcourt Science and Technology Company

San Diego San Francisco New York Boston
London Sydney Tokyo

This book is printed on acid-free paper. ∞

Academic Press
A Harcourt Science and Technology Company
525 B Street, Suite 1900, San Diego, California 92101-4495, USA
http://www.academicpress.com

Academic Press
Harcourt Place, 32 Jamestown Road, London NW1 7BY, UK
http://www.academicpress.com

Library of Congress Catalog Card Number: 00-111105

International Standard Book Number: 0-12-045144-1

PRINTED IN THE UNITED STATES OF AMERICA
00 01 02 03 04 05 ML 9 8 7 6 5 4 3 2 1

For Anne, Sipra, Caroline, and Claire

Contents

Preface

Since the publication of the first edition of *Nonlinear Fiber Optics* in 1989, this field has virtually exploded. A major factor behind such tremendous growth was the advent of fiber amplifiers, made by doping silica or fluoride fibers with rare-earth ions such as erbium and neodymium. Such amplifiers revolutionized the design of fiber-optic communication systems, including those making use of optical solitons whose very existence stems from the presence of nonlinear effects in optical fibers. Optical amplifiers permit propagation of lightwave signals over thousands of kilometers as they can compensate for all losses encountered by the signal in the optical domain. At the same time, fiber amplifiers enable the use of massive wavelength-division multiplexing (WDM) and have led to the development of lightwave systems with capacities exceeding 1 Tb/s. Nonlinear fiber optics plays an increasingly important role in the design of such high-capacity lightwave systems. In fact, an understanding of various nonlinear effects occurring inside optical fibers is almost a prerequisite for a lightwave-system designer.

While preparing the third edition of *Nonlinear Fiber Optics*, my intention was to bring the book up to date so that it remains a unique source of comprehensive coverage on the subject of nonlinear fiber optics. An attempt was made to include recent research results on all topics relevant to the field of nonlinear fiber optics. Such an ambitious objective increased the size of the book to the extent that it was necessary to split it into two separate books, thus creating this new book *Applications of Nonlinear Fiber Optics*. The third edition of *Nonlinear Fiber Optics* deals with the fundamental aspects of the field. This book is devoted to the applications of nonlinear fiber optics, and its use requires knowledge of the fundamentals covered in *Nonlinear Fiber Optics*. **Please note that when an equation or section number is prefaced with the letter A, that indicates that the topic is covered in more detail in the third edition of of *Nonlinear Fiber Optics*.**

Most of the material in this volume is new. The first three chapters deal with three important fiber-optic components—fiber-based gratings, couplers, and interferometers—that serve as the building blocks of lightwave technology. In view of the enormous impact of rare-earth-doped fibers, amplifiers and lasers made by using such fibers are covered in Chapters 4 and 5. The last three chapters describe important applications of nonlinear fiber optics and are devoted to pulse-compression techniques, fiber-optic communication systems, and soliton-based transmission schemes. This volume should serve well the need of the scientific community interested in such fields as ultrafast phenomena, optical amplifiers and lasers, and optical communications. It will also be useful to graduate students as well as scientists and engineers involved in lightwave technology.

The potential readership is likely to consist of senior undergraduate students, graduate students enrolled in the M.S. and Ph.D. programs, engineers and technicians involved with the telecommunication industry, and scientists working in the fields of fiber optics and optical communications. This volume may be a useful text for graduate and senior-level courses dealing with nonlinear optics, fiber optics, or optical communications that are designed to provide mastery of the fundamental aspects. Some universities may even opt to offer a high-level graduate course devoted solely to nonlinear fiber optics. The problems provided at the end of each chapter should be useful to instructors of such a course.

Many individuals have contributed either directly or indirectly to the completion of this book. I am thankful to all of them, especially to my students, whose curiosity led to several improvements. Some of my colleagues have helped me in preparing this book. I thank Taras Lakoba, Zhi Liao, Natalia Litchinitser, Bishnu Pal, and Stojan Radic for reading several chapters and making helpful suggestions. I am grateful to many readers for their feedback. Last, but not least, I thank my wife, Anne, and my daughters, Sipra, Caroline, and Claire, for understanding why I needed to spend many weekends on the book instead of spending time with them.

Govind P. Agrawal

Rochester, NY

Chapter 1

Fiber Gratings

Silica fibers can change their optical properties permanently when they are exposed to intense radiation from a laser operating in the blue or ultraviolet spectral region. This photosensitive effect can be used to induce periodic changes in the refractive index along the fiber length, resulting in the formation of an intracore Bragg grating. Fiber gratings can be designed to operate over a wide range of wavelengths extending from the ultraviolet to the infrared region. The wavelength region near 1.5 μm is of particular interest because of its relevance to fiber-optic communication systems. In this chapter on fiber gratings, the emphasis is on the role of the nonlinear effects. Sections 1.1 and 1.2 discuss the physical mechanism responsible for photosensitivity and various techniques used to make fiber gratings. The coupled-mode theory is described in Section 1.3, where the concept of the photonic bandgap is also introduced. Section 1.4 is devoted to the nonlinear effects occurring under continuous-wave (CW) conditions. Time-dependent features such as modulation instability, optical solitons, and optical switching are covered in Sections 1.5 and 1.6. Section 1.7 considers nonuniform and long-period gratings together with photonic-crystal fibers.

1.1 Basic Concepts

Diffraction gratings constitute a standard optical component and are used routinely in various optical instruments such as a spectrometer. The underlying principle was discovered more than 200 years ago [1]. From a practical standpoint, a diffraction grating is defined as any optical element capable of im-

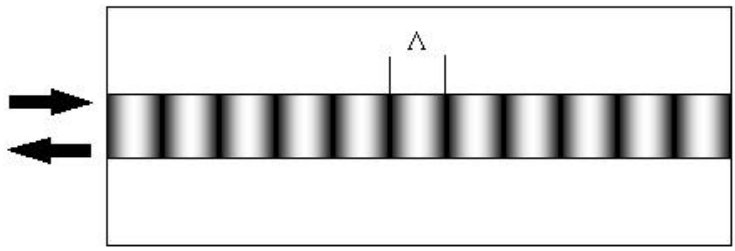

Figure 1.1 Schematic illustration of a fiber grating. Dark and light shaded regions within the fiber core show periodic variations of the refractive index.

posing a periodic variation in the amplitude or phase of light incident on it. Clearly, an optical medium whose refractive index varies periodically acts as a grating since it imposes a periodic variation of phase when light propagates through it. Such gratings are called *index gratings*.

1.1.1 Bragg Diffraction

The diffraction theory of gratings shows that when light is incident at an angle θ_i (measured with respect to the planes of constant refractive index), it is diffracted at an angle θ_r such that [1]

$$\sin\theta_i - \sin\theta_r = m\lambda/(\bar{n}\Lambda), \tag{1.1.1}$$

where Λ is the grating period, $\lambda/\bar{n}$ is the wavelength of light inside the medium with an average refractive index $\bar{n}$, and m is the order of Bragg diffraction. This condition can be thought of as a phase-matching condition, similar to that occurring in the case of Brillouin scattering or four-wave mixing, and can be written as

$$\mathbf{k}_i - \mathbf{k}_d = m\mathbf{k}_g, \tag{1.1.2}$$

where $\mathbf{k}_i$ and $\mathbf{k}_d$ are the wave vectors associated with the incident and diffracted light. The grating wave vector $\mathbf{k}_g$ has magnitude $2\pi/\Lambda$ and points in the direction in which the refractive index of the medium is changing in a periodic manner.

In the case of single-mode fibers, all three vectors lie along the fiber axis. As a result, $\mathbf{k}_d = -\mathbf{k}_i$ and the diffracted light propagates backward. Thus, as shown schematically in Fig. 1.1, a fiber grating acts as a reflector for a specific wavelength of light for which the phase-matching condition is satisfied. In

terms of the angles appearing in Eq. (1.1.1), $\theta_i = \pi/2$ and $\theta_r = -\pi/2$. If $m = 1$, the period of the grating is related to the vacuum wavelength as $\lambda = 2\bar{n}\Lambda$. This condition is known as the *Bragg condition*, and gratings satisfying it are referred to as *Bragg gratings*. Physically, the Bragg condition ensures that weak reflections occurring throughout the grating add up in phase to produce a strong reflection. For a fiber grating reflecting light in the wavelength region near 1.5 μm, the grating period $\Lambda \approx 0.5$ μm.

Bragg gratings inside optical fibers were first formed in 1978 by irradiating a germanium-doped silica fiber for a few minutes with an intense argon-ion laser beam [2]. The grating period was fixed by the argon-ion laser wavelength, and the grating reflected light only within a narrow region around that wavelength. It was realized that the 4% reflection occurring at the two fiber–air interfaces created a standing-wave pattern and that the laser light was absorbed only in the bright regions. As a result, the glass structure changed in such a way that the refractive index increased permanently in the bright regions. Although this phenomenon attracted some attention during the next 10 years [3]–[15], it was not until 1989 that fiber gratings became a topic of intense investigation, fueled partly by the observation of second-harmonic generation in photosensitive fibers. The impetus for this resurgence of interest was provided by a 1989 paper in which a side-exposed holographic technique was used to make fiber gratings with controllable period [16].

Because of its relevance to fiber-optic communication systems, the holographic technique was quickly adopted to produce fiber gratings in the wavelength region near 1.55 μm [17]. Considerable work was done during the early 1990s to understand the physical mechanism behind photosensitivity of fibers and to develop techniques that were capable of making large changes in the refractive index [18]–[48]. By 1995, fiber gratings were available commercially, and by 1997 they became a standard component of lightwave technology. In 1999, two books devoted entirely to fiber gratings focused on applications related to fiber sensors and fiber-optic communication systems [49], [50].

1.1.2 Photosensitivity

There is considerable evidence that photosensitivity of optical fibers is due to defect formation inside the core of Ge-doped silica fibers [28]–[30]. As mentioned in Section A.1.2, the fiber core is often doped with germania to increase its refractive index and introduce an index step at the core-cladding interface. The Ge concentration is typically 3–5%.

The presence of Ge atoms in the fiber core leads to formation of oxygen-deficient bonds (such as Si–Ge, Si–Si, and Ge–Ge bonds), which act as defects in the silica matrix [49]. The most common defect is the GeO defect. It forms a defect band with an energy gap of about 5 eV (energy required to break the bond). Single-photon absorption of 244-nm radiation from an excimer laser (or two-photon absorption of 488-nm light from an argon-ion laser) breaks these defect bonds and creates GeE' centers. Extra electrons associated with GeE' centers are free to move within the glass matrix until they are trapped at hole-defect sites to form color centers known as Ge(1) and Ge(2). Such modifications in the glass structure change the absorption spectrum $\alpha(\omega)$. However, changes in the absorption also affect the refractive index since $\Delta\alpha$ and Δn are related through the Kramers–Kronig relation [51]

$$\Delta n(\omega') = \frac{c}{\pi}\int_0^\infty \frac{\Delta\alpha(\omega)\,d\omega}{\omega^2-\omega'^2}. \tag{1.1.3}$$

Even though absorption modifications occur mainly in the ultraviolet region, the refractive index can change even in the visible or infrared region. Moreover, since index changes occur only in the regions of fiber core where the ultraviolet light is absorbed, a periodic intensity pattern is transformed into an index grating. Typically, index change Δn is $\sim 10^{-4}$ in the 1.3- to 1.6-μm wavelength range, but can exceed 0.001 in fibers with high Ge concentration [34].

The presence of GeO defects is crucial for photosensitivity to occur in optical fibers. However, standard telecommunication fibers rarely have more than 3% of Ge atoms in their core, resulting in relatively small index changes. The use of other dopants such as phosphorus, boron, and aluminum can enhance the photosensitivity (and the amount of index change) to some extent, but these dopants also tend to increase fiber losses. It was discovered in the early 1990s that the amount of index change induced by ultraviolet absorption can be enhanced by two orders of magnitude ($\Delta n > 0.01$) by soaking the fiber in hydrogen gas at high pressures (200 atm) and room temperature [39]. The density of Ge–Si oxygen-deficient bonds increases in hydrogen-soaked fibers because hydrogen can recombine with oxygen atoms. Once hydrogenated, the fiber needs to be stored at low temperature to maintain its photosensitivity. However, gratings made in such fibers remain intact over long periods of time, indicating the nearly permanent nature of the resulting index changes [46]. Hydrogen soaking is commonly used for making fiber gratings.

It should be stressed that understanding of the exact physical mechanism behind photosensitivity is far from complete, and more than one mechanism may be involved [52]. Localized heating can also affect grating formation. For instance, in fibers with a strong grating (index change > 0.001), damage tracks were seen when the grating was examined under an optical microscope [34]; these tracks were due to localized heating to several thousand degrees of the core region where ultraviolet light was most strongly absorbed. At such high temperatures the local structure of amorphous silica can change considerably because of melting.

1.2 Fabrication Techniques

Fiber gratings can be made by using several different techniques, each having its own merits. This section discusses briefly four major techniques commonly used for making fiber gratings: the single-beam internal technique, the dual-beam holographic technique, the phase mask technique, and the point-by-point fabrication technique. The reader is referred to Chapter 3 of Ref. [49] for further details.

1.2.1 Single-Beam Internal Technique

In this technique, used in the original 1978 experiment [2], a single laser beam, often obtained from an argon-ion laser operating in a single mode near 488 nm, is launched into a germanium-doped silica fiber. The light reflected from the near end of the fiber is then monitored. The reflectivity is initially about 4%, as expected for a fiber–air interface. However, it gradually begins to increase with time and can exceed 90% after a few minutes when the Bragg grating is completely formed [4]. Figure 1.2 shows the increase in reflectivity with time, observed in the 1978 experiment for a 1-m-long fiber having a numerical aperture of 0.1 and a core diameter of 2.5 μm. Measured reflectivity of 44% after 8 minutes of exposure implies more than 80% reflectivity of the Bragg grating when coupling losses are accounted for.

Grating formation is initiated by the light reflected from the far end of the fiber and propagating in the backward direction. The two counterpropagating waves interfere and create a standing-wave pattern with periodicity $\lambda/2\bar{n}$, where λ is the laser wavelength and $\bar{n}$ is the mode index at that wavelength. The refractive index of silica is modified locally in the regions of high intensity,

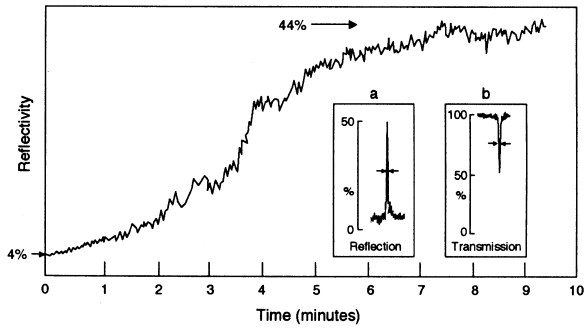

Figure 1.2 Increase in reflectivity with time during grating formation. Insets show the reflection and transmission spectra of the grating. (After Ref. [2], ©American Institute of Physics)

resulting in a periodic index variation along the fiber length. Even though the index grating is quite weak initially (4% far-end reflectivity), it reinforces itself through a kind of runaway process. Since the grating period is exactly the same as the standing-wave period, the Bragg condition is satisfied for the laser wavelength. As a result, some forward-traveling light is reflected backward through distributed feedback, which strengthens the grating, which in turn increases feedback. The process stops when the photoinduced index change saturates. Optical fibers with an intracore Bragg grating act as a narrowband reflection filter. The two insets in Fig. 1.2 show the measured reflection and transmission spectra of such a fiber grating. The full width at half maximum (FWHM) of these spectra is only about 200 MHz.

A disadvantage of the single-beam internal method is that the grating can be used only near the wavelength of the laser used to make it. Since Ge-doped silica fibers exhibit little photosensitivity at wavelengths longer than 0.5 μm, such gratings cannot be used in the 1.3- to 1.6-μm wavelength region that is important for optical communications. A dual-beam holographic technique, discussed next, solves this problem.

1.2.2 Dual-Beam Holographic Technique

The dual-beam holographic technique, shown schematically in Fig. 1.3, makes use of an external interferometric scheme similar to that used for holography. Two optical beams, obtained from the same laser (operating in the ultraviolet region) and making an angle 2θ are made to interfere at the exposed core of an

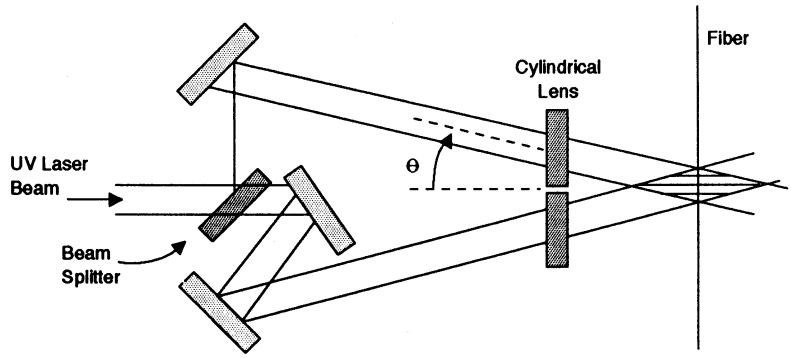

Figure 1.3 Schematic illustration of the dual-beam holographic technique.

optical fiber [16]. A cylindrical lens is used to expand the beam along the fiber length. Similar to the single-beam scheme, the interference pattern creates an index grating. However, the grating period Λ is related to the ultraviolet laser wavelength λ_{uv} and the angle 2θ made by the two interfering beams through the simple relation

$$\Lambda = \lambda_{\text{uv}}/(2\sin\theta). \tag{1.2.1}$$

The most important feature of the holographic technique is that the grating period Λ can be varied over a wide range by simply adjusting the angle θ (see Fig. 1.3). The wavelength λ at which the grating will reflect light is related to Λ as $\lambda = 2\bar{n}\Lambda$. Since λ can be significantly larger than λ_{uv}, Bragg gratings operating in the visible or infrared region can be fabricated by the dual-beam holographic method even when λ_{uv} is in the ultraviolet region. In a 1989 experiment, Bragg gratings reflecting 580-nm light were made by exposing the 4.4-mm-long core region of a photosensitive fiber for 5 minutes with 244-nm ultraviolet radiation [16]. Reflectivity measurements indicated that the refractive index changes were $\sim 10^{-5}$ in the bright regions of the interference pattern. Bragg gratings formed by the dual-beam holographic technique were stable and remained unchanged even when the fiber was heated to 500°C.

Because of their practical importance, Bragg gratings operating in the 1.55-μm region were made in 1990 [17]. Since then, several variations of the basic technique have been used to make such gratings in a practical manner. An inherent problem for the dual-beam holographic technique is that it requires an ultraviolet laser with excellent temporal and spatial coherence. Excimer lasers commonly used for this purpose have relatively poor beam quality and

require special care to maintain the interference pattern over the fiber core over a duration of several minutes.

It turns out that high-reflectivity fiber gratings can be written by using a single excimer laser pulse (with typical duration of 20 ns) if the pulse energy is large enough [31]–[34]. Extensive measurements on gratings made by this technique indicate a threshold-like phenomenon near a pulse energy level of about 35 mJ [34]. For lower pulse energies, the grating is relatively weak since index changes are only about 10^{-5}. By contrast, index changes of about 10^{-3} are possible for pulse energies above 40 mJ. Bragg gratings with nearly 100% reflectivity have been made by using a single 40-mJ pulse at the 248-nm wavelength. The gratings remained stable at temperatures as high as 800°C. A short exposure time has an added advantage. The typical rate at which a fiber is drawn from a preform is about 1 m/s. Since the fiber moves only 20 nm in 20 ns, and since this displacement is a small fraction of the grating period Λ, a grating can be written during the drawing stage while the fiber is being pulled and before it is sleeved [35]. This feature makes the single-pulse holographic technique quite useful from a practical standpoint.

1.2.3 Phase Mask Technique

This nonholographic technique uses a photolithographic process commonly employed for fabrication of integrated electronic circuits. The basic idea is to use a phase mask with a periodicity related to the grating period [36]. The phase mask acts as a master grating that is transferred to the fiber using a suitable method. In one realization of this technique [37], the phase mask was made on a quartz substrate on which a patterned layer of chromium was deposited using electron-beam lithography in combination with reactive-ion etching. Phase variations induced in the 242-nm radiation passing through the phase mask translate into a periodic intensity pattern similar to that produced by the holographic technique. Photosensitivity of the fiber converts intensity variations into an index grating of the same periodicity as that of the phase mask.

The chief advantage of the phase mask method is that the demands on the temporal and spatial coherence of the ultraviolet beam are much less stringent because of the noninterferometric nature of the technique. In fact, even a nonlaser source such as an ultraviolet lamp can be used. Furthermore, the phase mask technique allows fabrication of fiber gratings with a variable period (chirped gratings) and can also be used to tailor the periodic index profile

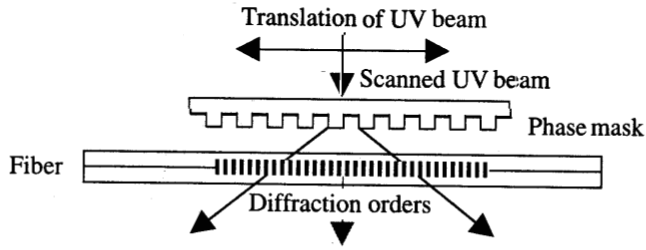

Figure 1.4 Schematic illustration of a phase mask interferometer used for making fiber gratings. (After Ref. [49], reprinted by permission of Academic Press)

along the grating length. It is also possible to vary the Bragg wavelength over some range for a fixed mask periodicity by using a converging or diverging wavefront during the photolithographic process [41]. On the other hand, the quality of fiber grating (length, uniformity, etc.) depends completely on the master phase mask, and all imperfections are reproduced precisely. Nonetheless, gratings with 5-mm length and 94% reflectivity were made in 1993, showing the potential of this technique [37].

The phase mask can also be used to form an interferometer using the geometry shown in Fig. 1.4. The ultraviolet laser beam falls normally on the phase mask and is diffracted into several beams in the Raman–Nath scattering regime. The zeroth-order beam (direct transmission) is blocked or canceled by an appropriate technique. The two first-order diffracted beams interfere on the fiber surface and form a periodic intensity pattern. The grating period is exactly one-half of the phase mask period. In effect, the phase mask produces both the reference and object beams required for holographic recording.

There are several advantages of using a phase mask interferometer. It is insensitive to the lateral translation of the incident laser beam and tolerant of any beam-pointing instability. Relatively long fiber gratings can be made by moving two side mirrors while maintaining their mutual separation. In fact, the two mirrors can be replaced by a single silica block that reflects the two beams internally through total internal reflection, resulting in a compact and stable interferometer [49]. The length of the grating formed inside the fiber core is limited by the size and optical quality of the silica block.

Long gratings can be formed by scanning the phase mask or by translating the optical fiber itself such that different parts of the optical fiber are exposed to the two interfering beams. In this way, multiple short gratings are formed in succession in the same fiber. Any discontinuity or overlap between the

two neighboring gratings, resulting from positional inaccuracies, leads to the so-called stitching errors (also called phase errors) that can affect the quality of the whole grating substantially if left uncontrolled. Nevertheless, this technique was used in 1993 to produce a 5-cm-long grating [42]. Since then, gratings longer than 1 meter have been made with success [53] by employing techniques that minimize phase errors [54].

1.2.4 Point-by-Point Fabrication Technique

This nonholographic scanning technique bypasses the need of a master phase mask and fabricates the grating directly on the fiber, period by period, by exposing short sections of width w to a single high-energy pulse [18]. The fiber is translated by a distance $\Lambda - w$ before the next pulse arrives, resulting in a periodic index pattern such that only a fraction w/Λ in each period has a higher refractive index. The method is referred to as point-by-point fabrication since a grating is fabricated period by period even though the period Λ is typically below 1 μm. The technique works by focusing the spot size of the ultraviolet laser beam so tightly that only a short section of width w is exposed to it. Typically, w is chosen to be $\Lambda/2$ although it could be a different fraction if so desired.

There are a few practical limitations of this technique. First, only short fiber gratings (< 1 cm) are typically produced because of the time-consuming nature of the point-to-point fabrication method. Second, it is hard to control the movement of a translation stage accurately enough to make this scheme practical for long gratings. Third, it is not easy to focus the laser beam to a small spot size that is only a fraction of the grating period. Recall that the period of a first-order grating is about 0.5 μm at 1.55 μm and becomes even smaller at shorter wavelengths. For this reason, the technique was first demonstrated in 1993 by making a 360-μm-long, third-order grating with a 1.59-μm period [38]. The third-order grating still reflected about 70% of the incident 1.55-μm light. From a fundamental standpoint, an optical beam can be focused to a spot size as small as the wavelength. Thus, the 248-nm laser commonly used in grating fabrication should be able to provide a first-order grating in the wavelength range from 1.3 to 1.6 μm with proper focusing optics similar to that used for fabrication of integrated circuits.

The point-by-point fabrication method is quite suitable for long-period gratings in which the grating period exceeds 10 μm and even can be longer than 100 μm, depending on the application [55]–[57]. Such gratings can

be used for mode conversion (power transfer from one mode to another) or polarization conversion (power transfer between two orthogonally polarized modes). Their filtering characteristics have been used for flattening the gain profile of erbium-doped fiber amplifiers and for mode conversion in all-fiber multimode devices.

1.3 Grating Characteristics

Two different approaches have been used to study how a Bragg grating affects wave propagation in optical fibers. In one approach, Bloch formalism—used commonly for describing motion of electrons in semiconductors—is applied to Bragg gratings [58]. In another, forward- and backward-propagating waves are treated independently, and the Bragg grating provides a coupling between them. This method is known as the *coupled-mode theory* and has been used with considerable success in several different contexts. In this section we derive the nonlinear coupled-mode equations and use them to discuss propagation of low-intensity CW light through a Bragg grating. We also introduce the concept of photonic bandgap and use it to show how a Bragg grating introduces a large amount of dispersion.

1.3.1 Coupled-Mode Equations

Wave propagation in a linear periodic medium has been studied extensively using coupled-mode theory [59]–[61]. This theory has been applied to distributed-feedback (DFB) semiconductor lasers [62], among other things. In the case of optical fibers, we need to include both the nonlinear changes and the periodic variation of the refractive index by using

$$\tilde{n}(\omega,z) = \bar{n}(\omega) + n_2|E|^2 + \delta n_g(z), \tag{1.3.1}$$

where n_2 is the nonlinear parameter and $\delta n_g(z)$ accounts for periodic index variations inside the grating. The coupled-mode theory can be generalized to include the fiber nonlinearity since the nonlinear index change $n_2|E|^2$ in Eq. (1.3.1) is so small that it can be treated as a perturbation [63].

The starting point consists of solving Maxwell's equations with the refractive index given in Eq. (1.3.1). However, as discussed in Section A.2.3, if the nonlinear effects are relatively weak, we can work in the frequency domain

and solve the Helmholtz equation

$$\nabla^2\tilde{E} + \tilde{n}^2(\omega,z)\omega^2/c^2\tilde{E} = 0, \tag{1.3.2}$$

where $\tilde{E}$ denotes the Fourier transform of the electric field with respect to time.

Noting that $\tilde{n}$ is a periodic function of z, it is useful to expand $\delta n_g(z)$ in a Fourier series as

$$\delta n_g(z) = \sum_{m=-\infty}^{\infty} \delta n_m \exp[2\pi i m(z/\Lambda)]. \tag{1.3.3}$$

Since both the forward- and backward-propagating waves should be included, $\tilde{E}$ in Eq. (1.3.2) is of the form

$$\tilde{E}(\mathbf{r},\omega) = F(x,y)[\tilde{A}_f(z,\omega)\exp(i\beta_B z) + \tilde{A}_b(z,\omega)\exp(-i\beta_B z)], \tag{1.3.4}$$

where $\beta_B = \pi/\Lambda$ is the Bragg wave number for a first-order grating. It is related to the Bragg wavelength through the Bragg condition $\lambda_B = 2\bar{n}\Lambda$ and can be used to define the Bragg frequency as $\omega_B = \pi c/(\bar{n}\Lambda)$. Transverse variations for the two counterpropagating waves are governed by the same modal distribution $F(x,y)$ in a single-mode fiber.

Using Eqs. (1.3.1)–(1.3.4), assuming that $\tilde{A}_f$ and $\tilde{A}_b$ vary slowly with z and keeping only the nearly phase-matched terms, the frequency-domain coupled-mode equations become [59]–[61]

$$\frac{\partial\tilde{A}_f}{\partial z} = i[\delta(\omega) + \Delta\beta]\tilde{A}_f + i\kappa\tilde{A}_b, \tag{1.3.5}$$

$$-\frac{\partial\tilde{A}_b}{\partial z} = i[\delta(\omega) + \Delta\beta]\tilde{A}_b + i\kappa\tilde{A}_f, \tag{1.3.6}$$

where δ is a measure of detuning from the Bragg frequency and is defined as

$$\delta(\omega) = (\bar{n}/c)(\omega - \omega_B) \equiv \beta(\omega) - \beta_B. \tag{1.3.7}$$

The nonlinear effects are included through $\Delta\beta$ defined as in Eq. (A.2.3.20). The coupling coefficient κ governs the grating-induced coupling between the forward and backward waves. For a first-order grating, κ is given by

$$\kappa = \frac{k_0 \int\int_{-\infty}^{\infty} \delta n_1 |F(x,y)|^2\, dx\, dy}{\int\int_{-\infty}^{\infty} |F(x,y)|^2\, dx\, dy}. \tag{1.3.8}$$

In this general form, κ can include transverse variations of δn_g occurring when the photoinduced index change is not uniform over the core area. For a transversely uniform grating $\kappa = 2\pi\delta n_1/\lambda$, as can be inferred from Eq. (1.3.8) by taking δn_1 as constant and using $k_0 = 2\pi/\lambda$. For a sinusoidal grating of the form $\delta n_g = n_a \cos(2\pi z/\Lambda)$, $\delta n_1 = n_a/2$ and the coupling coefficient is given by $\kappa = \pi n_a/\lambda$.

Equations (1.3.5) and (1.3.6) can be converted to time domain by following the procedure outlined in Section A.2.3. We assume that the total electric field can be written as

$$E(\mathbf{r},t) = \tfrac{1}{2}F(x,y)[A_f(z,t)e^{i\beta_B z} + A_b(z,t)e^{-i\beta_B z}]e^{-i\omega_0 t} + \text{c.c.}, \tag{1.3.9}$$

where ω_0 is the frequency at which the pulse spectrum is centered. We expand $\beta(\omega)$ in Eq. (1.3.7) in a Taylor series as

$$\beta(\omega) = \beta_0 + (\omega-\omega_0)\beta_1 + \tfrac{1}{2}(\omega-\omega_0)^2\beta_2 + \tfrac{1}{6}(\omega-\omega_0)^3\beta_3 + \cdots \tag{1.3.10}$$

and retain terms up to second order in $\omega - \omega_0$. The resulting equations can be converted into time domain by replacing $\omega - \omega_0$ with the differential operator $i(\partial/\partial t)$. The resulting coupled-mode equations become

$$\frac{\partial A_f}{\partial z} + \beta_1\frac{\partial A_f}{\partial t} + \frac{i\beta_2}{2}\frac{\partial^2 A_f}{\partial t^2} + \frac{\alpha}{2}A_f = i\delta A_f + i\kappa A_b + i\gamma(|A_f|^2 + 2|A_b|^2)A_f, \tag{1.3.11}$$

$$-\frac{\partial A_b}{\partial z} + \beta_1\frac{\partial A_b}{\partial t} + \frac{i\beta_2}{2}\frac{\partial^2 A_b}{\partial t^2} + \frac{\alpha}{2}A_b = i\delta A_b + i\kappa A_f + i\gamma(|A_b|^2 + 2|A_f|^2)A_b, \tag{1.3.12}$$

where δ in Eq. (1.3.7) is evaluated at $\omega = \omega_0$ and becomes $\delta = (\omega_0 - \omega_B)/v_g$. In fact, the δ term can be eliminated from the coupled-mode equations if ω_0 is replaced by ω_B in Eq. (1.3.9). The other parameters have the same meaning as in Section A.2.3. Specifically, $\beta_1 \equiv 1/v_g$ is related inversely to the group velocity, β_2 governs the group-velocity dispersion (GVD), and the nonlinear parameter γ is related to n_2 as $\gamma = n_2\omega_0/(cA_{\text{eff}})$, where A_{eff} is the effective core area as defined in Eq. (A.2.3.29).

The nonlinear terms in the time-domain coupled-mode equations contain the contributions of both self-phase modulation (SPM) and cross-phase modulation (XPM). The origin of the factor of 2 in the XPM term is discussed in

Section A.7.1. In fact, the coupled-mode equations are similar to and should be compared with Eqs. (A.7.1.15) and (A.7.1.16), which govern propagation of two copropagating waves inside optical fibers. The two major differences are: (i) the negative sign appearing in front of the $\partial A_b/\partial z$ term in Eq. (1.3.11) because of backward propagation of A_b and (ii) the presence of linear coupling between the counterpropagating waves governed by the parameter κ. Both of these differences change the character of wave propagation profoundly. Before discussing the general case, it is instructive to consider the case in which the nonlinear effects are so weak that the fiber acts as a linear medium.

1.3.2 CW Solution in the Linear Case

In this section, we will focus on the linear case in which the nonlinear effects are negligible. When the SPM and XPM terms are neglected in Eqs. (1.3.11) and (1.3.12), the resulting linear equations can be solved easily in the Fourier domain. In fact, we can use Eqs. (1.3.5) and (1.3.6). These frequency-domain coupled-mode equations include GVD to all orders. After setting the nonlinear contribution $\Delta\beta$ to zero, we obtain

$$\frac{\partial \tilde{A}_f}{\partial z} = i\delta\tilde{A}_f + i\kappa\tilde{A}_b, \tag{1.3.13}$$

$$-\frac{\partial \tilde{A}_b}{\partial z} = i\delta\tilde{A}_b + i\kappa\tilde{A}_f, \tag{1.3.14}$$

where $\delta(\omega)$ is given by Eq. (1.3.7).

A general solution of these linear equations takes the form

$$\tilde{A}_f(z) = A_1\exp(iqz) + A_2\exp(-iqz), \tag{1.3.15}$$

$$\tilde{A}_b(z) = B_1\exp(iqz) + B_2\exp(-iqz), \tag{1.3.16}$$

where q is to be determined. The constants A_1, A_2, B_1, and B_2 are interdependent and satisfy the following four relations:

$$(q-\delta)A_1 = \kappa B_1, \qquad (q+\delta)B_1 = -\kappa A_1, \tag{1.3.17}$$

$$(q-\delta)B_2 = \kappa A_2, \qquad (q+\delta)A_2 = -\kappa B_2. \tag{1.3.18}$$

These equations are satisfied for nonzero values of A_1, A_2, B_1, and B_2 if the possible values of q obey the dispersion relation

$$q = \pm\sqrt{\delta^2 - \kappa^2}. \tag{1.3.19}$$

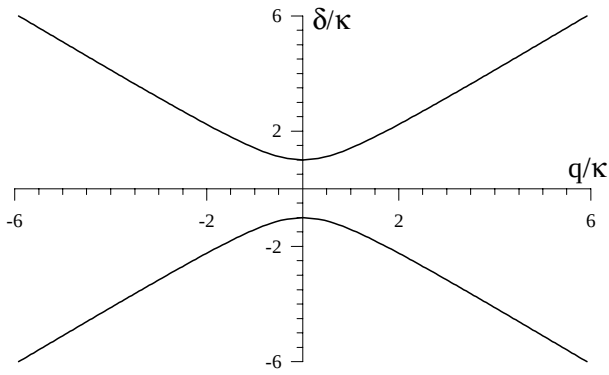

Figure 1.5 Dispersion curves showing variation of δ with q and the existence of the photonic bandgap for a fiber grating.

This equation is of paramount importance for gratings. Its implications will become clear soon.

One can eliminate A_2 and B_1 by using Eqs. (1.3.15)–(1.3.18) and write the general solution in terms of an effective reflection coefficient $r(q)$ as

$$\tilde{A}_f(z) = A_1 \exp(iqz) + r(q) B_2 \exp(-iqz), \tag{1.3.20}$$

$$\tilde{A}_b(z) = B_2 \exp(-iqz) + r(q) A_1 \exp(iqz), \tag{1.3.21}$$

where

$$r(q) = \frac{q-\delta}{\kappa} = -\frac{\kappa}{q+\delta}. \tag{1.3.22}$$

The q dependence of r and the dispersion relation (1.3.19) indicate that both the magnitude and the phase of backward reflection depend on the frequency ω. The sign ambiguity in Eq. (1.3.19) can be resolved by choosing the sign of q such that $|r(q)| < 1$.

1.3.3 Photonic Bandgap, or Stop Band

The dispersion relation of Bragg gratings exhibits an important property seen clearly in Fig. 1.5, where Eq. (1.3.19) is plotted. If the frequency detuning δ of the incident light falls in the range $-\kappa < \delta < \kappa$, q becomes purely imaginary. Most of the incident field is reflected in that case since the grating does not support a propagating wave. The range $|\delta| \leq \kappa$ is referred to as the *photonic*

bandgap, in analogy with the electronic energy bands occurring in crystals. It is also called the *stop band* since light stops transmitting through the grating when its frequency falls within the photonic bandgap.

To understand what happens when optical pulses propagate inside a fiber grating with their carrier frequency ω_0 outside the stop band but close to its edges, note that the effective propagation constant of the forward- and backward-propagating waves from Eqs. (1.3.4) and (1.3.15) is $\beta_e = \beta_B \pm q$, where q is given by Eq. (1.3.19) and is a function of optical frequency through δ. This frequency dependence of β_e indicates that a grating will exhibit dispersive effects even if it was fabricated in a nondispersive medium. In optical fibers, grating-induced dispersion adds to the material and waveguide dispersion. In fact, the contribution of grating dominates among all sources responsible for dispersion. To see this more clearly, we expand β_e in a Taylor series in a way similar to Eq. (1.3.10) around the carrier frequency ω_0 of the pulse. The result is given by

$$\beta_e(\omega) = \beta_0^g + (\omega-\omega_0)\beta_1^g + \tfrac{1}{2}(\omega-\omega_0)^2\beta_2^g + \tfrac{1}{6}(\omega-\omega_0)^3\beta_3^g + \cdots, \quad (1.3.23)$$

where β_m^g with $m = 1, 2, \ldots$ is defined as

$$\beta_m^g = \frac{d^m q}{d\omega^m} \approx \left(\frac{1}{v_g}\right)^m \frac{d^m q}{d\delta^m}, \quad (1.3.24)$$

where derivatives are evaluated at $\omega = \omega_0$. The superscript g denotes that the dispersive effects have their origin in the grating. In Eq. (1.3.24), v_g is the group velocity of pulse in the absence of the grating ($\kappa = 0$). It occurs naturally when the frequency dependence of $\bar{n}$ is taken into account in Eq. (1.3.7). Dispersion of v_g is neglected in Eq. (1.3.24) but can be included easily.

Consider first the group velocity of the pulse inside the grating. Using $V_G = 1/\beta_1^g$ and Eq. (1.3.24), it is given by

$$V_G = \pm v_g \sqrt{1 - \kappa^2/\delta^2}, \quad (1.3.25)$$

where the choice of $\pm$ signs depends on whether the pulse is moving in the forward or the backward direction. Far from the band edges ($|\delta| \gg \kappa$), optical pulse is unaffected by the grating and travels at the group velocity expected in the absence of the grating. However, as $|\delta|$ approaches κ, the group velocity decreases and becomes zero at the two edges of the stop band where $|\delta| = \kappa$. Thus, close to the photonic bandgap, an optical pulse experiences considerable

slowing down inside a fiber grating. As an example, its speed is reduced by 50% when $|\delta|/\kappa \approx 1.18$.

Second- and third-order dispersive properties of the grating are governed by β_2^g and β_3^g, respectively. Using Eq. (1.3.24) together with the dispersion relation, these parameters are given by

$$\beta_2^g = -\frac{\mathrm{sgn}(\delta)\kappa^2/v_g^2}{(\delta^2-\kappa^2)^{3/2}}, \qquad \beta_3^g = \frac{3|\delta|\kappa^2/v_g^3}{(\delta^2-\kappa^2)^{5/2}}. \tag{1.3.26}$$

The grating-induced GVD, governed by the parameter β_2^g, depends on the sign of detuning δ. The GVD is anomalous on the upper branch of the dispersion curve in Fig. 1.5, where δ is positive and the carrier frequency exceeds the Bragg frequency. In contrast, GVD becomes normal ($\beta_2^g > 0$) on the lower branch of the dispersion curve, where δ is negative and the carrier frequency is smaller than the Bragg frequency. Notice that the third-order dispersion remains positive on both branches of the dispersion curve. Also note that both β_2^g and β_3^g become infinitely large at the two edges of the stop band.

The dispersive properties of a fiber grating are quite different than those of a uniform fiber. First, β_2^g changes sign on the two sides of the stop band centered at the Bragg wavelength, whose location is easily controlled and can be in any region of the optical spectrum. This is in sharp contrast with β_2 for uniform fibers, which changes sign at the zero-dispersion wavelength that can be varied only in a range from 1.3 to 1.6 μm. Second, β_2^g is anomalous on the shorter wavelength side of the stop band whereas β_2 for fibers becomes anomalous for wavelengths longer than the zero-dispersion wavelength. Third, the magnitude of β_2^g exceeds that of β_2 by a large factor. Figure 1.6 shows how β_2^g varies with detuning δ for several values of κ. As seen there, $|\beta_2^g|$ can exceed 100 ps^2/cm for a fiber grating. This feature can be used for dispersion compensation in the transmission geometry [64]. Typically, a 10-cm-long grating can compensate the GVD acquired over fiber lengths of 50 km or more. Chirped gratings, discussed later in this chapter, can provide even more dispersion when the incident light is inside the stop band, although they reflect the dispersion-compensated signal [65].

1.3.4 Grating as an Optical Filter

What happens to optical pulses incident on a fiber grating depends very much on the location of the pulse spectrum with respect to the stop band associated

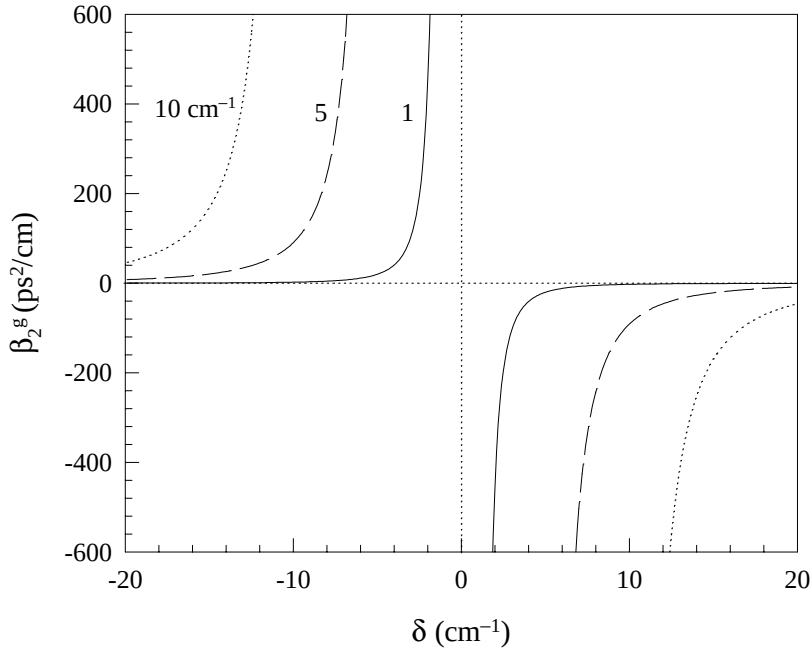

Figure 1.6 Grating-induced GVD plotted as a function of δ for several values of the coupling coefficient κ.

with the grating. If the pulse spectrum falls entirely within the stop band, the entire pulse is reflected by the grating. On the other hand, if a part of the pulse spectrum is outside the stop band, that part will be transmitted through the grating. The shape of the reflected and transmitted pulses will be quite different than that of the incident pulse because of the splitting of the spectrum and the dispersive properties of the fiber grating. If the peak power of pulses is small enough that nonlinear effects are negligible, we can first calculate the reflection and transmission coefficients for each spectral component. The shape of the transmitted and reflected pulses is then obtained by integrating over the spectrum of the incident pulse. Considerable distortion can occur when the pulse spectrum is either wider than the stop band or when it lies in the vicinity of a stop-band edge.

The reflection and transmission coefficients can be calculated by using Eqs. (1.3.20) and (1.3.21) with the appropriate boundary conditions. Consider a grating of length L and assume that light is incident only at the front end,

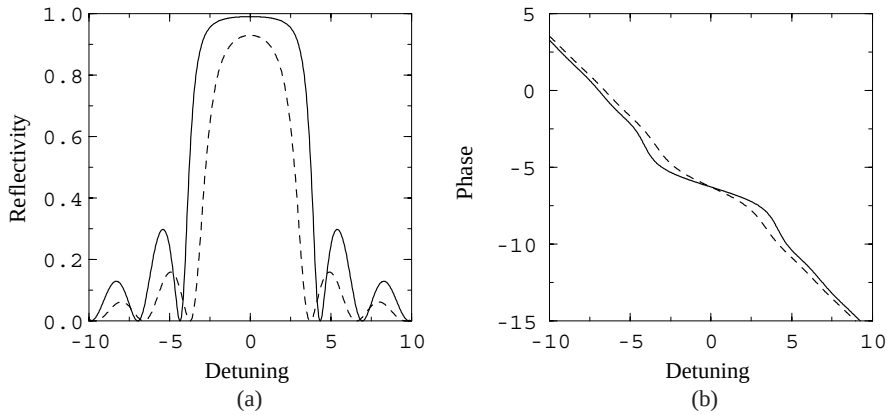

Figure 1.7 (a) The reflectivity $|r_g|^2$ and (b) the phase of r_g plotted as a function of detuning δ for two values of κL.

located at $z = 0$. The reflection coefficient is then given by

$$r_g = \frac{\tilde{A}_b(0)}{\tilde{A}_f(0)} = \frac{B_2 + r(q)A_1}{A_1 + r(q)B_2}. \tag{1.3.27}$$

If we use the boundary condition $\tilde{A}_b(L) = 0$ in Eq. (1.3.21),

$$B_2 = -r(q)A_1 \exp(2iqL). \tag{1.3.28}$$

Using this value of B_2 and $r(q)$ from Eq. (1.3.22) in Eq. (1.3.27), we obtain

$$r_g = \frac{i\kappa \sin(qL)}{q\cos(qL) - i\delta \sin(qL)}. \tag{1.3.29}$$

The transmission coefficient t_g can be obtained in a similar manner. The frequency dependence of r_g and t_g shows the filter characteristics associated with a fiber grating.

Figure 1.7 shows the reflectivity $|r_g|^2$ and the phase of r_g as a function of detuning δ for two values of κL. The grating reflectivity within the stop band approaches 100% for $\kappa L = 3$ or larger. Maximum reflectivity occurs at the center of the stop band and, by setting $\delta = 0$ in Eq. (1.3.29), is given by

$$R_{\max} = |r_g|^2 = \tanh^2(\kappa L). \tag{1.3.30}$$

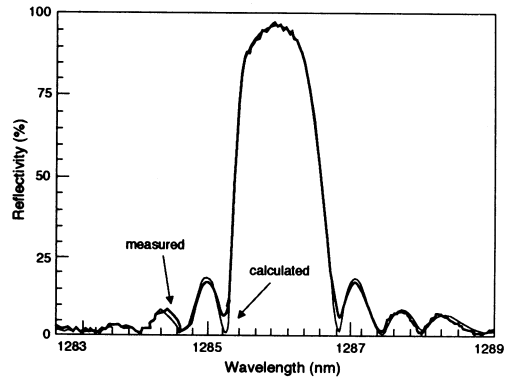

Figure 1.8 Measured and calculated reflectivity spectra for a fiber grating operating near 1.3 μm. (After Ref. [33])

For $\kappa L = 2$, $R_{\max} = 0.93$. The condition $\kappa L > 2$ with $\kappa = 2\pi\delta n_1/\lambda$ can be used to estimate the grating length required for high reflectivity inside the stop band. For $\delta n_1 \approx 10^{-4}$ and $\lambda = 1.55$ μm, L should exceed 5 mm to yield $\kappa L > 2$. These requirements are easily met in practice. Indeed, reflectivities in excess of 99% were achieved for a grating length of 1.5 cm [34].

1.3.5 Experimental Verification

The coupled-mode theory has been quite successful in explaining the observed features of fiber gratings. As an example, Figure 1.8 shows the measured reflectivity spectrum for a Bragg grating operating near 1.3 μm [33]. The fitted curve was calculated using Eq. (1.3.29). The 94% peak reflectivity indicates $\kappa L \approx 2$ for this grating. The stop band is about 1.7-nm wide. These measured values were used to deduce a grating length of 0.84 mm and an index change of 1.2×10^{-3}. The coupled-mode theory explains the observed reflection and transmission spectra of fiber gratings quite well.

An undesirable feature seen in Figs. 1.7 and 1.8 from a practical standpoint is the presence of multiple sidebands located on each side of the stop band. These sidebands originate from weak reflections occurring at the two grating ends where the refractive index changes suddenly compared to its value outside the grating region. Even though the change in refractive index is typically less than 1%, the reflections at the two grating ends form a Fabry–Perot cavity with its own wavelength-dependent transmission. An apodization technique is

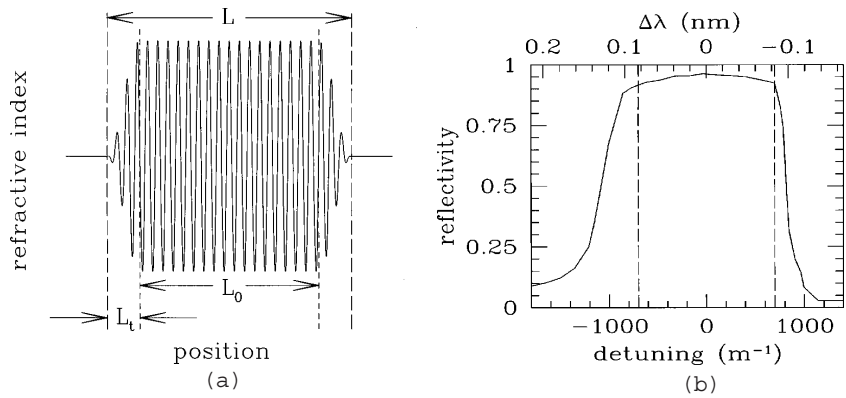

Figure 1.9 (a) Schematic variation of refractive index and (b) measured reflectivity spectrum for an apodized fiber grating. (After Ref. [66])

commonly used to remove the sidebands seen in Figs. 1.7 and 1.8 [49]. In this technique, the intensity of the ultraviolet laser beam used to form the grating is made nonuniform in such a way that the intensity drops to zero gradually near the two grating ends.

Figure 1.9(a) shows schematically the periodic index variation in an apodized fiber grating. In a transition region of width L_t near the grating ends, the value of the coupling coefficient κ increases from zero to its maximum value. These buffer zones can suppress the sidebands almost completely, resulting in fiber gratings with practically useful filter characteristics. Figure 1.9(b) shows the measured reflectivity spectrum for a 7.5-cm-long apodized fiber grating made by the scanning phase mask technique. The reflectivity exceeds 90% within the stop band, about 0.17-nm wide and centered at the Bragg wavelength of 1.053 μm, chosen to coincide with the wavelength of an Nd:YLF laser [66]. From the stop-band width, the coupling coefficient κ is estimated to be about 7 cm^{-1}. Note the sharp drop in reflectivity at both edges of the stop band and a complete absence of sidebands.

The same apodized fiber grating was used to investigate dispersive properties in the vicinity of a stop-band edge by transmitting 80-ps pulses (nearly Gaussian shape) through it [66]. Figure 1.10 shows the variation of the pulse width (a) and changes in the propagation delay during pulse transmission (b) as a function of the detuning δ from the Bragg wavelength on the upper branch of the dispersion curve. The most interesting feature is the increase in the arrival

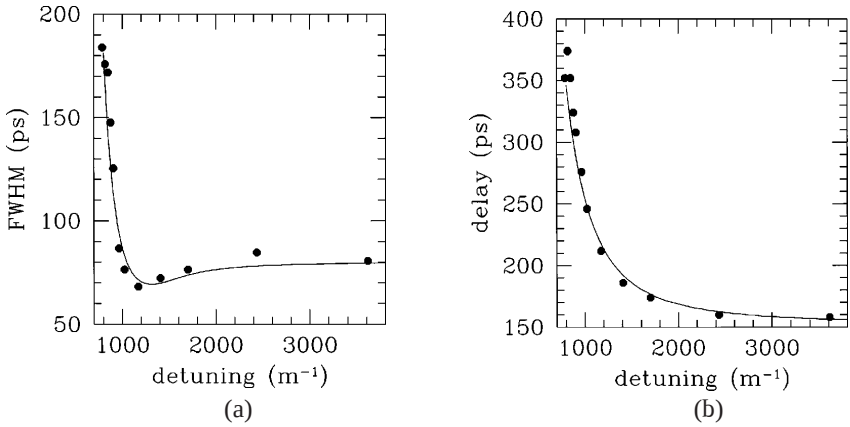

Figure 1.10 (a) Measured pulse width (FWHM) of 80-ps input pulses and (b) their arrival time as a function of detuning δ for an apodized 7.5-cm-long fiber grating. Solid lines show the prediction of the coupled-mode theory. (After Ref. [66])

time observed as the laser is tuned close to the stop-band edge because of the reduced group velocity. Doubling of the arrival time for δ close to 900 m^{-1} shows that the pulse speed was only 50% of that expected in the absence of the grating. This result is in complete agreement with the prediction of coupled-mode theory.

Changes in the pulse width seen in Figure 1.10 can be attributed mostly to the grating-induced GVD effects in Eq. (1.3.26). The large broadening observed near the stop-band edge is due to an increase in $|\beta_2^g|$. Slight compression near $\delta = 1200$ m^{-1} is due to a small amount of SPM that chirps the pulse. Indeed, it was necessary to include the γ term in Eqs. (1.3.11) and (1.3.12) to fit the experimental data. The nonlinear effects became quite significant at higher power levels. We turn to this issue next.

1.4 CW Nonlinear Effects

Wave propagation in a nonlinear, one-dimensional, periodic medium has been studied in several different contexts [67]–[87]. In the case of a fiber grating, the presence of an intensity-dependent term in Eq. (1.3.1) leads to SPM and XPM of counterpropagating waves. These nonlinear effects can be included by solving the nonlinear coupled-mode equations, Eqs. (1.3.11) and (1.3.12).

In this section, these equations are used to study the nonlinear effects for CW beams. The time-dependent effects are discussed in later sections.

1.4.1 Nonlinear Dispersion Curves

In almost all cases of practical interest, the β_2 term can be neglected in Eqs. (1.3.11) and (1.3.12). For typical grating lengths (< 1 m), the loss term can also be neglected by setting $\alpha = 0$. The nonlinear coupled-mode equations then take the following form:

$$i\frac{\partial A_f}{\partial z} + \frac{i}{v_g}\frac{\partial A_f}{\partial t} + \delta A_f + \kappa A_b + \gamma(|A_f|^2 + 2|A_b|^2)A_f = 0, \quad (1.4.1)$$

$$-i\frac{\partial A_b}{\partial z} + \frac{i}{v_g}\frac{\partial A_b}{\partial t} + \delta A_b + \kappa A_f + \gamma(|A_b|^2 + 2|A_f|^2)A_b = 0, \quad (1.4.2)$$

where v_g is the group velocity far from the stop band associated with the grating. These equations exhibit many interesting nonlinear effects. We begin by considering the CW solution of Eqs. (1.4.1) and (1.4.2) without imposing any boundary conditions. Even though this is unrealistic from a practical standpoint, the resulting dispersion curves provide considerable physical insight. Note that all grating-induced dispersive effects are included in these equations through the κ term.

To solve Eqs. (1.4.1) and (1.4.2) in the CW limit, we neglect the time-derivative term and assume the following form for the solution:

$$A_f = u_f \exp(iqz), \qquad A_b = u_b \exp(iqz), \quad (1.4.3)$$

where u_f and u_b are constant along the grating length. By introducing a parameter $f = u_b/u_f$ that describes how the total power $P_0 = u_f^2 + u_b^2$ is divided between the forward- and backward-propagating waves, u_f and u_b can be written as

$$u_f = \sqrt{\frac{P_0}{1+f^2}}, \qquad u_b = \sqrt{\frac{P_0}{1+f^2}}\, f. \quad (1.4.4)$$

The parameter f can be positive or negative. For values of $|f| > 1$, the backward wave dominates. By using Eqs. (1.4.1)–(1.4.4), both q and δ are found to depend on f and are given by

$$q = -\frac{\kappa(1-f^2)}{2f} - \frac{\gamma P_0}{2}\frac{1-f^2}{1+f^2}, \qquad \delta = -\frac{\kappa(1+f^2)}{2f} - \frac{3\gamma P_0}{2}. \quad (1.4.5)$$

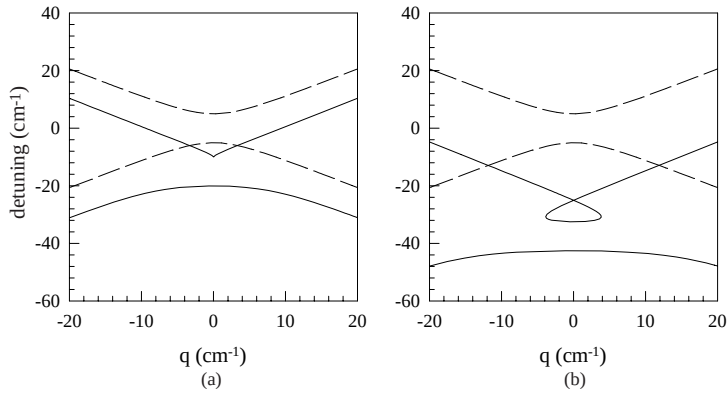

Figure 1.11 Nonlinear dispersion curves showing variation of δ with q for $\gamma P_0/\kappa = 2$ (a) and 5 (b) when $\kappa = 5\ \text{cm}^{-1}$. Dashed curves show the linear case ($\gamma = 0$).

To understand the physical meaning of Eq. (1.4.5), let us first consider the low-power case so that nonlinear effects are negligible. If we set $\gamma = 0$ in Eq. (1.4.5), it is easy to show that $q^2 = \delta^2 - \kappa^2$. This is precisely the dispersion relation (1.3.19) obtained previously. As f changes, q and δ trace the dispersion curves shown in Fig. 1.5. In fact, $f < 0$ on the upper branch while positive values of f belong to the lower branch. The two edges of the stop band occur at $f = \pm 1$. From a practical standpoint, the detuning δ of the CW beam from the Bragg frequency determines the value of f, which in turn fixes the values of q from Eq. (1.4.5). The group velocity inside the grating also depends on f and is given by

$$V_G = v_g \frac{d\delta}{dq} = v_g \left(\frac{1 - f^2}{1 + f^2} \right). \tag{1.4.6}$$

As expected, V_G becomes zero at the edges of the stop band corresponding to $f = \pm 1$. Note that V_G becomes negative for $|f| > 1$. This is not surprising if we note that the backward-propagating wave is more intense in that case. The speed of light is reduced considerably as the CW-beam frequency approaches an edge of the stop band. As an example, it reduces by 50% when f^2 equals 1/3 or 3.

Equation (1.4.5) can be used to find how the dispersion curves are affected by the fiber nonlinearity. Figure 1.11 shows such curves at two power levels. The nonlinear effects change the upper branch of the dispersion curve qualitatively, leading to the formation a loop beyond a critical power level. This

critical value of P_0 can be found by looking for the value of f at which q becomes zero while $|f| \neq 1$. From Eq. (1.4.5), we find that this can occur when

$$f \equiv f_c = -(\gamma P_0/2\kappa) + \sqrt{(\gamma P_0/2\kappa)^2 - 1}. \tag{1.4.7}$$

Thus, a loop is formed only on the upper branch where $f < 0$. Moreover, it can form only when the total power $P_0 > P_c$, where $P_c = 2\kappa/\gamma$. Physically, an increase in the mode index through the nonlinear term in Eq. (1.3.1) increases the Bragg wavelength and shifts the stop band toward lower frequencies. Since the amount of shift depends on the total power P_0, light at a frequency close to the edge of the upper branch can be shifted out of resonance with changes in its power. If the nonlinear parameter γ were negative (self-defocusing medium with $n_2 < 0$), the loop will form on the lower branch in Fig. 1.11, as is also evident from Eq. (1.4.7).

1.4.2 Optical Bistability

The simple CW solution given in Eq. (1.4.3) is modified considerably when boundary conditions are introduced at the two grating ends. For a finite-size grating, the simplest manifestation of the nonlinear effects occurs through optical bistability, first predicted in 1979 [67].

Consider a CW beam incident at one end of the grating and ask how the fiber nonlinearity would affect its transmission through the grating. It is clear that both the beam intensity and its wavelength with respect to the stop band will play an important role. Mathematically, we should solve Eqs. (1.4.1) and (1.4.2) after imposing the appropriate boundary conditions at $z = 0$ and $z = L$. These equations are quite similar to those occurring in Section A.6.3 and can be solved in terms of the elliptic functions by using the same technique used there [67]. The analytic solution is somewhat complicated and provides only an implicit relation for the transmitted power at $z = L$. We refer to Ref. [79] for details.

Figure 1.12 shows the transmitted versus incident power [both normalized to a critical power $P_{\rm cr} = 4/(3\gamma L)$] for several detuning values within the stop band by taking $\kappa L = 2$. The S-shaped curves are well known in the context of optical bistability occurring when a nonlinear medium is placed inside a cavity [88]. In fact, the middle branch of these curves with negative slope is unstable, and the transmitted power exhibits bistability with hysteresis, as shown by the arrows on the solid curve. At low powers, transmittivity is small,

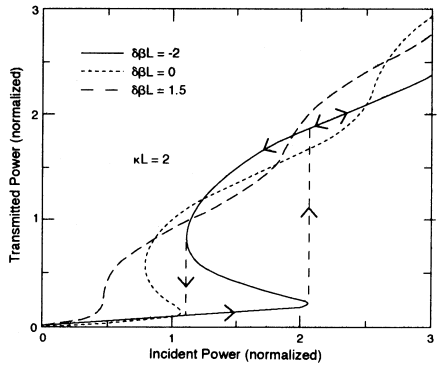

Figure 1.12 Transmitted versus incident power for three values of detuning within the stop band. (After Ref. [67], ©American Institute of Physics)

as expected from the linear theory since the nonlinear effects are relatively weak. However, above a certain input power, most of the incident power is transmitted. Switching from a low-to-high transmission state can be understood qualitatively by noting that the effective detuning δ in Eqs. (1.4.1) and (1.4.2) becomes power dependent because of the nonlinear contribution to the refractive index in Eq. (1.3.1). Thus, light that is mostly reflected at low powers because its wavelength is inside the stop band may tune itself out of the stop band and get transmitted when the nonlinear index change becomes large enough. In a sense, the situation is similar to that discussed in Section A.10.3, where SPM helped to satisfy the phase-matching condition associated with four-wave mixing.

The observation of optical bistability in fiber gratings is hampered by the large switching power required ($P_0 > P_{\rm cr} > 1$ kW). It turns out that the switching power can be reduced by a factor of 100 or more by introducing a $\pi/2$ phase shift in the middle of the fiber grating. Such gratings are called $\lambda/4$-shifted or phase-shifted gratings since a distance of $\lambda/4$ (half grating period) corresponds to a $\pi/2$ phase shift. They are used routinely for making distributed-feedback (DFB) semiconductor lasers [62]. Their use for fiber gratings was suggested in 1994 [89]. The $\pi/2$ phase shift opens a narrow transmission window within the stop band of the grating. Figure 1.13(a) compares the transmission spectra for the uniform and phase-shifted gratings at low powers. At high powers, the central peak bends toward left, as seen in the traces in Fig. 1.13(b). It is this bending that leads to low-threshold optical switching

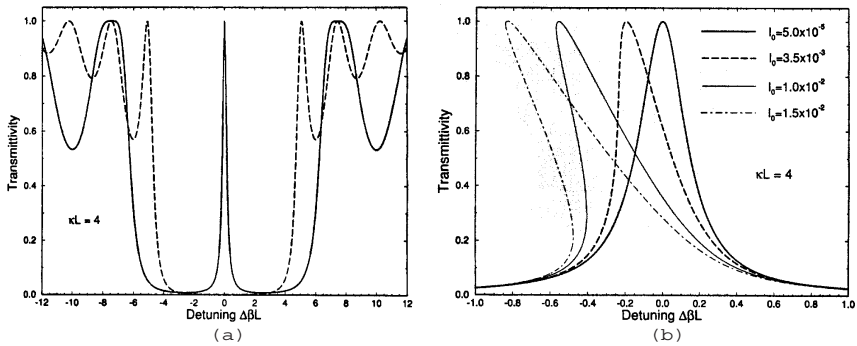

Figure 1.13 (a) Transmission spectrum of a fiber grating with (solid curve) and without (dashed curve) $\pi/2$ phase shift. (b) Bending of the central transmission peak with increasing power (normalized to the critical power). (After Ref. [82])

in phase-shifted fiber gratings [82]. The elliptic-function solution of uniform gratings can be used to construct the multivalued solution for a $\lambda/4$-shifted grating [83]. It turns out that the presence of a phase-shifted region lowers the switching power considerably.

The bistable switching does not always lead to a constant output power when a CW beam is transmitted through a grating. As early as 1982, numerical solutions of Eqs. (1.4.1) and (1.4.2) showed that transmitted power can become not only periodic but also chaotic under certain conditions [68]. In physical terms, portions of the upper branch in Fig. 1.12 may become unstable. As a result, the output becomes periodic or chaotic once the beam intensity exceeds the switching threshold. This behavior has been observed experimentally and is discussed in Section 1.6. In Section 1.5, we turn to another instability that occurs even when the CW beam is tuned outside the stop band and does not exhibit optical bistability.

1.5 Modulation Instability

The stability issue is of paramount importance and must be addressed for the CW solutions obtained in the previous section. Similar to the analysis of Section A.5.1, modulation instability can destabilize the steady-state solution and produce periodic output even when a CW beam is incident on one end of the fiber grating [90]–[95]. Moreover, the repetition rate of pulse trains generated

through modulation instability can be tuned over a large range because of large GVD changes occurring with the detuning δ.

1.5.1 Linear Stability Analysis

For simplicity, we discuss modulation instability using the CW solution given by Eqs. (1.4.3) and (1.4.4) and obtained without imposing the boundary conditions at the grating ends. Following the analysis of Section A.5.1, we perturb the steady state slightly as

$$A_j = (u_j + a_j)\exp(iqz), \quad (j = f, b), \tag{1.5.1}$$

and linearize Eqs. (1.4.1) and (1.4.2) assuming that the perturbation a_j is small. The resulting equations are [95]

$$\begin{aligned} i\frac{\partial a_f}{\partial z} + \frac{i}{v_g}\frac{\partial a_f}{\partial t} &+ \kappa a_b - \kappa f a_f \\ &+ \Gamma[(a_f + a_f^*) + 2f(a_b + a_b^*)] = 0, \end{aligned} \tag{1.5.2}$$

$$\begin{aligned} -i\frac{\partial a_b}{\partial z} + \frac{i}{v_g}\frac{\partial a_b}{\partial t} &+ \kappa a_f - \frac{\kappa}{f} a_b \\ &+ \Gamma[2f(a_f + a_f^*) + f^2(a_b + a_b^*)] = 0, \end{aligned} \tag{1.5.3}$$

where $\Gamma = \gamma P_0/(1+f^2)$ is an effective nonlinear parameter.

This set of two linear coupled equations can be solved assuming a plane-wave solution of the form

$$a_j = c_j \exp[i(Kz - \Omega t)] + d_j \exp[-i(Kz + \Omega t)], \tag{1.5.4}$$

where the subscript $j = f$ or b. Similar to the case discussed in Section A.6.4, we obtain a set of four homogeneous equations satisfied by c_j and d_j. This set has a nontrivial solution only when the 4×4 determinant formed by the coefficients matrix vanishes. This condition leads to the the following fourth-order polynomial:

$$\begin{aligned} (s^2 - K^2)^2 - 2\kappa^2(s^2 - K^2) - \kappa^2 f^2 (s+K)^2 \\ - \kappa^2 f^{-2}(s-K)^2 - 4\kappa\Gamma f(s^2 - 3K^2) = 0, \end{aligned} \tag{1.5.5}$$

where we have introduced a spatial frequency as $s = \Omega/v_g$.

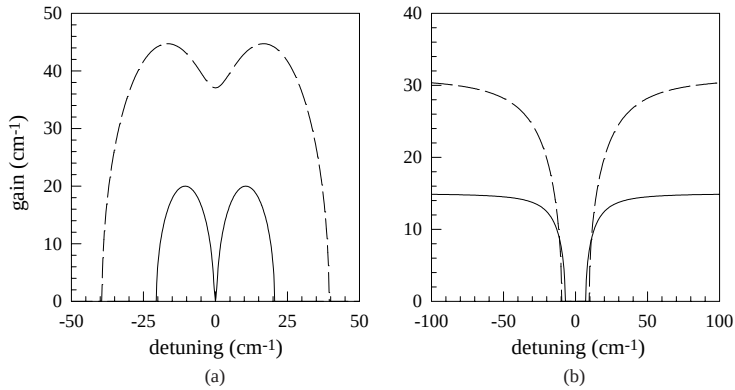

Figure 1.14 Gain spectra of modulation instability in the (a) anomalous- and (b) normal-GVD regions of a fiber grating ($f = \pm 0.5$) at two power levels corresponding to Γ/κ = 0.5 and 2.

The four roots of the polynomial in Eq. (1.5.5) determine the stability of the CW solution. However, a tricky issue must be first resolved. Equation (1.5.5) is a fourth-order polynomial in both s and K. The question is, which one determines the gain associated with modulation instability? In the case of the uniform-index fibers discussed in Section A.5.1, the gain g was related to the imaginary part of K since light was propagating in the forward direction. In a fiber grating, light travels both forward and backward simultaneously, and it is the time that moves forward for both of them. As a result, Eq. (1.5.5) should be viewed as a fourth-order polynomial in s whose roots depend on K. The gain of modulation instability is obtained using $g = 2\,\mathrm{Im}(s_m)$, where s_m is the root with the largest imaginary part.

The root analysis of the above polynomial leads to several interesting conclusions [95]. Figure 1.14 shows the gain spectra of modulation instability in the anomalous- and normal-GVD regions, corresponding to upper and lower branches of the dispersion curves, for two values of Γ/κ. In the anomalous-GVD case and at relatively low powers ($\Gamma < \kappa$), the gain spectrum is similar to that found for uniform-index fibers. As shown later in this section, the nonlinear coupled-mode equations reduce to a nonlinear Schrödinger (NLS) equation when $\Gamma \ll \kappa$. At high values of P_0 such that $\Gamma > \kappa$, the gain exists even at $s = 0$, as seen in Fig. 1.14(a) for $\Gamma/\kappa = 2$. Thus, the CW solution becomes unstable even to zero-frequency (dc) fluctuations at high power levels.

Modulation instability can occur even on the lower branch of the dispersion

curve ($f > 0$) where grating-induced GVD is normal. The instability occurs only when P_0 exceeds a certain value such that

$$P_0 > \tfrac{1}{2}\kappa(1+f^2)^2 f^p, \tag{1.5.6}$$

where $p = 1$ if $f \leq 1$ but $p = -3$ when $f > 1$. The occurrence of modulation instability in the normal-GVD region is solely a grating-induced feature.

The preceding analysis completely ignores boundary conditions. For a finite-length grating, one should examine the stability of the CW solution obtained in terms of the elliptic functions. Such a study is complicated and requires a numerical solution to the nonlinear coupled-mode equations [91]. The results show that portions of the upper branch of the bistability curves in Fig. 1.12 can become unstable, resulting in the formation of a pulse train through modulation instability. The resulting pulse train is not necessarily periodic and, under certain conditions, can exhibit period doubling and optical chaos.

1.5.2 Effective NLS Equation

The similarity of the gain spectrum in Fig. 1.14 with that occurring in uniform-index fibers (see Section A.5.1) indicates that, at not-too-high power levels, the nonlinear coupled-mode equations predict features that coincide with those found for the NLS equation. Indeed, under certain conditions, Eqs. (1.4.3) and (1.4.4) can be reduced formally to an effective NLS equation [96]–[100]. A multiple-scale method is commonly used to prove this equivalence; details can be found in Ref. [79].

The analysis used to reduce the nonlinear coupled-mode equations to an effective NLS equation makes use of the Bloch formalism well known in solid-state physics. Even in the absence of nonlinear effects, the eigenfunctions associated with the photonic bands, corresponding to the dispersion relation $q^2 = \delta^2 - \kappa^2$, are not A_f and A_b but the Bloch waves formed by a linear combination of A_f and A_b. If this basis is used for the nonlinear problem, Eqs. (1.4.3) and (1.4.4) reduce to an effective NLS equation provided two conditions are met. First, the peak intensity of the pulse is small enough that the nonlinear index change $n_2 I_0$ in Eq. (1.3.1) is much smaller than the maximum value of δn_g. This condition is equivalent to requiring that $\gamma P_0 \ll \kappa$ or $\kappa L_{\rm NL} \gg 1$, where $L_{\rm NL} = (\gamma P_0)^{-1}$ is the nonlinear length. This requirement is easy to satisfy in practice even at peak intensity levels as high as 100 GW/cm^2. Second, the third-order dispersion β_3^g induced by the grating should be negligible.

When the above two conditions are satisfied, pulse propagation in a fiber grating is governed by the following NLS equation [95]:

$$\frac{i}{v_g}\frac{\partial U}{\partial t} - \frac{(1-v^2)^{3/2}}{2\kappa\,\mathrm{sgn}(f)}\frac{\partial^2 U}{\partial \zeta^2} + \frac{1}{2}(3-v^2)\gamma|U|^2U, \tag{1.5.7}$$

where $\zeta = z - V_G t$. We have introduced a speed-reduction factor related to the parameter f through Eq. (1.4.6) as

$$v = \frac{V_G}{v_g} = \frac{1-f^2}{1+f^2} = \pm\sqrt{1-\kappa^2/\delta^2}. \tag{1.5.8}$$

The group velocity decreases by the factor v close to an edge of the stop band and vanishes at the two edges ($v = 0$) corresponding to $f = \pm 1$. The reason the first term is a time derivative, rather than the z derivative, was discussed earlier. It can also be understood from a physical standpoint if we note that the variable U does not correspond to the amplitude of the forward- or backward-propagating wave but represents the amplitude of the envelope associated with the Bloch wave formed by a superposition of A_f and A_b.

Equation (1.5.8) has been written for the case in which the contribution of A_f dominates ($|f| < 1$) so that the entire Bloch-wave envelope is propagating forward at the reduced group velocity V_G. With this in mind, we introduce $z = V_G t$ as the distance traveled by the envelope and account for changes in its shape through a local time variable defined as $T = t - z/V_G$. Equation (1.5.8) can then be written in the standard form used in Chapter A.5 as

$$i\frac{\partial U}{\partial z} - \frac{\beta_2^g}{2}\frac{\partial^2 U}{\partial T^2} + \gamma_g|U|^2U = 0, \tag{1.5.9}$$

where the effective GVD parameter β_2^g and the nonlinear parameter γ_g are defined as

$$\beta_2^g = \frac{(1-v^2)^{3/2}}{\mathrm{sgn}(f)v_g^2\kappa v^3}, \qquad \gamma_g = \left(\frac{3-v^2}{2v}\right)\gamma. \tag{1.5.10}$$

Using Eq. (1.5.8), the GVD parameter β_2^g can be shown to be the same as in Eq. (1.3.26).

Several features of Eq. (1.5.9) are noteworthy when this equation is compared with the standard NLS equations. First, the variable U represents the amplitude of the envelope associated with the Bloch wave formed by a superposition of A_f and A_b. Second, the parameters β_2^g and γ_g are not constants but

depend on the speed-reduction factor v. Both increase as v decreases and become infinite at the edges of the stop band where $v = 0$. Clearly, Eq. (1.5.9) is not valid at that point. However, it remains valid close to but outside the stop band. Far from the stop band ($v \to 1$), β_2^g becomes quite small (< 1 ps^2/km for typical values of κ). One should then include fiber GVD and replace β_2^g by β_2. Noting that $\gamma_g = \gamma$ when $v = 1$, Eq. (1.5.9) reduces to the standard NLS equation, and U corresponds to the forward-wave amplitude since no backward wave is generated under such conditions.

Before we can use Eq. (1.5.9) for predicting the modulation-instability gain and the frequency at which the gain peaks, we need to know the total power P_0 inside the grating when a CW beam with power P_{in} is incident at the input end of the grating located at $z = 0$. This is a complicated issue for apodized fiber gratings because κ is not constant in the transition or buffer zone. However, observing that the nonlinear coupled-mode equations require $|A_f^2| - |A_b^2|$ to remain constant along the grating, one finds that the total power P_0 inside the grating is enhanced by a factor $1/v$ [101]. The predictions of Eq. (1.5.9) are in agreement with the modulation-instability analysis based on the nonlinear coupled-mode equations as long as $\gamma P_0 \ll \kappa$ [95]. The NLS equation provides a shortcut to understanding the temporal dynamics in gratings within its regime of validity.

1.5.3 Experimental Results

Modulation instability implies that an intense CW beam should get converted into a pulse train if it passes through a fiber grating. The experimental observation of this phenomenon is difficult when a CW beam is used since the required input power is too large to be realistic. For this reason, experiments often use short optical pulses whose width is chosen to be much larger than the modulation period. In a 1996 experiment, 100-ps pulses—obtained from a Q-switched, mode-locked Nd:YLF laser operating close to 1.053 μm—were used and it was found that each pulse was transformed into two shorter pulses at the grating output [94]. The grating was only 3.5-cm long in this experiment and did not allow substantial growth of modulation instability.

In a 1998 experiment, a 6-cm-long fiber grating was used with a value of $\kappa = 12$ cm^{-1} [101]. Figure 1.15 shows transmitted pulse shapes when 100-ps pulses were propagated through this grating. The peak intensity of the input Gaussian pulse is 25 GW/cm^2. Its central frequency is tuned close to but outside the stop band such that the grating provides anomalous GVD (upper

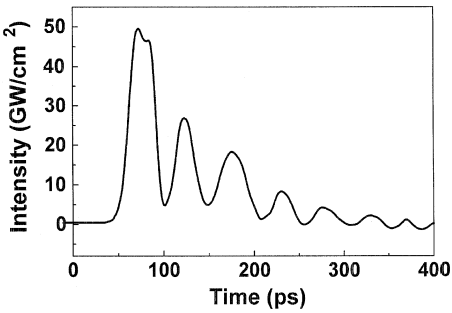

Figure 1.15 Transmitted pulse shape when 100-ps pulses with a peak intensity of 25 GW/cm^2 are propagated through a 6-cm-long fiber grating. (After Ref. [101], ©1998, reprinted with permission from Elsevier Science)

branch of the dispersion curve). At lower power levels, pulse is compressed because of the combination of GVD and SPM that leads to soliton-effect compression (discussed in Chapter 6). At the 25 GW/cm^2 power level, the transmitted pulse exhibits a multipeak structure that can be interpreted as a pulse train generated through modulation instability. This interpretation is supported by the observation that the repetition rate (spacing between two neighboring pulses) changes with the laser wavelength (equivalent to changing the detuning parameter δ), as expected from the theory of modulation instability.

1.6 Nonlinear Pulse Propagation

As discussed in Chapter A.5, modulation instability often indicates the possibility of soliton formation. In the case of Bragg gratings, it is closely related to a new kind of solitons referred to as *Bragg solitons* or *grating solitons*. Such solitons were first discovered in 1987 in the context of periodic structures known as superlattices [70] and were called *gap solitons* since they existed only inside the stop band. Later, a much larger class of Bragg solitons was identified by solving Eqs. (1.4.1) and (1.4.2) analytically [102]–[104].

The advent of fiber gratings provided an incentive during the 1990s for studying propagation of short optical pulses in such gratings [105]–[115]. The peak intensities required to observe the nonlinear effects are quite high (typically > 10 GW/cm^2) for Bragg gratings made in silica fibers because of a short interaction length (typically < 10 cm) and a low value of the nonlinear param-

eter n_2. The use of chalcogenide glass fibers for making gratings can reduce required peak intensities by a factor of 100 or more because the high values of n_2 in such glasses [116].

1.6.1 Bragg Solitons

It was realized in 1989 that the coupled-mode equations, Eqs. (1.4.1) and (1.4.2), become identical to the well-known massive Thirring model [117] if the SPM term is set to zero. The massive Thirring model of quantum field theory is known to be integrable by the inverse scattering method [118]–[120]. When the SPM term is included, the coupled-mode equations become non-integrable, and solitons do not exist in a strict mathematical sense. However, shape-preserving solitary waves can be obtained through a suitable transformation of the soliton supported by the massive Thirring model. These solitary waves correspond to the following solution [103]:

$$A_f(z,t) = a_+ \operatorname{sech}(\zeta - i\psi/2)e^{i\theta}, \tag{1.6.1}$$

$$A_b(z,t) = a_- \operatorname{sech}(\zeta + i\psi/2)e^{i\theta}, \tag{1.6.2}$$

where

$$a_\pm = \pm\left(\frac{1\pm v}{1\mp v}\right)^{1/4}\sqrt{\frac{\kappa(1-v^2)}{\gamma(3-v^2)}}\sin\psi, \quad \zeta = \frac{z-V_G t}{\sqrt{1-v^2}}\,\kappa\sin\psi, \tag{1.6.3}$$

$$\theta = \frac{v(z-V_G t)}{\sqrt{1-v^2}}\,\kappa\cos\psi - \frac{4v}{3-v^2}\tan^{-1}[|\cot(\psi/2)|\coth(\zeta)]. \tag{1.6.4}$$

This solution represents a two-parameter family of Bragg solitons. The parameter v is in the range $-1 < v < 1$ and the parameter ψ can be chosen anywhere in the range $0 < \psi < \pi$. The specific case $\psi = \pi/2$ corresponds to the center of the stop band [102]. Physically, Bragg solitons represent specific combinations of counterpropagating waves that pair in such a way that they move at the same but reduced speed ($V_G = v v_g$). Since v can be negative, the soliton can move forward or backward. The soliton width T_s is also related to the parameters v and ψ and is given by

$$T_s = \sqrt{1-v^2}/(\kappa V_G \sin\psi). \tag{1.6.5}$$

One can understand the reduced speed of a Bragg soliton by noting that the counterpropagating waves form a single entity that moves at a common speed.

The relative amplitudes of the two waves participating in soliton formation determine the soliton speed. If A_f dominates, the soliton moves in the forward direction but at a reduced speed. The opposite happens when A_b is larger. In the case of equal amplitudes, the soliton does not move at all since V_G becomes zero. This case corresponds to the stationary gap solitons predicted in the context of superlattices [70]. In the opposite limit in which $|v| \to 1$, Bragg solitons cease to exist since the grating becomes ineffective.

Another family of solitary waves is obtained by looking for the shape-preserving solutions of the nonlinear coupled-mode equations [104]. Such solitary waves exist both inside and outside the stop band. They reduce to the Bragg solitons described by Eqs. (1.6.2)–(1.6.4) in some specific limits. On the lower branch of the dispersion curve where the GVD is normal, solitary waves represent dark solitons, similar to those discussed in Section A.5.3.

1.6.2 Relation to NLS Solitons

As discussed earlier, the nonlinear coupled-mode equations reduce to the NLS equation when $\gamma P_0 \ll \kappa$, where P_0 is the peak power of the pulse propagating inside the grating. Since the NLS equation is integrable by the inverse scattering method, the fundamental and higher-order solitons found in Section A.5.2 should also exist for a fiber grating. The question then becomes how they are related to the Bragg soliton described by Eqs. (1.6.1) and (1.6.2).

To answer this question, we write the NLS equation (1.5.9) using soliton units in its standard form

$$i\frac{\partial u}{\partial \xi} + \frac{1}{2}\frac{\partial^2 u}{\partial \tau^2} + |u|^2 u = 0, \tag{1.6.6}$$

where $\xi = z/L_D$, $\tau = T/T_0$, $u = \sqrt{\gamma_g L_D}$, and $L_D = T_0^2/|\beta_2^g|$ is the dispersion length. The fundamental soliton of this equation, in its most general form, is given by (see Section A.5.2)

$$u(\xi,\tau) = \eta\,\mathrm{sech}[\eta(\tau - \tau_s + \varepsilon\xi)]\exp[i(\eta^2 - \varepsilon^2)\xi/2 - i\varepsilon\tau + i\phi_s], \tag{1.6.7}$$

where η, ε, τ_s, and ϕ_s are four arbitrary parameters representing amplitude, frequency, position, and phase of the soliton, respectively. The soliton width is related inversely to the amplitude as $T_s = T_0/\eta$. The physical origin of such solitons is the same as that for conventional solitons except that the GVD is provided by the grating rather than by material dispersion.

At first sight, Eq. (1.6.7) looks quite different than the Bragg soliton described by Eqs. (1.6.2)–(1.6.4). However, one should remember that u represents the amplitude of the Bloch wave formed by superimposing A_f and A_b. If the total optical field is considered and the low-power limit ($\gamma P_0 \ll \kappa$) is taken, the Bragg soliton indeed reduces to the fundamental NLS soliton [79]. The massive Thirring model also allows for higher-order solitons [121]. One would expect them to be related to higher-order NLS solitons in the appropriate limit. It has been shown that any solution of the NLS equation (1.5.9) can be used to construct an approximate solution of the coupled-mode equations [100].

The observation that Bragg solitons are governed by an effective NLS equation in the limit $\kappa L_{\rm NL} \gg 1$, where $L_{\rm NL}$ is the nonlinear length, allows us to use the concept of soliton order N and the soliton period z_0 developed in Chapter A.5. These parameters are defined as

$$N^2 = \frac{L_D}{L_{\rm NL}} \equiv \frac{\gamma_g P_0 T_0^2}{|\beta_2^g|}, \qquad z_0 = \frac{\pi}{2} L_D \equiv \frac{\pi}{2} \frac{T_0^2}{|\beta_2^g|}. \tag{1.6.8}$$

We need to interpret the meaning of the soliton peak power P_0 carefully since the NLS soliton represents the amplitude of the Bloch wave formed by a combination of A_f and A_b. This aspect is discussed later in this section.

An interesting issue is related to the collision of Bragg solitons. Since Bragg solitons described by Eqs. (1.6.1) and (1.6.2) are only solitary waves (because of the nonintegrablity of the underlying nonlinear coupled-mode equations), they may not survive collisions. On the other hand, the NLS solitons are guaranteed to remain unaffected by their mutual collisions. Numerical simulations based on Eqs. (1.4.1) and (1.4.2) show that Bragg solitons indeed exhibit features reminiscent of a NLS soliton in the low-power limit $\gamma P_0 \ll \kappa$ [113]. More specifically, two Bragg solitons attract or repel each other depending on their relative phase. The new feature is that the relative phase depends on the initial separation between the two solitons.

1.6.3 Formation of Bragg Solitons

Formation of Bragg solitons in fiber gratings was first observed in a 1996 experiment [105]. Since then, more careful experiments have been performed, and many features of Bragg solitons have been extracted. While comparing the experimental results with the coupled-mode theory, one needs to implement the boundary conditions properly. For example, the peak power P_0 of the

Bragg soliton formed inside the grating when a pulse is launched is not the same as the input peak power P_{in}. The reason can be understood by noting that the group velocity of the pulse changes as the input pulse crosses the front end of the grating located at $z = 0$. As a result, pulse length given by $v_g T_0$ just outside the grating changes to $V_G T_0$ on crossing the interface located at $z = 0$ [58], and the pulse peak power is enhanced by the ratio v_g/V_G. Mathematically, one can use the coupled-mode equations to show that $P_0 = |A_f^2| + |A_b^2| = P_{\text{in}}/v$, where $v = V_G/v_g$ is the speed-reduction factor introduced earlier. The argument becomes more complicated for apodized fiber gratings, used often in practice, because κ is not constant in the transition region [110]. However, the same power enhancement occurs at the end of the transition region.

From a practical standpoint, one needs to know the amount of peak power P_{in} required to excite the fundamental Bragg soliton. The soliton period z_0 is another important parameter relevant for soliton formation since it sets the length scale over which optical solitons evolve. We can use Eq. (1.6.8) with $N = 1$ to estimate both of them. Using the expressions for β_2^g and γ_g from Eq. (1.5.10), the input peak power and the soliton period are given by

$$P_{\text{in}} = \frac{2(1-v^2)^{3/2}}{v(3-v^2)v_g^2 T_0^2 \kappa \gamma}, \qquad z_0 = \frac{\pi v^3 v_g^2 T_0^2 \kappa}{2(1-v^2)^{3/2}}, \tag{1.6.9}$$

where T_0 is related to the FWHM as $T_{\text{FWHM}} \approx 1.76\,T_0$. Both P_{in} and z_0 depend through v on detuning of the laser wavelength from the edge of the stop band located at $\delta = \kappa$. As $v \to 0$ near the edge, P_{in} becomes infinitely large while z_0 tends toward zero.

Bragg solitons have been formed in a 7.5-cm-long apodized fiber grating by using 80-ps pulses obtained from a Q-switched, mode-locked Nd:YLF laser operating at 1053 nm [66]. Figure 1.16 shows pulse shapes at the output end of the grating when input pulses having a peak intensity of 11 GW/cm^2 are used. The coupling coefficient κ was estimated to be 7 cm^{-1} for this grating while the detuning parameter δ was varied over the range from 7 to 36 cm^{-1} on the blue side of the stop band (anomalous GVD). The arrival time of the pulse depends on δ because of the reduction in group velocity as δ is reduced and tuned closer to the stop-band edge. This delay occurs even when nonlinear effects are negligible as shown in Fig. 1.10, which was obtained under identical operating conditions but at a much lower value of the peak intensity.

At the high peak intensities used for Fig. 1.16, SPM in combination with the grating-induced anomalous GVD leads to formation of Bragg solitons.

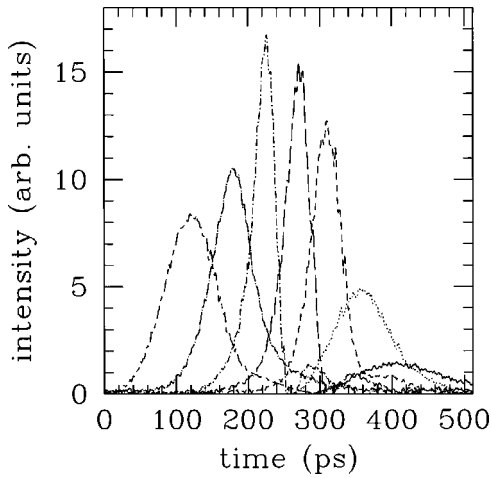

Figure 1.16 Output pulse shapes for different δ when 80-ps pulses with a peak intensity of 11 GW/cm^2 are propagated through a 7.5-cm-long fiber grating. Values of δ from left to right are 3612, 1406, 1053, 935, 847, 788, and 729 m^{-1}. (After Ref. [66])

However, since both β_2^g and γ_g depend on the detuning parameter δ through v, a Bragg soliton can form only in a limited range of δ. With this in mind, we can understand the pulse shapes seen in Fig. 1.16. Detuning is so large and β_2^g is so small for the leftmost trace that the pulse acquires some chirping through SPM but its shape remains nearly unchanged. This feature can also be understood from Eq. (1.6.9), where the soliton period becomes so long as $v \to 1$ that nothing much happens to the pulse over a few-cm-long grating. As δ is reduced, the pulse narrows down considerably. A reduction in pulse width by a factor of 3 occurs for $\delta = 1053$ m^{-1} in Fig. 1.16. This pulse narrowing is an indication that a Bragg soliton is beginning to form. However, the soliton period is still much longer than the grating length. In other words, the grating is not long enough to observe the final steady-state shape of the Bragg soliton. Finally, as the edge of the stop band is approached and δ becomes comparable to κ (rightmost solid trace), the GVD becomes so large that the pulse cannot form a soliton and becomes broader than the input pulse. This behavior is also deduced from Eq. (1.6.8), which shows that both N and z_0 tend toward zero as β_2^g tends toward infinity. A Bragg soliton can form only if $N > \frac{1}{2}$. Since the dispersion length becomes smaller than the grating length close to the stop-band edge, pulse can experience considerable broadening. This is precisely

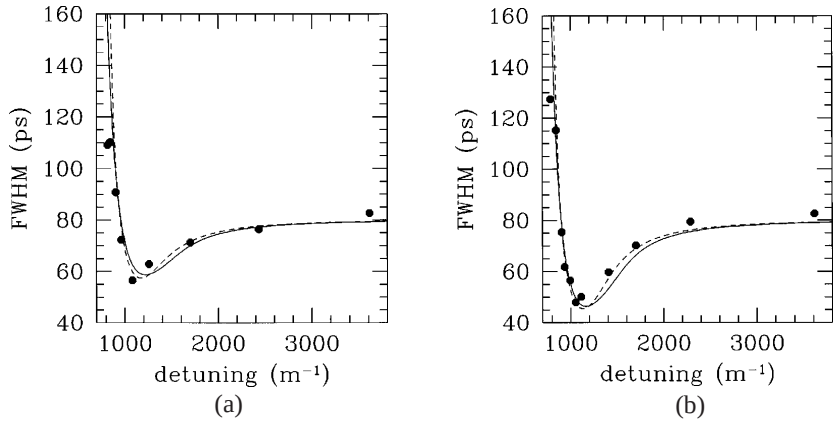

Figure 1.17 Measured pulse widths (circles) as a function of detuning for 80-ps pulses with a peak intensity of (a) 3 GW/cm^2 and (b) 6 GW/cm^2. Predictions of the coupled-mode theory (solid line) and the effective NLS equation (dashed line) are shown for comparison. (After Ref. [66])

what is observed for the smallest value of δ in Fig. 1.16 (solid curve).

A similar behavior was observed over a large range of pulse energies, with some evidence of the second-order soliton for input peak intensities in excess of 20 GW/cm^2 [66]. A careful comparison of the experimental data with the theory based on the nonlinear coupled-mode equations and the effective NLS equation showed that the NLS equation provides an accurate description within its regime of validity. Figure 1.17 compares the measured values of the pulse width with the two theoretical models for peak intensities of 3 and 6 GW/cm^2. The NLS equation is valid as long as $\kappa L_{\rm NL} \gg 1$. Using $\kappa = 7$ cm^{-1}, we estimate that the peak intensity can be as high as 50 GW/cm^2 for the NLS equation to remain valid. This is also what was found in Ref. [66].

Gap solitons that form within the stop band of a fiber grating have not been observed because of a practical difficulty: A Bragg grating reflects light whose wavelength falls inside the stop band. Stimulated Raman scattering may provide a solution to this problem since a pump pulse, launched at a wavelength far from the stop band, can excite a "Raman gap soliton" that is trapped within the grating and propagates much more slowly than the pump pulse itself [115]. The energy of such a gap soliton leaks slowly from the grating ends, but it can survive for durations greater than 10 ns even though it is excited by pump pulses of duration 100 ps or so.

1.6.4 Nonlinear Switching

As discussed in Section 1.4.2, a fiber grating can exhibit bistable switching even when a CW beam is incident on it. However, optical pulses should be used in practice because of the high intensities required for observing SPM-induced nonlinear switching. Even then, one needs peak-intensity values in excess of 10 GW/cm^2. For this reason, bistable switching was first observed during the 1980s using DFB semiconductor amplifiers for which large carrier-induced nonlinearities reduce the switching threshold to power levels below 1 mW [122]–[124]. Nonlinear switching in a passive grating was observed in a 1992 experiment using a semiconductor waveguide grating [76]. The nonlinear response of such gratings is not governed by the Kerr-type nonlinearity seen in Eq. (1.3.1) because of the presence of free carriers (electrons and holes) whose finite lifetime limits the nonlinear response time.

Nonlinear switching in a fiber Bragg grating was observed in 1998 in the 1.55-μm wavelength region useful for fiber-optic communications [109]. An 8-cm-long grating, with its Bragg wavelength centered near 1536 nm, was used in the experiment. It had a peak reflectivity of 98% and its stop band was only 4-GHz wide. The 3-ns input pulses were obtained by amplifying the output of a pulsed DFB semiconductor laser to power levels as high as 100 kW. Their shape was highly asymmetric because of gain saturation occurring inside the amplifier chain. The laser wavelength was inside the stop band on the short-wavelength side but was set very close to the edge (offset of about 7 pm or 0.9 GHz).

Figure 1.18(a) shows a sharp rise in the transmittivity from a few percent to 40% when the peak power of input pulses increases beyond 2 kW. Physically, the nonlinear increase in the refractive index at high powers shifts the Bragg wavelength far enough that the pulse finds itself outside the stop band and switches to the upper branch of the bistability curves seen in Fig. 1.12. The pulse shapes seen in Fig. 1.18(b) show what happens to the transmitted pulse. The initial spike near $t = 0$ in these traces is due to a sharp leading edge of the asymmetric input pulse and should be ignored. Multiple pulses form at the grating output whose number depends on the input power level. At a power level of 3 kW, a single pulse is seen but the number increases to five at a power level of 8 kW. The pulse width is smallest (about 100 ps) near the leading edge of the pulse train but increases substantially for pulses near the trailing edge.

Several conclusions can be drawn from these results. First, the upper bistability branch in Fig. 1.12 is not stable and converts the quasi-CW signal into a

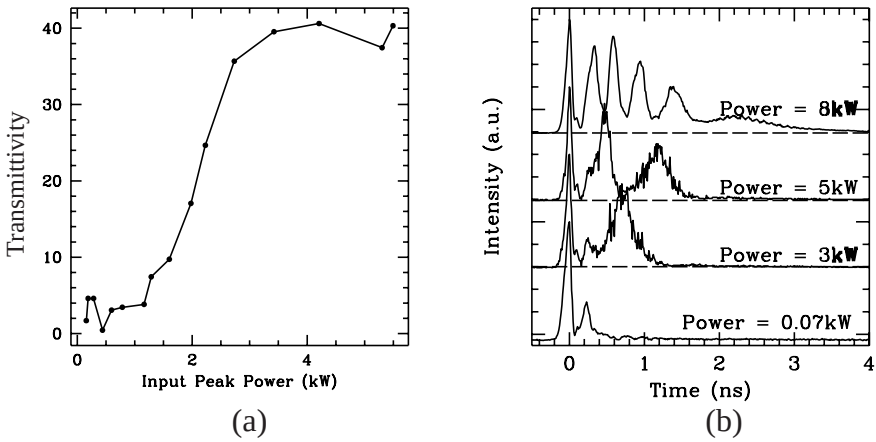

Figure 1.18 (a) Transmittivity as a function of input peak power showing nonlinear switching; (b) output pulse shapes at several peak power levels. (After Ref. [111])

pulse train [68]. Second, each pulse evolves toward a constant width. Pulses near the leading edge have had enough propagation time within the grating to stabilize their widths. These pulses can be thought of as a gap soliton since they are formed even though the input signal is inside the photonic bandgap and would be completely reflected in the absence of the nonlinear effects. Third, pulses near the trailing edge are wider simply because the fiber grating is not long enough for them to evolve completely toward a gap soliton. This interpretation was supported by a later experiment in which the grating length was increased to 20 cm [114]. Six gap solitons were found to form in this grating at a peak power level of 1.8 W. The observed data were in agreement with theory based on the nonlinear coupled-mode equations.

The nonlinear switching seen in Fig. 1.18 is sometimes called SPM-induced or self-induced switching since the pulse changes the refractive index to switch itself to the high-transmission state. Clearly, another signal at a different wavelength can also induce switching of the pulse by changing the refractive index through XPM, resulting in XPM-induced switching. This phenomenon was first observed in 1991 as an increase in the transmittivity of a 514-nm signal caused by a 1064-nm pump beam [74]. The increase in transmission was less than 10% in this experiment.

It was suggested later that XPM could be used to form a “push broom” such that a weak CW beam (or a broad pulse) would be swept by a strong pump

pulse and its energy piled up at the front end of the pump pulse [125]. The basic idea behind the optical push broom is quite simple. If the wavelength of the pump pulse is far from the stop band while that of the probe is close to but outside the stop band (on the lower branch of the dispersion curve), the pump travels faster than the probe. In the region where pump and probe overlap, the XPM-induced chirp changes the probe frequency such that it moves with the leading edge of the pump pulse. As the pump pulse travels further, it sweeps more and more of the probe energy and piles it up at its leading edge. In effect, the pump acts like a push broom. At the grating output, a significant portion of the probe energy appears at the same time as the pump pulse in the form of a sharp spike because of the XPM-induced increase in the probe speed. Such a push-broom effect has been seen in a 1997 experiment [126].

1.6.5 Effects of Birefringence

As discussed in Chapter A.6, fiber birefringence plays an important role and affects the nonlinear phenomena considerably. Its effects should be included if Bragg gratings are made inside the core of polarization-maintaining fibers. The coupled-mode theory can be easily extended to account for fiber birefringence [127]–[130]. However, the problem becomes quite complicated since one needs to solve a set of four coupled equations describing the evolution of two orthogonally polarized components, each containing both the forward- and backward-propagating waves. This complexity, however, leads to a rich class of nonlinear phenomena with practical applications such as optical logic gates.

From a physical standpoint, the two orthogonally polarized components have slightly different mode indices. Since the Bragg wavelength depends on the mode index, the stop bands of the two modes have the same widths but are shifted by a small amount with respect to each other. As a result, even though both polarization components have the same wavelength (or frequency), one of them may fall inside the stop band while the other remains outside it. Moreover, as the two stop bands shift due to nonlinear index changes, the shift can be different for the two orthogonally polarized components because of the combination of the XPM and birefringence effects. It is this feature that leads to a variety of interesting nonlinear effects.

In the case of CW beams, the set of four coupled equations was solved numerically in 1994 and several birefringence-related nonlinear effects were identified [128]. One such effect is related to the onset of polarization insta-

bility discussed in Chapter A.6. The critical power at which this instability occurs is reduced considerably in the presence of a Bragg grating [131]. Nonlinear birefringence also affects Bragg solitons. In the NLS limit ($\gamma P_0 \ll \kappa$), the four equations reduce a pair of coupled NLS equations, similar to those appearing in Chapter A.6. In the case of low-birefringence fibers, the two polarization components have nearly the same group velocity, and the coupled NLS equations take the following form [127]:

$$\frac{\partial U_x}{\partial z} + \frac{i\beta_2^g}{2}\frac{\partial^2 U_x}{\partial T^2} = i\gamma_g\left(|U_x|^2 + \frac{2}{3}|U_y|^2\right)U_x + \frac{i\gamma_g}{3}U_x^* U_y^2 \exp(-2i\Delta\beta z), \tag{1.6.10}$$

$$\frac{\partial U_y}{\partial z} + \frac{i\beta_2^g}{2}\frac{\partial^2 U_y}{\partial T^2} = i\gamma_g\left(|U_y|^2 + \frac{2}{3}|U_x|^2\right)U_y + \frac{i\gamma_g}{3}U_y^* U_x^2 \exp(2i\Delta\beta z), \tag{1.6.11}$$

where $\Delta\beta \equiv \beta_0 x - \beta_0 y$ is related to the beat length L_B as $\Delta\beta = 2\pi/L_B$. These equations support a vector soliton with equal amplitudes such that the peak power required for each component is only $\sqrt{3/5}$ of that required when only one component is present. Such a vector soliton is referred to as the *coupled-gap soliton* [127].

The coupled-gap soliton can be used for making an all-optical AND gate. The x and y polarized components of the input light represent bits for the gate, each bit taking a value of 0 or 1 depending on whether the corresponding signal is absent or present. The AND gate requires that a pulse appears at the output only when both components are present simultaneously. This can be achieved by tuning both polarization components inside the stop band but close to the upper branch of the dispersion curve. Their combined intensity can increase the refractive index (through a combination of SPM and XPM) enough that both components are transmitted. However, if one of the components is absent at the input (0 bit), the XPM contribution vanishes and both components are reflected by the grating. This occurs simply because the coupled gap soliton forms at a lower peak power level than the Bragg soliton associated with each individual component [127].

An all-optical AND gate was realized in a 1998 experiment in which a switching contrast of 17 dB was obtained at a peak power level of 2.5 kW [108]. Figure 1.19 shows the fraction of total pulse energy transmitted (a) as a func-

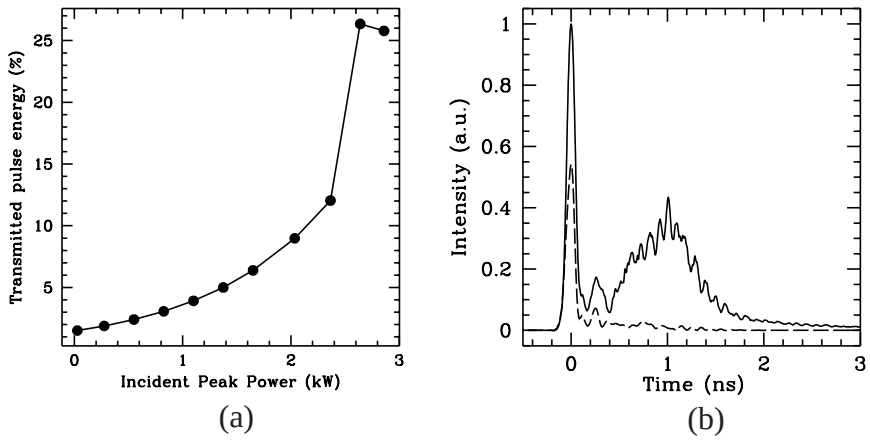

Figure 1.19 (a) Grating transmissivity as a function of input peak power showing the operation of the AND gate and (b) output pulse shapes at a peak power level of 3 kW when only one polarization component (dashed line) or both polarization components (solid line) are incident at the input end. (After Ref. [111])

tion of input peak power and the transmitted pulse shapes (b) at a peak power of 3 kW. When only one polarization component is incident at the input end, little energy is transmitted by the grating. However, when both polarization components are launched, each having the same peak power, an intense pulse is seen at the output end of the grating, in agreement with the prediction of the coupled NLS equations.

The XPM-induced coupling can be advantageous even when the two polarization components have different wavelengths. For example, it can be used to switch the transmission of a CW probe from low to high by using an orthogonally polarized short pump pulse at a wavelength far from the stop band associated with the probe [132]. In contrast with the self-induced bistable switching discussed earlier, XPM-induced bistable switching can occur for a CW probe too weak to switch itself. Furthermore, the short pump pulse switches the probe beam permanently to the high-transmission state.

1.7 Related Periodic Structures

This chapter has focused on uniform Bragg gratings (except for apodization) that are designed to couple the forward- and backward-propagating waves in-

side an optical fiber. Many variations of this simple structure exist. In this section we consider several other kinds of gratings and discuss nonlinear effects when intense light propagates through them.

1.7.1 Long-Period Gratings

Long-period gratings are designed to couple the fundamental fiber mode to a higher-order copropagating mode [133]–[136]. In the case of a single-mode fiber, the higher-order mode propagates inside the cladding and is called a *cladding mode*. The grating period required for coupling the two copropagating modes can be calculated from Eq. (1.1.2) and is given by $\Lambda = \lambda/\Delta n$, where Δn is the difference in the refractive indices of the two modes coupled by the grating. Since $\Delta n \sim 0.01$ typically, Λ is much larger than the optical wavelength. It is for this reason that such gratings are called *long-period gratings*.

The coupled-mode theory of Section 1.3 can be used for long-period gratings. In fact, the resulting equations are similar to Eqs. (1.3.11) and (1.3.12) and can be written as [135]

$$\frac{\partial A_1}{\partial z} + \frac{1}{v_{g1}}\frac{\partial A_1}{\partial t} + \frac{i\beta_{21}}{2}\frac{\partial^2 A_1}{\partial t^2} = i\delta A_1 + i\kappa A_2 + i\gamma_1(|A_1|^2 + c_1|A_2|^2)A_1, \tag{1.7.1}$$

$$\frac{\partial A_2}{\partial z} + \frac{1}{v_{g2}}\frac{\partial A_2}{\partial t} + \frac{i\beta_{22}}{2}\frac{\partial^2 A_2}{\partial t^2} = i\delta A_2 + i\kappa A_1 + i\gamma_2(|A_2|^2 + c_2|A_1|^2)A_2, \tag{1.7.2}$$

where A_1 and A_2 represent the slowly varying amplitudes of the two copropagating modes coupled by the grating. A comparison of these equations with Eqs. (1.3.11) and (1.3.12) reveals several important differences. First, the two z derivatives have the same sign since both waves travel in the forward direction. Second, the group velocities and the GVD parameters can be different for the two modes because of their different mode indices. Third, the SPM parameters γ_j and the XPM parameters c_j are also generally different for $j = 1$ and 2. The reason is related to different spatial profiles for the two modes, resulting in different overlap factors.

In the case of low-power CW beams, both the nonlinear effects and fiber-GVD effects can be neglected in Eqs. (1.7.1) and (1.7.2) by setting $\gamma_j = 0$ and $\beta_2 = 0$ $(j = 1, 2)$. These equations then reduce to Eqs. (1.3.13) and (1.3.14)

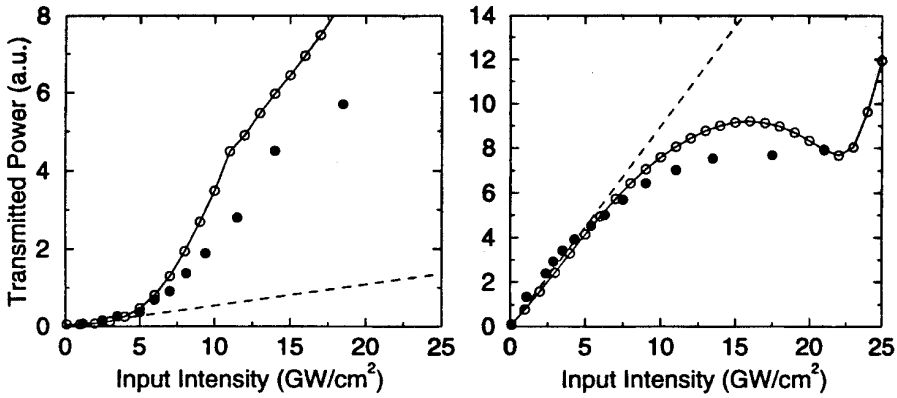

Figure 1.20 Transmitted power as a function of input peak power for (a) $\delta = 0$ and (b) -1.5 cm^{-1}. Experimental data (solid circles) are compared with coupled-mode theory (open circles). Dashed lines shows the behavior expected in the absence of nonlinear effects. (After Ref. [135] ©1997 IEEE)

with the only difference that both z derivatives have the same sign. They can be solved readily and exhibit features similar to those discussed in Section 1.3.2. When a single beam excites the A_1 mode at the fiber input, its transmission depends on its detuning δ from the Bragg wavelength and becomes quite small within the stop band centered at $\delta = 0$. The reason is easily understood by noting that the grating transfers power to the A_2 mode as light propagates inside the grating.

The nonlinear effects such as SPM and XPM can affect the amount of power transferred by changing the refractive index and shifting the Bragg wavelength toward longer wavelengths. As a result, a long-period grating should exhibit nonlinear switching. Moreover, the switching intensity is expected to be lower by a factor of $\bar{n}/\Delta n \sim 100$ compared with that required for short-period Bragg gratings. Figure 1.20 shows nonlinear changes in the transmitted power as a function of input peak intensity when 70-ps Gaussian pulses are transmitted through a 5-cm-long grating and compares the experimental data with the prediction of coupled-mode theory. Dashed lines shows the linear increase in transmission expected in the absence of nonlinear effects. For $\delta = 0$ [Fig. 1.20(a)], the input wavelength coincides with the Bragg wavelength, and little transmission occurs in the linear case. However, at intensity levels beyond 5 GW/cm^2, the nonlinear effects shift the Bragg wavelength

enough that a significant part of the incident power is transmitted through the grating. When the input wavelength is detuned by about 5.2 nm from the Bragg wavelength ($\delta = -1.5$ cm^{-1}), the transmitted power decreases at high peak intensities, as seen in Fig. 1.20(b).

Considerable pulse shaping was observed in the preceding experiment because of the use of short optical pulses. This feature can be used to advantage to compress and reshape an optical pulse. Nonlinear effects in long-period fiber gratings are likely to remain important and find practical applications.

1.7.2 Nonuniform Bragg Gratings

The properties of a Bragg grating can be considerably modified by introducing nonuniformities along their length such that the two grating parameters, κ and δ, become z dependent. Examples of such nonuniform gratings include chirped gratings, phase-shifted gratings, and superstructure gratings. It was seen in Section 1.4.2 that the use of a $\pi/2$ phase shift in the middle of an otherwise uniform grating can reduce the switching power by a factor of 100 or more. Here we focus on chirped and superstructure gratings.

In a chirped grating, the optical period $\bar{n}\Lambda$ of the grating changes along the fiber length, as shown in Fig. 1.21. Since the Bragg wavelength ($\lambda_B = 2\bar{n}\Lambda$) sets the frequency at which the stop band is centered, its axial variations translate into a shift of the stop band along the grating length. Mathematically, the parameter δ appearing in the nonlinear coupled-mode equations becomes z dependent. Typically, Λ is designed to vary linearly along the grating, and $\delta(z) = \delta_0 + \delta_c z$, where δ_c is a chirp parameter. Such gratings are called *linearly chirped gratings*.

Chirped fiber gratings have been fabricated using several different methods [49]. It is important to note that it is the optical period $\bar{n}\Lambda$ that needs to be varied along the grating (z axis). Thus, chirping can be induced either by varying the physical grating period Λ or by changing the effective mode index $\bar{n}$ along z. In the commonly used dual-beam holographic technique, the fringe spacing of the interference pattern is made nonuniform by using dissimilar curvatures for the interfering wavefronts, resulting in Λ variations. In practice, cylindrical lenses are used in one or both arms of the interferometer. Chirped fiber gratings can also be fabricated by tilting or stretching the fiber, by using strain or temperature gradients, or by stitching together multiple uniform sections.

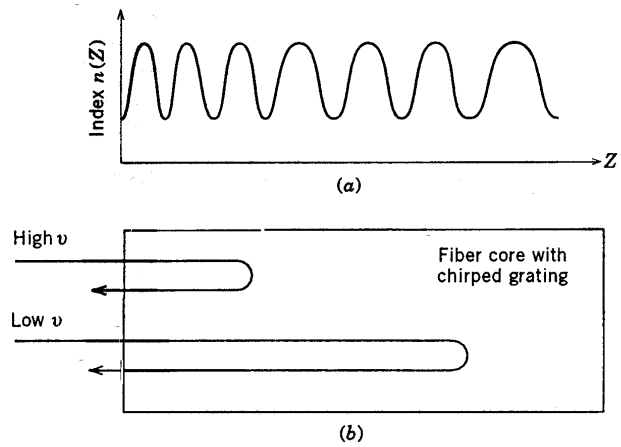

Figure 1.21 (a) Variations of refractive index in a chirped fiber grating. (b) Low and high frequency components of a pulse are reflected at different locations within the grating because of variations in the Bragg wavelength.

Chirped Bragg gratings have several important practical applications. As shown in Fig. 1.21, when a pulse—with its spectrum inside the stop band—is incident on a chirped grating, different spectral components of the pulse are reflected by different parts of the grating. As a result, even though the entire pulse is eventually reflected, it experiences a large amount of GVD whose nature (normal versus anomalous) and magnitude can be controlled by the chirp. For this reason, chirped gratings are commonly used for dispersion compensation [65]and pulse compression [137]–[139]. This aspect of chirped fiber gratings is discussed in Chapter 6. Chirped gratings also exhibit interesting nonlinear effects when the incident pulse is sufficiently intense. In one experiment, 80-ps pulses were propagated through a 6-cm-long grating whose linear chirp could be varied over a considerable range through a temperature gradient established along its length [140]. The reflected pulses were split into a pair of pulses by the combination of SPM and XPM for peak intensities close to 10 GW/cm^2.

In a variation of the chirping idea, it is the coupling coefficient κ that becomes nonuniform along the grating length. This occurs when the parameter δn_1 in Eq. (1.3.8) is made a function of z. In practice, variations in the intensity of the ultraviolet laser beam used to make the grating translate into axial variations of κ. From a physical standpoint, since the width of the photonic

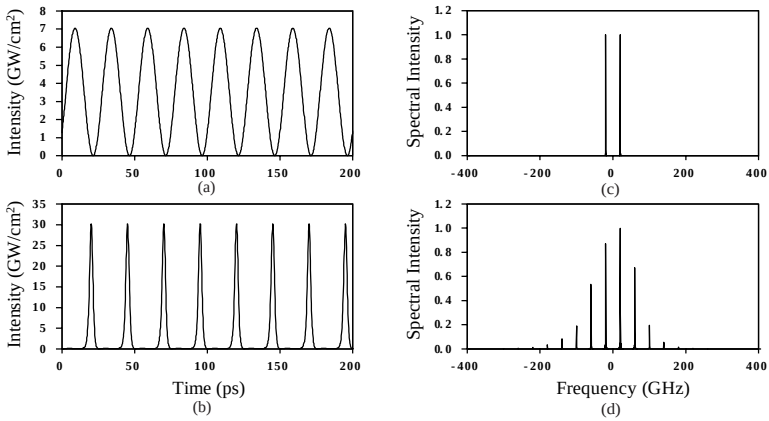

Figure 1.22 Temporal signal [(a) and (b)] and its spectrum [(c) and (d)] at the input [(a) and (c)] and output [(b) and (d)] end of a fiber grating designed with a linearly decreasing κ. (After Ref. [141])

bandgap is about 2κ, changes in κ translate into changes in the width of the stop band along the grating length. At a fixed wavelength of input light, such local variations in κ lead to axial variations of the group velocity V_G and the GVD parameter β_2^g, as seen from Eqs. (1.3.25) and (1.3.26). In effect, the dispersion provided by the grating becomes nonuniform and varies along its length. Such gratings can have a number of applications. For example, they can be used to generate a pulse train at high repetition rates by launching the output of two CW lasers with closely spaced wavelengths.

Figure 1.22 shows the numerical results obtained by solving Eqs. (1.4.1) and (1.4.2) with $\kappa(z) = \kappa_0(1 - \kappa_1 z)$ for the case in which laser frequencies are 40 GHz apart [141]. The grating is assumed to be 70 cm long with parameters $\kappa_0 = 70$ cm^{-1} and $\delta = 160$ cm^{-1}. The parameter κ_1 is chosen such that the sinusoidal oscillation seen at the grating input are compressed by a factor of 5 at the end of the grating. The pulse compression can be understood by noting that the nonlinear effects (SPM and XPM) chirp the pulse and broaden its spectrum, and the GVD compresses the chirped pulse. It can also be thought of in terms of a four-wave mixing process, phase-matched by the nonlinearity, that generates multiple sidebands at the grating output, as seen in Fig. 1.22.

In another class of gratings, the grating parameters are designed to vary periodically along the length of a grating. Such devices have double periodicity and are called *sampled* or *superstructure gratings*. They were first used

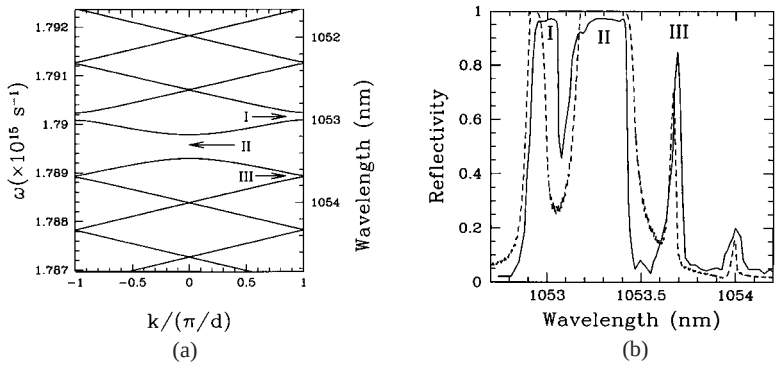

Figure 1.23 (a) Dispersion curves and (b) reflectivity spectrum for a 2.5-mm superstructure grating with $d = 1$ mm. (After Ref. [146])

in the context of DFB semiconductor lasers [142]. Fiber-based superstructure gratings were made in 1994 [143]. Since then, their properties have attracted considerable attention [144]–[149]. A simple example of a superstructure grating is provided by a long grating with constant phase-shift regions occurring at periodic intervals. In practice, such a structure can be realized by placing multiple gratings next to each other with a small constant spacing among them or by blocking small regions during fabrication of a grating such that $\kappa = 0$ in the blocked regions. It can also be made by etching away parts of an existing grating. In all cases, $\kappa(z)$ varies periodically along z. It is this periodicity that modifies the stop band of a uniform grating. The period d of $\kappa(z)$ is typically about 1 mm. If the average index $\bar{n}$ also changes with the same period d, both δ and κ become periodic in the nonlinear coupled-mode equations.

The most striking feature of a superstructure grating is the appearance of additional photonic bandgaps on both branches of the dispersion curve seen in Fig. 1.5 for a uniform grating. These bandgaps are referred to as *Rowland ghost gaps* [150]. Figure 1.23 shows the band structure of a 2.5-mm-long superstructure grating with $d = 1$ mm together with the measured reflectivity spectrum. The Rowland ghost gaps labeled I and III occur on the opposite sides of the stop band and lead to two additional reflectivity peaks. Dispersive properties near these gaps are similar to those expected near the edges of the stop band II. As a result, nonlinear effects are quite similar. In particular, Bragg solitons can form on the branch where GVD is anomalous [144]. Indirect evidence of such solitons was seen in an experiment in which a 100-ps pulse was

compressed to 38 ps within the 2.5-mm-long superstructure grating when it was tuned on the high-frequency side of the Rowland ghost gap I [146]. The pulse appeared to be evolving toward a Bragg soliton, which should form if the grating were long enough. Other nonlinear effects such as optical bistability, modulation instability, and optical switching should also occur near Rowland ghost gaps associated with a superstructure grating. In an interesting application, a superstructure grating was used to increase the repetition rate of a 3.4-ps pulse train from 10 to 40 GHz [149]. The grating was designed to have a band structure such that it reflected every fourth spectral peak of the input spectrum.

1.7.3 Photonic-Crystal Fibers

Fiber gratings constitute an example of a much larger class of periodic structures known as photonic crystals [151]–[154]. Whereas the refractive index is periodic only along one spatial dimension in a fiber grating, it is made periodic in all three spatial dimensions in the case of a photonic crystal. Starting in 1996, a new class of fibers, called *photonic-crystal fibers*, began to attract considerable attention, both experimentally and theoretically [155]–[167]. In such fibers, the refractive index is periodic in two spatial dimensions, perpendicular to the fiber axis. Since the periodicity does not occur along the direction of propagation, no backward-propagating wave is generated inside photonic-crystal fibers. As a result, such fibers do not perform the same function as a fiber grating. However, they can have new types of modes with quite different dispersive and nonlinear properties.

An interesting technique for fabricating photonic-crystal fibers consists of stacking multiple capillary tubes of pure silica (diameter about 1 mm) in a hexagonal pattern around a solid silica rod and drawing such a "preform" into a fiber form using the fiber-drawing apparatus [155]. A polymer coating is added on the outside to protect the resulting photonic-crystal fiber. When viewed under a scanning electron microscope, such a fiber shows a regular two-dimensional pattern of air holes around the central region acting as a core, as seen in Fig. 1.24(a). For this reason, such a photonic-crystal fiber is sometimes called a *holey fiber* [161]. The term *air–silica microstructure* is also used [165]. The absence of an air hole in the center creates a "defect" that can help to confine and guide an electromagnetic wave of right frequency. The contours seen in Fig. 1.24(a) correspond to such a guided mode at a wavelength of 1.55 μm [162].

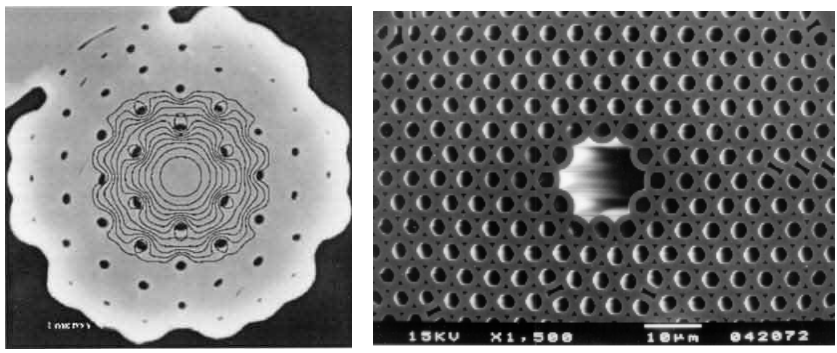

(a) (b)

Figure 1.24 Scanning electron micrograph of (a) a holey fiber and (b) a vacuum-guided fiber. The mode profile is shown in (a) as 1-dB contours of intensity. [(a) After Ref. [162] and (b) courtesy P. S. J. Russell]

Guiding and dispersive properties of holey fibers have been analyzed using several different methods [157]–[160]. Such fibers, when designed properly, can exhibit multiple photonic bandgaps resulting from the two-dimensional periodicity of air holes. When frequency of light is within a photonic bandgap, fiber does not transmit light since no guided mode exists. Outside each photonic bandgap, light travels along the central core region. Even though no built-in index difference exists between the core and cladding regions, air holes reduce the effective index of the region surrounded by the core, resulting in guided modes similar to those found in standard fibers. The GVD for holey fibers varies over a wide range and can become anomalous at visible wavelengths even though material dispersion remains normal up to a wavelength close to 1.3 μm. The zero-dispersion wavelength depends on the size of and spacing among air holes. It is close to 1 μm for the fiber of Fig. 1.24 (left part) because of a relatively large hole spacing, resulting in an air-fill fraction of only 20%. However, it can be reduced to below 0.8 μm by increasing the air-fill fraction close to 50%. Such fibers have anomalous GVD in the wavelength region near 0.8 μm, where Ti:sapphire lasers emit ultrashort optical pulses.

Nonlinearity of holey fibers has also been characterized by measuring the SPM-induced phase shift [162]. These measurements show that, even though n_2 has the same value as in standard silica fibers, the value of parameter γ can be larger by a factor of more than 3 because of a relatively low value of effective core area A_{eff}. As a result, almost all nonlinear effects are enhanced

considerably in the holey fiber shown in Fig. 1.24. Indeed, measurements of stimulated Brillouin scattering showed that the threshold was reduced by the same factor as A_{eff} compared with a dispersion-shifted regular fiber while the Brillouin shift was nearly the same.

Several experiments have used holey fibers for investigating the nonlinear effects in the 0.8-μm wavelength region where such fibers can provide anomalous GVD. In one experiment, the spectrum of a 110-fs input pulse (centered at 790 nm) broadened so much when the pulse was transmitted through a 10-cm section of a holey fiber that it extended from 390 to 1600 nm, forming a supercontinuum [165]. In another experiment, 200-fs input pulses at 850 nm were propagated through a 3.1-m section of a holey fiber [166]. The pulse width increased to 800 fs at low powers but formed a 140-fs-wide soliton when the peak power was close to 90 W. The soliton period was about 1 m in this experiment. Formation of a second-order soliton was also inferred indirectly from the pulse-width data.

Both short- and long-period gratings have been made inside the core of a photonic-crystal fiber with periodic air holes [163]. Such a device is not a three-dimensional photonic crystal in spite of periodic variation of the refractive index in all three spatial dimensions since the grating exists only inside the narrow core (radius ~ 1 μm). Nevertheless, it exhibits many interesting properties. In the case of a short-period Bragg grating, the transmission spectrum showed several dips in the wavelength region near 1.55 μm but the reflected signal had only one peak corresponding to the mode guided inside the core. The other transmission dips correspond to higher-order modes that travel outside the core and thus do not interact with the Bragg grating. Nonlinear effects in such gratings are yet to be studied.

A new kind of photonic-crystal fiber, called *vacuum-guided fiber*, was developed in 1999 [164]. Its cross section is shown in Fig 1.24(b). It was made using the same technique as a holey fiber except that the central core consisted of air and had a refractive index $n \approx 1$. The central hole was created by removing seven capillary tubes (one at the center and six surrounding it) before the preform was drawn into a fiber. The effective index of the cladding for such a fiber is considerably larger than the central air hole. As a result, no modes guided by total internal reflection can exist. Nonetheless, the fiber was found to transmit light along the central core in several frequency bands in the visible and infrared regions. This transmission is attributed to an optical mode that is created by the two-dimensional periodicity and confined to the central

air hole. Since light propagates in air, and not in silica, the Raman and Brillouin thresholds for such a fiber should be much larger than those of standard silica fibers.

The field of photonic-crystal fibers is in its infancy and is likely to evolve in the near future. Recent work has shown that even the periodicity of air holes within the cladding is not a necessary requirement for utilizing such fibers; that is, light can be guided in a holey fiber with randomly distributed air holes [167].

Problems

1.1 Derive Eq. (1.1.1) from the phase-matching condition in Eq. (1.1.2).

1.2 Use Eq. (1.1.1) to find the grating period Λ for a fiber Bragg grating reflecting light near 1.55 μm. Assume $m = 1$ and $\bar{n} = 1.45$.

1.3 Describe the mechanism through which absorption of ultraviolet light produces changes in the refractive index of silica fibers.

1.4 Discuss the holographic and phase mask techniques used to make fiber gratings. Sketch the experimental setup in each case.

1.5 Derive the nonlinear coupled-mode equations (1.3.11) and (1.3.12) for fiber gratings starting from the Helmholtz equation (1.3.2).

1.6 What is meant by the stop band of a grating? Starting from the linear coupled-mode equations (1.3.13) and (1.3.14), find the dispersion relation and the width of the stop band.

1.7 An optical pulse is transmitted through a fiber grating with its spectrum located close to but outside the stop band. Its energy is small enough that nonlinear effects are negligible. Derive an expression for the group velocity of the pulse.

1.8 For the previous problem, derive expressions for the second- and third-order dispersion induced by the grating. You can neglect the material and waveguide dispersion of silica fibers.

1.9 Derive an expression for the reflectivity of a fiber grating by solving the coupled-mode equations (1.3.13) and (1.3.14). Plot it as a function of δ/κ using $\kappa L = 3$.

1.10 The coupling coefficient of an apodized grating of length L varies as $\kappa(z) = \kappa_0 \exp[-(4-8z/L)^2 m]$. Solve the linear coupled-mode equations (1.3.13) and (1.3.14) numerically and plot the reflectivity spectrum for $m = 1, 2, 3$ as a function of δ/κ using $\kappa L = 3$.

1.11 Solve the nonlinear coupled-mode equations (1.4.1) and (1.4.2) assuming that the powers of the forward- and backward-propagating waves are constant in time and along the grating length. Find the relative power levels when $\delta/\kappa = 1.05$ and $\gamma P_0/\kappa = 2$, where P_0 is the total power.

1.12 Use the CW solution obtained in the previous problem to discuss how the stop band of a fiber grating is affected at high power levels because of the nonlinear effects.

1.13 Perturb the CW solution of Eqs. (1.4.1) and (1.4.2) and discuss the conditions under which it may become unstable.

1.14 Develop a computer program for solving Eqs. (1.4.1) and (1.4.2) numerically and use it to reproduce the results shown in Fig. 1.17.

References

[1] M. Born and E. Wolf, *Principles of Optics*, 7th ed. (Cambridge University Press, New York, 1999), Section 8.6.

[2] K. O. Hill, Y. Fujii, D. C. Johnson, and B. S. Kawasaki, *Appl. Phys. Lett.* **32**, 647 (1978).

[3] B. S. Kawasaki, K. O. Hill, D. C. Johnson, and Y. Fujii, *Opt. Lett.* **3**, 66 (1978).

[4] J. Bures, J. Lapierre, and D. Pascale, *Appl. Phys. Lett.* **37**, 860 (1980).

[5] J. Lapierre, J. Bures, and D. Pascale, *Opt. Commun.* **40**, 95 (1981).

[6] D. K. W. Lam and B. K. Garside, *Appl. Opt.* **20**, 440 (1982).

[7] J. Lapierre, J. Bures, and G. Chevalier, *Opt. Lett.* **7**, 37 (1982).

[8] J. Bures, S. Lacroix, and J. Lapierre, *Appl. Opt.* **21**, 3502 (1982).

[9] D. K. W. Lam, B. K. Garside, and K. O. Hill, *Opt. Lett.* **7**, 291 (1982).

[10] M. Parent, J. Bures, S. Lacroix, and J. Lapierre, *Appl. Opt.* **24**, 354 (1985).

[11] J. Stone, *J. Appl. Phys.* **62**, 4371 (1987).

[12] C. P. Kuo, U. Österberg, C. T. Seaton, G. I. Stegeman, and K. O. Hill, *Opt. Lett.* **13**, 1032 (1988).

[13] F. P. Payne, *Electron. Lett.* **25**, 498 (1989).

[14] H. G. Park and B. Y. Park, *Electron. Lett.* **25**, 737 (1989).

[15] F. Ouellette, *Electron. Lett.* **25**, 1590 (1989).

[16] G. Meltz, W. W. Morey, and W. H. Glen, *Opt. Lett.* **14**, 823 (1989).
[17] R. Kashyap, J. R. Armitage, R. Wyatt, S. T. Davey, and D. L. Williams, *Electron. Lett.* **26**, 730 (1990).
[18] K. O. Hill, B. Malo, K. A. Vineberg, F. Bilodeau, D. C. Johnson, and I. Skinner, *Electron. Lett.* **26**, 1270 (1990).
[19] S. La Rochelle, V. Mizrahi, G. I. Stegeman, and J. Sipe, *Appl. Phys. Lett.* **57**, 747 (1990).
[20] S. La Rochelle, Y. Hibino, V. Mizrahi, and G. I. Stegeman, *Electron. Lett.* **26**, 1459 (1990).
[21] J. P. Bernardin and N. M. Lawandy, *Opt. Commun.* **79**, 194 (1990).
[22] D. P. Hand and P. S. J. Russell, *Opt. Lett.* **15**, 104 (1990).
[23] B. Malo, K. A. Vineberg, F. Bilodeau, J. Albert, D. C. Johnson, and K. O. Hill, *Opt. Lett.* **15**, 953 (1990).
[24] G. A. Ball, W. W. Morey, and J. P. Waters, *Electron. Lett.* **26**, 1829 (1990).
[25] V. Mizrahi, S. La Rochelle, and G. I. Stegeman, *Phys. Rev. A* **43**, 433 (1991).
[26] S. E. Kanellopoulos, V. A. Handerek, H. Jamshidi, and A. J. Rogers, *IEEE Photon. Technol. Lett.* **3**, 244 (1991).
[27] S. Legoubin, E. Fertein, M. Douay, P. Bernage, P. Nidy, F. Bayon, and T. Georges, *Electron. Lett.* **27**, 1945 (1991).
[28] P. S. J. Russell, L. J. Poyntz-Wright, and D. P. Hand, *Proc. SPIE* **1373**, 126 (1991).
[29] G. Meltz and W. W. Morey, *Proc. SPIE* **1516**, 185 (1991).
[30] T. E. Tsai, C. G. Askins, and E. J. Friebele, *Appl. Phys. Lett.* **61**, 390 (1992).
[31] C. G. Askins, T. E. Tsai, G. M. Williams, M. A. Puttnam, M. Bashkansky, and E. J. Friebele, *Opt. Lett.* **17**, 833 (1992).
[32] S. J. Frisken, *Opt. Lett.* **17**, 1776 (1992).
[33] H. G. Limberger, P. Y. Fonjallaz, and R. P. Salathé, *Electron. Lett.* **29**, 47 (1993).
[34] J. L. Archambault, L. Reekie, and P. S. J. Russell, *Electron. Lett.* **29**, 28 (1993); *Electron. Lett.* **29**, 453 (1993).
[35] L. Long, J. L. Archambault, L. Reekie, P. S. J. Russell, and D. N. Payne, *Opt. Lett.* **18**, 861 (1993).
[36] K. O. Hill, B. Malo, F. Bilodeau, D. C. Johnson, and J. Albert, *Appl. Phys. Lett.* **62**, 1035 (1993).
[37] D. Z. Anderson, V. Mizrahi, T. Erdogan, and A. E. White, *Electron. Lett.* **29**, 566 (1993).
[38] B. Malo, D. C. Johnson, F. Bilodeau, J. Albert, and K. O. Hill, *Opt. Lett.* **18**, 1277 (1993).
[39] P. J. Lemaire, R. M. Atkins, V. Mizrahi, and W. A. Reed, *Electron. Lett.* **29**, 1191 (1993).

[40] L. Long, J. L. Archambault, L. Reekie, P. S. J. Russell, and D. N. Payne, *Electron. Lett.* **29**, 1577 (1993).

[41] J. D. Prohaska, E. Snitzer, S. Rishton, and V. Boegli, *Electron. Lett.* **29**, 1614 (1993).

[42] K. C. Byron, K. Sugden, T. Bricheno, and I. Bennion, *Electron. Lett.* **29**, 1659 (1993).

[43] B. Malo, K. O. Hill, F. Bilodeau, D. C. Johnson, and J. Albert, *Appl. Phys. Lett.* **62**, 1668 (1993).

[44] H. Patrick and S. L. Gilbert, *Opt. Lett.* **18**, 1484 (1993).

[45] K. O. Hill, B. Malo, F. Bilodeau, and D. C. Johnson, *Annu. Rev. Mater. Sci.* **23**, 125 (1993).

[46] T. Erdogan, V. Mizrahi, P. J. Lemaire, and D. Monroe, *J. Appl. Phys.* **76**, 73 (1994).

[47] S. J. Mihailor and M. C. Gower, *Electron. Lett.* **30**, 707 (1994).

[48] M. C. Farries, K. Sugden, D. C. J. Reid, I. Bennion, A. Molony, and M. J. Goodwin, *Electron. Lett.* **30**, 891 (1994).

[49] R. Kashyap, *Fiber Bragg Gratings* (Academic Press, San Diego, CA, 1999).

[50] A. Othonos and K. Kalli, *Fiber Bragg Gratings* (Artec House, Boston, 1999).

[51] P. N. Butcher and D. Cotter, *Elements of Nonlinear Optics* (Cambridge University Press, Cambridge, UK, 1990), p. 315.

[52] J. Canning, *Opt. Fiber Technol*. **6**, 275 (2000).

[53] R. Kashyap, H.-G. Froehlich, A. Swanton, and D. J. Armes, *Electron. Lett.* **32**, 1807 (1996).

[54] J. Albert, S. Theriault, F. Bilodeau, D. C. Johnson, K. O. Hill, P. Sixt, and M. J. Rooks, *IEEE Photon. Technol. Lett.* **8**, 1334 (1996).

[55] P. S. J. Russell and D. P. Hand, *Electron. Lett.* **26**, 1840 (1990).

[56] D. C. Johnson, F. Bilodeau, B. Malo, K. O. Hill, P. G. J. Wigley, and G. I. Stegeman, *Opt. Lett.* **17**, 1635 (1992).

[57] A. M. Vangsarkar, P. J. Lemaire, J. B. Judkins, V. Bhatia, T. Erdogan, and J. Sipe, *J. Lightwave Technol.* **14**, 58 (1996).

[58] P. S. J. Russell, *J. Mod. Opt.* **38**, 1599 (1991).

[59] H. A. Haus, *Waves and Fields in Optoelectronics* (Prentice-Hall, Englewood Cliffs, NJ, 1984).

[60] D. Marcuse, *Theory of Dielectric Optical Waveguides* (Academic Press, San Diego, CA, 1991).

[61] A. Yariv, *Optical Electronics in Modern Communications*, 5th ed. (Oxford University Press, New York, 1997).

[62] G. P. Agrawal and N. K. Dutta, *Semiconductor Lasers*, 2nd ed. (Van Nostrand Reinhold, New York, 1993).

[63] B. Crosignani, A. Cutolo, and P. Di Porto, *J. Opt. Soc. Am. B* **72**, 515 (1982).

[64] N. M. Litchinitser, B. J. Eggleton, and D. B. Patterson, *J. Lightwave Technol.* **15**, 1303 (1997).

[65] G. P. Agrawal, *Fiber-Optic Communication Systems*, 2nd ed. (Wiley, New York, 1997).

[66] B. J. Eggleton, C. M. de Sterke, and R. E. Slusher, *J. Opt. Soc. Am. B* **16**, 587 (1999).

[67] H. G. Winful, J. H. Marburger, and E. Garmire, *Appl. Phys. Lett.* **35**, 379 (1979).

[68] H. G. Winful and G. D. Cooperman, *Appl. Phys. Lett.* **40**, 298 (1982).

[69] H. G. Winful, *Appl. Phys. Lett.* **46**, 527 (1985).

[70] W. Chen and D. L. Mills, *Phys. Rev. Lett.* **58**, 160 (1987); *Phys. Rev. B* **36**, 6269 (1987).

[71] D. L. Mills and S. E. Trullinger, *Phys. Rev. B* **36**, 947 (1987).

[72] C. M. de Sterke and J. E. Sipe, *Phys. Rev. A* **38**, 5149 (1988); *Phys. Rev. A* **39**, 5163 (1989).

[73] C. M. de Sterke and J. E. Sipe, *J. Opt. Soc. Am. B* **6**, 1722 (1989).

[74] S. Larochelle, V. Mizrahi, and G. Stegeman, *Electron. Lett.* **26**, 1459 (1990).

[75] C. M. de Sterke and J. E. Sipe, *Phys. Rev. A* **43**, 2467 (1991).

[76] N. D. Sankey, D. F. Prelewitz, and T. G. Brown, *Appl. Phys. Lett.* **60**, 1427 (1992); *J. Appl. Phys.* **73**, 1 (1993).

[77] J. Feng, *Opt. Lett.* **18**, 1302 (1993).

[78] Y. S. Kivshar, *Phys. Rev. Lett.* **70**, 3055 (1993).

[79] C. M. de Sterke and J. E. Sipe, in *Progress in Optics*, Vol. 33, E. Wolf, Ed. (Elsevier, Amsterdam, 1994), Chap. 3.

[80] P. S. J. Russell and J. L. Archambault, *J. Phys. III France* **4**, 2471 (1994).

[81] M. Scalora, J. P. Dowling, C. M. Bowden, M. J. Bloemer, *Opt. Lett.* **19**, 1789 (1994).

[82] S. Radic, N. George, and G. P. Agrawal, *Opt. Lett.* **19**, 1789 (1994); *J. Opt. Soc. Am. B* **12**, 671 (1995).

[83] S. Radic, N. George, and G. P. Agrawal, *IEEE J. Quantum Electron.* **31**, 1326 (1995).

[84] A. R. Champneys, B. A. Malomed, M. J. Friedman, *Phys. Rev. Lett.* **80**, 4169 (1998).

[85] A. E. Kozhekin, G. Kurizki, and B. Malomed, *Phys. Rev. Lett.* **81**, 3647 (1998).

[86] C. Conti, G. Asanto, and S. Trillo, *Opt. Exp.* **3**, 389 (1998).

[87] Y. A. Logvin and V. M. Volkov, *J. Opt. Soc. Am. B* **16**, 774 (1999).

[88] H. M. Gibbs, *Optical Bistability: Controlling Light with Light* (Academic Press, San Diego, CA, 1985).

[89] G. P. Agrawal and S. Radic, *IEEE Photon. Technol. Lett.* **6**, 995 (1994).

[90] C. M. de Sterke and J. E. Sipe, *Phys. Rev. A* **42**, 2858 (1990).
[91] H. G. Winful, R. Zamir, and S. Feldman, *Appl. Phys. Lett.* **58**, 1001 (1991).
[92] A. B. Aceves, C. De Angelis, and S. Wabnitz, *Opt. Lett.* **17**, 1566 (1992).
[93] C. M. de Sterke, *Phys. Rev. A* **45**, 8252 (1992).
[94] B. J. Eggleton, C. M. de Sterke, R. E. Slusher, and J. E. Sipe, *Electron. Lett.* **32**, 2341 (1996).
[95] C. M. de Sterke, *J. Opt. Soc. Am. B* **15**, 2660 (1998).
[96] J. E. Sipe and H. G. Winful, *Opt. Lett.* **13**, 132 (1988).
[97] C. M. de Sterke and J. E. Sipe, *Phys. Rev. A* **42**, 550 (1990).
[98] C. M. de Sterke, D. G. Salinas, and J. E. Sipe, *Phys. Rev. E* **54**, 1969 (1996).
[99] T. Iizuka and M. Wadati, *J. Opt. Soc. Am. B* **14**, 2308 (1997).
[100] C. M. de Sterke and B. J. Eggleton, *Phys. Rev. E* **59**, 1267 (1999).
[101] B. J. Eggleton, C. M. de Sterke, A. B. Aceves, J. E. Sipe, T. A. Strasser, and R. E. Slusher, *Opt. Commun.* **149**, 267 (1998).
[102] D. N. Christodoulides and R. I. Joseph, *Phys. Rev. Lett.* **62**, 1746 (1989).
[103] A. B. Aceves and S. Wabnitz, *Phys. Lett. A* **141**, 37 (1989).
[104] J. Feng and F. K. Kneubühl, *IEEE J. Quantum Electron.* **29**, 590 (1993).
[105] B. J. Eggleton, R. R. Slusher, C. M. de Sterke, P. A. Krug, and J. E. Sipe, *Phys. Rev. Lett.* **76**, 1627 (1996).
[106] C. M. de Sterke, N. G. R. Broderick, B. J. Eggleton, and M. J. Steel. *Opt. Fiber Technol*. **2**, 253 (1996).
[107] B. J. Eggleton, C. M. de Sterke, and R. E. Slusher, *J. Opt. Soc. Am. B* **14**, 2980 (1997).
[108] D. Taverner, N. G. R. Broderick, D. J. Richardson, M. Isben, and R. I. Laming, *Opt. Lett.* **23**, 259 (1998).
[109] D. Taverner, N. G. R. Broderick, D. J. Richardson, R. I. Laming, and M. Isben, *Opt. Lett.* **23**, 328 (1998).
[110] C. M. de Sterke, *Opt. Exp.* **3**, 405 (1998).
[111] N. G. R. Broderick, D. Taverner, and D. J. Richardson, *Opt. Exp.* **3**, 447 (1998).
[112] B. J. Eggleton, G. Lenz, R. E. Slusher, and N. M. Litchinitser, *Appl. Opt.* **37**, 7055 (1998).
[113] N. M. Litchinitser, B. J. Eggleton, C. M. de Sterke, A. B. Aceves, and G. P. Agrawal, *J. Opt. Soc. Am. B* **16**, 18 (1999).
[114] N. G. R. Broderick, D. J. Richardson, and M. Isben, *Opt. Lett.* **25**, 536 (2000).
[115] H. G. Winful and V. Perlin, *Phys. Rev. Lett.* **84**, 3586 (2000).
[116] M. Asobe, *Opt. Fiber Technol*. **3**, 142 (1997).
[117] W. E. Thirring, *Ann. Phys. (NY)* **3**, 91 (1958).
[118] A. V. Mikhailov, *JETP Lett.* **23**, 320 (1976).
[119] E. A. Kuznetsov and A. V. Mikhailov, *Teor. Mat. Fiz.* **30**, 193 (1977).

[120] D. J. Kaup and A. C. Newell, *Lett. Nuovo Cimento* **20**, 325 (1977).

[121] D. David, J. Harnad, and S. Shnider, *Lett. Math. Phys.* **8**, 27 (1984).

[122] H. Kawaguchi, K. Inoue, T. Matsuoka, and K. Otsuka, *IEEE J. Quantum Electron.* **21**, 1314 (1985).

[123] M. J. Adams and R. Wyatt, *IEE Proc.* **134** 35 (1987).

[124] M. J. Adams, *Opt. Quantum Electron.* **19**, S37 (1987).

[125] C. M. de Sterke, *Opt. Lett.* **17**, 914 (1992).

[126] N. G. R. Broderick, D. Taverner, D. J. Richardson, M. Isben, and R. I. Laming, *Phys. Rev. Lett.* **79**, 4566 (1997); *Opt. Lett.* **22**, 1837 (1997).

[127] S. Lee and S. T. Ho, *Opt. Lett.* **18**, 962 (1993).

[128] W. Samir, S. J. Garth, and C. Pask, *J. Opt. Soc. Am. B* **11**, 64 (1994).

[129] W. Samir, C. Pask, and S. J. Garth, *Opt. Lett.* **19**, 338 (1994).

[130] S. Pereira and J. E. Sipe, *Opt. Exp.* **3**, 418 (1998).

[131] R. E. Slusher, S. Spälter, B. J. Eggleton, S. Pereira, and J. E. Sipe, *Opt. Lett.* **25**, 749 (2000).

[132] S. Broderick, *Opt. Commun.* **148**, 90 (1999).

[133] K. O. Hill, B. Malo, K. A. Vineberg, F. Bilodeau, D. C. Johnson, and I. Skinner, *Electron. Lett.* **26**, 1270 (1990).

[134] B. J. Eggleton, R. E. Slusher, J. B. Judkins, J. B. Stark, and A. M. Vengsarkar, *Opt. Lett.* **22**, 883 (1997).

[135] J. N. Kutz, B. J. Eggleton, J. B. Stark, and R. E. Slusher, *IEEE J. Sel. Topics Quantum Electron.* **3**, 1232 (1997).

[136] Y. Jeong and B. Lee, *IEEE J. Quantum Electron.* **35**, 1284 (1999).

[137] J. A. R Williams, I. Bennion, and L. Zhang, *IEEE Photon. Technol. Lett.* **7**, 491 (1995).

[138] A. Galvanauskas, P. A. Krug, and D. Harter, *Opt. Lett.* **21**, 1049 (1996).

[139] G. Lenz, B. J. Eggleton, and N. M. Litchinitser, *J. Opt. Soc. Am. B* **15**, 715 (1998).

[140] R. E. Slusher, B. J. Eggleton, T. A. Strasser, and C. M. de Sterke, *Opt. Exp.* **3**, 465 (1998).

[141] N. M. Litchinitser, G. P. Agrawal, B. J. Eggleton, and G. Lenz, *Opt. Exp.* **3**, 411 (1998).

[142] V. Jayaraman, D. Cohen, amd L. Coldren, *Appl. Phys. Lett.* **60**, 2321 (1992).

[143] B. J. Eggleton, P. A. Krug, L. Poladian, and F. Ouellette, *Electron. Lett.* **30**, 1620 (1994).

[144] N. G. R. Broderick, C. M. de Sterke, and B. J. Eggleton, *Phys. Rev. E* **55**, R5788 (1995).

[145] C. M. de Sterke and N. G. R. Broderick, *Opt. Lett.* **20**, 2039 (1995).

[146] B. J. Eggleton, C. M. de Sterke, and R. E. Slusher, *Opt. Lett.* **21**, 1223 (1996).

[147] N. G. R. Broderick and C. M. de Sterke, *Phys. Rev. E* **55**, 3232 (1997).

[148] C. M. de Sterke, B. J. Eggleton, and P. A. Krug, *J. Lightwave Technol.* **15**, 1494 (1997).

[149] P. Petropoulos, M. Isben, M. N. Zervas, and D. J. Richardson, *Opt. Lett.* **25**, 521 (2000).

[150] P. S. J. Russell, *Phys. Rev. Lett.* **56**, 596 (1986).

[151] E. Yablonovitch, *J. Opt. Soc. Am. B* **10**, 283 (1993).

[152] J. D. Joannopulos, J. N. Winn, and R. D. Meade, *Photonic Crystals: Molding the Flow of Light* (Princeton University Press, Princeton, NJ, 1995).

[153] C. M. Soukoulis, Ed., *Photonic Bandgap Materials* (Kluwer, Boston, 1996).

[154] Special issue, *J. Lightwave Technol.* **17**, 1928 (1999).

[155] J. C. Knight, T. A. Birks, P. S. J. Russell, and D. M. Atkin, *Opt. Lett.* **21**, 1547 (1996).

[156] T. A. Birks, J. C. Knight, and P. S. J. Russell, *Opt. Lett.* **22**, 961 (1997).

[157] J. C. Knight, T. A. Birks, P. S. J. Russell, and J. P. Sanders, *J. Opt. Soc. Am. A* **15**, 748 (1998).

[158] J. Broeng, S. B. Barkou, A. Bjarklev, J. C. Knight, T. A. Birks, and P. S. J. Russell, *Opt. Commun.* **156**, 240 (1998).

[159] T. M. Monro, D. J. Richardson, N. G. R. Broderick, and P. J. Bennett, *J. Lightwave Technol.* **17**, 1093 (1999).

[160] J. Broeng, D. Mogilevstev, S. B. Barkou, and A. Bjarklev, *Opt. Fiber Technol.* **5**, 305 (1999).

[161] P. J. Bennett, T. M. Monroe, and D. J. Richardson, *Opt. Lett.* **24**, 1203 (1999).

[162] N. G. R. Broderick, T. M. Monro, P. J. Bennett, and D. J. Richardson, *Opt. Lett.* **24**, 1395 (1999).

[163] B. J. Eggleton, P. S. Westbrook, R. S. Windeler, S. Spälter, and T. A. Sreasser, *Opt. Lett.* **24**, 1460 (1999).

[164] R. F. Cregan, B. J. Mangan, J. C. Knight, T. A. Birks, P. S. J. Russell, P. J. Roberts, and D. C. Allan, *Science* **285**, 1537 (1999).

[165] J. K. Ranka, R. S. Windeler, and A. J. Stentz, *Opt. Lett.* **25**, 25 (2000); *Opt. Lett.* **25**, 796 (2000).

[166] W. J. Wadsworth, J. C. Knight, A. Ortigosa-Blanch, J. Arriaga, E. Silvestre, and P. S. J. Russell, *Electron. Lett.* **36**, 53 (2000).

[167] T. M. Monro, P. J. Bennett, N. G. R. Broderick, and D. J. Richardson, *Opt. Lett.* **25**, 206 (2000).

Chapter 2

Fiber Couplers

Fiber couplers, also known as directional couplers, constitute an essential component of lightwave technology. They are used routinely for a multitude of fiber-optic devices that require splitting of an optical field into two coherent but physically separated parts (and vice versa). Although most applications of fiber couplers only use their linear characteristics, nonlinear effects have been studied since 1982 and can lead to all-optical switching among other applications. This chapter is devoted to describing nonlinear optical phenomena in fiber couplers. As an introduction, linear characteristics are described first in Section 2.1 using coupled-mode theory. In Section 2.2, the nonlinear effects are considered under continuous-wave (CW) conditions, along with the phenomenon of modulation instability. Section 2.3 focuses on propagation of short optical pulses through fiber couplers, with emphasis on optical solitons and nonlinear switching. Section 2.4 extends the discussion to asymmetric, active, birefringent, and multicore fiber couplers.

2.1 Coupler Characteristics

Fiber couplers are four-port devices (two input and two output ports) that are used routinely for a variety of applications related to fiber optics [1]–[4]. Their function is to split coherently an optical field, incident on one of the input ports, and direct the two parts to the output ports. Since the output is directed in two different directions, such devices are also referred to as *directional couplers*. They can be made using planar waveguides as well and have been studied

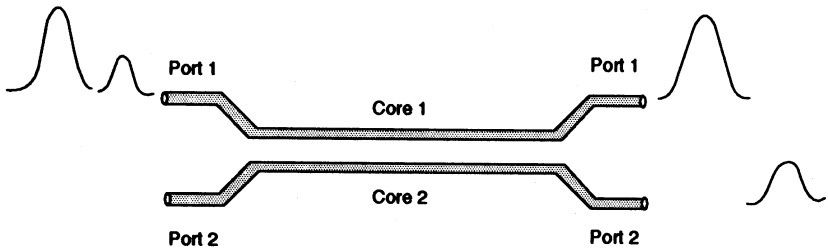

Figure 2.1 Schematic illustration of nonlinear switching in a fiber coupler. Input pulses appear at different output ports depending on their peak powers.

extensively in the context of $LiNbO_3$ and semiconductor waveguides. This chapter focuses exclusively on fiber-based directional couplers.

Several different techniques can be used to make fiber couplers [4]. Figure 2.1 shows schematically a fused fiber coupler in which the cores of two single-mode fibers are brought close together in a central region such that the spacing between the cores is comparable to their diameters. A dual-core fiber, designed to have two cores close to each other throughout its length, can also act as a directional coupler. In both cases, the cores are close enough that the fundamental modes propagating in each core overlap partially in the cladding region between the two cores. It will be seen in this section that such evanescent wave coupling between the two modes can lead to the transfer of optical power from one core to another under suitable conditions. An important application of the nonlinear effects in fiber couplers consists of using them for optical switching. As shown in Fig. 2.1, an optical pulse can be directed toward different output ports depending on its peak power.

Fiber couplers are called symmetric when their cores are identical in all respects. In general, the two cores need not be identical; such couplers are called asymmetric. In this section, we consider an asymmetric fiber coupler and discuss its operation using coupled-mode theory.

2.1.1 Coupled-Mode Equations

Coupled-mode theory is used commonly for directional couplers [5]–[9]. To derive the coupled-mode equations, we follow a procedure similar to that used in Section 1.3 for describing the grating-induced coupling between the counterpropagating waves inside the same core. Considering a specific frequency

component at the frequency ω, we solve the Helmholtz equation

$$\nabla^2\tilde{\mathbf{E}} + \tilde{n}^2(x,y)k_0^2\tilde{\mathbf{E}} = 0, \tag{2.1.1}$$

where $k_0 = \omega/c = 2\pi/\lambda_0$, λ_0 is the vacuum wavelength of light, and $\tilde{\mathbf{E}}(\mathbf{r},\omega)$ denotes the Fourier transform of the electric field $\mathbf{E}(\mathbf{r},t)$ with respect to time. The refractive index $\tilde{n}(x,y) = n_0$ everywhere in the x–y plane except in the region occupied by the two fiber cores, where it is larger by a constant amount.

The coupled-mode theory is based on the assumption that an approximate solution of Eq. (2.1.1) can be written as

$$\tilde{\mathbf{E}}(\mathbf{r},\omega) \approx \hat{e}[\tilde{A}_1(z,\omega)F_1(x,y) + \tilde{A}_2(z,\omega)F_2(x,y)]e^{i\beta z}, \tag{2.1.2}$$

where the propagation constant β is yet to be determined. The polarization direction $\hat{e}$ of the optical field is assumed to remain unchanged during propagation. The spatial distribution $F_m(x,y)$ with $m = 1,2$ corresponds to the fundamental mode supported by the mth core in the absence of the other core. It is obtained by solving Eq. (2.1.1) and satisfies the following equation:

$$\frac{\partial^2 F_m}{\partial x^2} + \frac{\partial^2 F_m}{\partial y^2} + [n_m^2(x,y)k_0^2 - \bar{\beta}_m^2]F_m = 0, \tag{2.1.3}$$

where $\bar{\beta}_m$ is the mode-propagation constant and $n_m(x,y) = n_0$ everywhere in the x–y plane except in the region occupied by the mth core, where it is larger by a constant amount. Equation (2.1.3) has been solved in Section A.2.2 in terms of the Bessel functions. The same solution applies here.

The amplitudes A_1 and A_2 vary along the coupler length because of the overlap between the two modes. To find how they evolve with z, we substitute Eq. (2.1.2) in Eq. (2.1.1), multiply the resulting equation by F_1^* or F_2^*, use Eq. (2.1.3), and integrate over the entire x–y plane. This procedure leads to the following set of two coupled-mode equations in the frequency domain:

$$\frac{d\tilde{A}_1}{dz} = i(\bar{\beta}_1 + \Delta\beta_1^{\mathrm{NL}} - \beta)\tilde{A}_1 + i\kappa_{12}\tilde{A}_2, \tag{2.1.4}$$

$$\frac{d\tilde{A}_2}{dz} = i(\bar{\beta}_2 + \Delta\beta_2^{\mathrm{NL}} - \beta)\tilde{A}_2 + i\kappa_{21}\tilde{A}_1, \tag{2.1.5}$$

where the coupling coefficient κ_{mp} and the nonlinear contribution $\Delta\beta_m^{\mathrm{NL}}$ are defined as ($m, p = 1$ or 2)

$$\kappa_{mp} = \frac{k_0^2}{2\beta}\int\int_{-\infty}^{\infty}(\tilde{n}^2 - n_p^2)F_m^* F_p\,dx\,dy, \tag{2.1.6}$$

$$\Delta\beta_m^{\mathrm{NL}} = \frac{k_0^2}{2\beta}\int\!\!\int_{-\infty}^{\infty}(\tilde{n}^2 - n_L^2)F_m^* F_m\,dx\,dy, \tag{2.1.7}$$

and n_L is the linear part of $\tilde{n}$. We have assumed that the modal distributions are normalized such that $\int\int_{-\infty}^{\infty}|F_m(x,y)|^2\,dx\,dy = 1$.

The frequency-domain coupled-mode equations can be converted to the time domain following the method used in Section A.2.3. In general, both $\bar{\beta}_m$ and κ_{mp} depend on frequency. We ignore the frequency dependence of κ_{mp} here but consider its impact on the coupler performance later (in Section 2.1.3). By expanding $\bar{\beta}_m(\omega)$ in a Taylor series around the carrier frequency ω_0 as

$$\bar{\beta}_m(\omega) = \beta_{0m} + (\omega-\omega_0)\beta_{1m} + \tfrac{1}{2}(\omega-\omega_0)^2\beta_{2m} + \cdots, \tag{2.1.8}$$

retaining terms up to second order, and replacing $\omega - \omega_0$ by a time derivative while taking the inverse Fourier transform, the time-domain coupled-mode equations can be written as

$$\begin{aligned}\frac{\partial A_1}{\partial z} &+ \beta_{11}\frac{\partial A_1}{\partial t} + \frac{i\beta_{21}}{2}\frac{\partial^2 A_1}{\partial t^2}\\ &= i\kappa_{12}A_2 + i\delta_a A_1 + (\gamma_1|A_1|^2 + C_{12}|A_2|^2)A_1, \qquad (2.1.9)\\ \frac{\partial A_2}{\partial z} &+ \beta_{12}\frac{\partial A_2}{\partial t} + \frac{i\beta_{22}}{2}\frac{\partial^2 A_2}{\partial t^2}\\ &= i\kappa_{21}A_1 - i\delta_a A_2 + (\gamma_2|A_2|^2 + C_{21}|A_1|^2)A_2, \qquad (2.1.10)\end{aligned}$$

where $v_{gm} \equiv 1/\beta_{1m}$ is the group velocity and β_{2m} is the group-velocity dispersion (GVD) in the mth core. We have introduced

$$\delta_a = \tfrac{1}{2}(\beta_{01} - \beta_{02}), \qquad \beta = \tfrac{1}{2}(\beta_{01} + \beta_{02}). \tag{2.1.11}$$

The parameter δ_a is a measure of asymmetry between the two cores. The nonlinear parameters γ_m and C_{mp} ($m, p = 1$ or 2) are defined as

$$\gamma_m = n_2 k_0 \int\!\!\int_{-\infty}^{\infty}|F_m|^4\,dx\,dy, \tag{2.1.12}$$

$$C_{mp} = 2n_2 k_0 \int\!\!\int_{-\infty}^{\infty}|F_m|^2|F_p|^2\,dx\,dy. \tag{2.1.13}$$

The parameter γ_m is responsible for self-phase modulation (SPM) while the effects of cross-phase modulation (XPM) are governed by C_{mp}.

Equations (2.1.9) and (2.1.10) are valid under quite general conditions and include both the linear and nonlinear coupling mechanisms between the optical fields propagating inside the two cores of an asymmetric fiber coupler. They simplify considerably for a symmetric coupler with two identical cores. Using $\delta_a = 0$, $\kappa_{12} = \kappa_{21} \equiv \kappa$, and $C_{12} = C_{21} \equiv \gamma\sigma$, the coupled-mode equations for symmetric couplers become:

$$\frac{\partial A_1}{\partial z} + \frac{1}{v_g}\frac{\partial A_1}{\partial t} + \frac{i\beta_2}{2}\frac{\partial^2 A_1}{\partial t^2} = i\kappa A_2 + i\gamma(|A_1|^2 + \sigma|A_2|^2)A_1, \quad (2.1.14)$$

$$\frac{\partial A_2}{\partial z} + \frac{1}{v_g}\frac{\partial A_2}{\partial t} + \frac{i\beta_2}{2}\frac{\partial^2 A_2}{\partial t^2} = i\kappa A_1 + i\gamma(|A_2|^2 + \sigma|A_1|^2)A_2, \quad (2.1.15)$$

where the subscript identifying a specific core has been dropped from the parameters v_g, β_2, and γ since they have the same values for both cores. The nonlinear parameter γ can be written as $\gamma = n_2 k_0 / A_{\text{eff}}$ and is identical to that introduced in Section A.2.3 for a fiber with the effective core area A_{eff}. The XPM parameter σ is quite small in practice and can often be neglected altogether. The reason is related to the fact that the integral in Eq. (2.1.13) involves overlap between the mode intensities and is relatively small even when the two cores are close enough that κ (involving overlap between the mode amplitudes) cannot be neglected. The coupling between A_1 and A_2 is essentially linear in that case.

2.1.2 Low-Power Optical Beams

Consider first the simplest case of a low-power CW beam incident on one of the input ports of a fiber coupler. The time-dependent terms can then be set to zero in Eqs. (2.1.9) and (2.1.10). Since the nonlinear terms are also negligible, the coupled-mode equations simplify considerably and become

$$\frac{dA_1}{dz} = i\kappa_{12}A_2 + i\delta_a A_1, \quad (2.1.16)$$

$$\frac{dA_2}{dz} = i\kappa_{21}A_1 - i\delta_a A_2. \quad (2.1.17)$$

By differentiating Eq. (2.1.16) and eliminating dA_2/dz using Eq. (2.1.17), we obtain the following equation for A_1:

$$\frac{d^2A_1}{dz^2} + \kappa_e^2 A_1 = 0, \quad (2.1.18)$$

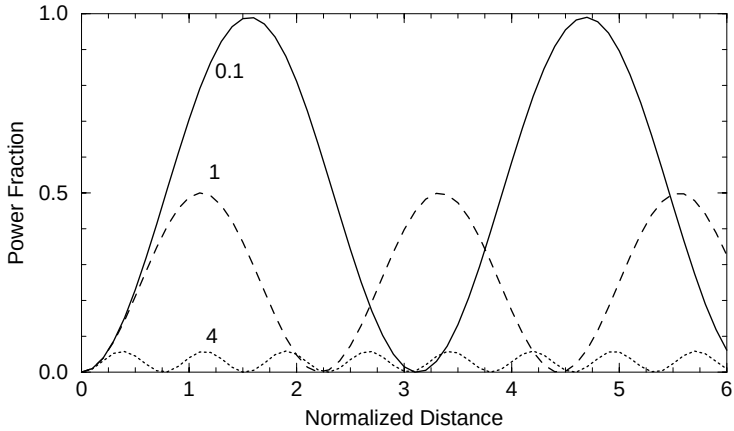

Figure 2.2 Fraction of power transferred to the second core plotted as a function of κz for three values of δ_a/κ when a CW beam is launched in one core at $z = 0$.

where the effective coupling coefficient κ_e is defined as

$$\kappa_e = \sqrt{\kappa^2 + \delta_a^2}, \qquad \kappa = \sqrt{\kappa_{12}\kappa_{21}}. \tag{2.1.19}$$

The same harmonic-oscillator-type equation is also satisfied by A_2.

By using the boundary condition that a single CW beam is incident on one of the input ports such that $A_1(0) = A_0$ and $A_2(0) = 0$, the solution of Eqs. (2.1.16) and (2.1.17) is given by

$$A_1(z) = A_0[\cos(\kappa_e z) + i(\delta_a/\kappa_e)\sin(\kappa_e z)], \tag{2.1.20}$$

$$A_2(z) = A_0(i\kappa_{21}/\kappa_e)\sin(\kappa_e z). \tag{2.1.21}$$

Thus, even though $A_2 = 0$ initially at $z = 0$, some power is transferred to the second core as light propagates inside the fiber coupler. Figure 2.2 shows the ratio $|A_2/A_0|^2$ as a function of z for several values of δ_a/κ. In all cases, power transfer to the second core occurs in a periodic fashion. The maximum power is transferred at distances such that $\kappa_e z = m\pi/2$, where m is an integer. The shortest distance at which maximum power is transferred to the second core for the first time is called the *coupling length* and is given by $L_c = \pi/(2\kappa_e)$.

The power coming out of the two output ports of a fiber coupler depends on the coupler length L and on the powers injected at the two input ends. For a symmetric coupler, the general solution of Eq. (2.1.18) can be written in a

matrix form as

$$\begin{pmatrix} A_1(L) \\ A_2(L) \end{pmatrix} = \begin{pmatrix} \cos(\kappa L) & i\sin(\kappa L) \\ i\sin(\kappa L) & \cos(\kappa L) \end{pmatrix} \begin{pmatrix} A_1(0) \\ A_2(0) \end{pmatrix}. \tag{2.1.22}$$

The determinant of the 2×2 transfer matrix on the right side is unity, as it should be for a lossless coupler. Typically, only one beam is injected at the input end. The output powers, $P_1 = |A_1|^2$ and $P_2 = |A_2|^2$, are then obtained from Eq. (2.1.22) by setting $A_2(0) = 0$ and are given by

$$P_1(L) = P_0 \cos^2(\kappa L), \qquad P_2(L) = P_0 \sin^2(\kappa L), \tag{2.1.23}$$

where $P_0 \equiv A_0^2$ is the incident power at the first input port. The coupler thus acts as a beam splitter, and the splitting ratio depends on the parameter κL.

If coupler length L is chosen such that $\kappa L = \pi/4$ or $L = L_c/2$, the power is equally divided between the two output ports. Such couplers are referred to as 50:50 or 3-dB couplers. Fiber couplers with $L = L_c$ transfer all of their input power to the second core (referred to as the cross state) whereas all of the launched power returns to the same core when $L = 2L_c$ (the bar state). It is important to realize that a directional coupler introduces a relative phase shift of $\pi/2$ between the two output ports, as indicated by the factor i in the off-diagonal term of the transfer matrix in Eq. (2.1.22). This phase shift plays an important role in the design of fiber interferometers (see Chapter 3).

The coupling length depends on the coupling coefficient κ, which in turn depends on the spacing d between the two cores. For a symmetric coupler, the integrals in Eq. (2.1.6) can be evaluated analytically [5]. The resulting expression is somewhat complicated as it involves the Bessel functions. The following empirical expression is useful in practice [10]:

$$\kappa = \frac{\pi V}{2k_0 n_0 a^2} \exp[-(c_0 + c_1 \bar{d} + c_2 \bar{d}^2)], \tag{2.1.24}$$

where V is the fiber parameter (see Section A.1.2), a is the core radius, and $\bar{d} \equiv d/a$ is the normalized center-to-center spacing between the two cores ($\bar{d} > 2$). The constants c_0, c_1, and c_2 depend on V as $c_0 = 5.2789 - 3.663V + 0.3841V^2$, $c_1 = -0.7769 + 1.2252V - 0.0152V^2$, and $c_2 = -0.0175 - 0.0064V - 0.0009V^2$. Equation (2.1.24) is accurate to within 1% for values of V and $\bar{d}$ in the range $1.5 \le V \le 2.5$ and $2 \le \bar{d} \le 4.5$. As an example, $\kappa \sim 1$ cm^{-1} for $\bar{d} = 3$, resulting in a coupling length of 1 cm or so. However, coupling length increases to 1 m or more when $\bar{d}$ exceeds 5.

One may ask whether the proximity of two cores always leads to periodic power transfer between the cores. In fact, the nature of power transfer depends on the launch conditions at the input end. The physics can be better understood by noting that, with a suitable choice of the propagation constant β in Eq. (2.1.2), the mode amplitudes $\tilde{A}_1$ and $\tilde{A}_2$ can be forced to become z independent. From Eqs. (2.1.4) and Eq. (2.1.5), this can occur when the amplitude ratio $f = \tilde{A}_2/\tilde{A}_1$ is initially such that

$$f = \frac{\beta - \bar{\beta}_1}{\kappa_{12}} = \frac{\kappa_{21}}{\beta - \beta_2}, \tag{2.1.25}$$

where the nonlinear contribution has been neglected. Equation (2.1.25) can be used to find the propagation constant β. Since β satisfies a quadratic equation, we find two values of β such that

$$\beta_\pm = \tfrac{1}{2}(\bar{\beta}_1 + \bar{\beta}_2) \pm \sqrt{\delta_a^2 + \kappa^2}. \tag{2.1.26}$$

The spatial distribution corresponding to the two eigenvalues is given by

$$F_\pm(x,y) = (1 + f_\pm^2)^{-1/2}[F_1(x,y) + f_\pm F_2(x,y)], \tag{2.1.27}$$

where $f_\pm$ is obtained from Eq. (2.1.25) using $\beta = \beta_\pm$. These two specific linear combinations of F_1 and F_2 constitute the eigenmodes of a fiber coupler (also called supermodes), and the eigenvalues $\beta_\pm$ correspond to their propagation constants. In the case of a symmetric coupler, $f_\pm = \pm 1$ and the eigenmodes reduce to the even and odd combinations of F_1 and F_2. When the input conditions are such that an eigenmode of the coupler is excited, no power transfer occurs between the two cores.

The periodic power transfer between the two cores, occurring when light is incident on only one core, can be understood using the above modal description as follows. Under such launch conditions, both supermodes of the fiber coupler are excited simultaneously. Each supermode propagates with its own propagation constant. Since β_+ and β_- are not the same, the two supermodes develop a relative phase difference on propagation. This phase difference, $\psi(z) = (\beta_+ - \beta_-)z \equiv 2\kappa_e z$, is responsible for the periodic power transfer between two cores. The situation is analogous to that occurring in birefringent fibers when linearly polarized light is launched at an angle from a principal axis. In that case, the relative phase difference between the two orthogonally polarized eigenmodes leads to periodic evolution of the state of polarization,

and the role of coupling length is played by the beat length (see Chapter A.6). The analogy between fiber couplers and birefringent fibers turns out to be quite useful even when the nonlinear effects are included.

2.1.3 Linear Pulse Switching

In the case of low-energy optical pulses, nonlinear effects can be neglected but the effects of fiber dispersion should be included. For symmetric couplers, the coupled-mode equations, Eqs. (2.1.14) and (2.1.15), become:

$$\frac{\partial A_1}{\partial z} + \frac{i\beta_2}{2}\frac{\partial^2 A_1}{\partial T^2} = i\kappa A_2, \tag{2.1.28}$$

$$\frac{\partial A_2}{\partial z} + \frac{i\beta_2}{2}\frac{\partial^2 A_2}{\partial T^2} = i\kappa A_1, \tag{2.1.29}$$

where $T = t - z/v_g$ is the reduced time and the parameter β_2 accounts for the effects of GVD in each core of the fiber coupler.

We can introduce the dispersion length in the usual way as $L_D = T_0^2/|\beta_2|$, where T_0 is related to the pulse width. The GVD effects are negligible if the coupler length $L \ll L_D$. Since L is comparable in practice to the coupling length ($L_c = \pi/2\kappa$), GVD has no effect on couplers for which $\kappa L_D \gg 1$. Since L_D exceeds 1 km for pulses with $T_0 > 1$ ps whereas $L_c < 1$ m typically, the GVD effects become important only for ultrashort pulses ($T_0 < 0.1$ ps). If we neglect the GVD term in Eqs. (2.1.28) and (2.1.29), the resulting equations become identical to those applicable for CW beams. Thus, picosecond optical pulses should behave in the same way as CW beams. More specifically, their energy is transferred to the neighboring core periodically when such pulses are incident on one of the input ports of a fiber coupler.

The above conclusion is modified if the frequency dependence of the coupling coefficient κ cannot be ignored [11]. It can be included by expanding $\kappa(\omega)$ in a Taylor series around the carrier frequency ω_0 in a way similar to Eq. (2.1.8) so that

$$\kappa(\omega) \approx \kappa_0 + (\omega - \omega_0)\kappa_1 + \tfrac{1}{2}(\omega - \omega_0)^2\kappa_2, \tag{2.1.30}$$

where $\kappa_m = d^m\kappa/d\omega^m$ is evaluated at $\omega = \omega_0$. When the frequency-domain coupled-mode equations are converted to time domain, two additional terms appear. With these terms included, Eqs. (2.1.28) and (2.1.29) become

$$\frac{\partial A_1}{\partial z} + \kappa_1\frac{\partial A_2}{\partial T} + \frac{i\beta_2}{2}\frac{\partial^2 A_1}{\partial T^2} + \frac{i\kappa_2}{2}\frac{\partial^2 A_2}{\partial T^2} = i\kappa_0 A_2, \tag{2.1.31}$$

$$\frac{\partial A_2}{\partial z} + \kappa_1 \frac{\partial A_1}{\partial T} + \frac{i\beta_2}{2}\frac{\partial^2 A_2}{\partial T^2} + \frac{i\kappa_2}{2}\frac{\partial^2 A_1}{\partial T^2} = i\kappa_0 A_1. \qquad (2.1.32)$$

In practice, the κ_2 term is negligible for pulses as short as 0.1 ps. The GVD term is also negligible if $\kappa L_D \gg 1$. Setting $\beta_2 = 0$ and $\kappa_2 = 0$, Eqs. (2.1.31) and (2.1.32) can be solved analytically to yield [11]:

$$A_1(z,T) = \tfrac{1}{2}\left[A_0(T-\kappa_1 z)e^{i\kappa_0 z} + A_0(T+\kappa_1 z)e^{-i\kappa_0 z}\right], \qquad (2.1.33)$$

$$A_2(z,T) = \tfrac{1}{2}\left[A_0(T-\kappa_1 z)e^{i\kappa_0 z} - A_0(T+\kappa_1 z)e^{-i\kappa_0 z}\right], \qquad (2.1.34)$$

where $A_0(T)$ represents the shape of the input pulse at $z = 0$. When $\kappa_1 = 0$, the solution reduces to

$$A_1(z,T) = A_0(T)\cos(\kappa_0 z), \qquad A_2(z,T) = A_0(T)\sin(\kappa_0 z). \qquad (2.1.35)$$

Equation (2.1.35) shows that the pulse switches back and forth between the two cores, while maintaining its shape, when the frequency dependence of the coupling coefficient can be neglected. However, when κ_1 is not negligible, Eq. (2.1.34) shows that the pulse will split into two subpulses after a few coupling lengths, and separation between the two would increase with propagation. This effect is referred to as intermodal dispersion and is similar in nature to polarization-mode dispersion occurring in birefringent fibers (see Chapter A.6). Intermodal dispersion was observed in a 1997 experiment by launching short optical pulses (width about 1 ps) in one core of a dual-core fiber with the center-to-center spacing $d \approx 4a$ [12]. The autocorrelation traces showed the evidence of pulse splitting after 1.25 m, and the subpulses separated from each other at a rate of 1.13 ps/m. The coupling length was estimated to be about 4 mm. Intermodal dispersion in fiber couplers becomes of concern only when the coupler length $L \gg L_c$ and pulse widths are ~ 1 ps or shorter. This effect is neglected in the following discussion of nonlinear effects in fiber couplers.

2.2 Nonlinear Effects

Nonlinear effects in directional couplers were studied starting in 1982 [13]–[33]. An important application of fiber couplers consists of using them for all-optical switching. Figure 2.1 showed schematically how an optical pulse can be directed toward different output ports, depending on its peak power. In this section, we focus on the quasi-CW case and consider a symmetric coupler with identical cores to simplify the discussion.

2.2.1 Quasi-CW Switching

The nonlinear coupled-mode equations for CW beams propagating inside a symmetric coupler are obtained from Eqs. (2.1.14) and (2.1.15) by neglecting the time-derivative terms. The resulting equations are

$$\frac{dA_1}{dz} = i\kappa A_2 + i\gamma(|A_1|^2 + \sigma|A_2|^2)A_1, \tag{2.2.1}$$

$$\frac{dA_2}{dz} = i\kappa A_1 + i\gamma(|A_2|^2 + \sigma|A_1|^2)A_2. \tag{2.2.2}$$

These equations are also applicable for optical pulses wide enough that the dispersion length L_D is much larger than the coupler length L (as the effects of GVD are then negligible). This is referred to as the quasi-CW case.

Equations (2.2.1) and (2.2.2) are similar to those studied in Section A.6.3 in the context of birefringent fibers and can be solved analytically using the same technique. Introducing the powers and phases through

$$A_j = \sqrt{P_j}\exp(i\phi_j), \quad (j = 1, 2), \tag{2.2.3}$$

and defining the phase difference $\phi = \phi_1 - \phi_2$, we obtain the following set of three equations:

$$\frac{dP_1}{dz} = 2\kappa\sqrt{P_1P_2}\sin\phi, \tag{2.2.4}$$

$$\frac{dP_2}{dz} = -2\kappa\sqrt{P_1P_2}\sin\phi, \tag{2.2.5}$$

$$\frac{d\phi}{dz} = \frac{P_2 - P_1}{\sqrt{P_1P_2}}\kappa\cos\phi + \frac{4\kappa}{P_c}(P_1 - P_2), \tag{2.2.6}$$

where the critical power P_c is defined as

$$P_c = 4\kappa/[\gamma(1-\sigma)]. \tag{2.2.7}$$

The critical power level plays an important role since the solution of Eqs. (2.2.4)–(2.2.6) exhibits qualitatively different behavior depending on whether the input power exceeds P_c.

Equations (2.2.4)–(2.2.6) can be solved analytically in terms of the elliptic functions after noting that they have the following two invariants [13]:

$$P_0 = P_1 + P_2, \qquad \Gamma = \sqrt{P_1P_2}\cos\phi - 2P_1P_2/P_c, \tag{2.2.8}$$

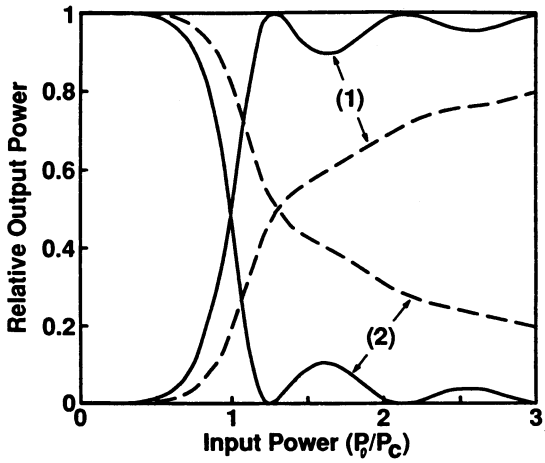

Figure 2.3 Nonlinear switching of CW beams in a fiber coupler with $\kappa L = \pi/2$. Solid lines show relative powers at the two output ports as a function of input power. Dashed lines show the coupler response in the quasi-CW case. (After Ref. [22], ©1989 IEEE)

where P_0 is the total power in both cores. In the specific case in which all the input power is initially launched into one core of a fiber coupler, the power remaining in that core after a distance z is given by

$$P_1(z) = |A_1(z)|^2 = \tfrac{1}{2}P_0[1 + \mathrm{cn}(2\kappa z|m)], \tag{2.2.9}$$

where $\mathrm{cn}(x|m)$ is a Jacobi elliptic function with modulus $m = (P_0/P_c)^2$. The power transferred to the second core is obtained using $P_2(z) = P_0 - P_1(z)$.

In the low-power limit ($m \ll 1$), Eq. (2.2.9) reduces to the result $P_1(z) = P_0\cos^2(\kappa z)$, as it should. Periodic transfer of the power between the two cores persists as long as $P_0 < P_c$ so that $m < 1$. However, as P_0 approaches P_c, the period begins to increase, becoming infinite when $P_0 = P_c$. The solution (2.2.9) reduces to $P_1(z) = \frac{1}{2}P_0[1 + \mathrm{sech}(2\kappa z)]$ when $m = 1$, and at most half of the power is transferred to the second core no matter how long the coupler is. For $P_0 > P_c$, the solution once again becomes periodic but the amount of power transferred to the second core is reduced to below 50% and becomes negligible for $P_0 \gg P_c$.

The solid lines in Fig. 2.3 show the relative powers as a function of the input power at the two output ports of a coupler of length $L = L_c$. For $P_0 \ll P_c$, the launched power is transferred completely to the second core (cross state). For $P_0 > P_c$, little power is transferred to the other core (bar state). Thus, an

optical beam can be switched from one output port to the other, depending on its input power.

The physics behind all-optical switching can be understood by noting that when an optical beam is launched in one core of the fiber coupler, the SPM-induced phase shift is not the same in both cores because of different mode powers. As a result, even a symmetric fiber coupler behaves asymmetrically because of the nonlinear effects. The situation is, in fact, similar to that occurring in asymmetric fiber couplers where the difference in the mode-propagation constants introduces a relative phase shift between the two cores and hinders complete power transfer between them. Here, even though the linear propagation constants are the same, a relative phase shift between the two cores is introduced by SPM. At sufficiently high input powers, the phase difference—or SPM-induced detuning—becomes large enough that the input beam remains confined to the same core in which it was initially launched.

2.2.2 Experimental Results

The experimental observation of optical switching in fiber couplers using CW beams is difficult because of relatively high values of the critical power in silica fibers. We can estimate P_c from Eq. (2.2.7) using appropriate values of κ and γ and setting the XPM parameter $\sigma \approx 0$. If we use $\kappa = 1$ cm^{-1} and $\gamma = 10$ W^{-1}/km as typical values, we find that $P_c = 40$ kW. It is difficult to launch such high CW power levels without damaging silica fibers. A common practical solution is to use short optical pulses with high peak powers but wide enough that the GVD effects are not important (the quasi-CW case).

There is an obvious problem with the use of optical pulses in the quasi-CW regime. Only the central intense part of an input pulse is switched since pulse wings exhibit the low-power behavior. Thus, a nonuniform intensity profile of optical pulses leads to distortion even when the effects of GVD are negligible. As one may expect, pulse distortion is accompanied by degradation in the switching behavior. As an example, the dashed curves in Fig. 2.3 show the response of a fiber coupler to input pulses whose intensity varies as $\operatorname{sech}^2(t/T_0)$. These curves represent relative energy levels in the two cores and are obtained by integrating over the pulse shape. When compared with the case of CW beams, pulse switching is not only more gradual but also incomplete. Less than 75% of the incident peak power remains in the core in which the input pulse is launched even at peak power levels in excess of $2P_c$. This behavior restricts severely the usefulness of fiber couplers as an all-optical switch.

The results shown in Fig. 2.3 do not include the effects of GVD. As one may anticipate, the situation becomes worse in the case of normal GVD because of pulse spreading. However, the performance of fiber couplers should improve significantly for optical pulses experiencing anomalous GVD and propagating as a soliton. The reason is related to the particle-like nature of optical solitons. This topic is covered in Section 2.3.

Nonlinear effects in dual-core fiber couplers were observed starting in 1985, and a clear evidence of high-contrast optical switching had been seen by 1988 [18]–[22]. All of the experiments used short optical pulses propagating in the normal-GVD region of the fiber and, therefore, did not make use of solitons. In the 1985 experiment [18], 80-ns pulses from a frequency-doubled Nd:YAG laser ($\lambda = 0.53\ \mu$m) were focused onto one core of a dual-core fiber. The 2.6-μm-diameter cores were separated by more than 8 μm (center-to-center spacing), resulting in a relatively small value of the coupling coefficient. Nonetheless, the transmitted power from a 18-cm-long coupler was found to increase as the launched peak power increased beyond the 100-W level. In a later experiment, the use of 50-ps pulses from a mode-locked laser provided better evidence of nonlinear switching [19].

In a 1987 experiment, 30-ps pulses from a 1.06-μm Nd:YAG laser were injected into one core of a 2-m-long dual-core fiber in which 5-μm-diameter cores were separated by 8 μm [20]. The critical power P_c was estimated to be 850 W for this coupler, and its length was about 3.8 L_c. At low input power levels, 90% of the pulse energy transferred to the neighboring core. However, the transferred energy was only 40% when the input peak power increased to about 700 W. The switching contrast improved considerably in a 1988 experiment [21] that used 100-fs pulses from a dye laser operating at 0.62 μm. The fiber coupler was only 5-mm long, consisted of two 2.8-μm-diameter cores separated by 8.4 μm, and required 32 kW of peak power for switching to occur. The measured switching characteristics were in good agreement with the theoretical prediction shown by the dashed lines in Fig. 2.3. Fiber dispersion played a relatively minor role even for 100-fs pulses because of the short length of the coupler used in the experiment ($L \ll L_D$). The autocorrelation measurements showed that only the central part of the pulse underwent switching. Use of square-shaped femtosecond pulses in 1989 resulted in considerable improvement since their use avoids the pulse breakup [22]. Figure 2.4 shows the switching characteristics measured using bell-shaped (Gaussian-like) and square-shaped pulses. Not only is the switching contrast better, the

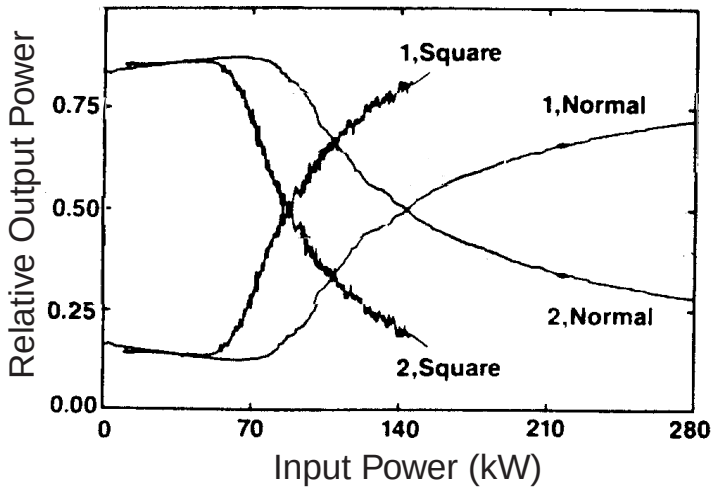

Figure 2.4 Switching data for a fiber coupler of length $L = L_c$. Relative output powers at ports 1 and 2 are shown as a function of input peak power for 90-fs bell-shaped (normal) pulses and 540-fs square-shaped pulses. (After Ref. [22] ©1989 IEEE)

switching peak power is also lower for square pulses.

The high power levels needed for nonlinear switching in fiber couplers have hindered the use of such devices for this purpose. The switching threshold can be reduced by using fibers made with a material whose nonlinear parameter n_2 is much larger compared with that of silica. Several such materials have been used to make fiber couplers. In one case, a dye-doped polymer fiber was used [31]. Both cores of this fiber were doped with a squarylium dye and were embedded in a PMMA polymer cladding. The 6-μm-radius cores were separated by 18 μm. The coupling length was estimated to be about 1 cm. Nonlinear transmission was observed using a Q-switched, mode-locked Nd:YAG laser. In another approach, GeS_2-based chalcohalide glass was used to make the fiber [32]. The nonlinear parameter for this glass was measured to be $n_2 \approx 7.5 \times 10^{-14}$ cm^2/W, a value that is larger by more than a factor of 200 compared with that of silica. As a result, the switching threshold should also be reduced by the same factor. A third approach used a polyconjugated polymer (DPOP-PPV) to make a nonlinear directional coupler [33]. Two-photon absorption plays an important role when dye-doped or semiconductor-doped fibersare used and can affect the switching characteristics adversely.

2.2.3 Nonlinear Supermodes

An alternative approach for understanding the nonlinear effects in fiber couplers makes use of the concept of nonlinear supermodes, which represent optical fields that propagate without any change in spite of the SPM and XPM effects. Mathematically, they represent z-independent solutions (the fixed points) of Eqs. (2.2.4)–(2.2.6) and can be obtained by setting the z derivatives to zero. Here we use an approach based on the rotation of a vector on the Poincaré sphere [16]. Let us introduce the following three real variables (in analogy with the Stokes parameters of Section A.6.3):

$$S_1 = |A_1|^2 - |A_2|^2, \qquad S_2 = 2\,\mathrm{Re}(A_1 A_2^*), \qquad S_3 = 2\,\mathrm{Im}(A_1 A_2^*), \quad (2.2.10)$$

and rewrite Eqs. (2.2.1) and (2.2.2) in terms of them as

$$\frac{dS_1}{dz} = 2\kappa S_3, \quad (2.2.11)$$

$$\frac{dS_2}{dz} = -\gamma(1-\sigma)S_1 S_3, \quad (2.2.12)$$

$$\frac{dS_3}{dz} = \gamma(1-\sigma)S_1 S_2 - 2\kappa S_1. \quad (2.2.13)$$

It can be easily verified from Eqs. (2.2.10)–(2.2.13) that $S_1^2 + S_2^2 + S_3^2 = |A_1|^2 + |A_2|^2 \equiv P_0$, where P_0 is the total power in both cores. Since P_0 is independent of z, the Stokes vector $\mathbf{S}$ with components S_1, S_2, and S_3 moves on the surface of a sphere of radius P_0 as the CW light propagates inside the fiber coupler. This sphere is known as the Poincaré sphere and provides a visual description of the coupler dynamics. In fact, Eqs. (2.2.11)–(2.2.13) can be written in the form of a single vector equation as

$$\frac{d\mathbf{S}}{dz} = \mathbf{W} \times \mathbf{S}, \quad (2.2.14)$$

where $\mathbf{W} = \mathbf{W}_L + \mathbf{W}_{\mathrm{NL}}$ such that $\mathbf{W}_L = 2\kappa\hat{y}$ and $\mathbf{W}_{\mathrm{NL}} = \gamma(1-\sigma)S_1\hat{x}$. Thus, the linear coupling rotates the Stokes vector $\mathbf{S}$ around the y axis while the SPM and XPM rotate it around the x axis. The combination of the two rotations determines the location of the Stokes vector on the Poincaré sphere at a given distance along the coupler length.

Figure 2.5 shows trajectories of the Stokes vector on the Poincaré sphere under three different conditions. In the low-power case, nonlinear effects can

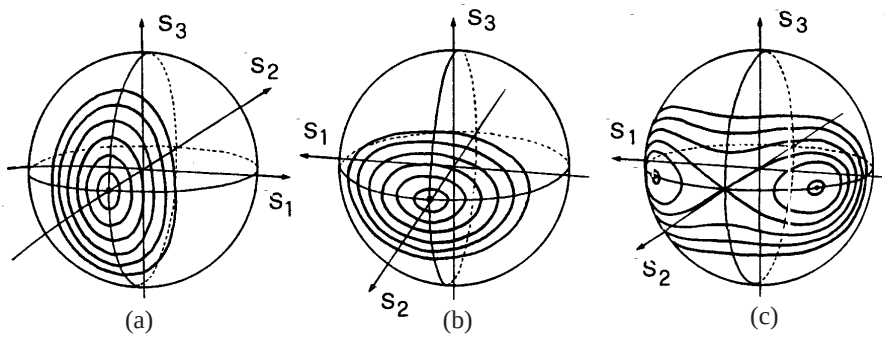

Figure 2.5 Trajectories showing motion of the Stokes vector on the Poincaré sphere. (a) Linear case; (b) $P_0 < P_c$; (c) $P_0 > P_c$. (After Ref. [16])

be neglected by setting $\gamma = 0$. Since $\mathbf{W}_{\rm NL} = 0$ in that case, the Stokes vector rotates around the S_2 or y axis with an angular velocity 2κ [Fig. 2.5(a)]. This is equivalent to the periodic solution obtained earlier. If the Stokes vector is initially oriented along the S_2 axis, it remains fixed. This can also be seen from the steady-state (z-invariant) solution of Eqs. (2.2.11)–(2.2.13) by noting that the Stokes vectors with components $(0, P_0, 0)$ and $(0, -P_0, 0)$ represent two fixed points in the linear case. These fixed points correspond to the even and odd supermodes of a fiber coupler discussed earlier.

In the nonlinear case, the behavior depends on the power level of the incident light. As long as $P_0 < P_c/2$, nonlinear effects play a minor role, and the situation is similar to the linear case, as shown in Fig. 2.5(b). At higher power levels, the motion of the Stokes vector on the Poincaré sphere becomes quite complicated since $\mathbf{W}_L$ is oriented along the y axis while $\mathbf{W}_{\rm NL}$ is oriented along the x axis. Moreover, the nonlinear rotation of the Stokes vector along the x axis depends on the magnitude of S_1 itself. Figure 2.5(c) shows the motion of the Stokes vector when $P_0 > P_c$.

To understand the dynamical behavior, we find the fixed points of Eqs. (2.2.11)–(2.2.13) by setting the z derivatives to zero. The location and the number of fixed points depend on the optical power P_0 launched inside the fiber. More specifically, the number of fixed points changes from two to four at a critical power level $P_0 = P_c/2$, where P_c is given in Eq. (2.2.7). For $P_0 < P_c/2$, only two fixed points, $(0, P_0, 0)$ and $(0, -P_0, 0)$, occur; these are identical to the low-power case. In contrast, when $P_0 > P_c/2$, two new fixed points emerge. The components of the Stokes vector, at the location of the new fixed points

on the Poincaré sphere, are given by [16]

$$S_1 = \pm\sqrt{P_0^2 - P_c^2/4}, \quad S_2 = P_c/2, \quad S_3 = 0. \tag{2.2.15}$$

The new fixed points represent the nonlinear supermodes of a fiber coupler in the sense that when input light excites one of these eigenmodes, the core powers do not change along the coupler length in spite of the close proximity of the two cores. Trajectories near the new fixed points are separated from those occurring near the fixed point $(0, P_0, 0)$ by a separatrix. The nonlinear switching corresponds to the transition from the low-power fixed point $(0, P_0, 0)$ to one of the new fixed points.

2.2.4 Modulation Instability

The CW solution of the coupled-mode equations (the fixed points) can become unstable in the presence of GVD in the same way as a CW beam propagating inside an optical fiber can break up into a pulse train under certain conditions. The modulation instability of couplers is similar in nature to the vector modulation instability discussed in Section A.6.4 since the underlying coupled nonlinear Schrödinger (NLS) equations have the same form. This analogy is not obvious from Eqs. (2.1.14) and (2.1.15) since the XPM term is often negligible in practice. By setting $\sigma = 0$, the coupled NLS equations for a fiber coupler reduce to

$$\frac{\partial A_1}{\partial z} + \frac{i\beta_2}{2}\frac{\partial^2 A_1}{\partial T^2} = i\kappa A_2 + i\gamma|A_1|^2 A_1, \tag{2.2.16}$$

$$\frac{\partial A_2}{\partial z} + \frac{i\beta_2}{2}\frac{\partial^2 A_2}{\partial t^2} = i\kappa A_1 + i\gamma|A_2|^2 A_2, \tag{2.2.17}$$

where we have introduced, as usual, the reduced time $T = t - z/v_g$ to eliminate the group-velocity term.

The analogy between a fiber coupler and a birefringent fiber becomes quite clear if Eqs. (2.2.16) and (2.2.17) are rewritten using the even and odd supermodes of a fiber coupler. For this purpose, we introduce two new variables

$$B_1 = (A_1 + A_2)/\sqrt{2}, \qquad B_2 = (A_1 - A_2)/\sqrt{2} \tag{2.2.18}$$

so that B_1 and B_2 correspond to the amplitudes associated with the even and odd supermodes introduced earlier [see Eq. (2.1.27)]. In terms of the new

variables, Eqs. (2.2.16) and (2.2.17) can be written as [35]

$$\frac{\partial B_1}{\partial z} + \frac{i\beta_2}{2}\frac{\partial^2 B_1}{\partial T^2} - i\kappa B_1 = \frac{i\gamma}{2}[(|B_1|^2 + 2|B_2|^2)B_1 + B_2^2 B_1^*], \quad (2.2.19)$$

$$\frac{\partial B_2}{\partial z} + \frac{i\beta_2}{2}\frac{\partial^2 B_2}{\partial T^2} + i\kappa B_2 = \frac{i\gamma}{2}[(|B_2|^2 + 2|B_1|^2)B_2 + B_1^2 B_2^*]. \quad (2.2.20)$$

The even and odd supermodes are uncoupled linearly but their phase velocities are not the same, as evident from different signs of the κ term in the above two equations. Since light in the even supermode travels more slowly than that in the odd supermode, the even and odd supermodes are analogous to the light polarized along the slow and fast axes in a birefringent fiber. As seen from Eqs. (2.2.19) and (2.2.20), the coupled NLS equations written in terms of the supermodes have three nonlinear terms that correspond to SPM, XPM, and four-wave-mixing-type coupling (identical to the case of birefringent fibers).

The steady-state or CW solution of Eqs. (2.2.19) and (2.2.20) is easily obtained when the input conditions are such that either the even or the odd supermode is excited exclusively. In the case of even supermode, the CW solution is given by

$$\bar{B_1} = \sqrt{P_0}\exp(i\theta), \qquad \bar{B_2} = 0, \quad (2.2.21)$$

where $\theta = (\gamma P_0/2 + \kappa)z$. The solution in the case of odd supermode is obtained from Eq. (2.2.21) by changing the sign of κ and the subscripts 1 and 2. In both cases, the input power remains equally divided between the two cores, with no power exchange taking place between them. In the Poincaré sphere representation, these two CW solutions correspond to the fixed points $(0, P_0, 0)$ and $(0, -P_0, 0)$, as discussed earlier.

We can follow the procedure of Section 5.1 to examine the stability of the CW solution in Eq. (2.2.21). Assuming a time-dependent solution of the form

$$B_1 = (\sqrt{P_0} + b_1)\exp(i\theta), \qquad B_2 = b_2\exp(i\theta), \quad (2.2.22)$$

where b_1 and b_2 are small perturbations, we linearize Eqs. (2.2.19) and (2.2.20) in terms of b_1 and b_2 and obtain a set of two coupled linear equations. These equations can be solved by assuming a solution of the form

$$b_m = u_m \exp[i(K_p z - \Omega T)] + iv_m \exp[-i(K_p z - \Omega T), \quad (2.2.23)$$

where $m = 1$ or 2, Ω is the frequency of perturbation, and K_p is the corresponding wave number.

The four algebraic equations obtained using this technique are found to have an interesting property. The two equations for u_1 and v_1 are coupled, and so are those for u_2 and v_2. However, these two sets of two equations are not coupled. This feature simplifies the analysis considerably. The dispersion relation for the even-mode perturbation b_1 turns out to be

$$K_p^2 = \tfrac{1}{2}\beta_2\Omega^2(\tfrac{1}{2}\beta_2\Omega^2 + \gamma P_0) \tag{2.2.24}$$

and is the same dispersion relation obtained in Section A.5.1 (except for a factor of 2 in the last term). The features associated with modulation instability are thus identical to those found in Section A.5.1. More specifically, no instability occurs in the case of normal GVD. When GVD is anomalous, gain curves are similar to those in Fig. A.5.1.

The new feature for fiber couplers is that, even when CW light is launched initially into the even supermode, perturbations in the odd supermode can grow because of the coupling between the two cores. The odd-mode perturbations satisfy the dispersion relation [35]

$$K_p^2 = (\tfrac{1}{2}\beta_2\Omega^2 - 2\kappa)(\tfrac{1}{2}\beta_2\Omega^2 - 2\kappa + \gamma P_0). \tag{2.2.25}$$

The presence of κ in this equation shows that the coupling between the two cores can lead to a new kind of modulation instability in fiber couplers. Indeed, it is easy to see that K_p becomes complex under certain conditions even in the normal-GVD regime. Introducing the instability gain as $g_0 = 2\,\mathrm{Im}(K_p)$, the gain is given by

$$g_0(f) = 2\kappa[(2 \pm f^2)(4p - 2 \pm f^2)]^{1/2}, \tag{2.2.26}$$

where $f = \Omega/\Omega_c$ is the normalized frequency and $p = P_0/P_c$ is the normalized input power. They are introduced using

$$\Omega_c = \sqrt{\frac{2\kappa}{|\beta_2|}}, \qquad P_c = \frac{4\kappa}{\gamma} \tag{2.2.27}$$

The critical power P_c is the same as defined earlier in Eq. (2.2.7) since $\sigma = 0$ has been assumed. The choice of sign in Eq. (2.2.26) depends on the sign of the GVD parameter β_2; a minus sign is chosen for anomalous GVD.

Figure 2.6 shows the gain spectra of modulation instability for both normal and anomalous GVD. In both cases, the gain exists at low frequencies, including $\Omega = 0$. This feature is similar to the polarization instability occurring in

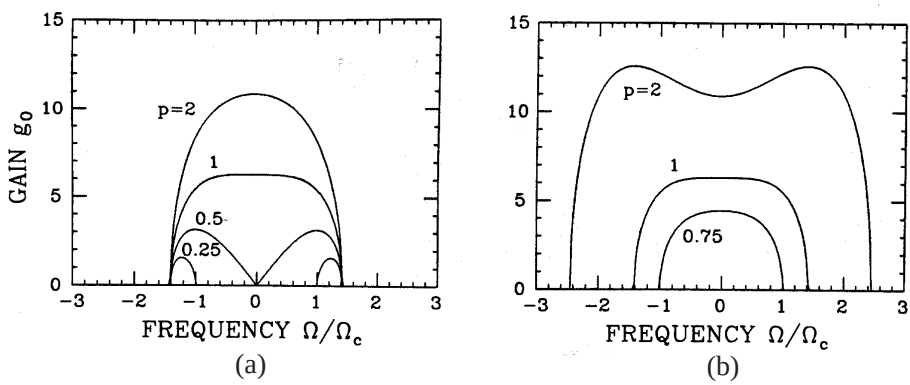

Figure 2.6 Gain spectra of modulation instability at several power levels in the cases of (a) normal and (b) anomalous GVD.

birefringent fibers (see Chapter A.6). The gain at $\Omega = 0$ occurs only when the input power exceeds $P_c/2$ ($p > 0.5$). This is related to the appearance of the two new fixed points on the Poincaré sphere (see Fig. 2.5). When GVD is normal, the gain peak occurs at $\Omega = 0$ only when $p > 1$. Thus, when the input power P_0 exceeds P_c, modulation instability is static in nature and does not lead to self-pulsing. In contrast, when GVD is anomalous, the gain peak occurs at $\Omega \neq 0$ for $p > 1$. In this case, CW light can be converted into a pulse train whose repetition rate depends on the input power. The repetition rate is close to $\Omega_c/2\pi$ and is estimated to be ~ 1 THz for typical values of κ and β_2.

Direct experimental observation of modulation instability in fiber couplers is hampered by the fact that it is difficult to excite the even or odd supermode alone. Typically, initial conditions are such that both supermodes are excited simultaneously. Another difficulty is related to the relatively short coupler lengths used in practice ($L \sim L_c$). The growth of sidebands from noise (spontaneous modulation instability) requires the use of dual-core fibers for which $L \gg L_c$ is possible. The effects of induced modulation instability can be observed using shorter lengths since sidebands are seeded by an input signal. As an example, induced modulation instability can be used to control switching of a strong pump beam launched in one core of the coupler through a much weaker signal launched into the other core with an appropriate relative phase [17].

2.3 Ultrashort Pulse Propagation

Because of the high power levels needed for all-optical switching in fiber couplers, optical pulses are often used in practice. For short pulses, the GVD term in the coupled-mode equations can affect the switching behavior considerably, and its effects have been studied extensively [34]–[60]. This section considers propagation of ultrashort optical pulses in fiber couplers, with emphasis on soliton effects.

2.3.1 Nonlinear Switching of Optical Pulses

To discuss pulse switching, it is useful to normalize Eqs. (2.2.16) and (2.2.17) using soliton units (see Section A.5.3) and write them as

$$i\frac{\partial u}{\partial \xi} - \frac{s}{2}\frac{\partial^2 u}{\partial \tau^2} + |u|^2 u + Kv = 0, \tag{2.3.1}$$

$$i\frac{\partial v}{\partial \xi} - \frac{s}{2}\frac{\partial^2 v}{\partial \tau^2} + |v|^2 v + Ku = 0, \tag{2.3.2}$$

where $s = \text{sgn}(\beta_2) = \pm 1$, $K = \kappa L_D$, and we have introduced the following normalized variables:

$$\xi = z/L_D, \quad \tau = T/T_0, \quad u = (\gamma L_D)^{1/2} A_1, \quad v = (\gamma L_D)^{1/2} A_2. \tag{2.3.3}$$

Here $L_D = T_0^2/|\beta_2|$ is the dispersion length and T_0 is a measure of the pulse width. For $K = 0$, these equations reduce to two uncoupled NLS equations.

The coupled NLS equations, Eqs. (2.3.1) and (2.3.2), cannot be solved analytically in general. They have been solved numerically using the split-step Fourier method of Section A.2.4. The switching behavior depends on whether GVD is normal or anomalous. As early as 1988, numerical simulations indicated that solitons, forming in the case of anomalous GVD, switch between the cores as an entire pulse in a manner analogous to the CW case [34]. In contrast, switching ceases to occur in the normal-dispersion regime if pulses are short enough that the dispersion length L_D becomes comparable to the coupling length L_c [36]. Soliton switching is, in fact, superior to the quasi-CW switching realized using relatively broad pulses.

Figure 2.7 compares the switching characteristics of fiber couplers in these two cases. These results are obtained by solving Eqs. (2.3.1) and (2.3.2) with the initial conditions

$$u(0,\tau) = N\,\text{sech}(\tau), \qquad v(0,\tau) = 0. \tag{2.3.4}$$

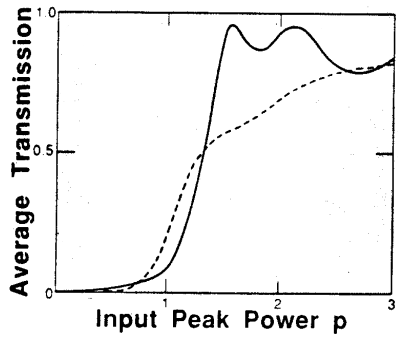

Figure 2.7 Transmitted pulse energy as a function of $p = P_0/P_c$ in the case of solitons (solid line) and quasi-CW pulses (dashed line) for a coupler of length $L = L_c$. (After Ref. [34])

The amplitude N is related to the peak power P_0 of the input pulse as $N^2 = \gamma L_d P_0 = 4Kp$, where $p = P_0/P_c$ is normalized to the CW switching power P_c. If we choose $K = 1/4$, N equals 1 when $p = 1$; that is, the input pulse propagates as a fundamental soliton when $P_0 = P_c$. The fraction of the pulse energy appearing in the core in which a soliton is initially launched is plotted as a solid line in Fig. 2.7 for values of p in the range from 0 to 3. The switching behavior near $p = 1$ for solitons is almost identical to that of a CW beam (compare with Fig. 2.5). Since $L = L_c \sim L_D$ is required for soliton switching to occur, the input pulse width and peak power should be about 0.1 ps and 1 kW, respectively, for a 1-m-long fiber coupler. Because of relatively short propagation distances involved, higher-order dispersive effects are not likely to affect the switching behavior considerably, unless pulses become much shorter than 100 fs.

The exact value of N required for switching depends on the choice of the single parameter K appearing in Eqs. (2.3.1) and (2.3.2). As an example, when $K = 1$, $p = 1$ is realized only when $N = 2$ since $N^2 = 4Kp$. The switching behavior in this case is shown in Fig. 2.8, where evolution of $|u|^2$ and $|v|^2$ along the coupler length is shown for $N = 1$ and 2. Since the first-order soliton is below the switching threshold, most of its power is transferred to the neighboring core at a distance $\xi = \pi/2$. In contrast, the second-order soliton keeps most of its power in the original core since $p = 1$ for it. The switching threshold appears to be below $p = 1$, in contrast with the results shown in Fig. 2.7. The reason can be understood by noting that a second-order soliton undergoes

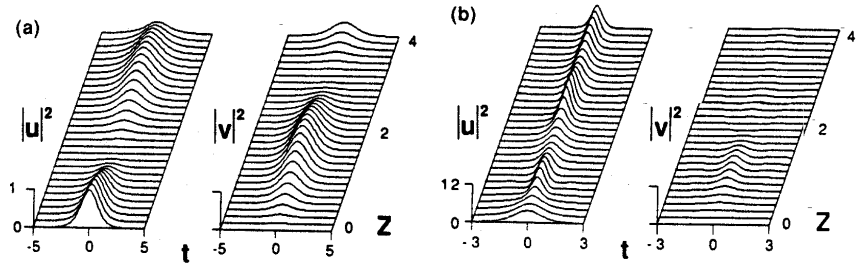

Figure 2.8 Evolution of pulses in two cores of a fiber coupler with coupling length $L_c = \pi L_D/2$ when an input pulse is launched in one core with (a) $N = 1$ and (b) $N = 2$. (After Ref. [34])

compression initially, resulting in higher peak powers. In fact, the pulse is compressed enough that the value of N at the output end is close to 1. The important point to note is that the entire pulse switches from one core to another. In the absence of the soliton effects, pulses are severely distorted since only central part is intense enough to undergo switching. Physically, this behavior is related to the fact that a fundamental soliton has the same phase over the entire pulse width in spite of SPM. A weak pulse, launched at the other input port, can also force a soliton to switch between the two output ports [37]. All-optical ultrafast logic gates have also been proposed using asymmetric fiber couplers [38].

2.3.2 Variational Approach

Particle-like switching of solitons suggests the use of a classical mechanics technique based on the Hamiltonian or Lagrangian formulation. Such an approach offers considerable physical insight [40]–[45]. The variational technique was first used in 1990 for solving Eqs. (2.3.1) and (2.3.2) approximately [41]. However, the width of solitons was assumed to remain constant in spite of changes in their amplitudes. As discussed in Chapter A.5, the width and the amplitude of a soliton are related inversely when solitons evolve adiabatically. This section discusses the adiabatic case [43].

In the Lagrangian formalism, Eqs. (2.3.1) and (2.3.2) are derived from the Euler–Lagrange equation

$$\frac{\partial}{\partial \xi}\left(\frac{\partial L_g}{\partial q_\xi}\right) + \frac{\partial}{\partial \tau}\left(\frac{\partial L_g}{\partial q_\tau}\right) - \frac{\partial L_g}{\partial q} = 0, \tag{2.3.5}$$

where q represents u, u^*, v, or v^*; the subscripts τ and ξ denote differentiation with respect to that variable; and the Lagrangian density L_g is given by [41]

$$L_g = \frac{i}{2}(u^* u_\xi - u u_\xi^*) + \frac{1}{2}(|u|^4 - |u_\tau|^2) + \frac{i}{2}(v^* v_\xi - v v_\xi^*) + \frac{1}{2}(|v|^4 - |v_\tau|^2) + K(u^* v + u v^*). \tag{2.3.6}$$

The crucial step in the variational analysis consists of choosing an appropriate functional form of the solution. In the case of adiabatic evolution, we anticipate solitons to maintain their "sech" shape even though their amplitude, width, and phase can change. We thus assume that

$$u(\xi,\tau) = \eta_1 \operatorname{sech}(\eta_1 \tau) e^{i\phi_1}, \qquad v(\xi,\tau) = \eta_2 \operatorname{sech}(\eta_2 \tau) e^{i\phi_2}, \tag{2.3.7}$$

where η_j is the amplitude and ϕ_j is the phase for the soliton propagating in the jth core of the coupler. Both η_j and ϕ_j are assumed to vary with ξ. The soliton width also changes with its amplitude, as expected. Note that solitons in both cores are assumed to remain unchirped. In general, one should also include chirp variations [55].

The next step consists of integrating the Lagrangian density over τ using $\bar{L}_g = \int_{-\infty}^{\infty} L_g \, d\tau$. The result is given by

$$\bar{L}_g = \frac{1}{3}(\eta_1^2 + \eta_2^2) - 2\eta_1 \frac{d\phi_1}{d\xi} - 2\eta_2 \frac{d\phi_2}{d\xi} + K\eta_1\eta_2 \cos(\phi_1 - \phi_2) \int_{-\infty}^{\infty} \operatorname{sech}(\eta_1 \tau) \operatorname{sech}(\eta_2 \tau) \, d\tau. \tag{2.3.8}$$

Using Eq. (2.3.8) in the Euler–Lagrange equation, we obtain a set of four ordinary differential equations for η_j and ϕ_j $(j = 1, 2)$. These equations can be simplified by noting that $\eta_1 + \eta_2 \equiv 2\eta$ is a constant of motion. Furthermore, the total phase $\phi_1 + \phi_2$ does not play a significant role since $\bar{L}_g$ depends only on the relative phase difference $\phi = \phi_1 - \phi_2$. Introducing a new dynamical variable

$$\Delta = (\eta_1 - \eta_2)/(\eta_1 + \eta_2), \qquad |\Delta| \le 1, \tag{2.3.9}$$

the switching dynamics is governed by the equations

$$\frac{d\Delta}{dZ} = G(\Delta) \sin\phi, \qquad \frac{d\phi}{dZ} = \mu\Delta + \cos\phi \frac{dG}{d\Delta}, \tag{2.3.10}$$

where $Z = 2K\xi \equiv 2\kappa z$, $\mu = \eta^2/K$, and

$$G(\Delta) = \int_0^\infty \frac{(1-\Delta^2)\,dx}{\cosh^2 x + \sinh^2(x\Delta)}. \tag{2.3.11}$$

The parameter η is related to the total energy Q of both solitons as

$$Q = \int_{-\infty}^{\infty} (|u|^2 + |v|^2)\,d\tau = 2(\eta_1 + \eta_2) \equiv 4\eta. \tag{2.3.12}$$

Equations (2.3.10) can be integrated easily by noting that they can be derived from the Hamiltonian

$$H(\Delta, \phi) = -\tfrac{1}{2}\mu\Delta^2 - G(\Delta)\cos\phi. \tag{2.3.13}$$

As a result, Δ and ϕ can be treated as the generalized coordinate and momentum of a fictitious particle. This analogy permits us to describe the switching dynamics of solitons in the Δ–ϕ phase plane. The qualitative behavior depends on the parameter μ. To understand soliton switching, we first find the fixed points of Eqs. (2.3.10) by setting the Z derivatives to zero. Two fixed points are given by $\Delta = 0$ with $\phi = 0$ or π. Since both solitons have equal energy when $\Delta = 0$, these fixed points correspond to the even and odd supermodes found earlier in the CW case.

Two other fixed points of Eqs. (2.3.10) correspond to the situation in which the soliton is confined to only one core and are given by

$$\Delta = \pm 1, \qquad \cos\phi = 2\mu/\pi. \tag{2.3.14}$$

They exist only for $\mu < \pi/2$ and are always unstable. For $\mu > \pi/2$, two new fixed points emerge for which $\sin\phi = 0$ and Δ is obtained from the implicit relation $\mu\Delta = -(dG/d\Delta)$. In the limit of small Δ, the integral in Eq. (2.3.13) can be performed analytically with the approximation

$$G(\Delta) \approx (1-\Delta^2)(1-\alpha\Delta^2), \tag{2.3.15}$$

with $\alpha = (\pi^2/6 - 1)/3 \approx 0.215$. These fixed points disappear when $\mu > \mu_c = 2(1+\alpha) \approx 2.43$. In this region, the even-mode fixed point is also unstable.

Figure 2.9 shows trajectories in the Δ–ϕ phase plane in three regimes with different sets of fixed points. The various trajectories correspond to different launch conditions at the input end of the fiber coupler. Consider the case in

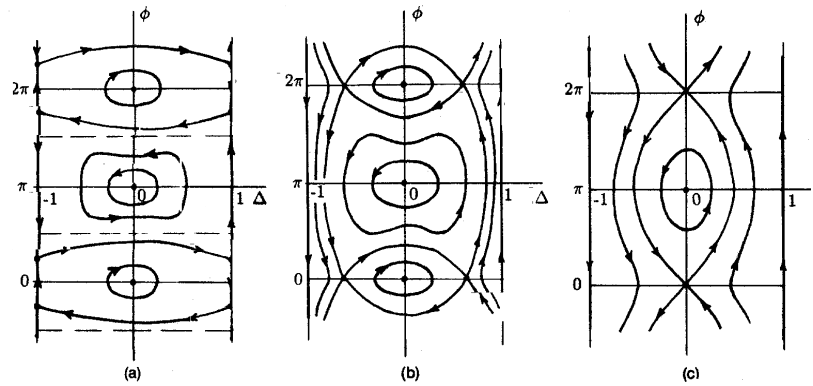

Figure 2.9 Phase-space trajectories in three different regimes corresponding to (a) $\mu < \pi/2$, (b) $\pi/2 < \mu < \mu_c$, and (c) $\mu > \mu_c$. (After Ref. [43])

which a single soliton is launched in one core such that $\eta_2(0) = 0$ or $\Delta(0) = 1$. The parameter μ is then related to the peak power P_0 of the launched soliton as $\mu = P_0/P_c$, where P_c is the CW critical power introduced earlier. As long as $\mu < \pi/2$, the soliton exhibits the same behavior as a low-power CW beam. More specifically, its energy will oscillate between the two cores in a periodic manner.

Nonlinear switching occurs in the region $\pi/2 < \mu < \mu_c$ since most of the soliton energy remains in the core in which the pulse is launched initially. This feature is equivalent to the CW switching discussed earlier except that the required peak power P_0 is larger by a factor of $\pi/2$. This increase is not surprising since even the low-power wings of the soliton switch together with its peak as one unit. Finally, when $\mu > \mu_c$, soliton energy oscillates around the stable point located at $\Delta = 0$ and $\phi = \pi$ (the odd supermode). Nonlinear switching is incomplete in this case. The main point to note is that whole-pulse switching of solitons is feasible with a proper control of soliton energy.

The CW-like switching behavior of solitons can be seen even more clearly if the soliton width is assumed to remain constant in spite of amplitude changes; that is, the ansatz (2.3.7) is replaced with [41]

$$u(\xi,\tau) = \eta_1 \operatorname{sech}(\tau) e^{i\phi_1}, \qquad v(\xi,\tau) = \eta_2 \operatorname{sech}(\tau) e^{i\phi_2}. \tag{2.3.16}$$

In this case, the integral in Eq. (2.3.11) can be evaluated analytically. Since $G(\Delta)$ is then known, Eqs. (2.3.10) can be integrated in a closed form in terms of the elliptic functions. Introducing the peak powers P_1 and P_2 using $\eta_j^2 =$

$\gamma L_D P_j$ $(j = 1,2)$, P_1 is found to vary along the coupler length as

$$P_1(z) = \tfrac{1}{2}P_0[1 + \mathrm{cn}(2\kappa z|m)], \tag{2.3.17}$$

where the modulus of the Jacobi elliptic function is given by $m = (2P_0/3P_c)^2$, where P_c is the CW critical power. This solution is identical to the CW case except that the critical power for switching is larger by a factor of 3/2. This value compares reasonably well with the enhancement factor of $\pi/2$ predicted before using Eqs. (2.3.10). The variational analysis also predicts a symmetry-breaking bifurcation at $m = 1/2$. At this value, the symmetric solution, with equal peak powers in the two cores, becomes unstable and is replaced with an asymmetric solution [41].

The variational analysis based on Eq. (2.3.7) assumes that solitons remain unchirped. More accurate results are obtained when both pulse width and chirp are allowed to evolve along the coupler length [55]. The variational approach has also been used to study the influence of XPM on soliton switching [44] by including the XPM term appearing in Eqs. (2.1.14) and (2.1.15). For the relatively small values of the XPM parameter σ that are relevant for fiber couplers, the effect of XPM is to increase the critical power as seen in Eq. (2.2.7). When σ becomes close to 1, the XPM modifies the switching characteristics considerably. In the limiting case of $\sigma = 1$, Eqs. (2.1.14) and (2.1.15) are integrable by the inverse scattering method [61].

2.4 Coupler-Paired Solitons

A different approach for studying the nonlinear effects in directional couplers focuses on finding the soliton pairs that can propagate through the coupler without changes in their amplitude and width in spite of the coupling induced by the proximity of the two cores. Such soliton pairs are analogous to the XPM-paired solitons discussed in Chapter A.7 except that the coupling between the two solitons is linear in nature. Several analytic solutions of Eqs. (2.3.1) and (2.3.2) have been obtained under different conditions [46]–[49]. It should be stressed that, strictly speaking, such solutions represent not solitons but solitary waves since Eqs. (2.3.1) and (2.3.2) are not integrable by the inverse scattering method.

The shape-preserving solutions of Eqs. (2.3.1) and (2.3.2) can be found by assuming a solution in the form [47]

$$u(\xi,\tau) = U(\tau)e^{iq\xi}, \qquad v(\xi,\tau) = V(\tau)e^{iq\xi}, \tag{2.4.1}$$

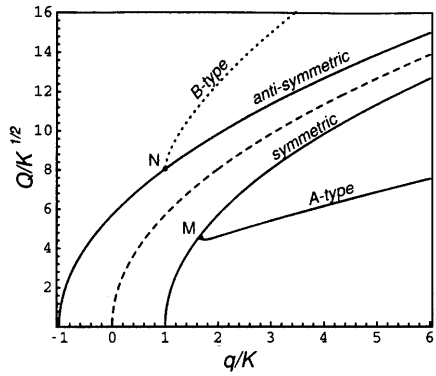

Figure 2.10 Energy Q and wave number K of soliton pairs that can propagate along the fiber coupler without change in their shape. (After Ref. [48], ©1993 by the American Physical Society)

where q is a constant representing change in the wave number (from its value β). The amplitudes U and V are ξ independent and govern the shape of the two pulses representing the soliton pair. By substituting Eq. (2.4.1) in Eqs. (2.3.1) and (2.3.2), U and V are found to satisfy the following set of two coupled ordinary differential equations:

$$\frac{1}{2}\frac{d^2U}{d\tau^2} + U^3 + KV - qU = 0, \tag{2.4.2}$$

$$\frac{1}{2}\frac{d^2V}{d\tau^2} + V^3 + KU - qV = 0, \tag{2.4.3}$$

where the GVD is taken to be anomalous by choosing $s = -1$.

Equations (2.4.2) and (2.4.3) can be solved analytically when $V = \pm U$ since they reduce to a single equation of the same form obtained in Chapter A.5. The resulting two solutions are given by

$$U(\tau) = V(\tau) = \sqrt{2(q-K)}\,\mathrm{sech}[\sqrt{2(q-K)}\tau], \tag{2.4.4}$$

$$U(\tau) = -V(\tau) = \sqrt{2(q+K)}\,\mathrm{sech}[\sqrt{2(q+K)}\tau]. \tag{2.4.5}$$

The solution (2.4.4) is called the symmetric state and exists only for $q > K$. The solution (2.4.5) represents an antisymmetric state and exists for all $q > -K$. These two solutions correspond to the even and odd supermodes introduced in Section 2.1.2. In both cases, identical pulses propagate in the two cores with the only difference being that they are in phase ($U = V$) for the even

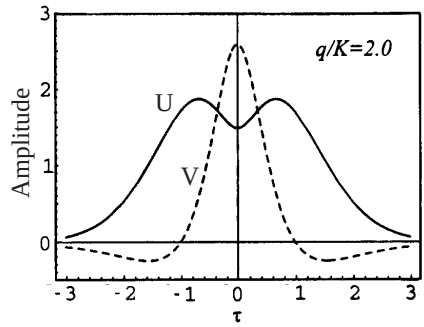

Figure 2.11 Example of B-type asymmetric soliton pair supported by a fiber coupler. (After Ref. [47], ©1993 by the American Physical Society)

supermode but out of phase ($U = -V$) for the odd supermode. The total energy of both solitons can be calculated using Eq. (2.3.12) and is given by $Q(K) = 4\sqrt{2(q \pm K)}$, where the minus sign corresponds to the symmetric state.

The symmetric and antisymmetric states represent soliton pairs with equal pulse energies in two cores of a fiber coupler. Depending on the total energy Q associated with the soliton pair, Eqs. (2.4.2) and (2.4.3) also have asymmetric solutions such that pulse energies are different in the two cores. The pulse shapes for such solutions are found numerically. Figure 2.10 shows possible solutions in the q–Q phase space [47]. The point M marks the location ($q/K = 5/3$) where the symmetric state bifurcates and results in soliton pairs with different amplitudes (A-type branch). The point N marks the location ($q/K = 1$) where the antisymmetric state bifurcates toward the B-type branch. The new feature of solitons on this branch is that their shape can be quite complicated with multiple humps. Figure 2.11 shows an example of the shapes associated with a soliton pair on the B-type branch.

Stability of soliton pairs can be examined using an extension of the modulation-stability analysis of Section 2.2.4. In this approach, the soliton state is perturbed as

$$u(\xi,\tau) = [U(\tau) + a_1(\xi,\tau)]e^{iq\xi}, \qquad v(\xi,\tau) = [V(\tau) + a_2(\xi,\tau)]e^{iq\xi}, \quad (2.4.6)$$

where perturbations a_1 and a_2 vary with both ξ and τ. If the perturbations grow exponentially with ξ, the corresponding soliton pair is unstable. The results of such a stability analysis are shown by dashed lines in Fig. 2.10 and can be summarized as follows [48]. Symmetric states are stable up to the bifurcation

point M in Fig. 2.10 and become unstable after that. The antisymmetric states are unstable for $q/K > -0.6$. Asymmetric solutions are always unstable on the B branch and stable on the A branch only if the slope $dQ/dq > 0$. Since the slope is negative in a small range—$5/3 < q/K < 1.85$—the asymmetric solutions on the A branch are stable except for a tiny region near the bifurcation point M. The existence of this tiny unstable region on the A branch implies that the symmetry-breaking bifurcation occurring at the point M is subcritical and leads to hysteresis with respect to pulse energy Q (first-order phase transition in the language of thermodynamics). It should be stressed that instability of a solution in Fig. 2.10 only indicates that the corresponding soliton pair cannot propagate without changes in its shape, width, or amplitude. In other words, the solid lines in Fig. 2.10 are analogous to the stable fixed points of the CW or the variational analysis.

Numerical simulations have been used to explore the propagation dynamics when the launch conditions at the input end of a fiber coupler do not correspond to a stable soliton pair [49]. The results show that if the input parameters are not too far from a stable point in Fig. 2.10, solitons exhibit oscillations around the stable state while losing a part of their energy through continuum radiation. The variational analysis should be used with caution in this case since it assumes a fixed "sech" shape *a priori* and does not include radiative energy losses. Such losses are relatively small for short couplers but must be accounted for when $L \gg L_c$.

In the case of normal dispersion, one should choose $s = 1$ in Eqs. (2.3.1) and (2.3.2). As discussed in Section A.5.3, the NLS equation supports dark solitons in each core in the absence of coupling. One may thus ask whether the coupled NLS equations have solutions in the form of dark-soliton pairs. This turns out to be the case. Mathematically, one can follow the same procedure adopted above and assume the solution of the form given in Eq. (2.4.1). The resulting equations for U and V are identical to Eqs. (2.4.2) and (2.4.3) except for a change in the sign of the second derivative term. These equations have the following symmetric and antisymmetric dark-soliton pairs [54]:

$$U(\tau) = V(\tau) = \sqrt{q-K}\tanh(\sqrt{q-K}\tau), \tag{2.4.7}$$

$$U(\tau) = -V(\tau) = \sqrt{q+K}\tanh(\sqrt{q+K}\tau). \tag{2.4.8}$$

Asymmetric dark-soliton pairs also exist after a bifurcation point on the symmetric branch, but their properties are quite different from those associated with the bright-soliton pairs.

2.5 Extensions and Applications

The discussion of nonlinear effects has so far focused on symmetric fiber couplers whose cores are identical in all respects. There are several different ways in which two cores can become dissimilar. For example, the cores may have different shapes or sizes. This case was discussed in Section 2.1 but the nonlinear effects were neglected. Nonlinear phenomena in asymmetric couplers can lead to new effects. An interesting situation occurs when the cores have different dispersive properties (normal versus anomalous). Cores can also be made different by selective doping and pumping. An example is provided by couplers in which one core is doped with erbium ions and pumped externally to provide gain. As another example, a Bragg grating can be integrated in one or both cores; such devices are called grating-assisted directional couplers. This section considers several extensions of the basic coupler design and discusses their practical applications.

2.5.1 Asymmetric Couplers

Nonlinear effects in asymmetric couplers with dissimilar cores have attracted increasing attention in recent years [62]–[66]. Several new effects can occur in directional couplers with cores of different sizes. Mathematically, we use Eqs. (2.1.9) and (2.1.10). In soliton units, these equations become

$$i\frac{\partial u}{\partial \xi}+\frac{1}{2}\frac{\partial^2 u}{\partial \tau^2}+|u|^2u+Kv+d_pu=0, \tag{2.5.1}$$

$$i\frac{\partial v}{\partial \xi}+id_g\frac{\partial u}{\partial \tau}+\frac{d_2}{2}\frac{\partial^2 v}{\partial \tau^2}+d_n|v|^2v+Ku-d_pu=0, \tag{2.5.2}$$

where we used normalized variables as defined in Eq. (2.3.3), assumed that GVD in one core is anomalous ($\beta_{21}<0$), and introduced the following four parameters related to the asymmetric nature of the coupler:

$$d_p=\delta_aL_D,\quad d_g=(\beta_{12}-\beta_{11})L_D/T_0,\quad d_2=\beta_{22}/\beta_{21},\quad d_n=\gamma_2/\gamma_1. \tag{2.5.3}$$

Physically, d_p and d_g represent, respectively, phase- and group-velocity mismatch while d_2 and d_n account for differences in the dispersive properties and effective core areas, respectively. The parameter d_2 can be negative if the GVD in the second core is normal.

The presence of four new parameters in the coupled NLS equations makes the analysis of asymmetric couplers quite involved. Differences in the GVD

parameters result from the waveguide contribution to GVD that depends on the core size. If the operating wavelength is close to the zero-dispersion wavelength of the fiber, small changes in the core shape and size can induce large enough changes in dispersion that even the nature of GVD (normal versus anomalous) can be different for the two cores. In contrast, if the operating wavelength is far from the zero-dispersion wavelength, the GVD parameters are nearly the same in both cores. We consider the latter case and assume that the two cores are similar enough that we can set $d_g = 0$, $d_2 = 1$, and $d_n = 1$ in Eqs. (2.5.1) and (2.5.2). The asymmetry in such couplers is due only to different phase velocities in the two cores.

We can use the same method used earlier to find the stationary soliton pairs that propagate without change in their shape. By substituting Eq. (2.4.1) in Eqs. (2.5.1) and (2.5.2), U and V are found to satisfy the following set of two ordinary differential equations:

$$\frac{1}{2}\frac{d^2U}{d\tau^2} + U^3 + KV - (q - d_p)U = 0, \tag{2.5.4}$$

$$\frac{1}{2}\frac{d^2V}{d\tau^2} + V^3 + KU - (q + d_p)V = 0. \tag{2.5.5}$$

These equations should be solved numerically to find $U(\tau)$ and $V(\tau)$. A variational technique can be used with a Gaussian-shaped ansatz [65]. The phase diagram in the q–Q plane [see Eq. (2.3.12) for the definition of Q] turns out to be quite different compared with that of Fig. 2.10 when $d_p \neq 0$. This is not surprising as all solutions for asymmetric couplers must be asymmetric such that $|U| \neq |V|$. However, one still finds solutions such that U and V have the same sign. Since the relative phase between the two components is zero, such in-phase solitons are analogous to the symmetric state such that $U > V$ when $d_p > 0$. Similarly, one finds out-of-phase soliton pairs that are analogous to the asymmetric state in the sense that U and V have opposite signs. It turns out that $|V| > |U|$ for such solitons when $d_p > 0$. In both cases, more and more energy remains confined to one core as $|d_p|$ becomes larger. This feature can be understood from Eqs. (2.5.4) and (2.5.5) by solving them in the limit of large $|d_p|$. If both the dispersive and nonlinear terms are neglected, q can have two values given by

$$q = \pm\sqrt{d_p^2 + K^2} \approx \pm d_p, \tag{2.5.6}$$

and the solutions corresponding to these values of q satisfy

$$U \approx 2d_pV, \qquad U \approx -V/(2d_p). \tag{2.5.7}$$

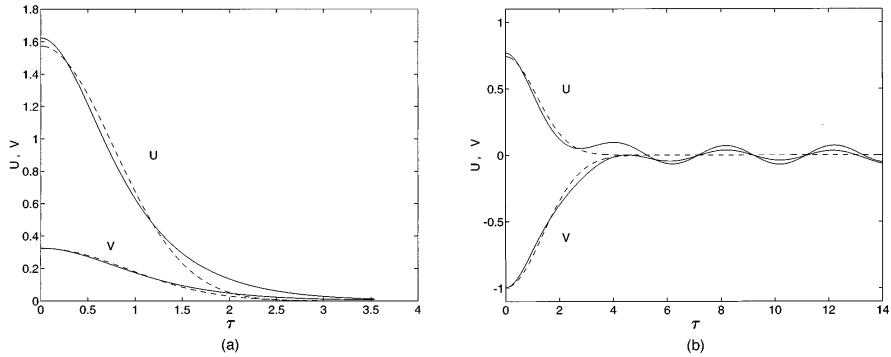

Figure 2.12 Pulse amplitudes associated with the (a) in-phase and (b) out-of-phase soliton pairs. Dashed curves show the Gaussian approximation based on the variational analysis. (After Ref. [65])

Clearly, almost all energy remains in one core of the coupler for large d_p.

A third solution of Eqs. (2.5.4) and (2.5.5) is found when $|d_p|$ exceeds a critical value [65]. The components U and V have opposite signs for this solution, and most of the energy is confined to one of them. The exact range of $|d_p|$ over which the third solution occurs depends on both K and the total energy Q. In fact, depending on the value of Q, only in-phase soliton pairs may exist for some values of $|d_p|$. Bistable behavior can also occur when Q is large enough.

The shapes and energies of the two solitons are quite different for the in-phase and out-of-phase solitons. Numerical solutions of Eqs. (2.5.4) and (2.5.5) show that soliton pairs for which U and V have the same signs are localized in the sense that their amplitude decreases exponentially far away from the center [65]. In contrast, soliton pairs for which U and V have opposite signs (out-of-phase solitons) are delocalized such that their amplitude oscillates and does not decrease to zero even far away from the center. Figure 2.12 shows an example of these two types of soliton pairs for $Q = 2$.

The effect of GVD mismatch between the two cores—governed by the parameter d_2 in Eqs. (2.5.1) and (2.5.2)—is even more interesting, especially in the case in which the GVD is normal in the second core [66]. The most striking new feature is related to the existence of gap solitons, similar to those found for Bragg gratings (see Section 1.6), that occur inside a gap region in which light cannot propagate when nonlinear effects are weak. Moreover, such bright solitons carry most of their energy in the core with normal GVD. The

shape of the soliton components U and V exhibits oscillatory tails that decay exponentially far away from the pulse center.

2.5.2 Active Couplers

Fiber losses are typically neglected in the context of fiber couplers. This is justified in view of short fiber lengths used in practice (typically $L < 10$ m) and relatively low losses associated with silica fibers. The situation is different when one or both cores of a coupler are doped with a rare-earth element such as erbium. The doped core will absorb considerable light when its wavelength is close to an atomic resonance or will amplify the propagating signal if that core is externally pumped to provide gain (see Chapter 4). The pumping level can be different for the two cores, resulting in different gains, or one core may be left unpumped. Because of differences in the amount of gain or loss in the two cores, doped couplers behave asymmetrically even if both cores are identical in shape and size. Such couplers are sometimes called *active directional couplers* and can be useful for a variety of applications [67]–[73].

To understand operation of such devices, we use Eqs. (2.3.1) and (2.3.2), appropriate for a symmetric coupler, but add an extra gain term [67]:

$$i\frac{\partial u}{\partial \xi} - \frac{s}{2}\frac{\partial^2 u}{\partial \tau^2} + |u|^2 u + Kv = \frac{i}{2} g_1 L_D \left(u + b\frac{\partial^2 u}{\partial \tau^2} \right), \tag{2.5.8}$$

$$i\frac{\partial v}{\partial \xi} - \frac{s}{2}\frac{\partial^2 v}{\partial \tau^2} + |v|^2 v + Ku = \frac{i}{2} g_2 L_D \left(v + b\frac{\partial^2 v}{\partial \tau^2} \right), \tag{2.5.9}$$

where g_1 and g_2 are the gain coefficients whose value depends on the pumping level. The parameter $b = (T_2/T_0)^2$ accounts for the finite gain bandwidth. It originates from the frequency dependence of the gain approximated as $\tilde{g}_j(\omega) = g_j(1 - \omega^2 T_2^2)$, where T_2 is the dipole relaxation time of dopants, related inversely to the gain bandwidth (see Chapter 4). For picosecond pulses (width > 5 ps), the spectrum is narrow enough that all frequency components of the pulse experience nearly the same gain. The parameter b can be set to zero for such pulses. In the absence of pumping, g_j becomes negative and accounts for dopant-induced losses in the jth core.

In the quasi-CW case, the two terms involving time derivatives can be set to zero. The resulting equations can be solved analytically in the low-power case but require a numerical solution to study nonlinear switching [68]. When both cores are pumped to provide equal gains, the power threshold is reduced at

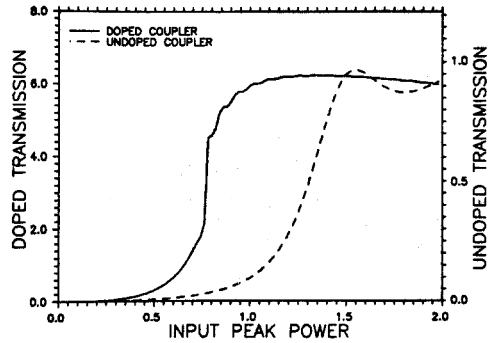

Figure 2.13 Switching characteristics (solid curve) of an active fiber coupler with equal gain in both cores. Dashed curve shows the behavior expected in the absence of gain. (After Ref. [67])

the expense of switch quality. The best performance occurs for active couplers with gain in one core and comparable loss in the other core. With proper choice of device parameters, the switching threshold can be reduced by a factor of more than 10 while maintaining a sharp, step-function-like response of the switch.

Soliton switching in active fiber couplers has been investigated numerically by choosing $s = -1$ (anomalous GVD), setting $g_1 = g_2 = g_0$ and $b = 0$ in Eqs. (2.5.8) and (2.5.9), and using the input conditions [67]

$$u(0,\tau) = N\,\mathrm{sech}(\tau), \qquad v(0,\tau) = 0. \tag{2.5.10}$$

Figure 2.13 shows improvement in switching of picosecond pulses occurring because of amplification for a coupler of length $L = 2\pi L_D$ by choosing $K = 0.25$ and $g_0 L_D = 0.3$. Several features are noteworthy. First, the switching threshold is reduced by about a factor of 2. Second, the switching is much sharper. A relatively small change in peak power of the pulse can switch the soliton from one core to another. Third, the switching contrast is improved because of the amplification provided by the coupler. In fact, the switched pulse is narrower than the input pulse by a factor in the range of 3 to 7, depending on the input peak power. For femtosecond pulses, gain dispersion must be included by choosing $b \neq 0$. Numerical simulations show that the main effect of gain dispersion is to reduce the overall switching efficiency without affecting the pulse quality significantly. It should be stressed that input pulse does not correspond to a fundamental soliton when $N \neq 1$. As a result, switching is

accompanied by dispersive radiation that appears in the other core because of its low power.

Asymmetric active couplers in which two cores have different gains ($g_1 \neq g_2$) can be used as saturable absorbers. Consider the case in which one core is pumped to provide gain while the other core is either undoped or unpumped. Low-energy pulses will then be transferred to the second core while high-energy pulses whose peak power exceeds the switching threshold will remain in the core with gain. Such a device acts as a saturable absorber and can be used for many applications. For example, it can be used for passive mode locking of fiber lasers by using the doped core as a gain medium within a cavity [70]. This scheme works even in the normal-GVD regime and can be used to generate picosecond pulse trains in the spectral region below 1.3 μm by using dopants such as neodymium [71]. Such a device can also be used to filter noise associated with solitons since noise can be transferred selectively to the lossy core because of its low power level [72]. The device acts as an optical amplifier whose gain is power dependent such that low-power signals are attenuated while high-power signals are amplified [73]. It should be stressed that the dopants used to provide gain or loss in fiber couplers can also have their own saturable nonlinearities that can affect the switching behavior significantly [69]. This issue is discussed in Chapter 4 in the context of fiber amplifiers.

2.5.3 Grating-Assisted Couplers

An important class of directional couplers makes use of a Bragg grating to improve the performance of asymmetric couplers. Such couplers are called *grating-assisted couplers* [74]–[85]. They have been studied mostly in the context of planar waveguides, in which grating-induced variations in the thickness of one waveguide lead to periodic modulation of the coupling coefficient. The grating period Λ is chosen such that the mismatch between the modal propagation constants equals the grating wave vector, that is,

$$\bar{\beta}_1 - \bar{\beta}_2 = \beta_g \equiv 2\pi/\Lambda. \tag{2.5.11}$$

This condition is similar to that of a long-period grating used for coupling the modes in a single-core fiber (see Section 1.7.1). In the case of a grating-assisted coupler, such a long-period grating couples the modes supported by two spatially separated waveguides (or the even and odd modes of the coupled

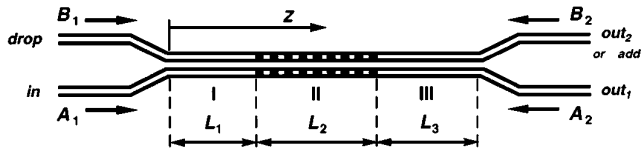

Figure 2.14 Schematic of a grating-assisted fiber coupler. (After Ref. [91])

waveguides) and allows complete transfer of a low-power beam between the two waveguides even though little power exchange occurs in the absence of the grating.

In the case of fiber couplers, it is difficult to vary the core diameter in a periodic fashion on a scale of about 10 μm. For this reason, gratings are formed by modulating the refractive index of the core. Since the spacing between cores does not vary in this case, the coupling coefficient remains nearly unchanged. Nevertheless, such phase gratings can be quite useful. Indeed, several kinds of grating-assisted fiber couplers have been proposed and analyzed for wavelength-division multiplexing (WDM) applications [86]–[96]. An example of such a coupler is shown in Fig. 2.14. Both long- and short-period gratings have been used. In a 1992 experiment, an acoustic wave, excited by a silica horn, coupled the forward-propagating normal modes of an asymmetric dual-core fiber coupler [86]. Such a device can be useful for a variety of applications related to WDM and signal processing. Periodic microbending induced by an acoustic wave or by a fixed mechanical grating has also been used to induce mode coupling [87].

Short-period Bragg gratings have been incorporated into one core of fiber couplers for making add–drop WDM filters [88], [89]. Such gratings produce a backward-propagating wave if the wavelength of the input signal falls within its stop band. When a multichannel WDM signal is injected into the core without the grating and transferred to the second core, a specific channel is selectively reflected back by the grating; it appears at the input end of the second core while the remaining channels appear at the output end of that core. A signal at the same specific wavelength can be added by injecting it from the output port of the core without the grating. The grating period is set by Eq. (2.5.11)—after changing the minus sign to a plus sign because of the backward propagation of the dropped channel—and is a fraction of the wavelength of that channel. Fabrication of a Bragg grating in the coupling region between the two cores allows the same add–drop functionality [90].

Fiber couplers in which both cores contain built-in Bragg gratings can also be used for adding or dropping a channel. In this case, forward- and backward-propagating waves are produced in both cores. Denoting the backward waves by B_1 and B_2 and neglecting the GVD, the operation of such a device is governed by the following four coupled-mode equations [91]:

$$\frac{dA_1}{dz} = i\delta_1 A_1 + i\kappa_{g1} B_1 + i\kappa_{12} A_2 + i\gamma_1(|A_1|^2 + 2|B_1|^2)A_1, \quad (2.5.12)$$

$$-\frac{dB_1}{dz} = i\delta_1 B_1 + i\kappa_{g1} A_1 + i\kappa_{12} B_2 + i\gamma_1(|B_1|^2 + 2|A_1|^2)B_1, \quad (2.5.13)$$

$$\frac{dA_2}{dz} = i\delta_2 A_2 + i\kappa_{g2} B_2 + i\kappa_{21} A_1 + i\gamma_2(|A_2|^2 + 2|B_2|^2)A_2, \quad (2.5.14)$$

$$-\frac{dB_2}{dz} = i\delta_2 B_2 + i\kappa_{g2} A_2 + i\kappa_{21} B_1 + i\gamma_2(|B_2|^2 + 2|A_2|^2)B_2, \quad (2.5.15)$$

where κ_{g1} and κ_{g2} are the coupling coefficients of the two gratings that can be designed to be different if necessary. The parameters δ_1 and δ_2 represent detuning between the Bragg and the modal propagation constants [96]. These equations can be easily generalized to include fiber dispersion by adding the first and second time-derivative terms as was done in Eqs. (2.1.9) and (2.1.10).

Equations (2.5.12)–(2.5.15) can be solved analytically only in the case of identical gratings and low-power CW beams by setting $\kappa_{g1} = \kappa_{g2}$ and $\gamma_1 = \gamma_2 = 0$; the results confirm the add–drop function offered by such a device [91]. In the general case in which gratings are different, occupy only a fraction of the coupling region, and are allowed to be nonuniform (e.g., apodized gratings), a numerical solution is required to optimize the performance of such add–drop multiplexers [96]. When a broadband WDM signal is launched inside one core of a coupler of length $L = L_c$, the channel whose wavelength falls within the stop band of the grating is reflected back and appears at the unused input port of the second core while the remaining channels appear at the output end. Such grating-assisted fiber couplers have been fabricated and exhibit large add–drop efficiency ($> 90\%$) with low losses [93].

Nonlinear effects can be studied by solving Eqs. (2.5.12)–(2.5.15) numerically. Similar to the case of grating-assisted codirectional couplers [80], the intensity-dependent shift of the Bragg frequency affects the channel to be dropped. As a result, the device can act as a nonlinear switch such that the channel is dropped only if its power exceeds a certain value. Propagation of short optical pulses should also lead to interesting nonlinear phenomena since

such a grating-assisted fiber coupler can support Bragg solitons in each core but these solitons are coupled by the proximity of two cores.

2.5.4 Birefringent Couplers

Another situation in which one needs to solve a set of four coupled-mode equations occurs when a fiber coupler exhibits large birefringence. In practice, birefringence can be induced either by using elliptical cores or through stress-induced anisotropy, the same techniques used for making polarization-maintaining fibers. As discussed in Chapter A.6, polarization in such fibers is maintained only when light is polarized along the fast or slow axis of the fiber. When incident light is polarized at an angle to these axes, the state of polarization changes along the core length in a periodic fashion.

The mathematical description of birefringent fiber couplers requires four coupled-mode equations corresponding to the two orthogonally polarized components of light in the two cores [97]–[100]. In the general case of asymmetric couplers and arbitrary birefringence, these equations are quite complicated since all four field components propagate with different group velocities. They can be simplified considerably for symmetric couplers with either very high or very low birefringence (as discussed in Section A.6.1).

Consider first the high-birefringence case. Using the notation that A_m and B_m denote the linearly polarized components in the mth core, the coupled-mode equations in this case become

$$\frac{\partial A_1}{\partial z}+\frac{1}{v_{gx}}\frac{\partial A_1}{\partial t}+\frac{i\beta_2}{2}\frac{\partial^2 A_1}{\partial T^2}=i\kappa A_2+i\gamma(|A_1|^2+\sigma|B_1|^2)A_1, \quad (2.5.16)$$

$$\frac{\partial B_1}{\partial z}+\frac{1}{v_{gy}}\frac{\partial B_1}{\partial t}+\frac{i\beta_2}{2}\frac{\partial^2 B_1}{\partial T^2}=i\kappa B_2+i\gamma(|B_1|^2+\sigma|A_1|^2)B_1, \quad (2.5.17)$$

$$\frac{\partial A_2}{\partial z}+\frac{1}{v_{gx}}\frac{\partial A_2}{\partial t}+\frac{i\beta_2}{2}\frac{\partial^2 A_2}{\partial T^2}=i\kappa A_1+i\gamma(|A_2|^2+\sigma|B_2|^2)A_2, \quad (2.5.18)$$

$$\frac{\partial B_2}{\partial z}+\frac{1}{v_{gy}}\frac{\partial B_2}{\partial t}+\frac{i\beta_2}{2}\frac{\partial^2 B_2}{\partial T^2}=i\kappa B_1+i\gamma(|B_2|^2+\sigma|A_2|^2)B_2, \quad (2.5.19)$$

where v_{gx} and v_{gy} are group velocities for the two polarization components. The XPM parameter takes a value of $\sigma = 2/3$ for linearly polarized components. In a low-birefringence coupler, all components propagate with the same group velocity but one cannot neglect four-wave mixing between the linearly polarized components. It is common to use circularly polarized components

in this case. The resulting equations are identical to Eqs. (2.5.16)–(2.5.19) provided we set $v_{gx} = v_{gy}$ and use $\sigma = 2$ for the XPM parameter.

The CW case in which all time-derivative terms in Eqs. (2.5.16)–(2.5.19) are set to zero was analyzed in 1988 using both the Hamiltonian and Stokes-parameter formalisms [97]. The new feature is that the state of polarization of the optical fields in the two cores can be different. This feature can be used to control the behavior of an intense beam launched in one core of the coupler by injecting a weak, orthogonally polarized probe in the other core. It can also be used to perform AND logic operation since the threshold for nonlinear switching is reduced when two orthogonally polarized pulses are launched simultaneously into the same core of the coupler. Another interesting result is that the power-dependent switching exhibits chaotic behavior when light is launched in both cores simultaneously to excite the even or odd supermode of the coupler.

Solutions of Eqs. (2.5.16)–(2.5.19) in the form of coupled soliton pairs have been studied using variational analysis with a Gaussian-shaped ansatz [99]. These solutions represent two vector solitons coupled by the proximity of two cores. They can again be classified as being symmetric or antisymmetric with equal energies in the two cores ($|A_1| = |A_2|$ and $|B_1| = |B_2|$) and being asymmetric such that the two cores have pulses with different energies. Stability properties of these soliton pairs are similar to those seen in Fig. 2.10, where birefringence effects were ignored [100].

A birefringent coupler can be converted into a dual-core rocking filter if the axis of birefringence is rocked periodically by twisting the preform during the fiber-drawing process [101]. Such periodic rotation of the birefringence axis at the beat length can be included in Eqs. (2.5.16)–(2.5.19) by adding an additional grating-like term on the right side. More specifically, one should add the term $i\kappa_g B_1 \exp(-4i\pi z/L_B)$ to Eq. (2.5.16), and similar terms to other equations, where L_B is the beat length of the birefringent fiber. Following the approach outlined in Section 1.5.2, the resulting four equations can be reduced to a pair of coupled NLS equations under suitable conditions [50]. These equations support pairs of coupled Bragg solitons that can propagate along the coupler length without changing their shapes.

2.5.5 Multicore Couplers

An interesting extension of fiber couplers consists of making fibers with multiple cores. Arrays of planar waveguides (active or passive) were studied ex-

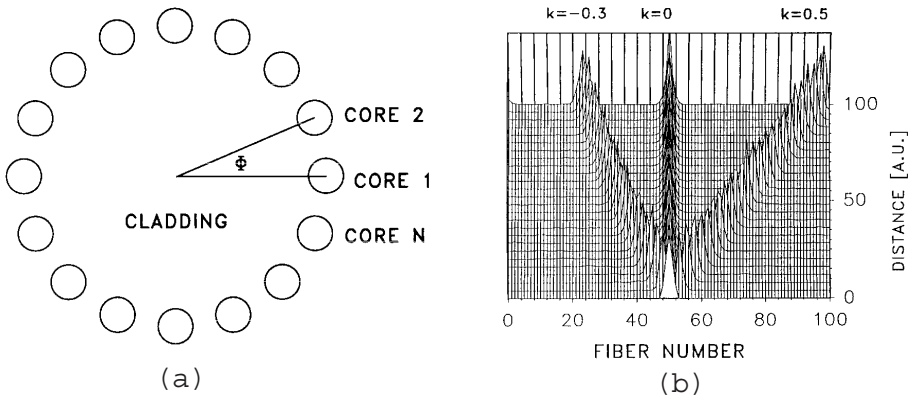

Figure 2.15 (a) Schematic of a circular fiber array. (b) Optical steering of a CW beam along the array. (After Ref. [123])

tensively during the 1980s and were used to make high-power semiconductor lasers [102]–[106]. Multicore fiber couplers were fabricated as early as 1989 [107]. Such couplers are needed for WDM technology and are used for making $N \times 1$ multiplexers and star couplers [108], although nonlinear effects are rarely needed for operation of such devices.

Nonlinear effects in fiber arrays (three or more cores sharing the same cladding) have been analyzed theoretically since the early 1990s using a set of coupled NLS equations [109]–[129]. When all cores are identical, these equations take a simple form and can be written, using soliton units, in the following compact form:

$$i\frac{\partial u_m}{\partial \xi} + \frac{1}{2}\frac{\partial^2 u_m}{\partial \tau^2} + |u_m|^2 u_m + K(u_{m+1} + u_{m-1}) = 0, \tag{2.5.20}$$

where u_m represents the field amplitude in the mth core and is coupled to the fields in the two neighboring cores. For a linear array of M cores, the cores at the two ends have only one neighbor. The resulting boundary conditions require $u_0 = u_{M+1} = 0$. This asymmetry can be avoided for a circular fiber array in which all cores are spaced equally and their centers lie along a circle, resulting in periodic boundary conditions. Figure 2.15(a) shows such a fiber array schematically.

The specific case of three-core couplers has attracted considerable attention since the resulting three coupled NLS equations permit analytical solution

in both the CW and pulsed cases [109]–[114]. The periodic boundary conditions can be used when the core centers form an equilateral triangle. In analogy with the two-core couplers, one can find soliton triplets that propagate through the three-core coupler without changing their shapes [56]. The bifurcation diagram in the q–Q plane is much more complicated in this case [112]. The reason is related to a vast variety of possible solutions that may exist even for couplers with only three cores. At low values of the total energy Q, the symmetric solution for which all three solitons are identical in all respects (in-phase solution) is stable. However, an antisymmetric solution also exists. In this case, two solitons are out of phase and have the same energy while the energy in the third core is zero. At a certain value of the energy Q, both the symmetric and antisymmetric solutions become unstable and give rise to partially or totally asymmetric solutions.

The analysis of multicore fiber couplers becomes increasingly more involved as the number of cores increases. Numerical solutions of Eq. (2.5.20) for a linear array, in which the input CW beam is launched initially at one end of the array, shows that nonlinear switching not only occurs but has a sharper threshold [109]. More specifically, the input beam is transferred to the outermost core at the other end at low powers (if the coupler length is chosen judiciously) but remains in the same core when the input power exceeds a threshold value. However, the threshold power increases and the power-transfer efficiency decreases as the number of intermediate cores is increased [116].

Power transfer from core to core also occurs in the case of a circular fiber array [123]. Figure 2.15(b) shows this behavior for a 101-core array by solving Eq. (2.5.20) numerically when a CW beam is launched initially with the amplitude

$$u_m = Ka\,\mathrm{sech}[a/\sqrt{2}(m-m_c)]\exp[-ik(m-m_c)], \tag{2.5.21}$$

where $m_c = 51$ and $a^2 = 1.1$. The integer m is varied from 51 to 55, resulting in the excitation of five cores at $\xi = 0$. The parameter k determines the initial phase difference between the excited cores. The beam remains confined to the same cores when $k = 0$. However, when $k \neq 0$, the power is transferred to successive cores as the CW beam propagates down the array. Since the shape of the envelope governing power distribution among cores is maintained during this process, this phenomenon is referred to as soliton-like optical switching. It should be stressed that the word *soliton* in this context refers to a spatial soliton.

The set of equations (2.5.20) has attracted considerable attention from a mathematical standpoint since it corresponds to a discrete version of the NLS equation in the quasi-CW limit in which the effects of GVD are negligible and the second-derivative term can be ignored. This feature can be seen more clearly by writing Eq. (2.5.20) as

$$i\frac{\partial u_m}{\partial \xi} + K(u_{m+1} - 2u_m + u_{m-1}) + 2Ku_m + |u_m|^2 u_m = 0. \tag{2.5.22}$$

The linear term $2Ku_m$ can be removed by shifting the propagation constant through the transformation $u'_m = u_m \exp(2iK\xi)$. The resulting equation is known as the discrete NLS equation since it is a discrete version of the following equation:

$$i\frac{\partial u}{\partial \xi} + Kd^2\frac{\partial^2 u}{\partial x^2} + |u|^2 u = 0, \tag{2.5.23}$$

where $x = md$ represents the position of the mth core along the array and the core spacing d is assumed to be small in the continuum limit. Equation (2.5.23) has spatially localized solutions in the form of spatial solitons. It is thus likely that Eq. (2.5.22) also possesses localized nonlinear modes such that the power is confined to only few neighboring cores. This indeed turns out to be the case [106]. The discrete NLS equation was studied extensively, both analytically and numerically, during the 1990s and continues to be of interest [117]–[129].

Problems

2.1 Explain in physical terms why proximity of two cores in a fiber coupler leads to power exchange between the two cores.

2.2 Starting from the wave equation, derive the coupled-mode equations for a fiber coupler in the frequency domain.

2.3 Convert Eqs. (2.1.4) and (2.1.5) into time-domain equations, treating both the propagation constants and the coupling coefficients as frequency dependent. Assume a symmetric coupler to simplify the algebra.

2.4 Evaluate the integral in Eq. (2.1.6) to find the coupling coefficient for a symmetric fiber coupler whose core centers are separated by a distance d. Assume that the fundamental mode in each waveguide has a Gaussian shape with width (FWHM) w_0.

2.5 Discuss how κ obtained in previous problem depends on the ratio d/w_0 by plotting it. Find the coupling length when $d/w_0 = 3$.

2.6 A CW optical beam with power P_0 is launched into one core of a symmetric fiber coupler. Solve the coupled-mode equations and find the power transferred to the second core. You can neglect the XPM-induced coupling. Discuss what happens when the input power exceeds $4\kappa/\gamma$.

2.7 Show that Eqs. (2.2.11)–(2.2.13) follow from the CW coupled-mode equations when the Stokes vector components are introduced as defined in Eq. (2.2.10).

2.8 Find all solutions of Eqs. (2.2.11)–(2.2.13) that remain invariant with z. Show the location of these fixed points on the Poincaré sphere. What happens when input power exceeds $2\kappa/\gamma$?

2.9 Find the dispersion relation associated with modulation instability when the CW solution of Eqs. (2.2.19) and (2.2.20) corresponds to the odd mode of a symmetric fiber coupler. Discuss the main differences from the even-mode case.

2.10 Show that the coupled NLS equations for a fiber coupler, Eqs. (2.3.1) and (2.3.2), indeed follow from the Lagrangian density in Eq. (2.3.6).

2.11 Evaluate the integral $\bar{L}_g = \int_{-\infty}^{\infty} L_g \, d\tau$ using the soliton ansatz given in Eq. (2.3.7) and derive the four equations describing the evolution of the soliton parameters along the coupler length.

2.12 Solve Eq. (2.3.10) numerically for μ = 1.5, 1.6, and 2.5 and plot Δ and ϕ along the coupler length. Interpret your results using phase diagrams of Fig. 2.8.

2.13 Repeat the previous problem using the ansatz given in Eq. (2.3.16) and solve the resulting four equations analytically.

2.14 Find the symmetric and antisymmetric shape-preserving soliton pairs by solving Eqs. (2.3.1) and (2.3.2).

2.15 Solve Eqs. (2.5.4) and (2.5.5) numerically and reproduce the pulse shapes shown in Fig. 2.11.

References

[1] V. J. Tekippe, *Fiber Integ. Opt.* **9**, 97 (1990).

[2] P. E. Green, Jr., *Fiber-Optic Networks* (Prentice-Hall, Upper Saddle River, NJ, 1993), Chap. 3.

[3] J. Hecht, *Understanding Fiber Optics* (Prentice-Hall, Upper Saddle River, NJ, 1999), Chap. 15.

[4] A. K. Ghatak and K. Thyagarajan, *Introduction to Fiber Optics* (Cambridge University Press, New York, 1999), Chap. 17.

[5] A. W. Snyder, *J. Opt. Soc. Am.* **62**, 1267 (1972); P. D. McIntyre and A. Snyder, *J. Opt. Soc. Am.* **63**, 1518 (1973).

[6] A. W. Snyder and J. D. Love, *Optical Waveguide Theory* (Chapman and Hall, London, 1983).

[7] D. Marcuse, *Theory of Dielectric Optical Waveguides* (Academic Press, San Diego, CA, 1991), Chap. 6.

[8] H. A. Haus and W. P. Huang, *Proc. IEEE* **79**, 1505 (1991).

[9] W. P. Huang, *J. Opt. Soc. Am. A* **11**, 963 (1994).

[10] R. Tewari and K. Thyagarajan, *J. Lightwave Technol.* **4**, 386 (1986).

[11] K. S. Chiang, *Opt. Lett.* **20**, 997 (1995); *IEEE J. Quantum Electron.* **33**, 950 (1997).

[12] K. S. Chiang, Y. T. Chow, D. J. Richardson, D. Taverner, L. Dong, L. Reekie, and K. M. Lo, *Opt. Commun.* **143**, 189 (1997).

[13] S. M. Jenson, *IEEE J. Quantum Electron.* **QE-18**, 1580 (1982).

[14] A. A. Maier, *Sov. J. Quantum Electron.* **12**, 1490 (1982); *Sov. J. Quantum Electron.* **14**, 101 (1984).

[15] K. Kitayama and S. Wang, *Appl. Phys. Lett.* **43**, 17 (1983).

[16] B. Daino, G. Gregori, and S. Wabnitz, *J. Appl. Phys.* **58**, 4512 (1985).

[17] S. Wabnitz, E. M. Wright, C. T. Seaton, and G. I. Stegeman, *Appl. Phys. Lett.* **49**, 838 (1986).

[18] D. D. Gusovskii, E. M. Dianov, A. A. Maier, V. B. Neustruev, E. I. Shklovskii, and I. A. Shcherbakov, *Sov. J. Quantum Electron.* **15**, 1523 (1985)

[19] D. D. Gusovskii, E. M. Dianov, A. A. Maier, V. B. Neustruev, V. V. Osiko, A. M. Prokhorov, K. Y. Sitarskii, and I. A. Shcherbakov, *Sov. J. Quantum Electron.* **17**, 724 (1987).

[20] S. R. Friberg, Y. Silberberg, M. K. Oliver, M. J. Andrejco, M. A. Saifi, and P. W. Smith, *Appl. Phys. Lett.* **51**, 1135 (1987).

[21] S. R. Friberg, A. M. Weiner, Y. Silberberg, B. G. Sfez, and P. W. Smith, *Opt. Lett.* **13**, 904 (1988).

[22] A. M. Weiner, Y. Silberberg, H. Fouckhardt, D. E. Leaird, M. A. Saifi, M. J. Andrejco, and P. W. Smith, *IEEE J. Quantum Electron.* **25**, 2648 (1989).

[23] S. Trillo, S. Wabnitz, W. C. Banyai, N. Finlayson, C. T. Seaton, G. I. Stegeman, and R. H. Stolen, *IEEE J. Quantum Electron.* **25**, 104 (1989).

[24] G. I. Stegeman and E. M. Wright, *Opt. Quantum Electron.* **22**, 95 (1990).

[25] A. T. Pham and L. N. Binh, *J. Opt. Soc. Am. B* **8**, 1914 (1991).

[26] A. W. Snyder, D. J. Mitchell, L. Poladian, D. R. Rowland, and Y. Chen, *J. Opt. Soc. Am. B* **8**, 2102 (1991).

[27] W. Samir, C. Pask, and S. J. Garth, *J. Opt. Soc. Am. B* **11**, 2193 (1994).

[28] A. A. Maier, *Sov. Phys. Usp.* **165**, 1037 (1995); *Sov. Phys. Usp.* **166**, 1171 (1996).

[29] K. Yasumoto, H. Maeda, and N. Maekawa, *J. Lightwave Technol.* **14**, 628 (1996).

[30] D. Artigas, F. Dios, and F. Canal, *J. Mod. Opt.* **44**, 1207 (1997).

[31] S. R. Vigil, Z. Zhou, B. K. Canfield, J. Tostenrude, and M. G. Kuzyk, *J. Opt. Soc. Am. B* **15**, 895 (1998).

[32] D. Marchese, M. De Sairo, A. Jha, A. K. Kar, and E. C. Smith, *J. Opt. Soc. Am. B* **15**, 2361 (1998).

[33] T. Gabler, A. Brauer, H. H. Horhold, T. Pertsch, and R. Stockmann, *Chem. Phys.* **245**, 507 (1999).

[34] S. Trillo, S. Wabnitz, E. M. Wright, and G. I. Stegeman, *Opt. Lett.* **13**, 672 (1988).

[35] S. Trillo, S. Wabnitz, G. I. Stegeman, and E. M. Wright, *J. Opt. Soc. Am. B* **6**, 899 (1989).

[36] S. Trillo, S. Wabnitz, and G. I. Stegeman, *IEEE J. Quantum Electron.* **25**, 1907 (1989).

[37] S. Trillo and S. Wabnitz, *Opt. Lett.* **16**, 1 (1991).

[38] C. C. Yang, *Opt. Lett.* **16**, 1641 (1991).

[39] S. Wabnitz, S. Trillo, E. M. Wright, and G. I. Stegeman, *J. Opt. Soc. Am. B* **8**, 602 (1991).

[40] E. Cagloti, S. Trillo, S. Wabnitz, B. Crosignani, and P. Di Porto, *J. Opt. Soc. Am. B* **7**, 374 (1990).

[41] C. Paré and M. Florjanczyk, *Phys. Rev. A* **41**, 6287 (1990).

[42] M. Romagnoli, S. Trillo, and S. Wabnitz, *Opt. Quantum Electron.* **24**, S1237 (1992).

[43] Y. S. Kivshar, *Opt. Lett.* **18**, 7 (1993).

[44] Y. S. Kivshar and M. L. Quiroga-Teixerio, *Opt. Lett.* **18**, 980 (1993).

[45] P. L. Chu, G. D. Peng, and B. A. Malomed, *Opt. Lett.* **18**, 328 (1993); *J. Opt. Soc. Am. B* **10**, 1379 (1993).

[46] E. M. Wright, G. I. Stegeman, and S. Wabnitz, *Phys. Rev. A* **40**, 4455 (1989).

[47] N. Akhmediev and A. Ankiewicz, *Phys. Rev. Lett.* **70**, 2395 (1993).

[48] J. M. Soto-Crespo and N. Akhmediev, *Phys. Rev. E* **48**, 4710 (1993).

[49] N. Akhmediev and J. M. Soto-Crespo, *Phys. Rev. E* **47**, 1358 (1993); *Phys. Rev. E* **49**, 4519 (1994).

[50] D. C. Psaila and C. M. de Sterke, *Opt. Lett.* **18**, 1905 (1993).

[51] C. Schmidt-Hattenberger, R. Muschall, F. Lederer, and U. Trutschel, *J. Opt. Soc. Am. B* **10**, 1592 (1993).

[52] W. Samir, S. J. Garth, and C. Pask, *Appl. Opt.* **32**, 4513 (1993).

[53] A. V. Buryak and N. Akhmediev, *Opt. Commun.* **110**, 287 (1994).

[54] A. Ankiewicz, M. Karlsson, and N. Akhmediev, *Opt. Commun.* **111**, 116 (1994).

[55] I. M. Uzunov, R. Muschall, M. Gölles, Y. S. Kivshar, B. A. Malomed, and F. Lederer, *Phys. Rev. E* **51**, 2527 (1995).

[56] N. Akhmediev and A. Ankiewicz, *Solitons: Nonlinear Pulses and Beams* (Chapman and Hall, New York, 1997).

[57] P. M. Ramos and C. R. Paiva, *IEEE J. Sel. Topics Quantum Electron.* **3**, 1224 (1997); *IEEE J. Quantum Electron.* **35**, 983 (1999).

[58] P. Shum, K. S. Chinag, and W. A. Gambling, *IEEE J. Quantum Electron.* **35**, 79 (1999).

[59] T. P. Valkering, J. van Honschoten, and H. J. Hoekstra, *Opt. Commun.* **159**, 215 (1999).

[60] B. A. Umarov, F. K. Abdullaev, and M. R. B. Wahiddin, *Opt. Commun.* **162**, 340 (1999).

[61] P. A. Bélanger and C. Paré, *Phys. Rev. A* **41**, 5254 (1990).

[62] P. B. Hansen, A. Kloch, T. Aaker, and T. Rasmussen, *Opt. Commun.* **119**, 178 (1995).

[63] B. A. Malomed, *Phys. Rev. E* **51**, R864 (1995).

[64] B. A. Malomed, I. M. Skinner, P. L. Chu, and G. D. Peng, *Phys. Rev. E* **53**, 4084 (1996).

[65] D. J. Kaup, T. I. Lakoba, and B. A. Malomed, *J. Opt. Soc. Am. B* **14**, 1199 (1997).

[66] D. J. Kaup and B. A. Malomed, *J. Opt. Soc. Am. B* **15**, 2838 (1998).

[67] J. Wilson, G. I. Stegeman, and E. M. Wright, *Opt. Lett.* **16**, 1653 (1991).

[68] Y. Chen, A. W. Snyder, and D. N. Payne, *IEEE J. Quantum Electron.* **28**, 239 (1992).

[69] P. L. Chu and B. Wu, *Opt. Lett.* **17**, 255 (1992).

[70] H. G. Winful and D. T. Walton, *Opt. Lett.* **17**, 1688 (1992).

[71] D. T. Walton and H. G. Winful, *Opt. Lett.* **18**, 720 (1993).

[72] P. L. Chu, B. A. Malomed, H. Hatami-Hanza, and I. M. Skinner, *Opt. Lett.* **20**, 1092 (1995).

[73] B. A. Malomed, G. D. Peng, and P. L. Chu, *Opt. Lett.* **21**, 330 (1996).

[74] D. Marcuse, *J. Lightwave Technol.* **5**, 268 (1987); *IEEE J. Quantum Electron.* **26**, 675 (1990).

[75] W. P. Huang and H. A. Haus, *J. Lightwave Technol.* **7**, 920 (1989).
[76] Y. J. Chen and A. W. Snyder, *Opt. Lett.* **16**, 217 (1991).
[77] Y. J. Chen, *J. Mod. Opt.* **38**, 1731 (1991).
[78] W. P. Huang, B. E. Little, and S. K. Chadhuri, *J. Lightwave Technol.* **9**, 721 (1991).
[79] L. P. Yuan, *IEEE J. Quantum Electron.* **29**, 171 (1993).
[80] B. E. Little and W. P. Huang, *J. Lightwave Technol.* **11**, 1990 (1993).
[81] B. E. Little, *J. Lightwave Technol.* **12**, 774 (1994).
[82] S. H. Zhang and T. Tamir, *Opt. Lett.* **20**, 803 (1995); *J. Opt. Soc. Am. A* **13**, 2403 (1997).
[83] N. H. Sun, J. K. Butler, G. A. Evans, L. Pang, and P. Congdon, *J. Lightwave Technol.* **15**, 2301 (1997).
[84] T. Liang and R. W. Ziolkowski, *Microwave Opt. Tech. Lett.* **17**, 17 (1998).
[85] N. Izhaky and A. Hardy, *J. Opt. Soc. Am. A* **16**, 1303 (1999); *Appl. Opt.* **38**, 6987 (1999).
[86] H. Sabert, L. Dong, and P. S. J. Russell, *Int. J. Optoelectron.* **7**, 189 (1992).
[87] L. Dong, T. A. Birks, M. H. Ober, and P. S. J. Russell, *J. Lightwave Technol.* **12**, 24 (1994).
[88] J. L. Archambault, P. S. J. Russell, S. Bacelos, P. Hua, and L. Reekie, *Opt. Lett.* **19**, 180 (1994).
[89] L. Dong, P. Hua, T. A. Birks, L. Reekie, and P. S. J. Russell, *IEEE Photon. Technol. Lett.* **8**, 1656 (1996).
[90] F. Bakhti, P. Sansonetti, C. Sinet, L. Gasca, L. Martineau, S. Lacroix, X. Daxhelet, and F. Gonthier, *Electron. Lett.* **33**, 803 (1997).
[91] S. S. Orlov, A. Yariv, and S. van Essen, *Opt. Lett.* **22**, 688 (1997).
[92] A. Ankiewicz and G. D. Peng, *Electron. Lett.* **33**, 2151 (1997).
[93] A. S. Kewitsch, G. A. Rakuljic, P. A. Willems, and A. Yariv, *Opt. Lett.* **23**, 106 (1998).
[94] T. Erdogan, *Opt. Commun.* **157**, 249 (1998).
[95] B. Ortega, L. Dong, and L. Reekie, *Appl. Opt.* **37**, 7712 (1998).
[96] J. Capmany, P. Muñoz, and D. Pastor, *IEEE J. Sel. Topics Quantum Electron.* **5**, 1392 (1999).
[97] S. Trillo and S. Wabnitz, *J. Opt. Soc. Am. B* **5**, 483 (1988).
[98] D. C. Psaila and C. M. de Sterke, *Opt. Lett.* **18**, 1905 (1993).
[99] T. I. Lakoba, D. J. Kaup, and B. A. Malomed, *Phys. Rev. E* **55**, 6107 (1997).
[100] T. I. Lakoba and D. J. Kaup, *Phys. Rev. E* **56**, 4791 (1997).
[101] R. H. Stolen, A. Ashkin, W. Pleibel, and J. M. Dziedzic, *Opt. Lett.* **9**, 200 (1984).
[102] H. A. Haus and L. Molter-Orr, *IEEE J. Quantum Electron.* **19**, 840 (1983).

[103] E. Kapon, J. Katz, and A. Yariv, *Opt. Lett.* **9**, 125 (1984).
[104] G. P. Agrawal, *J. Appl. Phys.* **58**, 2922 (1985).
[105] M. Kuznetsov, *IEEE J. Quantum Electron.* **21**, 1893 (1985).
[106] D. N. Christodoulides and R. I. Joseph, *Opt. Lett.* **13**, 794 (1988).
[107] J. W. Arkwright and D. B. Mortimore, *Electron. Lett.* **26**, 1534 (1989).
[108] D. B. Mortimore and J. W. Arkwright, *Appl. Opt.* **29**, 1814 (1990); *Appl. Opt.* **30**, 650 (1991).
[109] Y. Chen, A. W. Snyder, and D. J. Mitchell, *Electron. Lett.* **26**, 77 (1990).
[110] N. Finlayson and G. I. Stegeman, *Appl. Phys. Lett.* **56**, 2276 (1990).
[111] D. J. Mitchell, A. W. Snyder, and Y. Chen, *Electron. Lett.* **26**, 1164 (1990).
[112] N. Akhmediev and A. V. Buryak, *J. Opt. Soc. Am. B* **11**, 804 (1994).
[113] D. Artigas, J. Olivas, F. Dios, and F. Canal, *Opt. Commun.* **131**, 53 (1996).
[114] M. G. da Silva, A. F. Teles, and A. S. B. Sombra, *J. Appl. Phys.* **84**, 1834 (1998).
[115] J. M. Soto-Crespo and E. M. Wright, *J. Appl. Phys.* **70**, 7240 (1991).
[116] C. Schmidt-Hattenberger, U. Trutschel, and F. Lederer, *Opt. Lett.* **16**, 294 (1991).
[117] C. Schmidt-Hattenberger, U. Trutschel, R. Muschall, and F. Lederer, *Opt. Commun.* **82**, 461 (1991); *Opt. Commun.* **89**, 473 (1992).
[118] C. Schmidt-Hattenberger, R. Muschall, U. Trutschel, and F. Lederer, *Opt. Quantum Electron.* **24**, 691 (1992).
[119] P. E. Langridge and W. J. Firth, *Opt. Quantum Electron.* **24**, 1315 (1992).
[120] Y. Kivshar, *Opt. Lett.* **18**, 1147 (1993); *Phys. Lett. A* **173**, 172 (1993).
[121] C. Claude, Y. S. Kivshar, D. Kluth, and K. H. Spatschek, *Phys. Rev. B* **47**, 14228 (1993).
[122] B. A. Malomed, *Phys. Rev. E* **47**, 2874 (1993).
[123] W. Królikowski, U. Trutschel, M. Cronin-Golomb, and C. Schmidt-Hattenberger, *Opt. Lett.* **19**, 320 (1994).
[124] R. Muschall, C. Schmidt-Hattenberger, and F. Lederer, *Opt. Lett.* **19**, 323 (1994).
[125] A. B. Aceves, C. De Angelis, A. M. Rubenchik, and S. K. Turitsyn, *Opt. Lett.* **19**, 329 (1994).
[126] A. B. Aceves, C. De Angelis, S. Trillo, and S. Wabnitz, *Opt. Lett.* **19**, 332 (1994).
[127] A. B. Aceves, G. G. Luther, C. De Angelis, A. M. Rubenchik, and S. K. Turitsyn, *Phys. Rev. Lett.* **75**, 73 (1995); *Opt. Fiber Technol.* **1**, 244 (1995).
[128] E. W. Laedke, K. H. Spatschek, S. K. Turitsyn, and V. K. Mezentsev, *Phys. Rev. E* **52**, 5549 (1995).
[129] M. I. Weinstein and B. Yeary, *Phys. Lett. A* **222**, 157 (1996).

Chapter 3

Fiber Interferometers

The two fiber components covered in Chapters 1 and 2 can be combined to form a variety of fiber-based optical devices. Four common ones among them are the fiber version of the well-known Fabry–Perot, Sagnac, Mach–Zehnder, and Michelson interferometers [1]. They exhibit interesting nonlinear effects that are useful for optical-switching applications [2]–[4], when power levels are large enough for the self- and cross-phase modulation (SPM and XPM) to become important. This chapter is devoted to the nonlinear effects occurring in these fiber interferometers. Section 3.1 considers the Fabry–Perot and ring resonators and discusses several nonlinear effects such as optical bistability and modulation instability. Nonlinear fiber-loop mirrors, whose operation is based on Sagnac interferometers, are covered in Section 3.2. Nonlinear switching in Mach–Zehnder interferometers is described in Section 3.3. Finally, Section 3.4 is devoted to Michelson interferometers.

3.1 Fabry–Perot and Ring Resonators

Fabry–Perot and ring resonators are well-known devices used commonly for making lasers [5]. A fiber-based Fabry–Perot resonator can be constructed by simply making two ends of an optical fiber partially reflecting. This can be realized in practice by using external mirrors or by depositing high-reflectivity coatings at the two ends. An alternative approach, shown schematically in Fig. 3.1, splices a fiber grating at each end of the fiber. The construction of a fiber-ring resonator is even simpler. It can be made by connecting the two ends of a piece of fiber to an input and an output port of a fiber coupler, as

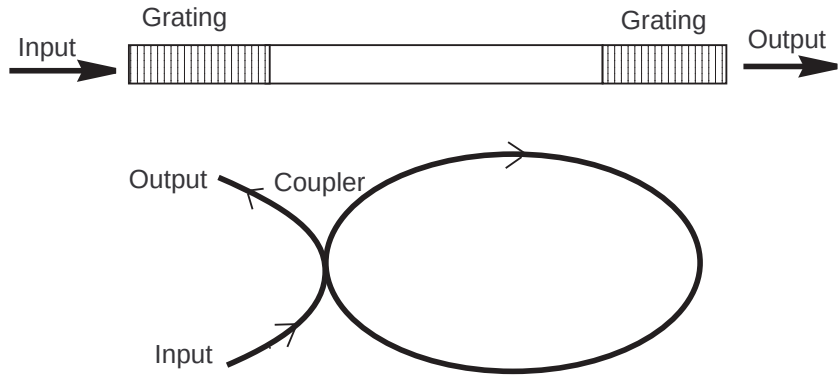

Figure 3.1 Fiber-based Fabry–Perot and ring resonators made by using Bragg gratings and directional couplers.

shown schematically in Fig. 3.1. This section is devoted to the nonlinear effects occurring in such resonators. The continuous-wave (CW) case is considered first with focus on optical bistability and chaos. It is followed by a discussion of modulation instability and other temporal phenomena.

3.1.1 Transmission Resonances

Several types of fiber-based Fabry–Perot interferometers have been developed for wavelength-division multiplexing (WDM) applications [6]–[8]. Some of them function in a linear fashion since they use air as the intracavity medium [9]. Others use a piece of fiber between two Bragg gratings [10] and thus are capable of exhibiting the nonlinear effects. Fiber-ring resonators were made as early as 1982 using a directional coupler [11], and a finesse of 1260 was realized by 1988 [12].

Transmittivity of a Fabry–Perot resonator, formed by using two identical mirrors (or Bragg gratings) of reflectivity R_m, can be calculated by adding coherently the optical fields transmitted on successive round trips. Consider a CW optical beam at the frequency ω. When it is incident at the left mirror, the field inside the resonator consists of forward- and backward-propagating waves and can be expressed as

$$E(\mathbf{r},t) = \tfrac{1}{2}F(x,y)\{A(z)\exp[i(\tilde{\beta}z-\omega t)] + B(z)\exp[-i(\tilde{\beta}z+\omega t)] + \text{c.c.}\}, \tag{3.1.1}$$

where $F(x,y)$ is the spatial distribution and $\tilde{\beta}$ is the propagation constant associated with the fundamental mode supported by the fiber. The transmitted field is obtained by adding contributions of an infinite number of round trips and is given by [5]

$$A(L) = \frac{(1-R_m)A(0)}{1-R_m \exp(i\tilde{\beta}L_R)} \tag{3.1.2}$$

where $L_R \equiv 2L$ is the round-trip distance for a fiber of length L.

Transmittivity of the resonator is obtained from Eq. (3.1.2) and is given by the well-known Airy formula [1]

$$T_R = \frac{P_t}{P_i} = \left|\frac{A(L)}{A(0)}\right|^2 = \frac{(1-R_m)^2}{(1-R_m)^2 + 4R_m \sin^2(\phi_R/2)}, \tag{3.1.3}$$

where $P_i = |A(0)|^2$ is the input power, P_t is the transmitted power, and $\phi_R = \tilde{\beta}L_R$ is the phase shift occurring over one round trip inside the resonator. The nonlinear and dispersive effects enter through this phase shift, which can be separated into two parts

$$\phi_R(\omega) \equiv \phi_0(\omega) + \phi_{\rm NL} = [\beta(\omega) + \Delta\beta_{\rm NL}]L_R. \tag{3.1.4}$$

The nonlinear part $\phi_{\rm NL}$ represents the contribution of SPM and can be related to the nonlinear parameter γ as

$$\phi_{\rm NL} = \gamma \int_0^L (|A(z)|^2 + |B(z)|^2)\, dz = \gamma P_{\rm av} L_R, \tag{3.1.5}$$

where $P_{\rm av}$ is the average power level inside the resonator.

At low power levels such that $\phi_{\rm NL} \ll 1$, the nonlinear effects can be neglected. In that case, 100% of the incident light is transmitted ($T_R = 1$) whenever $\phi_0 = 2m\pi$, where m is an integer. Frequencies that satisfy this condition correspond to the longitudinal modes of the resonator. Transmission drops as the frequency of incident light is detuned from the resonance. The solid curve in Fig. 3.2 shows the transmittivity of a fiber resonator as a function of ϕ_0 for $R_m = 0.8$. The frequency spacing $\Delta\nu_L$ between the successive transmission peaks is known as the *free-spectral range* (also called the longitudinal-mode spacing in laser literature). It is obtained using the phase-matching condition

$$[\beta(\omega + 2\pi\Delta\nu_L) - \beta(\omega)]L_R = 2\pi \tag{3.1.6}$$

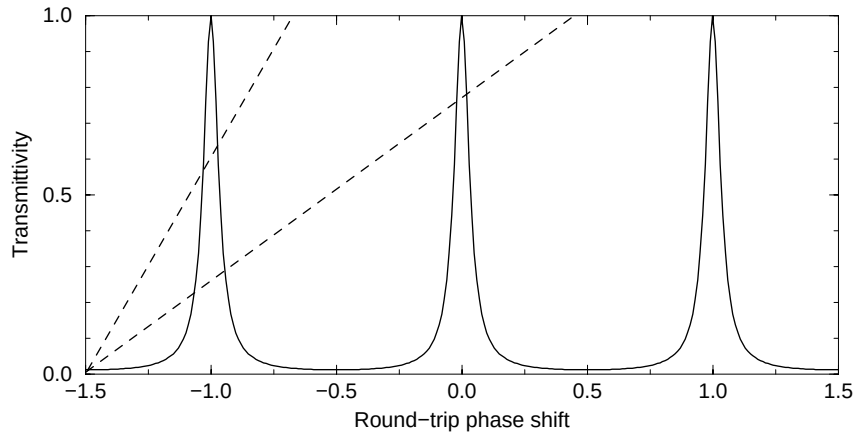

Figure 3.2 Transmittivity of a Fabry–Perot resonator as a function of $\phi_0/2\pi$ for $R_m = 0.8$. Dashed lines show changes in ϕ_R because of SPM at two power levels.

and is approximately given by $\Delta\nu_L = v_g/L_R \equiv 1/T_R$, where $v_g \equiv 1/\beta_1$ is the group velocity and T_R is the round-trip time within the resonator. Because of group-velocity dispersion (GVD), the free spectral range of a fiber resonator becomes frequency dependent. It can vary considerably in a Fabry–Perot resonator made by using Bragg gratings because of the large GVD associated with them [13]. The sharpness of the resonance peaks in Fig. 3.2 is quantified through the resonator finesse F_R defined as

$$F_R = \frac{\Delta\nu_L}{\Delta\nu_R} = \frac{\pi\sqrt{R_m}}{1-R_m}, \tag{3.1.7}$$

where $\Delta\nu_R$ is the width of each resonance peak (at half maximum).

Equation (3.1.3) changes somewhat for a fiber-ring resonator [11]. The changes are related to the constant phase shift of $\pi/2$ occurring when light crosses over from one core to another inside a fiber coupler (see Section 2.1). Note also that $B(z) = 0$ in Eq. (3.1.1) for a ring resonator since a backward-propagating wave is not generated in this case. This feature simplifies the mathematical description and has considerable implications for nonlinear phenomena since the XPM-induced coupling between the forward- and backward-propagating waves cannot occur in unidirectional ring resonators.

3.1.2 Optical Bistability

The nonlinear phenomenon of optical bistability has been studied in nonfiber resonators since 1976 by placing the nonlinear medium inside a cavity formed by using multiple mirrors [14]–[19]. The single-mode fiber was used in 1983 as the nonlinear medium inside a ring cavity [20]. Since then, the study of nonlinear phenomena in fiber resonators has remained a topic of considerable interest [21]–[38].

The origin of the nonlinear effects in fiber resonators is evident from Eq. (3.1.3): Note that the round-trip phase shift ϕ_R depends on input power because of the SPM-induced phase shift $\phi_{\rm NL}$. For high-finesse resonators, $P_t \approx (1-R_m)P_{\rm av}$. Using this relation in Eq. (3.1.5), the transmitted power from Eq. (3.1.3) is found to satisfy the transcendental equation

$$P_t\left\{1+\frac{4R_m}{(1-R_m)^2}\sin^2\left[\frac{\phi_0}{2}+\frac{\gamma P_t L_R}{2(1-R_m)}\right]\right\}=P_i. \tag{3.1.8}$$

It is clear from this equation that multiple values of P_t are possible at a fixed value of the incident power P_i because of SPM. Dashed lines in Fig. 3.2 show ϕ_R as a function of ϕ_0 for two values of P_i using Eq. (3.1.4). The intersection points of the dashed lines with the solid curve correspond to the multiple solutions of Eq. (3.1.8). At low powers, the dashed lines become nearly vertical, and only one solution is possible. With increasing input power, the dashed lines tilt, and the number of solutions increases from one to three, then to five and beyond. We focus on the case of three solutions since it requires the least input power.

Multiple solutions of Eq. (3.1.8) lead to dispersive optical bistability, a nonlinear phenomenon that has been observed using several different nonlinear media [19]. It occurs in fiber resonators when the linear phase shift ϕ_0 does not correspond to a resonance of the resonator so that little light is transmitted at low power levels. For a given detuning $\delta \equiv 2\pi M - \phi_0$ of the input signal from the nearest Mth resonance, the SPM-induced phase shift reduces the net detuning toward zero, resulting in higher transmission. However, the transmitted power P_t does not increase linearly with P_0, as is evident from the nonlinear nature of Eq. (3.1.8). Figure 3.3 shows the expected behavior for three values of δ. Over a certain range of δ, three solutions of Eq. (3.1.8) produce the well-known S-shaped curve associated with optical bistability. The middle branch with a negative slope is always unstable [19]. As a result, the transmitted power jumps up and down at specific values of P_i in such a way

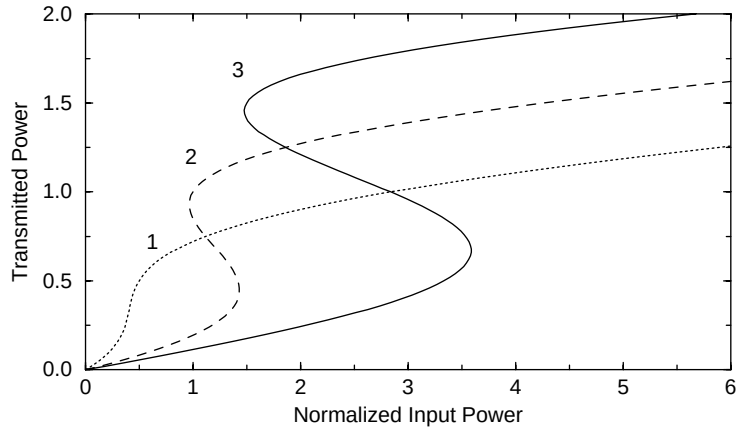

Figure 3.3 Bistable response of a fiber resonator with $R_m = 0.5$ for three values of detuning δ. Powers are normalized using $P_n = (\gamma L_R)^{-1}$.

that it exhibits hysteresis. The switching powers are of the order of $(\gamma L_R)^{-1}$, with numerical values ~ 10 W for $L_R \sim 100$ m.

Experimental observation of optical bistability using CW beams is hampered by a relatively low threshold of stimulated Brillouin scattering (SBS) in fiber resonators [39]. The evidence of bistability in a ring cavity was first seen in a 1983 experiment in which SBS was avoided using picosecond pulses [20]. In a later experiment, SBS was suppressed by placing an optical isolator inside the ring cavity that was formed using 13 m of low-birefringence fiber [22]. Bistable behavior was observed in this experiment at CW power levels below 10 mW. The nonlinear phase shift $\phi_{\rm NL}$ at this power level is relatively small in magnitude (below 0.01 rad) but still large enough to induce bistability.

In all experiments on optical bistability, it is important to stabilize the cavity length to subwavelength accuracy. An improved stabilization scheme was used in a 1998 experiment [37]. Figure 3.4 shows the observed behavior at four values of the detuning δ. The experiment used mode-locked pulses (width ~ 1 ps) emitted from a Ti:sapphire laser. The length of ring resonator (about 7.4 m) was adjusted precisely so that an entering laser pulse overlapped in time with another pulse already circulating inside the cavity (synchronous pumping). The observed bistable behavior was in qualitative agreement with the CW theory in spite of the use of short optical pulses since the GVD played a relatively minor role [24].

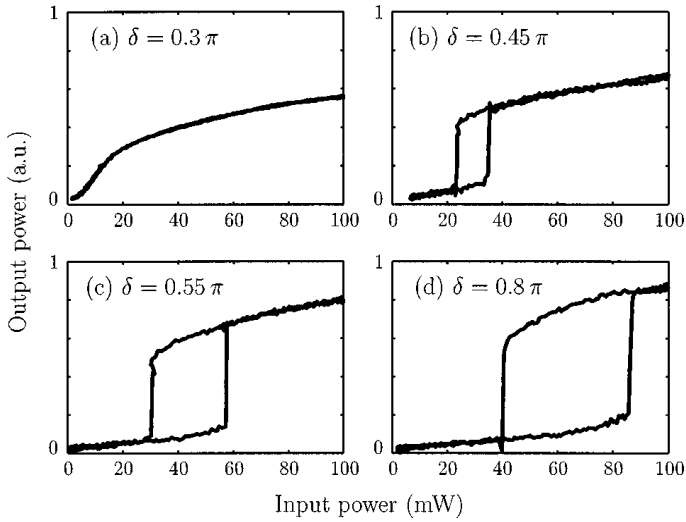

Figure 3.4 Hysteresis cycles observed in a fiber-ring resonator at four values of detuning δ. (After Ref. [37])

3.1.3 Nonlinear Dynamics and Chaos

It was discovered in 1979 that the nonlinear response of a ring resonator can initiate a period-doubling route to optical chaos [15]. The basic idea consists of recognizing that the dynamics in a ring cavity correspond to that of a nonlinear map in the sense that the intracavity field is mapped to a different function on each round trip inside the cavity [40]–[42]. Mathematically, the map can be written as

$$A^{(n+1)}(0,t) = \sqrt{\rho}A^{(n)}(L_R,t)\exp(i\phi_0) + i\sqrt{(1-\rho)P_i}, \tag{3.1.9}$$

where the superscript denotes the number of round trips inside the resonator and ρ represents the fraction of the power remaining in the resonator after the coupler (see Fig. 3.1). Evolution of the intracavity field $A(z,t)$ during each round trip is governed by the usual nonlinear Schrödinger (NLS) equation:

$$i\frac{\partial A}{\partial z} - \frac{\beta_2}{2}\frac{\partial^2 A}{\partial T^2} + \gamma|A|^2 A = 0, \tag{3.1.10}$$

where $T = t - z/v_g$ is the reduced time and β_2 is the GVD parameter. If the effect of GVD can be neglected in a CW or quasi-CW situation, this equation

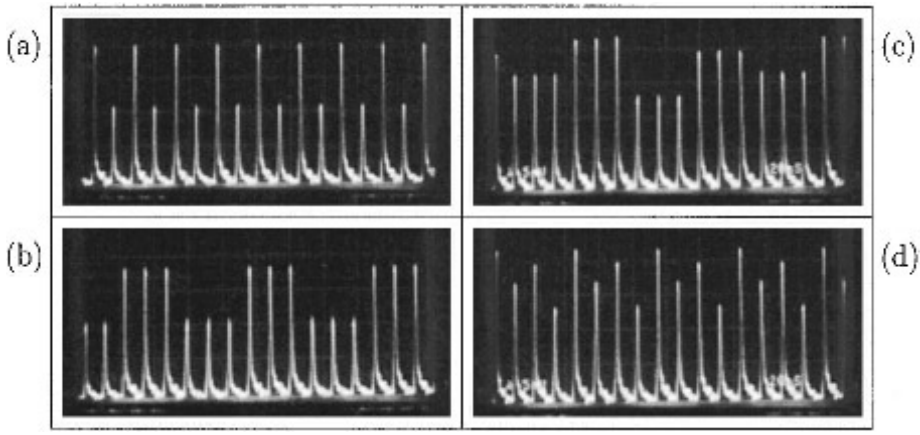

Figure 3.5 Period-2 patterns observed for $\delta = 0.35\pi$ at an average input power of (a) 200 mW and (b) 250 mW. Patterns change to period 4 for $\delta = 0.65\pi$ [(c) and (d)] at the same two power levels. (After Ref. [37])

can be solved analytically to obtain the simple result

$$A(L_R,t) = A(0,t)\exp[i\gamma|A(0,t)|^2 L_R]. \tag{3.1.11}$$

Using Eq. (3.1.11) in Eq. (3.1.9), the nonlinear map can be iterated for a given value of the input power P_i. The results show that the output of the ring resonator can become time dependent even for a CW input. Moreover, the output becomes chaotic following a period-doubling route in a certain range of input parameters [15]. This behavior was observed experimentally in a 1983 experiment by launching 140-ps pulses (obtained from a Q-switched, mode-locked Nd:YAG laser) into a fiber-ring cavity [20]. The cavity length was selected to precisely match the round-trip time to the 7.6-ns interval between the neighboring pulses (synchronous pumping).

In a 1998 experiment, a mode-locked Ti:sapphire laser was used to launch short pulses (width ~ 1 ps) into a well-stabilized fiber-ring resonator [37]. Figure 3.5 shows the period-2 and period-4 patterns observed using two different values of detuning at two different power levels. At higher power levels, the output became chaotic over a wide range of detuning δ, with period-3 windows embedded within the chaos. These features are consistent with the general theory of nonlinear dynamical systems [40]–[42].

3.1.4 Modulation Instability

Even in the absence of feedback, the combination of GVD and SPM can lead to modulation instability when a CW beam propagates inside optical fibers (see Section A.5.1). An interesting question is how the presence of feedback modifies this nonlinear phenomenon. Modulation instability in fiber resonators is of considerable interest as it can be used to convert a CW beam into a train of ultrashort pulses [43]–[49].

The theory of modulation instability has been extended to include the effects of feedback occurring inside a fiber resonator. The analysis is quite involved in the case of a Fabry–Perot cavity since one must use the coupled NLS equations describing the evolution of the forward- and backward-propagating waves [49]. It simplifies considerably for a ring resonator [46]. In fact, one can use Eqs. (3.1.9) and (3.1.10). The approach is similar to that used in Section A.5.1. It is useful to normalize Eq. (3.1.10) in the usual way and write it as

$$i\frac{\partial u}{\partial \xi} - \frac{s}{2}\frac{\partial^2 u}{\partial \tau^2} + |u|^2 u = 0, \tag{3.1.12}$$

where $s = \mathrm{sgn}(\beta_2) = \pm 1$ and we have introduced

$$\xi = z/L_R, \quad \tau = T/\sqrt{|\beta_2| L_R}, \quad u = (\gamma L_R)^{1/2} A. \tag{3.1.13}$$

Note that the resonator length L_R is used to define the time scale.

The CW solution of Eq. (3.1.12) is given by $u = u_0 \exp(i u_0^2 \xi)$. To examine its stability, we perturb it at a frequency Ω such that

$$u(\xi, \tau) = [u_0 + a_1 \exp(-i\Omega\tau) + a_2 \exp(i\Omega\tau)] \exp(i u_0^2 z), \tag{3.1.14}$$

where a_1 and a_2 represent weak perturbations whose growth results in the two sidebands associated with modulation instability. When the NLS equation is linearized in terms of a_1 and a_2, we obtain the coupled linear differential equations:

$$da_1/d\xi = i(\tfrac{1}{2} s\Omega^2 + u_0^2) a_1 + i u_0^2 a_2, \tag{3.1.15}$$

$$da_2/d\xi = i(\tfrac{1}{2} s\Omega^2 + u_0^2) a_1 + i u_0^2 a_1 \tag{3.1.16}$$

These equations should be solved subject to the boundary conditions imposed by the ring cavity:

$$a_j^{(n+1)}(0) = \sqrt{\rho}\, a_j^{(n)}(1) \exp[i(\phi_0 + u_0^2)], \quad (j = 1, 2), \tag{3.1.17}$$

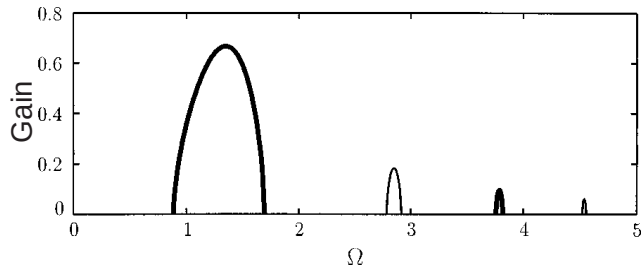

Figure 3.6 Gain spectrum of modulation instability in the normal-GVD region of a fiber-ring resonator. Thin and thick lines correspond to the resonance and anti-resonance conditions, respectively. (After Ref. [48], ©1997 by the American Physical Society)

where the superscript denotes the round-trip number.

Equations (3.1.15)–(3.1.17) relate the perturbation amplitudes a_1 and a_2 on two successive round trips. Modulation instability occurs if they grow after each round trip for a given set of parameters. The growth rate depends not only on the frequency Ω and the input power P_i but also on the fiber-ring parameters β_2, γ, ρ, and ϕ_0. The interesting new feature is that modulation instability can occur even in the normal-GVD region of the fiber [48]. Moreover, the instability occurs either close to a cavity resonance, $\phi_0 \approx 2m\pi$, or close to the anti-resonance condition $\phi_0 \approx (2m+1)\pi$. Modulation instability in the latter case is called period-2 type since the phase of perturbation is restored after two round trips inside the cavity. Figure 3.6 shows the gain spectra in the normal-GVD region of a ring cavity using $\rho = 0.95$ and $u_0 = 1$. Different peaks correspond to detuning of the CW beam such that ϕ_0 deviates from the resonance (thin line) or the antiresonance (thick line) condition by 0.1π. In real units, $\Omega = 1$ corresponds to a frequency of about 0.3 THz when $\beta_2 = 30$ ps^2/km and $L_R = 10$ m.

Evidence of modulation instability in a fiber-ring resonator has been seen experimentally [48] with the same setup used for Fig. 3.5. The 7.38-m ring cavity was driven synchronously using 1.25 ps from a 980-nm, mode-locked Ti:sapphire laser. When the peak power of input pulses exceeded a threshold value (about 500 W), the pulse spectrum developed peaks at the location corresponding to antiresonances of the fiber resonator. The spectrum exhibited peaks at cavity resonances also. However, such peaks appear even below the modulation-instability threshold. In contrast, the antiresonance spectral peaks

appear only above the instability threshold, and their presence constitutes a clear evidence of the cavity-induced modulation instability.

3.1.5 Ultrafast Nonlinear Effects

When short optical pulses are fed into a fiber resonator whose length is much larger than the dispersion and nonlinear length scales associated with the pulse, considerable pulse shaping is likely to occur over a single round trip. The combined effects of GVD and SPM on pulses circulating in a fiber resonator can lead to quite interesting nonlinear dynamics [50]–[56]. Depending on the input and fiber parameters, a steady-state pattern (along the fiber length) may or may not evolve (in the sense that it remains unchanged from one round trip to next). Moreover, evolution of pulses within the fiber ring depends on whether pulses experience normal or anomalous GVD.

Consider the situation in which ultrashort optical pulses are injected into a fiber-ring cavity synchronously using a mode-locked laser. Evolution of pulses over multiple round trips is governed by the generalized NLS equation of Section A.2.3.2. Including the terms related to third-order dispersion and intrapulse Raman scattering, Eq. (3.1.10) becomes

$$i\frac{\partial A}{\partial z} - \frac{\beta_2}{2}\frac{\partial^2 A}{\partial T^2} - \frac{i\beta_3}{6}\frac{\partial^3 A}{\partial T^3} + \gamma|A|^2 A - \gamma T_R A\frac{\partial |A|^2}{\partial T} = 0, \tag{3.1.18}$$

where T_R is the Raman parameter (with a value of about 3 fs). For a fiber ring of length L_R, this equation should be solved with the following boundary condition at the coupler after each round trip:

$$A^{(n+1)}(0,T) = \sqrt{\rho}A^{(n)}(L_R,T)\exp(i\phi_0) + i\sqrt{(1-\rho)}A_i(T), \tag{3.1.19}$$

where the superscript denotes the round-trip number. The amplitude A_i for "sech" input pulses can be written as

$$A_i(T) = \sqrt{P_0}\,\mathrm{sech}(T/T_0) \tag{3.1.20}$$

for pulses of width T_0 and peak power P_0. The full width at half maximum (FWHM) of pulses is related to T_0 as $T_p = 2\ln(1+\sqrt{2})T_0 \approx 1.763\,T_0$.

Numerical simulations for 10-ps pulses propagating inside a 100-m fiber ring show that each input pulse develops an internal substructure consisting of many subpulses of width ~ 1 ps. Moreover, a steady state is reached only if the input peak power is below a certain value. In the steady state, subpulses

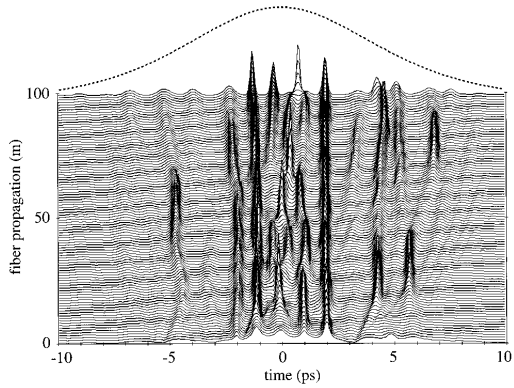

Figure 3.7 Evolution of substructure in a 100-m ring resonator when 10-ps pulses (dotted curve) are injected into it synchronously. (After Ref. [54], ©1997 by the American Physical Society)

have a uniform spacing that does not change from one round trip to next. Each subpulse corresponds to a fundamental soliton whose width and peak power are related such that the soliton order $N \approx 1$. When the input peak power exceeds the critical value, a phase-transition-like behavior occurs such that the position and width of subpulses change continuously in an apparently random manner. Since most subpulses retain their soliton character (in the sense that $N \approx 1$), such an ensemble of subpulses is referred to as a *soliton gas*. Figure 3.7 shows the evolution of substructure along the ring over one round trip.

Direct experimental observation of such a pattern is difficult because of the ultrashort time scale involved. However, the autocorrelation and spectral measurements agree with the theoretical predictions based on the NLS equation. In the experiment, 2-ps mode-locked pulses, obtained from a color-center laser operating at 1.57 μm, were injected into a ring resonator made by using 6 m of polarization-maintaining fiber. Both the autocorrelation trace and the spectrum changed qualitatively as the peak power increased beyond a certain value, resulting in the transition from a regular to irregular pattern of subpulses.

In the case of normal GVD, nonlinear dynamics becomes even more complex [52]. Numerical simulations show that each pulse still develops an internal substructure but the resulting pattern is not governed by soliton shaping. Depending on the linear detuning ϕ_0 of the ring resonator, the substructure varies from pulse to pulse and exhibits period-doubling bifurcations and chaos. Experiments performed using 12-ps pulses (obtained from a Nd:YAG laser op-

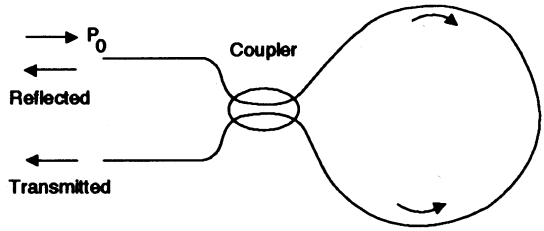

Figure 3.8 Schematic illustration of an all-fiber Sagnac interferometer acting as a nonlinear fiber-loop mirror.

erating near 1.32 μm) show that the pulse energy also varies from pulse to pulse and exhibits a period-doubling route toward chaos as ϕ_0 is varied in the vicinity of a cavity resonance.

3.2 Sagnac Interferometers

Sagnac interferometers can also exploit the nonlinear phase shift of optical fibers for optical switching [57]–[59]. Figure 3.8 shows schematically how a fiber coupler can be used to make a Sagnac interferometer. It is made by connecting a piece of long fiber to the two output ports of a fiber coupler to form a loop. It appears similar to a fiber-ring resonator but behaves quite differently because of two crucial differences. First, there is no feedback mechanism since all light entering from the input port exits from the resonator after a single round trip. Second, the entering optical field is split into two counterpropagating parts that share the same optical path and interfere at the coupler coherently.

The relative phase difference between the counterpropagating beams determines whether an input beam is reflected or transmitted by the Sagnac interferometer. In fact, if a 3-dB fiber coupler is used, any input is totally reflected, and the Sagnac loop acts as a perfect mirror. Such a device can be designed to transmit a high-power signal while reflecting it at low power levels, thus acting as an all-optical switch. For this reason, it is referred to as the *nonlinear fiber-loop mirror* and has attracted considerable attention not only for optical switching but also for mode locking and wavelength demultiplexing.

3.2.1 Nonlinear Transmission

The physical mechanism behind nonlinear switching can be easily understood by considering a CW or a quasi-CW input beam. When such an optical signal is incident at one port of the fiber coupler, the transmittivity of a Sagnac interferometer depends on the power-splitting ratio of the coupler. If a fraction ρ of the input power P_0 travels in the clockwise direction, the transmittivity for a loop of length L is obtained by calculating the phase shifts acquired during a round trip by the counterpropagating optical waves, and then recombining them interferometrically at the coupler. It is important to include any relative phase shift introduced by the coupler. If we use the transfer matrix of a fiber coupler given in Eq. (2.1.22) together with $A_2(0) = 0$, the amplitudes of the forward- (clockwise) and backward- (counterclockwise) propagating fields are given by

$$A_f = \sqrt{\rho} A_0, \qquad A_b = i\sqrt{1-\rho} A_0, \tag{3.2.1}$$

where $\rho = \cos^2(\kappa l_c)$ for a coupler of length l_c. Notice the $\pi/2$ phase shift for A_b introduced by the coupler. After one round trip, both fields acquire a linear phase shift as well as the SPM- and XPM-induced nonlinear phase shifts. As a result, the two fields reaching at the coupler take the following form:

$$A_f' = A_f \exp[i\phi_0 + i\gamma(|A_f|^2 + 2|A_b|^2)L], \tag{3.2.2}$$

$$A_b' = A_b \exp(i\phi_0 + i\gamma(|A_b|^2 + 2|A_f|^2)L], \tag{3.2.3}$$

where $\phi_0 \equiv \beta L$ is the linear phase shift for a loop of length L and β is the propagation constant within the loop.

The reflected and transmitted fields can now be obtained by using the transfer matrix of the fiber coupler and are given by

$$\begin{pmatrix} A_t \\ A_r \end{pmatrix} = \begin{pmatrix} \sqrt{\rho} & i\sqrt{1-\rho} \\ i\sqrt{1-\rho} & \sqrt{\rho} \end{pmatrix} \begin{pmatrix} A_f' \\ A_b' \end{pmatrix}. \tag{3.2.4}$$

Using Eqs. (3.2.1)–3.2.4), the transmittivity $T_S \equiv |A_t|^2/|A_0|^2$ of the Sagnac loop is given by [59]

$$T_S = 1 - 2\rho(1-\rho)\{1 + \cos[(1-2\rho)\gamma P_0 L]\}, \tag{3.2.5}$$

where $P_0 = |A_0|^2$ is the input power. The linear phase shift does not appear in this equation because of its exact cancellation. For $\rho = 0.5$, T_S equals zero, and the loop reflectivity is 100% at all power levels (hence the name *fiber-loop*

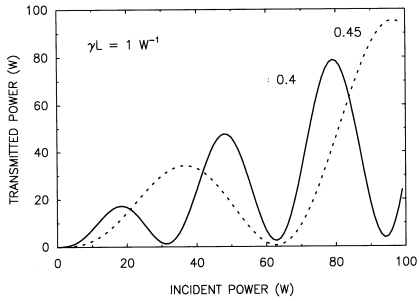

Figure 3.9 Transmitted power as a function of incident power for two values of ρ, showing the nonlinear response of an all-fiber Sagnac interferometer.

mirror). Physically, if the power is equally divided between the counterpropagating waves, the nonlinear phase shift is equal for both waves, resulting in no relative phase difference between the counterpropagating waves. However, if the power-splitting factor ρ is different than 0.5, the fiber-loop mirror exhibits different behavior at low and high powers and can act as an optical switch.

Figure 3.9 shows the transmitted power as a function of P_0 for two values of ρ. At low powers, little light is transmitted if ρ is close to 0.5 since $T_S \approx 1 - 4\rho(1-\rho)$. At high powers, the SPM-induced phase shift leads to 100% transmission of the input signal whenever

$$|1-2\rho|\gamma P_0 L = (2m-1)\pi, \tag{3.2.6}$$

where m is an integer. As seen in Fig. 3.9, the device switches from low to high transmission periodically as input power increases. In practice, only the first transmission peak ($m = 1$) is likely to be used for switching because it requires the least power. The switching power for $m = 1$ can be estimated from Eq. (3.2.6) and is 31 W for a 100-m-long fiber loop when $\rho = 0.45$ and $\gamma = 10$ W^{-1}/km. It can be reduced by increasing the loop length, but one should then consider the effects of fiber loss and GVD that were neglected in deriving Eq. (3.2.5).

3.2.2 Nonlinear Switching

Nonlinear switching in all-fiber Sagnac interferometers was observed beginning in 1989 in several experiments [60]–[66]. Most experiments used short optical pulses with high peak powers. In this case, the power dependence

of loop transmittivity in Eq. (3.2.5) can lead to considerable pulse distortion since only the central part of a pulse is intense enough to undergo switching. In a 1989 experiment, 180-ps pulses obtained from a Q-switched, mode-locked Nd:YAG laser were injected into a 25-m Sagnac loop [60]. Transmission increased from a few percent to 60% at when peak power was increased beyond 30 W. Transmitted pulses were narrower than input pulses, as expected, because only the central part of the pulse was switched. As discussed in Section 2.3, the shape-induced deformation of optical pulses can be avoided in practice by using soliton effects since solitons have a uniform nonlinear phase across the entire pulse. Their use requires ultrashort pulses (width < 10 ps) propagating in the anomalous-GVD regime of the fiber. The XPM-induced coupling between the counterpropagating solitons can be ignored for optical pulses short enough that they overlap for a relatively short time compared with the round-trip time. As a result, one can use two uncoupled NLS equations in the form of Eq. (3.1.12) for counterpropagating solitons inside the fiber loop.

SPM-Induced Switching

Soliton switching in Sagnac interferometers was observed in 1989 by launching ultrashort pulses at a wavelength in the anomalous-GVD regime of the fiber loop. In one experiment, mode-locked pulses (width about 0.4 ps), obtained from a color-center laser operating near 1.5 μm, were launched into a 100-m Sagnac loop formed using a 58:42 fiber coupler [61]. In another experiment, a 25-m-long loop was formed using a polarization-maintaining fiber (having its zero-dispersion wavelength near 1.58 μm), and 0.3-ps input pulses were obtained from a color-center laser operating near 1.69 μm [62]. Figure 3.10 shows the switching characteristics observed in this experiment. Energies of the transmitted and reflected pulses (E_{OUT} and E_{REFL}, respectively) vary with the input pulse energy E_{IN}, showing clear evidence of nonlinear switching. The energy of transmitted pulses increases from a few percent to 90% as the input pulse energy is ramped up close to 55 pJ (peak power ~ 100 W).

The experimental results obtained with 0.3-ps pulses cannot be explained using the simple CW theory given earlier since soliton effects play an important role. Good agreement was obtained by solving the generalized NLS equation given in Eq. (3.1.18) numerically with the appropriate boundary conditions [62]. The inclusion of intrapulse Raman scattering—a higher-order nonlinear effect that shifts the spectrum of solitons (see Section A.5.5)—was

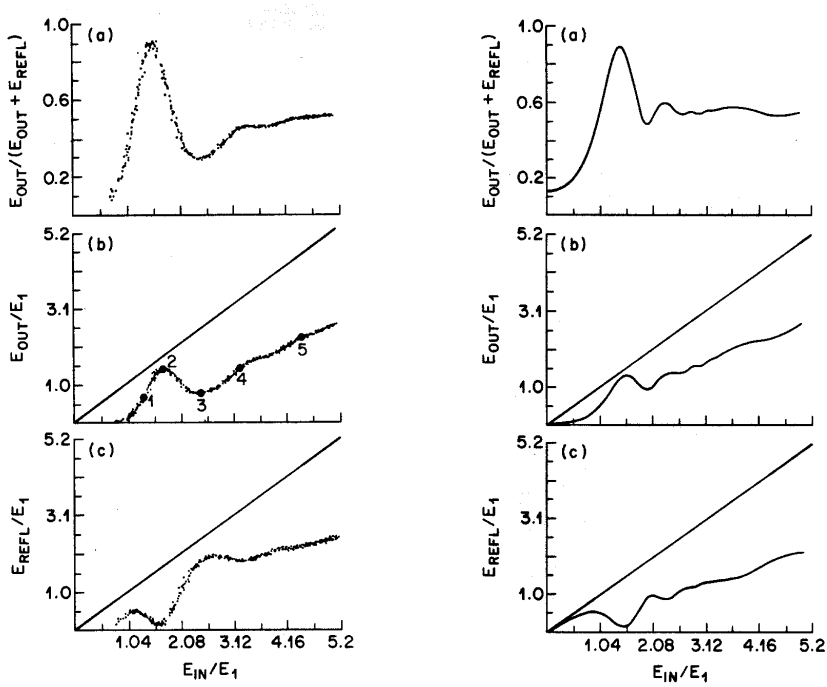

Figure 3.10 Measured (left) and simulated (right) switching characteristics of a nonlinear fiber-loop mirror. The energy level for forming a fundamental soliton was $E_1 = 33.2$ pJ for 0.3-ps input pulses used in the experiment. (After Ref. [62])

found to be important for such short pulses and limited the peak transmission from reaching 100%. It also led to pulse breakup at high powers.

The switching threshold of a Sagnac interferometer can be reduced by incorporating a fiber amplifier within the loop [65]. If the amplifier is located close to the fiber coupler, its presence introduces an asymmetry as the counterpropagating pulses are not amplified simultaneously. Since the Sagnac interferometer is unbalanced by the amplifier, even a 50:50 coupler ($\rho = 0.5$) can be used. The switching behavior in this case can be understood by noting that one wave is amplified at the entrance to the loop while the counterpropagating wave experiences amplification just before exiting the loop. Since the intensities of the two waves differ by a large amount throughout the loop, the differential phase shift can be quite large. In fact, assuming that the clockwise wave is amplified first by a factor G, we can use Eq. (3.2.4) to calculate the transmittivity provided that A_f in Eq. (3.2.2) is multiplied by $\sqrt{G}$. The result

is given by

$$T_S = 1 - 2\rho(1-\rho)\{1 + \cos[(1-\rho-G\rho)\gamma P_0 L]\}. \tag{3.2.7}$$

The condition for complete transmission is obtained from Eq. (3.2.6) by replacing $(1-2\rho)$ with $(1-\rho-G\rho)$. For $\rho = 0.5$, the switching power is given by (using $m = 1$)

$$P_0 = 2\pi/[(G-1)\gamma L]. \tag{3.2.8}$$

Since the amplification factor G can be as large as 30 dB, the switching power is reduced by a factor of up to 1000. Such a device, referred to as the *nonlinear amplifying-loop mirror*, can switch at peak power levels below 1 mW. Its implementation is relatively simple with the advent of fiber amplifiers (see Chapter 4). In a demonstration of the basic concept, 4.5 m of Nd-doped fiber was spliced within the 306-m fiber loop formed using a 3-dB coupler [65]. Quasi-CW-like switching was observed using 10-ns pulses. The switching power was about 0.9 W even when the amplifier provided only a 6-dB gain (a factor of 4). In a later experiment, the use of a semiconductor optical amplifier, providing different gains for counterpropagating waves, inside a 17-m fiber loop resulted in switching powers of less than 250 μW when 10-ns pulses obtained from a semiconductor laser were injected into the loop [66].

A Sagnac interferometer can also be unbalanced by using a fiber loop in which GVD is not constant but varies along the loop [67]–[74]. The GVD can vary continuously as in a dispersion-decreasing fiber, or in a steplike fashion (using fibers with different dispersive properties connected in series). The simplest situation corresponds to the case in which the Sagnac loop is made with two types of fibers and is similar to a dispersion-management scheme used in lightwave systems for GVD compensation. Dispersion-varying fiber loops unbalance a Sagnac interferometer since the counterpropagating waves experience different GVD as they complete a round trip. The most noteworthy feature of such Sagnac loops is that they remain balanced for CW beams of any power levels since GVD does not affect them. However, evolution of optical pulses is affected both by GVD and SPM, resulting in a net relative phase shift between the counterpropagating waves. As a result, optical pulses can be switched to the output port while any CW background noise is reflected by dispersion-imbalanced Sagnac loops. An extinction ratio of 22 dB for the CW background was observed in an experiment [69] in which the 20-m loop was made using equal lengths of standard telecommunication fiber ($\beta_2 = -23$ ps^2/km) and dispersion-shifted fiber ($\beta_2 = -2.3$ ps^2/km).

XPM-Induced Switching

An important class of applications is based on the XPM effects occurring when a control or pump signal is injected into the Sagnac loop such that it propagates in only one direction and induces a nonlinear phase shift on one of the counterpropagating waves through XPM while the other is not affected by it. In essence, the control signal is used to unbalance the Sagnac interferometer in a way similar to how an optical amplifier can be used to produce different SPM-induced phase shifts. As a result, the loop can be made using a 50:50 coupler so that a low-power CW beam is reflected in the absence of the control but transmitted when a control pulse is applied. Many experiments have shown the potential of XPM-induced switching [75]–[84]. As early as 1989, transmittivity of a 632-nm CW signal (obtained from a He–Ne laser) was switched from zero to close to 100% by using intense 532-nm picosecond pump pulses with peak powers of about 25 W [75].

When the signal and control wavelengths are far apart, one should consider the walk-off effects induced by the group-velocity mismatch. As discussed in Section A.7.2, in the absence of GVD effects, the XPM-induced relative phase shift at the coupler is given by

$$\phi_{\mathrm{XPM}} = 2\gamma \int_0^L |A_p(T - d_w z)|^2 \, dz, \tag{3.2.9}$$

where A_p is the pump-pulse amplitude, $T = t - z/v_{gs}$ is the reduced time in the frame moving with the signal pulse, and $d_w = v_{gp}^{-1} - v_{gs}^{-1}$ represents the group-velocity mismatch between the pump and signal pulses. The integral can be evaluated analytically for certain shapes of the pump pulse. For example, for a "sech" pump pulse with $A_p(T) = \sqrt{P_p}\,\mathrm{sech}(T/T_0)$, the phase shift becomes [76]

$$\phi_{\mathrm{XPM}}(\tau) = (\gamma P_p/\delta_w)[\tanh(\tau) - \tanh(\tau - \delta_w)], \tag{3.2.10}$$

where $\tau = T/T_0$ and $\delta_w = d_w L/T_0$. The relative phase is not only time dependent but its shape is also affected considerably by the group-velocity mismatch. Since loop transmittivity remains high as long as the phase shift is close to an odd multiple of π, the transmitted signal shape changes considerably with the shape and peak power of pump pulses.

The problem of pulse walk-off can be solved by using a fiber whose zero-dispersion wavelength lies between the pump and signal wavelengths such that

the two waves have the same group velocity ($d_w = 0$). Indeed, such a 200-m-long Sagnac loop was built in 1990 using polarization-maintaining fiber [77]. It was employed to switch the 1.54-μm signal using 120-ps pump pulses with 1.8-W peak power at 1.32 μm. In a later experiment, 14-ps pump pulses, obtained from a gain-switched 1.55-μm DFB laser and amplified using a fiber amplifier, were able to switch a CW signal in the wavelength region near 1.32 μm.

The pulse walk-off occurring because of wavelength difference between the pump and signal can also be avoided by using an orthogonally polarized pump at the same wavelength as that of the signal [78]. There is still a group-velocity mismatch because of polarization-mode dispersion, but it is relatively small. Moreover, it can be used to advantage by constructing a Sagnac loop in which the slow and fast axes of polarization-maintaining fibers are interchanged in a periodic fashion. In one implementation of this idea [79], a 10.2-m loop consisted of 11 such sections. Two orthogonally polarized pump and signal pulses (width about 230 fs) were injected into the loop and propagated as solitons. The pump pulse was polarized along the fast axis and delayed initially such that it overtook the signal pulse in the first section. In the second section, the signal pulse traveled faster because of the reversing of slow and fast axes and overtook the pump pulse. This process repeated in each section. As a result, two solitons collided multiple times inside the Sagnac loop, and the XPM-induced phase shift was enhanced considerably.

3.2.3 Applications

By exploiting different nonlinear effects—such as XPM, SPM, and four-wave mixing (FWM)—occurring inside the fiber used to make the Sagnac loop, one can use the nonlinear fiber-loop mirror in many applications. This section describes applications relevant to lightwave systems.

Pulse Shaping and Generation

A nonlinear Sagnac interferometer acts as a high-pass intensity filter in the sense that it reflects low-intensity signals but transmits high-intensity radiation without affecting it. This feature is similar to that of saturable absorbers, which absorb weak signals but become transparent at high intensities, with one crucial difference. The speed of saturable absorbers is limited in practice to time

scales longer than 10 ps while the nonlinear response of silica fibers is almost instantaneous (< 10 fs).

A simple application of Sagnac interferometers consists of using them for pulse shaping and pulse cleanup. For example, if a short optical pulse contains a broad low-intensity pedestal, the pedestal can be removed by passing it through such a device [85]. Similarly, a soliton pulse train, corrupted by dispersive radiation or amplified spontaneous emission, can be cleaned by passing it through an all-fiber Sagnac loop. Since solitons can be switched as one unit, they are transmitted by the loop while the low-energy dispersive radiation or noise is reflected back. The Sagnac loop can also be used for pulse compression (see Chapter 6) and for generating a train of short optical pulses at a high repetition rate by injecting a dual-wavelength signal [86].

Saturable absorbers are routinely used for passive mode locking of lasers to generate picosecond pulses. However, their use is limited by their sluggish nonlinear response. Since a nonlinear fiber-loop mirror responds on femtosecond timescales, its passive use for mode-locked lasers was suggested as early as 1990 [87]. Indeed, this approach led to a new class of fiber lasers known as figure-8 lasers [88]. Such lasers can generate femtosecond pulses and are covered in Chapter 5.

Another approach makes use of XPM-induced switching in a Sagnac loop for wavelength conversion and for generating high-quality optical pulses. The basic idea is to launch a CW beam together with control pulses at a different wavelength. In the absence of control signal, the CW light is reflected from a balanced Sagnac interferometer since it acts as a perfect mirror. However, each control pulse shifts the optical phase through XPM and directs a time slice of the CW beam to the output end, producing a pulse train at the CW-laser wavelength. In effect, the Sagnac loop acts as an all-optical gate that is open for the duration of each control pulse. Clearly, such a device acts as a wavelength converter, and this mode of operation should be useful for WDM networks. An added benefit is that the wavelength-converted pulse train can be of higher quality than the control pulses themselves. In one experiment, control pulses from a gain-switched DFB laser operating near 1533 nm were used to convert the 1554-nm CW radiation into a pulse train [89]. Even though 60-ps control pulses were highly chirped, the pulses produced by the Sagnac loop were nearly transform limited. The pulse quality was high enough that pulses could be propagated over 2400 km using a recirculating fiber loop [90]. The reflected light from such a Sagnac loop is in the form of a train of dark

pulses that could be useful for dark-soliton experiments.

Sagnac interferometers are also useful for all-optical signal regeneration in lightwave systems since they can reshape switched pulses while reducing the noise level [91]. The pulse-shaping capability of such interferometers can be improved significantly by concatenating several Sagnac loops in series [92]. The loop length can be reduced by using fibers with a relatively high value of the nonlinear parameter γ. Such fibers were used in a recent experiment to form two concatenated Sagnac loops [93]. The XPM-induced switching was used in the first loop to convert the wavelength of the 10-Gb/s data channel by using it as a control signal. The output of the first loop became the control signal for the second loop where the wavelength was switched back to the original wavelength. The net result was regeneration (noise reduction and pulse shaping) of the data without change in its wavelength.

All-Optical Signal Processing

An important category of applications is related to signal regeneration, format conversion, and logic operation on digital bit streams used in lightwave systems. Nonlinear Sagnac loops can be used as analog-to-digital and digital-to-analog converters [94]. They can also be used for converting frequency modulation into amplitude modulation [95]. The possibility of using a nonlinear Sagnac interferometer for all-optical logic operations was pointed out as early as 1983 [57]. A polarization-maintaining Sagnac loop was used in 1991 to demonstrate the elementary logic operations in the form of AND, XOR, and $\overline{\text{XOR}}$ gates [96]. Two control signals in counterpropagating directions were used to realize this functionality.

To understand how a Sagnac loop performs digital logic, consider the situation in which a regular pulse train (an optical clock) is launched into the loop through a 3-dB coupler. In the absence of control signals, all 1 bits are reflected. If two data streams (random sequences of 1 and 0 bits) are launched inside the loop as control signals, the clock pulse will be reflected if both controls have the same bit in that time slot but get transmitted otherwise. The reason is that a net XPM-induced phase shift is produced when the two controls have different types of bits in a given time slot. The transmitted and reflected signals thus correspond to the XOR and $\overline{\text{XOR}}$ gates, respectively. The AND gate requires only one control signal since a pulse is transmitted only when both the control and signal bits are present simultaneously. Inversion operation can also be carried out using only one control.

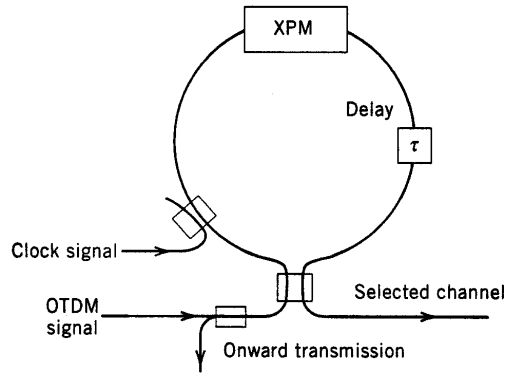

Figure 3.11 Demultiplexing of an OTDM signal using XPM-induced phase shift in a Sagnac interferometer. Delay τ corresponds to the round-trip time within the loop.

All of the above logic operations were demonstrated by injecting pulses from a 1.54-μm DFB laser into a polarization-maintaining Sagnac loop and using 100-ps control pulses from a 1.32-μm Nd:YAG laser [96]. The loop was 200-m long and required power levels of about 1 W to realize the π phase shift. The system-level applications of Sagnac logic gates have also been studied [97]. The use of Sagnac loops for signal regularization or regeneration in fiber-optic communication systems requires consideration of factors such as signal-clock walk-off, GVD-induced pulse broadening, and timing jitter [98].

Channel Demultiplexing

Although lightwave systems commonly employ the WDM technique, optical time-division multiplexing (OTDM) of multiple channels over a single wavelength carrier is a viable option [8]. Sagnac interferometers were used for demultiplexing of OTDM signals starting in 1991 [99]–[105]. A nonlinear fiber-loop mirror was used in 1992 to demultiplex a 64-Gb/s signal to individual 4-Gb/s channels [100]. The pulse energy required for switching was only 1.1 pJ. In another experiment, 10-Gb/s channels were demultiplexed from a 40-Gb/s OTDM signal by using a 11-km-long Sagnac loop [102]. Demultiplexing of a 6.3-Gb/s channel from a 100-Gb/s OTDM signal was demonstrated in 1993 [103].

The demultiplexing function of a nonlinear Sagnac interferometer is based on the XPM-induced switching discussed earlier. The control signal (an opti-

cal clock) consists of a train of optical pulses at the single-channel bit rate. It is injected into the loop such that it propagates only in the clockwise (or anticlockwise) direction, as shown schematically in Fig. 3.11. The OTDM signal enters from the input end and is split into counterpropagating directions by the 3-dB coupler. The clock signal is timed such that it overlaps with pulses belonging to a specific channel within the OTDM signal. As a result, it introduces a nonlinear phase shift through XPM only for those pulses. The power of the clock signal and the loop length are made large enough to introduce a relative phase shift of π. As a result, pulses belonging to the channel selected by the clock are transmitted by the loop while remaining channels are reflected back toward the input port. Different channels can be selected by delaying the clock signal by a suitable amount. All channels can be demultiplexed simultaneously by using several Sagnac loops in parallel [105].

The main limitation of a Sagnac interferometer making use of XPM stems from the weak fiber nonlinearity. The loop length should be 10 km or more in order to introduce a phase shift of π with practical power levels of the clock signal. In a variant of the basic idea, a semiconductor optical amplifier is inserted within the fiber loop and its nonlinearity is used for demultiplexing OTDM channels. The semiconductor optical amplifier induces a phase shift resulting from gain saturation. This phase shift depends on the power of the saturating signal and on a parameter known as the line-width enhancement factor [106]. A phase shift of π can be realized within an semiconductor optical amplifier of length < 1 mm at moderate clock-power levels. As a result of the XPM-induced phase shift within the semiconductor optical amplifier, data bits belonging to a specific channel are transmitted by the Sagnac loop, resulting in demultiplexing of that channel.

The use of a semiconductor optical amplifier as a nonlinear element in place of the fiber reduces the loop length to less than 1 m. However, the nonlinear response of such amplifiers is relatively slow because it requires recombination of electron–hole pairs within the active region of the amplifier and is governed by the carrier lifetime with values ~ 1 ns [106]. By injecting a CW signal with the clock signal (at different wavelengths), the carrier lifetime can be reduced to below 100 ps. In another approach, the semiconductor optical amplifier is placed asymmetrically within the loop in such a way that it is offset from the center by a small but controlled amount [107]–[110]. Such a device can operate at relatively high speeds in spite of the slow semiconductor optical amplifier nonlinearity since the switching time is determined by the offset of

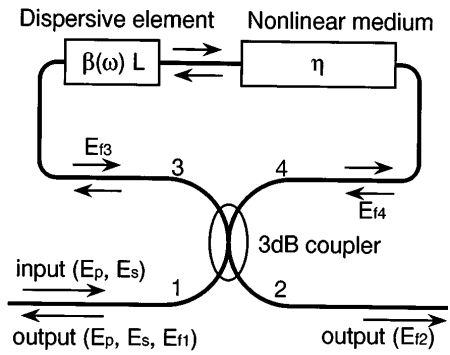

Figure 3.12 Schematic of FWM inside a Sagnac interferometer acting as a parametric-loop mirror. (After Ref. [112])

the semiconductor optical amplifier from the midpoint. This device is often referred to as the *terahertz optical asymmetric demultiplexer* (TOAD) because it can respond at timescales close to 1 ps [108]. Its operation at bit rates as high as 250 Gb/s has been demonstrated [109]. A combination of several such devices can be used for all-optical regenerative memory [111].

Parametric Amplification

An important class of applications is based on four-wave mixing (FWM) occurring inside a nonlinear Sagnac interferometer [112]–[121]. As discussed in Chapter A.10, simultaneous propagation of pump and signal waves at different wavelengths inside an optical fiber generates an idler wave through the nonlinear FWM process. Both the signal and idler waves experience gain through parametric amplification. Moreover, the phase of the idler wave is related to that of the signal wave through the phase-matching condition. For this reason, such a FWM process is also known as *phase conjugation*.

The FWM inside a Sagnac loop is considerably modified by the counterpropagating nature of the pump and signal fields and the nonlinear phase shifts induced by SPM and XPM. Such a device is referred to as the *optical parametric loop mirror* to emphasize the importance of the parametric gain [112]. Figure 3.12 shows the device configuration schematically. The pump and signal fields (E_p and E_s) are launched into the loop from the same port of the coupler. If the Sagnac interferometer is balanced by using a 3-dB coupler so that both pump and signal fields are split equally, they will be reflected by the

loop mirror. On the other hand, the FWM component E_f (idler wave) generated inside the loop behaves asymmetrically if a piece of dispersive fiber is placed near the coupler to unbalance the interferometer.

To understand the operation of a parametric loop mirror, we need to consider the relative phase difference between the counterpropagating components of the idler wave (E_{f3} and E_{f4}). Since the propagation constant β inside a dispersive fiber is different for the pump, signal, and conjugate fields because of their frequencies (ω_p, ω_s, and ω_c, respectively), a net relative phase shift, $\phi_d = [2\beta(\omega_p) - \beta(\omega_s) - \beta(\omega_c)]L_f$, is introduced by a dispersive fiber of length L_f. As a result, the FWM power coming out from the output port 2 of the Sagnac loop depends on this phase shift and is given by [112]

$$P_{\text{out}} = P_c \sin^2(\phi_d/2), \tag{3.2.11}$$

where P_c is the total power generated through FWM. The remaining power exits from the input port. Thus, when ϕ_d is an odd multiple of π, the FWM signal exits from the output port. In contrast, when ϕ_d is an even multiple of π, the loop acts as a phase-conjugate mirror since all FWM power appears to be reflected. From a practical standpoint, the FWM power at the frequency ω_c can be separated from both the pump and signal fields by choosing $\phi_d = \pi$ without requiring an optical filter. At the same time, low-power noise associated with the signal (e.g., amplified spontaneous emission) is filtered by the Sagnac loop since it gets reflected.

FWM in a Sagnac loop has been used for many applications. The phase-sensitive nature of parametric amplification can be used for all-optical storage of data packets consisting of a random string of 1 and 0 bits in the form of picosecond pulses [113]. It can also be used to produce amplitude-squeezed solitons using an asymmetric Sagnac loop [115]. FWM in a nonlinear Sagnac interferometer has been used to make parametric oscillators. Pulses shorter than 1 ps can be generated through synchronous pumping of a Sagnac loop [116]. Moreover, such parametric oscillators are tunable over a range as wide as 40 nm [117]. Parametric amplification is also useful for reducing the noise figure of amplifiers below the 3-dB quantum limit (see Chapter 4). In a recent experiment, 16-dB amplification was realized with a noise figure of only 2 dB [118].

Another important application consists of using the nonlinear Sagnac interferometer for phase conjugation. In one experiment, two orthogonally polarized pump waves were fed into different ports of the Sagnac interferometer

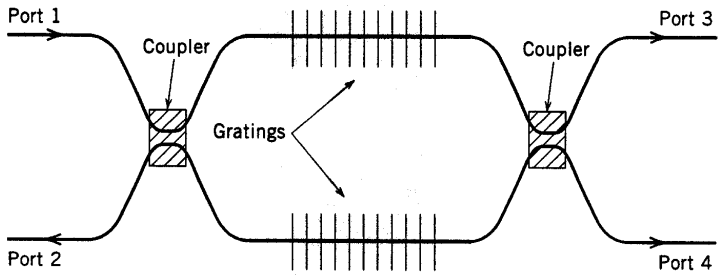

Figure 3.13 Schematic illustration of a Mach–Zehnder interferometer. Fiber gratings are useful for adding or dropping a WDM channel.

to realize a phase conjugator that was not only polarization insensitive but also wavelength-shift free [119]. In another experiment, a semiconductor optical amplifier was used for phase conjugation within a Sagnac loop [120]. Such a device was capable of compensating dispersion over 106 km of standard fiber at a bit rate of 80 Gb/s when the phase conjugator was placed nearly in the middle of the fiber span. This technique of dispersion compensation is also known as *midway spectral inversion* since the spectrum of the FWM signal is a mirror image of the signal spectrum because of phase conjugation [8].

3.3 Mach–Zehnder Interferometers

An all-fiber Mach–Zehnder interferometer (MZI) is constructed by connecting two fiber couplers in series, as shown schematically in Fig. 3.13. The first coupler splits the input signal into two parts, which acquire different phase shifts if arm lengths are different, before they interfere at the second coupler. Such a device has the same functionality as a Sagnac loop but has an added advantage that nothing is reflected back toward the input port. Moreover, a MZI can be unbalanced by simply using different lengths for its two arms since the two optical fields inside it take physically separated paths. However, the same feature also makes the interferometer susceptible to environmental fluctuations. Nonlinear effects in MZIs were considered starting in 1987 and have continued to be of interest [122]–[132].

3.3.1 Nonlinear Characteristics

The theory of nonlinear switching in a MZI is similar to that of Sagnac interferometers. The main difference is that the two fields produced at the output of the first fiber coupler take different physical paths, and thus acquire only SPM-induced phase shifts. In general, two couplers need not be identical and can have different power-splitting fractions, ρ_1 and ρ_2. Two arms of the interferometer can also have different lengths and propagation constants. We consider such an asymmetric MZI and find the powers transmitted from the two output ports when a single CW beam with power P_0 is incident at one input port. Using Eq. (3.2.1) at the first coupler and taking into account both the linear and nonlinear phase shifts, the optical fields at the second coupler are given by

$$A_1 = \sqrt{\rho_1} A_0 \exp(i\beta_1 L_1 + i\rho_1 \gamma |A_0|^2 L_1), \tag{3.3.1}$$

$$A_2 = i\sqrt{1-\rho_1} A_0 \exp[i\beta_2 L_2 + i(1-\rho_1)\gamma |A_0|^2 L_2], \tag{3.3.2}$$

where L_1 and L_2 are the lengths and β_1 and β_2 are the propagation constants for the two arms of the MZI.

The optical fields exiting from the output ports of a MZI are obtained by using the transfer matrix of the second fiber coupler:

$$\begin{pmatrix} A_3 \\ A_4 \end{pmatrix} = \begin{pmatrix} \sqrt{\rho_2} & i\sqrt{1-\rho_2} \\ i\sqrt{1-\rho_2} & \sqrt{\rho_2} \end{pmatrix} \begin{pmatrix} A_1 \\ A_2 \end{pmatrix}. \tag{3.3.3}$$

The fraction of power transmitted from the bar port of the MZI is obtained using $T_b = |A_3|^2/|A_0|^2$ and is given by

$$T_b = \rho_1\rho_2 + (1-\rho_1)(1-\rho_2) - 2[\rho_1\rho_2(1-\rho_1)(1-\rho_2)]^{1/2}\cos(\phi_L + \phi_{\mathrm{NL}}), \tag{3.3.4}$$

where the linear and nonlinear parts of the relative phase shift are given by

$$\phi_L = \beta_1 L_1 - \beta_2 L_2, \quad \phi_{\mathrm{NL}} = \gamma P_0[\rho_1 L_1 - (1-\rho_1)L_2]. \tag{3.3.5}$$

This equation simplifies considerably for a symmetric MZI made using two 3-dB couplers so that $\rho_1 = \rho_2 = \frac{1}{2}$. The nonlinear phase shift vanishes for such a coupler when $L_1 = L_2$, and the transmittivity of the bar port is given as $T_b = \sin^2(\phi_L/2)$. Since the linear phase shift ϕ_L is frequency dependent, the output depends on the wavelength of light. Thus, an MZI acts as an optical filter. The spectral response can be improved by using a cascaded chain of such interferometers with relative path lengths adjusted suitably.

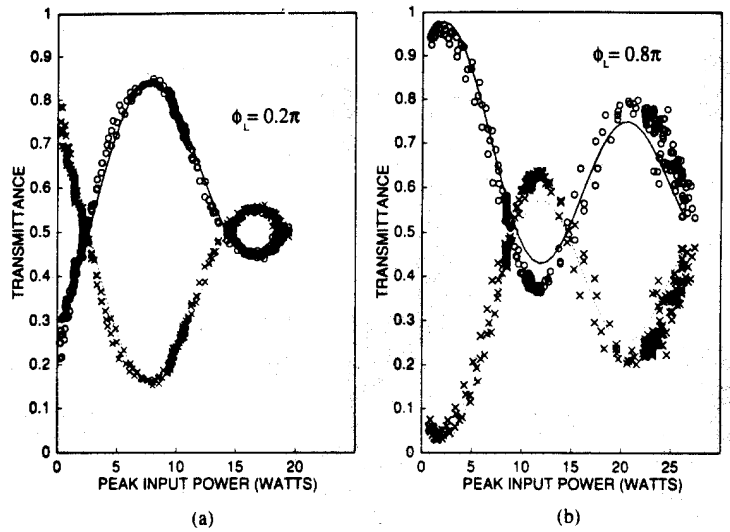

Figure 3.14 Nonlinear switching in a Mach–Zehnder interferometer for two values of ϕ_L. Data from the bar and cross ports are shown by circles and crosses. Theoretical predictions are shown as solid and dotted curves. (After Ref. [128])

The nonlinear response of an MZI is similar to that of a Sagnac loop in the sense that the output from one of the ports can be switched from low to high (or vice versa) by changing the input peak power of the incident signal. Figure 3.14 shows the experimentally observed transmittance from the bar port (circles) and the cross port (crosses) as input peak power is varied over a range of 0 to 25 W for two values of ϕ_L [128]. Predictions of Eq. (3.3.4) are also shown for comparison using $\rho_1 = 0.34$ and $\rho_2 = 0.23$ for the power-splitting ratios of the two couplers. The arm lengths were identical in this experiment ($L_1 = L_2$) as the MZI was made using a dual-core fiber whose two identical cores were connected on each side to a fiber coupler. This configuration avoids temporal fluctuations occurring on a millisecond timescale. Such fluctuations occur invariably when two separate fiber pieces are used in each arm of the MZI and require an active stabilization scheme for controlling them [123].

Similar to the case of Sagnac interferometers, switching can also be accomplished using pump-induced phase shift in an arm of the MZI. In one experiment, one arm of the MZI incorporated 1.6 m of Yb-doped fiber while the fiber in the other arm was undoped [131]. Doping did not affect the signal launched in one of the input ports of the MZI using 1.31-μm and 1.55-

μm semiconductor lasers, and most of the power appeared at the cross port. However, when a 980-nm pump was injected in the arm with doped fiber, the signal switched to the bar port at pump power levels of less than 5 mW. The physical mechanism behind switching is the phase shift induced at the signal wavelength resulting from saturation of absorption near 980 nm. Remarkably, phase shifts of π or more can be induced with only a few milliwatts of the pump power. This mechanism should be distinguished from the XPM-induced phase shift, discussed earlier in the context of Sagnac interferometers, since the phase shift is induced by the dopants rather than fiber nonlinearity.

3.3.2 Applications

MZIs are used for a variety of applications. Most of them are based on the ability of an MZI to produce large changes in its output with small changes in the refractive index in one of its arms. MZIs made by using $LiNbO_3$ or semiconductor waveguides are used routinely as high-speed modulators since such electro-optic materials permit voltage-induced changes in the refractive index. Silica fibers do not have this property, but their refractive index can be changed either optically (through SPM and XPM) or through changes in the environment (such as temperature or pressure). The latter property is useful for making fiber sensors [133]–[135]. Such applications are not discussed here since they do not make use of fiber nonlinearity.

Another class of applications uses MZIs as optical filters. Several kinds of add–drop filters have been developed using MZIs [136]–[140]. The simplest scheme uses a series of interconnected fiber couplers, forming a chain of MZIs. Such a device is sometimes referred to as a *resonant coupler* since it resonantly couples out a specific-wavelength channel from a WDM signal to one output port while the remaining channels appear at the other output port. Its performance can be optimized by controlling the power-splitting ratios of various directional couplers [136]. The wavelength selectivity of Bragg gratings can also be used to make add–drop filters [10]. In one scheme, two identical Bragg gratings are formed in the center of each arm of an MZI [137]. Operation of such a device can be understood from Fig. 3.13. A single channel, whose wavelength λ_g falls within the stop band of the Bragg grating, is totally reflected and appears at port 2. The remaining channels are not affected by the gratings and appear at port 4. The same device can add a channel at the wavelength λ_g if the signal at that wavelength is injected from port 3. Stability of the MZI is of primary concern in these devices and requires active

phase control in practice [138]. Such MZIs are quite important for WDM networks [140]. They are not discussed further here since their operation does not require fiber nonlinearity.

Nonlinear applications of MZIs make use of the SPM- or XPM-induced phase shifts. In fact, nearly all applications discussed in Section 3.2.3 in the context of Sagnac interferometers can use an MZI in place of the Sagnac loop. As an example, demultiplexers based on the XPM-induced phase shift have attracted considerable attention [105]. The main advantage is that multiple MZIs can be cascaded as remaining channels appear at the output end of the MZI (rather than being reflected). The drawback is that active stabilization is often necessary to avoid fluctuations induced by environmental changes.

The pump power required for XPM-induced switching can be reduced to manageable levels by using several different techniques. The nonlinear parameter γ can be increased by reducing the effective core area A_{eff}. In a 1988 experiment, an XPM-induced phase shift of 10° was measured at a pump power of about 15 mW by reducing A_{eff} to only 2 μm^2 in an MZI with 38 m of fiber in each arm [124]. The use of a ring resonator in one arm of the resonator can increase the XPM-induced phase shift by several orders of magnitude [132]. The pump power required for the π phase shift is reduced to under 10 mW for a 10-m-long fiber ring, although the switching speed is also reduced to below 1 GHz for such devices.

3.4 Michelson Interferometers

A Michelson interferometer is made by connecting two separate pieces of fibers to the output ports of a fiber coupler and attaching 100% reflecting mirrors or Bragg gratings at the other end of the fibers [10]. Bragg gratings reflect completely the light whose wavelength falls within the stop band of the grating (see Fig. 3.12). A Michelson interferometer functions much like an MZI with the crucial difference that the light propagating in its two arms is forced to interfere at the same coupler where it was split. Because of this feature, a Michelson interferometer acts as a nonlinear mirror, similar to a Sagnac interferometer, with the important difference that the interfering optical fields do not share the same physical path. Nonlinear Michelson interferometers can also be made using bulk optics (beam splitters and mirrors) with a long piece of fiber in one arm acting as a nonlinear medium. Nonlinear effects in Michel-

son interferometers were first studied in the context of passive mode locking and have continued to remain of interest [141]–[145].

We can apply the analysis of Section 3.3.1 developed for an MZI to the case of a Michelson interferometer because of the similarity between the two. In both cases, an optical field is split into two parts at a fiber coupler, each part acquires a phase shift, and the two parts recombine interferometrically at the coupler. Since the same coupler is used for splitting and combining the optical fields in the case of a Michelson interferometer, we should set $\rho_1 = \rho_2 \equiv \rho$ in Eq. (3.3.4). For the same reason, transmission from the bar port of the coupler turns into reflection from the input port, and the reflectivity is given by

$$R_M = \rho^2 + (1-\rho)^2 - 2\rho(1-\rho)\cos(\phi_L + \phi_{\mathrm{NL}}). \tag{3.4.1}$$

The lengths L_1 and L_2 appearing in Eq. (3.3.5) should be interpreted as round-trip lengths in each arm of the Michelson interferometer. The transmittivity is, of course, given by $T_M = 1 - R_M$. The reflection and transmission characteristics of a Michelson interferometer are similar to those of a Sagnac loop with two major differences. First, the round-trip path lengths L_1 and L_2 can be different for a Michelson interferometer. Second, the reflectivity and transmittivity are reversed for the Sagnac loop. Indeed, Eq. (3.4.1) reduces to Eq. (3.2.5) if $\phi_L = 0$.

Because of the SPM-induced nonlinear phase shift, the reflectivity of a Michelson interferometer is power dependent. As a result, such an interferometer tends to shorten an optical pulse and acts effectively as a fast-responding saturable absorber [141]. The pulse-shortening mechanism can be understood as follows. When the relative linear phases are set appropriately, the nonlinear phase shift may lead to constructive interference near the peak of the pulse, while the wings of the pulse experience destructive interference. The pulse-shortening capability of Michelson interferometers can be exploited for passive mode locking of lasers. This technique is commonly referred to as *additive-pulse mode locking* since it is the interferometric addition of an optical pulse at the coupler that is responsible for mode locking [146]. The discovery of additive-pulse mode locking led to a revolution in the field of lasers and has resulted in mode-locked lasers capable of generating pulses shorter than 10 fs. SPM in optical fibers played an important role in this revolution. This topic is discussed further in Chapter 5 in the context of mode-locked fiber lasers.

Problems

3.1 Derive Eq. (3.1.3) by considering multiple round trips inside a Fabry–Perot resonator.

3.2 Derive an expression for the transmittivity of a fiber-ring resonator of length L formed using a fiber coupler with bar-state transmission of ρ.

3.3 Prove that the free spectral range of a ring resonator of length L is given by v_g/L, where v_g is the group velocity. How much does it change for a 10-m ring when the input wavelength is changed by 10 nm in the wavelength region near 1.55 μm? Assume that GVD of the fiber near this wavelength is -20 ps^2/km and $n_g = 1.46$.

3.4 Reproduce the bistability curves shown in Fig. 3.3 using Eq. (3.1.8). Explore the impact of resonator finesse on bistability by varying R_m in the range from 0.4 to 0.8. Explain your results qualitatively.

3.5 Iterate the nonlinear map given in Eq. (3.1.9) numerically assuming that the phase changes during each round trip inside the ring resonator as indicated in Eq. (3.1.11). Plot the transmittivity as a function of round-trip number for values of $\gamma P_i L_R$ = 1, 5, and 10. Assume $\rho = 0.95$.

3.6 Derive Eq. (3.2.5) by considering the phase shifts experienced by the counterpropagating waves inside a Sagnac loop. Use it to estimate the minimum switching power required when ρ = 0.4 and $\gamma L = 0.1$ W^{-1}.

3.7 Use Eq. (3.2.5) for a Gaussian pulse for which $P_i(t) = P_0 \exp[-(t/T_0)^2]$. Plot the shape of the transmitted pulse using $T_0 = 1$ ps, $\rho = 0.45$, and $\gamma P_0 L$ = 1, 2, and 4. Estimate the compression factor in each case.

3.8 Derive an expression for the transmittivity of a Sagnac loop containing an optical amplifier next to the fiber coupler. Assume G is the amplifier gain, ρ is the bar-state transmission of the coupler, and a CW beam with power P_0 is injected into the loop.

3.9 Use the expression derived in the previous problem to find the switching power when a 3-dB coupler is used ($\rho = 0.5$) to make the Sagnac loop. Estimate its numerical value for a 100-m loop when $G = 30$ dB. Use $\gamma = 2$ W^{-1}/km.

3.10 Show that the XPM-induced phase shift for a "sech" pump pulse is given by Eq. (3.2.10).

3.11 Explain how a Sagnac loop can be used for demultiplexing a single channel from an OTDM bit stream.

3.12 Derive an expression for the bar-state transmittivity of a Mach–Zehnder interferometer. Allow for different path lengths of the two arms and different power-splitting ratios of the two couplers.

References

[1] M. Born and E. Wolf, *Principles of Optics*, 7th ed. (Cambridge University Press, New York, 1999), Chap. 7.

[2] J. E. Midwinter, Ed., *Photonics in Switching* (Academic Press, San Diego, CA, 1993).

[3] A. Marrakchi, Ed., *Selected Papers on Photonic Switching* (SPIE Press, Bellingham, WA, 1996).

[4] H. T. Mouftah, *Photonic Switching Technology* (IEEE Press, Piscataway, NJ, 1998).

[5] O. Svelto, *Principles of Lasers*, 4th ed. (Plenum Press, New York, 1998).

[6] I. P. Kaminow, *IEEE J. Sel. Areas Commun.* **8**, 1005 (1990).

[7] P. E. Green, Jr., *Fiber-Optic Networks* (Prentice-Hall, Englewood Cliffs, NJ, 1993), Chap. 4.

[8] G. P. Agrawal, *Fiber-Optic Communication Systems*, 2nd ed. (Wiley, New York, 1997).

[9] J. Stone and L. W. Stulz, *Electron. Lett.* **23**, 781 (1987); *Electron. Lett.* **26**, 1290 (1990).

[10] R. Kashyap, *Fiber Bragg Gratings* (Academic Press, San Diego, CA, 1999).

[11] L. F. Stokes, M. Chodorow, and H. J. Shaw, *Opt. Lett.* **7**, 288 (1982).

[12] C. Y. Yue, J. D. Peng, Y. B. Liao, and B. K. Zhou, *Electron. Lett.* **24**, 622 (1988).

[13] S. Legoubin, M. Douay, P. Bernage, and P. Niay, *J. Opt. Soc. Am. A* **12**, 1687 (1995).

[14] H. M. Gibbs, S. L. McCall, and T. N. C. Venkatesan, *Phys. Rev. Lett.* **36**, 1135 (1976).

[15] K. Ikeda, *Opt. Commun.* **30**, 257 (1979).

[16] G. P. Agrawal and H. J. Carmichael, *Phys. Rev. A* **19**, 2074 (1979); *Optica Acta* **27**, 651 (1980).

[17] G. P. Agrawal and C. Flytzanis, *Phys. Rev. Lett.* **44**, 1058 (1980); *IEEE J. Quantum Electron.* **17**, 374 (1981).

[18] L. A. Lugiato, in *Progess in Optics*, Vol. 21, E. Wolf, Ed. (North-Holland, Amsterdam, 1984).

[19] H. M. Gibbs, *Optical Bistability: Controlling Light with Light* (Academic Press, San Diego, CA, 1985).

[20] H. Nakatsuka, S. Asaka, H. Itoh, K. Ikeda, and M. Matsuoka, *Phys. Rev. Lett.* **50**, 109 (1983).

[21] B. Crosignani, B. Daino, P. Di Porto, and S. Wabnitz, *Opt. Commun.* **59**, 309 (1986).

[22] R. M. Shelby, M. D. Levenson, and S. H. Perlmutter, *J. Opt. Soc. Am. B* **5**, 347 (1988).

[23] F. J. Fraile-Pelaez, J. Campany, and M. A. Muriel, *Opt. Lett.* **16**, 907 (1991).

[24] R. Vallée, *Opt. Commun.* **81**, 419 (1991).

[25] M. Haelterman, *Appl. Phys. Lett.* **61**, 2767 (1992).

[26] K. Ogusu and S. Yamamoto, *J. Lightwave Technol.* **11**, 1774 (1993).

[27] Y. H. Ja, *Appl. Opt.* **32**, 5310 (1993); *IEEE J. Quantum Electron.* **30**, 329 (1994).

[28] J. Capmany, F. J. Fraile-Pelaez, and M. A. Muriel, *IEEE J. Quantum Electron.* **30**, 2578 (1994).

[29] M. Haelterman, S. Trillo, and S. Wabnitz, *J. Opt. Soc. Am. B* **11**, 446 (1994).

[30] G. Steinmeyer, D. Jasper, and F. Mitschke, *Opt. Commun.* **104**, 379 (1994).

[31] M. Haelterman and M. D. Tolley, *Opt. Commun.* **108**, 165 (1994).

[32] T. Fukushima and T. Sakamoto, *Opt. Lett.* **20**, 1119 (1995).

[33] K. Ogusu, H. Shigekuni, and Y. Yokota, *Opt. Lett.* **20**, 2288 (1995).

[34] K. Ogusu, *IEEE J. Quantum Electron.* **32**, 1537 (1996).

[35] K. Ogusu, A. L. Steel, J. E. Hood, and S. Lynch, *IEEE J. Quantum Electron.* **33**, 2128 (1997).

[36] K. Ogusu, H. Li, and T. Kamizono, *Opt. Rev.* **5**, 185 (1998).

[37] S. Coen, M. Haelterman, P. Emplit, L. Delage, L. M. Simohamed, and F. Reynaud, *J. Opt. Soc. Am. B* **15**, 2283 (1998).

[38] S. Coen and M. Haelterman, *Opt. Lett.* **24**, 80 (1999).

[39] L. F. Stokes, M. Chodorow, and H. J. Shaw, *Opt. Lett.* **7**, 509 (1982).

[40] E. Ott, *Chaos in Dynamical Systems* (Cambridge University Press, New York, 1993).

[41] O. Williams, *Nonlinear Dynamics and Chaos* (World Scientific, Boston, 1997).

[42] E. Infeld and G. Rowlands, *Nonlinear Waves, Solitons, and Chaos*, 2nd ed. (Cambridge University Press, New York, 2000).

[43] M. Nakazawa, K. Suzuki, and H. A. Haus, *Phys. Rev. A* **38**, 5193 (1988); *Phys. Rev. A* **39**, 5788 (1989); *IEEE J. Quantum Electron.* **25**, 2036 (1989).

[44] M. Nakazawa, K. Suzuki, H. Kubota, and H. A. Haus, *IEEE J. Quantum Electron.* **25**, 2045 (1989).

[45] E. J. Greer, D. M. Patrick, and P. G. J. Wigley, *Electron. Lett.* **25**, 1246 (1989).

[46] M. Haelterman, S. Trillo, and S. Wabnitz, *Opt. Lett.* **17**, 745 (1992).

[47] M. Haelterman, S. Trillo, and S. Wabnitz, *Electron. Lett.* **29**, 119 (1993).

[48] S. Coen and M. Haelterman, *Phys. Rev. Lett.* **79**, 4139 (1997).

[49] M. Yu, C. J. McKinstrie, and G. P. Agrawal, *J. Opt. Soc. Am. B* **15**, 607 (1998); *J. Opt. Soc. Am. B* **15**, 617 (1998).

[50] R. Vallée, *Opt. Commun.* **93**, 389 (1992).

[51] M. B. van der Mark, J. M. Schins, and A. Lagendijk, *Opt. Commun.* **98**, 120 (1993).

[52] G. Steinmeyer, A. Buchholz, M. Hänsel, M. Heuer, A. Schwache, and F. Mitschke, *Phys. Rev. A* **52**, 830 (1995).

[53] F. Mitschke, G. Steinmeyer, and A. Schwache, *Physica D* **96**, 251 (1996).

[54] A. Schwache and F. Mitschke, *Phys. Rev. E* **55**, 7720 (1997).

[55] B. A. Malomed, A. Schwache, and F. Mitschke, *Fiber Integ. Opt.* **17**, 267 (1998).

[56] F. Mitschke, I. Halama, and A. Schwache, *Chaos, Solitons & Fractals* **10**, 913 (1999).

[57] K. Otsuka, *Opt. Lett.* **8**, 471 (1983).

[58] D. B. Mortimore, *J. Lightwave Technol.* **6**, 1217 (1988).

[59] N. J. Doran and D. Wood, *Opt. Lett.* **13**, 56 (1988).

[60] N. J. Doran, D. S. Forrester, and B. K. Nayar, *Electron. Lett.* **25**, 267 (1989).

[61] K. J. Blow, N. J. Doran, and B. K. Nayar, *Opt. Lett.* **14**, 754 (1989).

[62] M. N. Islam, E. R. Sunderman, R. H. Stolen, W. Pleibel, and J. R. Simpson, *Opt. Lett.* **14**, 811 (1989).

[63] N. Takato, T. Kaminato, A. Sugita, K. Jinguji, H. Toba, and M. Kawachi, *IEEE J. Sel. Areas Commun.* **8**, 1120 (1990).

[64] K. J. Blow, N. J. Doran, and B. P. Nelson, *Electron. Lett.* **26**, 962 (1990).

[65] M. E. Fermann, F. Haberl, M. Hofer, and H. Hochstrasser, *Opt. Lett.* **15**, 752 (1990).

[66] A. W. O'Neill and R. P. Webb, *Electron. Lett.* **26**, 2008 (1990).

[67] A. L. Steele, *Electron. Lett.* **29**, 1972 (1993).

[68] A. L. Steele and J. P. Hemingway, *Opt. Commun.* **123**, 487 (1996).

[69] W. S. Wong, S. Namiki, M. Margalit, H. A. Haus, and I. P. Ippen, *Opt. Lett.* **22**, 1150 (1997).

[70] M. G. da Silva and A. S. B. Sombra, *Opt. Commun.* **145**, 281 (1998).

[71] I. Y. Khrushchev, R. V. Penty, and I. H. White, *Electron. Lett.* **34**, 1009 (1998)

[72] I. Y. Khrushchev, I. D. Philips, A. D. Ellis, R. J. Manning, D. Nesset, D. G. Moodie, R. V. Penty, and I. H. White, *Electron. Lett.* **35**, 1183 (1999).

[73] J. L. S. Lima and A. S. B. Sombra, *Opt. Commun.* **163**, 292 (1999).

[74] Y. J. Chai, I. Y. Khrushchev, and I. H. White, *Electron. Lett.* **36**, 1565 (2000).

[75] M. C. Farries and D. N. Payne, *Appl. Phys. Lett.* **55**, 25 (1989).

[76] K. J. Blow, N. J. Doran, B. K. Nayar, and B. P. Nelson, *Opt. Lett.* **15**, 248 (1990).

[77] M. Jinno and T. Matsumoto, *IEEE Photon. Technol. Lett.* **2**, 349 (1990); *Electron. Lett.* **27**, 75 (1991).

[78] H. Avramopoulos, P. M. W. French, M. C. Gabriel, H. H. Houh, N. A. Whitaker, and T. Morse, *IEEE Photon. Technol. Lett.* **3**, 235 (1991).

[79] J. D. Moores, K. Bergman, H. A. Haus, and E. P. Ippen, *Opt. Lett.* **16**, 138 (1991); *J. Opt. Soc. Am. B* **8**, 594 (1991).

[80] A. D. Ellis and D. A. Cleland, *Electron. Lett.* **28**, 405 (1992).

[81] M. Jinno and T. Matsumoto, *IEEE J. Quantum Electron.* **28**, 875 (1992).

[82] M. Jinno, *J. Lightwave Technol.* **10**, 1167 (1992); *Opt. Lett.* **18**, 726 (1993); *Opt. Lett.* **18**, 1409 (1993).

[83] N. A. Whitaker, P. M. W. French, M. C. Gabriel, and H. Avramopoulos, *IEEE Photon. Technol. Lett.* **4**, 260 (1992).

[84] H. Bülow and G. Veith, *Electron. Lett.* **29**, 588 (1993).

[85] K. Smith, N. J. Doran, and P. G. J. Wigley, *Opt. Lett.* **15**, 1294 (1990).

[86] S. V. Chernikov and J. R. Taylor, *Electron. Lett.* **29**, 658 (1993).

[87] A. G. Bulushev, E. M. Dianov, and O. G. Okhotnikov, *IEEE Photon. Technol. Lett.* **2**, 699 (1990); *Opt. Lett.* **26**, 968 (1990).

[88] I. N. Duling III, *Electron. Lett.* **27**, 544 (1991); *Opt. Lett.* **16**, 5394 (1991).

[89] R. A. Betts, J. W. Lear, S. J. Frisken, and P. S. Atherton, *Electron. Lett.* **28**, 1035 (1992).

[90] R. A. Betts, J. W. Lear, N. T. Dang, R. D. Shaw, and P. S. Atherton, *IEEE Photon. Technol. Lett.* **4**, 1290 (1992).

[91] J. K. Lucek and K. Smith, *Opt. Lett.* **15**, 1226 (1993).

[92] B. K. Nayar, N. Finlayson, and N. J. Doran, *J. Mod. Opt.* **40**, 2327 (1993).

[93] S. Watanabe and S. Takeda, *Electron. Lett.* **36**, 52 (2000).

[94] J. M. Jeong and M. E. Marhic, *Opt. Commun.* **91**, 115 (1992).

[95] F. Mogensen, B. Pedersen, and B. Nielsen, *Electron. Lett.* **29**, 1469 (1993).

[96] M. Jinno and T. Matsumoto, *Opt. Lett.* **16**, 220 (1991).

[97] A. Huang, N. Whitaker, H. Avramopoulos, P. French, H. Houh, and I. Chuang, *Appl. Opt.* **33**, 6254 (1994).

[98] M. Jinno, *J. Lightwave Technol.* **12**, 1648 (1994).

[99] B. P. Nelson, K. J. Blow, P. D. Constantine, N. J. Doran, J. K. Lucek, I. W. Marshall, and K. Smith, *Electron. Lett.* **27**, 704 (1991).

[100] P. A. Andrekson, N. A. Olsson, J. R. Simpson, D. J. Digiovanni, P. A. Morton, T. Tanbun-Ek, R. A. Logan, and K. W. Wecht, *IEEE Photon. Technol. Lett.* **4**, 644 (1992).

[101] K. Uchiyama, H. Takara, S. Kawanishi, T. Marioka, and M. Saruwatari, *Electron. Lett.* **28**, 1864 (1992); *Electron. Lett.* **29**, 1313 (1993).

[102] D. M. Patrick, A. D. Ellis, and D. M. Spirit, *Electron. Lett.* **29**, 702 (1993).

[103] K. Uchiyama, H. Takara, S. Kawanishi, T. Morioka, M. Saruwatari, and T. Kitoh, *Electron. Lett.* **29**, 1870 (1993).

[104] M. Jinno, *IEEE J. Quantum Electron.* **30**, 2842 (1994).

[105] E. Bødtker and J. E. Bowers, *J. Lightwave Technol.* **13**, 1809 (1995).

[106] G. P. Agrawal and N. K. Dutta, *Semiconductor Lasers*, 2nd ed. (Van Nostrand Reinhold, New York, 1993).

[107] M. Eiselt, *Electron. Lett.* **28**, 1505 (1992).

[108] J. P. Sokoloff, P. R. Prucnal, I. Glesk, and M. Kane, *IEEE Photon. Technol. Lett.* **5**, 787 (1993); *IEEE Photon. Technol. Lett.* **6**, 98 (1994).

[109] I. Glesk, J. P. Sokoloff, and P. R. Prucnal, *Electron. Lett.* **30**, 339 (1994).

[110] M. Eiselt, W. Peiper, and H. G. Weber, *J. Lightwave Technol.* **13**, 2099 (1995).

[111] A. J. Poustie, A. E. Kelly, R. J. Manning, and K. J. Blow, *Opt. Commun.* **154**, 277 (1998).

[112] K. Mori, T. Morioka, and M. Saruwatari, *Opt. Lett.* **20**, 1424 (1995).

[113] G. D. Bartiolini, D. K. Serkland, P. Kumar, and W. L. Kath, *IEEE Photon. Technol. Lett.* **9**, 1020 (1997).

[114] S. Schmitt, J. Ficker, M. Wolff, F. Konig, A. Sizmann, and G. Leuchs, *Phys. Rev. Lett.* **81**, 2446 (1998).

[115] D. Krylov and K. Bergman, *Opt. Lett.* **23**, 1390 (1998).

[116] D. K. Serkland, G. D. Bartiolini, A. Agarwal, P. Kumar, and W. L. Kath, *Opt. Lett.* **23**, 795 (1998).

[117] D. K. Serkland and P. Kumar, *Opt. Lett.* **24**, 92 (1999).

[118] W. Imajuku, A. Takada, and Y. Yamabayashi, *Electron. Lett.* **36**, 63 (2000).

[119] H. C. Lim, F. Futami, and K. Kikuchi, *IEEE Photon. Technol. Lett.* **11**, 578 (1999).

[120] U. Feiste, R. Ludwig, C. Schmidt, E. Dietrich, S. Diez, H. J. Ehrke, E. H. Patzak, G. Weber, and T. Merker, *IEEE Photon. Technol. Lett.* **11**, 1063 (1999).

[121] H. C. Lim, F. Futami, K. Taira, and K. Kikuchi, *IEEE Photon. Technol. Lett.* **11**, 1405 (1999).

[122] N. J. Doran and D. Wood, *J. Opt. Soc. Am. B* **4**, 1843 (1987).

[123] N. Imoto, S. Watkins, and Y. Sasaki, *Opt. Commun.* **61**, 159 (1987).

[124] I. H. White, R. V. Penty, and R. E. Epworth, *Electron. Lett.* **24**, 340 (1988).
[125] M. N. Islam, S. P. Dijaili, and J. P. Gordon, *Opt. Lett.* **13**, 518 (1988).
[126] D. V. Khaidatov, *Sov. J. Quantum Electron.* **20**, 379 (1990).
[127] T. V. Babkina, F. G. Bass, S. A. Bulgakov, V. V. Grogoryants, and V. V. Konotop, *Opt. Commun.* **78**, 398 (1990).
[128] B. K. Nayar, N. Finlayson, N. J. Doran, S. T. Davey, W. L. Williams, and J. W. Arkwright, *Opt. Lett.* **16**, 408 (1991).
[129] D. Yao, *Phys. Rev. A* **52**, 4871 (1995).
[130] K. I. Kang, T. G. Chang, I. Glesk, and P. R. Prucnal, *Appl. Opt.* **35**, 1485 (1996).
[131] P. Elango, J. W. Arkwright, P. L. Chu, and G. R. Atkins, *IEEE Photon. Technol. Lett.* **8**, 1032 (1996).
[132] J. E. Heebner and R. W. Boyd, *Opt. Lett.* **24**, 847 (1999).
[133] M. A. Marcus and B. Culshaw, Eds., *Fiber Optic Sensor Technology and Applications* (SPIE Press, Bellingham, 1999).
[134] K. T. Gratten and B. T. Meggitt, *Optical Fiber Sensor Technology* (Chapman and Hall, New York, 1999).
[135] J. Sirkis, *Design of Fiber Optic Sensor Systems* (Marcel Dekker, New York, 2000).
[136] M. Kuznetsov, *J. Lightwave Technol.* **12**, 226 (1994).
[137] T. J. Cullen, H. N. Rourke, C. P. Chew, S. R. Baker, T. Bircheno, K. Byron, and A. Fielding, *Electron. Lett.* **30**, 2160 (1994).
[138] G. Nykolak, M. R. X. de Barros, T. N. Nielsen, and L. Eskildsen, *IEEE Photon. Technol. Lett.* **9**, 605 (1997).
[139] K. N. Park, T. T. Lee, M. H. Kim, K. S. Lee, and Y. H. Won, *IEEE Photon. Technol. Lett.* **10**, 555 (1998).
[140] T. Mizuochi, T. Kitayama, K. Shimizu, and K. Ito, *J. Lightwave Technol.* **16**, 265 (1998).
[141] F. Ouellette and M. Piché, *Opt. Commun.* **60**, 99 (1986); *Canadian J. Phys.* **66**, 903 (1988).
[142] E. M. Dianov and O. G. Okhotnikov, *IEEE Photon. Technol. Lett.* **3**, 499 (1991).
[143] C. Spielmann, F. Krausz, T. Brabec, E. Wintner, and A. J. Schmidt, *Appl. Phys. Lett.* **58**, 2470 (1991).
[144] P. Heinz, A. Reuther, and A. Laubereau, *Opt. Commun.* **97**, 35 (1993).
[145] C. X. Shi, *Opt. Lett.* **18**, 1195 (1993).
[146] H. A. Haus, J. G. Fujimoto, and E. P. Ippen, *J. Opt. Soc. Am. B* **7**, 2068 (1991).

Chapter 4

Fiber Amplifiers

Optical fibers attenuate light like any other material. In the case of silica fibers, losses are relatively small, especially in the wavelength region near 1.55 μm ($\alpha \approx 0.2$ dB/km). For this reason, losses can simply be ignored if fiber length is 1 km or less. In the case of long-haul fiber-optic communication systems, transmission distances may exceed thousands of kilometers. Fiber amplifiers are commonly used to overcome transmission losses and restore the optical signal in such systems. This chapter is devoted to fiber amplifiers. Section 4.1 discusses general concepts such as gain spectrum and amplifier bandwidth. Section 4.2 describes the operating characteristics of erbium-doped fiber amplifiers (EDFAs). The nonlinear and dispersive effects are included in Section 4.3 using the Maxwell–Bloch formalism. The resulting Ginzburg–Landau equation is used in Sections 4.4–4.6 to discuss a variety of nonlinear effects in fiber amplifiers.

4.1 Basic Concepts

Although fiber amplifiers were made as early as 1964 [1], their use became practical only after 1986 when the techniques for fabrication and characterization of low-loss, rare-earth-doped fibers were perfected [2]. The rare earths (or lanthanides) form a group of 14 similar elements with atomic numbers in the range from 58 to 71. When these elements are doped in silica or other glass fibers, they become triply ionized. Many different rare-earth ions, such as erbium, holmium, neodymium, samarium, thulium, and ytterbium, can be used to make fiber amplifiers that operate at wavelengths covering a wide range

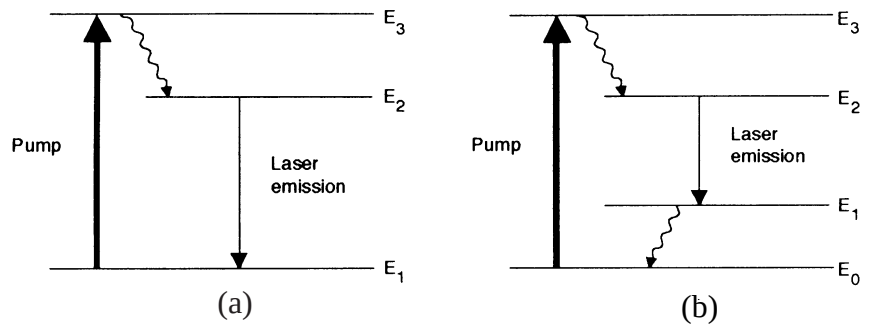

Figure 4.1 Schematic illustration of (a) three-level and (b) four-level pumping schemes. Wavy arrows indicate fast relaxation of the level population through nonradiative processes.

from visible to infrared. Amplifier characteristics, such as the operating wavelength and the gain bandwidth, are determined by dopants rather than by the fiber, which plays the role of a host medium. EDFAs have attracted the most attention as they operate near 1.55 μm and are useful for modern fiber-optic communication systems [3]–[9].

4.1.1 Pumping and Gain Coefficient

Fiber amplifiers amplify incident light through stimulated emission, the same mechanism used by lasers. Indeed, an optical amplifier is just a laser without feedback. Its main ingredient is the optical gain, occurring when the amplifier is pumped optically to realize population inversion. Depending on the energy levels of the dopant, pumping schemes can be classified as a three- or four-level scheme [10]–[12]. Figure 4.1 shows the two kinds of pumping schemes. In both cases, dopants absorb pump photons to reach a higher energy state and then relax rapidly to a lower-energy excited state (level 2). The stored energy is used to amplify the incident signal through stimulated emission. The main difference between the three- and four-level pumping schemes is related to the energy state occupied by the dopant after each stimulated-emission event. In the case of a three-level scheme, the ion ends up in the ground state, whereas it remains in an excited state in the case of a four-level pumping scheme. It will be seen later that this difference affects the amplifier characteristics significantly. EDFAs make use of a three-level pumping scheme.

For understanding the physics behind signal amplification, details of pumping are not important. Optical pumping creates the necessary population inversion between the two energy states, which in turn provides the optical gain $g = \sigma(N_1 - N_2)$, where σ is the transition cross section and N_1 and N_2 are atomic densities in the two energy states. The gain coefficient g can be calculated for both the three- and four-level pumping schemes by using the appropriate rate equations [10]–[12].

The gain coefficient of a homogeneously broadened gain medium can be written as [11]

$$g(\omega) = \frac{g_0}{1 + (\omega - \omega_a)^2 T_2^2 + P/P_s}, \tag{4.1.1}$$

where g_0 is the peak value, ω is the frequency of the incident signal, ω_a is the atomic transition frequency, and P is the optical power of the continuous-wave (CW) signal being amplified. The saturation power P_s depends on dopant parameters such as the fluorescence time T_1 and the transition cross section σ. The parameter T_2 in Eq. (4.1.1) is known as the dipole relaxation time and is typically quite small (~ 0.1 ps) for fiber amplifiers. The fluorescence time T_1 varies in the range from 0.1 μs to 10 ms, depending on the dopant. Equation (4.1.1) can be used to discuss the important characteristics of optical amplifiers such as gain bandwidth, amplification factor, and output saturation power. We begin by considering the case in which $P/P_s \ll 1$ throughout the amplifier. This is referred to as the *unsaturated regime* since the gain remains unsaturated during amplification.

4.1.2 Amplifier Gain and Bandwidth

By neglecting the term P/P_s in Eq. (4.1.1), the gain coefficient becomes

$$g(\omega) = \frac{g_0}{1 + (\omega - \omega_a)^2 T_2^2}. \tag{4.1.2}$$

This equation shows that the gain is maximum when the signal frequency ω coincides with the atomic transition frequency ω_a. The gain reduction for $\omega \neq \omega_a$ is governed by a Lorentzian profile (see Fig. 4.2) that is characteristic of homogeneously broadened systems [10]–[12]. As discussed later, the actual gain spectrum of fiber amplifiers can deviate considerably from the Lorentzian profile. The gain bandwidth is defined as the full width at half maximum (FWHM) of the gain spectrum $g(\omega)$. For the Lorentzian spectrum, the gain

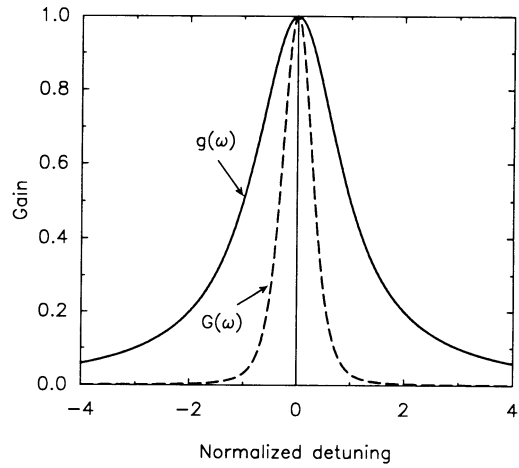

Figure 4.2 Lorentzian spectrum $g(\omega)$ and the corresponding amplifier-gain spectrum $G(\omega)$ for a fiber amplifier.

bandwidth is given by

$$\Delta\nu_g = \frac{\Delta\omega_g}{2\pi} = \frac{1}{\pi T_2}. \tag{4.1.3}$$

As an example, $\Delta\nu_g \approx 3$ THz when $T_2 = 0.1$ ps. Amplifiers with a relatively large bandwidth are preferred for optical communication systems.

A related concept of amplifier bandwidth is commonly used in place of the gain bandwidth. The difference becomes clear when one considers the amplification factor defined as $G = P_{\text{out}}/P_{\text{in}}$, where P_{in} and P_{out} are the input and output powers of the CW signal being amplified. The amplification factor is obtained by solving

$$dP/dz = g(\omega)P(z), \tag{4.1.4}$$

where $P(z)$ is the optical power at a distance z from the input end of the amplifier. A straightforward integration with the conditions $P(0) = P_{\text{in}}$ and $P(L) = P_{\text{out}}$ shows that the amplification factor for an amplifier of length L is given by

$$G(\omega) = \exp\left(\int_0^L g(\omega)dz\right) = \exp[g(\omega)L], \tag{4.1.5}$$

where g is assumed to be constant along the amplifier length.

Both $G(\omega)$ and $g(\omega)$ are maximum at $\omega = \omega_a$ and decrease when $\omega \neq \omega_a$. However, $G(\omega)$ decreases much faster than $g(\omega)$ because of the exponential

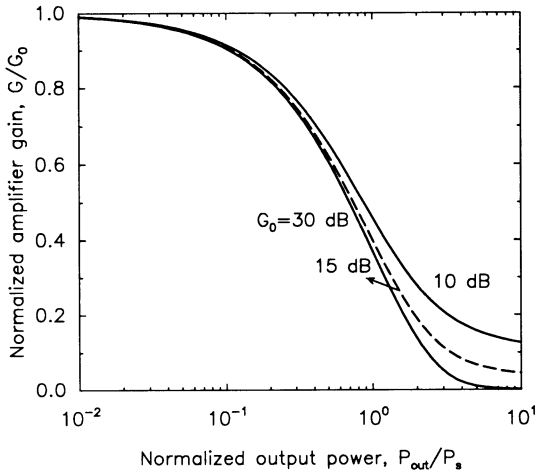

Figure 4.3 Saturated amplifier gain as a function of output power (normalized to the saturation power) for several values of the unsaturated amplifier gain G_0.

dependence seen in Eq. (4.1.5). The amplifier bandwidth $\Delta\nu_A$ is defined as the FWHM of $G(\omega)$ and is related to the gain bandwidth $\Delta\nu_g$ as

$$\Delta\nu_A = \Delta\nu_g \left(\frac{\ln 2}{\ln G_0 - \ln 2}\right)^{1/2}, \tag{4.1.6}$$

where G_0 is the peak value of the amplifier gain. Figure 4.2 shows the gain profile $g(\omega)$ and the amplification factor $G(\omega)$ by plotting both g/g_0 and G/G_0 as a function of $(\omega - \omega_a)T_2$. As expected, the amplifier bandwidth is smaller than the gain bandwidth, and the difference depends on the amplifier gain itself.

The origin of gain saturation lies in the power dependence of the gain coefficient in Eq. (4.1.1). Since g is reduced when P becomes comparable to P_s, the amplification factor G is also expected to decrease. To simplify the discussion, let us consider the case in which the signal frequency is exactly tuned to the atomic transition frequency ω_a. By substituting g from Eq. (4.1.1) in Eq. (4.1.4), we obtain

$$\frac{dP}{dz} = \frac{g_0 P}{1 + P/P_s}. \tag{4.1.7}$$

This equation can be easily integrated over the amplifier length. By using the initial condition $P(0) = P_{\text{in}}$ together with $P(L) = P_{\text{out}} = GP_{\text{in}}$, the amplifier

gain is given by the implicit relation

$$G = G_0 \exp\left(-\frac{G-1}{G}\frac{P_{\text{out}}}{P_s}\right). \tag{4.1.8}$$

Figure 4.3 shows the saturation characteristics by plotting G as a function of P_{out}/P_s for several values of G_0. A quantity of practical interest is the output saturation power P_{out}^s, defined as the output power at which the amplifier gain G is reduced by a factor of 2 from its unsaturated value G_0. By using $G = G_0/2$ in Eq. (4.1.8), P_{out}^s is given by

$$P_{\text{out}}^s = \frac{G_0 \ln 2}{G_0 - 2} P_s. \tag{4.1.9}$$

By noting that $G_0 \gg 2$ in practice, $P_{\text{out}}^s \approx (\ln 2) P_s \approx 0.69 P_s$. As seen in Fig. 4.3, P_{out}^s becomes nearly independent of G_0 for $G_0 > 20$ dB.

4.1.3 Amplifier Noise

All amplifiers degrade the signal-to-noise ratio (SNR) of the amplified signal because of spontaneous emission that is added to the signal during its amplification. The SNR degradation is quantified through the noise figure F_n defined as

$$F_n = (\text{SNR})_{\text{in}}/(\text{SNR})_{\text{out}}, \tag{4.1.10}$$

where both SNRs refer to the electrical power generated when an optical signal is converted to electric current by using a photodetector. In general, F_n depends on several parameters governing the shot and thermal noises associated with the detector. We can obtain a simple expression for F_n by considering an ideal detector whose performance is limited by shot noise only [13].

In the shot-noise limit, the SNR of the input signal is given by [8]

$$(\text{SNR})_{\text{in}} = \frac{I^2}{\sigma_s^2} = \frac{(RP_{\text{in}})^2}{2q(RP_{\text{in}})\Delta f} = \frac{P_{\text{in}}}{2h\nu\Delta f}, \tag{4.1.11}$$

where $I = RP_{\text{in}}$ is the average photocurrent, $R = q/h\nu$ is the responsivity of an ideal photodetector with 100% quantum efficiency, and

$$\sigma_s^2 = 2q(RP_{\text{in}})\Delta f \tag{4.1.12}$$

represents the contribution of shot noise. Here Δf is the detector bandwidth, ν is the optical frequency, and q is the magnitude of the electron's charge. To

evaluate the SNR of the amplified signal, we should add the contribution of spontaneous emission to the detector noise.

The spectral density of spontaneous-emission noise is nearly constant for broadband amplifiers (white noise) and is given by [14]

$$S_{sp}(\nu) = (G-1)n_{sp}h\nu, \tag{4.1.13}$$

where n_{sp} is called the spontaneous-emission (or population-inversion) factor and is defined as

$$n_{sp} = N_2/(N_2 - N_1). \tag{4.1.14}$$

The effect of spontaneous emission is to add fluctuations to the amplified signal, which are converted to current fluctuations during the detection process.

The dominant contribution to the noise current comes from the beating of spontaneous emission with the signal. This beating phenomenon is similar to heterodyne detection: Spontaneously emitted radiation mixes coherently with the amplified signal at the photodetector and produces a heterodyne component of the photocurrent. The variance of the photocurrent can be written as [8]

$$\sigma^2 = 2q(RGP_{\text{in}})\Delta f + 4(RGP_{\text{in}})(RS_{sp})\Delta f, \tag{4.1.15}$$

where the first term is due to shot noise and the second term results from signal–spontaneous emission beating. Since $I = RGP_{\text{in}}$ is the average current, the SNR of the amplified signal is given by

$$(\text{SNR})_{\text{out}} = \frac{(RGP_{\text{in}})^2}{\sigma^2} \approx \frac{GP_{\text{in}}}{4S_{sp}\Delta f}, \tag{4.1.16}$$

where the last relation was obtained by neglecting the first term in Eq. (4.1.15) and is valid for $G \gg 1$.

The amplifier noise figure is obtained by substituting Eqs. (4.1.11) and (4.1.16) in Eq. (4.1.10) and is given by

$$F_n = 2n_{sp}(G-1)/G \approx 2n_{sp}. \tag{4.1.17}$$

This equation shows that the SNR of the amplified signal is degraded by a factor of 2 (or 3 dB) even for an ideal amplifier for which $n_{sp} = 1$. In practice, F_n exceeds 3 dB. For its application in optical communication systems, an optical amplifier should have F_n as low as possible.

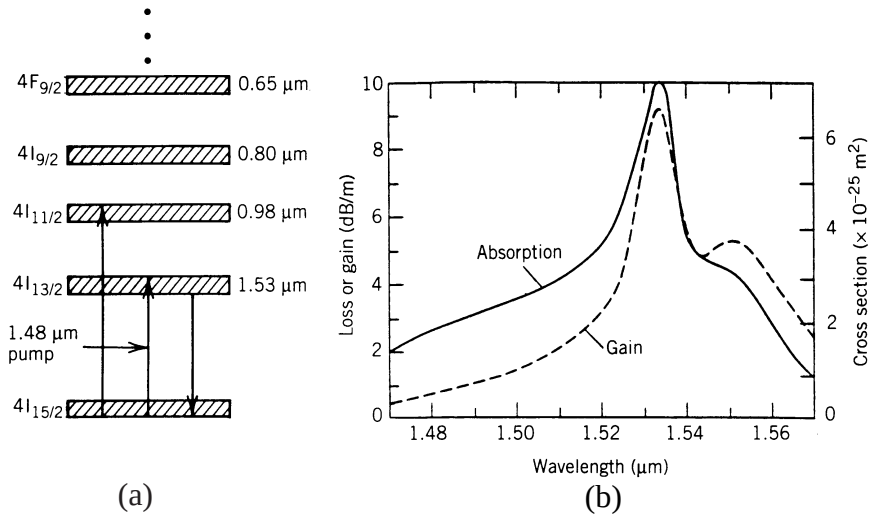

Figure 4.4 (a) Energy levels of erbium ions in silica fibers. (b) Absorption and gain spectra of an erbium-doped fiber. (After Ref. [34], ©1991 IEEE)

4.2 Erbium-Doped Fiber Amplifiers

In this section we focus on EDFAs because of their importance for lightwave systems. Figure 4.4(a) shows the relevant energy levels of Er^{3+} in silica glasses. The amorphous nature of silica broadens each energy level into bands. Many transitions can be used for pumping. Initial experiments used visible pump wavelengths even though their use is relatively inefficient [15], [16]. Efficient pumping is possible using semiconductor lasers operating near 0.98-μm and 1.48-μm wavelengths [17]–[20]. High gains in the range of 30 to 40 dB can be obtained with pump powers ~ 10 mW. The transition ${}^4I_{15/2} \rightarrow {}^4I_{9/2}$ allows the use of GaAs pump lasers operating near 0.8 μm, but the pumping efficiency is relatively poor [21]. It can be improved by codoping the fiber with aluminum and phosphorus [22]. EDFAs can also be pumped in the wavelength region near 650 nm. In one experiment, 33-dB gain was realized with 27 mW of pump power at 670 nm [23].

The pump and signal beams inside an EDFA may propagate in the same or opposite directions. The performance is nearly the same in the two pumping configurations when the signal power is small enough for the amplifier to remain unsaturated. In the saturation regime, power-conversion efficiency

is better in the backward-pumping configuration because of lower amplified spontaneous emission [24]. In the bidirectional pumping configuration, the amplifier is pumped in both directions simultaneously using two semiconductor lasers located at the two fiber ends. This configuration requires two pump lasers but has the advantage that the small-signal gain remains relatively constant along the entire amplifier length.

4.2.1 Gain Spectrum

The gain spectrum of an EDFA is affected considerably by the amorphous nature of silica and by the presence of other codopants such as germania and alumina within the fiber core [25]. The gain spectrum of isolated erbium ions is homogeneously broadened, and its bandwidth is determined by the dipole relaxation time T_2. However, it is considerably broadened by the silica host. Structural disorders lead to inhomogeneous broadening of the gain profile, whereas Stark splitting of various energy levels is responsible for additional homogeneous broadening [9]. Mathematically, the gain is obtained by averaging over the distribution of transition frequencies ω_a so that

$$g(\omega) = \int_{-\infty}^{\infty} g_h(\omega, \omega_a) f_a(\omega_a)\, d\omega_a, \tag{4.2.1}$$

where $g_h(\omega, \omega_a)$ is the homogeneously broadened gain profile and $f_a(\omega_a)$ is the distribution function whose form depends on the glass composition within the fiber core.

Figure 4.4(b) shows the gain and absorption spectra of an EDFA whose core was doped with germania. The gain spectrum is quite broad with a double-peak structure. The shape and the width of the gain spectrum is sensitive to core composition. Figure 4.5 shows the emission spectra for four different core compositions. The gain spectrum is narrowest in the case of pure silica but can be broadened considerably by codoping the core with alumina. Attempts have been made to isolate the relative contributions of homogeneous and inhomogeneous broadening. For silica-based EDFAs, the contribution of homogeneous broadening, as deduced from spectral hole-burning measurements, is in the range of 4 to 10 nm, depending on the signal wavelength [9]. With a proper choice of dopants and host fiber, the spectral bandwidth over which EDFAs are able to amplify signals can exceed 30 nm. However, the gain is not uniform over the entire bandwidth.

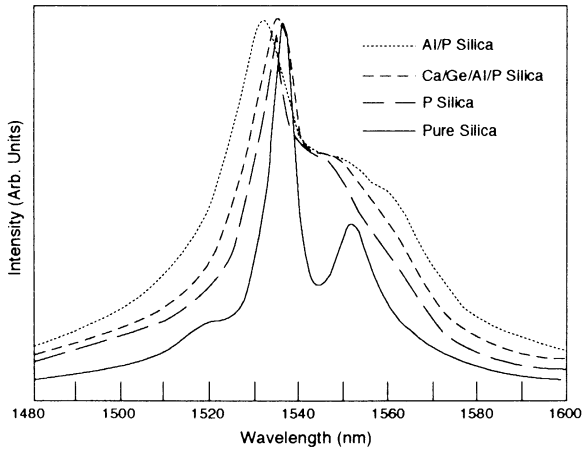

Figure 4.5 Gain spectra of four EDFAs with different core compositions. Codoping of silica core with aluminum or phosphorus broadens the emission spectrum considerably. (After Ref. [25], ©1991 IEEE)

With the advent of wavelength-division multiplexing (WDM), one EDFA is used to amplify a large number of channels simultaneously. Moreover, the WDM signal is propagated through a chain of such cascaded EDFAs covering distances longer than 1000 km. If the gain spectrum of EDFAs is not flat over the entire bandwidth of the WDM signal and the gain varies as little as a few percent from channel to channel, large variations (> 10 dB) among channel powers occur when the signal arrives at the receiver; such variations can degrade the system performance considerably. For this reason, many techniques have been developed for flattening the gain spectrum of EDFAs and extending the usable bandwidth to a range as large as 80 nm [9]. One solution consists of using an optical filter whose spectral response is tailored such that the filter transmits more light at wavelengths where gain is lower (and vice versa). Optical filters based on Mach–Zehnder interferometers were used as early as 1991 [26]. More recently, long-period fiber gratings have been used for this purpose with considerable success [27]. Another approach makes use of acousto-optic tunable filters [28].

With a proper design, the use of optical filters can provide flat gain over a bandwidth as large as 30 nm. However, dense WDM systems, designed to transmit more than 50 channels, require uniform EDFA gain over a bandwidth exceeding 50 nm. It is difficult to achieve such large gain bandwidths with a

single amplifier. A hybrid two-stage approach is commonly used in practice. In one design, two amplifiers are cascaded to produce flat gain (to within 0.5 dB) over the wavelength range of 1544 to 1561 nm [29]. The second EDFA is codoped with ytterbium and phosphorus and is optimized such that it acts as a power amplifier. In a variation of this idea, the second EDFA uses fluoride fiber as a host and is pumped at 1480 nm [30]. Another approach combines Raman amplification with one or two EDFAs to realize uniform gain over a 65-nm bandwidth extending from 1549 to 1614 nm [31].

A two-arm design has also been developed to solve the gain-flattening problem for dense WDM systems [32]. In this approach, the WDM signal is divided into two bands, known as the conventional or C band (1530–1560 nm) and the long-wavelength or L band (1570–1600 nm). The incoming WDM signal is split into two branches containing optimized EDFAs for C and L bands. The L-band EDFA requires long fiber lengths (> 100 m) since the inversion level is kept relatively low. The two-arm design has produced a relatively uniform gain of 24 dB over a bandwidth as large as 80 nm when pumped using 980-nm semiconductor lasers while maintaining a noise figure of about 6 dB [9].

4.2.2 Amplifier Gain

The gain of EDFAs depends on a large number of parameters such as erbium-ion concentration, amplifier length, core radius, and pump power [33]–[37]. A three-level rate-equation model, used commonly for lasers, can be adapted for EDFAs [9]. It is sometimes necessary to add a fourth level to include the effects of excited-state absorption. Another complication stems from the nonuniform nature of inversion along the amplifier length. Since a fiber amplifier is pumped from one end, the pump power decreases along the fiber length. As a result, it is necessary to include axial variations of the pump, the signal, and the atomic-level populations. In general, the resulting set of coupled equations must be solved numerically.

Much insight can be gained by using a simple model that neglects amplified spontaneous emission and excited-state absorption. The model assumes that the pump level of the three-level system remains nearly unpopulated because of a rapid transfer of the pumped population to the excited state 2 (see Fig. 4.1). It also neglects differences between the emission and absorption cross sections. With these simplifications, the excited-state density $N_2(z,t)$ is

obtained by solving the following rate equation [12]

$$\frac{\partial N_2}{\partial t} = W_p N_1 - W_s(N_2 - N_1) - \frac{N_2}{T_1}, \tag{4.2.2}$$

where $N_1 = N_t - N_2$, N_t is the total ion density, and W_p and W_s are the transition rates for the pump and signal, respectively. These rates are given by

$$W_p = \frac{\Gamma_p \sigma_p P_p}{a_p h\nu_p}, \qquad W_s = \frac{\Gamma_s \sigma_s P_s}{a_s h\nu_s}, \tag{4.2.3}$$

where Γ_p is the overlap factor representing the fraction of pump power P_p within the doped region of the fiber, σ_p is the transition cross section at the pump frequency ν_p, and a_p is the mode area of the pump inside the fiber. The quantities Γ_s, σ_s, P_s, a_s, and ν_s are defined similarly for the signal. The steady-state solution of Eq. (4.2.2) is given by

$$N_2 = \frac{(P_p' + P_s')N_t}{1 + 2P_s' + P_p'}, \tag{4.2.4}$$

where $P_p' = P_p/P_p^{\text{sat}}$, $P_s' = P_s/P_s^{\text{sat}}$, and the saturation powers are defined as

$$P_p^{\text{sat}} = \frac{a_p h\nu_p}{\Gamma_p \sigma_p T_1}, \qquad P_s^{\text{sat}} = \frac{a_s h\nu_s}{\Gamma_s \sigma_s T_1}. \tag{4.2.5}$$

The pump and signal powers vary along the amplifier length because of absorption, stimulated emission, and spontaneous emission. Their variation also depends on whether the signal and pump waves propagate in the same or opposite directions. If the contribution of spontaneous emission is neglected and forward pumping is assumed, P_p and P_s satisfy

$$\frac{dP_p}{dz} = -\Gamma_p \sigma_p N_1 - \alpha' P_p, \qquad \frac{dP_s}{dz} = \Gamma_s \sigma_s (N_2 - N_1) - \alpha P_s, \tag{4.2.6}$$

where α and α' take into account fiber losses at the signal and pump wavelengths, respectively. By substituting N_2 from Eq. (4.2.4) together with $N_1 = N_t - N_2$, we obtain a set of two coupled equations,

$$\frac{dP_p'}{dz} = -\frac{(P_s' + 1)\alpha_p P_p'}{1 + 2P_s' + P_p'} - \alpha' P_p', \tag{4.2.7}$$

$$\frac{dP_s'}{dz} = \frac{(P_p' - 1)\alpha_s P_s'}{1 + 2P_s' + P_p'} - \alpha P_s', \tag{4.2.8}$$

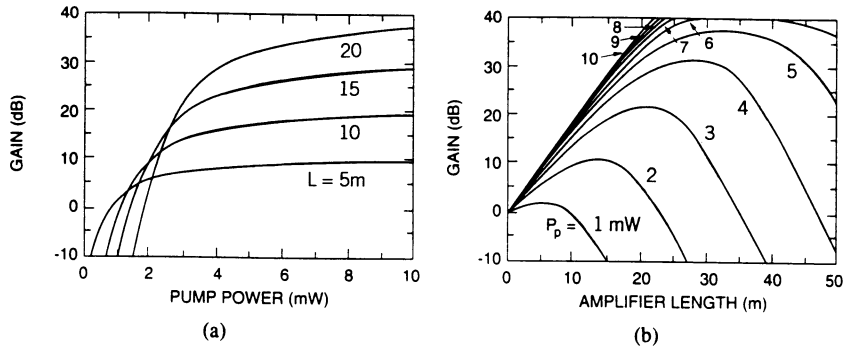

Figure 4.6 Small-signal gain at 1.55 μm as a function of (a) pump power and (b) amplifier length for an EDFA pumped at 1.48 μm. (After Ref. [34], ©1991 IEEE)

where $\alpha_p \equiv \Gamma_p \sigma_p N_t$ and $\alpha_s \equiv \Gamma_s \sigma_s N_t$ are the absorption coefficients at the pump and signal wavelengths, respectively. These equations govern the evolution of signal and pump powers inside an EDFA. Their predictions are in good agreement with experiments as long as the amplified spontaneous emission (ASE) remains negligible [36]. The inclusion of fiber losses is essential for distributed-gain amplifiers, which amplify signals over long fiber lengths. For lumped amplifiers with fiber lengths under 1 km, α and α' can be set to zero.

A drawback of the above model is that the absorption and emission cross sections are taken to be the same for both the pump and signal beams. As was seen in Fig. 4.4(b), these cross sections are generally different. It is easy to extend the model to include such differences [34]. An analytic solution can still be obtained [33]. Figure 4.6 shows the small-signal gain at 1.55 μm as a function of the pump power and the amplifier length by using typical parameter values. For a given amplifier length L, the gain increases exponentially with pump power initially, but at a much reduced rate when pump power exceeds a certain value [corresponding to the "knee" in Fig. 4.6(a)]. For a given pump power, amplifier gain becomes maximum at an optimum value of L and drops sharply when L exceeds this optimum value. The reason is that the end portion of the amplifier remains unpumped and absorbs the amplified signal.

Since the optimum value of L depends on the pump power P_p, it is necessary to choose both L and P_p appropriately. Figure 4.6(b) shows that for 1.48-μm pumping, 35-dB gain can be realized at a pump power of 5 mW for $L = 30$ m. It is possible to design high-gain amplifiers using fiber lengths as

short as a few meters. The qualitative features shown in Fig. 4.6 are observed in all EDFAs; the agreement between theory and experiment is generally quite good [36].

The preceding analysis assumes that both pump and signal waves are in the form of CW beams. In practice, EDFAs are pumped by using CW semiconductor lasers, but the signal is generally not a CW beam. For example, in lightwave system applications the signal is in the form of a pulse train (containing a random sequence of 1 and 0 bits). It is often required that all pulses experience the same gain. Fortunately, this occurs naturally in EDFAs for pulses shorter than a few microseconds. The reason is related to the relatively large value of the fluorescence time associated with erbium ions ($T_1 \approx 10$ ms). When the timescale of signal power variations is much shorter than T_1, erbium ions are unable to follow such fast variations. Since single-pulse energies are typically much below the saturation energy ($\sim 10\ \mu$J), EDFAs respond to the average power. As a result, gain saturation is governed by the average signal power, and amplifier gain does not vary from pulse to pulse.

In some applications related to packet-switched and reconfigurable WDM networks, the transient nature of gain dynamics becomes of concern [37]. It is possible to implement a built-in gain-control mechanism that keeps the amplifier gain pinned at a constant value [38]–[44]. The basic idea consists of forcing the EDFA to oscillate at a controlled wavelength outside the range of interest (typically below 1.5 μm). Since the gain remains clamped at the threshold value for a laser, the signal is amplified by the same factor in spite of variations in the signal power. A simple scheme uses an all-optical feedback loop at a specific wavelength to initiate lasing [38]. In another implementation, an EDFA is forced to oscillate at 1.48 μm by fabricating fiber Bragg gratings at the two ends of the amplifier [40]. One of the gratings can also be replaced by a fiber-loop mirror [43]. With this change, the signal wavelength can be close to the lasing wavelength without affecting the amplifier performance.

4.2.3 Amplifier Noise

Since amplifier noise is the ultimate limiting factor for system applications, it has been studied extensively [45]–[58]. As discussed earlier, amplifier noise is quantified through the noise figure $F_n = 2n_{sp}$, where the spontaneous-emission factor n_{sp} depends on the relative populations N_1 and N_2 of the two energy states, as indicated in Eq. (4.1.14). Since EDFAs operate on the basis of a

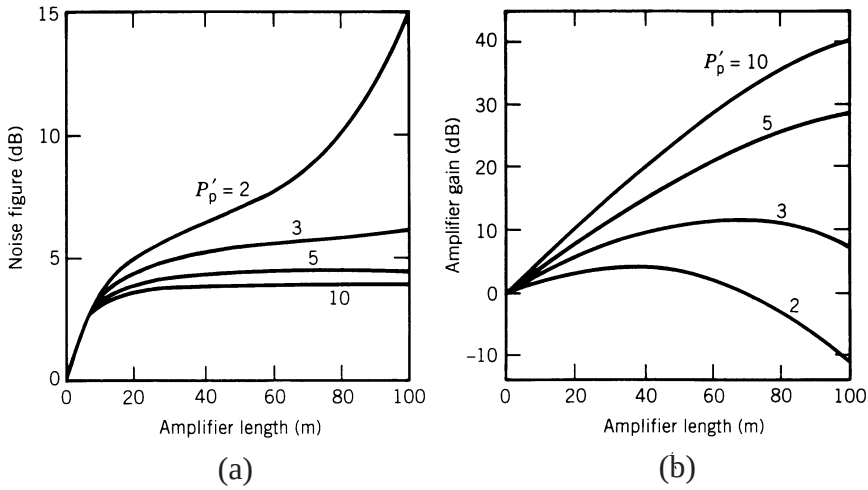

Figure 4.7 (a) Noise figure and (b) amplifier gain at several pumping levels as a function of fiber length. (After Ref. [50], ©1990 IEE)

three-level pumping scheme, N_1 is not negligible and n_{sp} exceeds 1. Thus, the noise figure of EDFAs is expected to be larger than the ideal value of 3 dB.

The spontaneous-emission factor for EDFAs can be calculated by using the three-level rate-equation model discussed earlier. However, one should take into account the fact that both N_1 and N_2 vary along the fiber length because of their dependence on the pump and signal powers [see Eq. (4.2.4)], and n_{sp} should be averaged along the amplifier length. As a result, the noise figure depends both on the amplifier length L and the pump power P_p, just as the amplifier gain does. Figure 4.7(a) shows the variation of F_n with the amplifier length for several values of P_p/P_p^{sat} when a 1.53-μm signal is amplified with an input power of 1 mW [50]. The amplifier gain under the same conditions is shown in Fig. 4.7(b). The results show that a noise figure close to 3 dB can be obtained for high-gain amplifiers.

The experimental results confirm that F_n close to 3 dB can be realized in EDFAs. A noise figure of 3.2 dB was measured in a 30-m long EDFA, pumped at 0.98 μm with 11 mW of power [47]. A similar value was measured in another experiment with only 5.8 mW of pump power [49]. In general, it is difficult to achieve high gain, low noise, and high pumping efficiency simultaneously. The main limitation is imposed by the ASE traveling backward toward the pump and depleting the pump power. An internal isolator allevi-

ates this problem to a large extent. In one implementation, a 51-dB gain was realized with a 3.1-dB noise figure at a pump power of only 48 mW [54]. The relatively low noise levels of EDFAs make them an ideal choice for WDM lightwave systems. In spite of low noise, the performance of long-haul systems employing multiple EDFAs is often limited by the ASE.

The effects of amplifier noise are most severe when a low-power signal is amplified by a large factor. In practice, the noise in a chain of cascaded EDFAs can be reduced by decreasing the amplifier spacing. For this reason, considerable attention has focused on *distributed* fiber amplifiers in which the gain is distributed over long lengths (~ 50 km) of lightly doped silica fibers such that fiber losses are nearly compensated all along the fiber length [59]–[66]. Such fibers are referred to as being *transparent*, although they become nearly transparent only when pumped at a suitable wavelength. The optimal pumping wavelength is 1.48 μm since fiber losses for the pump at this wavelength are minimal compared to other pumping wavelengths (such as 0.98 μm). In general, one should consider the effect of stimulated Raman scattering (SRS) in distributed EDFAs pumped at 1.48 μm since the signal wavelength lies within the Raman gain bandwidth [62]. As a result, the signal experiences not only the gain provided by the dopants but also the gain provided by SRS. In practice, SRS increases the net gain and reduces the noise figure for a given amount of pump power. Nonlinear and dispersive effects associated with the silica host play an important role in distributed fiber amplifiers. We turn to them in the following section.

4.3 Dispersive and Nonlinear Effects

Because of their large bandwidths, fiber amplifiers can be used to amplify, without distortion, short optical pulses. Indeed, EDFAs were used to amplify ultrashort pulses soon after their development. We discuss in this section how the nonlinear Schrödinger (NLS) equation, useful for describing pulse propagation in undoped fibers, can be extended to include the gain provided by dopants.

4.3.1 Maxwell–Bloch Equations

Rare-earth ions in doped fibers can be modeled as a two-level system by considering only the two energy levels that participate in light-induced transitions.

The dynamic response of a two-level system is governed by the well-known Maxwell–Bloch equations [11]. We can extend these equations to the case of fiber amplifiers. The starting point is the wave equation (A.2.1.7), but the induced polarization $\mathbf{P}(\mathbf{r},t)$ in Eq. (A.2.1.8) should include a third term $\mathbf{P}_d(\mathbf{r},t)$ representing the contribution of dopants. This contribution is calculated by using a semiclassical approach in which dopants interact with the optical field $\mathbf{E}(\mathbf{r},t)$ through the induced dipole moment. In the slowly varying envelope approximation, $\mathbf{P}_d(\mathbf{r},t)$ is written as

$$\mathbf{P}_d(\mathbf{r},t) = \tfrac{1}{2}\hat{x}[P(\mathbf{r},t)\exp(-i\omega_0 t) + \text{c.c.}], \tag{4.3.1}$$

where $\hat{x}$ is the polarization unit vector associated with the optical field $\mathbf{E}(\mathbf{r},t)$. The slowly varying part $P(\mathbf{r},t)$ is obtained by solving the Bloch equations, which can be written as [11]

$$\frac{\partial P}{\partial t} = -\frac{P}{T_2} - i(\omega_a - \omega_0)P - \frac{i\mu^2}{\hbar}EW, \tag{4.3.2}$$

$$\frac{\partial W}{\partial t} = \frac{W_0 - W}{T_1} + \frac{1}{\hbar}\text{Im}(E^* P), \tag{4.3.3}$$

where μ is the dipole moment, ω_a is the atomic transition frequency, $W = N_2 - N_1$ is the population-inversion density with the initial value W_0, and T_1 and T_2 are the population and dipole relaxation times introduced earlier. Here $E(\mathbf{r},t)$ is the slowly varying amplitude associated with the optical field defined as in Eq. (A.2.3.2). Following the analysis of Section A.2.3, the net effect of dopants is to modify the NLS equation as

$$\frac{\partial A}{\partial z} + \beta_1\frac{\partial A}{\partial t} + \frac{i\beta_2}{2}\frac{\partial^2 A}{\partial t^2} + \frac{\alpha}{2}A = i\gamma|A|^2 A + \frac{i\omega_0}{2\varepsilon_0 c}\langle P\exp(-i\beta_0 z)\rangle, \tag{4.3.4}$$

where angle brackets denote spatial averaging over the mode profile $|F(x,y)|^2$. An average over the atomic transition frequencies should also be performed if one wants to include the effects of inhomogeneous broadening.

The set of Maxwell–Bloch equations (4.3.2)–(4.3.4) must be solved for pulses whose width is shorter or comparable to the dipole relaxation time ($T_2 < 0.1$ ps). However, the analysis is simplified considerably for broader optical pulses since one can make the rate-equation approximation in which the dopants respond so fast that the induced polarization follows the optical field adiabatically [11].

Dispersive effects associated with dopants can be included by working in the Fourier domain and defining the dopant susceptibility through the standard relation

$$\tilde{P}(\mathbf{r},\omega) = \varepsilon_0 \chi_d(\mathbf{r},\omega)\tilde{E}(\mathbf{r},\omega), \tag{4.3.5}$$

where ε_0 is the vacuum permittivity and the tilde represents the Fourier transform. The susceptibility is found to be given by

$$\chi_d(\mathbf{r},\omega) = \frac{\sigma_s W(\mathbf{r}) n_0 c/\omega_0}{(\omega-\omega_a)T_2 + i}, \tag{4.3.6}$$

where the transition cross section σ_s is related to the dipole moment μ as $\sigma_s = \mu^2\omega_0 T_2/(\varepsilon_0 n_0 \hbar c)$ and n_0 is the background linear refractive index of the host medium at the frequency ω_0.

4.3.2 Ginzburg–Landau Equation

The propagation equation for optical pulses is obtained from Eqs. (4.3.2) and (4.3.6) by following the analysis of Section A.2.3. In the frequency domain, Eqs. (A.2.3.10) and (A.2.3.16) remain valid provided χ_d is added to the dielectric constant ε. The index change Δn from Eq. (A.2.3.18) then becomes

$$\Delta n = n_2|E|^2 + \frac{i\alpha}{2k_0} + \frac{\chi_d}{2n}. \tag{4.3.7}$$

The major change is that $\Delta\beta$ in Eq. (A.2.3.22) becomes frequency dependent because of the frequency dependence of χ_d. When the optical field is transformed back to the time domain, we must expand both β and $\Delta\beta$ in a Taylor series to include the dispersive effects associated with the dopants. Writing $\omega-\omega_a = (\omega-\omega_0)+(\omega_0-\omega_a)$ and using the Taylor-series expansion, the resulting equation is given by [67]

$$\frac{\partial A}{\partial z} + \beta_1^{\text{eff}}\frac{\partial A}{\partial t} + \frac{i}{2}\beta_2^{\text{eff}}\frac{\partial^2 A}{\partial t^2} + \frac{1}{2}(\alpha+\alpha_2|A|^2)A = i\gamma|A|^2A + \frac{g_0}{2}\frac{1+i\delta}{1+\delta^2}A, \tag{4.3.8}$$

where

$$\beta_1^{\text{eff}} = \beta_1 + \frac{g_0 T_2}{2}\left[\frac{1-\delta^2+2i\delta}{(1+\delta^2)^2}\right], \tag{4.3.9}$$

$$\beta_2^{\text{eff}} = \beta_2 + g_0 T_2^2\left[\frac{\delta(\delta^2-3)+i(1-3\delta^2)}{(1+\delta^2)^3}\right], \tag{4.3.10}$$

and the detuning parameter $\delta = (\omega_0 - \omega_a)T_2$. The gain g_0 is defined as

$$g_0(z,t) = \frac{\sigma_s \int\int_{-\infty}^{\infty} W(\mathbf{r},t)|F(x,y)|^2\,dx\,dy}{\int\int_{-\infty}^{\infty} |F(x,y)|^2\,dx\,dy}, \tag{4.3.11}$$

where integration is over the entire range of x and y. Spatial averaging results from the use of Eq. (4.3.7) in Eq. (A.2.3.20). Equation (4.3.8) includes the effects of two-photon absorption through the parameter α_2. Even though two-photon absorption is negligible for silica fibers, it may become important for fibers made using materials with high nonlinearities [68].

Equation (4.3.8) shows how the dispersion parameters of the host fiber change because of the dopant contribution. Since $v_g = \beta_1^{-1}$, changes in β_1 indicate that the group velocity of the pulse is affected by the dopants. However, the dopant-induced change in the group velocity is negligible in practice since the second term in Eq. (4.3.9) is smaller by more than a factor of 10^4 under typical operating conditions. In contrast, changes in β_2 cannot be neglected since the two terms in Eq. (4.3.10) can become comparable, especially near the zero-dispersion wavelength of the amplifier. Even in the special case $\delta = 0$, β_2^{eff} does not reduce to β_2. In fact, Eq. (4.3.10) shows that for $\delta = 0$,

$$\beta_2^{\text{eff}} = \beta_2 + ig_0 T_2^2 \tag{4.3.12}$$

is a complex parameter whose imaginary part results from the gain provided by dopants. The physical origin of this contribution is related to the finite gain bandwidth of fiber amplifiers and is referred to as *gain dispersion* since it originates from the frequency dependence of the gain. Equation (4.3.12) is a consequence of the parabolic-gain approximation in which the gain spectrum of fiber amplifiers is approximated by a parabola over the spectral bandwidth of the pulse.

It is difficult to perform integration in Eq. (4.3.11) exactly since the inversion W depends not only on the spatial coordinates x, y, and z but also on the mode profile $|F(x,y)|^2$ because of gain saturation. In practice, only a small portion of the fiber core is doped with rare-earth ions. If the mode intensity and the dopant density are nearly uniform over the doped portion, W can be assumed to be a constant in the doped region and zero outside it. The integration is then readily performed to yield the simple relation

$$g_0(z,t) = \Gamma_s \sigma_s W(z,t), \tag{4.3.13}$$

where Γ_s represents the fraction of mode power within the doped portion of the fiber. Using Eqs. (4.3.3) and (4.3.13), the gain dynamics is governed by

$$\frac{\partial g_0}{\partial t} = \frac{g_{ss} - g_0}{T_1} - \frac{g_0 |A|^2}{T_1 P_s^{\text{sat}}}, \tag{4.3.14}$$

where $g_{ss} = \Gamma_s \sigma_s W_0$ is the small-signal gain and the saturation power P_s^{sat} is defined in Eq. (4.2.5). Note that g_0 is not constant along the fiber length because of pump power variations. The z dependence of g_0 depends on the pumping configuration and requires the use of Eq. (4.2.6).

In general, one must solve Eqs. (4.3.8) and (4.3.14) together in a self-consistent manner. However, for most fiber amplifiers the fluorescence time T_1 is so long (0.1–10 ms) compared with typical pulse widths that we can assume that spontaneous emission and pumping do not occur over the pulse duration. Equation (4.3.14) is then readily integrated to obtain the result

$$g_0(z,t) \approx g_{ss} \exp\left(-\frac{1}{E_s} \int_{-\infty}^{t} |A(z,t)|^2 dt \right), \tag{4.3.15}$$

where the saturation energy is defined as $E_s = \hbar\omega_0 (a_s/\sigma_s)$.

Typical values of E_s for fiber amplifiers are close to 1 μJ. However, pulse energies used in practice are much smaller than the saturation energy E_s. As a result, gain saturation is negligible over the duration of a single pulse. However, it cannot be neglected for a long pulse train since the amplifier gain will saturate over timescales longer than T_1. The average power within the amplifier then determines the saturated gain as $g_0 = g_{ss}(1 + P_{av}/P_s^{\text{sat}})^{-1}$.

Pulse propagation in fiber amplifiers is thus governed by a generalized NLS equation, with coefficients β_1^{eff} and β_2^{eff} that are not only complex but also vary with z along the fiber length. In the specific case in which $\delta = 0$, Eq. (4.3.8) simplifies considerably and can be written as

$$\frac{\partial A}{\partial z} + \frac{i}{2}(\beta_2 + i g_0 T_2^2) \frac{\partial^2 A}{\partial T^2} = i\left(\gamma + \frac{i}{2}\alpha_2\right) |A|^2 A + \frac{1}{2}(g_0 - \alpha) A, \tag{4.3.16}$$

where $T = t - \beta_1^{\text{eff}} z$ is the reduced time. This equation governs amplification of optical signals in fiber amplifiers. The T_2 term accounts for decrease in gain for spectral components of an optical pulse located far from the gain peak. Equation (4.3.16) is a generalized NLS equation with complex coefficients. It can be reduced to a Ginzburg–Landau equation, which has been studied extensively in the context of fluid dynamics. We discuss in the next section the stability of its steady-state solutions.

4.4 Modulation Instability

Modulation instability, discussed in Section A.5.1, should play an important role if a CW beam propagates in a distributed fiber amplifier in which amplification occurs along long fiber lengths. Also, a new type of modulation instability can occur if signals are periodically amplified in a chain of short-length amplifiers, a situation that occurs in soliton communication systems (see Chapter 8). In this section we discuss the two cases separately.

4.4.1 Distributed Amplification

Consider the propagation of CW or quasi-CW signals inside a distributed fiber amplifier. The steady-state solution can be obtained by neglecting the time-derivative term in Eq. (4.3.16). Assuming for simplicity that g_0 is z independent, the solution is given by

$$\bar{A}(z) = \sqrt{P_0}\exp[b(z)], \tag{4.4.1}$$

where P_0 is the incident power and

$$b(z) = \tfrac{1}{2}(g_0 - \alpha)z + i\gamma P_0 \int_0^z \exp[(g_0 - \alpha)z]\, dz. \tag{4.4.2}$$

Equation (4.4.1) shows that the CW signal is amplified exponentially and acquires a nonlinear phase shift induced by self-phase modulation (SPM).

Following the procedure of Section A.5.1, we perturb the steady state slightly such that

$$A(z,T) = [\sqrt{P_0} + a(z,T)]\exp[b(z)] \tag{4.4.3}$$

and examine the evolution of the weak perturbation $a(z,T)$ using a linear stability analysis. By substituting Eq. (4.4.3) in Eq. (4.3.16) and linearizing in a, we obtain a linear equation that can be solved approximately and has a solution in the form

$$a(z,T) = a_1 \exp[i(\textstyle\int_0^z K(z)\, dz - \Omega T)] + a_2 \exp[-i(\int_0^z K(z)\, dz - \Omega T)], \tag{4.4.4}$$

where Ω is the frequency of perturbation. The wave number K is z dependent because of the gain provided by the amplifier and is found to satisfy the following dispersion relation [69]:

$$K(\Omega, z) = \tfrac{1}{2} i g_0 T_2^2 \Omega^2 \pm \tfrac{1}{2}|\beta_2 \Omega|[\Omega^2 + (4\gamma P_0/\beta_2)e^{(g_0-\alpha)z}]^{1/2}. \tag{4.4.5}$$

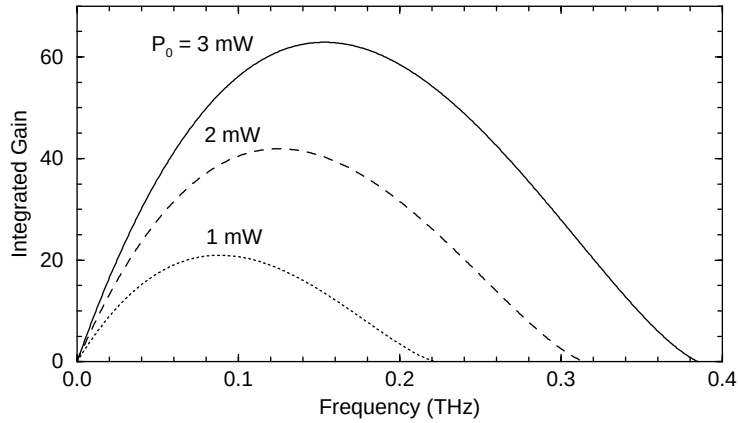

Figure 4.8 Gain spectra of modulation instability at three power levels for a distributed fiber amplifier with 30-dB gain over 10 km. Values of other parameters are $\beta_2 = -20$ ps^2/km and $\gamma = 10$ W^{-1}/km.

The dispersion relation (4.4.5) reduces to that obtained for undoped fibers in Section A.5.1 when gain and loss are neglected. Modulation instability occurs when $K(\Omega, z)$ has a negative imaginary part over a large length of the fiber amplifier. It is useful to define the total integrated gain at a frequency Ω as

$$h(\Omega) = -2\int_0^L \mathrm{Im}[K(\Omega, z)]\, dz, \tag{4.4.6}$$

where L is the amplifier length. Stability of the steady state depends critically on whether light experiences normal or anomalous GVD inside the amplifier. In the case of normal GVD, $h(\Omega)$ is negative for all values of Ω, and the steady state is stable against small perturbations.

The situation is quite different in the case of anomalous GVD ($\beta_2 < 0$). Similar to the case of undoped fibers, $h(\Omega)$ becomes positive in a certain range of Ω. Figure 4.8 shows the gain spectrum of modulation instability by plotting $h(\Omega)$ at three input power levels for a fiber amplifier with 30-dB gain distributed over a length of 10 km. Modulation instability occurs for input power levels of about 1 mW. It can transform a CW beam into a pulse train at a repetition rate around 100 GHz.

4.4.2 Periodic Lumped Amplification

Most long-haul fiber-optic communication systems use optical amplifiers in which the doped fiber is only a few meters long. The length of such amplifiers is much shorter than both the dispersion and nonlinear length scales. In essence, the role of a fiber amplifier is to amplify the signal without introducing any temporal or spectral changes. Such amplifiers are called *lumped amplifiers* since they amplify the signal by a factor of 20 dB or so over a length of about 10 m and compensate for fiber losses acquired over a distance as large as 100 km. With this scheme, optical signals can be transmitted over distances ~ 1000 km by simply placing multiple amplifiers periodically along the fiber link.

Modulation instability affects the performance of such periodically amplified fiber-optic communication systems in several different ways. As early as 1990, computer simulations showed that modulation instability can be a limiting factor for lightwave systems employing the nonreturn-to-zero (NRZ) format for data transmission [70]. Since then, the impact of modulation instability has been studied, both analytically and experimentally, for single-channel as well as WDM systems [71]–[85].

The use of optical amplifiers can induce modulation instability in both the normal and anomalous GVD regimes of optical fibers because of the periodic nature of amplification [74]. The new instability mechanism has its origin in the periodic sawtooth variation of the optical power along the link length. To understand the physics more clearly, note that a periodic variation of power in z is equivalent to formation of an index grating since the nonlinear part of the refractive index depends on the local power level. The period of this grating is equal to the amplifier spacing and is typically in the range of 40 to 80 km. Such a long-period grating provides a new coupling mechanism between the modulation-instability sidebands and allows them to grow when the perturbation frequency Ω satisfies the Bragg condition.

Mathematically, the evolution of the optical field outside fiber amplifiers is governed by the standard NLS equation

$$i\frac{\partial A}{\partial z} - \frac{\beta_2}{2}\frac{\partial^2 A}{\partial T^2} + \gamma|A|^2 A = -\frac{i\alpha}{2}A, \tag{4.4.7}$$

where α accounts for fiber losses. Within each amplifier, $-\alpha$ is replaced by the net gain g_0, and the dispersive and nonlinear effects are negligible. By introducing a new variable B through $A = B\exp(-\alpha z/2)$, Eq. (4.4.7) can be

written as

$$i\frac{\partial B}{\partial z} - \frac{\beta_2}{2}\frac{\partial^2 B}{\partial T^2} + \gamma f(z)|B|^2 B = 0, \tag{4.4.8}$$

where $f(z)$ is a periodic function such that it decreases exponentially as $f(z) = \exp(-\alpha z)$ in each fiber section between amplifiers and jumps to 1 at the location of each amplifier.

The analysis of Section A.5.1 can be extended to include periodic variations of $f(z)$. If we expand $f(z)$ in a Fourier series as

$$f(z) = \sum_{n=-\infty}^{\infty} c_n \exp(2\pi i n z/L_A), \tag{4.4.9}$$

the frequency at which the gain of modulation instability peaks is found to be given by [74]

$$\Omega_m = \pm\left(\frac{2\pi m}{\beta_2 L_A} - \frac{2\gamma P_0 c_0}{\beta_2}\right)^{1/2}, \tag{4.4.10}$$

where the integer m represents the order of Bragg diffraction, L_A is the spacing between amplifiers (grating period), and the Fourier coefficient c_0 is related to the fiber loss α, or the amplifier gain $G \equiv \exp(\alpha L_A)$, as

$$c_0 = \frac{1-\exp(-\alpha L_A)}{\alpha L_A} = \frac{G-1}{G\ln G}. \tag{4.4.11}$$

In the absence of periodic gain–loss variations, or when $m = 0$, Ω_0 exists only when the CW signal experiences anomalous GVD. However, when $m \neq 0$, modulation sidebands can occur even for normal GVD ($\beta_2 > 0$). For this reason, this instability is referred to as *sideband instability*. Physically, the creation of sidebands can be understood by noting that the nonlinear index grating helps to satisfy the phase-matching condition necessary for four-wave mixing when $m \neq 0$. This phenomenon can be avoided in practice by ensuring that the amplifier spacing is not uniform along the fiber link.

4.4.3 Noise Amplification

Modulation instability can degrade the system performance considerably in the presence of noise produced by optical amplifiers. Physically, spontaneous emission within fiber amplifiers adds broadband noise to the amplified signal. This noise can seed the growth of modulation-instability sidebands and is thus

amplified through *induced* modulation instability [77]–[85]. Such noise amplification affects system performance in two ways. First, it degrades the SNR at the receiver. Second, it broadens the signal spectrum. Since GVD-induced broadening of optical signals depends on their spectral bandwidth, system performance is compromised.

We can study the noise amplification process in each section of the fiber between two optical amplifiers by adding noise to the CW solution of Eq. (4.4.8) so that

$$B(z,T) = [\sqrt{P_0} + a(z)e^{i\Omega T})]\exp(i\phi_{\rm NL}), \tag{4.4.12}$$

where $\phi_{\rm NL} = \gamma P_0 \int_0^z f(z)\,dz$ is the SPM-induced nonlinear phase shift and $a(z)$ is the noise amplitude at the frequency Ω. Substituting Eq. (4.4.12) in Eq. (4.4.8), we obtain

$$\frac{da}{dz} = \frac{i}{2}\beta_2\Omega^2 + i\gamma P_0 f(z)(a + a^*). \tag{4.4.13}$$

This equation can be solved easily in the lossless case in which $\alpha = 0$, and $f(z) \equiv 1$ is z independent [77]. It can also be solved when $\alpha \neq 0$ but the solution is quite complicated as it involves the Hankel functions [80]. An approximate solution is obtained when $f(z)$ is replaced by its average value c_0 and is given by [85]

$$\begin{pmatrix} a_1(z) \\ a_2(z) \end{pmatrix} = \begin{pmatrix} \cos(Kz) & -r_0^{-1}\sin(Kz) \\ r_0\sin(Kz) & \cos(Kz) \end{pmatrix} \begin{pmatrix} a_1(0) \\ a_2(0) \end{pmatrix}, \tag{4.4.14}$$

where a_1 and a_2 are the real and imaginary parts of the noise amplitude ($a = a_1 + ia_2$) and K and r_0 are defined as

$$K = \tfrac{1}{2}\beta_2\Omega^2 r_0, \qquad r_0 = [1 + 4\gamma P_0 c_0/(\beta_2\Omega^2)]^{1/2}. \tag{4.4.15}$$

Fiber amplifiers generate noise over their entire gain bandwidth (typically > 30 nm). Frequency components of the noise that fall within the gain spectrum of modulation instability are amplified exponentially since r_0, and hence the propagation constant K, becomes purely imaginary for them. In practice, optical filters are placed just after each amplifier to reduce the noise bandwidth. Figure 4.9 shows an example of a numerically simulated optical spectrum at the end of a 2500-km fiber link with 50 amplifiers placed 50 km apart [85]. A 1-mW signal at the 1.55-μm wavelength is transmitted through the amplifier chain. Optical filters with a 8-nm passband (Lorentzian shape) are placed after every amplifier. The broad pedestal represents the contribution of ASE to

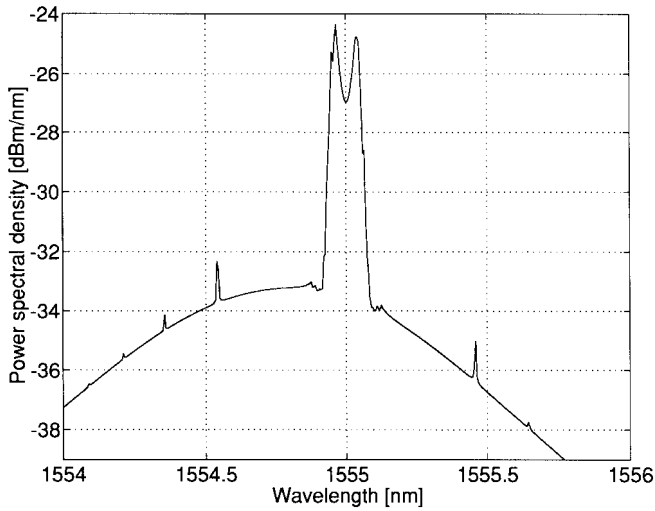

Figure 4.9 Optical spectrum for a 2500-km fiber link with 50 amplifiers showing effects of modulation instability. Values of fiber parameters are $\beta_2 = -1$ ps^2/km, $\gamma = 2$ W^{-1}/km, and $\alpha = 0.22$ dB/km. (After Ref. [85], ©1999 IEEE)

the signal spectrum located at 1.55 μm. The double-peak structure near this wavelength is due to the standard modulation instability occurring even in the absence of amplifiers. The weak satellite peaks result from the nonlinear index grating formed by periodic power variations. Their location is in agreement with the prediction of Eq. (4.4.10).

The enhancement of amplifier noise degrades the SNR of the signal at the receiver. Experimental results for a lightwave system operating at 10 Gb/s showed considerable degradation after a transmission distance of only 455 km [81]. The system performance improved considerably when the GVD was partially compensated using a dispersion-compensating fiber. In the case of WDM systems, a signal in one channel can act as a seed for induced modulation instability—resulting in interchannel crosstalk—if the channel spacing falls within the gain bandwidth of the instability. This phenomenon is called *resonant four-wave mixing* and can occur because of SPM-mediated phase matching, in spite of large GVD [84]. In general, the impact of modulation instability on lightwave systems can be reduced by reducing amplifier spacing and by using the normal-GVD regime of the fiber link for signal transmission.

4.5 Optical Solitons

In this section we consider propagation of optical pulses in fiber amplifiers. Considerable attention has also been paid to understanding the amplification process through theoretical modeling [86]–[119]. Before considering amplification of ultrashort pulses, it is instructive to inquire whether doped fibers can support solitons similar to those found for undoped fibers in Chapter A.5. Since the Ginzburg–Landau equation [Eq. (4.3.16)] is not integrable by the inverse scattering method, it does not support solitons in a strict mathematical sense. However, it may have solitary-wave solutions that represent optical pulses whose shape does not change on propagation. Such a solution of Eq. (4.3.16) was found as early as 1977 in the context of fluid dynamics [120]; it was rediscovered in 1989 in the context of nonlinear fiber optics [86]. Since then, solutions of the Ginzburg–Landau equation have been studied both analytically and numerically [121]–[129].

4.5.1 Autosolitons

Similar to the case of conventional solitons in undoped fibers, it is useful to introduce the dimensionless variables (soliton units)

$$\xi = z/L_D, \qquad \tau = T/T_0, \qquad u = \gamma L_D A, \tag{4.5.1}$$

where $L_D = T_0^2/|\beta_2|$ is the dispersion length. Equation (4.3.16) then takes the normalized form [95]

$$i\frac{\partial u}{\partial \xi} - \frac{1}{2}(s+id)\frac{\partial^2 u}{\partial \tau^2} + (1+i\mu_2)|u|^2 u = \frac{i}{2}\mu u, \tag{4.5.2}$$

where $s = \mathrm{sgn}(\beta_2) = \pm 1$ and the other parameters are defined as

$$d = g_0 L_D (T_2/T_0)^2, \quad \mu = (g_0 - \alpha)L_D, \quad \mu_2 = \alpha_2/2\gamma. \tag{4.5.3}$$

Equation (4.5.2) reduces to the standard NLS equation when the three parameters d, μ, and μ_2 are set to zero. Physically, d is related to the amplifier bandwidth (through the parameter T_2), μ is related to the amplifier gain, and μ_2 governs the effect of two-photon absorption. Numerical values of these parameters for most EDFAs are such that $\mu \sim 1$, $d \sim 10^{-3}$, and $\mu_2 \sim 10^{-4}$ when $T_0 \sim 1$ ps.

An extended version of Eq. (4.5.2), known as the quintic Ginzburg–Landau equation, has also attracted considerable attention [123]–[129]. It adds a fifth-order term $\varepsilon|u|^4u$ to Eq. (4.5.2), where ε is a constant parameter that may be complex in general. Physically, the quintic term results from saturation of the fiber nonlinearity and is negligible for silica fibers at practical power levels. For this reason, its effects are not considered in this chapter.

Since the inverse scattering method is not applicable, the solitary-wave solutions of Eq. (4.5.2) are found by a trial-and-error method. In this method, an analytic form of the solution is guessed, and the constants are adjusted to satisfy Eq. (4.5.2). An appropriate functional form of the solitary-wave solution of this equation is [120]

$$u(\xi,\tau) = N_s[\mathrm{sech}(p\tau)]^{1+iq}\exp(iK_s\xi). \tag{4.5.4}$$

The constants N_s, p, q, and K_s are determined by substituting this solution in Eq. (4.5.2) and are

$$N_s^2 = \tfrac{1}{2}p^2[s(q^2-2)+3qd], \tag{4.5.5}$$

$$p^2 = -\mu[d(1-q^2)+2sq]^{-1}, \tag{4.5.6}$$

$$K_s = -\tfrac{1}{2}p^2[s(1-q^2)-2qd], \tag{4.5.7}$$

where q is a solution of the quadratic equation

$$(d-\mu_2 s)q^2 - 3(s+\mu_2 d)q - 2(d-\mu_2 s) = 0. \tag{4.5.8}$$

It is easy to verify that when $s=-1$ (anomalous GVD) and d, μ, and μ_2 are set to zero, the solution (4.5.4) reduces to the standard soliton of the NLS equation. The parameter p remains undetermined in that limit since the NLS equation supports a whole family of fundamental solitons such that $N_s = p$. By contrast, both p and N_s are fixed for the Ginzburg–Landau equation by the amplifier parameters μ and d. This is a fundamental difference introduced by the dopants: Fiber amplifiers select a single soliton from the entire family of solitons supported by the undoped fiber. The width and the peak power of this soliton are uniquely determined by the amplifier parameters (such as the gain and its bandwidth). Such a soliton is often called the *autosoliton* since all input pulses, irrespective of their width and peak power, automatically evolve toward this unique soliton [90].

An important property of autosolitons is that, unlike conventional NLS solitons, they represent chirped pulses. This feature is seen clearly from Eq.

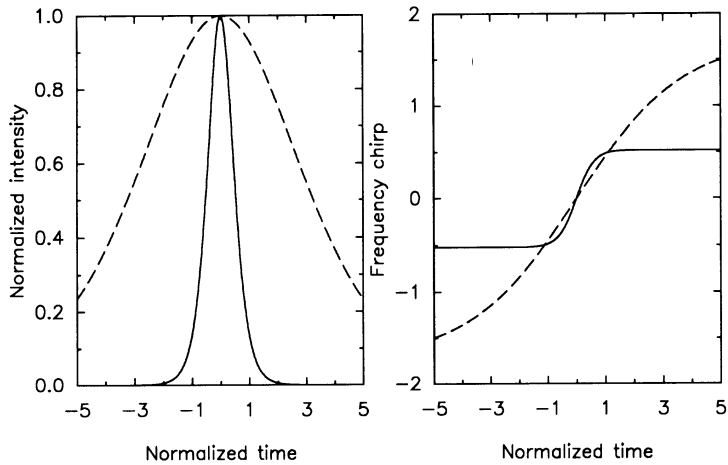

Figure 4.10 (a) Intensity and (b) chirp profiles for a soliton supported by fiber amplifiers when $d = 0.5$. Solid and dashed curves correspond to the cases of normal and anomalous GVD, respectively.

(4.5.4) by noting that the phase of the soliton becomes time dependent when $q \neq 0$. In fact, Eq. (4.5.4) can be written as

$$u(\xi,\tau) = N_s \operatorname{sech}(p\tau)\exp[iK_s\xi - iq\ln(\cosh\, p\tau)]. \tag{4.5.9}$$

By defining the frequency chirp as $\delta\omega = -\partial\phi/\partial\tau$, the chirp is given by

$$\delta\omega(\tau) = qp\tanh(p\tau). \tag{4.5.10}$$

The parameter q governs the magnitude of chirp. As seen from Eq. (4.5.8), $q \neq 0$ only when d or μ_2 are nonzero. For silica fiber amplifiers, μ_2 is small enough that it can be set to zero. The parameter q is then given by

$$q = [3s \pm (9 + 8d^2)^{1/2}]/2d, \tag{4.5.11}$$

where the sign is chosen such that both p and N_s are real.

The existence of solitons in a fiber amplifier is somewhat surprising. For the soliton to preserve its shape and energy in spite of the gain provided by the amplifier, a loss mechanism must exist. Both gain dispersion and two-photon absorption provide such a loss mechanism. Although the role of two-photon absorption as a loss mechanism is easily understood, it is not obvious

how gain dispersion leads to loss. Because of a finite gain bandwidth, the frequency dependence of the gain is such that spectral wings of an optical pulse experience less gain—and may even experience loss—if the pulse spectrum becomes wider than the gain bandwidth. Thus, gain dispersion can act as a loss mechanism for pulses with a wide spectrum. The frequency chirp imposed on the soliton of Eq. (4.5.9) helps to maintain balance between gain and loss since it can tailor the pulse spectrum through the chirp parameter q. This is why autosolitons are chirped. This mechanism also explains why amplifier solitons can exist even in the normal GVD region of a doped fiber.

Figure 4.10 compares the intensity and chirp profiles of an amplifier soliton in the cases of normal (dashed curve) and anomalous (solid curve) GVD using $d = 0.5$, $\mu = 0.5$, and $\mu_2 = 0$. In both cases, the chirp is nearly linear over most of the intensity profile, but the soliton is considerably broader in the case of normal GVD. Dependence of soliton parameters on the gain-dispersion parameter d is shown in Fig. 4.11, where the width parameter p^{-1} and the chirp parameter q are plotted as a function of d using $\mu = d$ and $\mu_2 = 0$. Solid and dashed curves correspond to the cases of normal ($s = 1$) and anomalous ($s = -1$) GVD, respectively. For large values of d, the difference between normal and anomalous GVD disappears since the soliton behavior is determined by gain dispersion (rather than index dispersion of the silica host). In contrast, both the width and chirp parameters are much larger in the case of normal GVD when $d < 1$. Indeed, both of these parameters tend to infinity as $d \to 0$ since undoped fibers do not support bright solitons in the case of normal GVD. In the presence of two-photon absorption, the soliton amplitude decreases and its width increases. For most fiber amplifiers μ_2 is so small that its effects can be ignored.

Since gain dispersion and two-photon absorption permit the existence of bright solitons in the normal-GVD region, one is justified in asking whether the Ginzburg–Landau equation has solutions in the form of dark solitary waves that exist in both normal- and anomalous-GVD regions. This turns out to be the case. Since $\mathrm{sech}(\tau)$ is replaced by $\tanh(\tau)$ for dark solitons in undoped fibers, a simple guess is to replace Eq. (4.5.9) with

$$u(\xi, \tau) = N_s \tanh(p\tau) \exp[iK_s\xi - iq \ln(\cosh p\tau)]. \tag{4.5.12}$$

Equation (4.5.12) is indeed a solution of the Ginzburg–Landau equation [86]. The parameters N_s, p, q, and K_s are determined by a set of equations similar to Eqs. (4.5.5)–(4.5.8). The qualitative behavior of dark solitons is also similar

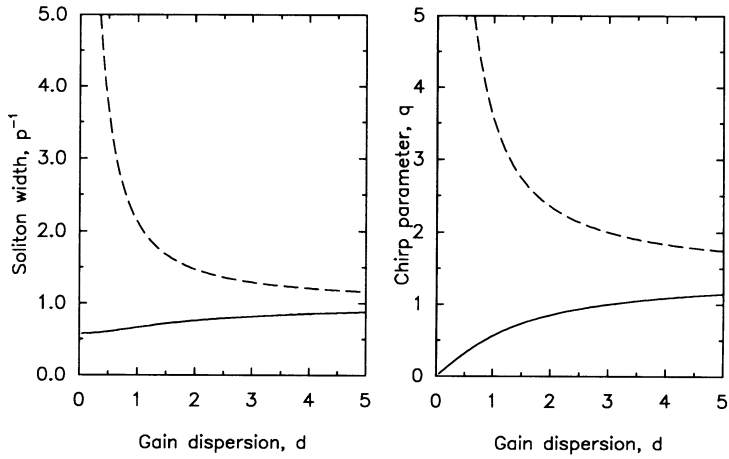

Figure 4.11 Variation of (a) soliton width p^{-1} and (b) chirp parameter q as a function of d. Solid and dashed curves correspond to the cases of normal and anomalous GVD, respectively.

to that of bright solitons governed by Eq. (4.5.9). In particular, gain dispersion determines the frequency chirp imposed on the dark soliton.

Just as modulation instability can destabilize the CW solution, a solitary-wave solution of the Ginzburg–Landau equation can also become unstable under some conditions. For this reason, the stability of such solutions has been studied extensively [123]–[125]. It is evident from Eqs. (4.5.4)–(4.5.8) that the parameters N_s and p can have real positive values only in a certain range of the three parameters μ, d, and μ_2 for $s = \pm 1$. A stable autosoliton exists only when $\mu > 0$ and amplifier parameters are such that both N_s and p are positive numbers. However, when $\mu > 0$, the background is not stable since any small fluctuation can be amplified by the fiber gain. Instability of background noise has important implications for fiber amplifiers and lasers, as will become clear later.

4.5.2 Maxwell–Bloch Solitons

The soliton solution (4.5.9) shows that the width of autosolitons can become comparable to the dipole relaxation time T_2 (see Fig. 4.11). The validity of the Ginzburg–Landau equation then becomes questionable since the rate-equation

approximation used in its derivation [see Eq. (4.3.5)] becomes invalid under such conditions. In its place, we should look for the solitary-wave solutions of the Maxwell–Bloch equations themselves by solving Eqs. (4.3.2)–(4.3.4).

Such solutions were first obtained in 1967 for nonfiber media in which both β_2 and γ are negligible [130]. The underlying nonlinear phenomenon is known as self-induced transparency (SIT). Since 1967, SIT solitons have been studied extensively [131]–[135]. Soliton solutions of the Maxwell–Bloch equations exist even for a nonlinear host (without dispersion), but the resulting solitons are chirped [132]. Chirped solitons for an amplifying two-level medium in a dispersive nonlinear host have also been obtained [134].

Equations (4.3.2)–(4.3.4) can be simplified considerably in the case of SIT. The terms containing T_1 and T_2 can be neglected because SIT requires coherent interaction between atoms and the optical field that occurs only for optical pulses much shorter than T_1 and T_2. The amplitude $A(z,t)$ can be assumed real if the laser frequency ω_0 coincides with the atomic transition frequency ω_a. For a two-level absorber (no pumping), the SIT soliton is given by [130]

$$A(z,t) = N_0 \operatorname{sech}\left(\frac{t - z/V}{\tau_p}\right), \tag{4.5.13}$$

where the pulse velocity V and the pulse width τ_p are related as

$$\frac{1}{V} = \frac{1}{c} + \frac{\rho\mu^2\omega_0}{2\varepsilon_0 hc}\int_{-\infty}^{\infty} \frac{\tau_p^2 h(\Delta)\, d\Delta}{1 + (\Delta\tau_p)^2}. \tag{4.5.14}$$

In this equation, ρ is the atomic density, $\Delta = \omega - \omega_0$, and $h(\Delta)$ is distribution function over which the integration is performed for an inhomogeneously broadened two-level system.

Equation (4.5.13) shows that a "sech" pulse can propagate without change in its shape, width, or amplitude—even in an absorbing medium—provided that its input amplitude N_0 is related to its width to form a 2π pulse [135]. The effect of absorption is to slow down the optical pulse. Indeed, the soliton velocity V may be reduced by several orders of magnitude ($V/c \sim 10^{-3}$). Physically, the pulse slows down because of continuous absorption and emission of radiation occurring inside the medium. Qualitatively speaking, energy is absorbed from the leading edge of the pulse and is emitted back near the trailing edge. For the pulse amplitude given in (4.5.13), the two processes can occur coherently in such a manner that the pulse shape remains unchanged on propagation. In essence, the role of dispersion is played by absorption for SIT

solitons. Similar to the case of fiber solitons, SIT solitons describe an entire family of solitons whose width and group velocities are related by Eq. (4.5.14).

The situation becomes much more interesting in the case of fiber amplifiers since the two kinds of solitons can exist simultaneously. The silica host supports NLS solitons whereas the dopants can support SIT solitons. The question thus arises: What happens in a fiber amplifier where dopants are inside a dispersive nonlinear host? To answer this question, we should look for soliton solutions of Eqs. (4.3.2)–(4.3.4) in the coherent limit in which the terms containing T_1 and T_2 can be neglected [96]–[106]. Detuning effects can be ignored by setting $\omega_a = \omega_0$. It turns out that the SIT solution given by Eq. (4.5.13) remains valid but the group velocity of the soliton is determined by [97]

$$\frac{1}{V} = \left(\frac{1}{v_g^2} + \frac{2n_2 n_0 \omega_0^2 h^2}{\mu^2 c^2} \right)^{1/2}, \tag{4.5.15}$$

where v_g is the group velocity in the undoped fiber.

A remarkable feature of Eq. (4.5.15) is that the soliton velocity depends on the nonlinear parameter n_2 but is independent of the dopant density and the soliton width. Another noteworthy feature is that both the width and the peak power of the soliton are uniquely determined by the amplifier. More specifically, the peak power and the width of the soliton must satisfy not only the fundamental-soliton condition $N = 1$ but also the SIT condition that the pulse area equals 2π [98]. Such a SIT soliton exists for both normal and anomalous GVD. The situation is similar to that occurring for autosolitons [see Eq. (4.5.4)] in the sense that a single soliton is selected from the entire family of SIT solitons. The surprising feature is that an SIT soliton can be chirp free, in contrast to the solitary-wave solution of the Ginzburg–Landau equation.

Experimental realization of SIT solitons is difficult in practice because of the relatively small value of the dipole relaxation time ($T_2 \sim 100$ fs). In the coherent regime, the soliton width should be smaller than T_2. The required peak power for such a 2π pulse is prohibitively large ($P_0 > 1$ GW). Nevertheless, coherent effects associated with the SIT solitons were observed in an experiment in which an EDFA was cooled to 4.2 K [136]. Cooling of a doped fiber to such low temperatures increases T_2 by orders of magnitude ($T_2 \sim 1$ ns) because of reduced phonon-related effects. As a result, SIT solitons can be observed by using pulses widths of about 100 ps and peak powers of about 10 W. Indeed, 400-ps pulses with peak power levels of about 50 W were used in the

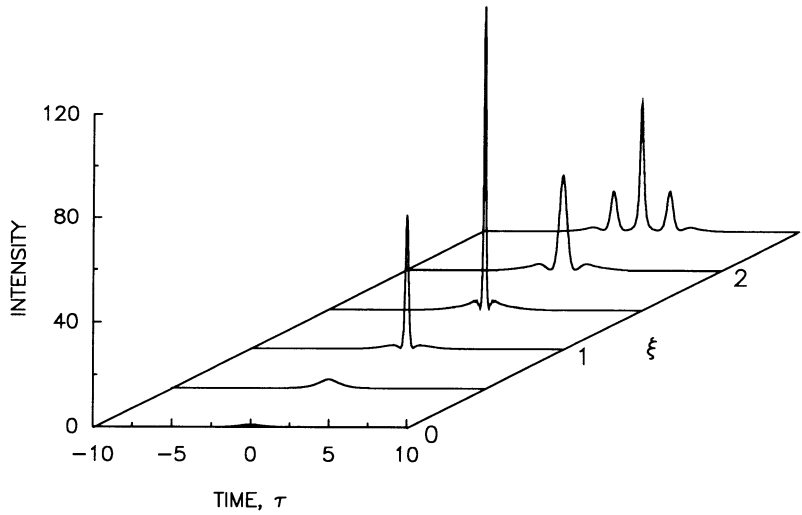

Figure 4.12 Evolution of a fundamental soliton ($N = 1$) in a fiber amplifier with parameters $d = 0.092$, $\mu = 2.3$, and $\mu_2 = 0$.

experiment [136]. When such pulses were propagated in a 1.5-m-long cooled fiber, they formed the SIT soliton when the peak power was large enough to form the 2π pulse. Another coherent effect, known as *photon echo*, has also been observed in EDFAs cooled to liquid-helium temperatures [100].

4.6 Pulse Amplification

Amplification of short optical pulses can be studied by solving the Ginzburg–Landau equation numerically. Since that equation is valid only for pulses of duration $T_0 \gg T_2$, picosecond pulses are considered first; femtosecond pulses require the use of full Maxwell–Bloch equations. The split-step Fourier method (see Section A.2.4) can be easily extended for solving these equations.

4.6.1 Picosecond Pulses

Consider the case in which the input pulse amplitude is given by $A(0,t) = \sqrt{P_0}\,\mathrm{sech}(t/T_0)$, and its width T_0 is related to the peak power P_0 such that the pulse will propagate as a fundamental soliton in the absence of dopants and fiber losses. The evolution of such a pulse in distributed fiber amplifiers is

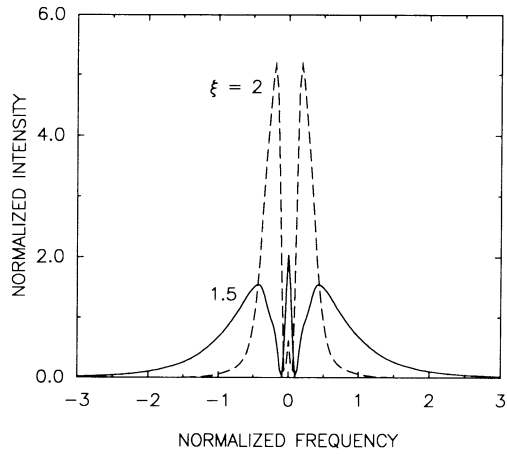

Figure 4.13 Pulse spectra at ξ = 1.5 and 2 corresponding to the pulse shapes shown in Fig. 4.12. Spectral narrowing at ξ = 2 is due to gain dispersion.

studied by solving Eq. (4.5.2) numerically with the input $u(0,\tau) = \text{sech}(\tau)$. The amplification process depends strongly on the value of the gain parameter μ. One can distinguish two regions depending on whether $\mu \ll 1$ or becomes comparable to or larger than 1. In the former case, the soliton is amplified adiabatically. In fact, one can treat Eq. (4.5.2) as a perturbed NLS equation (since all three parameters d, μ, and μ_2 are much less than 1) and apply soliton perturbation theory [104]. In essence, the soliton adjusts its parameters adiabatically and evolves toward the chirped amplifier soliton given in Eq. (4.5.9).

Practical fiber amplifiers can provide gains of 30 dB or more over a length of only a few meters. For such high-gain amplifiers, the parameter μ can easily exceed 1 and the amplification process is not adiabatic. Figure 4.12 shows the evolution of a fundamental soliton over a distance $L = 2.5L_D$ for an EDFA pumped to provide 10-dB gain over each dispersion length [$\exp(\mu) = 10$ or $\mu \approx 2.3$]. The width T_0 is chosen such that $T_2/T_0 = 0.2$ ($d = 0.092$). Two-photon absorption is neglected by setting $\mu_2 = 0$. The input soliton is compressed by more than a factor of 10 at $\xi = 1.5$, a feature that can be used to amplify and compress ultrashort optical pulses simultaneously by passing them through an EDFA. The soliton develops additional structure in the form of subpulses as it propagates beyond $\xi = 2$ [67].

The compression stage seen in Fig. 4.12 is similar to that occurring for higher-order solitons and can be understood by noting that the initial stage of

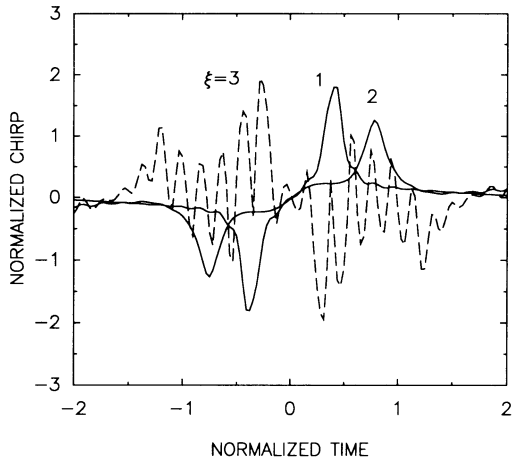

Figure 4.14 Frequency chirp profiles at $\xi = 1$, 2, and 3. The chirp is absent at the amplifier input (ξ = 0). Parameter values are the same as for Fig. 4.12.

amplification raises the peak power such that N exceeds 1. As discussed in Section A.5.2, the pulse tries to maintain $N = 1$ by reducing its width. As long as the amplification process remains adiabatic, this process continues and the pulse width keeps decreasing, as seen in Fig. 4.12 for distances up to $\xi = 1.5$. However, by that time the pulse has become so short, and its spectrum has become so broad (comparable to the gain bandwidth), that the effects of gain dispersion take over. Gain dispersion reduces the spectral bandwidth and broadens the pulse in the propagation region beyond $\xi > 1.5$. Spectral narrowing is clearly seen in Fig. 4.13 where pulse spectra are compared for ξ = 1.5 and 2. The soliton is also considerably chirped because of SPM and gain dispersion. Figure 4.14 shows chirp profiles for ξ = 1, 2, and 3. For ξ = 1 and 2, the features of frequency chirp are similar to those expected from SPM alone (see Section A.4.1). However, the chirp behavior becomes qualitatively different for $\xi > 2$, as is evident by the rapid oscillations seen in Fig. 4.14.

The qualitative changes seen in Fig. 4.14 beyond $\xi = 2$ can be attributed to the generation of subpulses seen in Fig. 4.12. The number of such subpulses grows with further propagation. Figure 4.15 shows pulse shapes and spectra at ξ = 3 and 5. Each subpulse, once it has stabilized, has the same width and about the same amplitude. Spacing between subpulses is nearly uniform (except for subpulses that are still in the process of formation) and does not change with propagation. These features can be understood qualitatively in terms of

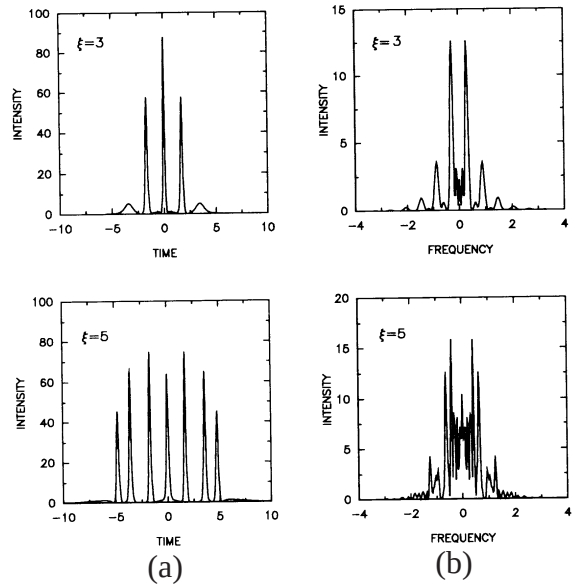

Figure 4.15 (a) Pulse shapes and (b) pulse spectra at $\xi = 3$ and 5 for the case shown in Fig. 4.12. New subpulses are generated continuously as the pulse propagates along the amplifier.

chirped autosolitons. The width and the peak power (parameters p and N_s) of such solitons are fixed by the amplifier parameters [μ and d in Eq. (4.5.2)]. Thus, the input pulse evolves toward such a soliton by reducing its width and increasing its peak power (see Fig. 4.12). However, during this process it sheds a part of its energy as dispersive waves. Because of the gain provided by the amplifier and instability of the background, parts of the dispersive wave can grow and evolve toward another chirped soliton. This mechanism explains continuous generation of subpulses during the amplification process.

In the absence of soliton interactions, each subpulse will correspond to the solitary-wave solution given by Eq. (4.5.9). However, soliton interactions cannot be ignored, especially for chirped solitons since chirp profiles overlap considerably. It is this interaction of chirped solitons that leads to the oscillatory structure in Fig. 4.13 and to the amplitude differences seen in Fig. 4.14. The structure within the pulse spectra in Fig. 4.15(b) is also due to soliton interaction. This effect has been studied for the Ginzburg–Landau equation by using perturbation theory [137]. The results show that the origin of multiple-pulse

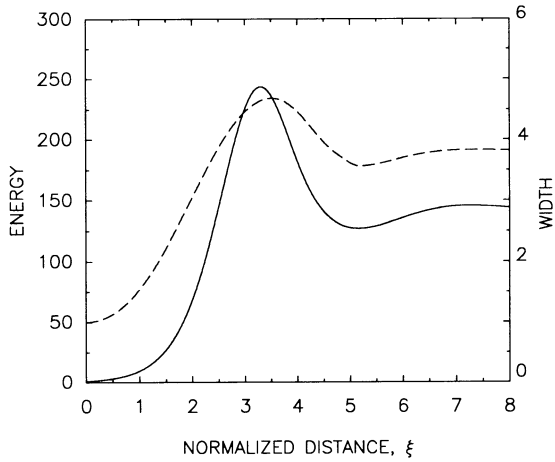

Figure 4.16 Energy (solid line) and RMS width (dashed line) of the amplified pulse in the case of normal dispersion. Parameter values are the same as in Fig. 4.12.

solitons similar to those seen in Fig. 4.15 lies in the frequency chirp associated with such solitons.

One may wonder what happens when optical pulses propagate in the normal-dispersion region of fiber amplifiers. Solitary-wave solutions of the Ginzburg–Landau equation exist in the form of a chirped soliton even in the case of normal GVD ($\beta_2 > 0$). Thus, one can expect an input pulse to evolve toward this soliton, similar to the case of anomalous GVD. Numerical simulations confirm this expectation. The surprising feature, however, turns out to be the absence of pulse splitting. The input pulse evolves toward a single chirped soliton of the form given in Eq. (4.5.9). This feature is seen in Fig. 4.16, where the energy and the root-mean-square (RMS) width of pulses are plotted as a function of distance over the range ξ = 0–8 for the same parameter values used in Fig. 4.12 except that $s = 1$ instead of -1. Both the energy and the RMS width become constant after initial transients have died out. In contrast with the features seen in Fig. 4.12, the pulse width actually increases by about a factor of 4. This is easily understood from the results shown in Fig. 4.11 by noting that the chirped soliton supported by fiber amplifiers is much wider in the case of normal GVD. The absence of pulse splitting indicates that interaction between chirped solitons is repulsive for normal GVD.

4.6.2 Ultrashort Pulses

When input pulses are relatively short (~ 1 ps or shorter), it becomes necessary to include the higher-order nonlinear and dispersive effects. The parabolic-gain approximation made in deriving the Ginzburg–Landau equation should also be relaxed for such short pulses. This can be done by keeping the denominator in Eq. (4.3.6) intact while using Eqs. (4.3.4) and (4.3.5). Following the analysis of Section A.2.3 and including the higher-order effects, the generalized Ginzburg–Landau equation can be written as

$$i\frac{\partial u}{\partial \xi} \pm \frac{1}{2}\frac{\partial^2 u}{\partial \tau^2} + |u|^2 u - i\delta_3 \frac{\partial^3 u}{\partial \tau^3} - is_0 \frac{\partial |u|^2 u}{\partial \tau} - \tau_R u \frac{\partial |u|^2}{\partial \tau} = \frac{i}{2} g_0 L_d \int_{-\infty}^{\infty} \frac{\tilde{u}(\xi, f)\exp(-if\tau)\,df}{1 - i(f - f_0)(T_2/T_0)} - \frac{i}{2}\alpha L_d u, \quad (4.6.1)$$

where $\tilde{u}(\xi, f)$ is the Fourier transform of $u(\xi, \tau)$, $f_0 = \omega_0 T_0$; and δ_3, s_0, and τ_R are the same three parameters introduced in Section A.5.5. The self-steepening parameter s_0 is negligible except for extremely short pulses (~ 10 fs) for which Eq. (4.6.1) itself is likely to break down. Third-order dispersive effects are also negligible unless the fiber amplifier operates very close to the zero-dispersion wavelength. In contrast, the parameter τ_R governs the frequency shift induced by intrapulse Raman scattering, and its effects should be included for pulse widths below 5 ps.

As early as 1988, it was shown that the Raman-induced spectral shift of solitons may be suppressed in fiber amplifiers because of gain-dispersion effects [138]. Indeed, in an early experiment [139], in which gain was provided by SRS (rather than dopants), little frequency shift was observed even for 100-fs pulses. Physically, this behavior can be understood by noting that a shift of the pulse spectrum from the gain peak reduces the gain experienced by the center frequency of the pulse. At the same time, spectral components located near the gain peak are amplified more. Thus, the amplifier has a built-in mechanism that tries to pull the pulse spectrum toward the gain peak, resulting in a decrease in the Raman-induced frequency shift of solitons.

One may ask how intrapulse Raman scattering affects chirped solitons in fiber amplifiers. Equation (4.6.1) does not appear to have pulselike solitary-wave solutions when τ_R is nonzero although shocklike solutions, similar to those discussed in Section A.5.5 for undoped fibers, may exist under certain conditions [140]. One can use numerical simulations to study the effect of SRS on pulse amplification. For $g_0 L_d \ll 1$, soliton evolution is similar to the case

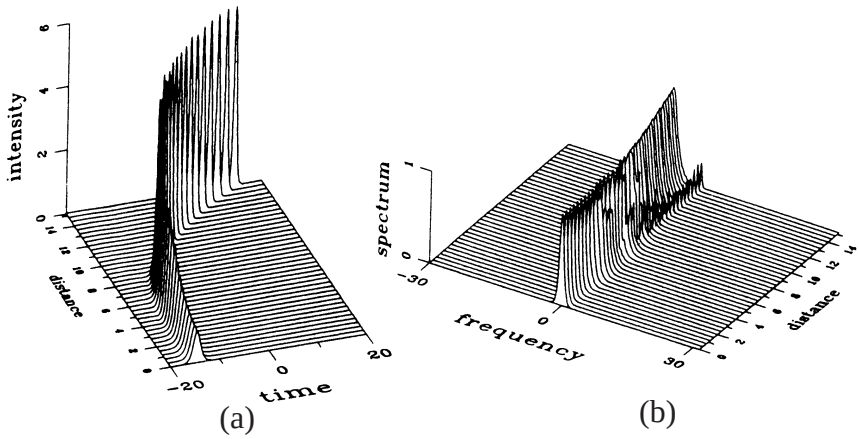

Figure 4.17 Soliton amplification for T_0 = 100 fs and $g_0 L_d$ = 0.2 showing the effects of Raman-induced frequency shift on (a) pulse shape and (b) pulse spectrum. (After Ref. [104])

of undoped fibers. As the soliton amplifies adiabatically, it compresses and, at the same time, its group velocity decreases because of the Raman-induced frequency shift. Figure 4.17 shows the results of numerical simulations when a 100-fs soliton is amplified [104]. For values of $g_0 L_d \sim 1$, the pulse splitting seen in Fig. 4.15 still occurs, but both the soliton amplitude and the width vary from subpulse to subpulse [88]. Pulse spectra show that the magnitude of Raman-induced frequency shift is quite sensitive to the input parameters. The shift also depends on the shape of the gain spectrum [104].

Several experiments have focused on amplification of ultrashort pulses in fiber amplifiers [141]–[149]. Pulse shortening for femtosecond input pulses was observed in several of these experiments. In one experiment, the dependence of the pulse width and the spectrum on amplifier gain was studied by using 240-fs input pulses [146]. Pulses as short as 60-fs were observed at the output end of a 3-m-long fiber amplifier. This experiment also showed that the Raman-induced frequency shift was nearly absent at low pump powers—an effect referred to as *soliton trapping*—but became dominant when the amplifier gain was large enough. Figure 4.18 shows the experiment pulse spectra for three values of pump powers and compares them to the input spectrum (dashed curve). The pulse spectrum did not shift significantly for pump powers of 7 and 13 mW but exhibited a shift of more than 20 nm for 25 mW of pump power.

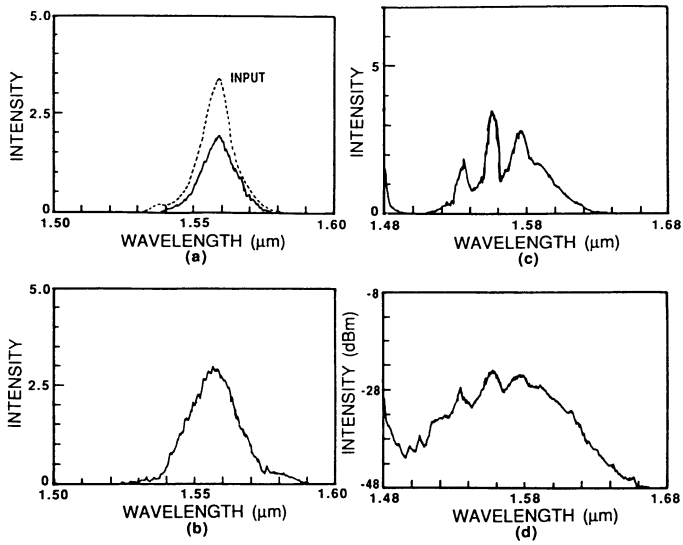

Figure 4.18 Experimental pulse spectra at three pump powers showing effects of Raman-induced frequency shift; (a)–(c) correspond to pump powers of 7, 13, and 25 mW, respectively; (d) shows the 25-mW spectrum on a logarithmic scale. (After Ref. [146], ©American Institute of Physics)

For optical pulses shorter than T_2, one should use, in principle, the complete set of Maxwell–Bloch equations in place of the Ginzburg–Landau equation. These equations have been solved numerically by using the split-step Fourier method [103]. The results show significant deviations between the exact and approximate solutions. For example, whereas the soliton amplitude increases exponentially and its width decreases exponentially in the case of $T_0 \gg T_2$ (see Fig. 4.12), in the coherent regime in which $T_0 \ll T_2$ the changes are linear in ξ rather than being exponential [96]. Even when $T_0 > T_2$ initially, the coherent effects should be included whenever the pulse width becomes comparable to T_2 during propagation. Both qualitative and quantitative differences were found to occur in a numerical study in which $T_0 = 3T_2$ initially but the amplifier gain of 10 dB per dispersion length was large enough to lead to considerable pulse narrowing during the amplification process [103].

One may ask how the solitary-wave solution of the Ginzburg–Landau equation—obtained in the parabolic-gain approximation and given by Eq. (4.5.4)—changes when the Lorentzian shape of the gain spectrum is taken into account

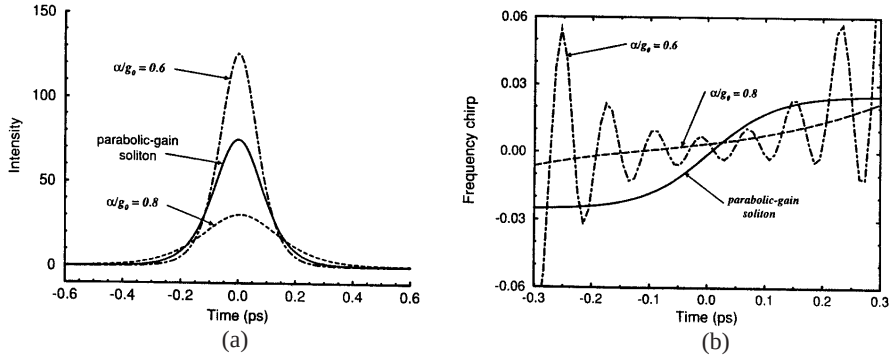

Figure 4.19 (a) Intensity and (b) frequency chirp across the autosoliton for two values α/g_0 using $T_2 = T_0 = 0.2$ ps, $\delta_3 = s_0 = \tau_R = 0$, and $\exp(g_0 L_D) = 2$. The solid line shows the chirp in the parabolic-gain approximation. (After Ref. [115], ©1996, reprinted with permission from Elsevier Science)

through Eq. (4.6.1). Numerical solutions show that autosolitons still exist in the sense that any input pulse evolves toward a unique solitary pulse whose shape, amplitude, width, and chirp are determined by the amplifier parameters [115]. However, the pulse characteristics are quite different than those of the solitary-wave solution (4.5.4). A new feature is that the parameter α/g_0 plays an important role in determining the properties of the autosoliton. As an example, Fig. 4.19 shows the intensity and chirp profiles obtained numerically for α/g_0 = 0.6 and 0.8 using $T_2 = 0.2$ ps. The corresponding profiles for the parabolic-gain soliton obtained from Eq. (4.5.4) are also shown for comparison. In general, the autosoliton becomes narrower and more intense as α/g_0 decreases. The reason can be understood by noting that the pulse spectrum can expand as long as the gain in the spectral wings exceeds the loss level, resulting in shorter pulses for smaller values of α/g_0. However, chirp variations along the pulse also then become large and nonuniform with a periodic structure. It should be stressed that such autosolitons are not absolutely stable since background noise is amplified by the amplifier.

From a practical standpoint, fiber amplifiers can be used to amplify and compress picosecond optical pulses simultaneously, but the amplification process becomes less useful for femtosecond pulses because of temporal and spectral distortions occurring as a result of the higher-order nonlinear effects such as the Raman-induced frequency shift. One can use the technique of chirped-pulse amplification to advantage in that case (see Section 6.5). In this tech-

nique, input femtosecond pulses are first chirped. The pulse width increases substantially during the chirping process. The chirped pulse is then amplified in a fiber amplifier, and the amplified pulse is recompressed by passing it through a dispersive delay line such as a grating pair. Numerical results show that highly efficient and practically distortionless amplification of femtosecond pulses can be realized by this method [150]. The reason is that initial chirping of the pulse stretches its width by as much as two orders of magnitude and decreases the peak power accordingly. As a result, the peak power becomes so small that nonlinear effects are almost negligible during the amplification process. The amplified pulse is then recompressed close to its original width. In a 1994 experiment, the technique of chirped-pulse amplification was used to generate subpicosecond pulses with 100-nJ energy levels from an all-fiber source [151].

Problems

4.1 Assuming that the gain spectrum of a fiber amplifier can be approximated by a Lorentzian profile of 30-nm bandwidth (FWHM), calculate the amplifier bandwidths when it is operated to provide 20- and 30-dB gain. Neglect gain saturation.

4.2 A fiber amplifier can amplify a 1-μW signal to the 1-mW level. What is the output power when a 1-mW signal is incident on the same amplifier? Assume a saturation power of 10 mW.

4.3 Explain the concept of noise figure for a fiber amplifier. Why does the SNR of the amplified signal degrade by 3 dB even for an ideal amplifier?

4.4 Derive an expression for the small-signal gain of an EDFA by using rate equations for the three-level pumping scheme. Assume a rapid transfer of the pumped population to the excited state.

4.5 Solve Eqs. (4.2.7) and (4.2.8) analytically, or numerically if an analytic solution is not possible. Plot the saturated amplifier gain as a function of the pump power for $\alpha_p L = 5$ and $\alpha_s L = 2$, where L is the amplifier length. Neglect fiber losses by setting $\alpha = \alpha' = 0$.

4.6 Derive the Ginzburg–Landau equation (4.3.8) by adding the contribution of dopants to the nonlinear polarization and following the method of Section A.2.3.

4.7 Show by direct substitution that the chirped soliton given by Eq. (4.5.4) is indeed a solution of the Ginzburg–Landau equation (4.5.2) when the soliton parameters are given by Eqs. (4.5.5)–(4.5.8).

4.8 Use the chirped soliton solution given by Eq. (4.5.4) to obtain an expression for the frequency chirp. How would you operate a fiber amplifier to minimize the chirp?

4.9 Solve the Ginzburg–Landau equation of the form in Eq. (4.5.2) numerically by using the split-step Fourier method. Use it to reproduce the results shown in Fig. 4.15 when a fundamental soliton is amplified in a fiber amplifier.

4.10 Modify the numerical scheme used in the previous problem and solve Eq. (4.6.1) numerically. Use your computer code to find the autosoliton in the anomalous-GVD regime, setting δ_3, s_0, and τ_R to zero and choosing $T_2 = T_0 = 0.2$ ps, $\exp(g_0 L_D) = 2$, and $\alpha/g_0 = 0.5$ and 0.7. Plot the intensity and chirp profiles of the autosolitons obtained in the two cases.

References

[1] C. J. Koester and E. Snitzer, *Appl. Opt.* **3**, 1182 (1964).

[2] S. B. Poole, D. N. Payne, R. J. Mears, M. E. Fermann, and R. E. Laming, *J. Lightwave Technol.* **LT-4**, 870 (1986).

[3] M. J. F. Digonnet, Ed., *Rare-Earth Doped Fiber Lasers and Amplifiers* (Marcel Dekker, New York, 1993).

[4] A. Bjarklev, *Optical Fiber Amplifiers: Design and System Applications* (Artech House, Boston, 1993).

[5] E. Desurvire, *Erbium-Doped Fiber Amplifiers* (Wiley, New York, 1994).

[6] R. Jopson, Ed., *Optical Amplifiers and Their Applications* (Optical Society of America, Washington, DC, 1996).

[7] S. Sudo, Ed., *Optical Fiber Amplifiers: Materials, Devices, and Applications* (Artech House, Boston, 1997).

[8] G. P. Agrawal, *Fiber-Optic Communication Systems*, 2nd ed. (Wiley, New York, 1997).

[9] P. C. Becker, N. A. Olsson, and J. R. Simpson, *Erbium-Doped Fiber Amplifiers: Fundamentals and Technology* (Academic, San Diego, CA, 1999).

[10] A. E. Siegman, *Lasers* (University Science Books, Mill Valley, CA, 1986).

[11] P. W. Milonni and J. H. Eberly, *Lasers* (Wiley, New York, 1988).

[12] O. Svelto, *Principals of Lasers*, 4th ed. (Plenum, New York, 1998).

[13] A. Yariv, *Opt. Lett.* **15**, 1064 (1990).

[14] H. Kogelnik and A. Yariv, *Proc. IEEE* **52**, 165 (1964).

[15] R. J. Mears, L. Reekie, I. M. Jauncey, and D. N. Payne, *Electron. Lett.* **23**, 1026 (1987).

[16] E. Desurvire, J. R. Simpson, and P. C. Becker, *Opt. Lett.* **12**, 888 (1987).

[17] M. Nakazawa, Y. Kimura, and K. Suzuki, *Appl. Phys. Lett.* **54**, 295 (1989).

[18] P. C. Becker, J. R. Simpson, N. A. Olsson, and N. K. Dutta, *IEEE Photon. Technol. Lett.* **1**, 267 (1989).

[19] M. Yamada, M. Shimizu, T. Takeshita, M. Okayasu, M. Horiguchi, S. Uehara, and E. Sugita, *IEEE Photon. Technol. Lett.* **1**, 422 (1989)

[20] M. Shimizu, M. Yamada, M. Horiguchi, T. Takeshita, and M. Okayasu, *Electron. Lett.* **26**, 1641 (1990).

[21] M. Nakazawa, Y. Kimura, E. Yoshida, and K. Suzuki, *Electron. Lett.* **26**, 1936 (1990).

[22] B. Pederson, A. Bjarklev, H. Vendeltorp-Pommer, and J. H. Povlsen, *Opt. Commun.* **81**, 23 (1991).

[23] M. Horiguchi, K. Yoshino, M. Shimizu, and M. Yamada, *Electron. Lett.* **29**, 593 (1993).

[24] R. I. Laming, J. E. Townsend, D. N. Payne, F. Meli, G. Grasso, and E. J. Tarbox, *IEEE Photon. Technol. Lett.* **3**, 253 (1991).

[25] W. J. Miniscalco, *J. Lightwave Technol.* **9**, 234 (1991).

[26] K. Inoue, T. Korninaro, and H. Toba, *IEEE Photon. Technol. Lett.* **3**, 718 (1991).

[27] R. Kashyap, *Fiber Bragg Gratings* (Academic Press, San Diego, CA, 1999).

[28] S. H. Yun, B. W. Lee, H. K. Kim, and B. Y. Kim, *IEEE Photon. Technol. Lett.* **11**, 1229 (1999).

[29] P. F. Wysocki, N. Park, and D. DiGiovanni, *Opt. Lett.* **21**, 1744 (1996).

[30] H. Ono, M. Yamada, T. Kanamori, and Y. Ohishi, *Electron. Lett.* **33**, 1477 (1997).

[31] M. Masuda, K. I. Suzuki, S. Kawai, and K. Aida, *Electron. Lett.* **33**, 753 (1997).

[32] M. Yamada, H. Ono, T. Kanamori, S. Sudo, and Y. Ohishi, *Electron. Lett.* **33**, 710 (1997).

[33] A. A. M. Saleh, R. M. Jopson, J. D. Evankow, and J. Aspell, *IEEE Photon. Technol. Lett.* **2**, 714 (1990).

[34] C. R. Giles and E. Desurvire, *J. Lightwave Technol.* **9**, 271 (1991).

[35] B. Pedersen, A. Bjarklev, J. H. Povlsen, K. Dybdal, and C. C. Larsen, *J. Lightwave Technol.* **9**, 1105 (1991).

[36] K. Nakagawa, S. Nishi, K. Aida, and E. Yoneda, *J. Lightwave Technol.* **9**, 198 (1991).

[37] Y. Sun, J. L. Zyskind, and A. K. Srivastava, *IEEE J. Sel. Topics Quantum Electron.* **3**, 991 (1997).

[38] M. Zirngibl, *Electron. Lett.* **27**, 560 (1991).

[39] H. Okamura, *J. Lightwave Technol.* **10**, 1110 (1992).

[40] E. Delevaque, T. Georges, J. F. Bayon, M. Monerie, P. Niay, and P. Benarge, *Electron. Lett.* **29**, 1112 (1993).

[41] A. Yu and M. J. O'Mahony, *IEEE J. Sel. Topics Quantum Electron.* **3**, 1013 (1997).

[42] N. Takahashi, T. Hirono, H. Akashi, S. Takahashi, and T. Sasaki, *IEEE J. Sel. Topics Quantum Electron.* **3**, 1019 (1997).

[43] K. Inoue, *IEEE Photon. Technol. Lett.* **11**, 533 (1999).

[44] Y. Liu and M. F. Kroll, *IEEE Photon. Technol. Lett.* **11**, 1381 (1999).

[45] R. Olshansky, *Electron. Lett.* **24**, 1363 (1988).

[46] C. R. Giles, E. Desurvire, J. L. Zyskind, and J. R. Simpson, *IEEE Photon. Technol. Lett.* **1**, 367 (1989).

[47] M. Yamada, M. Shimizu, M. Okayasu, T. Takeshita, M. Horiguchi, Y. Tachikawa, and E. Sugita, *IEEE Photon. Technol. Lett.* **2**, 205 (1990).

[48] E. Desurvire, *IEEE Photon. Technol. Lett.* **2**, 208 (1990).

[49] R. I. Laming and D. N. Payne, *IEEE Photon. Technol. Lett.* **2**, 418 (1990).

[50] K. Kikuchi, *Electron. Lett.* **26**, 1851 (1990).

[51] G. R. Walker, *Electron. Lett.* **27**, 745 (1991).

[52] B. Pedersen, J. Chirravuri, and W. J. Miniscalco, *IEEE Photon. Technol. Lett.* **4**, 351 (1992).

[53] R. G. Smart, J. L. Zyskind, J. W. Sulhoff, and D. J. DiGiovanni, *IEEE Photon. Technol. Lett.* **4**, 1261 (1992).

[54] R. I. Laming, M. N. Zervas, and D. N. Payne, *IEEE Photon. Technol. Lett.* **4**, 1345 (1992).

[55] F. W. Willems, J. C. van der Plaats, and D. J. DiGiovanni, *Electron. Lett.* **30**, 645 (1994).

[56] M. N. Zervas, R. I. Laming, and D. N. Payne, *IEEE J. Quantum Electron.* **31**, 472 (1995).

[57] R. Lebref, B. Landousies, T. Georges, and E. Delevaque, *J. Lightwave Technol.* **15**, 766 (1997).

[58] M. Yamada, H. Ono, and Y. Ohishi, *Electron. Lett.* **34**, 1747 (1998).

[59] G. R. Walker, D. M. Spirit, D. L. Williams, and S. T. Davey, *Electron. Lett.* **27**, 1390 (1991).

[60] D. N. Chen and E. Desurvire, *IEEE Photon. Technol. Lett.* **4**, 52 (1992).

[61] K. Rottwitt, J. H. Povlsen, A. Bjarklev, O. Lumholt, B. Pedersen, and T. Rasmussen, *Electron. Lett.* **28**, 287 (1992); *IEEE Photon. Technol. Lett.* **5**, 218 (1993).

[62] S. Wen and S. Chi, *IEEE Photon. Technol. Lett.* **4**, 189 (1992); *J. Lightwave Technol.* **10**, 1869 (1992).

[63] K. Rottwitt, J. H. Povlsen, and A. Bjarklev, *J. Lightwave Technol.* **11**, 2105 (1993).

[64] C. Lester, K. Rottwitt, J. H. Povlsen, P. Varming, M. A. Newhouse, and A. J. Antos, *Opt. Lett.* **20**, 1250 (1995).

[65] A. Altuncu, L. Noel, W. A. Pender, A. S. Siddiqui, T. Widdowson, A. D. Ellis, M. A. Newhouse, A. J. Antos, G. Kar, and P. W. Chu, *Electron. Lett.* **32**, 233 (1996).

[66] M. Nissov, H. N. Poulsen, R. J. Pedersen, B. F. Jørgensen, M. A. Newhouse, and A. J. Antos, *Electron. Lett.* **32**, 1905 (1996).

[67] G. P. Agrawal, *Phys. Rev. A* **44** , 7493 (1991).

[68] M. Asobe, T. Kanamori, and K. Kubodera, *IEEE Photon. Technol. Lett.* **4**, 362 (1992); *IEEE J. Quantum Electron.* **2**, 2325 (1993).

[69] G. P. Agrawal, *IEEE Photon. Technol. Lett.* **4**, 562 (1992).

[70] J. P. Hamide, P. Emplit, and J. M. Gabriagues, *Electron. Lett.* **26**, 1452 (1990).

[71] S. Ryu, *Electron. Lett.* **28**, 2212 (1992).

[72] M. Murakami and S. Saito, *IEEE Photon. Technol. Lett.* **4**, 1269 (1992).

[73] K. Kikuchi, *IEEE Photon. Technol. Lett.* **5**, 221 (1993).

[74] F. Matera, A. Mecozzi, M. Romagnoli, and M. Settembre, *Opt. Lett.* **18**, 1499 (1993).

[75] A. Mecozzi, *J. Opt. Soc. Am. B* **11**, 462 (1994).

[76] S. B. Cavalcanti, G. P. Agrawal, and M. Yu, *Phys. Rev. A* **51**, 4086 (1995).

[77] M. Yu, G. P. Agrawal, and C. J. McKinstrie, *J. Opt. Soc. Am. B* **12**, 1126 (1995).

[78] M. O. van Deventer, S. Wingstrand, B. Hermansson, A. Bolle, P. Jalderot, C. Backdahl, and J. Karlsson, *Opt. Fiber Technol*. **2**, 183 (1996).

[79] C. Lorattanasane and K. Kikuchi, *IEEE J. Quantum Electron.* **33**, 1084 (1997).

[80] A. Carena, V. Curri, R. Gaudino, P. Poggiolini, and S. Benedetto, *IEEE Photon. Technol. Lett.* **9**, 535 (1997).

[81] R. A. Saunders, B. A. Patel, and D. Garthe, *IEEE Photon. Technol. Lett.* **9**, 699 (1997).

[82] R. Q. Hui, M. O'Sullivan, A. Robinson, and M. Taylor, *J. Lightwave Technol.* **15**, 1071 (1997).

[83] D. F. Grosz and H. L. Fragnito, *Microwave Opt. Tech. Lett.* **18**, 275 (1998); **19**, 149 (1998); **20**, 389 (1999).

[84] D. F. Grosz, C. Mazzali, S. Celaschi, A. Paradisi, and H. L. Fragnito, *IEEE Photon. Technol. Lett.* **11**, 379 (1999).

[85] M. Norgia, G. Giuliani, and S. Donati, *J. Lightwave Technol.* **17**, 1750 (1999).

[86] P. A. Bélanger, L. Gagnon, and C. Paré, *Opt. Lett.* **14**, 943 (1989).

[87] P. Heist, W. Rudolph, and V. Petrov, *Appl. Phys. B* **49**, 113 (1989).

[88] G. P. Agrawal, *IEEE Photon. Technol. Lett.* **2**, 875 (1990); *Opt. Lett.* **16**, 226 (1991).

[89] L. Gagnon and P. A. Bélanger, *Phys. Rev. A* **43**, 6187 (1991).

[90] V. S. Grigor'yan and T. S. Muradyan, *J. Opt. Soc. Am. B* **8**, 1757 (1991).

[91] I. R. Gabitov, M. Romagnoli, and S. Wabnitz, *Appl. Phys. Lett.* **20**, 1881 (1991).

[92] E. M. Dianov, K. K. Konstantinov, A. N. Pilipetskii, and A. N. Starodumov, *Sov. Lightwave Commun.* **1**, 169 (1991).

[93] W. Hodel, J. Schülz, and H. P. Weber, *Opt. Commun.* **88**, 173 (1992).

[94] M. Romagnoli, F. S. Locati, F. Matera, M. Settembre, M. Tamurrini, and S. Wabnitz, *Opt. Lett.* **17**, 1456 (1992).

[95] G. P. Agrawal, *Phys. Rev. E* **48**, 2316 (1993).

[96] V. Petrov and W. Rudolph, *Opt. Commun.* **76**, 53 (1990).

[97] I. V. Melnikov, R. F. Nabiev, and A. V. Nazarkin, *Opt. Lett.* **15**, 1348 (1990).

[98] T. Y. Wang and S. Chi, *Opt. Lett.* **16**, 1575 (1991).

[99] M. Nakazawa, E. Yamada, and H. Kubota, *Phys. Rev. Lett.* **66**, 2625 (1991); *Phys. Rev. A* **44**, 5973 (1991).

[100] V. L. da Silva, Y. Siberberg, J. P. Heritage, E. W. Chase, M. A. Saifi, and M. J. Andrejco, *Opt. Lett.* **16**, 1340 (1991).

[101] M. Nakazawa, K. Suzuki, Y. Kimura, and H. Kubota, *Phys. Rev. A* **45**, 2682 (1992).

[102] S. Chi and T. Y. Wang, *Opt. Commun.* **89**, 463 (1992).

[103] B. Gross and J. T. Manassah, *Opt. Lett.* **17**, 340 (1992).

[104] V. V. Afanasjev, V. N. Serkin, and V. A. Vysloukh, *Sov. Lightwave Commun.* **2**, 35 (1992).

[105] A. I. Maimistov, *Sov. J. Quantum Electron.* **22**, 271 (1992); *Opt. Commun.* **94**, 33 (1992).

[106] S. Chi, C. W. Chang, and S. Wen, *Opt. Commun.* **106**, 183 (1994); *Opt. Commun.* **111**, 132 (1994).

[107] M. F. S. Ferreira, *Opt. Commun.* **107**, 365 (1994).

[108] M. N. Islam, L. Rahman, and J. R. Simpson, *J. Lightwave Technol.* **12**, 1952 (1994).

[109] K. Kurokawa and M. Nakazawa, *IEEE J. Quantum Electron.* **28**, 1922 (1992).

[110] K. Kurokawa, H. Kubota, and M. Nakazawa, *IEEE J. Quantum Electron.* **30**, 2220 (1994).

[111] D. Shenoy and A. Puri, *Opt. Commun.* **113**, 401 (1995).

[112] K. Porsezian and K. Nakkeeran, *Phys. Rev. Lett.* **74**, 2941 (1995); *J. Mod. Opt.* **42**, 1953 (1995).

[113] H. Ammamm, W. Hodel, and H. P. Weber, *Opt. Commun.* **115**, 347 (1995).

[114] J. T. Manassah and B. Gross, *Opt. Commun.* **122**, 71 (1995).

[115] L. W. Liou and G. P. Agrawal, *Opt. Commun.* **124**, 500 (1996).

[116] K. Nakkeeran and K. Porsezian, *Opt. Commun.* **123**, 169 (1996); *J. Mod. Opt.* **43**, 693 (1996).

[117] G. H. M. van Tartwijk and G. P. Agrawal, *J. Opt. Soc. Am. B* **14**, 2618 (1997).

[118] J. R. Costa and C. R. Paival, *Microwave Opt. Tech. Lett.* **19**, 309 (1998).

[119] N. Akozbek and S. John, *Phys. Rev. E* **58**, 3876 (1998).

[120] N. N. Pereira and L. Stenflo, *Phys. Fluids* **20**, 1733 (1977).

[121] W. van Saarloos and P. Hohenberg, *Physica D* **56**, 303 (1992).

[122] P. Marcq, H. Chatë, and R. Conte, *Physica D* **73**, 305 (1994).

[123] N. N. Akhmediev, V. V. Afanasjev, and J. M. Soto-Crespo, *Phys. Rev. E* **53**, 1190 (1996).

[124] J. M. Soto-Crespo, N. N. Akhmediev, and V. V. Afanasjev, *J. Opt. Soc. Am. B* **13**, 1439 (1996).

[125] N. N. Akhmediev and A. Ankiewicz, *Solitons: Nonlinear Pulses and Beams* (Chapman and Hall, London, 1997), Chap. 13.

[126] V. Afanasjev, P. L. Chu, and B. A. Malomed, *Phys. Rev. E* **57**, 1088 (1998).

[127] T. Kapitula, *Physica D* **116**, 121 (1998).

[128] T. Kapitula and B. Sandstede, *J. Opt. Soc. Am. B* **15**, 2757 (1998).

[129] M. F. S. Ferreira, M. M. V. Facao, and S. C. V. Latas, *Fiber Integ. Opt.* **19**, 31 (2000).

[130] S. L. McCall and E. L. Hahn, *Phys. Rev. Lett.* **18**, 908 (1967); *Phys. Rev.* **183**, 457 (1969).

[131] J. E. Armstrong and E. Courtens, *IEEE J. Quantum Electron.* **QE-4**, 411 (1968); *IEEE J. Quantum Electron.* **QE-5**, 249 (1969).

[132] J. H. Eberly and L. Matulic, *Opt. Commun.* **1**, 241 (1969).

[133] L. Matulic and J. H. Eberly, *Phys. Rev. A* **6**, 822 (1972).

[134] S. B. Barone and S. Chi, *Opt. Commun.* **3**, 343 (1973).

[135] A. A. Maimistov, A. M. Basharov, S. O. Elyutin, and Yu. M. Sklyarov, *Phys. Rep.* **191**, 1 (1990).

[136] M. Nakazawa and K. Kurokawa, *Electron. Lett.* **27**, 1369 (1991); K. Kurokawa and M. Nakazawa, *Electron. Lett.* **27**, 1765 (1991).

[137] B. A. Malomed, *Phys. Rev. A* **44**, 6954 (1991); *Phys. Rev. E* **47**, 2874 (1993).

[138] K. J. Blow, N. J. Doran, and D. Wood, *J. Opt. Soc. Am. B* **5**, 1301 (1988).

[139] A. S. Gouveia-Neto, A. S. L. Gomes, and J. R. Taylor, *Opt. Lett.* **12**, 1035 (1987).

[140] D. N. Christodoulides and M. J. Cavelho, *Opt. Lett.* **19**, 251 (1994).

[141] K. Suzuki, Y. Kimura, and M. Nakazawa, *Opt. Lett.* **14**, 865 (1989).

[142] A. Takada, K. Iwatsuki, and M. Saruwatari, *IEEE Photon. Technol. Lett.* **2**, 122 (1990).

[143] B. J. Ainslie, K. J. Blow, A. S. Gouveia-Neto, P. G. J. Wigley, A. S. B. Sombra, and J. R. Taylor, *Electron. Lett.* **26**, 186 (1990).

[144] I. Y. Khrushchev, A. B. Grudinin, E. M. Dianov, D. V. Korobkin, V. A. Semenov, and A. M. Prokhorov, *Electron. Lett.* **26**, 186 (1990).

[145] A. B. Grudinin, E. M. Dianov, D. V. Korobkin, A. Y. Makarenko, A. M. Prokhorov, and I. Y. Khrushchev, *JETP Lett.* **51**, 135 (1990).

[146] M. Nakazawa, K. Kurokawa, H. Kubota, K. Suzuki, and Y. Kimura, *Appl. Phys. Lett.* **57** , 653 (1990).

[147] M. Nakazawa, K. Kurokawa, H. Kubota, and E. Yamada, *Phys. Rev. Lett.* **65**, 1881 (1990).

[148] M. Nakazawa, K. Suzuki, E. Yamada, and H. Kubota, *Electron. Lett.* **27**, 1662 (1991).

[149] D. S. Peter, W. Hodel, and H. P. Weber, *Opt. Commun.* **130**, 75 (1996).

[150] W. Hodel, D. S. Peter, and H. P. Weber, *Opt. Commun.* **97**, 233 (1993).

[151] M. E. Fermann, A. Galvanauskas, and D. Harter, *Appl. Phys. Lett.* **64**, 1315 (1994).

Chapter 5

Fiber Lasers

A fiber amplifier can be converted into a laser by placing it inside a cavity designed to provide optical feedback. Such lasers are called *fiber lasers*, and this chapter is devoted to them. Section 5.1 covers general concepts such as pumping, cavity design, and laser threshold. The characteristics of continuous-wave (CW) fiber lasers are covered in Section 5.2. Sections 5.3 and 5.4 discuss active and passive mode-locking techniques used to generate short optical pulses from fiber lasers. The effects of fiber dispersion and nonlinearities on the mode-locking process are considered in Section 5.5, using the Ginzburg–Landau equation that represents generalization of the nonlinear Schrödinger (NLS) equation for doped fibers with gain.

5.1 Basic Concepts

Many different rare-earth ions, such as erbium, neodymium, and ytterbium, can be used to make fiber lasers capable of operating over a wide wavelength range extending from 0.4 to 4 μm. The first fiber laser, demonstrated in 1961, used a Nd-doped fiber with the 300-μm core diameter [1]. Low-loss silica fibers were used to make diode-laser-pumped fiber lasers in 1973 soon after such fibers became available [2]. Although there was some research activity in between [3], it was not until the late 1980s that fiber lasers were fully developed. The initial emphasis was on Nd- and Er-doped fiber lasers [4]–[17], but other dopants such as holmium, samarium, thulium, and ytterbium were also used [18]–[21]. Starting in 1989, the focus turned to the development of mode-locked, erbium-doped fiber lasers (EDFLs) since such lasers are capable

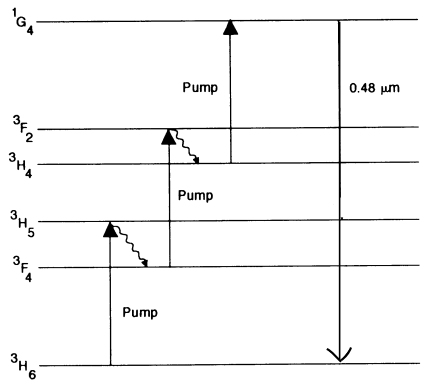

Figure 5.1 Pumping scheme for an up-conversion laser. Energy levels of Tm^{3+} ions are shown. Wavy arrows indicate rapid relaxation between the states. Three 1.06-μm pump photons are absorbed for each photon emitted at 0.48 μm.

of producing short optical pulses in the 1.55-μm spectral region and are useful for optical communications, ultrafast phenomena, and fiber-based sensors [30]–[33].

5.1.1 Pumping and Optical Gain

Pumping schemes for lasers can be classified as three- or four-level schemes [34]–[36]; both are shown in Fig. 4.1. A third kind of pumping scheme is also possible in lasers known as *up-conversion lasers* [37]–[43]. As an example, Fig. 5.1 shows pumping of an up-conversion Tm-doped laser. In this pumping scheme, two or more photons from the same pump laser (or from different lasers) are absorbed by the dopant such that it is raised to an excited state whose transition energy exceeds the energy of individual pump photons. As a result, the laser operates at a frequency higher than that of the pump laser, a phenomenon known as up-conversion in nonlinear optics. This kind of pumping has attracted attention since it can be used to make "blue" fiber lasers that are pumped with semiconductor lasers operating in the infrared region. In the example shown in Fig. 5.1, three 1.06-μm pump photons raise the Tm^{3+} ion to the excited state $^1G_4$. Blue light near 475 nm is emitted though the $^1G_4 \rightarrow {}^3H_5$ transition. Each level in Fig. 5.1 is actually an energy band because of host-induced broadening of the atomic transition.

Three- and four-level pumping schemes were discussed in Section 4.2 in

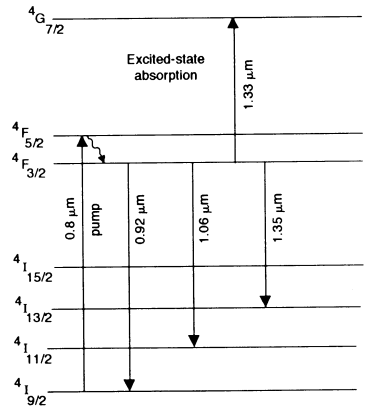

Figure 5.2 Pumping scheme for a four-level laser. Energy levels of Nd^{3+} ions are shown. An Nd-doped fiber laser can emit in three wavelength regions near 0.92, 1.06, and 1.35 μm with 0.8-μm pumping.

the context of fiber amplifiers. EDFLs use a three-level pumping scheme and can be pumped efficiently using semiconductor lasers operating at 0.98 or 1.48 μm. To illustrate the case of a four-level fiber laser, Fig. 5.2 shows the energy levels involved in the operation of Nd-doped fiber lasers. Such lasers can be pumped efficiently through the $^4I_{9/2} \rightarrow {}^4F_{5/2}$ transition by using 0.8-μm GaAs semiconductor lasers. They can be designed to operate in the spectral regions near 0.92, 1.06, and 1.35 μm. Pumping is most efficient for the 1.06-μm transition. Although the 1.35-μm transition can also be pumped using a four-level scheme, it suffers from the problem of excited-state absorption since the laser light can be absorbed by the transition $^4F_{3/2} \rightarrow {}^4G_{7/2}$. The first fiber laser in 1961 used the 1.06-μm transition [1]. Fiber lasers pumped using semiconductor lasers were built in 1973 [2]. Modern Nd-doped fiber lasers can generate CW power levels in excess of 10 W using arrays of semiconductor lasers for pumping.

5.1.2 Cavity Design

Fiber lasers can be designed with a variety of choices for the laser cavity [30]. The most common type of laser cavity is known as the *Fabry–Perot cavity*, which is made by placing the gain medium between two high-reflecting mirrors. In the case of fiber lasers, mirrors are often butt-coupled to the fiber ends to avoid diffraction losses. This approach was adopted in 1985 for a Nd-doped

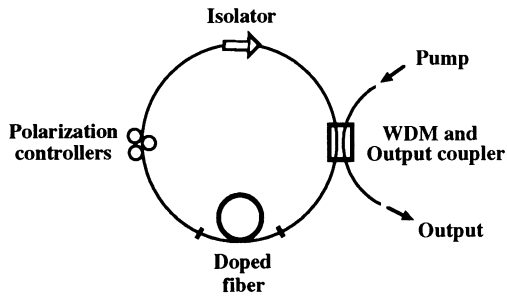

Figure 5.3 Schematic of a unidirectional ring cavity used for fiber lasers.

fiber [4]. The dielectric mirrors were highly reflective at the 1.088-μm laser wavelength but, at the same time, highly transmissive at the pump wavelength of 0.82 μm. Cavity losses were small enough that the laser reached threshold at a remarkably low pump power of 100 μW. Alignment of such a cavity is not easy since cavity losses increase rapidly with a tilt of the fiber end or the mirror, where tolerable tilts are less than 1°. This problem can be solved by depositing dielectric mirrors directly onto the polished ends of a doped fiber [8]. However, end-coated mirrors are quite sensitive to imperfections at the fiber tip. Furthermore, since pump light passes through the same mirrors, dielectric coatings can be easily damaged when high-power pump light is coupled into the fiber.

Several alternatives exist to avoid passing the pump light through dielectric mirrors. For example, one can take advantage of fiber couplers. It is possible to design a fiber coupler such that most of the pump power comes out of the port that is a part of the laser cavity. Such couplers are called *wavelength-division multiplexing* (WDM) couplers. Another solution is to use fiber gratings as mirrors [44]. As discussed in Chapter 1, a fiber Bragg grating can act as a high-reflectivity mirror for the laser wavelength while being transparent to pump radiation. The use of two such gratings results in an all-fiber Fabry–Perot cavity [45]. An added advantage of Bragg gratings is that the laser can be forced to operate in a single longitudinal mode. A third approach makes use of fiber-loop mirrors [46]. As discussed in Section 3.2, fiber-loop mirrors can be designed to reflect the laser light but transmit pump radiation.

Ring cavities are often used to realize unidirectional operation of a laser. In the case of fiber lasers, an additional advantage is that a ring cavity can be made without using mirrors, resulting in an all-fiber cavity. In the simplest

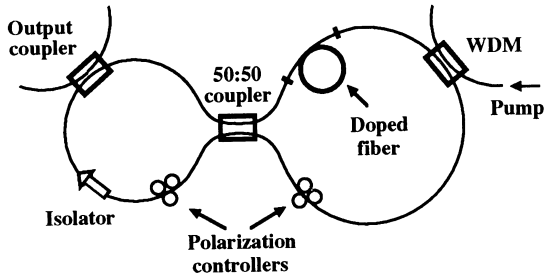

Figure 5.4 Schematic of a figure-8 cavity useful for mode-locked fiber lasers.

design, two ports of a WDM coupler are connected together to form a ring cavity containing the doped fiber, as shown in Fig. 5.3. An isolator is inserted within the loop for unidirectional operation. A polarization controller is also needed for conventional doped fiber that does not preserve polarization.

A ring cavity was used as early as 1985 for making an Nd-doped fiber laser [4]. Since then, several new designs have emerged. Figure 5.4 shows a specific design used for mode-locked fiber lasers. This configuration is referred to as the *figure-8 cavity* because of its appearance. The ring cavity on the right acts as a nonlinear amplifying-loop mirror, whose switching characteristics were discussed in Section 3.2. Indeed, the nonlinear effects play an important role in the operation of figure-8 lasers. At low powers, loop transmittivity is relatively small, resulting in relatively large cavity losses for CW operation. The Sagnac loop becomes fully transmissive for pulses whose peak power attains a critical value [see Eq. (3.2.8)]. For this reason, a figure-8 cavity favors mode locking. An isolator in the left cavity ensures unidirectional operation. The laser output is taken through a fiber coupler with low transmission ($< 10\%$) to minimize cavity losses. An interesting property of the figure-8 cavity is that it permits passive mode locking without a saturable absorber.

Many other cavity designs are possible. For example, one can use two coupled Fabry–Perot cavities. In the simplest scheme, one mirror is separated from the fiber end by a controlled amount. The 4% reflectivity of the fiber–air interface acts as a low-reflectivity mirror that couples the fiber cavity with the empty air-filled cavity. Such a compound resonator has been used to reduce the line width of an Er-doped fiber laser [23]. Three fiber gratings in series also produce two coupled Fabry–Perot cavities. Still another design makes use of a Fox–Smith resonator [47].

5.1.3 Laser Threshold and Output Power

The two most important parameters characterizing a laser are the threshold pump power and the efficiency with which the laser converts the pump power into laser power once it has reached threshold. Laser threshold is determined by requiring that the gain compensate total cavity losses during each round trip [34]–[36]. If we consider a Fabry–Perot cavity, formed by placing two mirrors of reflectivities R_1 and R_2 at the two ends of a fiber of length L, the threshold condition becomes

$$G^2 R_1 R_2 \exp(-2\alpha_{\text{int}} L) = 1, \tag{5.1.1}$$

where G is the single-pass amplification factor and α_{int} accounts for internal losses within the cavity.

The single-pass amplification factor should include the nonuniform nature of the gain coefficient and is obtained using

$$G = \exp\left[\int_0^L g(z)\,dz\right], \qquad g(z) = \sigma_s[N_2(z) - N_1(z)], \tag{5.1.2}$$

where σ_s is the transition cross section and N_1 and N_2 are the dopant densities in the two energy states participating in the stimulated-emission process. By substituting Eq. (5.1.2) in Eq. (5.1.1), the threshold condition becomes

$$\frac{1}{L}\int_0^L g(z)\,dz = \alpha_{\text{mir}} + \alpha_{\text{int}} \equiv \alpha_{\text{cav}}, \tag{5.1.3}$$

where $\alpha_{\text{mir}} = -\ln(R_1 R_2)/2L$ is the effective mirror loss and α_{cav} is the total cavity loss.

The population inversion $N_2 - N_1$ depends on the pumping strength. In general, it is obtained by using a set of three or four rate equations for the energy levels involved in the pumping process. It was calculated in Section 4.2.3 for a three-level laser, and a similar procedure can be followed for a four-level laser. In fact, the calculation is even simpler since $N_1 \approx 0$ and $N_2 \ll N_t$ for a four-level laser, where N_t is the total ion density. For this reason, Eq. (4.2.2) can be replaced with

$$\frac{\partial N_2}{\partial t} = W_p N_t - W_s N_2 - \frac{N_2}{T_1}, \tag{5.1.4}$$

where the transition rates W_p and W_s are given in Eq. (4.2.3). The steady-state solution of Eq. (5.1.4) is given by

$$N_2 = \frac{(P_p/P_p^{\text{sat}})N_t}{1 + P_s/P_s^{\text{sat}}}, \tag{5.1.5}$$

where the saturation powers P_p^{sat} and P_s^{sat} are defined as in Eq. (4.2.5).

The z dependence of N_2 stems from variations in the pump and signal powers along the cavity length. Below or near laser threshold, gain saturation can be neglected since $P_s/P_s^{\text{sat}} \ll 1$. Using the exponential decrease in the pump power through $P_p(z) = P_p(0)\exp(-\alpha_p z)$, where α_p accounts for pump losses, the integral in Eq. (5.1.3) is easily performed. The pump power needed to reach threshold is thus given by

$$P_p(0) = \frac{\alpha_{\text{cav}} L}{1-\exp(-\alpha_p L)} \left(\frac{\alpha_p}{\alpha_s}\right) P_p^{\text{sat}}, \tag{5.1.6}$$

where $\alpha_p = \sigma_p N_t$ and $\alpha_s = \sigma_s N_t$ are the absorption coefficients at the pump and signal wavelengths, respectively. This expression shows how the laser threshold depends on the cavity length. It is common to write the threshold power in terms of the absorbed pump power using

$$P_{\text{abs}} = P_p(0)[1-\exp(-\alpha_p L)]. \tag{5.1.7}$$

From Eqs. (5.1.6) and (5.1.7), the threshold power P_{th} is given by

$$P_{\text{th}} = \alpha_{\text{cav}} L(\alpha_p/\alpha_s) P_p^{\text{sat}} \equiv \alpha_{\text{cav}} L(a_p h\nu_p/\Gamma_s \sigma_s T_1), \tag{5.1.8}$$

where P_p^{sat} was obtained from Eq. (4.2.5). This equation shows how laser threshold depends on parameters associated with the gain medium (dopants) and the laser cavity.

The output power can also be obtained from the threshold condition (5.1.3) since the saturated gain remains clamped to its threshold value once the pump power exceeds the threshold. By using Eqs. (5.1.2) and (5.1.5) in Eq. (5.1.3), we obtain

$$\frac{\alpha_s}{L}\int_0^L \frac{P_p/P_p^{\text{sat}}}{1+P_s/P_s^{\text{sat}}}\,dz = \alpha_{\text{cav}}. \tag{5.1.9}$$

The integral is difficult to evaluate analytically since the intracavity laser power P_s varies with z along the fiber. However, in most cases of practical interest, mirror reflectivities are large enough that P_s can be treated approximately as constant. The integral then reduces to that evaluated earlier, and P_s is given by the remarkably simple expression

$$P_s = P_s^{\text{sat}}(P_{\text{abs}}/P_{\text{th}} - 1), \tag{5.1.10}$$

where P_{abs} is the absorbed pump power.

A fraction of the intracavity power P_s is transmitted from each mirror as the output power. The output from the mirror of reflectivity R_1 (or from a port of the output fiber coupler in the case of a ring cavity) can be written as

$$P_{\text{out}} = (1 - R_1)P_s = \eta_s(P_{\text{abs}} - P_{\text{th}}). \tag{5.1.11}$$

This equation shows that the laser power increases linearly with the absorbed pump power. The slope efficiency, defined as the ratio $dP_{\text{out}}/dP_{\text{abs}}$, is given by

$$\eta_s = \left(\frac{1 - R_1}{\alpha_{\text{cav}} L}\right)\left(\frac{a_s h\nu_s}{a_p h\nu_p}\right). \tag{5.1.12}$$

The slope efficiency is a measure of the efficiency with which the laser converts pump power into output power once it has reached threshold. It can be maximized by reducing cavity losses as much as possible. Typical values of η_s are around 10% although values as high as 50% are possible in some fiber lasers.

5.2 CW Fiber Lasers

Fiber lasers can be used to generate CW radiation as well as ultrashort optical pulses. This section focuses on the CW operation. The nonlinear effects associated with the host fiber play a relatively small role in the case of CW operation until power levels exceed several watts.

5.2.1 Nd-Doped Fiber Lasers

Nd-doped fiber lasers are of considerable practical interest as they can be pumped using GaAs semiconductor lasers operating near 0.8 μm [30]. Such a laser was first demonstrated in 1973 using a silica fiber whose core was codoped with alumina [2]. The graded-index fiber had a core diameter of 35 μm. A Fabry–Perot cavity was made by coating polished ends of an 1-cm-long fiber with dielectric mirrors having high reflectivity ($> 99.5\%$ at the laser wavelength of 1.06 μm). The laser reached threshold at 0.6 mW of pump power; the absorbed pump power was estimated to be only 0.2 mW.

Single-mode silica fibers were first used in 1985 for making Nd-doped fiber lasers [4]. The 2-m-long fiber had Nd^{3+} concentration of about 300 ppm (parts per million). The laser cavity was made by butt-coupling the cleaved

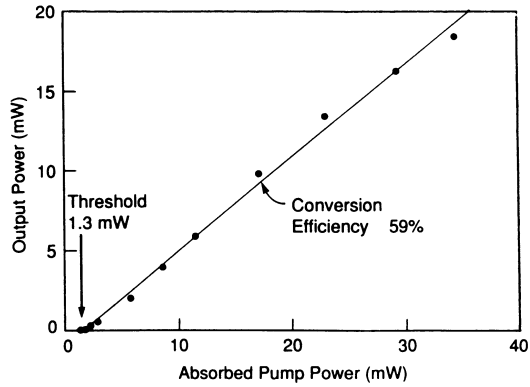

Figure 5.5 Output power as a function of absorbed pump power for an Nd-doped fiber laser. (After Ref. [12], ©1988 IEE)

fiber ends against dielectric mirrors having $> 99.5\%$ reflectivity at the 1.088-μm laser wavelength and $> 80\%$ transmission at the 0.82-μm pump wavelength. Laser threshold was reached at an absorbed pump power of only 0.1 mW. The output power was relatively low. In a later experiment, an Nd-doped fiber laser pumped with a 0.82-μm dye laser [12]. Figure 5.5 shows the output power as a function of the absorbed pump power for this laser. Ring cavities have also been used for Nd-doped fiber lasers. As early as 1985, a 2.2-m ring-cavity laser produced 2 mW of output power in each direction at an absorbed pump power of 20 mW when pumped using a 595-nm dye laser [4].

Much higher power levels have been realized using double-clad fibers [48]–[52]. In such fibers, the doped core is surrounded by an inner cladding that is used to guide the pump light. The large size and a large numerical aperture of the inner cladding permit efficient coupling of the pump power using GaAs laser-diode bars capable of emitting high powers (> 10 W) near 800 nm. Since pump light is guided by the inner cladding, the laser is pumped all along the length of the doped fiber (side pumping in place of the commonly used end pumping). In a 1995 experiment, a double-clad Nd-doped fiber laser emitted 9.2 W of CW power in the form of a high-quality beam when 35 W of pump power was launched into the inner cladding of 400-μm diameter [52]. The 12-μm-diameter core of the double-clad fiber was doped with 1300 ppm of Nd ions. Power levels in excess of 10 W are possible using the double-clad geometry, although the nonlinear effects become increasingly more important and limit the beam quality.

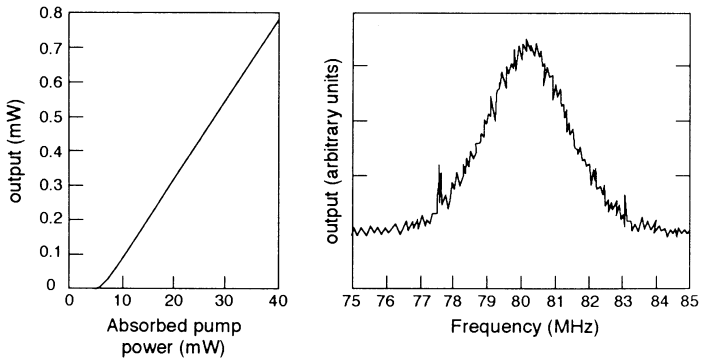

Figure 5.6 (a) Output power versus absorbed pump power and (b) measured spectral line shape for an Nd-doped fiber laser forced to oscillate in a single longitudinal mode through an internal Bragg grating. (After Ref. [11], ©1988 IEE)

Fiber lasers normally operate in multiple longitudinal modes because of a large gain bandwidth (> 30 nm) and a relatively small longitudinal-mode spacing (< 100 MHz). The spectral bandwidth of laser output can exceed 10 nm under CW operation [12]. The large gain bandwidth is a boon for generating ultrashort pulses. However, many applications of CW lasers require operation in a narrow-linewidth single mode whose wavelength can be tuned over the gain bandwidth. Several methods have been used to realize narrow-linewidth fiber lasers [53]. An intracavity étalon, commonly used for solid-state lasers, can be used for fiber lasers as well. However, fiber Bragg gratings are preferred for this purpose since they can be fabricated with a reflectivity spectrum of less than 0.1 nm. A 1986 experiment used such a grating to realize narrowband operation (about 16 GHz bandwidth) of a Nd-doped fiber laser [6]. The laser provided output powers in excess of 1.5 mW at 10 mW of input pump power. This laser did not operate in a single longitudinal mode because a relatively small mode spacing. In a later experiment, single-longitudinal-mode operation was achieved by using a fiber length of only 5 cm [11]. The Nd^{3+} concentration was relatively high to ensure pump absorption over such a short length. Figure 5.6 shows the output power as a function of absorbed pump power together with the observed spectral line shape measured through a self-heterodyne technique. The spectral line width was only 1.3 MHz for this laser.

The large gain bandwidth of fiber lasers is useful for tuning them over a wavelength range exceeding 50 nm [53]. The simplest scheme for tuning

replaces one mirror of the Fabry–Perot cavity by a dispersive grating. An Nd-doped fiber laser was tuned in 1986 over the range of 1.07 to 1.14 μm by this technique [5]. An intracavity birefringent filter can also be used for tuning [7]. However, both of these techniques make use of bulky optical components. A remarkably simple technique uses a ring cavity with a fiber coupler whose coupling efficiency can be varied mechanically (see Fig. 5.3). Such lasers are tuned by varying the wavelength at which reflectivity of the fiber coupler is maximum since the cavity loss becomes minimum for that wavelength. In a 1989 experiment, an Nd-doped fiber laser could be tuned over 60 nm by this technique [54].

Nd-doped fiber lasers can also operate in the wavelength regions near 0.92 and 1.35 μm. Operation at 0.92 μm requires higher pump powers because of the three-level nature of the laser transition involved. It is necessary to use cavity mirrors with a high reflectivity near 0.92 μm but a low reflectivity near 1.06 μm so that cavity losses are high for the latter transition. In a 1986 experiment, such an Nd-doped fiber laser was tuned over 45 nm by using a birefringent filter as a tuning device [7]. It is difficult to operate Nd-doped silica fiber lasers at the 1.35-μm transition because of excited-state absorption (see Fig. 5.2). With a proper design, such lasers can be made to operate at wavelengths > 1.36 μm since excited-state absorption is less important for such wavelengths [55]. Shorter wavelengths (< 1.35 μm) can be obtained by Nd-doping of fluorozirconate fibers. In one experiment, the laser operated near 1.33 μm when the cavity mirrors were selected to defavor the 1.06-μm transition [11].

5.2.2 Erbium-Doped Fiber Lasers

EDFLs can operate in several wavelength regions, ranging from visible to far infrared. The 1.55-μm region has attracted the most attention because it coincides with the low-loss region of silica fibers used for optical communications. At first sight, 1.55-μm EDFLs do not appear very promising because the transition ${}^4I_{13/2} \rightarrow {}^4I_{15/2}$ terminates in the ground state of the Er^{3+} ion. Since a three-level laser requires that at least half of the ion population be raised to the excited state, it has a high threshold. Indeed, early attempts to make EDFLs used high-power argon-ion lasers as a pump source [5]. The threshold pump powers were ~ 100 mW with slope efficiencies $\sim 1\%$. In one experiment, the slope efficiency was improved to 10%, but the laser reached threshold at 44 mW [23].

EDFLs pumped near 0.8-μm using GaAs semiconductor lasers suffer from the problem of excited-state absorption. The situation improves in silica fibers sensitized with ytterbium [14]–[16]. The core of such fibers is codoped with Yb_2O_3 such that the ratio of Yb^{3+} to Er^{3+} concentrations is more than 20. Such EDFLs can be pumped using 0.8-μm semiconductor lasers or miniature 1.06-μm Nd:YAG lasers. The improved performance of Yb-sensitized EDFLs is due to the near coincidence of the $^2F_{5/2}$ state of Yb^{3+} ions with the $^4I_{11/2}$ state of Er^{3+} ions. The excited state of Yb^{3+} is broad enough that it can be pumped in the range from 0.85 to 1.06 μm. In one Er:Yb fiber laser, pumped using a 0.82-μm semiconductor laser, the threshold pump power was 5 mW with a slope efficiency of 8.5% [14].

The performance of EDFLs improves considerably when they are pumped at the 0.98 or 1.48 μm wavelength because of the absence of excited-state absorption. Indeed, semiconductor lasers operating at these wavelengths have been developed solely for the purpose of pumping Er-doped fibers. Their use has resulted in commercial 1.55-μm fiber lasers. As early as 1989, a 0.98-μm-pumped EDFL exhibited a slope efficiency of 58% against absorbed pump power [26], a figure that is close to the quantum limit of 63% obtained by taking the ratio of signal to pump photon energies. EDFLs pumped at 1.48 μm also exhibit good performance. In fact, the choice between 0.98 and 1.48 μm is not always clear since each pumping wavelength has its own merits. Both have been used for developing practical EDFLs with excellent performance characteristics [56]–[68].

An important property of continuously operating EDFLs from a practical standpoint is their ability to provide output that is tunable over a wide range. Similar to the case of Nd-doped fiber lasers, many techniques can be used to reduce the spectral bandwidth of tunable EDFLs [53]. In a 1989 experiment [23], an intracavity étalon formed between a bare fiber end and the output mirror led to a 620-MHz line width even though the fiber was 13 m long. The laser wavelength can also be tuned by using an external grating in combination with an étalon. Figure 5.7 shows the experimental setup together with the tuning curves obtained for two different fiber lengths. This laser was tunable over a 70-nm range [29]. The output power was more than 250 mW in the wavelength range from 1.52 to 1.57 μm.

Ring cavities can also be used to make tunable EDFLs [57]–[67]. A common technique uses a fiber intracavity étalon that can be tuned electrically [60]. Such EDFLs have shown low threshold (absorbed pump power of 2.9 mW)

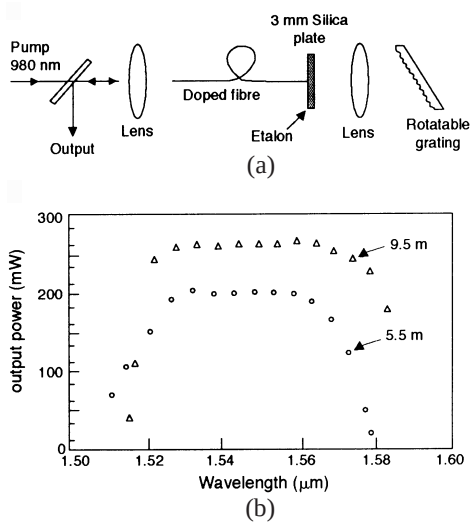

Figure 5.7 (a) Experimental setup for a broadly tunable EDFL. (b) Tuning curves for two different fiber lengths at 540 mW of launched power. (After Ref. [29], ©IEE)

with 15% slope efficiency [61]. They can be tuned over 60 nm. They can also be designed to provide a line width as small as 1.4 kHz [58]. In an optimized EDFL, 15.6-mW of output power was obtained with 48% slope efficiency (68% with respect to absorbed pump power) while the tuning range (at the 3-dB point) was 42 nm [67].

Many other tuning techniques have been used for fiber lasers. In one experiment, a fiber laser was tuned over 33 nm through strain-induced birefringence [66]. In another, a fiber laser could be tuned over 39 nm by using a reflection Mach–Zehnder interferometer that acts as a wavelength-selective loss element within the ring-laser cavity [68]. The wavelength for which cavity losses are minimum is changed by controlling the optical path length in one of the interferometer arms either electro-optically or by applying stress.

Fiber gratings can also be used to improve the performance of EDFLs [33]. As early as 1990, a Bragg grating was used to realize a line width of about 1 GHz [44]. Since then, fiber gratings have been used in EDFAs for a variety of reasons [69]–[82]. The simplest configuration splices a Bragg grating at each end of an erbium-doped fiber, forming a Fabry–Perot cavity. Such devices are called *distributed Bragg reflector* (DBR) lasers, following the terminology used for semiconductor lasers [83]. DBR fiber lasers can be tuned continuously

while exhibiting a narrow line width [70]. They can also be made to oscillate in a single longitudinal mode by decreasing the fiber length. In a novel scheme, an EDFL was made to oscillate at two distinct wavelengths, with a narrow line width at each wavelength, by fabricating two different gratings or by using a single grating with dual-peak reflectivity [72].

Multiple fiber gratings can be used to make coupled-cavity fiber lasers. Such lasers have operated at two different wavelengths (0.5 nm apart) simultaneously such that each spectral line was stable to within 3 MHz and had a line width of only 16 kHz [73]. Fiber gratings have been used to make efficient, low-noise EDFLs. In one such laser, up to 7.6 mW of output power was obtained without self-pulsation while the relative intensity-noise level was below -145 dB/Hz at frequencies above 10 MHz [74]. Even higher powers can be obtained by using the master oscillator/power amplifier (MOPA) configuration in which a fiber laser acting as a master oscillator is coupled to a fiber amplifier through an intracore Bragg grating. Output powers of up to 62 mW have been obtained by using such a configuration through active feedback while maintaining intensity-noise levels below -110 dB/Hz at all frequencies [75].

Another approach consists of making a distributed-feedback (DFB) fiber laser. In analogy with DFB semiconductor lasers [83], a Bragg grating is formed directly into the erbium-doped fiber that provides gain [77]. Phase-shifted DFB lasers have also been made by leaving a small region of the doped fiber in the middle without a grating [78]. Multiple gratings with slightly different Bragg wavelengths can also be formed into the same doped fiber, resulting in several DFB lasers cascaded together.

Multiwavelength optical sources, capable of emitting light at several well-defined wavelengths simultaneously, are useful for WDM lightwave systems. Fiber lasers can be used for this purpose, and several schemes have been developed [84]–[91]. A dual-frequency fiber laser was demonstrated in 1993 by using a coupled-cavity configuration [72]. Since then, simultaneous operation of a fiber laser at up to 29 wavelengths has been realized by cooling the doped fiber to 77 K using liquid nitrogen [89]. The cavity length is made quite small ($\sim$ 1 mm or so) since spacing between the lasing wavelengths is governed by the longitudinal-mode spacing. A 1-mm cavity length corresponds to a 100-GHz wavelength spacing. Such fiber lasers operate as standard multimode lasers. Cooling of the doped fiber helps to reduce the homogeneous broadening of the gain spectrum to below 0.5 nm. The gain spectrum is then predominantly inhomogeneously broadened, resulting in multimode operation

through spectral hole burning [34]. Long cavities with several meters of doped fibers can also be used. Wavelength selection is then made using an intracavity comb filter such as a Fabry–Perot interferometer [84]. In a dual-filter approach, a tunable comb filter in combination with a set of fiber gratings provides a multiwavelength source that is switchable on a microsecond timescale to precise preselected wavelengths [90].

5.2.3 Other Fiber Lasers

Many other rare-earth ions can be used to make fiber lasers. Holmium, samarium, thulium, and ytterbium were used in 1988 nearly simultaneous experiments [18]–[21] to make fiber lasers emitting at wavelengths ranging from visible to infrared. Attention later shifted to Pr^{3+} ions in an attempt to realize fiber lasers and amplifiers operating at 1.3 μm [92]–[95]. Pr-doped fiber lasers can also operate at 1.05-μm. A tuning range of 86 nm was realized in an experiment in which the laser was pumped at 592 nm by using a dye laser [96]. Pr-doped fiber lasers can also be operated in the visible region using an up-conversion pumping scheme [97].

Thulium-doped fiber lasers have attracted considerable attention because of their potential applications [98]–[100]. They can be operated either in the blue region of the optical spectrum through an up-conversion pumping scheme (see Fig. 5.1) or at the $^3F_4 \rightarrow {}^3H_6$ transition that allows tuning over a range extending from 1.71 to 2.1 μm. A diode-pumped blue fiber laser is useful for several applications. By 1997, 230 mW of blue light at 481 nm was obtained by pumping a Tm-doped fiber laser with a diode-pumped Nd:YAG laser [99].

Operation at several other important wavelengths can be realized by using fluoride fibers as a host in place of silica fibers. The $^3H_5 \rightarrow {}^3H_4$ transition provides emission in the 2.25- to 2.4-μm wavelength range, which is useful for sensing hydrocarbon gases [100]. The $^3F_4 \rightarrow {}^3H_4$ transition can provide tunable lasers in the 1.45- to 1.51-μm wavelength range, which is useful for pumping EDFAs and Raman amplifiers. Output powers of 1 W have been obtained at this transition by pumping at 1.06 μm from a compact Nd:YAG laser [101]. Laser threshold and slope efficiency were respectively 175 mW and 29%, and the laser could be tuned from 1.445 to 1.51 μm.

Holmium-doped fiber lasers have attracted attention because they operate near 2 μm, a wavelength useful for medical and other eye-safe applications. Such lasers were first made in 1988 using fluoride fibers [18]. Thulium-codoping permits these lasers to be pumped with GaAs lasers operating near

0.8 μm [102]. By 1994, Ho-doped fiber lasers, made by using silica fibers and pumped near 0.8 μm, provided output powers of about 10 mW while being tunable over the wavelength range from 2.037 to 2.096 μm [103].

Ytterbium-doped fiber lasers, operating near 1.01 μm and tunable over 60 nm, were first made in 1988 [21]. In 1992, the use of fluoride fibers as the host medium provided output powers of up to 100 mW [104]. In a later experiment, more than 200-mW power with a quantum efficiency of 80% was obtained from a silica-based Yb-doped fiber laser pumped at 869 nm [105]. Two intracavity Bragg gratings, fabricated directly onto the doped fiber with reflectivities of 65% and 99%, formed the 7-m-long Fabry–Perot cavity of the fiber laser. Power levels as high as 110 W have been realized from Yb-doped fiber lasers by using double-clad fibers. In the 1999 demonstration of this technique, the inner cladding of the Yb-doped fiber had a rectangular cross section [106]. Four diode-laser bars, each emitting 45 W of power near the 915-nm wavelength, were used for pumping the fiber laser. The laser emitted up to 110 W of CW radiation at a wavelength near 1.12 μm, with an optical conversion efficiency of 58.3%. In another approach to high-power levels, the output of a low-power Yb-doped fiber laser (master oscillator) is amplified using a power amplifier (the MOPA configuration). Power levels of several watts have been obtained using a single amplifier [107], [108]. This scheme has the potential for realizing ultrahigh power levels by using an array of fiber amplifiers seeded by a single master oscillator.

5.2.4 Self-Pulsing and Chaos

Some fiber lasers emit a train of optical pulses even when pumped continuously. This phenomenon is referred to as *self-pulsing* and is a specific example of laser instabilities that occur in many kinds of lasers [109]. Its occurrence requires a nonlinear mechanism within the laser cavity. Self-pulsing in EDFLs has been observed, and its origin is attributed to two different nonlinear mechanisms [110]–[113]. In one study, ion–ion interactions in erbium clusters were found to produce self-pulsing [111]. Another model shows that self-pulsing can result from destabilization of relaxation oscillations [112], the same mechanism that leads to self-pulsing in semiconductor lasers [109]. This origin of self-pulsing was confirmed in an experiment in which the Er-doped fiber was codoped with alumina to minimize production of erbium-ion clusters within the silica core [113]. In fact, the repetition rate of pulses agreed quite well with relaxation-oscillation frequency. A rate-equation model, generalized to

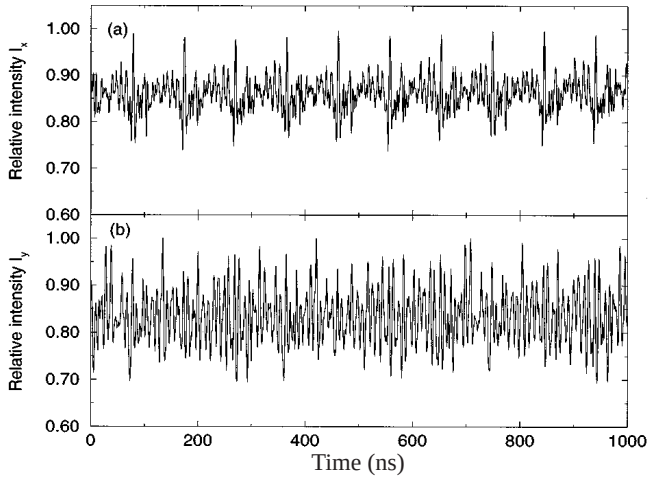

Figure 5.8 Chaotic power fluctuations for the two polarization components observed experimentally at the output of an EDFL. (After Ref. [118], ©1997 by the American Physical Society)

include the excited-state absorption of pump radiation, reproduced most of the features of self-pulsing observed experimentally.

It is well known that self-pulsing often leads to optical chaos in the laser output, following a period-doubling or a quasi-periodic route [109]. Chaotic behavior in fiber lasers has been observed and attributed to several different nonlinear mechanisms [114]–[120]. Since fiber lasers constitute an example of class-B lasers, the single-mode rate equations do not predict chaos [109]. However, chaos can be induced through pump modulation, optical feedback, or external injection [116]. In the case of fiber lasers, chaos can also occur because of nonlinear coupling between the orthogonally polarized components of the optical field. In an interesting set of experiments, chaos in an EDFL originated from the nonlinear polarization dynamics occurring on a timescale shorter than the round-trip time inside the laser cavity [118]. The two polarization components inside the laser cavity were coupled nonlinearly through cross saturation and gain sharing. A polarization controller inside the cavity acted as a half-wave plate and introduced additional coupling. Figure 5.8 shows an example of chaotic power fluctuations occurring for the two polarization components. Depending on the pumping and loss levels, a variety of chaotic patterns were observed experimentally. The experimental data can be

modeled quite well using a stochastic delay difference model.

In general, the outputs of two chaotic fiber lasers are not synchronized. This feature can be used for transmitting data in a secure manner if the signal is generated by modulating the output of a chaotic laser. Several experiments have used chaotic fiber lasers to demonstrate the possibility of secure optical communications [121]–[124]. In one set of experiments, the signal is enclosed on the chaotic waveform by injecting it into the EDFA [121]. The laser output is then transmitted through a fiber link (as long as 35 km). At the receiver end, a part of the chaotic signal is injected into another EDFL, designed to be nearly identical to the one at the transmitter, for chaos synchronization. The data can be recovered from the remaining received signal because of this synchronization. Signal recovery at a bit rate of up to 250 Mb/s was demonstrated in the 1999 experiment [123]. The bit rate can be extended to beyond 1 Gb/s [124].

5.3 Short-Pulse Fiber Lasers

Two techniques used for generating short optical pulses from lasers are known as *Q-switching* and *mode locking* [34]–[36]. An intracavity acousto-optic modulator was used as early as 1986 to obtain Q-switched optical pulses from fiber lasers [5]. Q-switching remains a useful technique for fiber lasers since it can generate high peak-power (> 1 kW) pulses whose wavelengths are tunable over a wide range covering the entire gain spectrum [125]–[133]. In a 1999 experiment, Q-switched pulses from a double-clad Yb-fiber laser could be tuned from 1060 to 1100 nm while maintaining peak powers as large as 2 kW [131]. In another experiment, a Fabry–Perot étalon, with a free spectral range of 0.535 nm and a finesse of 76, allowed emission of Q-switched pulses from an EDFL at more than 90 distinct wavelengths simultaneously [132]. Pulse energies as high as 2.3 mJ have been generated at a repetition rate of 500 Hz from a cladding-pumped Yb-doped fiber laser [133].

Q-switching produces relatively broad optical pulses (~ 100 ns). In contrast, mode locking can generate pulses shorter than 100 fs. Early experiments on Nd-doped fiber lasers produced pulses of $>$ 1-ns duration [7]. Pulse widths of 120 ps were obtained by 1988 using a laser-diode array for pumping [17]. Starting in 1989, attention focused on the development of mode-locked EDFLs because of their potential applications in lightwave systems [134]–[138]. In this section we focus on actively mode-locked fiber lasers; passive mode locking is discussed in the next section.

5.3.1 Physics of Mode Locking

Fiber lasers operate simultaneously in a large number of longitudinal modes falling within the gain bandwidth. The frequency spacing among the modes is given by $\Delta\nu = c/L_{\text{opt}}$, where L_{opt} is the optical length during one round trip inside the cavity. Multimode operation is due to a wide gain bandwidth compared with a relatively small mode spacing of fiber lasers ($\Delta\nu \sim 10$ MHz). The total optical field can be written as

$$E(t) = \sum_{m=-M}^{M} E_m \exp(i\phi_m - i\omega_m t), \tag{5.3.1}$$

where E_m, ϕ_m, and ω_m are the amplitude, phase, and frequency of a specific mode among $2M+1$ modes. If all modes operate independently of each other with no definite phase relationship among them, the interference terms in the total intensity $|E(t)|^2$ averages out to zero. This is the situation in multimode CW lasers.

Mode locking occurs when phases of various longitudinal modes are synchronized such that the phase difference between any two neighboring modes is locked to a constant value ϕ such that $\phi_m - \phi_{m-1} = \phi$. Such a phase relationship implies that $\phi_m = m\phi + \phi_0$. The mode frequency ω_m can be written as $\omega_m = \omega_0 + 2m\pi\Delta\nu$. If we use these relations in Eq. (5.3.1) and assume for simplicity that all modes have the same amplitude E_0, the sum can be performed analytically. The result is given by [36]

$$|E(t)|^2 = \frac{\sin^2[(2M+1)\pi\Delta\nu t + \phi/2]}{\sin^2(\pi\Delta\nu t + \phi/2)} E_0^2. \tag{5.3.2}$$

The total intensity $|E(t)|^2$ is shown in Fig. 5.9 for nine coupled modes ($M = 4$). It is a periodic function of time with period $\tau_r = 1/\Delta\nu$, which is just the round-trip time inside the laser cavity. The laser output is in the form of a pulse train whose individual pulses are spaced by τ_r. A simple way to interpret this result is that a single pulse circulates inside the laser cavity and a fraction of its energy is emitted by the laser each time the pulse arrives at the output coupler.

The pulse width is estimated from Eq. (5.3.2) to be $\tau_p = [(2M+1)\Delta\nu]^{-1}$. Since $(2M+1)\Delta\nu$ represents the total bandwidth of all phase-locked modes, the pulse width is inversely related to the spectral bandwidth over which phases of various longitudinal modes can be synchronized. The exact relationship between the pulse width and the gain bandwidth $\Delta\nu_g$ depends on the nature of gain broadening (homogeneous versus inhomogeneous).

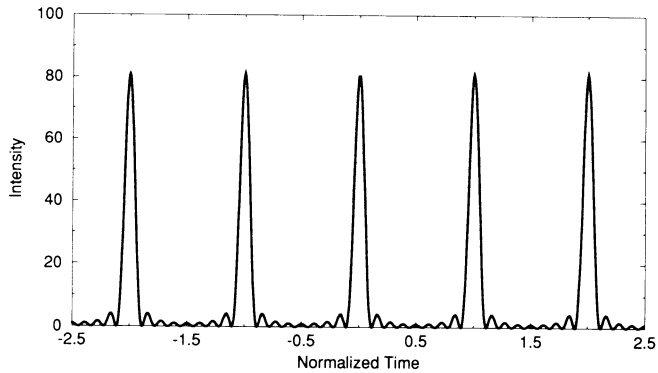

Figure 5.9 Pulse train formed when nine modes of equal amplitudes are mode locked.

5.3.2 Active Mode Locking

Active mode locking requires modulation of either the amplitude or the phase of the intracavity optical field at a frequency f_m equal to (or a multiple of) the mode spacing $\Delta\nu$. It is referred to as AM (amplitude modulation) or FM (frequency modulation) mode locking depending on whether amplitude or phase is modulated. One can understand the locking process as follows. Both the AM and FM techniques generate modulation sidebands, spaced apart by the modulation frequency f_m. These sidebands overlap with the neighboring modes when $f_m \approx \Delta\nu$. Such an overlap leads to phase synchronization. The mode-locking process can be modeled by using a set of multimode rate equations in which the amplitude of each mode is coupled to its nearest neighbors [34].

One can also understand the process of pulse formation in the time domain. Figure 5.10 shows the case of AM mode locking in which cavity losses are modulated at the frequency $\Delta\nu$. Since the laser generates more light at the loss minima, the intracavity field is modulated at the same frequency. This slight intensity difference builds up on successive round trips, and the laser emits a train of mode-locked pulses in the steady state. Stated another way, the laser threshold is lower for pulsed operation. As a result, the laser emits a train of pulses in place of the CW output.

The time-domain theory of mode locking considers the evolution of a mode-locked pulse over one round trip inside the laser cavity [139]–[141]. As usual, even though the pulse amplitude $A(z,t)$ is modified by the gain medium and the modulator, it should recover its original value after one round trip

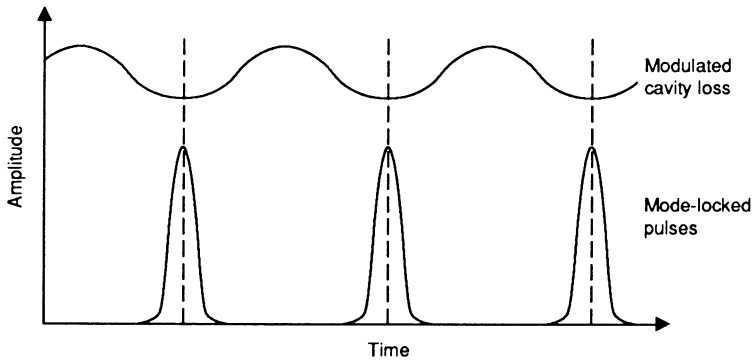

Figure 5.10 Schematic illustration of active AM mode locking through modulation of cavity losses.

under steady-state conditions. We can adapt the Ginzburg–Landau equation, derived in Section 4.3 for fiber amplifiers, to the case of fiber lasers by adding the losses introduced by the amplitude modulator and cavity mirrors. This requires replacing the loss parameter α in Eq. (4.3.17) with

$$\alpha = \alpha_c + \alpha_M[1 - \cos(\omega_M t)], \tag{5.3.3}$$

where α_c accounts for all cavity losses and α_M is the additional loss, periodic at the frequency ω_M, introduced by the modulator. In the context of fiber lasers, Eq. (4.3.17) becomes

$$\frac{\partial A}{\partial z} + \frac{i}{2}(\beta_2 + ig_c T_2^2)\frac{\partial^2 A}{\partial t^2} = i\left(\gamma + \frac{i}{2}\alpha_2\right)|A|^2 A + \frac{1}{2}(g_c - \alpha)A, \tag{5.3.4}$$

where g_c is the saturated gain averaged over the cavity length L. The parameter T_2 is related inversely to the gain bandwidth as $T_2 = 1/\Omega_g$. This equation is sometimes called the *master equation of mode locking* [141].

Consider first the case in which the effects of group-velocity dispersion (GVD) and self-phase modulation (SPM) can be ignored by setting $\beta_2 = 0$ and $\gamma = 0$ in Eq. (5.3.4). Two-photon absorption can also be neglected ($\alpha_2 = 0$). If we use $\cos(\omega_M t) \approx 1 - \frac{1}{2}(\omega_M t)^2$ in Eq. (5.3.3), assuming that the pulse width is much shorter than a modulation cycle, Eq. (5.3.4) takes the form

$$\frac{\partial A}{\partial z} = \frac{g_c}{2}\left(A + \Omega_g^{-2}\frac{\partial^2 A}{\partial t^2}\right) - \frac{1}{2}\left(\alpha_c + \frac{1}{2}\alpha_M \omega_M^2 t^2\right)A. \tag{5.3.5}$$

In the steady state, we look for solutions of the form $A(z,t) = B(t)\exp(iKz)$, where $B(t)$ governs the pulse shape that does not change from one round trip to next. The resulting ordinary differential equation for $B(t)$ is identical to that of a harmonic oscillator and has the following solution in terms of the Hermite–Gauss functions [141]:

$$B_n(t) = C_n H_n(t/T_0)\exp[-\tfrac{1}{2}(t/T_0)^2], \tag{5.3.6}$$

where $n = 0, 1, 2, \ldots$, H_n is the Hermite polynomial of order n,

$$T_0 = [2g_c/(\alpha_M \Omega_g^2 \omega_M^2)]^{1/4} \tag{5.3.7}$$

is a measure of the width of mode-locked pulses, and C_n is a normalization constant related to the pulse energy. The propagation constant K depends on various laser parameters as

$$iK = g_c - \alpha_c - \alpha_M \omega_M^2 T_0^2 (n + \tfrac{1}{2}). \tag{5.3.8}$$

In the steady state, K should be real. Equation (5.3.8) provides the saturated gain needed for various Hermite–Gauss temporal modes supported by the laser. Since the lowest gain occurs for $n = 0$, an actively mode-locked laser emits a Gaussian pulse with a full width at half maximum (FWHM) $T_p \approx 1.665 T_0$. The pulse width depends on both the gain bandwidth Ω_g and the modulator frequency $\omega_M = 2\pi\Delta\nu$, where $\Delta\nu$ is the longitudinal-mode spacing.

The situation changes considerably when the effects GVD and SPM are included in Eq. (5.3.4). In the absence of gain and losses, this equation reduces to the NLS equation and has the soliton solutions discussed in Chapter A.5. The solution corresponding to a fundamental soliton is given by

$$A(z,t) = \sqrt{P_0}\,\mathrm{sech}(t/T_s)\exp(iz/2L_D), \tag{5.3.9}$$

where the peak power P_0 and the width T_0 are related by the usual soliton condition

$$N = \gamma P_0 T_0^2/|\beta_2| = 1, \tag{5.3.10}$$

where N is the soliton order.

The important question is how the soliton solution is affected by the gain and losses inside the laser cavity. If the pulse formation is dominated by the GVD and SPM effects, one should expect the mode-locked pulse to behave as a fundamental soliton and have the "sech" shape in place of the Gaussian

shape predicted above in the absence of GVD and SPM. Soliton perturbation theory has been used to find the width of the steady-state soliton pulse. The results show that the mode-locked pulse is shorter than that predicted by Eq. (5.3.6) when soliton effects are significant. The maximum possible reduction factor is limited by [142]

$$(T_0/T_s)^2 < \tfrac{1}{2}\left(3d_g + \sqrt{9d_g^2 - \pi^2}\right), \quad d_g = \mathrm{Re}\left(\sqrt{1 + i|\beta_2|\Omega_g^2/g_c}\right). \quad (5.3.11)$$

In general, pulses become shorter as the amount of anomalous GVD increases; reduction by a factor of 2 occurs when $|\beta_2| = 5g_c/\Omega_g^2$. Note also that a minimum amount of GVD is required for solitons to form since d_g should exceed $\pi/3$.

5.3.3 Harmonic Mode Locking

The most common technique for active mode locking of fiber lasers makes use of an amplitude or phase modulator. Both acousto-optic and electro-optic modulators have been used for this purpose. However, most bulk modulators are not suitable for fiber lasers because of their size. They also introduce large coupling losses when light is coupled into and out of the modulator. An exception occurs in the case of $LiNbO_3$ modulators, which are relatively compact and can be integrated within the fiber cavity with relatively small coupling losses. They can also be modulated at speeds as high as 40 GHz [143]. For these reasons, $LiNbO_3$ modulators are commonly used for mode-locking fiber lasers.

Active mode locking of EDFLs initially produced pulses of widths > 10 ps. In a 1989 experiment, 4-ps pulses were generated using a ring cavity that included 2-km of standard fiber with large anomalous GVD [144]. Generation of short pulses was attributed to the soliton effects. In fact, the peak power of pulses was in good agreement with the expected peak power for the fundamental soliton from Eq. (5.3.10). The soliton-like nature of emitted pulses was also confirmed by the inferred "sech" shape and by the measured time-bandwidth product of 0.35. The pulse width was reduced to below 2 ps in an FM mode-locking experiment that used a Fabry–Perot cavity [145]. The fiber was only 10 m long, resulting in a longitudinal-mode spacing of about 10 MHz. This laser was referred to as the *fiber-soliton laser* since the "sech" pulses were nearly chirp free, with a time-bandwidth product of only 0.3. The laser wavelength could be tuned over the range of 1.52 to 1.58 μm, indicating

that such lasers can serve as a source of tunable picosecond pulses in the 1.55-μm wavelength region of interest for optical communication systems. In this experiment, the $LiNbO_3$ modulator was operated at 420 MHz. This kind of mode locking, where modulation frequency is an integer multiple of the mode spacing, is called *harmonic mode locking* [34].

The performance of harmonically mode-locked EDFLs has continued to improve [146]–[174]. As early as 1990, the pulse-repetition rate was extended to 30 GHz by using a high-speed $LiNbO_3$ modulator [146]. A ring cavity of 30-m length was used with an intracavity isolator for unidirectional operation. In a 1992 experiment, a fiber laser provided transform-limited 3.5- to 10-ps pulses with a time-bandwidth product of 0.32 at repetition rates of up to 20 GHz [147]. The laser was used in a system experiment to demonstrate that such pulses can be used for soliton communication systems at bit rates of up to 8 Gb/s.

A common problem with harmonically mode-locked fiber lasers is that they are unable to produce stable, equal-amplitude pulse trains over extended periods unless a stabilization technique is used. A phase-locking technique in which the optical phase is locked to the electrical drive of the modulator has been used with success [148]. In another approach, the use of a high-finesse Fabry–Perot étalon with a free spectral range equal to the repetition rate has resulted in a stable harmonically mode-locked EDFL suitable for soliton communication systems [149]. Polarization-maintaining fibers have also been used to make actively mode-locked EDFLs. In 1993, such a laser produced 6-ps pulses at repetition rates of up to 40 GHz and at wavelengths tunable over a wide range from 40 to 50 nm [151].

In a different approach, a cavity design known as the *sigma configuration*is used for making environmentally stable fiber lasers [156]. Figure 5.11 shows the σ-shaped cavity schematically consisting of two parts. A loop made of polarization-maintaining fiber contains a $LiNbO_3$ amplitude modulator and an output coupler. The loop is coupled to a linear section through a polarizing beam splitter. This section is made of traditional fibers and does not preserve the polarization state. However, it terminates with a Faraday rotator placed in front of a mirror. Such a Faraday mirror produces orthogonally polarized light on reflection. As a result, all birefringence effects are totally compensated during each round trip in the linear section.

A dispersion-compensating fiber can be used in the linear branch for reducing the average GVD. Such a dispersion-management technique has many ad-

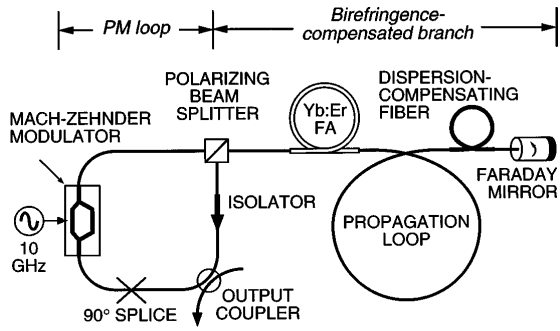

Figure 5.11 Schematic of a harmonically mode-locked fiber laser employing the sigma configuration. The 10-m-long fiber amplifier (FA) is connected to a 90-m propagation loop in the linear section. (After Ref. [156])

vantages, which will be discussed in Chapter 7. It is important to note that the sigma cavity is functionally equivalent to a ring cavity because of the Faraday mirror. In 1996 experiment, such a laser produced 1.3-ps pulses at the 10-GHz repetition rate through soliton-shaping effects while maintaining a negligible pulse-dropout rate and low noise [156]. The pulse shape was close to Gaussian in the center but fitted the "sech" shape better in the wings. This is a well-known feature of dispersion-managed solitons (see Chapter 8). The pulse width also decreased at higher power levels because of the increased nonlinear phase shift produced by SPM. This feature is in agreement with Eq. (5.3.10).

Active mode locking requires the modulation frequency of the $LiNbO_3$ modulator to remain matched to the longitudinal-mode spacing $\Delta\nu$ (or a multiple of it) quite precisely. This is difficult to realize in practice because of fluctuations in $\Delta\nu$ induced by environmental changes. The matching problem can be solved automatically by using the technique of regenerative mode locking [153]. In this technique, the electrical signal for the modulator at the correct modulation frequency is generated from the laser output using a clock-extraction circuit, a phase controller, and a microwave amplifier. Even though the laser is not initially mode locked, its power spectrum contains the beat signal at frequencies corresponding to multiples of the longitudinal-mode spacing. This signal can be used to produce pulse trains at high repetition rates through harmonic mode locking. As early as 1995, 1.8-ps pulses were produced at the 20-GHz repetition rate using regenerative mode locking of a ring cavity made by using polarization-maintaining fiber components [155]. The

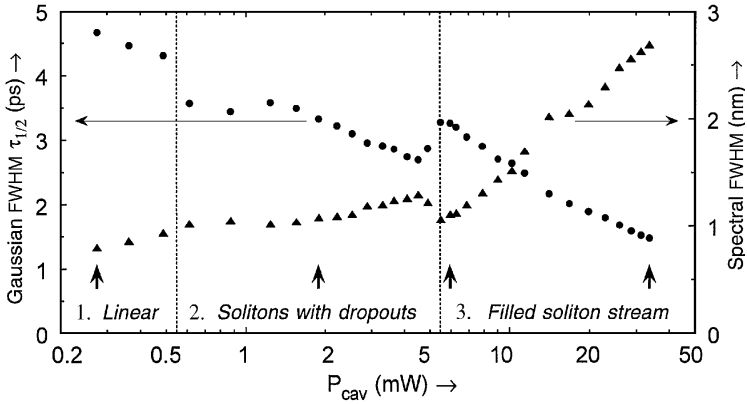

Figure 5.12 Temporal (circles) and spectral (triangles) widths for a sigma laser as a function of intracavity optical power P_{cav}. (After Ref. [171])

output pulses could be compressed to below 0.2 ps in a fiber amplifier made with dispersion-decreasing fiber. The wavelength of the regeneratively mode-locked laser was tunable over a considerable range within the gain spectrum of erbium ions. Moreover, the mode-locked pulse train exhibited low timing jitter (about 120 fs) and small energy fluctuations (about 0.2%) at a repetition rate of 10 GHz [168]. In a 1999 experiment, the technique of regenerative mode locking produced a 40-GHz pulse train tunable over 1530 to 1560 nm while maintaining pulse widths close to 1 ps [169].

A harmonically mode-locked fiber laser can also be stabilized with an electronic feedback loop that is used to adjust the cavity length. Such a scheme has been used for a sigma-configuration laser whose cavity included a piezoelectric transducer for fine adjustment of the cavity length [171]. The cavity also included an optical filter (bandwidth 16 nm). A careful analysis of this sigma laser showed that it has three distinct regions of operation. Figure 5.12 shows how temporal and spectral widths of the mode-locked pulses change with increasing intracavity power. At low power levels, the nonlinear effects (SPM) in silica fibers are negligible, and the laser produces Gaussian-shaped pulses of width close to 5 ps. As the intracavity power increases, the soliton effects become important, and the pulses become narrower, more intense, and attain a certain fixed energy level (as required for autosolitons). If the average power is not large enough to sustain such pulses in all time slots (because of a high repetition rate enforced by the modulator), pulse dropouts occur in a random fash-

ion. Finally, when the intracavity power exceeds a certain value (about 5 mW), the laser emits a train of short optical pulses (width 1–3 ps) with a negligible dropout rate, low noise, and low timing jitter. This behavior is in agreement with numerical simulations based on the Maxwell–Bloch equations [172]. The theory predicts a fourth regime in which more than one pulse may occupy the same time slot at high power levels when GVD is uniform inside the cavity.

In general, the use of dispersion management improves the laser performance considerably. It helps to reduce the timing jitter in the position of mode-locked pulses within the pulse train. The jitter reduction is similar in nature to that occurring for periodically amplified lightwave systems (see Chapter 8). Fiber lasers employing dispersion management and polarization-maintaining fibers can be designed to emit 10-GHz pulse trains simultaneously at two different wavelengths [170]. At a single wavelength, the repetition rate of the mode-locked pulse train can be made as high as 40 GHz using AM mode locking. The repetition rate of 64 GHz has been realized in an FM mode-locked fiber laser in which the optical phase was modulated at 16 GHz, and a Fabry–Perot filter with a 64-GHz free spectral range was used to initiate harmonic mode locking [166]. Such fiber lasers should prove useful for lightwave systems employing the return-to-zero (RZ) format for data transmission.

5.3.4 Other Techniques

An undesirable aspect of actively mode-locked fiber lasers is that the use of a $LiNbO_3$ modulator introduces a nonfiber element inside the laser cavity. Several techniques have been used to produce mode locking without requiring an electro-optic modulator. In one scheme, the nonlinear phenomenon of cross-phase modulation (XPM) is used to produce an all-fiber mode-locked EDFL [175]–[179]. Figure 5.13 shows the design of such a laser schematically. A relatively long length (several kilometers) of fiber is inserted into the ring cavity through two WDM couplers. Pump pulses from an external laser propagate into this fiber and modulate the phase of laser light through XPM. If the repetition rate of pump pulses is an integer multiple of the mode spacing, XPM forces the fiber laser to produce mode-locked pulses. Pulses shorter than 10 ps have been obtained by this technique at repetition rates up to 40 GHz. Such a laser has been used to transfer an arbitrary bit pattern from the pump-pulse wavelength to the laser wavelength [176], resulting in wavelength conversion. This technique can also be used to make an optically programmable mode-

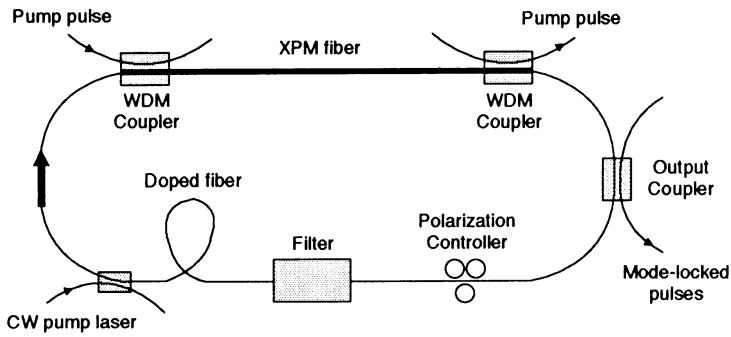

Figure 5.13 Experimental setup for observation of XPM-induced mode locking in fiber lasers. (After Ref. [175], ©1992 IEE)

locked laser such that emitted pulses represent the result of logic operations between elements of the driving pulse train [177].

Synchronous pumping can also be used for FM mode locking of fiber lasers. Implementation of this technique is extremely simple for EDFLs pumped with semiconductor lasers since one can simply modulate the pump-laser current at the appropriate frequency. Because of a relatively long fluorescence time (~ 10 ms) of erbium ions, it is not possible to modulate the gain at frequencies in excess of 1 MHz. However, pump pulses can modulate the laser field through XPM although XPM-induced phase shift is expected to be quite small. In a 1992 experiment in which an EDFL was pumped at 980 nm, mode-locked pulses were relatively broad with widths > 100 ps [180]. Since the XPM-induced phase shift depends on the group-velocity mismatch, it can be increased by decreasing the mismatch. Indeed, pulses shorter than 50 ps were generated when a 1.48-μm pump laser was used [181]. Another way to increase the XPM-induced phase shift is to increase the peak power of pump pulses. Mode-locked pulses as short as 2 ps were generated in an EDFL pumped with a Nd:YAG laser producing 100-ps pulses at the 100-MHz repetition rate [182]. Soliton shaping plays an important role in these experiments since phase-modulated CW laser radiation is converted into nearly chirp-free soliton pulses through the combined action of GVD and SPM.

Several other variations have been used for actively mode-locked fiber lasers. In one scheme, a semiconductor optical amplifier is used as the mode-locking element [183]. In essence, the long piece of silica fiber in Fig. 5.13 is replaced with a pigtailed amplifier. When pump pulses and laser light prop-

agate inside the amplifier, the nonlinear phenomenon of cross-gain saturation modulates both the amplitude and the phase of laser light. GVD and SPM occurring inside the fiber cavity convert the modulated signal into a train of mode-locked soliton pulses. Pulses shorter than 10 ps at repetition rates of up to 20 GHz have been generated by this technique [184].

In another scheme, an acousto-optic modulator and an optical filter are placed inside the laser cavity [185]–[188]. The modulator's role is to shift the laser frequency by a small amount ($\sim$ 100 MHz). Such a frequency-shifted feedback in combination with the fiber nonlinearity leads to formation of picosecond optical pulses inside the laser cavity. Pulses shorter than 10 ps have been generated by using a narrowband optical filter [186]. The theory of such lasers is similar to that used for soliton communication systems making use of sliding-frequency guiding filters (see Chapter 8). In both cases, the soliton maintains itself by changing its frequency adiabatically so that its spectrum remains close to the gain peak. The CW light, in contrast, moves away from the gain peak after a few round trips because of the frequency shift, and thus experiences higher losses than the soliton. As a result, the fiber laser emits mode-locked soliton pulses. Such a laser can also be classified as passively mode locked since nothing modulates the amplitude or phase of laser light at the round-trip frequency or its multiple. We focus on passive mode locking in the following two sections.

5.4 Passive Mode Locking

Passive mode locking is an all-optical nonlinear technique capable of producing ultrashort optical pulses, without requiring any active component (such as a modulator) inside the laser cavity. It makes use of a nonlinear device whose response to an entering optical pulse is intensity dependent such that the exiting pulse is narrower than the input pulse. Several implementations of this basic idea have been used to make passively mode-locked fiber lasers. This section discusses mostly experimental results.

5.4.1 Saturable Absorbers

Saturable absorbers have been used for passive mode locking since the early 1970s. In fact, their use was the sole method available for this purpose until the advent of additive-pulse mode locking. The basic mechanism behind mode

locking is easily understood by considering a fast saturable absorber whose absorption can change on a timescale of the pulse width. When an optical pulse propagates through such an absorber, its wings experience more loss than the central part, which is intense enough to saturate the absorber. The net result is that the pulse is shortened during its passage through the absorber. Pulse shortening provides a mechanism through which a laser can minimize cavity losses by generating intense pulses if the CW radiation is unable to saturate the absorber.

To quantify the extent of pulse shortening in a saturable absorber, we should replace g_0 by α_0 in Eq. (4.1.9), where α_0 is the small-signal absorption coefficient. The resulting equation can be integrated analytically to obtain

$$\ln(P_{\text{out}}/P_{\text{in}}) + (P_{\text{out}} - P_{\text{in}})/P_{\text{sa}} + \alpha_0 l_a = 0, \tag{5.4.1}$$

where P_{in} and P_{out} are the input and output powers, P_{sa} is the saturation power, and l_a is the length of the saturable absorber. For a fast-responding saturable absorber, Eq. (5.4.1) applies along the entire pulse and can be used to obtain the output shape $P_{\text{out}}(t)$ for a given input shape $P_{\text{in}}(t)$. The output pulse is always slightly narrower than the input pulse because of the absorption of low-intensity wings.

The pulse-formation process is quite complex in passively mode-locked lasers [34]. Fluctuations induced by spontaneous emission are enhanced by the saturable absorber during multiple round trips inside the laser cavity until an intense pulse capable of saturating the absorber is formed. The pulse continues to shorten until it becomes so short that its spectral width is comparable to the gain bandwidth. The reduced gain in spectral wings then provides the broadening mechanism that stabilizes the pulse width to a specific value. In the case of fiber lasers, GVD and SPM also play an important role in evolution of mode-locked pulses and should be included.

It is not easy to find a fast saturable absorber responding at timescales of 1 ps or faster. The most suitable material for fiber lasers is a semiconductor absorbing medium [189]–[200]. Its use is more practical with a Fabry–Perot cavity since the absorber can be attached to one of the cavity mirrors. The saturable absorber can be made using either a single or a large stack (> 100 layers) of quantum-well layers. In the latter case, it forms a periodic structure called the *superlattice*. Each period of the superlattice consists of alternating absorbing and transparent layers. In the case of EDFLs, all layers are made using the InGaAsP material but the layer composition is altered appropriately.

In some cases, the mirror attached to the saturable absorber is also made using a periodic arrangement of quarter-wavelength-thick layers that form a grating and reflect light through Bragg diffraction. Such a device is referred to as a *saturable Bragg reflector* to emphasize the use of a Bragg grating.

A superlattice was first used in 1991 for passive mode locking of a ring-cavity EDFL [189]. It produced mode-locked pulses of 1.2-ps duration with a "sech" shape, as expected from theory. In a 1993 experiment [190], the superlattice saturable absorber consisted of 82 periods, and each period used a 7.8-nm-thick absorbing InGaAs layer and a 6.5-nm-thick transparent InP layer. The absorber was integrated with a Bragg reflector (made of alternating InGaAsP and InP layers) that acted as one of the mirrors of the Fabry–Perot laser cavity. Mode-locked pulses obtained from this laser were relatively broad ($\approx$ 22 ps) for a 6.2-m cavity, but their width could be reduced to 7.6 ps by shortening the doped fiber to 2 m. With further refinements, mode-locked pulses as short as 0.84 ps with pulse energies of 0.85 nJ were obtained at a repetition rate of 22 MHz [191]. The same technique was also used for mode locking a Nd-doped fiber laser, and 4-ps pulses were obtained using a heavily doped fiber of 6-cm length [192].

A superlattice saturable absorber integrated with a Bragg reflector requires the growth of hundreds of thin layers using molecular-beam epitaxy. In a different approach, a single 2-μm-thick epitaxial layer of InGaAsP, grown on an InP substrate, acted as a saturable absorber [193]. It was directly mounted on a mirror serving as the output coupler. The 1.2-m-long erbium-doped fiber was the polarization-preserving type. The mode-locked laser produced 320-fs pulses with 40 pJ energy. The laser was self-starting and its output was linearly polarized along a principal axis of the fiber. By codoping the gain-producing fiber with ytterbium, such a laser can be pumped with diode-pumped Nd:YAG or Nd:YLF lasers or directly with a semiconductor laser.

A semiconductor laser amplifier can also be used as a saturable absorber when it is biased below threshold. Its use allows the construction of a self-starting, passively mode-locked EDFL that can be switched between mode-locked and CW states by simply changing the amplifier bias current. In a 1993 experiment, such a laser produced mode-locked pulses of 1.25-ps width at a repetition rate in the range from 10 to 50 MHz in a ring-cavity configuration [194].

Fiber lasers that are mode-locked using a saturable Bragg reflector inside a short Fabry–Perot cavity have quite interesting properties. Figure 5.14 shows

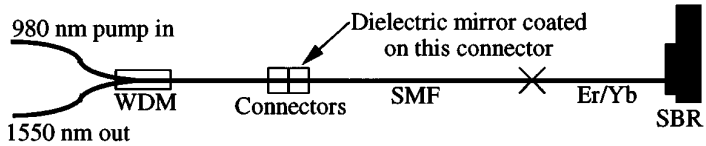

Figure 5.14 Schematic of a fiber laser that was mode locked using a saturable Bragg reflector. (After Ref. [197])

the cavity design schematically. A short piece (length 15 cm) of doped fiber is butt-coupled to the saturable Bragg reflector. Its other end is sliced to a section of standard telecommunication fiber (length about 30 cm) and terminated with a connector on which a high-reflectivity dielectric mirror has been coated. A piece of dispersion-compensating fiber can also be included for dispersion management.

In a series of experiments, total cavity length was changed from 0.5 to 2.5 m, and the average GVD was varied over wide range (normal to anomalous) by using the dispersion-compensating fiber [196]. A mode-locked pulse train could be formed even in the case of normal GVD, but the pulse width was close to 16 ps at a repetition rate of about 40 MHz. This is expected from the results of Section 4.6. Much shorter pulses were observed when the average GVD was anomalous. Pulse widths below 0.5 ps formed over a wide range of average GVD ($\beta_2 = -2$ to -14 ps^2/km) although they were not transform limited. This is expected because of the chirp associated with the autosolitons (see Section 4.5). For short laser cavities (under 50 cm), harmonic mode locking was found to occur. A 45-cm-long laser produced transform-limited, 300-fs pulses at a repetition rate of 2.6 GHz through harmonic passive mode locking [197]. The laser was able to self-organize into a steady state such than 11 pulses with nearly uniform spacing were present simultaneously inside the cavity. Cross-correlation measurements indicated that spacing between pulses was uniform to within 4% of the expected value.

5.4.2 Nonlinear Fiber-Loop Mirrors

An undesirable aspect of semiconductor-based saturable absorbers is that fiber lasers using them loose their all-fiber nature. A solution is provided by the nonlinear fiber-loop mirrors (Sagnac interferometers) whose power-dependent transmission can shorten an optical pulse just as saturable absorbers do (see Section 3.2). Fiber lasers making use of a Sagnac loop for passive mode lock-

ing are referred to as figure-8 lasers because of the appearance of their cavity (see Fig. 5.4). The physical mechanism responsible for mode locking is known as the interferometric or additive-pulse mode locking.

The operation of a figure-8 laser can be understood as follows. The central 3-dB coupler in Fig. 5.4 splits the entering radiation into two equal counterpropagating parts. The doped fiber providing amplification is placed close to the central coupler such that one wave is amplified at the entrance to the loop while the other experiences amplification just before exiting the loop, resulting in a nonlinear amplifying-loop mirror (NALM). As discussed in Section 3.2, the counterpropagating waves acquire different nonlinear phase shifts while completing a round trip inside the NALM. Moreover, the phase difference is not constant but varies along the pulse profile. If the NALM is adjusted such that the phase shift is close to π for the central intense part, this part of the pulse is transmitted, while pulse wings get reflected because of their lower power levels and smaller phase shifts. The net result is that the pulse exiting from the NALM is narrower compared with that entering it. Because of this property, a NALM behaves similarly to a fast saturable absorber except for one major difference—it is capable of responding at femtosecond timescales because of the electronic origin of fiber nonlinearity.

NALMs were first used in 1991 for mode locking a fiber laser [201]–[205]. Pulses shorter than 0.4 ps were generated in the form of fundamental solitons even in early experiments in which the fiber laser was pumped using a Ti:sapphire laser [202]. In a later experiment, 290-fs pulses were produced from an EDFL pumped by 1.48-μm InGaAsP semiconductor lasers [205]. The threshold for mode-locked operation was only 50 mW. Once mode locking initiated, pump power could be decreased to as low as 10 mW.

It is generally difficult to produce pulses shorter than 100 fs from figure-8 lasers. However, mode-locked pulses as short as 30 fs were obtained by amplifying the laser output and then compressing the amplified pulse in a dispersion-shifted fiber [206]. Pulse shortening inside a fiber amplifier occurs because of adiabatic amplification of fundamental solitons (see Section 4.3). Since the amplified pulse is chirped, it can be further compressed by using a fiber with the appropriate dispersion. Pulses as short as 98 fs were generated directly from a figure-8 laser by using a polarization-sensitive isolator and a short piece of normal-GVD fiber for chirp compensation [207].

Passively mode-locked fiber lasers suffer from a major drawback that has limited their usefulness. It was observed in several experiments that the repeti-

tion rate of mode-locked pulses was essentially uncontrollable and could vary over a wide range. Typically, several pulses circulate simultaneously inside the laser cavity, and the spacing among them is not necessarily uniform. In contrast with the case of active mode locking, nothing in the cavity determines the relative location of pulses. As a result, the position of each pulse is determined by various other effects such as fiber birefringence and soliton interactions.

When a single pulse circulates inside the laser cavity, the repetition rate is equal to the round-trip frequency $\Delta\nu$. However, since pulses in a fiber laser propagate as fundamental solitons, their energy is fixed such that

$$E_s = P_0 \int_{-\infty}^{\infty} |A(z,t)|^2 \, dt = 2P_0 T_s. \tag{5.4.2}$$

Since both the soliton width T_s and the peak power P_0 are limited by the laser design, the pulse energy E_s is fixed or quantized [208]. On the other hand, the average intracavity power P_{av} is determined by the pumping level and gain saturation. If $P_{\text{av}} > (\Delta\nu)E_s$, multiple pulses—each of quantized energy E_s—must coexist inside the laser cavity. If these pulses were uniformly spaced, the fiber laser would behave similarly to a harmonically mode-locked laser. However, multiple pulses need not necessarily be uniformly spaced. Most fiber lasers emit pulse trains at the fundamental repetition rate $\Delta\nu$ such that spacing among pulses in each period is virtually random. Under some operating conditions, the laser emits a train of bunched pulses such that each bunch contains 10 or more closely spaced solitons, each with the quantized energy E_s. The number of pulses within each fundamental period depends on the pumping level, among other things.

The key to stabilizing a figure-8 laser consists of implementing a scheme that can adjust the repetition rate f_r in such a way that $f_r E_s$ nearly equals the average circulating power inside the laser cavity. In one scheme, a subring was added to the left ring in Fig. 5.5 containing the isolator [209]. The subring was only 1.6-m long while the total loop length was 60.8 m. In this arrangement, the repetition rate of the subring cavity is 38 times that of the main laser cavity. Pulses circulating inside the subring provide a seed and lead to the formation of 38 uniformly spaced pulses in the main laser cavity under mode-locked operation. Such a laser emitted 315-fs pulses at a fixed repetition rate of 125 MHz. A similar control of the repetition rate can be realized by placing a mirror close to one port of the output coupler [210]. In this case, the optical feedback from the external mirror provides the seed and fixes the relative location of pulses

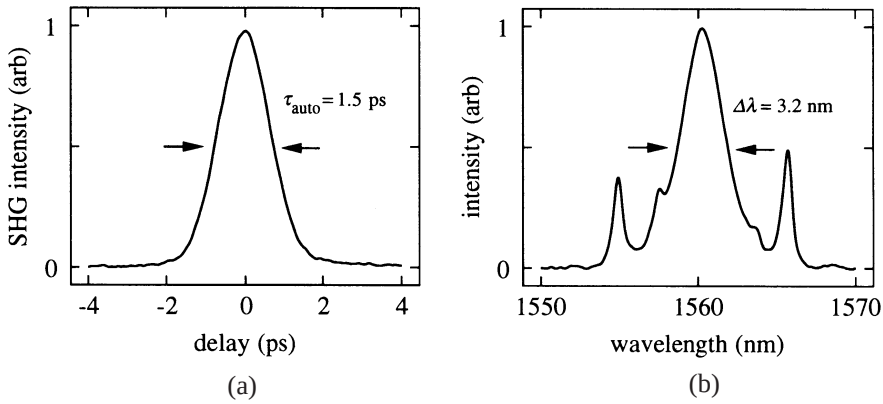

Figure 5.15 (a) Autocorrelation trace and (b) spectrum of mode-locked pulses obtained from a figure-8 laser employing a 94:6 central coupler. (After Ref. [214])

in a periodic manner. The mirror distance controls the repetition rate of such fiber lasers.

The performance of figure-8 lasers has continued to improve [211]–[219]. Transform-limited pulses of 1.35-ps duration, at wavelengths continuously tunable over a 20-nm range, were generated in 1993 by using an intracavity Fabry–Perot filter for spectral stabilization and a feedback loop for temporal stabilization [213]. In another experiment, the central coupler (see Fig. 5.4) was unbalanced such that 94% of the intracavity power was propagating in the direction in which laser emission occurred [214]. Such a laser had lower cavity losses and was found to be more easily mode locked than figure-8 lasers with balanced (50:50) central couplers. The laser was able to generate pulses shorter than 1 ps. Figure 5.15 shows the autocorrelation trace of 970-fs pulses together with the corresponding spectrum. The origin of spectral sidebands seen in this figure is discussed later.

Shorter and more energetic pulses were obtained in a 1997 experiment in which the erbium-doped fiber had normal dispersion ($\beta_2 > 0$) at the operating wavelength [219]. Pulses inside the cavity were stretched considerably during amplification inside the doped fiber. This permitted energy levels as high as 0.5 nJ. Pulses were compressed down to 125 fs by using a long length of dispersion-shifted fiber inside the cavity. Both the central wavelength and the spectral width of mode-locked pulses were tunable by adjusting the polarization-controllers within the laser cavity.

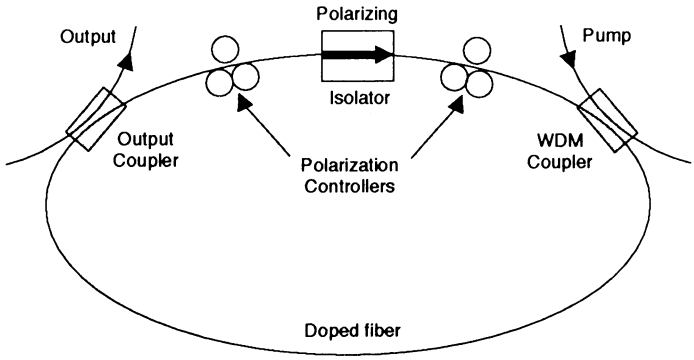

Figure 5.16 Schematic design of a fiber laser passively mode locked via nonlinear polarization-rotation.

5.4.3 Nonlinear Polarization Rotation

Fiber lasers can also be mode locked by using intensity-dependent changes in the state of polarization (occurring because of SPM and XPM) when the orthogonally polarized components of a single pulse propagate inside an optical fiber (see Chapter A.6). The physical mechanism behind mode locking makes use of the nonlinear birefringence and is similar to that of a Kerr shutter (see Section A.7.2). From a conceptual point of view, the mode-locking mechanism is identical to that used for figure-8 lasers (additive-pulse mode locking) except that the orthogonally polarized components of the same pulse are used in place of counterpropagating waves. From a practical standpoint, passive mode locking can be accomplished by using a cavity with a single fiber ring.

The mode-locking process can be understood using the ring cavity shown in Fig. 5.16. A polarizing isolator placed between two polarization controllers acts as the mode-locking element. It plays the double role of an isolator and a polarizer such that light leaving the isolator is linearly polarized. Consider a linearly polarized pulse just after the isolator. The polarization controller placed after the isolator changes the polarization state to elliptical. The polarization state evolves nonlinearly during propagation of the pulse because of SPM- and XPM-induced phase shifts imposed on the orthogonally polarized components. The state of polarization is nonuniform across the pulse because of the intensity dependence of the nonlinear phase shift. The second polarization controller (one before the isolator) is adjusted such that it forces the polarization to be linear in the central part of the pulse. The polarizing isolator

lets the central intense part of the pulse pass but blocks (absorbs) the low-intensity pulse wings. The net result is that the pulse is slightly shortened after one round trip inside the ring cavity, an effect identical to that produced by a fast saturable absorber.

The technique of nonlinear polarization rotation was first used in 1992 for passive mode locking of fiber lasers and has resulted in considerable improvement of of such lasers [220]–[224]. By the end of 1992, stable, self-starting pulse trains of subpicosecond pulses (452-fs pulse width) at a 42-MHz repetition rate were generated by using this technique [223]. Further improvements occurred when it was realized that the presence of anomalous GVD within the laser cavity is not necessarily beneficial since it limits both the width and the energy of mode-locked pulses. In a 1993 experiment, 76-fs pulses—with 90-pJ energy and 1 kW of peak power—were generated by using a ring cavity in which the average GVD was normal [224].

Considerable research has been done to understand and to improve fiber lasers making use of nonlinear polarization rotation for passive mode locking [225]–[242]. The shortest pulses (42 fs) with high energies (up to 1 nJ) were obtained from an Nd-doped fiber laser in a Fabry–Perot configuration in which a moving mirror was used to start mode locking [229]. In the case of EDFLs, high-energy (> 0.5 nJ), ultrashort (< 100 fs) pulses at a repetition rate of 48 MHz were obtained in a ring-cavity configuration in which the net dispersion was positive [235]. The ring cavity of this fiber laser consisted of a piece of erbium-doped fiber (length about 1 m) with normal GVD ($\beta_2 \approx 5$ ps^2/km) and several types of optical fibers (total length 2–6 m) with anomalous GVD in the wavelength region near 1.56 μm. The average dispersion could be changed from anomalous to normal by adjusting the cavity length. Such cavities are called dispersion managed since the net dispersion can be tailored to any desired value. The laser is referred to as a *stretched-pulse fiber laser* since pulses circulating inside the cavity stretch considerably in the section with normal GVD. It was found that high-energy pulses could be generated only when the average or net dispersion in the cavity was normal. The emitted pulses were relatively broad (> 1 ps) but could be compressed down to below 100 fs by using an appropriate length of fiber because of their highly chirped nature. The location of the output coupler plays an important role in such lasers since pulse width varies by a large amount along the cavity length. Mode-locked pulses as short as 63 fs have been generated with proper optimization [241].

For practical applications, environmental stability is often an important is-

sue. The main source of environmental instability is the relatively long length of the fiber inside the laser cavity required to produce a large enough nonlinear phase shift. Temperature and stress variations can lead to birefringence fluctuations that affect the mode-locking process. The problem can be solved to a large extent by reducing the fiber length to under 10 m and using a fiber with high built-in birefringence (polarization-maintaining fiber) so that linear birefringence is not affected by environmental changes. In one scheme, a Fabry–Perot cavity in which one of the mirrors acts as a Faraday rotator has been used to realize environmentally stable operation [237]. The Faraday mirror rotates the polarization such that the reflected light is orthogonally polarized. As a result, the phase shift induced by linear birefringence is exactly canceled after one round trip, while the nonlinear phase shift remains unaffected. The Faraday mirror also eliminates the walk-off effects induced by the group-velocity mismatch in high-birefringence fibers. Such a laser was capable of producing 360-fs pulses of 60-pJ energy at a stable repetition rate of 27 MHz. In a 1999 experiment, pulse energy was increased to 4 nJ using the double-clad fiber for an Nd-doped fiber laser [242].

5.4.4 Hybrid Mode Locking

Hybrid mode locking combines more than one mode-locking technique within the same laser cavity to improve the laser performance. The most obvious combination incorporates an amplitude or phase modulator inside a passively mode-locked fiber laser. The modulator provides periodic timing slots to produce a regular pulse train, while a passive mode-locking technique shortens the pulse compared to that expected from active mode locking alone. An added benefit is that the modulator can be operated at a frequency that is a high multiple of the round-trip frequency, resulting in a well-defined repetition rate that can exceed 10 GHz or more while the mode spacing remains close to 10 MHz.

As early as 1991, the active and passive mode-locking techniques were combined by using a phase modulator [243]. Since then, this combination has led to considerable improvement in the performance of fiber lasers. In a 1994 experiment, it was used to generate subpicosecond pulses at the 0.5-GHz repetition rate from a single-polarization EDFL [244]. The laser used the sigma configuration discussed earlier in the context of active mode locking. A polarization-maintaining loop containing the $LiNbO_3$ modulator was coupled to a linear section through a polarizing beam splitter. This section contained

the fiber amplifier and the passive mode-locking element composed of quarter-wave plates and a Faraday rotator.

The sigma configuration has been used to make a diode-pumped stretched-pulse EDFL with excellent environmental stability [245]. The polarization-maintaining loop containing the $LiNbO_3$ modulator was made using 7.5 m of standard fiber with a GVD of -20 ps^2/km. The linear section contained 1 m of erbium-doped fiber with normal GVD ($\beta_2 \approx 100$ ps^2/km), together with a quarter-wave plate, a half-wave plate, and two Faraday rotators (whose presence makes the sigma-laser cavity equivalent to a ring cavity). The net dispersion in the cavity was normal with a value of about 0.02 ps^2. The doped fiber was pumped using 980-nm diode lasers. The laser produced mode-locked pulses with 1.2-nJ energy (average power 20 mW) at a pump power of 200 mW. The pulse width from the laser was about 1.5 ps but could be compressed down to below 100 fs using a dispersive delay line (see Chapter 6).

It is also possible to combine two passive mode-locking techniques within the same fiber laser. In one approach, a superlattice saturable absorber is added to a laser that is passively mode locked via nonlinear polarization rotation. This combination was used in 1996 for a cladding-pumped fiber laser [246]. The laser produced 200-fs pulses with pulse energies of up to 100 pJ at a wavelength near 1560 nm. Pulse energies of up to 1 nJ were obtained by increasing the GVD inside the fiber cavity while maintaining a pulse width close to 3 ps. The intracavity saturable absorber is helpful for initiating mode locking (self-starting capability), whereas the steady-state pulse shape is governed by the nonlinear polarization evolution. The laser is also environmentally stable because of the use of a compensation scheme for linear polarization drifts.

In another implementation of hybrid mode locking, an Nd-doped fiber laser was tuned continuously over a 75-nm bandwidth [247]. Such a wide tuning range (more than twice the FWHM of the gain spectrum) was realized by optimizing the reflection characteristics of the semiconductor saturable absorber. The duration of mode-locked pulses was 0.3 to 0.4 ps over the entire tuning range. A chirped fiber grating has also been used for dispersion compensation in the cavity of an Nd-doped fiber laser [248]. Such a laser is self-starting and can be passively mode locked by using just the saturable absorber as the mode-locking element. No intracavity polarization controllers were required for its optimization. The laser generated mode-locked pulses of 6-ps duration with output energies as high as 1.25 nJ.

In still another application of hybrid mode locking, an Nd-doped fiber laser

was mode locked at two wavelengths simultaneously [249]. A prism pair, used for dispersion compensation, also separated the paths taken by the two intracavity beams. The 1.06-μm beam was mode locked using a saturable absorber, whereas the technique of nonlinear polarization rotation was used for mode locking the 1.1-μm beam. Such a device operates as if the two lasers share the same gain medium, and cross-gain saturation plays an important role in its operation. Indeed, it was necessary to mismatch the cavity lengths slightly to introduce an offset of at least 0.5 kHz between the repetition rates of the two mode-locked pulse trains. The difference between the repetition rates was tunable from 0.5 kHz to >1 MHz.

5.4.5 Other Mode-Locking Techniques

Several other techniques have been suggested for passively mode locking fiber lasers. In one scheme, a dual-core fiber with one core doped with erbium ions provides not only gain but also the saturable absorption necessary for mode locking [250]. The operation of such a laser makes use of optical switching in nonlinear directional couplers (see Section 2.3). At low powers, a part of the mode energy is transferred to the undoped core and constitutes a loss mechanism for the laser cavity. At high powers, such an energy transfer ceases to occur, and most of the energy remains confined to the doped core. As a result, a dual-core fiber acts as a fast saturable absorber and shortens an optical pulse propagating through it. Mode locking can also be achieved by using a dual-core fiber as a fiber-loop mirror or simply by placing it inside the Fabry–Perot cavity of a fiber laser [251].

In another scheme, fiber gratings are used to make a coupled-cavity fiber laser that can be mode locked through additive-pulse mode locking. In a simple implementation of this idea, three Bragg gratings were used to form two coupled Fabry–Perot cavities [252]. In one cavity, the fiber was doped with erbium and pumped at 980 nm while the other cavity had the standard undoped fiber. Both cavities had the same nominal length with total length ranging from 1 to 6 m. The laser produced relatively wide mode-locked pulses (width > 50 ps) without requiring stabilization of individual cavity lengths. The latter feature is somewhat surprising since additive-pulse mode locking in coupled-cavity lasers normally requires precise matching of the cavity lengths. It can be understood by noting that the effective penetration distance in a fiber grating before light is reflected depends on the wavelength of light. As a result, the laser can adjust its wavelength to match the cavity lengths automatically. The

self-matching capability of coupled-cavity fiber lasers can be extended by using chirped gratings [253]. Such a laser produced 5.5-ps mode-locked pulses, which could be compressed down to below 1 ps (because of their chirped nature) using a piece of fiber with the appropriate GVD (see Chapter 6).

5.5 Role of Fiber Nonlinearity and Dispersion

Nonlinear effects such as SPM and XPM play a dominant role in the operation of most passively mode-locked fiber lasers. Fiber dispersion also plays an important role, especially when the soliton effects are relevant. Both numerical and analytical methods have been used to understand and to quantify the role of fiber nonlinearity and dispersion [254]–[274].

5.5.1 Saturable-Absorber Mode Locking

The theory of passive mode locking is based on the same Ginzburg–Landau equation used earlier for active mode locking. The main difference is in the functional form of the cavity-loss parameter α appearing in Eq. (5.3.4), which should include the intensity dependence of losses produced by the saturable absorber [140]. More specifically, α is given by

$$\alpha = \alpha_c + \alpha_0(1+|A|^2/P_{\rm sa})^{-1} \approx \alpha_c + \alpha_0 - \alpha_0|A|^2/P_{\rm sa}, \tag{5.5.1}$$

where $P_{\rm sa}$ is the saturation power of the absorber, assumed to be much larger than the peak power levels associated with optical pulses circulating inside the laser cavity. This assumption is made only to simplify the following analysis.

If we substitute Eq. (5.5.1) in Eq. (5.3.4), we find that the presence of saturated absorption modifies the parameter α_2 such that $\alpha_2 \approx -\alpha_0/P_{\rm sa}$ if two-photon absorption is negligible. The new value of α_2 is negative. This is understandable from a physical viewpoint since the intensity dependence of a saturable absorber is just the opposite that of a two-photon absorber (absorption decreases with increasing intensity). In the following discussion we use Eq. (5.3.4) with negative values of α_2.

A change in the sign of α_2 does not affect the form of the solution given in Eq. (4.4.4). We can thus conclude that a passively mode-locked fiber laser emits pulses in the form of a chirped soliton whose amplitude is given by [141]

$$u(\xi,\tau) = N_s[\mathrm{sech}(p\tau)]^{1+iq}\exp(iK_s\xi). \tag{5.5.2}$$

The three parameters N_s, p, and q are determined in terms of the laser parameters as indicated in Eqs. (4.4.5)–(4.4.8). They are in turn related to the soliton width T_s, peak power P_s, and the frequency chirp $\delta\omega$ as (see Section 4.4)

$$T_s = T_2/p, \quad P_s = |\beta_2|N_s^2/(\gamma T_2^2), \quad \delta\omega = q\tanh(p\tau)/T_s. \tag{5.5.3}$$

Using p from Eq. (4.4.6), the pulse width can be written in terms of the laser parameters (assuming anomalous GVD) as

$$T_s = \left\{ \frac{|\beta_2|[2q + d(q^2-1)]}{g_c - \alpha_c - \alpha_0} \right\}^{1/2}, \tag{5.5.4}$$

where $d = g_c/(\beta_2\Omega_g^2)$ is related to the gain bandwidth. It is evident that GVD and SPM play a major role in establishing the width of the mode-locked pulse train.

This simple theory needs modification for modeling fiber lasers that are mode-locked using semiconductor saturable absorbers. The reason is that a semiconductor does not response instantaneously. In fact, the response time of a quantum well is typically longer than the width of mode-locked pulses. The carrier dynamics can be included by replacing Eq. (5.5.1) with $\alpha = \alpha_c + \alpha_s$. The absorption coefficient α_s of the saturable absorber satisfies the following rate equation:

$$\frac{\partial\alpha_s}{\partial t} = \frac{\alpha_0 - \alpha_s}{\tau_s} - \frac{|A|^2}{E_{\rm sa}}\alpha_s, \tag{5.5.5}$$

where τ_s is the recovery time and $E_{\rm sa} \equiv \tau_s P_{\rm sa}$ is the saturation energy of the absorber. For a fast-responding absorber, α_s is given by the steady-state solution of this equation, and the chirped-soliton solution of Eq. (5.5.2) is recovered.

Equation (5.5.5) can be solved approximately in the opposite limit of a relatively slow absorber and leads to the following expression for α:

$$\alpha = \alpha_c + \alpha_0 \exp\left[-\frac{1}{E_{\rm sa}} \int_0^t |A(z,t)|^2\, dt \right]. \tag{5.5.6}$$

The use of this equation in Eq. (5.4.1) leads to a modified Ginzburg–Landau equation that can be solved analytically in several important cases [272]. Actual quantum-well absorbers are found to have both fast and slow recovery mechanisms. A realistic model for such saturable absorbers has been developed [271]. The resulting Ginzburg–Landau equation is solved numerically; its predictions agree well with the experimental data.

5.5.2 Additive-Pulse Mode Locking

The Ginzburg–Landau equation can be extended for fiber lasers making use of additive-pulse mode locking [265]. The pulse-shortening effect of the mode-locking element (nonlinear fiber-loop mirror or nonlinear polarization rotation) is included through amplitude and phase changes induced on the pulse circulating inside the cavity.

Consider first the figure-8 laser in which a Sagnac loop imposes amplitude and phase changes on each pulse as it circulates inside it. Transmittivity of a Sagnac loop in which an amplifier is located at the entrance of the loop is given in Section 3.2 for CW beams. For an optical pulse with amplitude $A(t)$, it can be written as

$$T_S(t) = 1 - 2\rho(1-\rho)\{1 + \cos[(1-\rho-G\rho)\gamma|A(t)|^2 L_s]\}, \tag{5.5.7}$$

where ρ is the bar-port transmission of the coupler and L_s is the loop length. For a 50:50 or 3-dB coupler, $\rho = 0.5$ and Eq. (5.5.7) reduces to

$$T_S(t) = \sin^2[(G-1)\gamma|A(t)|^2 L_s/4]. \tag{5.5.8}$$

If loop length L_s is chosen such that $(G-1)\gamma P_0 L_s = 2\pi$, where P_0 is the peak power, the central part of a pulse is transmitted without loss, but the pulse wings experience loss. This intensity-dependent loss is referred to as *self-amplitude modulation* and is similar to that induced by a fast saturable absorber.

We can distribute the intensity-dependent loss introduced by the Sagnac loop over the cavity length and include its effects through the parameter α_2 in the Ginzburg–Landau equation. The effect of loop-induced nonlinear phase shift can also be included by modifying the parameter γ. The steady-state solution of the Ginzburg–Landau equation remains in the form of the chirped soliton of Eq. (5.5.2), but its width and peak power are affected by the loop parameters. This analytic solution can be used to study the effect of fiber dispersion and nonlinearity on the performance of figure-8 fiber lasers [31]. A similar technique can be used for fiber lasers that are mode locked via nonlinear polarization rotation [265].

Modeling of realistic mode-locked fiber lasers requires consideration of several other factors. For example, spontaneous emission seeds the growth of mode-locked pulses and should be included. Another effect that becomes

important for ultrashort pulses is the self-frequency shift of solitons resulting from intrapulse Raman scattering. It is common to solve the Ginzburg–Landau equation numerically since such an approach automatically includes the effects of SPM, XPM, GVD, and intrapulse Raman scattering [259]–[263]. This equation reduces to a generalized NLS equation in the parts of the laser cavity where the fiber is undoped. In the case of figure-8 lasers, the evolution of counterpropagating pulses should be considered separately inside the Sagnac loop, and the two optical fields should be combined coherently at the central coupler to determine the transmitted field. For fiber lasers making use of nonlinear polarization rotation, one must consider the evolution of orthogonally polarized components of the optical pulse by solving a set of two coupled Ginzburg–Landau equations generalized to include the XPM effects. The effects of spontaneous emission can be included approximately by starting numerical simulations with a broadband noise pulse acting as a seed [263]. The noise pulse is propagated around the laser cavity repeatedly until a steady state is reached. Gain saturation is included by considering average power circulating inside the laser cavity. Such numerical simulations are capable of predicting most features observed experimentally.

5.5.3 Spectral Sidebands

The Ginzburg–Landau equation provides only an approximate description of passively mode-locked fiber lasers. Real lasers show features not explained by this model. For example, pulse spectra of most fiber lasers exhibit sidebands, similar to those seen in Fig. 5.15. In fact, several pairs of such sidebands appear under some operating conditions. Figure 5.17 shows an example of such a pulse spectrum obtained from a fiber laser that was passively mode-locked via nonlinear polarization rotation [222]. The ring cavity of this laser incorporated 122 m of standard fiber (undoped) with a total loop length of 148 m.

The origin of spectral sidebands seen in the output of fiber lasers is well understood [275]–[278]. The chirped soliton, found by solving the Ginzburg–Landau equation, represents the average situation since this equation ignores discrete nature of perturbations experienced by such solitons during each round trip. In reality, a part of the soliton energy leaves the cavity at the output coupler and constitutes a loss to the soliton circulating inside the cavity. The energy builds up to its original value as the pulse is amplified during each round trip. The net result is that the soliton energy and the peak power vary

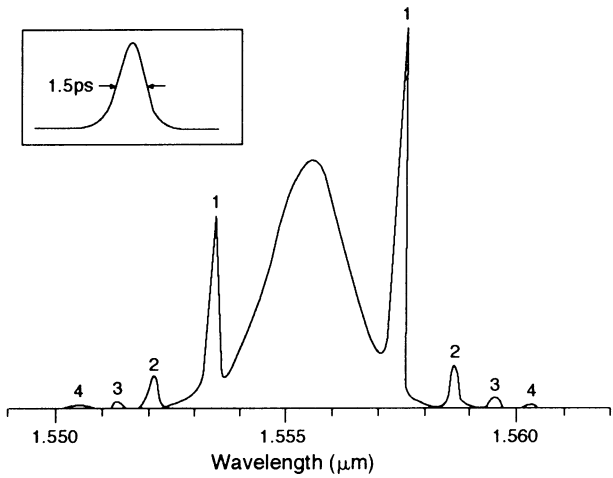

Figure 5.17 Pulse spectrum of an EDFL mode locked via nonlinear polarization rotation technique. Inset shows the autocorrelation trace of mode-locked pulses. (After Ref. [222])

periodically, with a period equal to the cavity length. This amounts to creating a nonlinear-index grating that can affect soliton properties through Bragg diffraction, among other things. The situation is similar to that occurring in optical communication systems when pulses are amplified periodically to overcome fiber losses (see Section 4.3.2). In both cases, solitons adjust to perturbations by shading a part of their energy in the form of dispersive waves, also known as the *continuum radiation*.

Normally, dispersive waves produced by perturbations form a low-level, broadband background that accompanies the soliton. However, in the case of periodic perturbations, dispersive waves of certain frequencies can be resonantly enhanced, resulting in the spectral sidebands seen in Fig. 5.17. The frequency and the amplitude of sidebands can be calculated using the perturbation theory of solitons [277]. The frequency can also be calculated by using a phase-matching condition if spectral sidebands are interpreted to result from a four-wave mixing process that is phase matched by the index grating created by periodic perturbations.

A simple physical approach to understanding the growth of spectral sidebands makes use of a constructive interference condition. If the dispersive wave at a frequency $\omega_0 + \delta\omega$, where ω_0 is the soliton carrier frequency, is to

grow on successive round trips, the phase difference between the soliton and that dispersive wave must be a multiple of 2π during a single round trip, i.e.,

$$|\beta(\omega_0) + \beta_1 \delta\omega + K_s - \beta(\omega_0 + \delta\omega)|L = 2\pi m, \tag{5.5.9}$$

where m is an integer, $\beta(\omega_0 + \delta\omega)$ is the propagation constant of the dispersive wave, and K_s is the soliton wave number appearing in Eq. (4.4.7).

In general, one must use Eq. (4.4.8) to determine K_s. However, if the soliton is nearly unchirped, $K_s = (2L_D)^{-1}$, where $L_D = T_s^2/|\beta_2|$ is the dispersion length for a soliton of width T_s. By expanding $\beta(\omega_0 + \delta\omega)$ in a Taylor series and retaining terms up to quadratic in $\delta\omega$, Eq. (5.5.9) leads to the following expression for the sideband frequencies [275]:

$$\delta\omega = \pm T_s^{-1}(8mz_0/L - 1)^{1/2}, \tag{5.5.10}$$

where $z_0 = (\pi/2)L_D$ is the soliton period. The predictions of Eq. (5.5.10) agree quite well with the position of sidebands seen in Fig. 5.17 when mode-locked pulses are nearly transform limited. In the case of chirped solitons, the use of Eq. (4.4.5)–(4.4.7) with $s = -1$ ($\beta_2 < 0$) and $p = T_2/T_s$ leads to the result

$$\delta\omega = \pm T_s^{-1}(8mz_0/L - 1 + q^2 - 2qd)^{1/2}, \tag{5.5.11}$$

where the chirp parameter q is obtained from Eq. (4.4.8). The effect of third-order dispersion on the location of spectral sidebands can also be taken into account [278] by including the cubic term in the Taylor-series expansion of $\beta(\omega_0 + \delta\omega)$ in Eq. (5.5.9).

Periodic perturbations occurring in a fiber laser also limit the duration of mode-locked pulses. This limit is similar to that restricting amplifier spacing in soliton communication systems and has the same origin [32]. If the solitons were to recover from periodic perturbations, they should be perturbed as little as possible during each round trip. In particular, the phase shift $K_s L$ acquired by the soliton over the cavity length L must be a small fraction of 2π. By using $K_s = (2L_D)^{-1}$ with $L_D = T_s^2/|\bar{\beta}_2|$, the soliton width T_s is limited by

$$T_s \gg (|\bar{\beta}_2|L/4\pi)^{1/2}. \tag{5.5.12}$$

Here $\bar{\beta}_2$ represents the average value of GVD inside the laser cavity if different types of fibers are used in a dispersion-managed cavity. If we use L = 20 m and $\beta_2 = -4$ ps^2/km as typical values for a figure-8 laser, $T_s \gg 80$ fs. Indeed, it is

difficult to generate pulses much shorter than 100 fs from mode-locked fiber lasers. Equation (5.5.12) also shows that shorter mode-locked pulses can be generated by reducing the cavity length and net GVD inside the laser cavity. If we use $L = 2$ m and $\beta_2 = -1$ ps^2/km as optimized values for a mode-locked fiber laser, the condition (5.5.12) becomes $T_s \gg 25$ fs. Such lasers can generate pulses shorter than 100 fs. This is indeed what has been observed experimentally [224]. Measurements of pulse widths over a wide range of residual dispersion show that the pulse width is approximately given by $T_s \approx (|\bar{\beta}_2|L)^{1/2}$ [278]. These observations are consistent with the preceding simple argument.

As mentioned earlier, the average GVD inside the cavity does not have to be anomalous for mode-locked fiber lasers. The general solution given in Eq. (5.5.2) exists for both normal and anomalous GVD. Moreover, Eqs. (4.4.5)–(4.5.8) show that the chirp is relatively large in the case of normal GVD. Indeed, mode-locked pulses emitted from dispersion-managed fiber lasers with normal average GVD are heavily chirped. For this reason, they can be compressed considerably outside the laser cavity (see Chapter 6). In a 1994 experiment, the shortest pulse width (76 fs) was obtained from a mode-locked EDFL when the output pulse was compressed by using a piece of fiber with appropriate dispersion [235].

5.5.4 Polarization Effects

So far in this chapter, we have not addressed the issue of the state of polarization of light emitted from mode-locked fiber lasers. As discussed in Chapter A.6, optical fibers do not preserve polarization unless they are specifically designed to do so. As a result, the state of polarization of output light may not be constant in time. It may change from pulse to pulse or even over the duration of a single pulse. The situation is quite interesting for short-cavity fiber lasers for which the cavity length is a small fraction of the beat length. In general, polarization evolution is important in all mode-locked fiber lasers and should be included for a proper understanding of such lasers [279]–[284].

The polarization effects were investigated thoroughly in a 1997 experiment where a fiber laser of cavity length ~ 1 m or less was mode locked passively using a saturable Bragg reflector [279]. The cavity design was similar to that shown in Figure 5.10 except for the addition of a polarization controller. It was made by wrapping standard single-mode fiber on two 5.5-cm-diameter paddles and allowed continuous adjustment of the linear birefringence within

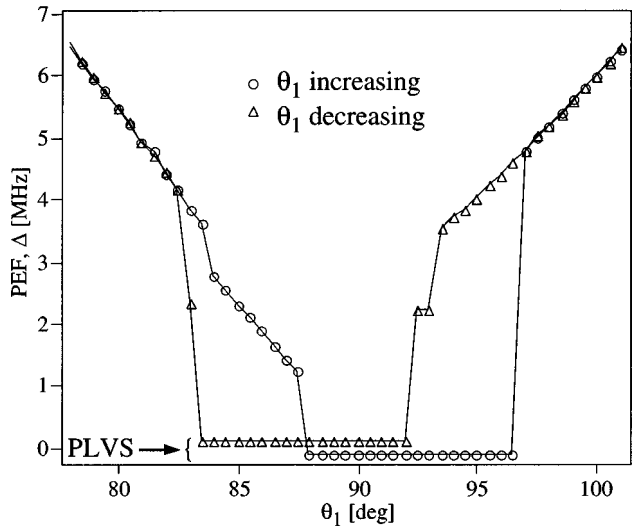

Figure 5.18 Measured variation of polarization-evolution frequency (PEF) Δ with θ_1. Polarization locking (PLVS) occurs when Δ equals 0 and exhibits hysteresis. (After Ref. [282])

the cavity by changing the azimuthal angles θ_1 and θ_2 of the paddles. A linear polarizer was placed at the output of the laser to analyze the polarization state. It converted polarization changes into periodic amplitude changes and introduced AM sidebands in the optical spectrum around each longitudinal mode. The presence of these sidebands is a sign that the state of polarization is not constant from pulse to pulse. Moreover, their frequency spacing Δ provides a quantitative measure of the temporal period over which polarization evolves. For this reason, this frequency is called the *polarization-evolution frequency*.

It was discovered experimentally that the AM sidebands disappear ($\Delta = 0$) for a certain combination of the angles θ_1 and θ_2. Figure 5.18 shows variations in Δ with θ_1 at a fixed value of θ_2. The polarization-evolution frequency decreases as θ_1 approaches $\pi/2$ and drops to zero in the vicinity of this value. The range of angles over which $\Delta = 0$ depends on the direction from which θ_1 approaches $\pi/2$, indicating that this phenomenon exhibits hysteresis. When $\Delta = 0$, the polarization of mode-locked pulses is locked in such a way that all pulses have the same state of polarization in spite of the presence of linear birefringence within the laser cavity [280]. Such pulses are referred to as *polarization-locked vector solitons* (PLVSs).

Properties of the PLVS have been investigated in a 2000 experiment [282]. It turns out that the polarization state of a PLVS can be linear or elliptical. In the case of elliptical polarization, the two linearly polarized components have different amplitudes and phases. The relative phase difference is fixed at $\pm\pi/2$ in all cases but the amplitude difference depends on the linear birefringence within the cavity. In the case of a linearly polarized PLVS, the total energy of the soliton is carried by the component polarized along the slow axis. The existence of such solitons is related to the polarization instability of light polarized along the fast axis (see Chapter A.6). A theoretical model based on a set of two coupled Ginzburg–Landau equations is able explain most of the experimental data [283].

Vector solitons can also form in a fiber laser using a birefringent Sagnac loop for mode locking [281]. In the case of fiber lasers mode locked via nonlinear polarization rotation, birefringence effects can lead to pulse-to-pulse periodic variations in both the peak power and the state of polarization [284]. An amplitude- and polarization-locked pulse train is generated only when the axis of polarization of the polarizing isolator is aligned with the slow axis of the fiber.

Problems

5.1 Why does the gain in fiber lasers vary along the fiber length? Derive the threshold condition by including such axial variations and considering a round trip inside the laser cavity.

5.2 Use the threshold condition [Eq. (5.1.3)] to derive an expression for the pump power required to reach threshold in fiber lasers.

5.3 Why is the gain in a laser clamped at its threshold value? Use this feature to derive expressions for the output power and the slope efficiency of fiber lasers.

5.4 How would you design the Fabry–Perot cavity of a fiber laser without using actual mirrors? Show two such designs and explain their operation.

5.5 Derive an expression for the output intensity by considering N longitudinal modes of the cavity such that the phase difference between two neighboring modes is constant. Estimate the pulse width when 10,000

modes in a fiber laser are mode locked in this way. Assume a ring cavity of 5-m perimeter.

5.6 Explain how XPM can be used to induce mode locking in fiber lasers. Use diagrams as necessary.

5.7 The absorption of a fast saturable absorber saturates with power P as $\alpha = \alpha_0(1+P/P_{\text{sa}})^{-1}$, where P_{sa} is the saturation power. Estimate the extent of pulse shortening occurring when a 1-ps hyperbolic-secant pulse of peak power $P_0 = 100P_{\text{sa}}$ passes through the saturable absorber. Assume that only 0.1% of low-power light is transmitted.

5.8 Explain the mode-locking process in a figure-8 fiber laser. What limits the pulse width in such lasers?

5.9 How can nonlinear birefringence be used to advantage for passive mode locking of fiber lasers? Draw the laser cavity schematically and explain the purpose of each component.

5.10 What is the origin of sidebands often seen in the spectrum of pulses emitted from passively mode-locked fiber lasers? Derive an expression for their frequencies.

References

[1] E. Snitzer, *Phys. Rev. Lett.* **7**, 444 (1961).

[2] J. Stone and C. A. Burrus, *Appl. Phys. Lett.* **23**, 388 (1973); *Appl. Opt.* **13**, 1256 (1974).

[3] M. I. Dzhibladze, Z. G. Esiashvili, E. S. Teplitskii, S. K. Isaev, and V. R. Sagaradze, *Sov. J. Quantum Electron.* **13**, 245 (1983).

[4] R. J. Mears, L. Reekie, S. B. Poole, and D. N. Payne, *Electron. Lett.* **21**, 738 (1985).

[5] L. Reekie, R. J. Mears, S. B. Poole, and D. N. Payne, *J. Lightwave Technol.* **4**, 956 (1986).

[6] I. M. Jauncey, L. Reekie, R. J. Mears, D. N. Payne, C. J. Rowe, D. C. J. Reid, I. Bennion, and C. Edge, *Electron. Lett.* **22**, 987 (1986).

[7] I. P. Alcock, A. I. Ferguson, D. C. Hanna, and A. C. Tropper, *Opt. Lett.* **11**, 709 (1986); *Electron. Lett.* **22**, 268 (1986).

[8] M. Shimizu, H. Suda, and M. Horiguchi, *Electron. Lett.* **23**, 768 (1987).

[9] L. Reekie, I. M. Jauncey, S. B. Poole, and D. N. Payne, *Electron. Lett.* **23**, 884 (1987); *Electron. Lett.* **23**, 1078 (1987).

[10] W. J. Miniscalco, L. J. Andrews, B. A. Thompson, R. S. Quimby, L. J. B. Vacha, and M. G. Drexhage, *Electron. Lett.* **24**, 28 (1988).
[11] I. M. Jauncey, L. Reekie, J. E. Townsend, D. N. Payne, and C. J. Rowe, *Electron. Lett.* **24**, 24 (1988).
[12] K. Liu, M. Digonnet, K. Fesler, B. Y. Kim, and H. J. Shaw, *Electron. Lett.* **24**, 838 (1988).
[13] Y. Kimura and M. Nakazawa, *J. Appl. Phys.* **64**, 518 (1988).
[14] D. C. Hanna, R. M. Percival, I. M. Perry, R. G. Smart, and A. C. Trooper, *Electron. Lett.* **24**, 1068 (1988).
[15] M. E. Fermann, D. C. Hanna, D. P. Shepherd, and J. E. Townsend, *Electron. Lett.* **24**, 1135 (1988).
[16] G. T. Maker and A. I. Ferguson, *Electron. Lett.* **24**, 1160 (1988).
[17] I. N. Duling, L. Goldberg, and J. F. Weller, *Electron. Lett.* **24**, 1333 (1988).
[18] M. C. Brierley, P. W. France, and C. A. Miller, *Electron. Lett.* **24**, 539 (1988).
[19] M. C. Farries, P. R. Morkel, and J. E. Townsend, *Electron. Lett.* **24**, 709 (1988).
[20] L. Esterowitz, R. Allen, and I. Aggarwal, *Electron. Lett.* **24**, 1104 (1988).
[21] D. C. Hanna, R. M. Percival, I. R. Perry, R. G. Smart, P. J. Suni, J. E. Townsend, and A. C. Trooper, *Electron. Lett.* **24**, 1111 (1988).
[22] R. Wyatt, B. J. Ainslie, and S. P. Craig, *Electron. Lett.* **24**, 1362 (1988).
[23] M. S. O'Sullivan, J. Chrostowski, E. Desurvire, and J. R. Simpson, *Opt. Lett.* **14**, 438 (1989).
[24] K. Susuki, Y. Kimura, and M. Nakazawa, *Jpn. J. Appl. Phys.* **28**, L1000 (1989).
[25] P. L. Scrirener, E. J. Tarbox, and P. D. Maton, *Electron. Lett.* **25**, 549 (1989).
[26] W. J. Barnes, S. B. Poole, J. E. Townsend, L. Reekie, D. J. Taylor, and D. N. Payne, *J. Lightwave Technol.* **7**, 1461 (1989).
[27] M. C. Farries, P. R. Morkel, R. I. Laming, T. A. Birks, D. N. Payne, and E. J. Tarbox, *J. Lightwave Technol.* **7**, 1473 (1989).
[28] Y. Kimura, K. Susuki, and M. Nakazawa, *Opt. Lett.* **14**, 999 (1989).
[29] R. Wyatt, *Electron. Lett.* **26**, 1498 (1989).
[30] M. J. F. Digonnet, Ed., *Rare Earth Doped Fiber Lasers and Amplifiers* (Marcel Dekker, New York, 1993).
[31] I. N. Duling III, Ed., *Compact Sources of Ultrashort Pulses* (Cambridge University Press, New York, 1995).
[32] G. P. Agrawal, *Fiber-Optic Communication Systems*, 2nd ed. (Wiley, New York, 1997).
[33] R. Kashyap, *Fiber Bragg Gratings* (Academic Press, San Diego, CA, 1999), Chap. 8.
[34] A. E. Siegman, *Lasers* (University Science Books, Mill Valley, CA, 1986).
[35] W. T. Silfvast, *Laser Fundamentals* (Cambridge University Press, New York, 1996).

[36] O. Svelto, *Principles of Lasers*, 4th ed. (Plenum, New York, 1998).

[37] D. C. Hanna, R. M. Percival, I. R. Perry, R. G. Smart, J. E. Townsend, and A. C. Tropper, *Opt. Commun.* **78**, 187 (1990).

[38] J. Y. Allain, M. Monerie, and H. Poignant, *Electron. Lett.* **26**, 166 (1990); *Electron. Lett.* **26**, 261(1990); *Electron. Lett.* **27**, 189 (1991).

[39] R. G. Smart, D. C. Hanna, A. C. Trooper, S. T. Davey, S. F. Carter, and D. Szebesta, *Electron. Lett.* **27**, 1307 (1991).

[40] D. S. Funk, S. B. Stevens, and J. G. Eden, *IEEE Photon. Technol. Lett.* **5**, 154 (1993).

[41] S. Sanders, R. G. Waarts, D. G. Mehuys, and D. F. Welch, *Appl. Phys. Lett.* **67**, 1815 (1995).

[42] R. Scheps, *Prog. Quantum Electron.* **20**, 271 (1996).

[43] E. B. Mejia, A. N. Starodumov, and Y. O. Barmenkov, *Appl. Phys. Lett.* **74**, 1540 (1999).

[44] R. P. Kashyap, I. R. Armitage, R. Wyatt, S. T. Davey, and D. L. Williams, *Electron. Lett.* **26**, 730 (1990).

[45] G. A. Ball, W. W. Morey, and W. H. Glenn, *IEEE Photon. Technol. Lett.* **3**, 613 (1991).

[46] D. B. Mortimore, *J. Lightwave Technol.* **6**, 1217 (1988).

[47] P. Barnsley, P. Urquhart, C. A. Miller, and M. C. Brierley, *J. Opt. Soc. Am. A* **5**, 1339 (1988).

[48] H. Po, J. D. Cao, B. M. Laliberte, R. A. Minns, R. F. Robinson, B. H. Rockney, R. R. Tricca, and Y. H. Zhang, *Electron. Lett.* **29**, 1500 (1993).

[49] L. Zenteno, *J. Lightwave Technol.* **11**, 1435 (1993).

[50] T. Weber, W. Luthy, H. P. Weber, V. Neuman, H. Berthou, G. Kotrotsios, J. P. Dan, and H. E. Hintermann, *IEEE J. Quantum Electron.* **31**, 326 (1995).

[51] W. Luthy and T. Weber, *Opt. Eng.* **34**, 2361 (1995).

[52] H. Zellmer, U. Willamowski, A. Tunnermann, H. Welling, S. Unger, V. Reichel, H.-R. Muller, T. Kirchhof, and P. Albers, *Opt. Lett.* **20**, 578 (1995).

[53] P. R. Morkel, in *Rare Earth Doped Fiber Lasers and Amplifiers*, M. J. F. Digonnet, Ed. (Marcel Dekker, New York, 1993), Chap. 6.

[54] Y. Chaoyu, P. Jiangde, and Z. Bingkun, *Electron. Lett.* **25**, 101 (1989).

[55] F. Hakimi, H. Po, T. Tumminelli, B. C. McCollum, L. Zenteno, N. M. Cho, and E. Snitzer, *Opt. Lett.* **14**, 1060 (1989).

[56] W. L. Barnes, P. R. Morkel, L. Reekie, and D. N. Payne, *Opt. Lett.* **14**, 1002 (1989).

[57] Y. Kimura, K. Susuki, and M. Nakazawa, *Opt. Lett.* **14**, 999 (1989).

[58] K. Iwatsuki, H. Okumura, and M. Saruwatari, *Electron. Lett.* **26**, 2033 (1990).

[59] G. J. Cowle, D. N. Payne, and D. Reid, *Electron. Lett.* **27**, 229 (1991).

[60] J. L. Zyskind, J. W. Sulhoff, Y. Sun, J. W. Stone, L. W. Stulz, G. T. Harvey, D. J. DiGiovanni, H. M. Presby, A. Piccirilli, U. Koren, and R. M. Jopson, *Electron. Lett.* **27**, 1950 (1991).

[61] J. L. Zyskind, J. W. Sulhoff, J. W. Stone, D. J. DiGiovanni, L. W. Stultz, H. M. Presby, A. Piccirilli, and P. E. Pramayon, *Electron. Lett.* **27**, 2148 (1991).

[62] N. K. Park, J. W. Dawson, and K. J. Vahala, *Appl. Phys. Lett.* **59**, 2369 (1991).

[63] D. A. Smith, M. W. Maeda, J. J. Johnson, J. S. Patel, M. A. Saifi, and A. V. Lehman, *Opt. Lett.* **16**, 387 (1991).

[64] H. Schmuck, T. H. Pfeiffer, and G. Veith, *Electron. Lett.* **27**, 2117 (1991).

[65] T. H. Pfeiffer, H. Schmuck, and H. Blow, *IEEE Photon. Technol. Lett.* **4**, 847 (1992).

[66] P. D. Humphrey and J. E. Bowers, *IEEE Photon. Technol. Lett.* **5**, 32 (1993).

[67] C. V. Poulsen and M. Sejka, *IEEE Photon. Technol. Lett.* **5**, 646 (1993).

[68] Y. T. Chieng and R. A. Minasian, *IEEE Photon. Technol. Lett.* **6**, 153 (1994).

[69] G. A. Ball and W. W. Morey, *Opt. Lett.* **17**, 420 (1992).

[70] G. A. Ball and W. H. Glenn, *J. Lightwave Technol.* **10**, 1338 (1982).

[71] J. L. Zyskind, V. Mizrahi, D. J. DiGiovanni, and J. W. Sulhoff, *Electron. Lett.* **28**, 1385 (1992).

[72] S. V. Chernikov, R. Kashyap, P. F. McKee, and J. R. Taylor, *Electron. Lett.* **29**, 1089 (1993).

[73] S. V. Chernikov, J. R. Taylor, and R. Kashyap, *Opt. Lett.* **18**, 2024 (1993); *Electron. Lett.* **29**, 1788 (1993).

[74] J. T. Kringlebton, P. R. Morkel, L. Reekie, J. L. Archambault, and D. N. Payne, *IEEE Photon. Technol. Lett.* **5**, 1162 (1993).

[75] G. A. Ball, C. E. Holton, G. Hull-Allen, and W. W. Morey, *IEEE Photon. Technol. Lett.* **6**, 192 (1994).

[76] W. H. Loh, R. I. Lamming, and M. N. Zervas, *Appl. Phys. Lett.* **66**, 3422 (1995).

[77] W. H. Loh and R. I. Lamming, *Electron. Lett.* **31**, 1440 (1995).

[78] M. Sejka, P. Varming, J. Hübner, and M. Kristensen, *Electron. Lett.* **31**, 1445 (1995).

[79] A. J. Gloag, N. Langford, I. Bennion, and L. Zhang, *Opt. Commun.* **123**, 553 (1996).

[80] J. L. Archambault and S. G. Grubb, *J. Lightwave Technol.* **15**, 1378 (1997).

[81] K. Hsu, W. H. Loh, L. Dong, and C. M. Miller, *J. Lightwave Technol.* **15**, 1438 (1997).

[82] W. H. Loh, B. N. Samson, L. Dong, G. J. Cowle, and K. Hsu, *J. Lightwave Technol.* **16**, 114 (1998).

[83] G. P. Agrawal and N. K. Dutta, *Semiconductor Lasers*, 2nd ed. (Van Nostrand Reinhold, New York, 1993).

[84] J. Chow, G. Town, B. Eggleton, M. Isben, K. Sugden, and I. Bennion, *IEEE Photon. Technol. Lett.* **8**, 60 (1996).

[85] O. Graydon, W. H. Loh, R. I. Laming, and L. Dong, *IEEE Photon. Technol. Lett.* **8**, 63 (1996).

[86] S. Yamashita and K. Hotate, *Electron. Lett.* **32**, 1298 (1996).

[87] N. Park and P. F. Wysocki, *IEEE Photon. Technol. Lett.* **8**, 1459 (1996).

[88] J. Hübner, P. Varming, and M. Kristensen, *Electron. Lett.* **33**, 139 (1997).

[89] S. Yamashita, K. Hsu, and W. H. Loh, *IEEE J. Sel. Topics Quantum Electron.* **3**, 1058 (1997).

[90] N. J. C. Libatique and R. K. Jain, *IEEE Photon. Technol. Lett.* **11**, 1584 (1999).

[91] J. Sun, J. Qiu, and D. Huang, *Opt. Commun.* **182**, 193 (2000).

[92] J. E. Pedersen, M. C. Brierley, S. F. Carter, and P. W. France, *Electron. Lett.* **26**, 329 (1990).

[93] T. Sugawa, Y. Miyajima, and T. Komukai, *Electron. Lett.* **26**, 2042 (1990).

[94] Y. Durteste, M. Monerie, J. Y. Allain, and H. Poignant, *Electron. Lett.* **27**, 628 (1991).

[95] S. F. Carter, D. Szebesta, S. T. Davey, R. Wyatt, M. C. Brierley, and P. W. France, *Electron. Lett.* **27**, 628 (1991).

[96] Y. Shi, C. V. Poulsen, M. Sejka, M. Isben, and O. Poulsen, *Electron. Lett.* **29**, 1426 (1993).

[97] A. C. Trooper, J. N. Carter, R. D. T. Lauder, D. C. Hanna, S. T. Davey, and D. Szebesta, *J. Opt. Soc. Am. B* **5**, 886 (1994).

[98] I. J. Booth, C. J. MacKechnie, and B. F. Ventrudo, *IEEE J. Quantum Electron.* **32**, 118 (1996).

[99] R. Paschotta, N. Moore, W. A. Clarkson, A. C. Trooper, D. C. Hanna, and G. Mazé, *IEEE J. Sel. Topics Quantum Electron.* **3**, 1100 (1997).

[100] F. J. McAleavey, J. O'Gorman, J. F. Donegan, B. D. MacCraith, J. Hegarty, and G. Mazé, *IEEE J. Sel. Topics Quantum Electron.* **3**, 1103 (1997).

[101] Y. Miyajima, T. Komukai, and T. Sugawa, *Electron. Lett.* **29**, 663 (1993).

[102] R. M. Percival, D. Szebesta, and S. T. Davey, *Electron. Lett.* **28**, 2231 (1992).

[103] K. Oh, T. F. Morse, A. Kilian, L. Reinhart, and P. M. Weber, *Opt. Lett.* **19**, 278 (1994).

[104] J. Y. Allain, M. Monerie, and H. Poignant, *Electron. Lett.* **28**, 988 (1992).

[105] J. Y. Allain, J.-F. Bayon, M. Monerie, P. Bernage, and P. Niay, *Electron. Lett.* **29**, 309 (1993).

[106] V. Dominic, S. MacCormack, R. Waarts, S. Sanders, S. Bicknese, R. Dohle, E. Wolak, P. S. Yeh, and E. Zucker, *Electron. Lett.* **35**, 1158 (1999).

[107] J. M. Sousa, J. Nilsson, C. C. Renaud, J. A. Alvarez-Chavez, A. B. Grudinin, and J. D. Minelly, *IEEE Photon. Technol. Lett.* **11**, 39 (1999).

[108] I. Zawischa, K. Plamann, C. Fallnich, H. Welling, H. Zellmer, and A. Tunnermann, *Opt. Lett.* **24**, 469 (1999).

[109] G. H. M. van Tartwijk and G. P. Agrawal, *Prog. Quant. Electron.* **22**, 43 (1998).

[110] P. LeBoudec, M. Le Flohic, P. I. François, F. Sanchez, and G. Stefan, *Opt. Quantum Electron.* **25**, 359 (1993).

[111] F. Sanchez, P. LeBoudec, P. I. François, and G. Stefan, *Phys. Rev. A* **48**, 2220 (1993).

[112] M. Dinand and C. Schütte, *J. Lightwave Technol.* **13**, 14 (1995).

[113] R. Rangel-Rojo and M. Mohebi, *Opt. Commun.* **137**, 98 (1997).

[114] S. Bielawski, D. Derozier, and P. Glorieux, *Phys. Rev. A* **46**, 2811 (1992).

[115] M. Haeltermann, S. Trillo, and S. Wabnitz, *Phys. Rev. A* **47**, 2344 (1993).

[116] E. Lacot, F. Stoeckel, and M. Chenevier, *Phys. Rev. A* **49**, 3997 (1994).

[117] F. Sanchez and G. Stefan, *Phys. Rev. E* **53**, 2110 (1996).

[118] Q. L. Williams, J. Garcia-Ojalvo, and R. Roy, *Phys. Rev. A* **55**, 2376 (1997).

[119] L. G. Luo, T. J. Lee, and P. L. Chu, *J. Opt. Soc. Am. B* **15**, 972 (1998).

[120] H. D. I. Abarbanel, M. B. Kennel, M. Buhl, and C. T. Lewis, *Phys. Rev. A* **60**, 2360 (1999).

[121] G. D. van Wiggeren and R. Roy, *Science* **279**, 2524 (1998); *Phys. Rev. Lett.* **81**, 3547 (1998).

[122] L. G. Luo and P. L. Chu, *J. Opt. Soc. Am. B* **15**, 2524 (1998).

[123] G. D. van Wiggeren and R. Roy, *Int. J. Bifur. Chaos* **9**, 2129 (1999).

[124] L. G. Luo, P. L. Chu, and H. F. Liu, *IEEE Photon. Technol. Lett.* **12**, 269 (2000).

[125] Y. Shi, J. P. Ragey, and O. Poulsen, *IEEE J. Quantum Electron.* **29**, 1402 (1993).

[126] P. R. Morkel, K. P. Jedrzejewski, and E. R. Taylor, *IEEE J. Quantum Electron.* **29**, 2178 (1993).

[127] I. Abdulhalim, C. N. Pannell, L. Reekie, K. P. Jedrzejewski, E. R. Taylor, and D. N. Payne, *Opt. Commun.* **99**, 355 (1993).

[128] O. G. Okhotnikov and J. R. Salcedo, *Electron. Lett.* **30**, 702 (1994).

[129] S. V. Chernikov, Y. Zhu, J. R. Taylor, and V. P. Gapontse, *Opt. Lett.* **22**, 298 (1997).

[130] R. Paschotta, R. Haring, E. Gini. H. Melchior, U. Keller, H. L. Offerhaus, and D. J. Richardson, *Opt. Lett.* **24**, 388 (1999).

[131] C. C. Renaud, R. J. Selvas-Aguilar, J. Nilsson, P. W. Turner, and A. B. Grudinin, *IEEE Photon. Technol. Lett.* **8**, 976 (1999).

[132] J. M. Sousa and O. G. Okhotnikov, *IEEE Photon. Technol. Lett.* **8**, 1117 (1999).

[133] J. A. Alvarez-Chavez, H. L. Offerhaus, J. Nilsson, P. W. Turner, W. A. Clarkson, and D. J. Richardson, *Opt. Lett.* **25**, 37 (2000).

[134] D. C. Hanna, A. Kazer, M. W. Phillips, D. P. Shepherd, and P. I. Suni, *Electron. Lett.* **25**, 95 (1989).

[135] I. N. Duling III, *Laser Focus* **29** (4), 213 (1993).

[136] K. Smith and J. K. Lucek, *Laser Focus* **29** (10), 85 (1993).

[137] M. E. Fermann, A. Galvanauskas, G. Sucha, and D. Harter, *Appl. Phys. B* **65**, 259 (1997).

[138] L. E. Nelson, D. J. Jones, K. Tamura, H. A. Haus, and I. P. Ippen, *Appl. Phys. B* **65**, 277 (1997).

[139] D. J. Kuizenga and A. E. Siegman, *IEEE J. Quantum Electron.* **6**, 694 (1970).

[140] H. A. Haus, *J. Appl. Phys.* **46**, 3049 (1975); *IEEE J. Quantum Electron.* **11**, 323 (1975).

[141] H. A. Haus, in *Compact Sources of Ultrashort Pulses*, I. N. Duling III, Ed., (Cambridge University Press, New York, 1995).

[142] F. X. Kärtner, D. Kopf, and U. Keller, *J. Opt. Soc. Am. B* **12**, 486 (1995).

[143] K. Noguchi, O. Mitomi, and H. Miyazawa, *J. Lightwave Technol.* **16**, 615 (1998).

[144] J. D. Kafka, T. Baer, and D. W. Hall, *Opt. Lett.* **14**, 1269 (1989).

[145] K. Smith, J. R. Armitage, R. Wyatt, N. J. Doran, and S. M. J. Kelly, *Electron. Lett.* **26**, 1149 (1990).

[146] A. Takada and H. Miyazawa, *Electron. Lett.* **26**, 216 (1990).

[147] H. Takara, S. Kawanishi, M. Saruwatari, and K. Noguchi, *Electron. Lett.* **28**, 2095 (1992).

[148] X. Shan, D. Cleland, and A. Elis, *Electron. Lett.* **28**, 182 (1992).

[149] G. T. Harvey and L. F. Mollenauer, *Opt. Lett.* **18**, 107 (1993).

[150] F. Fontana, G. Bordogna, P. Franco, M. Midrio, and M. Romagnoli, *Electron. Lett.* **29**, 1652 (1993).

[151] T. Pfeiffer and G. Veith, *Electron. Lett.* **29**, 1849 (1993).

[152] D. M. Pataca, M. L. Rocha, K. Smith, T. J. Whitley, and R. Wyatt, *Electron. Lett.* **30**, 964 (1994).

[153] M. Nakazawa, E. Yoshida, and Y. Kimura, *Electron. Lett.* **30**, 1603 (1994).

[154] E. Marti-Panameno, J. J. Sanchez-Mondragon, and V. A. Vysloukh, *IEEE J. Quantum Electron.* **30**, 822 (1994).

[155] E. Yoshida, Y. Kimura, and M. Nakazawa, *Electron. Lett.* **31**, 377 (1995).

[156] T. F. Carruthers and I. N. Duling III, *Opt. Lett.* **21**, 1927 (1996).

[157] H. A. Haus, D. J. Jones, E. P. Ippen, and W. S. Wong, *J. Lightwave Technol.* **14**, 622 (1996).

[158] D. J. Jones, H. A. Haus, and E. P. Ippen, *Opt. Lett.* **21**, 1818 (1996).

[159] M. Baldo, G. E. Town, and M. Romagnoli, *Opt. Commun.* **140**, 19 (1997).

[160] J. S. Wey, J. Goldhar, and G. L. Burdge, *J. Lightwave Technol.* **15**, 1171 (1997).

[161] C. X. Shi, *J. Opt. Commun.* **19**, 27 (1998).
[162] B. Bakshi, P. A. Andrekson, and X. Zhang, *Electron. Lett.* **34**, 884 (1998).
[163] Y. Zhao and C. Shu, *Appl. Phys. Lett.* **72**, 1556 (1998).
[164] M. Y. Jeon, H. K. Lee, K. H. Kim, E. H. Lee, W. Y. Oh, B. Y. Kim, and H. W. Lee, *Opt. Commun.* **149**, 312 (1998).
[165] R. Kiyan, O. Deparis, O. Pottiez, P. Megret, and M. Blondel, *Opt. Lett.* **24**, 1029 (1999).
[166] K. S. Abedin, N. Onodera, and M. Hyodo, *Opt. Lett.* **24**, 1564 (1999).
[167] A. D. Ellis, R. J. Manning, I. D. Phillips, and D. Nesset, *Electron. Lett.* **35**, 645 (1999).
[168] E. Yoshida and M. Nakazawa, *IEEE Photon. Technol. Lett.* **10**, 1753 (1998); *IEEE Photon. Technol. Lett.* **11**, 548 (1999).
[169] E. Yoshida, N. Shimizu, and M. Nakazawa, *IEEE Photon. Technol. Lett.* **11**, 1587 (1999).
[170] B. Bakshi and P. A. Andrekson, *IEEE Photon. Technol. Lett.* **11**, 1387 (1999); *Electron. Lett.* **36**, 411 (2000).
[171] T. F. Carruthers, I. N. Duling III, M. Horowitz, and C. R. Menyuk, *Opt. Lett.* **25**, 153 (2000).
[172] M. Horowitz, C. R. Menyuk, T. F. Carruthers, and I. N. Duling III, *IEEE Photon. Technol. Lett.* **12**, 266 (2000).
[173] J. Li, P. A. Andrekson, and B. Bakshi, *IEEE Photon. Technol. Lett.* **12**, 1150 (2000).
[174] E. R. Thoen, M. E. Grein, E. M. Koontz, E. P. Ippen, H. A. Haus, and L. A. Kolodziejski, *Opt. Lett.* **25**, 948 (2000).
[175] E. J. Greer and K. Smith, *Electron. Lett.* **28**, 1741 (1992).
[176] J. K. Lucek and K. Smith, *Opt. Lett.* **18**, 12,226 (1993).
[177] M. Obro, K. Lucek, K. Smith, and K. J. Blow, *IEEE Photon. Technol. Lett.* **6**, 799 (1994).
[178] D. S. Peter, G. Onishchukov, W. Hodel, and H. P. Weber, *Electron. Lett.* **30**, 1595 (1994).
[179] T. Aakjer and J. H. Povlsen, *Opt. Commun.* **112**, 315 (1994).
[180] E. M. Dianov, T. R. Martirosian, O. G. Okhotnikov, V. M. Paramonov, and A. M. Prokhorov, *Sov. Lightwave Commun.* **2**, 275 (1992).
[181] O. G. Okhotnikov, F. M. Araujo, and J. R. Salcedo, *IEEE Photon. Technol. Lett.* **6**, 933 (1994).
[182] D. U. Noske, A. Boskovic, M. J. Guy, and J. R. Taylor, *Electron. Lett.* **29**, 1863 (1993).
[183] C. R. Ó. Cochláin, R. J. Mears, and G. Sherlock, *IEEE Photon. Technol. Lett.* **5**, 25 (1993).
[184] D. M. Patrick, *Electron. Lett.* **30**, 43 (1994).

[185] H. Sabert and E. Brinkmeyer, *Electron. Lett.* **29**, 2124 (1993); *J. Lightwave Technol.* **12**, 1360 (1994).

[186] F. Fontana, N. Ridi, M. Romagnoli, and P. Franco, *Opt. Commun.* **107**, 240 (1994).

[187] M. Romagnoli, S. Wabnitz, P. Franco, M. Midrio, F. Fontana, and G. E. Town, *J. Opt. Soc. Am. B* **12**, 72 (1992).

[188] D. O. Culverhouse, D. J. Richardson, T. A. Birks, and P. S. J. Russell, *Opt. Lett.* **20**, 2381 (1995).

[189] M. Zirngibl, L. W. Stulz, J. Stone, J. Hugi, D. DiGiovanni, and P. B. Hansen, *Electron. Lett.* **27**, 1734 (1991).

[190] W. H. Loh, D. Atkinson, P. R. Morkel, M. Hopkinson, A. Rivers, A. J. Seeds, and D. N. Payne, *IEEE Photon. Technol. Lett.* **5**, 35 (1993).

[191] W. H. Loh, D. Atkinson, P. R. Morkel, M. Hopkinson, A. Rivers, A. J. Seeds, and D. N. Payne, *Appl. Phys. Lett.* **63**, 4 (1993).

[192] W. H. Loh, D. Atkinson, P. R. Morkel, R. Grey, A. J. Seeds, and D. N. Payne, *Electron. Lett.* **29**, 808 (1993).

[193] E. A. De Souza, M. N. Islam, C. E. Soccolich, W. Pleibel, R. H. Stolen, J. R. Simpson, and D. J. DiGiovanni, *Electron. Lett.* **29**, 447 (1993).

[194] D. Abraham, R. Nagar, V. Mikhelashvili, and G. Eisenstein, *Appl. Phys. Lett.* **63**, 2857 (1993).

[195] B. C. Barnett, L. Rahman, M. N. Islam, Y. C. Chen, P. Bhattacharya, W. Riha, K. V. Reddy, A. T. Howe, K. A. Stair, H. Iwamura, S. R. Friberg, and T. Mukai, *Opt. Lett.* **20**, 471 (1995).

[196] B. C. Collings, K. Bergman, S. T. Cundiff, S. Tsuda, J. N. Kutz, J. E. Cunningham, W. Y. Jan, M. Koch, and W. H. Knox, *IEEE J. Sel. Topics Quantum Electron.* **3**, 1065 (1997).

[197] B. C. Collings, K. Bergman, and W. H. Knox, *Opt. Lett.* **23**, 123, (1998).

[198] M. Hofer, M. E. Fermann, and L. Goldberg, *IEEE Photon. Technol. Lett.* **10**, 1247, (1998).

[199] M. Jiang, G. Sucha, M. E. Fermann, J. Jimenez, D. Harter, M. Dagenais, S. Fox, and Y. Hu, *Opt. Lett.* **24**, 1074 (1999).

[200] J. W. Haus, M. Hapduk, W. Kaechele, G. Shaulov, J. Theimer, K. Teegarden, and G. Wicks, *Opt. Commun.* **174**, 204 (2000).

[201] D. J. Richardson, R. I. Laming, D. N. Payne, V. Matsas, and M. W. Phillips, *Electron. Lett.* **27**, 542 (1991).

[202] I. N. Duling III, *Electron. Lett.* **27**, 544 (1991); *Opt. Lett.* **16**, 539 (1991).

[203] D. J. Richardson, R. I. Laming, D. N. Payne, M. W. Phillips, and V. Matsas, *Electron. Lett.* **27**, 730 (1991).

[204] D. J. Richardson, R. I. Laming, D. N. Payne, V. J. Matsas, and M. W. Phillips, *Electron. Lett.* **27**, 1451 (1991).

[205] M. Nakazawa, E. Yoshida, and Y. Kimura, *Appl. Phys. Lett.* **59**, 2073 (1991).

[206] D. J. Richardson, A. B. Grudinin, and D. N. Payne, *Electron. Lett.* **28**, 778 (1992).

[207] M. Nakazawa, E. Yoshida, and Y. Kimura, *Electron. Lett.* **29**, 63 (1993).

[208] A. B. Grudinin, D. J. Richardson, and D. N. Payne, *Electron. Lett.* **28**, 67 (1992).

[209] E. Yoshida, Y. Kimura, and M. Nakazawa, *Appl. Phys. Lett.* **60**, 932 (1992).

[210] M. L. Dennis and I. N. Duling III, *Electron. Lett.* **28**, 1894 (1992); *Electron. Lett.* **29**, 409 (1993); *Appl. Phys. Lett.* **62**, 2911 (1993).

[211] S. Wu, J. Strait, R. L. Fork, and T. F. Morse, *Opt. Lett.* **18**, 1444 (1993).

[212] M. J. Guy, D. U. Noske, and J. R. Taylor, *Opt. Lett.* **18**, 1447 (1993).

[213] D. U. Noske and J. R. Taylor, *Electron. Lett.* **29**, 2200 (1993).

[214] A. J. Stentz and R. W. Boyd, *Electron. Lett.* **30**, 1302 (1994); *Opt. Lett.* **19**, 1462 (1994).

[215] D. U. Noske, M. J. Guy, K. Rottwitt, R. Kashyap, and J. R. Taylor, *Opt. Commun.* **108**, 297 (1994).

[216] D. U. Noske, N. Pandit, and J. R. Taylor, *Opt. Commun.* **115**, 105 (1995).

[217] G. Town, J. Chow, and M. Romagnoli, *Electron. Lett.* **31**, 1452 (1995).

[218] W. Y. Oh, B. Y. Kim, and H. W. Lee, *IEEE J. Quantum Electron.* **32**, 333 (1996).

[219] T. O. Tsun, M. K. Islam, and P. L. Chu, *Opt. Commun.* **141**, 65 (1997).

[220] V. J. Matsas, T. P. Newson, D. J. Richardson, and D. N. Payne, *Electron. Lett.* **28**, 1391 (1992).

[221] V. J. Matsas, T. P. Newson, and M. N. Zervas, *Opt. Commun.* **92**, 61 (1992).

[222] D. U. Noske, N. Pandit, and J. R. Taylor, *Opt. Lett.* **17**, 1515 (1992); *Electron. Lett.* **28**, 2185 (1992).

[223] K. Tamura, H. A. Haus, and E. P. Ippen, *Electron. Lett.* **28**, 2226 (1992).

[224] K. Tamura, E. P. Ippen, H. A. Haus, and L. E. Nelson, *Opt. Lett.* **18**, 1080 (1993).

[225] M. E. Fermann, M. J. Andrejco, M. L. Stock, Y. Silberberg, and A. M. Weiner, *Appl. Phys. Lett.* **62**, 910 (1993).

[226] R. P. Davey, N. Langford, and A. I. Ferguson, *Electron. Lett.* **29**, 758 (1993).

[227] K. Tamura, J. Jacobseon, E. P. Ippen, H. A. Haus, and J. G. Fujimoto, *Opt. Lett.* **18**, 220 (1993).

[228] V. J. Matsas, D. J. Richardson, T. P. Newson, and D. N. Payne, *Opt. Lett.* **18**, 358 (1993).

[229] M. H. Ober, M. Hofer, and M. E. Fermann, *Opt. Lett.* **18**, 367 (1993).

[230] D. Abraham, R. Nagar, M. N. Ruberto, G. Eisenstein, U. Koren, J. L. Zyskind, and D. J. DiGiovanni, *IEEE Photon. Technol. Lett.* **5**, 377 (1993).

[231] V. J. Matsas, W. H. Loh, and D. J. Richardson, *IEEE Photon. Technol. Lett.* **5**, 492 (1993).

[232] M. E. Fermann, M. J. Andrejco, Y. Silberberg, and A. M. Weiner, *Opt. Lett.* **18**, 48 (1993).

[233] M. Nakazawa, E. Yoshida, T. Sugawa, and Y. Kimura, *Electron. Lett.* **29**, 1327 (1993).

[234] A. B. Grudinin, D. J. Richardson, and D. N. Payne, *Electron. Lett.* **29**, 1860 (1993).

[235] K. Tamura, L. E. Nelson, H. A. Haus, and E. P. Ippen, *Appl. Phys. Lett.* **64**, 149 (1994).

[236] K. Tamura, C. R. Doerr, L. E. Nelson, H. A. Haus, and E. P. Ippen, *Opt. Lett.* **19**, 46 (1994).

[237] M. E. Fermann, L.-M. Yang, M. L. Stock, and M. J. Andrejco, *Opt. Lett.* **19**, 43 (1994).

[238] W. H. Loh, A. B. Grudinin, and D. N. Payne, *Electron. Lett.* **30**, 413 (1994).

[239] M. E. Fermann, K. Sugden, and I. Bennion, *Opt. Lett.* **20**, 172 (1995).

[240] G. Lenz, K. Tamura, H. A. Haus, and E. P. Ippen, *Opt. Lett.* **20**, 1289 (1995).

[241] K. Tamura, E. P. Ippen, and H. A. Haus, *Appl. Phys. Lett.* **67**, 158 (1995).

[242] R. Hofer, M. Hofer, and G. A. Reider, *Opt. Commun.* **169**, 135 (1999).

[243] R. P. Davey, R. P. E. Fleming, K. Smith, R. Kashyap, and J. R. Armitage, *Electron. Lett.* **27**, 2087(1991).

[244] T. F. Carruthes, I. N. Duling III, and M. L. Dennis, *Electron. Lett.* **30**, 1051 (1994).

[245] D. J. Jones, L. E. Nelson, H. A. Haus, and E. P. Ippen, *IEEE J. Sel. Topics Quantum Electron.* **3**, 1076 (1997).

[246] M. E. Fermann, D. Harter, J. D. Minelly, and G. G. Vienne, *Opt. Lett.* **21**, 967 (1996).

[247] M. H. Ober, M. Hofer, G. A. Reider, G. D. Sucha, M. E. Fermann, D. Harter, C. A. C. Mendonca, and T. H. Chiu, *Opt. Lett.* **20**, 2305 (1995).

[248] M. Hofer, M. H. Ober, R. Hofer, M. E. Fermann. G. D. Sucha, D. Harter, K. Sugden, I. Bennion, C. A. C. Mendonca, and T. H. Chiu, *Opt. Lett.* **20**, 1701 (1995).

[249] M. H. Ober, G. D. Sucha, and M. E. Fermann, *Opt. Lett.* **20**, 195 (1995).

[250] H. G. Winful and D. T. Walton, *Opt. Lett.* **17**, 1688 (1992).

[251] R.-J. Essiambre and R. Vallé, *Opt. Commun.* **105**, 142 (1994).

[252] P. K. Cheo, L. Wang, and M. Ding, *IEEE Photon. Technol. Lett.* **8**, 66 (1996).

[253] D. W. Huang, G. C. Lin, and C. C. Yang, *IEEE J. Quantum Electron.* **35**, 138 (1999).

[254] A. G. Bulushev, E. M. Dianov, and O. G. Okhotnikov, *Opt. Lett.* **15**, 968 (1990); *Opt. Lett.* **16**, 88 (1991).

[255] H. A. Haus, J. G. Fujimoto, and E. P. Ippen, *J. Opt. Soc. Am. B* **8**, 2068 (1991).
[256] P. A. Bélanger, *J. Opt. Soc. Am. B* **8**, 2077 (1991).
[257] H. A. Haus and E. P. Ippen, *Opt. Lett.* **16**, 1331 (1991).
[258] S. M. J. Kelly, K. Smith, K. J. Blow, and N. J. Doran, *Opt. Lett.* **16**, 1337 (1991).
[259] M. P. Soerensen, K. A. Shore, T. Geisler, P. L. Christiansen, J. Mork, and J. Mark, *Opt. Commun.* **90**, 65 (1992).
[260] T. Geisler, K. A. Shore, M. P. Soerensen, P. L. Christiansen, J. Mork, and J. Mark, *J. Opt. Soc. Am. B* **10**, 1166 (1993).
[261] M. L. Dennis and I. N. Duling III, *Appl. Phys. Lett.* **63**, 2911 (1993).
[262] V. Tzelepis, S. Markatos, S. Kalpogiannis, T. Sphicopoulos, and C. Caroubalos, *J. Lightwave Technol.* **11**, 1729 (1993).
[263] V. Tzelepis, Th. Sphicopoulos, and C. Caroubalos, *IEEE Photon. Technol. Lett.* **6**, 47 (1994).
[264] I. N. Duling III, C.-J. Chen, P. K. A. Wai, and C. R. Menyuk, *IEEE J. Quantum Electron.* **30**, 194 (1994).
[265] H. A. Haus, E. P. Ippen, and K. Tamura, *IEEE J. Quantum Electron.* **30**, 200 (1994).
[266] C. J. Chen, P. K. A. Wai, and C. R. Menyuk, *Opt. Lett.* **19**, 198 (1994); *Opt. Lett.* **20**, 350 (1995).
[267] G. Sucha, S. R. Bolton, S. Weiss, and D. S. Chemla, *Opt. Lett.* **20**, 1794 (1995).
[268] M. Margalit and M. Orenstein, *Opt. Commun.* **124**, 475 (1996).
[269] S. Namiki and H. A. Haus, *IEEE J. Quantum Electron.* **33**, 649 (1997); C. X. Yu, S. Namiki, and H. A. Haus, *IEEE J. Quantum Electron.* **33**, 660 (1997).
[270] G. H. M. van Tartwijk and G. P. Agrawal, *J. Opt. Soc. Am. B* **14**, 2618 (1997).
[271] J. N. Kutz, B. C. Collings, K. Bergman, S. Tsuda, S. T. Cundiff, W. H. Knox, P. Holmes, and M. Weinstein, *J. Opt. Soc. Am. B* **14**, 2681 (1997).
[272] N. N. Akhmediev, A. Ankiewicz, M. J. Lederer, and B. Luther-Davies, *Opt. Lett.* **23**, 280 (1988).
[273] G. H. M. van Tartwijk and G. P. Agrawal, *IEEE J. Quantum Electron.* **34**, 1854 (1998).
[274] D. Arbel and M. Orenstein, *IEEE J. Quantum Electron.* **35**, 977 (1999).
[275] S. M. J. Kelly, *Electron. Lett.* **28**, 806 (1992).
[276] N. Pandit, D. U. Noske, S. M. J. Kelly, and J. R. Taylor, *Electron. Lett.* **28**, 455 (1992).
[277] J. P. Gordon, *J. Opt. Soc. Am. B* **9**, 91 (1992).
[278] M. L. Dennis and I. N. Duling III, *IEEE J. Quantum Electron.* **30**, 1469 (1994).
[279] S. T. Cundiff, B. C. Collings, and W. H. Knox, *Opt. Exp.* **1**, 12 (1997).
[280] S. T. Cundiff, B. C. Collings, N. N. Akhmediev, J. M. Soto-Crespo, K. Bergman, and W. H. Knox, *Phys. Rev. Lett.* **82**, 3988 (1999).

[281] J. W. Haus, G. Shaulov, E. A. Kuzin, and J. Sanchez-Mondragon, *Opt. Lett.* **24**, 376 (1999).

[282] B. C. Collings, S. T. Cundiff, N. N. Akhmediev, J. M. Soto-Crespo, K. Bergman, and W. H. Knox, *J. Opt. Soc. Am. B* **17**, 354 (2000).

[283] J. M. Soto-Crespo, N. N. Akhmediev, B. C. Collings, S. T. Cundiff, K. Bergman, and W. H. Knox, *J. Opt. Soc. Am. B* **17**, 366 (2000).

[284] A. D. Kim, J. N. Kutz, and D. J. Muraki, *IEEE J. Quantum Electron.* **36**, 465 (2000).

Chapter 6

Pulse Compression

An important application of nonlinear fiber optics consists of compressing optical pulses. Pulses shorter than 5 fs have been produced by using the nonlinear and dispersive effects occurring simultaneously inside silica fibers. This chapter is devoted to the study of pulse-compression techniques, the theory behind them, and the experimental issues related to them. Section 6.1 presents the basic idea and introduces the two kinds of compressors commonly used for pulse compression. The grating-fiber compressors discussed in Section 6.2 use a fiber with normal group-velocity dispersion (GVD) followed by a grating pair. The soliton-effect compressors described in Section 6.3 make use of higher-order solitons forming when self-phase modulation (SPM) and anomalous GVD occur simultaneously. The use of fiber gratings for pulse compression is discussed in Section 6.4. Section 6.5 focuses on the technique of chirped-pulse amplification while Section 6.6 is devoted to dispersion-decreasing fibers. Several other techniques that use optical fibers for pulse compression are discussed in Section 6.7.

6.1 Physical Mechanism

The basic idea behind optical pulse compression is borrowed from *chirp radar*, where chirped pulses at microwave frequencies are compressed by passing them through a dispersive delay line [1]. The physical mechanism can be understood by referring to Section A.3.2, where propagation of chirped optical pulses in a linear dispersive medium is discussed. Such a medium imposes a dispersion-induced chirp on the pulse during its propagation. If the initial

chirp is in the opposite direction of that imposed by GVD, the two tend to cancel each other, resulting in an output pulse that is narrower than the input pulse.

To see how such cancellation can produce shorter pulses, consider the propagation of a chirped Gaussian pulse inside an optical fiber. The optical field after a distance z is given by Eq. (A.3.2.17). This equation can be written as

$$U(z,T) = [1 - i\xi(1+iC)]^{-1/2} \exp\left\{ -\frac{(1+iC)T^2}{2T_0^2[1 - i\xi(1+iC)]} \right\}, \qquad (6.1.1)$$

where $T = t - z/v_g$ is the reduced time, T_0 is the input pulse width, and C is the initial chirp. The propagation distance $\xi = z/L_D$ is normalized to the dispersion length $L_D = T_0^2/|\beta_2|$. For an unchirped pulse ($C = 0$), the GVD-induced chirp varies linearly across the pulse. This can be verified from Eq. (6.1.1) by calculating the chirp using $\delta\omega = -\partial\phi/\partial T$. It is easy to conclude that the input pulse should also be linearly chirped for maximum chirp cancellation.

Equation (6.1.1) can be used to find the compression factor $F_c = T_0/T_p$ as a function of propagation distance, where T_p is the width of the compressed Gaussian pulse. It is given by the simple expression

$$F_c(\xi) = [(1 + sC\xi)^2 + \xi^2]^{-1/2}, \qquad (6.1.2)$$

where $s = \mathrm{sgn}(\beta_2) = \pm 1$, depending on the nature of GVD. This equation shows that pulse is compressed only if $sC < 0$. This condition just states that chirp cancellation occurs only if the initial chirp and GVD-induced chirp are of opposite kinds. Positively chirped pulses ($C > 0$) require anomalous GVD for compression (and vice versa).

Equation (6.1.2) also shows that the shortest pulse is obtained only at a specific distance given by $\xi = |C|/(1+C^2)$. The maximum compression factor at that distance is also fixed by the input chirp and is $F_c = (1+C^2)$. This limit is easily understood by noting that spectrum of a chirped input pulse is broader by a factor of $1+C^2$ compared with that of an unchirped pulse. In the time domain, the compression process can be visualized as follows. Different frequency components of the pulse travel at different speeds in the presence of GVD. If the leading edge of the pulse is delayed by just the right amount to arrive nearly with the trailing edge, the output pulse is compressed. Positively chirped pulses (frequency increasing toward the trailing side) require anomalous or negative GVD in order to slow down the red-shifted leading edge. By

contrast, negatively chirped pulses require normal or positive GVD to slow down the blue-shifted leading edge.

Early pulse-compression studies made use of both normal and anomalous GVD, depending on the technique through which frequency chirp was initially imposed on the pulse [2]–[9]. In the case of negatively chirped pulses, pulses were transmitted through liquids or gases such that they experienced normal GVD [3]. In the case of positively chirped pulses, a grating pair was found to be most suitable for providing anomalous GVD [7]. In these early experiments, pulse compression did not make use of any nonlinear optical effects. Although the use of the nonlinear process of SPM for pulse compression was suggested as early as 1969 [10], the experimental work on SPM-based pulse compression took off only during the 1980s when the use of single-mode silica fibers as a nonlinear medium became widespread [11]–[29]. It led in 1987 to the creation of optical pulses as short as 6 fs in the 620-nm wavelength region [16]. By 1988, compression factors as large as 5000 had been attained. Such advances were possible only after the evolution of optical pulses in silica fibers was properly understood.

Pulse compressors based on nonlinear fiber optics can be classified into two broad categories: *grating-fiber* and *soliton-effect* compressors. In a grating-fiber compressor, the input pulse is propagated in the normal-dispersion regime of the fiber and then compressed externally using a grating pair. The role of fiber is to impose a nearly linear, positive chirp on the pulse through a combination of SPM and GVD. The grating pair provides the anomalous GVD required for compression of positively chirped pulses [7].

A soliton-effect compressor, in contrast, consists of only a piece of fiber whose length is suitably chosen. The input pulse propagates in the anomalous-GVD regime of the fiber and is compressed through an interplay between SPM and GVD. Compression occurs because of an initial pulse-narrowing phase through which all higher-order solitons go before the input shape is restored after one soliton period. The compression factor depends on the peak power of the pulse, which determines the soliton order N. The two types of compressors are complementary and generally operate in different regions of the optical spectrum. Grating-fiber compressors are useful for compressing pulses in the visible and near-infrared regions while soliton-effect compressors work typically in the range from 1.3 to 1.6 μm. The wavelength region near 1.3 μm offers special opportunities since both kinds of compressors can be combined to yield large compression factors by using dispersion-shifted fibers.

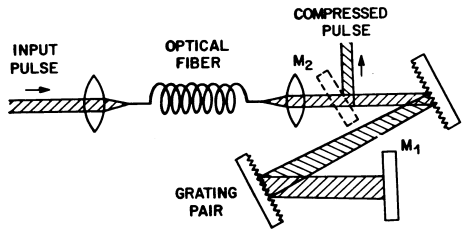

Figure 6.1 Schematic drawing of a grating-fiber compressor in the double-pass configuration. Mirror M_2 (shown dashed) is located above the plane of the figure. Mirror M_1 is slightly tilted to separate the outgoing beam from the incoming beam.

6.2 Grating-Fiber Compressors

In the visible and near-infrared regions ($\lambda < 1.3\ \mu$m), a grating-fiber compressor is commonly used for pulse compression [12]–[29]. Figure 6.1 shows such a compressor schematically in the double-pass configuration [17]. The input pulse is coupled into a single-mode fiber where it broadens spectrally and develops a positive chirp across its entire width. The output pulse is then sent through a grating pair where it experiences anomalous GVD and gets compressed. The optical beam is sent back through the grating pair to reconvert it to the original cross section. The mirror M_1 is slightly tilted to separate the outgoing beam from the incoming one. The mirror M_2 deflects the compressed pulse out of the compressor without introducing any additional losses.

6.2.1 Grating Pair

A pair of two parallel gratings acts as a dispersive delay line. Optical pulses propagating through such a grating pair behave as if they were transmitted through an optical fiber with anomalous GVD [7]. In this subsection we focus on the theory behind a grating pair [30]–[33].

When an optical pulse is incident at one grating of a pair of two parallel gratings, different frequency components associated with the pulse are diffracted at slightly different angles. As a result, they experience different time delays during their passage through the grating pair. It turns out that the blue-shifted components arrive earlier than the red-shifted components. In a positively chirped pulse, blue-shifted components occur near the trailing edge of the pulse whereas the leading edge consists of red-shifted components.

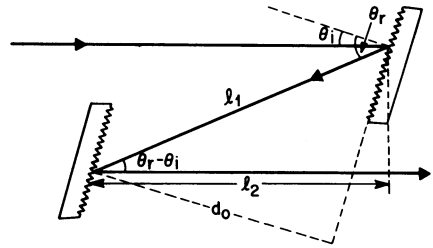

Figure 6.2 Geometry of a grating pair used as a dispersive delay line.

Thus, the trailing edge catches up with the leading edge during passage of the pulse through the grating pair, and the pulse is compressed.

Mathematically, the phase shift acquired by a specific spectral component of the pulse at the frequency ω passing through the grating pair is given by $\phi_g(\omega) = \omega l_p(\omega)/c$, where the optical path length $l_p(\omega)$ is obtained from Fig. 6.2 using simple geometrical arguments and is given by [32]

$$l_p(\omega) = l_1 + l_2 = d_0 \sec\theta_r[1 + \cos(\theta_r - \theta_i)], \tag{6.2.1}$$

where d_0 is the grating separation (see Fig. 6.2). The diffraction theory of gratings shows that when light is incident at an angle θ_i, the diffraction angle θ_r is given by Eq. (1.1.1). We use this relation and assume first-order diffraction ($m = 1$). The frequency dependence of θ_r is responsible for the dispersion induced by a grating pair.

If the spectral width of the optical pulse is a small fraction of its center frequency ω_0, it is useful to expand $\phi_g(\omega)$ in a Taylor series around ω_0 as

$$\phi_g(\omega) = \phi_0 + \phi_1(\omega - \omega_0) + \tfrac{1}{2}\phi_2(\omega - \omega_0)^2 + \tfrac{1}{6}\phi_3(\omega - \omega_0)^3 + \cdots, \tag{6.2.2}$$

where ϕ_0 is a constant and ϕ_1 is related to the transit time through the grating pair. The parameters ϕ_2 and ϕ_3 take into account the dispersive effects associated with the grating pair and can be obtained by expanding $l_p(\omega)$ in a Taylor series and using Eq. (1.1.1) for θ_r. The result is given by

$$\phi_2 = \frac{-8\pi^2 c b_0}{\omega_0^3 \Lambda^2 \cos^2\theta_{r0}}, \quad \phi_3 = \frac{24\pi^2 c b_0(1 + \sin\theta_i \sin\theta_{r0})}{\omega_0^4 \Lambda^2 \cos^4\theta_{r0}}, \tag{6.2.3}$$

where θ_{r0} is the diffraction angle for ω_0 and d_g is the center-to-center spacing between the gratings ($d_g = d_0 \sec\theta_{r0}$).

In most cases of practical interest, the spectral width of the pulse satisfies the condition $\Delta\omega \ll \omega_0$, and the cubic and higher-order terms in the expansion (6.2.2) can be neglected. If we ignore the unimportant constant and linear terms, the frequency-dependent part of the phase shift is governed by ϕ_2. Since ϕ_2 is negative from Eq. (6.2.3), a grating pair introduces anomalous GVD. This can be seen more clearly by considering the optical field at the output end of the grating pair. If $U_{\text{in}}(T)$ is the input field, the output field is given by

$$U_{\text{out}}(T) = \frac{1}{2\pi}\int_{-\infty}^{\infty} \tilde{U}_{\text{in}}(\omega-\omega_0)\exp\left[\frac{i}{2}\phi_2(\omega-\omega_0)^2 - i\omega T\right] d\omega, \qquad (6.2.4)$$

where $\tilde{U}_{\text{in}}$ is the Fourier transform of U_{in}. Comparing Eq. (6.2.4) with Eq. (A.3.2.5), the effective GVD parameter for a grating pair is given by $\beta_2^{\text{eff}} = \phi_2/d_g$. It is also possible to introduce an effective dispersion length as $L_D^{\text{eff}} = T_0^2/|\beta_2^{\text{eff}}|$, where T_0 is the input pulse width. An order of magnitude estimate of β_2^{eff} is obtained from Eqs. (6.2.3). In the visible region ($\lambda_0 \approx 0.5\ \mu$m), $\beta_2^{\text{eff}} \sim 1000$ ps^2/km if we use $\Lambda \sim 1\ \mu$m. This corresponds to $L_D^{\text{eff}} \sim 1$ m for $T_0 = 1$ ps.

The grating separation required for pulse compression depends on the amount of positive chirp; typically d_g is a fraction of L_D^{eff}. For subpicosecond pulses $d_g \sim 10$ cm or less. However, it becomes impractically large (~ 10 m) for $T_0 > 10$ ps. It is possible to increase β_2^{eff} by letting the pulse be incident at the grazing angle so that θ_{r0} in Eq. (6.2.3) approaches $\pi/2$. However, as is evident from this equation, such a scheme increases the contribution of third-order dispersion (TOD) and the cubic term in Eq. (6.2.2) must be included. Inclusion of the TOD term becomes necessary for ultrashort pulses ($T_0 \sim 10$ fs) whose bandwidth $\Delta\omega$ is comparable to ω_0 [47]. The effects of TOD can be minimized by using special gratings that are engraved directly on a prism [33].

A drawback of the grating pair is that spectral components of a pulse are dispersed not only temporally but also spatially. As a result, the optical beam diverges between the two gratings, acquiring a cross section that resembles an elongated ellipse rather than a circle. Such a beam deformation is undesirable and becomes intolerable in the case of large grating separations. A simple solution is to reflect the beam back through the grating pair [34]. This double-pass configuration not only recollimates the beam back into its original cross section but also doubles the amount of GVD, thereby reducing the grating separation by a factor of 2 [17]. A slight tilt of the reflecting mirror can separate the path of the compressed pulse from that of the input pulse. The double-pass configuration is used almost exclusively in practice.

Another disadvantage of the grating pair is related to the diffraction losses associated with it. Typically, 60 to 80% of the pulse energy remains in the pulse during first-order diffraction at a grating. This results in an energy loss of about a factor of 2 during a single pass through the grating pair or a factor of 4 in the double-pass configuration. Two alternative schemes can produce anomalous GVD with significantly smaller losses. One scheme makes use of a Gires–Tournois interferometer for the purpose of pulse compression [2]. Such an interferometer can reflect almost all of the pulse energy while imposing a dispersive phase shift of the quadratic form on various spectral components. In another scheme, a pair of two prisms provides anomalous GVD through refraction [35]. However, the required prism spacing is typically quite large ($>$10 m) because of the relatively small dispersion of fused quartz.

The prism spacing can be reduced by using other materials such as dense flint glass or TeO_2 crystal. In the case of TeO_2 crystal prisms, the spacing becomes comparable to that of a grating pair. In a 1988 experiment, 800-fs pulses were compressed to 120 fs by using a prism-pair spacing of 25 cm [37]. The energy loss of a prism pair can be reduced to 2% or less. A phase grating induced in a crystal by a chirped ultrasonic wave provides an alternative to the grating pair [38]. The use of fiber gratings is also quite attractive for this purpose [39]. As discussed in Chapter 1, a fiber grating can provide anomalous GVD even when it is fabricated within the core of a normal-GVD fiber.

6.2.2 Optimum Compressor Design

Several important questions need to be answered for optimum performance of grating-fiber compressors. The most important among them are: (i) What is the optimum fiber length for given values of input pulse parameters? (ii) How far apart should the two gratings be to obtain high-quality pulses with maximum compression? To answer these questions, we should consider how an input pulse of certain width and peak power evolves inside optical fibers in the presence of both SPM and GVD [40]–[50].

It is useful to employ a normalized form of the nonlinear Schrödinger (NLS) equation for this purpose. In the case of positive GVD ($\beta_2 > 0$), the NLS equation can be written as

$$i\frac{\partial U}{\partial \xi} - \frac{1}{2}\frac{\partial^2 U}{\partial \tau^2} + N^2 \exp(-\alpha L_D \xi)|U|^2 U = 0, \tag{6.2.5}$$

where $\tau = T/T_0$, $\xi = z/L_D$, α accounts for fiber losses, and the parameter N^2 is given by

$$N^2 = \frac{L_D}{L_{\rm NL}} = \frac{\gamma P_0 T_0^2}{|\beta_2|}. \tag{6.2.6}$$

In Eqs. (6.2.5) and (6.2.6), $U = Ae^{-\alpha z}/P_0^{1/2}$ is the normalized amplitude, P_0 is the peak power of input pulses of width T_0, and γ is the nonlinear parameter. The length scales L_D and $L_{\rm NL}$ are defined in the usual manner. The soliton period $z_0 = (\pi/2)\xi$ can also be used in place of ξ. It serves as a useful length scale even in the normal-dispersion regime with the interpretation that the pulse width nearly doubles at $z = z_0$ in the absence of SPM [42].

The performance of a grating-fiber compressor can be simulated by solving Eq. (6.2.5) numerically to obtain $U(z,\tau)$ at the fiber output and then using it as the input field in Eq. (6.2.4) to find the compressed pulse shape. The parameter ϕ_2 in Eq. (6.2.3) can be adjusted to optimize the compressor performance. The optimum compressor is one for which the grating separation corresponds to an optimum value of ϕ_2 such that the peak power of the compressed pulse is largest. This is precisely how a grating-fiber compressor is optimized in practice. In the following discussion, fiber losses are neglected since the fiber lengths used in practice are relatively short ($\alpha L \ll 1$).

Consider first the case of pure SPM by neglecting GVD. As discussed in Section A.4.1, in the absence of GVD, the shape of the input pulse remains unchanged while its spectrum broadens with propagation. More important, however, from the standpoint of pulse compression, is the SPM-induced frequency chirp. For a Gaussian pulse, the chirp is linear only over the central part of the pulse (see Fig. A.4.1). When such a pulse is passed through a grating pair, only the central part is compressed. Since a significant amount of pulse energy remains in the wings, the compressed pulse is not of high quality.

It turns out that GVD of fibers can improve the pulse quality considerably [40]. As discussed in Section A.4.2, normal GVD broadens the pulse and reshapes it to become nearly rectangular (see Fig. A.4.9). At the same time, the pulse develops a nearly linear chirp across its entire width. As a result of this linear chirp, the grating pair can compress most of the pulse energy into a narrow pulse. Figure 6.3 shows the pulse shape at the fiber output, the frequency chirp across the pulse, and the compressed pulse for $N = 5$ and $z/z_0 = 0.5$ [42]. For comparison, the upper row shows the corresponding plots in the absence of GVD for a fiber length chosen such that the pulse is compressed by about the same factor in both cases ($N^2 z/z_0 = 4.5$). Even though neither N^2 nor z_0 is

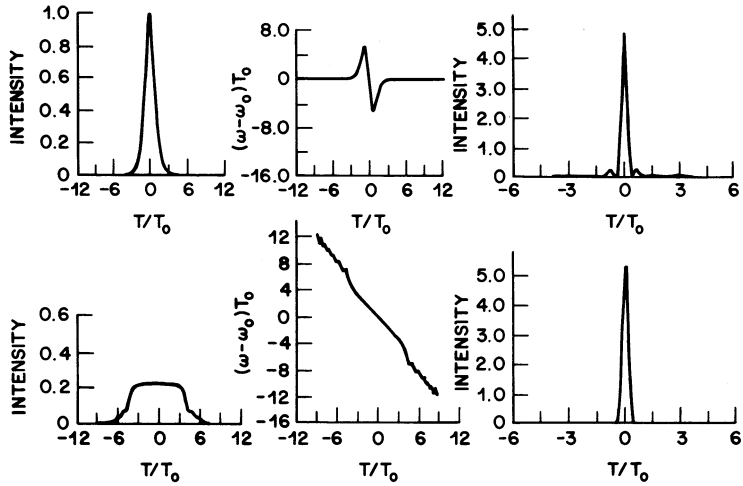

Figure 6.3 Pulse shape and chirp profile at fiber output and compressed pulse after grating pair. Effects of GVD are ignored in the upper row and $N^2 z/z_0 = 4.5$. In the lower row, $N = 5$, $z/z_0 = 0.5$, and GVD is included. (After Ref. [42])

finite in the limit $\beta_2 = 0$, their ratio remains finite and can be used to compare the two cases. A comparison of the two rows in Fig. 6.3 reveals the beneficial effect of GVD on the pulse quality when $\beta_2 > 0$ for the fiber used for chirping the pulse. However, this benefit is realized only at the expense of reduced compression at a given value of the input peak power [42].

To quantify the performance of grating-fiber compressors, it is useful to introduce two parameters:

$$F_c = T_{\text{FWHM}}/T_{\text{comp}}, \qquad Q_c = |U_{\text{out}}(0)|^2/F_c, \tag{6.2.7}$$

where T_{comp} is the FWHM of the compressed pulse. Clearly, F_c is the compression factor. The parameter Q_c is a measure of the quality of the compressed pulse. Its value at the fiber input is 1, and $Q_c \approx 1$ is desirable for the compressed pulse if nearly all of the pulse energy has to reappear in it.

Numerical simulations based on the NLS equation show that an optimum value of the fiber length exists for which both F_c and Q_c are maximum [42]. Figure 6.4 shows variations in F_c and Q_c with z/z_0 for values of N in the range from 1 to 20, assuming a "sech" shape for input pulses. For values of $N >$ 5, the maxima of F_c and Q_c are evident, indicating the need to optimize the fiber length. The existence of an optimum fiber length z_{opt} can be understood

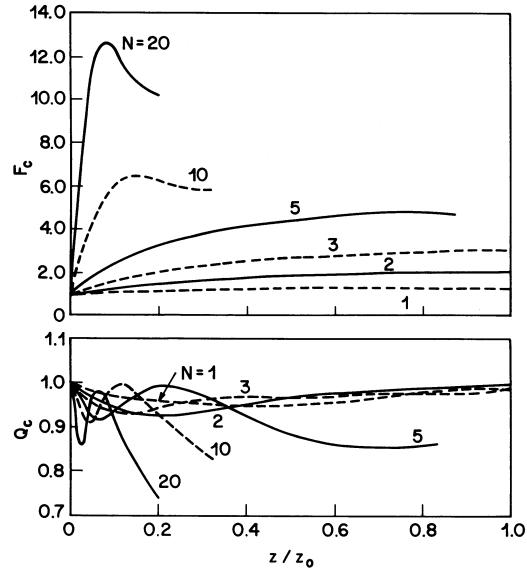

Figure 6.4 Compression factor F_c and quality factor Q_c as a function of fiber length for values of N in the range from 1 to 20. Grating separation is optimized in each case to maximize the peak power of the compressed pulse. (After Ref. [42])

qualitatively as follows. For $z < z_{\text{opt}}$ the SPM-induced chirp has not yet been linearized, whereas for $z > z_{\text{opt}}$ the GVD effects broaden the pulse so much that SPM loses its effectiveness. Indeed, z_{opt} is well approximated by $(6L_D L_{\text{NL}})^{1/2}$, showing the relative importance of both the GVD and SPM effects for pulse compression.

From the standpoint of compressor design, it is useful to provide simple design rules that govern the optimum fiber length and the optimum grating separation for realizing maximum compression for given values of the pulse and fiber parameters. The numerical results of Fig. 6.4 can be used to obtain the following relations valid for $N \gg 1$:

$$z_{\text{opt}}/z_0 \approx 1.6/N, \tag{6.2.8}$$

$$\tfrac{1}{2}|\phi_2|/T_{\text{FWHM}}^2 \approx 1.6/N, \tag{6.2.9}$$

$$1/F_c \approx 1.6/N, \tag{6.2.10}$$

where the grating parameter ϕ_2 is related to the optimum grating separation through Eq. (6.2.3). The numerical factor depends on the input pulse shape

and would be slightly different than 1.6 for shapes other than a hyperbolic secant. Equations (6.2.8)–(6.2.10) are fairly accurate for all pulse shapes as long as $N > 10$. Similar relations have been obtained using the inverse scattering method and making certain approximations about the pulse shape and the chirp [41]. In applying Eqs. (6.2.8)–(6.2.10) in practice, the parameter N is first estimated from Eq. (6.2.6) for given values of the peak power P_0 and the width T_0 associated with a pulse. Then, the fiber length z_{opt} is obtained from Eq. (6.2.8) while Eqs. (6.2.3) and (6.2.9) provide the grating separation. Finally, the compression factor is estimated from Eq. (6.2.10).

6.2.3 Practical Limitations

Although the preceding theory of pulse compression is applicable in most practical situations, it is important to keep in mind its limitations [51]–[58]. First, input pulses were assumed to be unchirped. It is easy to include the effect of a linear initial chirp by solving Eq. (6.2.5) numerically [51]. For down-chirped pulses $(C < 0)$, the optimum fiber length increases since the positive chirp provided by the fiber has to compensate for the initial negative chirp. At the same time, the compression factor is slightly reduced because such a compensation is not perfect all along the pulse width. The opposite occurs in the case of up-chirped pulses $(C > 0)$. However, for large values of N $(N > 10)$ the changes in z_{opt} and F_c are relatively small ($< 10\%$) for pulses whose spectral width is up to twice of that expected in the absence of chirp. A related issue is the effect of a random chirp on pulse compression because of phase fluctuations associated with some input pulses. Numerical simulations show that the average compression factor is reduced by an amount that depends on the noise variance but the optimum value of the fiber length remains relatively unaffected [52].

Another limitation of the results shown in Fig. 6.4 is that they are based on Eq. (6.2.5), which neglects the higher-order nonlinear and dispersive effects. This is justified as long as the spectral width $\Delta\omega \ll \omega_0$, and the results are fairly accurate for pulse widths $T_0 > 1$ ps. For shorter pulses, one must use the generalized NLS equation derived in Section A.2.3. In general, both the pulse shape and spectrum become asymmetric. The enhanced spectral broadening on the high-frequency side in Fig. A.4.18 is a manifestation of a larger chirp near the trailing edge compared with that occurring near the leading edge. Since the chirp is not as linear as it would be in the absence of higher-order nonlinear effects, the compression factor is generally reduced for femtosecond pulses from the predictions of Fig. 6.4.

A more severe limitation on the performance of grating-fiber compressors for ultrashort pulses ($T_0 < 50$ fs) is imposed by the grating pair that no longer acts as a quadratic compressor. For such short pulses, the spectral width is large enough that the cubic term in the expansion (6.2.2) becomes comparable to the quadratic term and must be included in Eq. (6.2.4). Numerical results show that the compressed pulse then carries a significant part of its energy in the form of an oscillatory trailing edge [53]. As a result, the compression factor is smaller than that shown in Fig. 6.4. This limitation is fundamental and can be overcome only if a way is found to counteract the effect of the cubic term in Eq. (6.2.2). On the positive side, the cubic term can be exploited to compensate partially for the TOD of the fiber [47] or the nonlinear chirp induced by self-steepening [54].

An ultimate limitation on the performance of grating-fiber compressors is imposed by stimulated Raman scattering [55]–[58]. Even though the compression factor $F_c \propto N$, according to Eq. (6.2.10), and can in theory be increased by increasing the peak power of the incident pulse, it is limited in practice since the peak power must be kept below the Raman threshold to avoid the transfer of pulse energy to the Raman pulse. Furthermore, even if some energy loss is acceptable, the Raman pulse can interact with the pump pulse through cross-phase modulation and deform the linear nature of the frequency chirp. It is possible to achieve large compression factors even in the Raman regime with an optimization of the design parameters [58]. Numerical simulations show that a significant part of the pulse energy remains uncompressed because of mutual interaction between the pump and Raman pulses. For highly energetic pulses, parametric processes such as four-wave mixing can suppress the Raman process to some extent, but they eventually limit the extent of pulse compression [59].

The performance of a grating-fiber compressor can be improved by using the spectral-window method [20], in which a suitable aperture is placed near the mirror M_1 in Fig. 6.1 to filter the pulse spectrum selectively. The technique of spectral filtering is a powerful technique that can be used not only to improve the performance of a grating-fiber compressor but also to control the pulse shape through spectral modifications inside the compressor [60]–[62]. This is possible since the grating pair separates the spectral components spatially and allows one to modify them (both in amplitude and phase) by using masks placed near the mirror M_1 in Fig. 6.2.

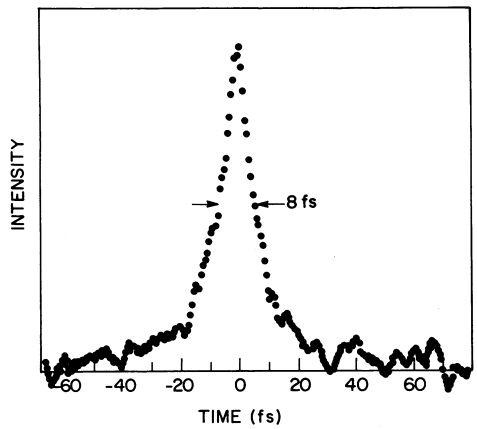

Figure 6.5 Measured autocorrelation trace of a 40-fs input pulse compressed by a grating-fiber compressor. The 12-fs width of the trace corresponds to 8-fs pulse width. (After Ref. [15], ©American Institute of Physics)

6.2.4 Experimental Results

In the 1981 experiment in which an optical fiber was first used for pulse compression, 5.5-ps (FWHM) input pulses at 587 nm, with peak powers of 10 W, were propagated through a 70-m-long fiber [11]. The 20-ps output pulses were nearly rectangular in shape and had an SPM-broadened spectrum with a nearly linear chirp across the entire pulse. This experiment used sodium vapor, instead of a grating pair, as a dispersive-delay line. The compressed pulse was 1.5-ps wide. Compression factor of 3.7 is in agreement with the results of Fig. 6.4 if we note that the experimental values of the parameters correspond to $N \approx 7$ and $z/z_0 \approx 0.25$. Even the pulse shape at the fiber output was in close agreement with the numerical simulations based on the NLS equation.

The compression technique was extended in 1982 to the femtosecond domain by using a grating pair as a dispersive delay line [12]. In this experiment, 90-fs pulses at 619 nm were passed through a 15-cm-long fiber and were compressed to about 30 fs after passing through the grating pair. The fiber and pulse parameters were such that $N \approx 3$ and $z/z_0 \approx 1.5$. The compression factor of about 3 is expected from Fig. 6.4. This experiment led to a series of experiments [14]–[16] in which the pulse width was reduced in succession to about 6 fs. In one experiment, 40-fs pulses at 620 nm, with a peak intensity of about 10^{12} W/cm^2, were passed through a 7-mm-long fiber and then compressed to

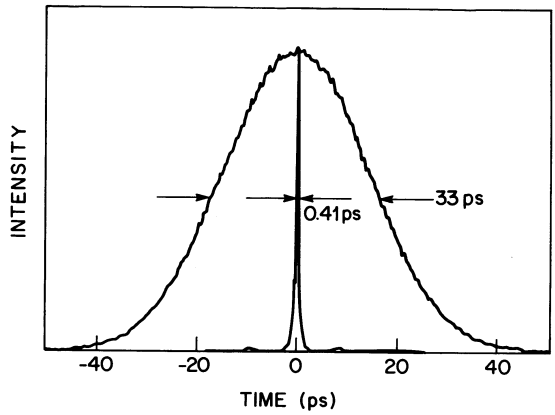

Figure 6.6 Measured autocorrelation traces of the input and compressed pulses showing a single-stage compression by a factor of 80. (After Ref. [17], ©American Institute of Physics)

8 fs by using a grating pair [15]. Figure 6.5 shows the autocorrelation trace of the compressed pulse. The corresponding spectrum can be seen in Fig. A.4.18 (the topmost trace). The spectral width of about 70 nm indicates that a pulse width of 6 fs is possible if the compressed pulse were transform limited. The most important factor that limited compression was the TOD of the grating pair resulting from the ϕ_3 term in Eq. (6.2.2). In a later experiment, the effects of TOD were compensated for by using a combination of gratings and prisms, and the pulse indeed compressed to 6 fs [16]. Such a pulse at 620 nm consists of only three optical cycles.

In a different set of experiments, the objective was to maximize the compression factor. Compression by a factor of 12 was achieved in a 1983 experiment in which 5.4-ps input pulses from a dye laser were compressed to 0.45 ps using a 30-m-long fiber [13]. A higher compression factor of 65 was obtained using a two-stage compression scheme in which the pulse was passed through two grating pairs in succession. In a 1984 experiment, single-stage compression by a factor of 80 was realized using 33-ps pulses at 532 nm from a frequency-doubled Nd:YAG laser [17]. Passage of these pulses through a 105-m-long fiber, followed by a grating pair (separation $d_g = 7.24$ m), resulted in compressed pulses of 0.41-ps duration. The experiment utilized a double-pass configuration. Figure 6.6 shows the compressed pulse and compares it to the input pulse. The corresponding spectra are similar to those shown in

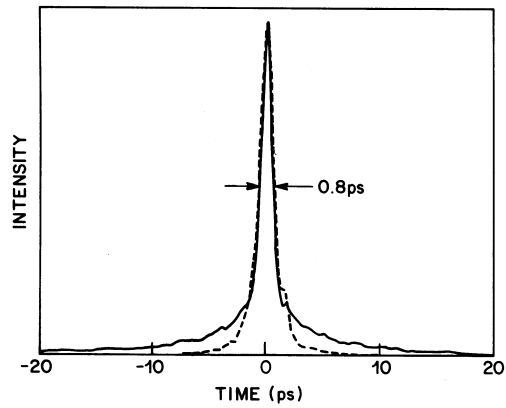

Figure 6.7 Autocorrelation traces of compressed pulses with (dashed curve) and without (solid line) spectral windowing. (After Ref. [61])

Fig. A.4.12. The input peak power of 240 W corresponds to $N \approx 145$. Equation (6.2.10) predicts a compression factor of about 90 for this value of N, in reasonable agreement with the experimental value of 80. Although larger values of the compression factor are possible in principle, peak powers cannot be increased much more in practice because of the onset of stimulated Raman scattering.

The experiments described above were performed in the visible region of the optical spectrum. The grating-fiber compression technique has been extended to the near-infrared region to obtain ultrashort pulses at 1.06 and 1.32 μm. Input pulses at these wavelengths are generally obtained from mode-locked Nd:YAG lasers and are typically 100-ps wide. As a result, the dispersion length and the parameter z_0 are relatively large ($\sim$ 100 km). Equation (6.2.8) indicates that the optimum fiber length exceeds 1 km even for values of $N \sim 100$. The optimum value of the grating separation is also relatively large ($d_g > 1$ m), as seen from Eqs. (6.2.3) and (6.2.9).

In a 1984 experiment, 60-ps pulses at 1.06 μm were compressed by a factor of 15 after passing through a 10-m-long fiber and a grating pair with spacing of about 2.5 m [18]. In a different experiment, a compression factor of 45 was achieved by using a 300-m-long fiber and a compact grating pair [19]. The compressed pulses at 1.06 μm generally carry a significant amount of energy in the uncompressed wings because a smaller fiber length than that dictated by Eq. (6.2.8) is often used in practice to reduce optical losses. In the absence

of fully developed GVD effects only the central part of the pulse is linearly chirped, and the energy in the wings remains uncompressed. The energy in uncompressed pulse wings can also be reduced by using the nonlinear birefringence (see Chapter A.6) in such a way that the fiber acts as an intensity discriminator [63].

The technique of spectral windowing has been used to remove energy from pulse wings [20]. It makes use of the observation that the wings contain spectral components at the extreme end of the pulse spectrum, which can be filtered by placing an aperture (or window) near the mirror M_1 in Fig. 6.2. Figure 6.7 compares the autocorrelation traces of compressed pulses obtained with and without spectral windowing [61]. The 75-ps input pulses were compressed to about 0.8 ps in a conventional grating-fiber compressor, resulting in a compression factor of more than 90. The use of spectral windowing nearly eliminated the pulse wings while the pulse width increased slightly to 0.9 ps. This technique can also be used to modify the pulse shape by using suitable masks in place of a simple aperture [60]–[62]. Temporal modulation of the chirped pulses at the fiber output (before entering the grating pair) has also been used for this purpose [64]. Such techniques convert the grating-fiber compressor into a versatile tool that can be used for pulse synthesis.

It is generally difficult to achieve compression factors larger than 100 for 1.06-μm pulses because of the onset of stimulated Raman scattering. Compression by a factor of 110 was realized in an experiment in which 60-ps pulses were propagated through a 880-m-long fiber [29]. Even higher compression factors can be obtained by using two grating-fiber compressors in series [22]. In one experiment, 90-ps pulses were compressed to 0.2 ps, resulting in an overall compression factor of 450 [27]. At the same time, the peak power increased from 480 W to 8 kW. Two compressors provided the same compression factor of about 21. It was noticed that, even though pulses after the first compressor had significant amounts of energy in their wings, pulses emerging from the second compressor were of high quality. The reason is related to the different input pulse widths. The 4.2-ps pulses fed to the second compressor were short enough that GVD was able to linearize the chirp across the whole pulse. The experimental results were in close agreement with theory.

The grating-fiber compression technique has been extended to 1.32 μm, a wavelength at which mode-locked Nd:YAG lasers can provide powerful pulses of about 100-ps duration [23]. However, since standard fibers provide normal dispersion only for $\lambda < 1.3$ μm, it is necessary to use a dispersion-shifted

fiber with its zero-dispersion wavelength around 1.55 μm. The optimum fiber length typically exceeds 2 km. This is not, however, a limiting factor because of smaller fiber losses (≈ 0.4 dB/km) near 1.32 μm. Compression by a factor of 50 was realized when 100-ps pulses were chirped using a 2-km-long dispersion-shifted fiber [26] (zero dispersion at 1.59 μm). The fiber length was less than optimum ($z_{\text{opt}} \approx 3.3$ km) to reduce the grating separation to manageable dimensions. Equation (6.2.10) predicts a compression factor of 80 if the optimum fiber length with optimum grating separation were employed ($N \approx 130$).

An advantage of operating at the 1.32-μm wavelength is that the grating pair can be replaced by a piece of fiber, making it possible to realize a compact all-fiber compressor. Two fibers with positive and negative values of the GVD parameter β_2 are fused together to make the compressor. The fiber with positive β_2 produces linear chirp across the pulse while the fiber with negative β_2 compresses it. The lengths of the two fibers need to be optimized using Eqs. (6.2.8) and (6.2.9). The grating parameter ϕ_2 is replaced by $\beta_2 L_2$, where L_2 is the optimum length of the second fiber with negative β_2. In a feasibility demonstration of this concept, 130-ps pulses were compressed to about 50 ps using a 2-km-long fiber ($\beta_2 \approx 18.4$ ps^2/km) followed by a 8-km-long fiber with $\beta_2 \approx -4.6$ ps^2/km [23]. In later experiments [78]–[80], a two-stage compression technique in which a grating-fiber compressor is followed by an anomalous-GVD fiber was used to obtain compression factors of up to 5000. The second-stage compression in these experiments results from the effects of higher-order solitons, a topic covered in the next section.

With the advent of mode-locked Ti:sapphire lasers, considerable attention focused during the 1990s on reducing the pulse width below 5 fs [65]. By 1996, optical pulses shorter than 8 fs were generated directly from a Ti:sapphire laser [66]. If a 10-fs pulse could be compressed even by a factor of 3 using a grating-fiber compressor, one would be able to attain pulses shorter than 4 fs in the 800-nm wavelength region. Such a pulse would contain less than two optical cycles! It is not easy to realize such short pulses in practice because of several higher-order nonlinear effects that limit the extent of pulse compression. Nonetheless, pulse widths in the range of 4 to 5 fs have been obtained in several experiments [67]–[72]. The spectral width of a 5-fs pulse exceeds 100 THz. It is hard to find a grating or prism pair whose GVD is constant over such a large spectral range. As a result, the TOD limits the compressor performance considerably.

A number of techniques are employed to circumvent the limitations imposed by the higher-order dispersive and nonlinear effects. In a 1997 experiment, a polarization-maintaining fiber with a 2.75-μm-diameter core was used to chirp 13-fs input pulses [67]. Although the optimum fiber length was estimated to be only 1 mm [see Eq. (6.2.8)], practical considerations forced the use of 3-mm-long fiber. The spectrum of the chirped pulse was more than 250-nm wide. A grating pair, followed by a four-prism combination, was used for pulse compression. The width of the compressed pulse was 4.9 fs and was found to be limited by the TOD effects. The use of a Gires–Tournois interferometer formed using a *chirped mirror* reduced the pulse width to 4.6 fs [69]. A chirped mirror is made by depositing multiple layers of two different dielectrics on a substrate, similar to the saturable Bragg mirror used for mode locking of fiber lasers (see Section 5.4). Just as a chirped fiber grating (see Section 6.4) provides large GVD, a chirped mirror can introduce large GVD on reflection. Such mirrors can be designed, by varying layer thicknesses, in such a way that their GVD is uniform over a large bandwidth ($>$150 THz) with little residual TOD [73].

A shortcoming of using optical fibers for chirping the input pulse is that peak powers of compressed pulses are limited by the damage threshold of silica. This problem can be solved by using a hollow fiber with a relatively large diameter that is filled with a noble gas. In one set of experiments, a 60-cm-long hollow fiber (diameter 80 μm) was filled with argon or krypton [70]. The nonlinear and dispersive effects of the gas were used to chirp 20-fs pulses with 40-μJ energy. Pulses as short as 4.5 fs were produced by compressing the chirped pulses using a chirped mirror in combination with two pairs of fused silica prisms. Pulse energies as large as 0.5 mJ were realized by this technique in the form of 5-fs compressed pulses.

6.3 Soliton-Effect Compressors

Optical pulses at wavelengths exceeding 1.3 μm generally experience both SPM and anomalous GVD during their propagation in silica fibers. Such a fiber can act as a compressor by itself without the need of an external grating pair and has been used since 1983 for this purpose [74]–[93]. The compression mechanism is related to a fundamental property of higher-order solitons. As discussed in Section A.5.2, these solitons follow a periodic evolution pattern such that they undergo an initial narrowing phase at the beginning of each

period (see Fig. A.5.4). Because of this property, with an appropriate choice of the fiber length, input pulses can be compressed by a factor that depends on the soliton order N. Such a compressor is referred to as the *soliton-effect compressor* to emphasize the role of solitons.

6.3.1 Compressor Optimization

The evolution of a soliton of order N inside optical fibers is governed by the NLS equation. One can neglect fiber losses ($\alpha = 0$) since fiber lengths employed in practice are relatively small ($\alpha L \ll 1$). In the case of anomalous GVD ($\beta_2 < 0$), Eq. (6.2.5) becomes

$$i\frac{\partial U}{\partial \xi} + \frac{1}{2}\frac{\partial^2 U}{\partial \tau^2} + N^2|U|^2 U = 0, \tag{6.3.1}$$

where the parameter N is given by Eq. (6.2.6). Even though higher-order solitons follow an exact periodic pattern only for integer values of N, Eq. (6.3.1) can be used to describe pulse evolution for arbitrary values of N. In general, the input pulse goes through an initial narrowing phase for all values of $N > 1$. The optimum fiber length z_{opt} corresponds to the location at which the width of the central spike is minimum. The compression factor is the ratio of the FWHM of the compressed pulse to that of the input pulse.

Numerical techniques have been used to obtain the compression factor F_c and the optimum fiber length z_{opt} as a function of N [74]. The inverse scattering method can also be used to obtain these quantities for integer values of N. Figure 6.8 shows the variation of F_c^{-1} and z_{opt}/z_0 with N for values of N from 1 to 15. Also shown is the quality factor Q_c, defined as the fraction of input pulse energy appearing in the compressed pulse. In contrast to the case of a grating-fiber compressor, Q_c is significantly smaller than its ideal value of unity and decreases monotonically as N increases. This drawback is inherent in all soliton-effect compressors. The remaining pulse energy appears in the form of a broad pedestal around the compressed pulse. The physical origin of the pedestal can be understood as follows. During the initial narrowing stage, the evolution of higher-order solitons is dominated by SPM. Since the SPM-induced chirp is linear only over the central part of the pulse, only the central part is compressed by anomalous GVD. Energy in the pulse wings remains uncompressed and appears as a broad pedestal.

Numerical simulations performed for values of N up to 50 show that the compression factor F_c and the optimum fiber length of a soliton-effect com-

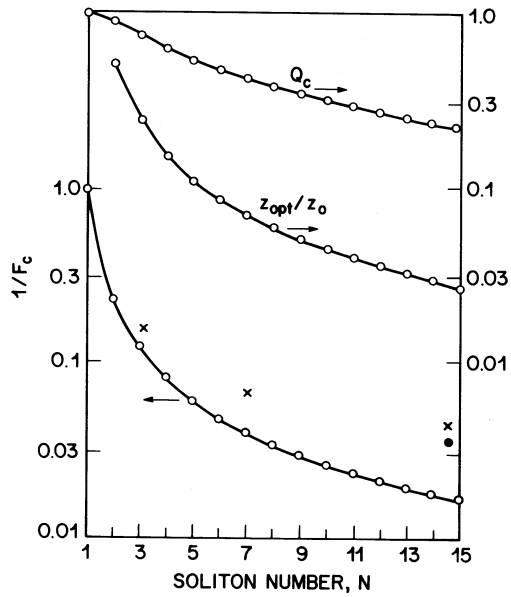

Figure 6.8 Variation of compression factor F_c, optimum fiber length z_{opt}, and quality factor Q_c with the parameter N. Data points correspond to experiments performed with 320-m (crosses) and 100-m (solid dots) fibers. (After Ref. [74]).

pressor are well approximated by the empirical relations [43]

$$F_c \approx 4.1N, \tag{6.3.2}$$

$$\frac{z_{\text{opt}}}{z_0} \approx \frac{0.32}{N} + \frac{1.1}{N^2}. \tag{6.3.3}$$

These relations are accurate to within a few percent for $N > 10$ and can serve as simple design rules, similar to those given by Eqs. (6.2.8)–(6.2.10) for grating-fiber compressors. A direct comparison shows that for the same values of N and z_0, a soliton-effect compressor provides pulse compression that is larger by a factor of 6.5 with a fiber that is shorter by a factor of 5. However, the pulse quality is poorer since the compressed pulse carries only a fraction of the input energy, with the remaining energy appearing in the form of a broad pedestal. The results of Fig. 6.8 assume an unchirped input pulse with "sech" shape. Much higher compression factors are possible for chirped input pulses having specific pulse shapes [84].

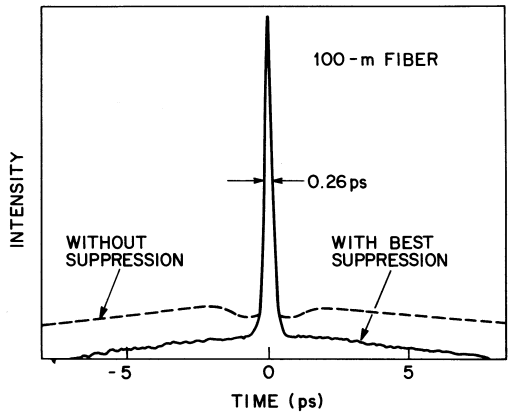

Figure 6.9 Autocorrelation trace of a 7-ps input pulse compressed to 0.26 ps by using a soliton-effect compressor. Dashed and solid curves compare the pedestal with and without the nonlinear birefringence effect. (After Ref. [74])

6.3.2 Experimental Results

In a 1983 experiment [74], 7-ps pulses from a color-center laser operating near 1.5 μm were propagated through a 320-m-long fiber ($z/z_0 \approx 0.25$). As the input peak power was increased beyond 1.2 W (the power level corresponding to a fundamental soliton), the output pulse became narrower than the input pulse by a factor that increased with increasing N. The observed values of the compression factor are shown in Fig. 6.8 (crosses) for three values of N. The compression factor was close to the theoretical value of 8 for $N = 3$ but became significantly smaller for larger values of N. This can be understood by noting that the fiber length of 320 m was close to optimum for $N = 3$ but became far too large for $N > 3$. Indeed, a reduction in the fiber length to 100 m ($z/z_0 \approx 0.077$) increased the compression factor to 27 for $N = 13$. The autocorrelation trace of the 0.26-ps compressed pulse is shown in Fig. 6.9.

It was observed experimentally that the broad pedestal associated with the compressed pulse could be partially suppressed under certain experimental conditions. As discussed in Chapter A.6, the origin of pedestal suppression is related to the nonlinear birefringence of optical fibers that can make the fiber act as an intensity discriminator [63]. This mechanism can, in principle, eliminate the pedestal almost completely. Another possibility for removing the pedestal is to filter out the low-frequency components of the compressed

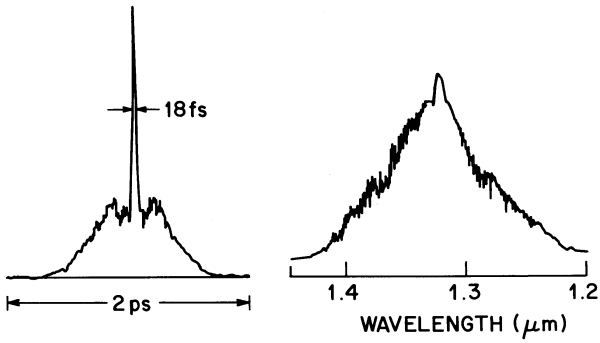

Figure 6.10 Autocorrelation trace and spectrum of an 18-fs pulse obtained by compressing 90-ps input pulses using a two-stage compression scheme. (After Ref. [80], reprinted with permission from Taylor & Francis, http://www.tandf.co.uk/journals)

pulse that are associated with the pedestal. The numerical results show that the bandwidth $\Delta\nu_f$ of such a filter is related to the parameter N and the input pulse width T_{FWHM} by the relation [76]

$$\Delta\nu_f \approx 0.2(N/T_{\text{FWHM}}), \tag{6.3.4}$$

where the numerical factor depends slightly on the input pulse shape.

Soliton-effect compressors can provide quite high compression factors. A compression factor of 110 was realized when 30-ps pulses were compressed to 275 fs by passing them through a 250-m-long fiber [75]. The fiber length is nearly optimum in this experiment if we take $N \approx 28$ (corresponding to a peak power of 0.6 kW) and note that $z_0 \approx 20$ km for 30-ps input pulses. The observed compression is also in agreement with Eq. (6.3.2). Compression factors of about 1000 have been realized using a two-stage scheme in which a grating-fiber compressor is followed by a soliton-effect compressor [78]–[80]. These experiments used 100-ps input pulses, emitted by a mode-locked Nd:YAG laser operating at 1.32 μm. In the first stage, a grating-fiber compressor was used to obtain compressed pulses of widths in the range of 1 to 2 ps. These pulses were fed into a soliton-effect compressor whose fiber length was carefully optimized to achieve compression factors of about 50. In one experiment [80], the initial 90-ps pulse was compressed to only 18 fs (consisting of only four optical cycles) by such a two-stage scheme, resulting in a net compression factor of 5000. Figure 6.10 shows the autocorrelation trace and the spectrum of the 18-fs pulse. The narrow central feature in the spectrum corre-

sponds to the pedestal seen in the autocorrelation trace that carries 69% of the total energy.

6.3.3 Higher-Order Nonlinear Effects

In pulse-compression experiments producing femtosecond pulses [79], the optimum fiber length was found to be larger by more than a factor of 2.5 than that predicted by Eq. (6.3.3). This is not unexpected since Eq. (6.3.3) is based on the numerical solution of Eq. (6.3.1), which neglects the higher-order dispersive and nonlinear effects that become increasingly more important as pulses get shorter than 100 fs. For an accurate prediction of the optimum fiber length, one must include the effects of TOD, self-steepening, and intrapulse Raman scattering by solving the generalized NLS equation,

$$i\frac{\partial U}{\partial \xi}+\frac{1}{2}\frac{\partial^2 U}{\partial \tau^2}-i\delta_3\frac{\partial^3 U}{\partial \tau^3}+N^2\left(|U|^2U-is_0\frac{\partial |U|^2U}{\partial \tau}-\tau_R U\frac{\partial |U|^2}{\partial \tau}\right)=0, \tag{6.3.5}$$

where the three parameters δ_3, s_0, and τ_R govern respectively the effects of TOD, self-steepening, and intrapulse Raman scattering (see Section A.5.5). For not-too-short pulses (width > 50 fs) propagating not too close to the zero-dispersion wavelength of the fiber, the dominant contribution comes from intrapulse Raman scattering. It manifests as a shift of the pulse spectrum toward the red side (see Fig. A.5.25). Associated with the red shift is a delay of the optical pulse resulting from a change in the group velocity. Such a delay affects substantially the interplay between GVD and SPM that is responsible for pulse compression. Numerical simulations indeed show that the optimum fiber length is longer than that predicted by Eq. (6.3.1) when the higher-order nonlinear effects are included in the analysis.

Interestingly, intrapulse Raman scattering improves the quality of the compressed pulse by producing pedestal-free pulses [82]. Figure 6.11 shows the evolution of the $N = 10$ soliton for $\tau_R = 0.01$, a value appropriate for 1-ps input pulses. The pulse begins to compress, and a narrow spike riding on a broad pedestal is formed near $\xi = 0.06$. This behavior is similar to that occurring when $\tau_R = 0$. However, the evolution becomes qualitatively different for $\xi > 0.06$ because of intrapulse Raman scattering. More specifically, the narrow spike travels more slowly than the pedestal and separates from it because of the change in its group velocity induced by the soliton self-frequency shift.

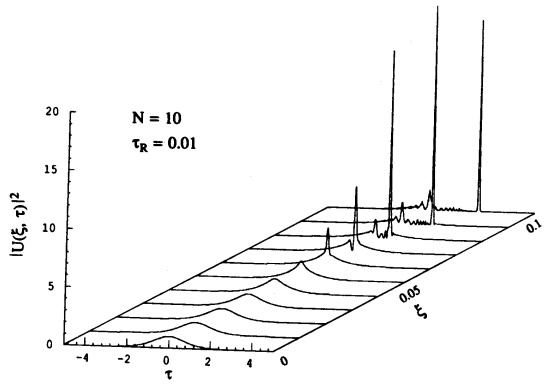

Figure 6.11 Evolution of a 10th-order soliton in the presence of intrapulse Raman scattering. The compressed pulse separates from the pedestal because of Raman-induced frequency shift. (After Ref. [82])

Moreover, the pedestal can be removed by spectral filtering. The net result is to produce a red-shifted, pedestal-free compressed pulse. At the same time, the optimum fiber length is longer and the compression factor is larger compared to the values obtained from Fig. 6.8.

Intrapulse Raman scattering, in combination with the induced modulation instability, can be used to obtain a train of pedestal-free ultrashort optical pulses at high repetition rates [83]. The basic idea consists of injecting a sinusoidally modulated CW beam into an optical fiber. Weak AM sidebands are amplified through the gain provided by modulation instability if the modulation frequency falls within the bandwidth of the instability gain. At the same time, the pulse compresses through the soliton-effect compression if the peak power is large enough to excite a higher-order soliton. In the absence of intrapulse Raman scattering, compressed pulses ride on a broad pedestal forming from the CW background. However, because of the Raman-induced frequency shift, the spectrum of the pulse train separates from the pedestal spectrum. A bandpass filter can be used to remove the pedestal and obtain a train of ultrashort optical pulses at a repetition rate determined by the initial modulation frequency. Numerical simulations reveal that a pulse train of width ~ 100 fs at repetition rates ~ 100 GHz can be generated by this technique [86].

The TOD, in general, degrades the quality of compressed pulses when femtosecond pulses propagate close to the zero-dispersion wavelength of the fiber used for soliton-effect compression [88]. However, if the TOD parameter δ_3

is negative, the combination of TOD and intrapulse Raman scattering can improve the performance of a soliton-effect compressor. Numerical simulations based on Eq. (6.3.5) show that negative values of β_3 result in larger compression factors and higher peak powers [90]. Although β_3 is positive for most fibers, dispersion-compensating fibers with negative values of β_3 were developed during the late 1990s. The use of dispersion management, a technique in which two or more fibers with different dispersion characteristics are spliced together, can provide soliton-effect compressors for which the average GVD is small but anomalous while the average value of β_3 is negative. Such compressors should prove useful for compressing femtosecond pulses.

6.4 Fiber Bragg Gratings

As discussed in Chapter 1, fiber Bragg gratings exhibit large GVD in the vicinity of the stop-band edges. The grating-induced GVD can be varied from normal to anomalous, and its magnitude can be tailored over a wide range by chirping the grating period. Since a fiber grating acts as a dispersive delay line, it can be used for compressing chirped pulses in place of the bulk-grating pair [94]. Moreover, the onset of various nonlinear effects within the fiber grating points to the possibility realizing pulse compression using a compact, all-fiber device [95]. For these reasons, the use of fiber gratings for pulse compression attracted attention soon after such gratings became available [96]–[111]. In this section we discuss the important role played by fiber gratings in pulse compressors.

6.4.1 Gratings as a Compact Dispersive Element

A uniform grating reflects light whose wavelength falls within the stop band centered at the Bragg wavelength λ_B. Outside but close to the stop-band edges, the grating provides large dispersion. The effective values of the grating-induced GVD and TOD depend on the detuning δ and are given by [see Eq. (1.3.26)]

$$\beta_2^g = -\frac{\mathrm{sgn}(\delta)\kappa^2/v_g^2}{(\delta^2-\kappa^2)^{3/2}}, \qquad \beta_3^g = \frac{3|\delta|\kappa^2/v_g^3}{(\delta^2-\kappa^2)^{5/2}}. \tag{6.4.1}$$

where κ is the coupling coefficient as defined in Section 1.3. The GVD parameter β_2^g depends on the sign of the detuning δ. The GVD is anomalous on the high-frequency side of the stop band where δ is positive. In contrast, GVD

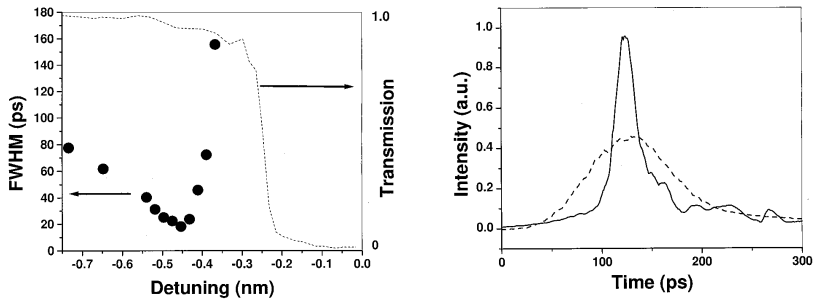

Figure 6.12 (a) Changes in width (FWHM) of pulses compressed by a fiber grating as a function of wavelength detuning $\Delta\lambda$. Dotted curve shows changes in transmittivity. (b) Shape of compressed pulse for $\Delta\lambda = -0.45$ nm. Dashed curve shows the input pulse. (After Ref. [110])

becomes normal ($\beta_2^g > 0$) on the low-frequency side of the stop band ($\delta < 0$). The TOD remains positive in all cases. Both β_2^g and β_3^g become infinitely large if the optical frequency falls close to the edges of the stop band such that $\delta = \kappa$. Figure 1.6 showed how GVD varies in the vicinity of the stop-band edges of a grating. Typical values of $|\beta_2^g|$ can easily exceed 10^7 ps^2/km. As a result, a 1-cm-long fiber grating may provide as much dispersion as 10-km of silica fiber or a bulk-grating pair with more than one meter spacing.

A simple application thus consists of replacing the bulk-grating pair in a grating-fiber compressor with a fiber grating. The resulting all-fiber device can be quite compact. Unfortunately, the TOD affects the quality of compressed pulses significantly since β_3^g increases rapidly as δ approaches the stop-band edges located at $\delta = \pm\kappa$. Figure 6.12 shows how the pulse width changes with wavelength detuning when 80-ps (FWHM) pulses—obtained from a Q-switched, mode-locked Nd:YLF laser and chirped through SPM within the laser—are transmitted through a 6.5-cm-long apodized grating. The shortest pulse width of about 15 ps is obtained for $\Delta\lambda = -0.45$ nm, where $\Delta\lambda = -(\lambda_B^2/2\pi\bar{n})\delta$ and $\bar{n}$ is the average value of the refractive index. The shape of the compressed pulse for this case is also shown in Fig. 6.12. Both the pulse shape and the compression factor of 5.3 are in agreement with the theory based on Eq. (6.4.1).

The compression factor as well as pulse quality can be improved considerably by using chirped fiber gratings. As discussed in Section 1.7.2, the optical period in a chirped grating changes along its length. As a result, the Bragg

wavelength at which the stop band is centered also shifts along the grating length. Physically speaking, different frequency components of the pulse are reflected from different regions of the grating. Such a device can introduce a large amount of GVD in the reflected pulse. We can estimate it by considering the time delay introduced by the total shift $\Delta\lambda_t$ in the Bragg wavelength. With $T_r = D_g L_g \Delta\lambda_t = 2\bar{n}L_g/c$, where T_r is the round-trip time for a grating of length L_g, the dispersion parameter is given by

$$D_g = -(2\pi c/\lambda^2)\beta_2^g = 2\bar{n}/(c\Delta\lambda_t). \tag{6.4.2}$$

Values of $|\beta_2^g|$ can exceed 5×10^7 ps^2/km for $\Delta\lambda_t = 0.2$ nm. Such shifts in the Bragg wavelength can be realized by chirping the grating period linearly such that it changes by only 0.1% at the two ends of the grating.

Several experiments in 1994 used chirped gratings for pulse compression [97]–[99]. A major motivation was to compensate for dispersion-induced broadening of pulses in fiber-optic communication systems [112]. In a 1995 experiment, dispersion compensation at 10 Gb/s over 270 km of standard fiber ($\beta_2 \approx -20$ ps^2/km) was realized using a 12-cm-long chirped grating [100]. Compression factors in excess of 100 can be realized by this technique. The only disadvantage of a chirped fiber grating from a practical standpoint is that the compressed pulse is reflected rather than transmitted. An optical circulator is commonly used to separate the reflected pulse from the incident pulse because of its relatively low insertion losses.

6.4.2 Grating-Induced Nonlinear Chirp

In a grating-fiber compressor, a long piece of normal-GVD fiber is used to chirp the input before it can be compressed. Since a fiber grating can also provide both SPM and normal GVD, it can be used to generate the frequency chirp. Such a device results in a compact compressor, but it requires high input pulse energies. Moreover, the fiber grating should be designed carefully to minimize the effects of TOD and to avoid the onset of stimulated Raman scattering [108].

The effect of TOD on the chirping process within the grating can be studied numerically by solving the nonlinear coupled-mode equations of Section 1.3. However, as pointed out there, these equations reduce to a modified NLS equation of the form

$$i\frac{\partial U}{\partial \xi} - \frac{1}{2}\frac{\partial^2 U}{\partial \tau^2} - \delta_3 \frac{\partial^3 U}{\partial \tau^3} + N^2|U|^2 U = 0, \tag{6.4.3}$$

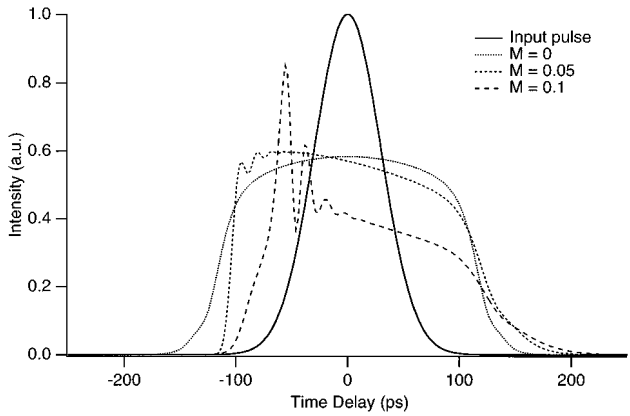

Figure 6.13 Effect of TOD on a 70-ps Gaussian pulse chirped using a fiber grating. Parameter $M = 3.6\delta_3$ is a measure of the relative strength of TOD. (After Ref. [108])

where $\delta_3 = \beta_3^g/(6\beta_2^g T_0)$ is the effective TOD parameter for a grating. Fiber losses within the grating can be neglected because of its short length. Figure 6.13 shows how the shape of a 70-ps Gaussian pulse is affected by TOD when it is chirped using a 10-cm-long fiber grating with normal GVD ($\beta_2 =$ 50 ps^2/cm). The peak intensity of the pulse is taken to be 170 GW/cm^2. The effects of TOD are included by changing δ_3. In the absence of TOD ($\delta_3 = 0$), the chirped pulse is nearly rectangular, as found to Section 6.2. However, the pulse becomes asymmetric and develops considerable internal structure as δ_3 increases. This structure affects the quality of the compressed pulse and should be minimized while designing the fiber grating [108].

The TOD parameter δ_3 depends on the detuning parameter δ and can be reduced by moving the stop-band edge of the grating away from the optical wavelength so that the pulse is not too close to the edge. However, the GVD parameter β_2^g becomes smaller as $|\delta|$ increases, resulting in a longer dispersion length. Since the optimum length of the grating is about $z_{\text{opt}} = (6L_D L_{\text{NL}})^{1/2}$, a longer grating is needed. The compression factor is limited by the onset of stimulated Raman scattering since the parameter N cannot be made very large by increasing input peak powers. A careful consideration of various dispersive and nonlinear effects shows that the maximum compression factor is limited to a value of about 6 [108]. It should also be stressed that pulses chirped nonlinearly by a grating cannot be compressed by another fiber grating acting as a dispersive element, because of their high peak power levels. The nonlinear

effects in the second grating can be avoided by reducing the pulse energy. Alternatively, a grating or prism pair can be used for pulse compression.

6.4.3 Bragg-Soliton Compression

As discussed in Section 1.6, fiber gratings support Bragg solitons. These solitons can be used for pulse compression in the same way that higher-order solitons produce soliton-effect compression in fibers without a grating. The advantage of a fiber grating is that the compressor length can be reduced from hundreds of meters to a few centimeters.

Since the nonlinear coupled-mode equations describing pulse propagation in fiber gratings reduce to an effective NLS equation under appropriate conditions (see Section 1.5.2), the analysis of Section 6.3 applies to fiber gratings as well, as long as the GVD parameter β_2 and the nonlinear parameter γ are replaced by their equivalent values given in Eq. (1.5.10). An estimate of the compression factor for values of N in the range from 2 to 15 is provided by $F_c \approx 4.6(N-1)$ [87]. The pulse shapes shown in Fig. 1.16 were obtained at the output end of a 7.5-cm-long apodized fiber grating for 80-ps input pulses having a peak intensity of 11 GW/cm^2. The soliton order N is different for different curves, seen in Fig. 1.16, since the GVD parameter β_2^g changes with detuning δ. Choosing the values of β_2^g and the pulse peak power P_0 such that the input pulse corresponds to a $N = 2$ soliton while the grating length $L = z_0/2$, the compression factor is expected to be 4.6. Indeed, pulse compression by a factor of 4 was observed experimentally under such conditions [110].

Another grating-based nonlinear scheme for compressing optical pulses makes use of the push-broom effect in which a weak broad pulse is swept by a strong pump pulse such that most of the energy of the broad pulse piles up at the front end of the pump pulse [101]. The physical mechanism behind optical push broom was discussed in Section 1.6.4. The nonlinear chirp in this case is generated not by SPM but by cross-phase modulation (XPM). Pulse compression induced by the push-broom effect was seen in a 1997 experiment [107]. XPM-induced pulse compression is discussed in more detail later in this chapter.

Although soliton-based compression has been observed in fiber gratings, its use is likely to be limited in practice. The reason is related to the combination of a relatively low value of n_2 in silica glasses and relatively short lengths of fiber gratings. A nonlinear phase shift ($\phi_{\rm NL} = \gamma P_0 L$) of π requires values of P_0 in excess of 1 kW even for a relatively long grating ($L = 50$ cm). The power

levels can be reduced by more than a factor of 100 if chalcogenide glasses are used for making the fiber grating.

6.5 Chirped-Pulse Amplification

Many applications require optical pulses with high energies (1 J or more) that are not readily available from the laser producing the pulse train. It is then necessary to amplify the pulse externally by using one or more amplifiers. The technique of chirped-pulse amplification has been found extremely useful for this purpose [113]–[132]. This technique was used as early as 1974 [113] but drew widespread attention only after 1985 when it was used to obtain ultrashort pulses with terawatt peak powers [114]–[118].

The basic idea behind chirped-pulse amplification consists of chirping and stretching the pulse before it is amplified. Nonlinear effects in optical fibers (SPM) are often used for this purpose. During its passage through the fiber, the pulse is not only chirped but it also broadens, as discussed in Section 6.2. Pulse broadening reduces the peak power substantially, making it possible to amplify the pulse by a large amount before gain saturation limits the energy-extraction efficiency. The amplified pulse is then compressed by using a grating pair. In essence, the scheme is similar to that shown in Fig. 6.1 except that an amplifier is inserted between the fiber and the grating pair.

The use of chirped-pulse amplification has resulted in the advent of table-top terawatt laser systems in which mode-locked pulses emitted from solid-state lasers are amplified to obtain picosecond, or even femtosecond, pulses with terawatt peak powers. In a 1991 experiment, this technique was used to produce 1.052-μm pulses of 3.5-ps duration and 28-J energy [118]. The 100-ps input pulse generated from a Q-switched, mode-locked Nd:glass laser was injected into a polarization-maintaining single-mode fiber of 1-m length. The input pulse energy of 1.8 μJ was chosen such that the optical fiber chirped the pulse through SPM without inducing stimulated Raman scattering. The spectrum of the output pulse broadened to about 0.7 nm, while the pulse width remained nearly the same because of negligible GVD in such a short fiber. A chain of amplifiers boosted the pulse energy to about 100 J. The amplified pulse was then compressed by using a grating pair. The quality of the compressed pulse was improved by selecting only a central portion of the pulse where the frequency chirp is linear; a saturable absorber was used for this purpose. The 3.5-ps compressed pulse had 28-J energy with 8-TW peak power.

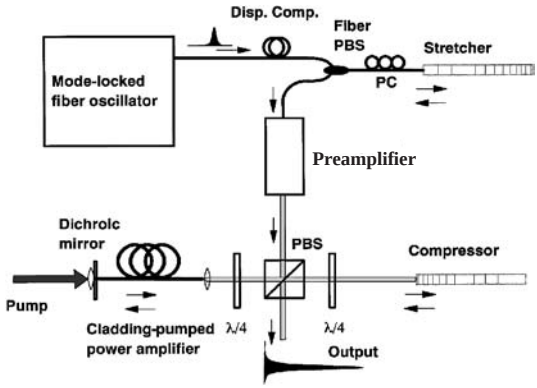

Figure 6.14 Chirped-pulse amplification using two chirped fiber gratings. (PBS: polarization beam splitter; PC: polarization controller) (After Ref. [126])

Although the use of optical fibers is not essential for chirped-pulse amplification, their nonlinearity provides a simple way to impose the frequency chirp on the pulse.

Starting in 1993, the technique of chirped-pulse amplification was applied to fiber amplifiers to obtain ultrashort optical pulses with high energies in the 1.55-μm spectral region [120]–[128]. As discussed in Chapter 5, mode-locked fiber lasers can produce pulses shorter than 1 ps but their energy is typically below 0.1 nJ. The energy level can be increased considerably by amplifying such pulses in an erbium-doped fiber amplifier, but the nonlinear effects occurring during amplification limit the pulse quality. Thus, it is useful to stretch the pulse by a factor of 100 or so (while chirping it) before amplification. The amplified pulse is then compressed back using a suitable compressor. By 1994, this technique produced 800-fs pulses with pulse energies of 100 nJ at a repetition rate of 200 kHz by using bulk gratings [122]. Bulk gratings were later replaced by chirped fiber gratings to realize a compact, all-fiber device. Figure 6.14 shows the experimental setup schematically for this technique. In one experiment, a chirped fiber grating stretched 330-fs pulses to 30 ps while the second grating recompressed the amplified pulse back to 408 fs [125]. In another experiment, the pulse energy was boosted to 20 nJ by using a cladding-pumped fiber amplifier [126]. In both experiments, the quality of compressed amplified pulses deteriorated at energy levels beyond 5 nJ because of the onset of nonlinear effects inside the compressor grating.

Higher pulse energies can be obtained if the pulse width is in the picosec-

ond regime. In a 1996 experiment, 1.9-ps pulses with 300-nJ energy levels were obtained using the technique of chirped-pulse amplification [128]. Linearly chirped pulses were obtained using a semiconductor laser and were relatively wide (> 1 ns) with low energy levels (< 10 pJ). They were amplified to energy levels as high as 3 μJ using two fiber amplifiers. A 12-cm-long chirped fiber grating compressed the pulse to under 2 ps. Nonlinear effects inside the grating were relatively small since the pulse was compressed fully near the output end of the grating. In fact, the onset of nonlinear effects in the 5-cm-long pigtail (attached to the grating) was believed to limit pulse energies in this experiment.

In a 1999 experiment, the pulse energy was increased to beyond 1 μJ (peak powers up to 500 kW) by forming a chirped grating inside the core of a large-mode-area fiber [131]. Figure 6.14 shows the experimental setup schematically. Optical pulses (width 1.5 ps) from a 1.53-μm fiber laser were first stretched to 600 ps using a chirped fiber grating before being amplified to an energy of 15 μJ using three fiber amplifiers and then compressed back to below 4 ps using a second chirped grating made using a fiber with large mode area (450 μm^2). Since the nonlinear parameter γ scales inversely with the effective mode area, nonlinear effects are reduced considerably in the second grating at the same pulse-energy level. Nonlinear effects were found to be negligible at energies of up to 0.9 μJ in this experiment. In another approach to high-energy pulses, a multimode fiber amplifier was used to overcome the peak-power limitations of single-mode fibers [132]. Femtosecond pulses with peak power levels in excess of 50 kW (average power 1.2 W) were generated in the 1.55-μm spectral region with this technique. Moreover, average powers of up to 420 mW were produced at the 775-nm wavelength using second-harmonic generation in a $LiNbO_3$ device periodically poled to realize quasi-phase matching. Chirping of the poling period compressed the pulse simultaneously while generating the second harmonic.

6.6 Dispersion-Decreasing Fibers

An interesting pulse-compression technique makes use of optical fibers in which the magnitude of the GVD parameter $|\beta_2|$ decreases along the direction of propagation of optical pulses [133]–[138]. Such fibers are referred to as dispersion-decreasing fibers (DDFs) and can be made by tapering the core diameter of the fiber at the preform-drawing stage [137]. As the waveguide

contribution to $|\beta_2|$ depends on the core size, its value decreases along the fiber length. The basic idea was proposed in 1988 but it was not until 1992 that compression factors as large as 16 were realized experimentally [135].

6.6.1 Compression Mechanism

The physical mechanism behind DDF-induced compression can be understood from Eq. (6.2.6), which shows how the soliton order N depends on the GVD parameter β_2. Consider a fundamental soliton launched at the fiber input so that $N = 1$ initially. If the numerical value of $|\beta_2|$ decreases along the fiber length, N would increase if the pulse width were to remain constant. However, the soliton order can be preserved at its input value $N = 1$ if the pulse width decreases as $|\beta_2|^{1/2}$. In essence, the situation is similar to that occurring in fiber amplifiers where an increase in the pulse peak power results in pulse compression in order to maintain $N = 1$. The analogy between a fiber amplifier and a DDF can be established mathematically by using the NLS equation [see Eq. (6.3.1)]. For a DDF this equation can be written as

$$i\frac{\partial U}{\partial \xi} + \frac{1}{2}p(\xi)\frac{\partial^2 U}{\partial \tau^2} + N^2|U|^2U = 0, \tag{6.6.1}$$

where the parameter $p(\xi) = |\beta_2(\xi)/\beta_2(0)|$ governs dispersion variations along the fiber length. If we make the transformation [139]

$$\eta = \int_0^\xi p(y)\,dy, \qquad v = NU/\sqrt{p}, \tag{6.6.2}$$

Eq. (6.6.1) is reduced to

$$i\frac{\partial v}{\partial \eta} + \frac{1}{2}\frac{\partial^2 v}{\partial \tau^2} + |v|^2 v = i\Gamma v, \tag{6.6.3}$$

where

$$\Gamma(\eta) = -\frac{1}{2p}\frac{dp}{d\eta}. \tag{6.6.4}$$

Equation (6.6.3) shows that the effect of decreasing dispersion is mathematically equivalent to adding a gain term to the NLS equation. The effective gain coefficient Γ is related to the rate at which GVD decreases along the fiber. Equation (6.6.3) can be used to study pulse compression in DDFs [86]. It is important to include the contribution of Raman-induced frequency shift of solitons in the femtosecond regime since changes in GVD affect the frequency shift considerably [135].

6.6.2 Experimental Results

Starting in 1991, DDFs were used for pulse compression in several experiments. In an early experiment, 130-fs pulses were compressed to 50 fs by using a 10-m section of a DDF [134]. Much larger compression factors were realized in 1992 by using 3.5-ps pulses from a mode-locked fiber laser operating near 1.55 μm [135]. Such pulses were transmitted through a fiber whose dispersion decreased from 10 to 0.5 ps/(km-nm) over a length of 1.6 km. The input pulse was compressed by a factor of 16 (to 230 fs) while its spectrum shifted by 10 nm due to the frequency shift induced by intrapulse Raman scattering. In another experiment, 630-fs pulses were compressed down to 115 fs by using a fiber whose dispersion decreased from 10 to 1.45 ps/(km-nm) over a length of 100 m [136].

Pulse compression has also been realized in a fiber whose dispersion was constant over the fiber length but decreased with wavelength in the 1.55- to 1.65-μm wavelength region [138]. A 95-fs input pulse at 1.57 μm compressed to 55 fs over 65 m of such fiber. The Raman-induced frequency shift plays a crucial role in this experiment. In effect, the GVD decreased along the fiber length in the reference frame of the pulse because of the frequency shift induced by intrapulse Raman scattering. The pulse spectrum was indeed observed to shift from 1.57 to 1.62 μm as the pulse compressed.

The DDF pulse-compression mechanism has been used to generate a train of ultrashort pulses [139]–[145]. The basic idea consists of injecting a CW beam, with weak sinusoidal modulation imposed on it, into an optical fiber exhibiting gain [139]. Since decreasing dispersion is equivalent to an effective gain, such fibers can be used in place of a fiber amplifier [140]. As the sinusoidal signal propagates, individual pulses within each modulation cycle are also compressed. The combined effect of GVD, SPM, and decreasing GVD is to convert a nearly CW signal into a high-quality train of ultrashort solitons [86]. The repetition rate of pulses is governed by the frequency of initial sinusoidal modulation.

Several experiments have used DDFs to generate ultrashort pulses at high repetition rates [140]–[144]. Sinusoidal modulation in these experiments is imposed by beating two optical signals. In a 1992 experiment [141], the outputs of two distributed-feedback (DFB) semiconductor lasers, operating continuously at slightly different wavelengths near 1.55 μm, were combined in a fiber coupler to produce a sinusoidally modulated signal at a beat frequency that could be varied in the 70 to 90 GHz range by controlling the laser temperature.

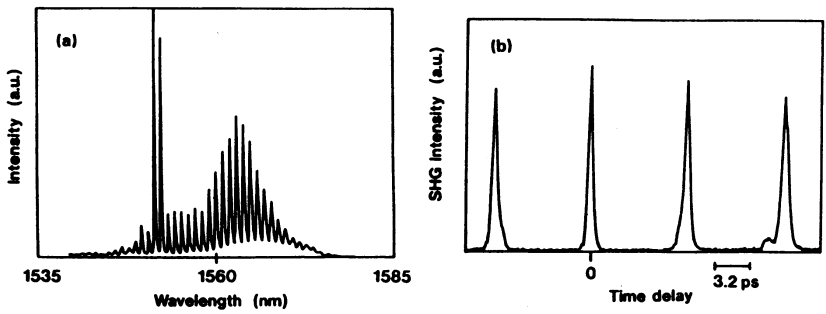

Figure 6.15 (a) Spectrum and (b) autocorrelation trace of a 114-GHz pulse train generated by using a dispersion-decreasing fiber. (After Ref. [144], ©American Institute of Physics)

The beat signal was amplified to power levels of about 0.3 W by using a fiber amplifier. It was then propagated through a 1-km dispersion-shifted fiber, followed by a DDF whose dispersion decreased from 10 to 0.5 ps/(km-nm) over a length of 1.6 km. The output consisted of a high-quality pulse train at 70 GHz with individual pulses of 1.3-ps width. By 1993, this technique had led to the generation of a 250-fs soliton train at 80- to 120-GHz repetition rates when the peak power of the beat signal was enhanced to about 0.8 W by synchronous modulation of the laser current [144]. Figure 6.15 shows the spectrum and the autocorrelation trace of such a soliton train at the 114-GHz repetition rate. Even though the laser wavelengths are near 1.5 μm, the spectrum of the soliton train is centered at 1.565 μm because of the Raman-induced frequency shift.

The use of a DDF is not essential for producing pulse trains of ultrashort solitons. In a 1993 experiment, a comblike dispersion profile was produced by splicing pieces of low- and high-dispersion fibers [145]. A dual-frequency fiber laser, integrated with a fiber amplifier, was used to generate the high-power beat signal. The output consisted of a 2.2-ps pulse train at the 59-GHz repetition rate. Such a device can be used as an integrated, all-fiber source useful for soliton communication systems. It operates by separating the effects of SPM and GVD in low- and high-dispersion fibers. Specifically, SPM dominates in low-dispersion sections and induces a frequency chirp on the beat signal. By contrast, GVD dominates in high-dispersion sections and compresses the chirped pulse. Since this alternating process is similar to that occurring for higher-order solitons, the pulse train can also be produced in conventional fibers. Indeed, in a 1994 experiment, a 123-GHz soliton train

of 1.3-ps pulses was generated by launching the high-power beat signal into a 5-km-long dispersion-shifted fiber [146]. The experimental results were in good agreement with numerical simulations based on the NLS equation. This technique was later extended to generate a 100-GHz pulse train using a single DFB laser [147]. The phase of laser output was modulated at 16.9 GHz using a $LiNbO_3$ modulator to create FM sidebands. The beat signal was generated by mixing the third-order FM sidebands, located on each side of the optical carrier and filtered using a fiber Fabry–Perot filter with a 100-GHz free spectral range. A 8.9-km-long DDF was used to produce 1.37-ps pulses at the 100-GHz repetition rate.

Pulse compression is DDFs remains a topic of active interest [149]–[158]. In one set of experiments, the objective was to produce a train of ultrashort pulses at high repetition rates. A 40-GHz train of 3.4-ps pulses was generated by compressing the sinusoidal signal (obtained beating two DFB lasers) using a combination of standard, dispersion-shifted, and dispersion-decreasing fibers [149]. In another experiment, 0.8-ps pulses at a repetition rate of 160 GHz were produced starting with a 10-GHz train of relatively wide ($>$10 ps) pulses obtained from a gain-switched semiconductor laser [150]. Chirped pulses were first compressed down to 6.3 ps in a normal-GVD fiber. They were then amplified and compressed to 0.8 ps using two sections (2 and 5 km long) of DDFs. Finally, time-division multiplexing was used to increase the repetition rate to 160 GHz. Pulses as short as 170 fs have been produced by combining decreasing GVD with amplification [151]. Such sources of ultrashort optical pulses are useful for fiber-optic communication systems [112].

In another set of experiments, the DDF is used for transmission of ultrashort pulses over relatively long lengths. The objective in this case is to maintain the width of a fundamental soliton in spite of fiber losses. In a constant-dispersion fiber, solitons broaden as they loose energy because of weakening of the nonlinear effects. However, soliton width can be maintained if GVD decreases exponentially. This behavior was indeed observed in a 40-km DDF [152]. The Raman-induced spectral shift can disturb the balance between the GVD and SPM since GVD changes with frequency. Soliton width can still be maintained if the dispersion profile is designed such that it remains exponential in the reference frame of the soliton. Indeed, lightwave systems operating at a bit rate of 100 Gb/s are feasible by using parametric amplifiers in combination with DDFs [153].

The optimum GVD profile is not exponential in the presence of the Raman-

induced spectral shift. Numerical simulations indicate that linear and Gaussian dispersion profiles result in better-quality compressed pulses and larger compression factors for subpicosecond pulses [154]. An analytic approach can also be used to find the optimum GVD profile [153]. It shows that in a long DDF, the GVD should be normal far from the input end to counteract the effect of the Raman-induced spectral shift. A variational approach has also been developed to determine the optimum GVD profile and its dependence on the width and peak power of input pulses [157]. Compression factors larger than 50 are possible by launching input pulses (with peak powers such that the soliton order $N \sim 1$) into a DDF whose length is about one soliton period [155]. This technique takes advantage of soliton-effect compression but requires lower peak powers and produces compressed pulses of better quality.

The TOD becomes the ultimate limiting factor for compression of ultrashort pulses in DDFs. Dispersion-flattened fibers, in which the TOD parameter β_3 is reduced considerably from its standard value (about 0.08 ps^3/km), became available in the late 1990s. The use of such a DDF has resulted in improved compression characteristics. In one set of experiments, 3-ps pulses at the 10-GHz repetition rate, obtained from a mode-locked fiber laser, were compressed down to 100 fs by using a 1.1-km-long DDF for which β_3 varied from 0.023 to 0.003 ps^3/km in the 1530- to 1565-nm wavelength range [158]. Both the compression factor and pulse quality were better than those obtained using a standard DDF with larger TOD ($\beta_3 = 0.073$ ps^3/km). Numerical simulations showed that the minimum pulse width was limited by the fourth-order dispersion in this experiment.

6.7 Other Compression Techniques

The pulse compression techniques described so far show how the interplay between SPM and GVD can be used to compress optical pulses by using fibers. Several other techniques based on this basic idea have been developed. This section discusses how these methods use nonlinear effects in optical fibers to produce ultrashort optical pulses.

6.7.1 Cross-Phase Modulation

The use of SPM-induced chirp for pulse compression requires input pulses to be intense enough that their spectrum broadens considerably during propaga-

tion inside an optical fiber. Clearly, such a technique cannot be used for compressing low-energy pulses. Since cross-phase modulation (XPM) also imposes a frequency chirp on optical pulses, it can be used for compressing weak optical pulses [159]–[172]. Of course, the use of XPM requires an intense pump pulse that must be copropagated with the weak input pulse (referred to as the probe pulse in pump-probe experiments). However, the pump pulse is allowed to have a different wavelength. As discussed in Section A.7.5, the XPM-induced chirp is affected by pulse walk-off and depends critically on the initial pump-probe delay. As a result, the practical use of XPM-induced pulse compression requires a careful control of the pump-pulse parameters such as its width, peak power, wavelength, and synchronization with the signal pulse.

Two cases must be distinguished depending on the relative magnitudes of the walk-off length L_W and the dispersion length L_D. If $L_D \gg L_W$ throughout the fiber, the GVD effects are negligible. In that case, the fiber imposes the chirp through XPM, and an external grating pair is needed to compress the chirped pulse. A nearly linear chirp can be imposed across the probe pulse when the pump pulse is much wider compared with it [161]. The compression factor depends on the pump-pulse energy and can easily exceed 10.

Another pulse-compression mechanism can be used when L_D and L_W are comparable. In this case, the same piece of fiber that is used to impose the XPM-induced chirp also compresses the pulse through the GVD. In some sense, this scheme is analogous to the soliton-effect compressor for the XPM case. However, in contrast with the SPM case where compression can occur only in the anomalous-GVD regime, the XPM offers the possibility of pulse compression even in the visible region (normal GVD) without the need of a grating pair. The performance of such a compressor is studied by solving the following set of two coupled NLS equations numerically (see Section A.7.4):

$$\frac{\partial U_1}{\partial \xi} + \frac{i}{2}\mathrm{sgn}(\beta_{21})\frac{\partial^2 U_1}{\partial \tau^2} = iN^2(|U_1|^2 + 2|U_2|^2)U_1, \tag{6.7.1}$$

$$\frac{\partial U_2}{\partial \xi} \pm \frac{L_D}{L_W}\frac{\partial U_2}{\partial \tau} + \frac{i}{2}\frac{\beta_{22}}{\beta_{21}}\frac{\partial^2 U_2}{\partial \tau^2} = iN^2\frac{\omega_2}{\omega_1}(|U_2|^2 + 2|U_1|^2)U_2, \tag{6.7.2}$$

where $U_j = A_j/P_j^{1/2}$ is the normalized amplitude, ω_j is the frequency, P_j is the peak power, and β_{2j} is the GVD parameter for the pump ($j = 1$) and probe ($j = 1$) pulses. The soliton order N and the walk-off length L_W are introduced

using

$$N^2 = \frac{\gamma_1 P_1 T_0^2}{|\beta_{21}|}, \qquad L_W = \frac{v_{g1} v_{g2} T_0}{|v_{g1} - v_{g2}|}, \tag{6.7.3}$$

where v_{g1} and v_{g2} are the group velocities of the pump and probe pulses. These equations govern how pump and probe pulses evolve in the presence of SPM, XPM, and group-velocity mismatch [161]. One can introduce a relative time delay T_d between the input pump and probe pulses such that the faster-moving pulse overtakes the slower pulse and passes through it. In general, a trade-off exists between the magnitude and the quality of compression. This issue is discussed in Section A.7.5.

XPM-induced pulse compression in the normal-GVD region of a fiber can also occur when the XPM coupling is due to interaction between the orthogonally polarized components of a single beam [163]. Indeed, an experiment in 1990 demonstrated pulse compression by using just such a technique [164]. A polarizing Michelson interferometer was used to launch 2-ps pulses in a 1.4-m birefringent fiber (with a 2.1-mm beat length) such that the peak power and the relative delay of the two polarization components were adjustable. For a relative delay of 1.2 ps, the weak component was compressed by a factor of about 6.7 when the peak power of the other polarization component was 1.5 kW.

When both the pump and signal pulses propagate in the normal-GVD region of the fiber, the compressed pulse is necessarily asymmetric because of the group-velocity mismatch and the associated walk-off effects. The group velocities can be made nearly equal when wavelengths of the two pulses lie on opposite sides of the zero-dispersion wavelength (about 1.3 μm in standard silica fibers). One possibility consists of compressing 1.55-μm pulses by using 1.06-μm pump pulses. The probe pulse by itself is too weak to form an optical soliton. However, the XPM-induced chirp imposed on it by a copropagating pump pulse may be strong enough that the probe pulse goes through an initial compression phase associated with the higher-order solitons. As an example, weak picosecond pulses can be compressed by a factor of 10 using pump pulses with $N = 30$ by optimizing the fiber length. This method of pulse compression is similar to that provided by higher-order solitons even though the compressed pulse never forms a soliton. Using dispersion-shifted fibers, the technique can be used even when both pump and probe wavelengths are in the 1.55-μm region as long as the zero-dispersion wavelength of the fiber lies in the middle. In a 1993 experiment [165], 10.6-ps signal pulses were compressed to 4.6 ps by using 12-ps pump pulses. Pump and signal pulses

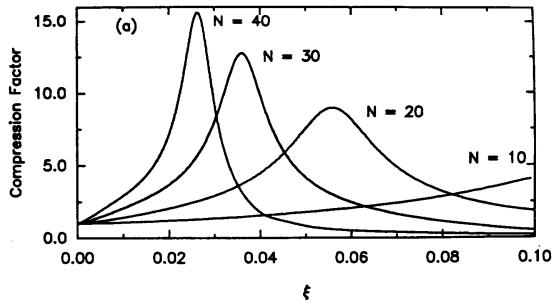

Figure 6.16 Compression factor as a function of fiber length during Raman amplification of a probe pulse by a pump pulse propagating as an Nth-order soliton. (After Ref. [166])

were obtained from mode-locked semiconductor lasers operating at 1.56 and 1.54 μm, respectively, with a 5-GHz repetition rate. Pump pulses were amplified to an average power of 17 mW by using a fiber amplifier. This experiment demonstrates that XPM-induced pulse compression can occur at power levels achievable with semiconductor lasers.

An extension of this idea makes use of Raman amplification for simultaneous amplification and compression of picosecond optical pulses [166]. The probe pulse extracts energy from the pump pulse through stimulated Raman scattering (see Chapter A.8) and is amplified. At the same time, it interacts with the pump pulse through XPM, which imposes a nearly linear frequency chirp on it and compresses it in the presence of anomalous GVD. Equations (6.3.1) and (6.3.2) can be used to study this case provided a Raman-gain term is added to these equations (see Section A.8.3). Numerical simulations show that compression factors as large as 15 can be realized while the pulse energy is amplified a millionfold [166]. The quality of the compressed pulses is also quite good, with no pedestal and little ringing. Figure 6.16 shows the compression factor as the probe pulse is amplified by a pump pulse intense enough to form a soliton of order N. Pulse compression is maximum for an optimum fiber length, a feature similar to that of soliton-effect compressors. This behavior is easily understood by noting that GVD reduces the XPM-induced chirp to nearly zero at the point of maximum compression. Simultaneous Raman-induced amplification and XPM-induced compression of picosecond optical pulses was observed in a 1996 experiment [167].

Several other XPM-based techniques can be used for pulse compression.

In one scheme, a probe pulse is compressed as it travels with a pump pulse that is launched as a higher-order soliton and is thus compressed through soliton-effect compression [169]. Compression factors as large as 25 are predicted by the coupled NLS equations. In this technique, a pump pulse transfers its compression to the copropagating probe pulse through XPM-induced coupling between the two pulses. Both pulses must propagate in the anomalous-GVD regime of the optical fiber and their wavelengths should not be too far apart. This is often the situation for WDM lightwave systems with channel spacing of 1 nm or so.

Another technique is based on propagation of two ultrashort pulses (widths below 100 fs) inside an optical fiber [170]. The second pulse is produced using second-harmonic generation. As a result, carrier frequencies of the two pulses are far apart but their relative phase is locked. Both pulses are launched into an optical fiber where they interact through XPM. The pulse spectra are relatively broad to begin with for ultrashort pulses. They broaden further through SPM and XPM to the extent that the two spectra merge at the fiber output, producing an extremely broad continuum. A grating pair, in combination with a spatial phase modulator, can then be used to compensate the chirp and realize a single supershort pulse whose spectrum corresponds to the merge spectra of the two input pulses. Pulses shorter than 3 fs are predicted theoretically.

In a 1999 experiment, a three-wave mixing technique was used to generate 8-fs pulses in the deep ultraviolet region near 270 nm [171]. Ultrashort 35-fs pulses, from a Ti:sapphire laser operating near 800 nm, and second-harmonic pulses were coupled together into a hollow silica fiber containing argon gas. The sum-frequency pulse generated was chirped because of XPM and could be compressed to 8 fs using a grating pair.

6.7.2 Gain-Switched Semiconductor Lasers

The technique of gain switching can produce pulses of about 20-ps duration from semiconductor lasers directly. As a rule, pulses emitted from gain-switched semiconductor lasers are chirped because of refractive-index variations occurring during pulse generation. In contrast with the positive chirp induced through SPM in optical fibers, the frequency chirp of gain-switched pulses is negative, i.e., frequency decreases toward the trailing edge. As seen in Fig. 3.2, such pulses with negative values of the chirp parameter C can be compressed if an optical fiber having positive GVD is used and its length is suitably optimized. This technique has been used in many experiments to

generate trains of ultrashort optical pulses suitable for optical communications [173]–[185]. Nonlinear properties of optical fibers are not used in this technique since laser pulses entering the fiber are already chirped. The role of the fiber is to provide positive dispersion. The output pulse is not only compressed but also becomes nearly transform limited. The use of dispersion-shifted fibers is necessary in the 1.5-μm wavelength region.

As early as 1986, the gain-switching technique was used to obtain 5- to 6-ps optical pulses at a repetition rate of 12 GHz [173]. The repetition rate was increased to 100 GHz by 1988 through time-division multiplexing of compressed pulses. Since the frequency chirp imposed by the gain-switched laser is not perfectly linear, the compressed pulse is not generally transform limited. The quality of the compressed pulse can be significantly improved by using a bandpass filter that passes the central part of the pulse spectrum where the chirp is nearly linear [174]. Transform-limited optical pulses of duration less than 6 ps were generated in this way [176]. In another experiment, the pulse width was reduced below 3 ps [175].

Even shorter pulses can be obtained if the compressed pulse is further compressed in a fiber with anomalous GVD by using the soliton-effect compression technique of Section 6.4. In one experiment [177], 1.26-ps optical pulses were generated by compressing a 17.5-ps gain-switched pulse through such a two-stage compression scheme. It was necessary to boost the pulse energy by using semiconductor laser amplifiers before launching the pulse into the second fiber so that the pulse energy would be large enough to excite a higher-order soliton. By 1993, the pulse width was reduced to below 1 ps [178]. Pulses as short as 230 fs were obtained by using a tunable distributed Bragg reflector (DBR) laser [179]. The ultimate performance of the gain-switching technique is limited by SPM occurring in the normal-GVD fiber used for pulse compression since the resulting positive chirp tends to cancel the negative chirp of gain-switched pulses. Numerical simulations are often used to optimize the performance [180].

Much shorter pulses were obtained in 1995 by using fiber birefringence during pulse compression in such a way that pulses were reshaped as they were being compressed [181]. A train of 185-fs high-quality pedestal-free pulses were successfully generated by this technique. In a later experiment, 16-ps pulses from a gain-switched laser were compressed down to 110 fs [182]. Linear compression of chirped pulses in a normal-GVD fiber resulted in transform-limited 4.2-ps pulses. Such pulses were then amplified and compressed to be-

low 0.2 ps by launching them into a dispersion-shifted fiber as a higher-order soliton (N = 10 to 12) to use soliton-effect compression. The effects of TOD as well as intrapulse Raman scattering become quite important for such short pulses. Experimental results were in agreement with the predictions of Eq. (6.3.5). The shortest optical pulses (as short as 21 fs) have been obtained by pumping synchronously a surface-emitting laser in the external-cavity configuration [85]. Pulses emitted from such a laser were heavily chirped (time-bandwidth product of more than 100) and could be compressed down to 21 fs by using a grating pair followed by a soliton-effect compressor.

6.7.3 Optical Amplifiers

Under certain conditions, amplification of optical pulses can chirp the pulse such that it can be compressed if it is subsequently propagated through an optical fiber having appropriate GVD. An example is provided by semiconductor optical amplifiers. When picosecond optical pulses are amplified in such amplifiers, gain saturation leads to nonlinear changes in the refractive index of the semiconductor gain medium [186]–[190]. In essence, the amplifier imposes a frequency chirp on the amplified pulse through the process of SPM [187]. However, in contrast with the gain-switched semiconductor lasers, the chirp imposed on the pulse is such that the frequency increases with time over a large portion of the pulse (similar to the SPM-induced chirp in optical fibers). As a result, the amplified pulse can be compressed if it is passed through a fiber having anomalous GVD ($\beta_2 < 0$). The compression mechanism is similar to the soliton-effect compression scheme of Section 6.4 with the difference that the SPM-induced chirp is imposed by the amplifier instead of the fiber. The main advantage of this technique stems from the fact that low-energy pulses, which cannot be compressed in fibers directly because their peak power is below the $N = 1$ level, can be simultaneously amplified and compressed by using an amplifier followed by the right kind of optical fiber.

Amplifier-induced pulse compression was observed in a 1989 experiment in which 40-ps pulses, emitted from a 1.52-μm mode-locked semiconductor laser, were first amplified in a semiconductor laser amplifier and then propagated through 18 km of optical fiber having $\beta_2 = -18$ ps^2/km [187]. The compression factor was about 2 because of relatively low pulse energies (~ 0.1 pJ). Pulse-shape measurements through a streak camera were in good agreement with the theoretical prediction [188]. The technique can be used for simultaneous compensation of fiber loss and dispersion in fiber-optic communication

systems. In a demonstration of the basic concept [189], a 16-Gb/s signal could be transmitted over 70 km of conventional fiber having large dispersion when a semiconductor laser amplifier was used as an in-line amplifier. In the absence of amplifier-induced chirp, the signal could not be transmitted over more than 15 km since optical pulses experienced excessive broadening.

As discussed in Section 4.6, fiber amplifiers can also compress optical pulses [191]–[200]. The compression mechanism is similar to that associated with higher-order solitons and occurs only in the case of anomalous GVD. Specifically, the amplifying pulse forms a fundamental soliton ($N = 1$) when its peak power becomes large enough. With further increase in the peak power, N begins to exceed 1. As seen from Eq. (6.2.6), the soliton order can be maintained ($N = 1$) if pulse width decreases with amplification. Thus, the amplified pulse keeps on compressing as long as the amplification process remains adiabatic. This compression mechanism is evident in Fig. 4.12, which was obtained by solving the Ginzburg–Landau equation that governs the amplification process in fiber amplifiers. The compression process eventually stops because of the finite gain bandwidth associated with fiber amplifiers. Compression of femtosecond pulses was achieved in erbium-doped fiber amplifiers soon after they became available [194]. In a 1990 experiment, 240-fs input pulses were compressed by about a factor of 4 [195]. In a later experiment, 124-fs pulses emitted from a mode-locked fiber laser were shortened to 50 fs by using a 6-m-long fiber amplifier [198].

Amplification can also improve the performance of standard grating-fiber compressors [200]. It turns out that if the normal-GVD fiber—used for imposing SPM-induced chirp—is doped and pumped to provide gain, the pulse acquires a nearly parabolic shape. As seen in Fig. 4.3, the pulse shape is close to being rectangular in the absence of gain. Sharp edges of such pulses leads to optical wave breaking, a phenomenon that does not occur easily for parabolic-shaped pulses. The SPM-induced chirp remains linear even when pulses are amplified in a normal-GVD fiber amplifier. As a result, the amplified pulse can be compressed by using a grating or prism pair. In the experiment, 350-fs pulses were compressed to 77 fs using a 4-m fiber amplifier with 18-dB gain followed by a prism pair. An added benefit of this technique is that it can be used for relatively weak input pulses as long as the amplified pulse becomes intense enough to undergo SPM-induced phase shift.

A Raman fiber amplifier can also compress optical pulses. The compression mechanism is identical to that of a doped fiber amplifier and is governed

by the same Ginzburg–Landau equation. In one experiment, 10-ps pulses were compressed down to 1 ps in a backward-pumped Raman amplifier made by using 20 km of standard telecommunication fiber [201]. The compression factor depended on the CW pump power, and power levels in excess of 1.5 W were needed to compress the pulse by a factor of 10. The Raman gain was nonuniform along the fiber because of the absorption of the pump power. In the backward-pumping configuration, the gain increases as the pulse is compressed. The reduction in the soliton period compensates for the increase in Raman gain. This feature helps to maintain the regime of adiabatic compression.

Frequency chirping can also be produced using four-wave mixing (FWM), a nonlinear process that produces gain. An example is provided by parametric amplification in which pump and probe (called signal in this context) pulses generate a new pulse at the idler wavelength. The new pulse can acquire significant chirp during four-wave mixing and can be compressed either externally or during the FWM process. In one approach, degenerate FWM of counterpropagating pulses in a birefringent fiber was proposed to compress a pulse train at a high repetition rate [202]. In another, 93-ps signal pulses were compressed down to 20 ps when 50-ps pump pulses (wavelength separation 4.9 nm) were copropagated with them inside a 5-km-long fiber [203]. Signal pulses were amplified simultaneously by 29 dB through FWM. An idler pulse was also generated during parametric amplification. Its width and peak powers were close to those of the signal pulse.

6.7.4 Fiber Couplers and Interferometers

The operation of nonlinear fiber couplers and interferometers and their use for optical switching was discussed in Chapters 2 and 3. The intensity-dependent transmission of these devices can be used for pulse shaping and compression [204]–[213]. For example, compressed pulses are often accompanied by a broad pedestal (see Section 6.3). If such a low-quality pulse is passed through a nonlinear fiber-loop mirror, the central intense part of the pulse can be separated from the low-power pedestal [204]. In general, any nonsoliton pulse is compressed by a Sagnac interferometer designed to transmit the central part while blocking the low-intensity pulse wings. A fiber amplifier is sometimes incorporated within the fiber loop if the input pulse energy is below the switching threshold. Compression factors are relatively small (two or less) since the technique works by clipping pulse wings [205]. The use of multiple sections

with different dispersion characteristics inside the Sagnac loop (dispersion management) can improve the performance of such pulse compressors [207]. A Sagnac loop with a semiconductor optical amplifier can also provide compression factors as large as 3 for a high-repetition-rate pulse train but its use requires a source of control pulses [213].

A dual-core fiber also exhibits nonlinear switching between the two cores (see Section 2.3), which can be exploited for pulse shaping and compression. The use of such a fiber in a Sagnac-loop configuration offers several advantages since it combines two nonlinear mechanisms in a single device. Numerical simulations show that it can be used for pulse shaping, pedestal suppression, and pulse compression [208]. An interesting feature of such a device is that one can introduce additional coupling between the two cores by twisting the dual-core fiber within the loop. The operation of the device is quite complex and requires the solution of coupled NLS equations since the energy can be transferred between the two cores in a way similar to that of a nonlinear directional coupler (see Chapter 2). With a proper design, a dual-core fiber loop can provide compression factors of 5 or more. Even larger compression factors (up to 20) are possible in symmetric dual-core fibers using higher-order solitons [211]. Moreover, the compressed pulse is nearly pedestal free.

A multicore fiber in which multiple cores are arranged in either a linear or a circular fashion (fiber array) can also lead to pulse compression [210]. If a pulse is launched into such a device such that its energy is spread over all cores, nonlinear effects such as SPM and XPM can collapse the energy distribution in such a way that almost all the energy appears in a single core in the form of a compressed pulse. Compression in fiber arrays has been studied numerically but not yet observed experimentally.

Problems

6.1 Explain the operation of a grating-fiber compressor. Use diagrams as necessary.

6.2 Derive an expression for the effective GVD coefficient of a grating pair.

6.3 Develop a computer simulation program capable of modeling the performance of a grating-fiber compressor. Use the split-step Fourier method for solving Eq. (6.2.5) and implement the action of a grating pair through Eq. (6.2.4).

6.4 A 100-ps pulse with 1-μJ energy (emitted from a 1.06-μm Nd:YAG laser) is compressed by using a grating-fiber compressor. Estimate the maximum compression factor, optimum fiber length, and optimum grating separation for typical parameter values.

6.5 Solve numerically the NLS equation that models the performance of a soliton-effect compressor. Find the maximum compression factor and the optimum fiber length when a 10th-order soliton is launched and the soliton period is 10 km.

6.6 What is the origin of pedestal formation in soliton-effect compressors? How can the pedestal be removed from the compressed pulse?

6.7 Solve numerically the generalized NLS equation and reproduce the results shown in Fig. 6.11 for the 10th-order soliton.

6.8 How a chirped fiber grating can be used for pulse compression? Estimate the dispersion provided by such a grating if its period changes by 0.1% over a 10-cm length. Assume $\lambda = 1.55$ μm and $\bar{n} = 1.45$.

6.9 What is meant by chirped-pulse amplification? How can this technique produce high-energy compressed pulses?

6.10 Dispersion of a fiber decreases exponentially from 20 to 1 ps/(km-nm) over a length of 1 km. Estimate the compression factor for a 1-ps pulse launched as a fundamental soliton at the high-GVD end.

6.11 Explain how a pulse can be compressed using the technique of Raman amplification. Reproduce the results shown in Fig. 6.16 by solving the appropriate equations from Chapter A.8.

References

[1] J. R. Klauder, A. C. Price, S. Darlington, and W. J. Albersheim, *Bell Syst. Tech. J.* **39**, 745 (1960).

[2] F. Gires and P. Tournois, *Compt. Rend. Acad. Sci.* **258**, 6112 (1964).

[3] J. A. Giordmaine, M. A. Duguay, and J. W. Hansen, *IEEE J. Quantum Electron.* **QE-4**, 252 (1968).

[4] E. B. Treacy, *Phys. Lett.* **28A**, 34 (1968).

[5] M. A. Duguay and J. W. Hansen, *Appl. Phys. Lett.* **14**, 14 (1969).

[6] A. Laubereau, *Phys. Lett.* **29A**, 539 (1969).

[7] E. B. Treacy, *IEEE J. Quantum Electron.* **QE-5**, 454 (1969).

[8] D. Grischkowsky, *Appl. Phys. Lett.* **25**, 566 (1974).

[9] J. K. Wigmore and D. R. Grischkowsky, *IEEE J. Quantum Electron.* **QE-14**, 310 (1978).

[10] R. A. Fisher, P. L. Kelley, and T. K. Gustafson, *Appl. Phys. Lett.* **14**, 140 (1969).

[11] H. Nakatsuka, D. Grischkowsky, and A. C. Balant, *Phys. Rev. Lett.* **47**, 910 (1981).

[12] C. V. Shank, R. L. Fork, R. Yen, R. H. Stolen, and W. J. Tomlinson, *Appl. Phys. Lett.* **40**, 761 (1982).

[13] B. Nikolaus and D. Grischkowsky, *Appl. Phys. Lett.* **42**, 1 (1983); *Appl. Phys. Lett.* **43**, 228 (1983).

[14] J. G. Fujimoto, A. M. Weiner, and E. P. Ippen, *Appl. Phys. Lett.* **44**, 832 (1984).

[15] W. H. Knox, R. L. Fork, M. C. Downer, R. H. Stolen, C. V. Shank, and J. A. Valdmanis, *Appl. Phys. Lett.* **46**, 1120 (1985).

[16] R. L. Fork, C. H. Brito Cruz, P. C. Becker, and C. V. Shank, *Opt. Lett.* **12**, 483 (1987).

[17] A. M. Johnson, R. H. Stolen, and W. M. Simpson, *Appl. Phys. Lett.* **44**, 729 (1984).

[18] E. M. Dianov, A. Y. Karasik, P. V. Mamyshev, G. I. Onischukov, A. M. Prokhorov, M. F. Stel'makh, and A. A. Fomichev, *Sov. J. Quantum Electron.* **14**, 726 (1984).

[19] J. D. Kafka, B. H. Kolner, T. Baer, and D. M. Bloom, *Opt. Lett.* **9**, 505 (1984).

[20] J. P. Heritage, R. N. Thurston, W. J. Tomlinson, A. M. Weiner, and R. H. Stolen, *Appl. Phys. Lett.* **47**, 87 (1985).

[21] T. Damm, M. Kaschke, F. Noack, and B. Wilhelmi, *Opt. Lett.* **10**, 176 (1985).

[22] A. S. L. Gomes, W. Sibbett, and J. R. Taylor, *Opt. Lett.* **10**, 338 (1985).

[23] K. J. Blow, N. J. Doran, and B. P. Nelson, *Opt. Lett.* **10**, 393 (1985).

[24] A. S. L. Gomes, U. Osterberg, W. Sibbett, and J. R. Taylor, *Opt. Commun.* **53**, 377 (1985).

[25] B. Strickland and G. Mourou, *Opt. Commun.* **55**, 447 (1985).

[26] K. Tai and A. Tomita, *Appl. Phys. Lett.* **48**, 309 (1986).

[27] B. Zysset, W. Hodel, P. Beaud, and H. P. Weber, *Opt. Lett.* **11** 156 (1986).

[28] B. Valk, K. Vilhelmsson, and M. M. Salour, *Appl. Phys. Lett.* **50**, 656 (1987).

[29] E. M. Dianov, A. Y. Karasik, P. V. Mamyshev, A. M. Prokhorov, and D. G. Fursa, *Sov. J. Quantum Electron.* **17**, 415 (1987).

[30] J. M. McMullen, *Appl. Opt.* **18**, 737 (1979).

[31] I. P. Cristov and I. V. Tomov, *Opt. Commun.* **58**, 338 (1986).

[32] S. D. Brorson and H. A. Haus, *Appl. Opt.* **27**, 23 (1988); *J. Opt. Soc. Am. B* **5**, 247 (1988).

[33] P. Tournois, *Electron. Lett.* **29**, 1414 (1993); *Opt. Commun.* **106**, 253 (1994).

[34] J. Debois, F. Gires, and P. Tournois, *IEEE J. Quantum Electron.* **QE-9**, 213 (1973).

[35] O. E. Martinez, J. P. Gordon, and R. L. Fork, *J. Opt. Soc. Am. A* **1**, 1003 (1984).

[36] J. D. Kafka and T. Baer, *Opt. Lett.* **12**, 401 (1987).

[37] M. Nakazawa, T. Nakashima, H. Kubota, and S. Seikai, *J. Opt. Soc. Am. B* **5**, 215 (1988).

[38] V. E. Pozhar and V. I. Pustovoit, *Sov. J. Quantum Electron.* **17**, 509 (1987).

[39] R. Kashyap, *Fiber Bragg Gratings* (Academic Press, San Diego, CA, 1999).

[40] D. Grischkowsky and A. C. Balant, *Appl. Phys. Lett.* **41**, 1 (1982).

[41] R. Meinel, *Opt. Commun.* **47**, 343 (1983).

[42] W. J. Tomlinson, R. H. Stolen, and C. V. Shank, *J. Opt. Soc. Am. B* **1**, 139 (1984).

[43] E. M. Dianov, Z. S. Nikonova, A. M. Prokhorov, and V. N. Serkin, *Sov. Tech. Phys. Lett.* **12**, 311 (1986).

[44] E. A. Golovchenko, E. M. Dianov, P. V. Mamyshev, and A. M. Prokhorov, *Opt. Quantum Electron.* **20**, 343 (1988).

[45] E. M. Dianov, L. M. Ivanov, P. V. Mamyshev, and A. M. Prokhorov, *Sov. J. Quantum Electron.* **19**, 197 (1989).

[46] D. G. Fursa, P. V. Mamyshev, and A. M. Prokhorov, *Sov. Lightwave Commun.* **2**, 59 (1992).

[47] M. Stern, J. P. Heritage, and E. W. Chase, *IEEE J. Quantum Electron.* **28**, 2742 (1992).

[48] R. F. Mols and G. J. Ernst, *Opt. Commun.* **94**, 509 (1992).

[49] E. M. Dianov, A. B. Grudinin, A. M. Prokhorov, and V. N. Serkin, in *Optical Solitons—Theory and Experiment*, J. R. Taylor, Ed. (Cambridge University Press, Cambridge, UK, 1992), Chap. 7.

[50] M. Karlsson, *Opt. Commun.* **112**, 48 (1994).

[51] D. Mestdagh, *Appl. Opt.* **26**, 5234 (1987).

[52] V. A. Vysloukh and L. K. Muradyan, *Sov. J. Quantum Electron.* **17**, 915 (1987).

[53] W. J. Tomlinson and W. H. Knox, *J. Opt. Soc. Am. B* **4**, 1404 (1987).

[54] H. Kubota and M. Nakazawa, *Opt. Commun.* **66**, 79 (1988).

[55] T. Nakashima, M. Nakazawa, K. Nishi, and H. Kubota, *Opt. Lett.* **12**, 404 (1987).

[56] A. M. Weiner, J. P. Heritage, and R. H. Stolen, *J. Opt. Soc. Am. B* **5**, 364 (1988).

[57] A. S. L. Gomes, A. S. Gouveia-Neto, and J. R. Taylor, *Opt. Quantum Electron.* **20**, 95 (1988).

[58] M. Kuckartz, R. Schulz, and H. Harde, *J. Opt. Soc. Am. B* **5**, 1353 (1988).

[59] A. P. Vertikov, P. V. Mamyshev, and A. M. Prokhorov, *Sov. Lightwave Commun.* **1**, 363 (1991).

[60] J. P. Heritage, A. M. Weiner, and R. H. Thurston, *Opt. Lett.* **10**, 609 (1985).

[61] A. M. Weiner, J. P. Heritage, and R. N. Thurston, *Opt. Lett.* **11**, 153 (1986).

[62] R. N. Thurston, J. P. Heritage, A. M. Weiner, and W. J. Tomlinson, *IEEE J. Quantum Electron.* **QE-22**, 682 (1986).

[63] R. H. Stolen, J. Botineau, and A. Ashkin, *Opt. Lett.* **7**, 512 (1982).

[64] M. Haner and W. S. Warren, *Appl. Phys. Lett.* **52**, 1458 (1988).

[65] C. P. J. Barty, W. White, W. Sibbett, and R. Trebino, Eds., Special Issue on Ultrafast Optics, *IEEE J. Sel. Topics Quantum Electron.* **4**, 157 (1998).

[66] L. Xu, C. Spielmann, F. Krausz, and R. Szipöcs, *Opt. Lett.* **21**, 1259 (1996).

[67] A. Baltuska, Z. Wei, M. S. Pshenichnikov, and D. A. Wiersma, *Opt. Lett.* **22**, 102 (1997).

[68] S. Sartania, Z. Cheng, M. Lenzner, G. Tempea, C. Spielmann, F. Krausz, and K. Ferencz, *Opt. Lett.* **22**, 1562 (1997).

[69] A. Baltuska, Z. Wei, M. S. Pshenichnikov, D. A. Wiersma, and R. Szipöcs, *Appl. Phys. B* **65**, 175 (1997).

[70] M. Nisoli, S. Stagira, S. De Silvestri, O. Svelto et al., *Appl. Phys. B* **65**, 189 (1997); *IEEE J. Sel. Topics Quantum Electron.* **4**, 414 (1998).

[71] L. Xu, N. Karasawa, N. Nakagawa, R. Morita, H. Shigekawa, and M. Yamashita, *Opt. Commun.* **162**, 256 (1999).

[72] G. Steinmeyer, D. H. Sutter, L. Gallmann, N. Matuschek, and U. Keller, *Science* **286**, 1507 (1999).

[73] G. Tempea, F. Krausz, C. Spielmann, and T. Barbec, *IEEE J. Sel. Topics Quantum Electron.* **4**, 193 (1998).

[74] L. F. Mollenauer, R. H. Stolen, J. P. Gordon, and W. J. Tomlinson, *Opt. Lett.* **8**, 289 (1983).

[75] E. M. Dianov, A. Y. Karasik, P. V. Mamyshev, G. I. Onischukov, A. M. Prokhorov, M. F. Stel'makh, and A. A. Fomichev, *JETP Lett.* **40**, 903 (1984).

[76] E. M. Dianov, Z. S. Nikonova, A. M. Prokhorov, and V. N. Serkin, *Sov. Tech. Phys. Lett.* **12**, 310 (1986).

[77] P. Beaud, W. Hodel, B. Zysset, and H. P. Weber, *IEEE J. Quantum Electron.* **23**, 1938 (1987).

[78] K. Tai and A. Tomita, *Appl. Phys. Lett.* **48**, 1033 (1986).

[79] A. S. Gouveia-Neto, A. S. L. Gomes, and J. R. Taylor, *Opt. Lett.* **12**, 395 (1987).

[80] A. S. Gouveia-Neto, A. S. L. Gomes, and J. R. Taylor, *J. Mod. Opt.* **35**, 7 (1988).

[81] E. M. Dianov, Z. S. Nikinova, and V. N. Serkin, *Sov. J. Quantum Electron.* **19**, 937 (1989).

[82] G. P. Agrawal, *Opt. Lett.* **15**, 224 (1990).

[83] P. V. Mamyshev, S. V. Chernikov, E. M. Dianov, and A. M. Prokhorov, *Opt. Lett.* **15**, 1365 (1990).

[84] N. N. Akhmediev and N. V. Mitzkevich, *IEEE J. Quantum Electron.* **27**, 849 (1991).

[85] W. H. Xiang, S. R. Friberg, K. Watanabe, S. Machida, Y. Sakai, H. Iwamura, and Y. Yamamoto, *Appl. Phys. Lett.* **59**, 2076 (1991).

[86] P. V. Mamyshev, in *Optical Solitons—Theory and Experiment*, J. R. Taylor, Ed. (Cambridge University Press, Cambridge, UK, 1992), Chap. 8.

[87] S. A. Akhmanov, V. A. Vysolukh, and A. S. Chirkin, (AIP Press, New York, 1992).

[88] K. C. Chan and H. F. Liu, *Opt. Lett.* **19**, 49 (1994); *IEEE J. Quantum Electron.* **31**, 2226 (1995).

[89] J. Yu, K. Guan, and B. Yang, *Microwave Opt. Tech. Lett.* **16**, 27 (1997).

[90] K. C. Chan and W. H. Cao, *J. Opt. Soc. Am. B* **15**, 2371 (1998).

[91] D. Huhse, O. Reimann, E. H. Bottcher, and D. Bimberg, *Appl. Phys. Lett.* **75**, 2530 (1999).

[92] W. Cao and S. Liu, *Chin. J. Quant. Electron.* **16**, 9 (1999).

[93] K. R. Tamura, H. Kuhota, and M. Nakazawa, *IEEE J. Quantum Electron.* **36**, 773 (2000).

[94] F. Ouellette, *Opt. Lett.* **12**, 847 (1987); *Appl. Opt.* **29**, 4826 (1990); *Opt. Lett.* **16**, 303 (1991).

[95] H. G. Winful, *Appl. Phys. Lett.* **46**, 527 (1985).

[96] D. S. Peter, W. Hodel, and H. P. Weber, *Opt. Commun.* **112**, 59 (1994).

[97] B. J. Eggleton, K. A. Ahmed, L. Poladian, K. A. Ahmed, and H. F. Liu, *Opt. Lett.* **19**, 877 (1994).

[98] J. A. R. William, I. Bennion, K. Sugden, and N. Doran, *Electron. Lett.* **30**, 985 (1994).

[99] R. Kashyap, S. V. Chernikov, P. F. McKee, and J. R. Tyalor, *Electron. Lett.* **30**, 1078 (1994).

[100] P. A. Krug, T. Stefans, G. Yoffe, F. Ouellette, P. Hill, and G. Dhosi, *Electron. Lett.* **31**, 1091 (1995).

[101] C. M. de Sterke, *Opt. Lett.* **17**, 914 (1992); M. J. Steel and C. M. de Sterke, *Phys. Rev. A* **49**, 5048 (1994).

[102] S. V. Chernikov, J. R. Taylor, and R. Kashyap, *Opt. Lett.* **20**, 1586 (1995).

[103] D. Taverner, D. J. Richardson, M. N. Zervas, L. Reekie, L. Dong, and J. L. Cruz, *IEEE Photon. Technol. Lett.* **7**, 1436 (1995).

[104] K. Tamura, T. Komukai, T. Yamamoto, T. Imai, E. Yoshida, amd M. Nakazawa, *Electron. Lett.* **31**, 2194 (1995).

[105] C. M. de Sterke, N. G. R. Broderick, B. J. Eggleton, and M. J. Steel, *Opt. Fiber Technol*. **2**, 253 (1996).

[106] C. M. de Sterke, B. J. Eggleton, and P. A. Krug, *J. Lightwave Technol.* **15**, 1494 (1997).

[107] N. G. R. Broderick, D. Taverner, D. J. Richardson, M. Isben, and R. I. Laming, *Phys. Rev. Lett.* **79**, 4566 (1997); *Opt. Lett.* **22**, 1837 (1997).

[108] G. Lenz, B. J. Eggleton, and N. M. Litchinitser, *J. Opt. Soc. Am. B* **15**, 715 (1998).

[109] G. Lenz and B. J. Eggleton, *J. Opt. Soc. Am. B* **15**, 2979 (1998).

[110] B. J. Eggleton, G. Lenz, R. E. Slusher, and N. M. Litchinitser, *Appl. Opt.* **37**, 7055 (1998).

[111] B. J. Eggleton, G. Lenz, and N. M. Litchinitser, *Fiber Integ. Opt.* **19**, 383 (2000).

[112] G. P. Agrawal, *Fiber-Optic Communication Systems*, 2nd ed. (Wiley, New York, 1997).

[113] R. A. Fisher and W. K. Bischel, *Appl. Phys. Lett.* **24**, 468 (1974); *IEEE J. Quantum Electron.* **QE-11**, 46 (1975).

[114] D. Strickland and G. Mourou, *Opt. Commun.* **56**, 219 (1985).

[115] P. Maine, D. Strickland, P. Bado, M. Pessot, and G. Mourou, *IEEE J. Quantum Electron.* **24**, 398 (1988).

[116] M. Pessot, J. Squier, G. Mourou, and D. J. Harter, *Opt. Lett.* **14**, 797 (1989).

[117] M. Ferray, L. A. Lompre, O. Gobert, A. L. Huillier, G. Mainfray, C. Manus, A. Sanchez, and A. S. Gomes, *Opt. Commun.* **75**, 278 (1990).

[118] K. I. Yamakawa, C. P. J. Barty, H. Shiraga, and Y. Kato, *IEEE J. Quantum Electron.* **27**, 288 (1991).

[119] J. L. Tapie and G. Mourou, *Opt. Lett.* **17**, 136 (1991).

[120] W. Hodel, D. S. Peter, H. P. Weber, *Opt. Commun.* **97**, 233 (1993).

[121] M. L. Stock and G. Mourou, *Opt. Commun.* **106**, 249 (1994).

[122] M. E. Fermann, A. Galvanauskas, and D. Harter, *Appl. Phys. Lett.* **64**, 1315 (1994).

[123] A. Galvanauskas, M. E. Fermann, and D. Harter, *Opt. Lett.* **19**, 1201 (1994).

[124] L. M. Yang, T. Sosnowski, M. L. Stock, T. B. Norris, J. Squier, G. Mourou, M. L. Dennis, and I. N. Duling III, *Opt. Lett.* **20**, 1044 (1995).

[125] A. Galvanauskas, M. E. Fermann, D. Harter, K. Sugden, and I. Bennion, *Appl. Phys. Lett.* **66**, 1053 (1995).

[126] J. D. Minelly, A. Galvanauskas, M. E. Fermann, D. Harter, J. E. Caplan, Z. J. Chen, and D. N. Payne, *Opt. Lett.* **20**, 1797 (1995).

[127] S. Kane and J. Squier, *IEEE J. Quantum Electron.* **31**, 2052 (1995).

[128] A. Galvanauskas, P. A. Krug, and D. Harter, *Opt. Lett.* **21**, 1049 (1996).

[129] D. S. Peter, W. Hodel, and H. P. Weber, *Opt. Commun.* **130**, 75 (1996).

[130] A. Galvanauskas, D. Harter, M. A. Arbore, M. H. Chou, and M. M. Fejer, *Opt. Lett.* **23**, 1695 (1998).

[131] N. G. R. Broderick, D. J. Richardson, D. Taverner, J. E. Caplen, L. Dong, and M. Ibsen, *Opt. Lett.* **24**, 566 (1999).

[132] M. Hofer, M. E. Fermann, A. Galvanauskas, D. Harter, and R. S. Windeler, *IEEE Photon. Technol. Lett.* **11**, 650 (1999).

[133] H. H. Kuehl, *J. Opt. Soc. Am. B* **5**, 709 (1988).

[134] S. V. Chernikov and P. V. Mamyshev, *J. Opt. Soc. Am. B* **8**, 1633 (1991).

[135] S. V. Chernikov, D. J. Richardson, E. M. Dianov, and D. N. Payne, *Electron. Lett.* **28**, 1842 (1992).

[136] S. V. Chernikov, E. M. Dianov, D. J. Richardson, and D. N. Payne, *Opt. Lett.* **18**, 476 (1993).

[137] V. A. Bogatyrjov, M. M. Bubnov, E. M. Dianov, and A. A. Sysoliatin, *Pure Appl. Opt.* **4**, 345 (1995).

[138] P. V. Mamyshev, P. G. J. Wigley, J. Wilson, G. I. Stegeman, V. A. Smenov, E. M. Dianov, and S. I. Miroshnichenko, *Phys. Rev. Lett.* **71**, 73 (1993).

[139] E. M. Dianov, P. V. Mamyshev, A. M. Prokhorov, and S. V. Chernikov, *Opt. Lett.* **14**, 1008 (1989).

[140] P. V. Mamyshev, S. V. Chernikov, and E. M. Dianov, *IEEE J. Quantum Electron.* **27**, 2347 (1991).

[141] S. V. Chernikov, J. R. Taylor, P. V. Mamyshev, and E. M. Dianov, *Electron. Lett.* **28**, 931 (1992).

[142] S. V. Chernikov, D. J. Richardson, R. I. Laming, and E. M. Dianov, *Electron. Lett.* **28**, 1210 (1992).

[143] S. V. Chernikov, P. V. Mamyshev, E. M. Dianov, D. J. Richardson, R. I. Laming, and D. N. Payne, *Sov. Lightwave Commun.* **2**, 161 (1992).

[144] S. V. Chernikov, D. J. Richardson, and R. I. Laming, *Appl. Phys. Lett.* **63**, 293 (1993).

[145] S. V. Chernikov, J. R. Taylor, and R. Kashyap, *Electron. Lett.* **29**, 1788 (1993); *Opt. Lett.* **19**, 539 (1994).

[146] E. A. Swanson and S. R. Chinn, *IEEE Photon. Technol. Lett.* **6**, 796 (1994).

[147] E. A. Swanson, S. R. Chinn, K. Hall, K. A. Rauschenbach, R. S. Bondurant, and J. W. Miller, *IEEE Photon. Technol. Lett.* **6**, 1194 (1994).

[148] P. Schell, D. Bimberg, V. A. Bogatyrjov, E. M. Dianov, A. S. Kurkov, V. A. Semenov, and A. A. Sysoliatin, *IEEE Photon. Technol. Lett.* **6**, 1191 (1994).

[149] A. V. Shipulin, E. M. Dianov, R. J. Richardson, and D. N. Payne, *IEEE Photon. Technol. Lett.* **6**, 1380 (1994).

[150] K. Suzuki, K. Iwatsuki, S. Nishi, M. Samwatari, and T. Kitoh, *IEEE Photon. Technol. Lett.* **6**, 352 (1994).

[151] M. Nakazawa, E. Yoshida, K. Kubota, and Y. Kimura, *Electron. Lett.* **30**, 2038 (1994).

[152] A. J. Stentz, R. W. Boyd, and A. F. Evans, *Opt. Lett.* **20**, 1770 (1995).

[153] R. J. Essiambre and G. P. Agrawal, *Opt. Lett.* **21**, 116 (1996).

[154] A. Mostofi, H. Hatami-Hanza, and P. L. Chu, *IEEE J. Quantum Electron.* **33**, 620 (1997).

[155] M. D. Pelusi and H. F. Liu, *IEEE J. Quantum Electron.* **33**, 1430 (1997).

[156] J. Wu, C. Lou, Y. Gao, W. Xu, Q. Guo, C. Liao, and S. Liu, *High Technol. Lett.* **8**, 8 (1998).

[157] K. I. M. McKinnon, N. F. Smyth, and A. L. Worthy, *J. Opt. Soc. Am. B* **16**, 441 (1999).

[158] K. R. Tamura and M. Nakazawa, *IEEE Photon. Technol. Lett.* **11**, 319 (1999).

[159] E. M. Dianov, P. V. Mamyshev, A. M. Prokhorov, and S. V. Chernikov, *Sov. J. Quantum Electron.* **18**, 1211 (1988).

[160] J. T. Manassah, *Opt. Lett.* **13**, 755 (1988).

[161] G. P. Agrawal, P. L. Baldeck, and R. R. Alfano, *Opt. Lett.* **14**, 137 (1989); *Phys. Rev. A* **40**, 5063 (1989).

[162] M. Yamashita and K. Torizuka, *Jpn. J. Appl. Phys.* **29**, 294 (1990).

[163] Q. Z. Wang, P. P. Ho, and R. R. Alfano, *Opt. Lett.* **15**, 1023 (1990); *Opt. Lett.* **16**, 496 (1991).

[164] J. E. Rothenberg, *Opt. Lett.* **15**, 495 (1990).

[165] A. D. Ellis and D. M. Patrick, *Electron. Lett.* **29**, 149 (1993).

[166] C. Headley III and G. P. Agrawal, *J. Opt. Soc. Am. B* **10**, 2383 (1993); *IEEE J. Quantum Electron.* **31**, 2058 (1995).

[167] R. F. de Souza , E. J. S. Fonseca, M. J. Hickmann, and A. S. Gouveia-Neto, *Opt. Commun.* **124**, 79 (1996).

[168] W. H. Cao and Y. W. Zhang, *Opt. Commun.* **128**, 23 (1996).

[169] C. Yeh and L. Bergman, *Phys. Rev. E* **57**, 2398 (1998).

[170] M. Yamashita, H. Sone, R. Morita, and H. Shigekawa, *IEEE J. Quantum Electron.* **34**, 2145 (1998).

[171] C. G. Durfee III, S. Backus, H. C. Kapteyn, and M. M. Murnane, *Opt. Lett.* **24**, 697 (1999).

[172] K. C. Chan and W. H. Cao, *Opt. Commun.* **178**, 79 (2000).

[173] A. Takada, T. Suigi, and M. Saruwatari, *Electron. Lett.* **22**, 1347 (1986).

[174] M. Nakazawa, K. Suzuki, and Y. Kimura, *Opt. Lett.* **15**, 588 (1990); *IEEE Photon. Technol. Lett.* **2**, 216 (1990).

[175] R. T. Hawkins, *Electron. Lett.* **26**, 292 (1990).

[176] K. Iwatsuki, K. Suzuki, and S. Nishi, *Electron. Lett.* **27**, 1981 (1991).

[177] H. F. Liu, Y. Ogawa, S. Oshiba, and T. Tonaka, *IEEE J. Quantum Electron.* **27**, 1655 (1991).

[178] J. T. Ong, R. Takahashi, M. Tsuchiya, S. H. Wong, R. T. Sahara, Y. Ogawa, and T. Kamiya, *IEEE J. Quantum Electron.* **29**, 1701 (1993).

[179] A. Galvanauskas, P. Blixt, and J. A. Tellefsen, Jr., *Appl. Phys. Lett.* **63**, 1742 (1993).

[180] L. Chusseau, *IEEE J. Quantum Electron.* **30**, 2711 (1994).

[181] K. A. Ahmed, K. C. Chan, and H. F. Liu, *IEEE J. Sel. Topics Quantum Electron.* **1**, 592 (1995).

[182] L. Chusseau and E. Delevaque, *IEEE J. Sel. Topics Quantum Electron.* **2**, 500 (1996).

[183] S. D. Cho, C. H. Lee, and S. Y. Shin, *IEEE Photon. Technol. Lett.* **11**, 782 (1999).

[184] Y. Matsui, M. D. Pelusi, and A. Suzuki, *IEEE Photon. Technol. Lett.* **11**, 1217 (1999).

[185] R. Yatsu, K. Taira, and M. Tsuchiya, *Opt. Lett.* **24**, 1172 (1999).

[186] G. P. Agrawal and N. A. Olsson, *Opt. Lett.* **14**, 500 (1989).

[187] N. A. Olsson and G. P. Agrawal, *Appl. Phys. Lett.* **55**, 13 (1989).

[188] G. P. Agrawal and N. A. Olsson, *IEEE J. Quantum Electron.* **25**, 2297 (1989).

[189] N. A. Olsson, G. P. Agrawal, and K. W. Wecht, *Electron. Lett.* **25**, 603 (1989).

[190] G. P. Agrawal and N. K. Dutta, *Semiconductor Lasers*, 2nd ed. (Van Nostrand Reinhold, New York, 1993).

[191] K. J. Blow, N. J. Doran, and D. Wood, *J. Opt. Soc. Am. B* **5**, 381 (1988); *J. Opt. Soc. Am. B* **5**, 1301 (1988).

[192] P. A. Bélanger, L. Gagnon, and C. Paré, *Opt. Lett.* **14** 943 (1989); L. Gagnon and P. A. Bélanger, *Phys. Rev. A* **43**, 6187 (1991).

[193] G. P. Agrawal, *IEEE Photon. Technol. Lett.* **2**, 216 (1990); *Opt. Lett.* **16**, 226 (1991); *Phys. Rev. A* **44**, 7493 (1991).

[194] I. Y. Khrushchev, A. B. Grudinin, E. M. Dianov, D. V. Korobkin, V. A. Semenov, and A. M. Prokhorov, *Electron. Lett.* **26**, 456 (1990).

[195] M. Nakazawa, K. Kurokawa, H. Kobota, K. Suzuki, and Y. Kimura, *Appl. Phys. Lett.* **57**, 653 (1990).

[196] V. S. Grigoryan and T. S. Muradyan, *J. Opt. Soc. Am. B* **8**, 1757 (1991).

[197] V. V. Afanasjev, V. N. Serkin, and V. A. Vysloukh, *Sov. Lightwave Commun.* **2**, 35 (1992).

[198] E. Yoshida, Y. Kimura, and M. Nakazawa, *Jpn. J. Appl. Phys.* **32**, 3461 (1993).

[199] M. L. Quiroga-Teixeiro, D. Anderson, P. A. Andrekson, A. Berntson, and M. Lisak, *J. Opt. Soc. Am. B* **13**, 687 (1996).

[200] K. Tamura and M. Nakazawa, *Opt. Lett.* **21**, 68 (1996).

[201] P. C. Reeves-Hall, S. A. E. Lewis, S. V. Chernikov, and J. R. Taylor, *Electron. Lett.* **36**, 622 (2000).

[202] A. N. Starodumov, *Opt. Commun.* **124**, 365 (1996).

[203] Y. Yamamoto and M. Nakazawa, *IEEE Photon. Technol. Lett.* **9**, 1595 (1997).

[204] K. Smith, N. J. Doran, and P. G. J. Wigley, *Opt. Lett.* **15**, 1294 (1990).

[205] R. A. Betts, S. J. Frisken, C. A. Telford, and P. S. Atherton, *Electron. Lett.* **27**, 858 (1991).

[206] A. G. Bulushev, T. R. Martirosyan, O. G. Okhotnikov, V. M. Paramonov, and V. A. Tsarjov, *Sov. Lightwave Commun.* **1**, 113 (1991).

[207] A. L. Steele, *Electron. Lett.* **29**, 1971 (1993).

[208] R. J. Essiambre and A. Vallé, *Can. J. Phys.* **71** , 11 (1993).

[209] J. H. Xy, Z. J. Fang, W. Z. Zhang, and F. X. Gan, *Fiber Integ. Opt.* **13**, 365 (1994).

[210] A. B. Aceves, G. G. Luther, C. De Angelis, A. M. Rubenchik, and S. K. Turitsyn, *Opt. Fiber Technol*. **1**, 244 (1995); *Phys. Rev. Lett.* **75**, 73 (1995).

[211] H. Hatami-Hanza, P. L. Chu, M. A. Malomed, and G. D. Peng, *Opt. Commun.* **134**, 59 (1997).

[212] D. K. Serkland, G. D. Bartiolini, A. Agarwal, P. Kumar, and W. L. Kath, *Opt. Lett.* **23**, 795 (1998).

[213] X. Hong and J. Lin, *Microwave Opt. Tech. Lett.* **24**, 187 (2000).

Chapter 7

Fiber-Optic Communications

Soon after the nonlinear effects in optical fibers were observed experimentally, it was realized that they would limit the performance of fiber-optic communication systems [1]. However, nonlinear effects were found to be mostly irrelevant for system design in the 1980s because both the bit rate and link lengths were limited by fiber losses and group-velocity dispersion (GVD). The situation changed dramatically during the 1990s with the advent of optical amplification, dispersion management, and wavelength-division multiplexing (WDM). These advances increased fiber-link lengths to beyond 1000 km and single-channel bit rates to beyond 10 Gb/s. As a result, the nonlinear effects in optical fibers became of paramount concern in the system design [2]–[6]. This chapter focuses on how the nonlinear effects influence the design of WDM lightwave systems. The loss- and dispersion-management techniques are discussed first in Section 7.1 as an introduction to system-related issues. Sections 7.2 and 7.3 consider the impact of stimulated Brillouin and Raman scattering (SBS and SRS). The role of self- and cross-phase modulation (SPM and XPM) is discussed in Sections 7.4 and 7.5, respectively, while Section 7.6 is devoted to the detrimental effects of four-wave mixing (FWM). Finally, Section 7.7 focuses on the design and performance of WDM systems.

7.1 System Basics

All digital lightwave systems transmit information as a continuous stream of 1 and 0 bits. The bit rate B determines the duration of each bit, or the bit slot, as $T_B = 1/B$. An optical pulse is present in the bit slot of each 1 bit. It

occupies a fraction of the bit slot when the return-to-zero (RZ) format is used. In the case of the nonreturn-to-zero (NRZ) format, the optical pulse occupies the entire bit slot. The most important issue for lightwave systems is how an optical bit stream is affected by losses, GVD, and various nonlinear effects as it propagates down the fiber link [7]–[10]. In this section the focus is on the effects of fiber losses and dispersion; the nonlinear effects are considered in later sections.

7.1.1 Loss Management

As discussed in Section A.1.2, optical fibers have minimum losses in the wavelength region near 1.55 μm (about 0.2 dB/km). In fact, most modern lightwave systems operate near this wavelength to minimize the impact of fiber losses. Even then, the optical signal is attenuated by a factor of 100 or more over a link length of only 100 km. Since long-haul lightwave systems typically extend over thousands of kilometers, it is evident that fiber losses must be compensated periodically to boost the signal power back to its original value.

A common technique, used exclusively during the 1980s, regenerates the optical signal using a "repeater" in which the bit stream is first converted to the electric domain (using an optical receiver) and then regenerated with the help of an optical transmitter [7]. This technique becomes quite cumbersome (and expensive) for WDM systems as it requires demultiplexing of all channels at each repeater. As discussed in Chapter 4, fiber amplifiers can amplify multiple WDM channels simultaneously. For this reason, almost all WDM lightwave systems use optical amplifiers for compensating fiber losses. Figure 7.1 shows how amplifiers can be cascaded in a periodic manner to form a chain, and thus extend fiber-optic transmission to distances as large as 10,000 km, while retaining the signal in its original optical form. Most systems employ lumped amplifiers in which losses accumulated over 50 to 100 km of fiber lengths are compensated using short lengths ($\sim$ 10 m) of erbium-doped fibers. The distributed-amplification scheme in which the transmission fiber itself is used for amplification (with the gain provided by SRS or erbium ions) compensates losses all along the fiber length. It requires periodic injection of pump power through the fiber couplers, as shown in Fig. 7.1.

The loss-management technique based on optical amplification degrades the signal-to-noise ratio (SNR) of the optical bit stream since all amplifiers add noise to the signal through spontaneous emission. Mathematically, this noise can be included by adding a Langevin-noise term to the Ginzburg–Landau

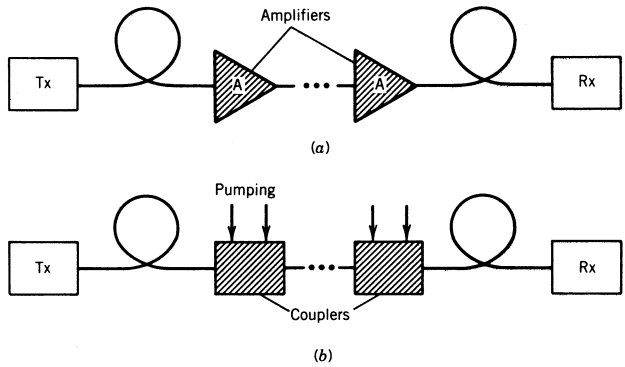

Figure 7.1 Schematic illustration of fiber-optic links making use of (a) lumped and (b) distributed amplification for compensation of fiber losses.

equation of Section 4.3. If the two-photon absorption term in Eq. (4.3.16) is neglected because of its smallness, the amplification process is governed by

$$\frac{\partial A}{\partial z}+\frac{i}{2}(\beta_2+ig_0T_2^2)\frac{\partial^2 A}{\partial T^2}=i\gamma|A|^2A+\frac{1}{2}(g_0-\alpha)A+f_n(z,T), \qquad (7.1.1)$$

where g_0 is the gain coefficient and the T_2 term accounts for the decrease in the gain for spectral components of an optical pulse located far from the gain peak. The noise induced by spontaneous emission vanishes on average such that $\langle f_n(z,T)\rangle = 0$. If noise is modeled as a Markovian stochastic process with Gaussian statistics, its second moment can be written as

$$\langle f_n(z,T)\, f_n(z',T')\rangle = n_{\rm sp}h\nu_0 g_0\delta(z-z')\delta(T-T'), \qquad (7.1.2)$$

where $n_{\rm sp}$ is the spontaneous-emission factor introduced in Section 4.1 and $h\nu_0$ is the average photon energy. The two delta functions ensure that all spontaneous-emission events are independent of each other. The noise variance is higher by factor of 2 when both polarization components are considered [11].

In the case of distributed amplification, Eq. (7.1.1) should be solved along the entire fiber link. However, when lumped amplifiers are used periodically, the amplifier length is typically much shorter than the dispersive and nonlinear lengths. For this reason, one can set α, β_2, and γ to zero in Eq. (7.1.1). If gain dispersion is also ignored by setting $T_2 = 0$, this equation can be integrated over the amplifier length l_a with the result

$$A_{\rm out}(T)=\sqrt{G}A_{\rm in}(T)+a_n(T), \qquad (7.1.3)$$

where $G = \exp(g_0 l_a)$ is the amplification factor of the lumped amplifier. The spontaneous-emission noise added by the amplifier is given by

$$a_n(T) = \int_0^{l_a} f_n(z,T) \exp\left[\frac{1}{2} g_0 (l_a - z)\right] dz. \tag{7.1.4}$$

If we use Eq. (7.1.2), the second moment of $a_n(T)$ satisfies

$$\langle a_n(T) a_n(T') \rangle = S_{\text{sp}} \delta(T - T'), \tag{7.1.5}$$

where $S_{\text{sp}} = (G-1) n_{\text{sp}} h\nu_0$ is the spectral density of amplified spontaneous emission (ASE), introduced earlier in Section 4.1.3. The delta function indicates that the ASE spectral density is frequency independent (white noise). In real amplifiers, the gain spectrum sets the bandwidth over which ASE occurs. An optical filter is often placed just after the amplifier to reduce the amplifier-induced noise. If that is the case, noise is added only over the filter bandwidth, and the ASE power becomes

$$P_{\text{sp}} = \int_{-\infty}^{\infty} S_{\text{sp}} H_f(\nu - \nu_0)\, d\nu \approx S_{\text{sp}} \Delta\nu_f, \tag{7.1.6}$$

where H_f is the transfer function, ν_0 is the center frequency, and $\Delta\nu_f$ is the 3-dB bandwidth (FWHM) of the filter.

In a chain of cascaded lumped amplifiers (see Fig. 7.1), ASE accumulates from amplifier to amplifier and can build up to high levels [11]. If we assume that all amplifiers are spaced apart by a constant distance L_A and the amplifier gain $G \equiv \exp(\alpha L_A)$ is just large enough to compensate for fiber losses in each fiber section, the total ASE power for a chain of N_A amplifiers is given by

$$P_{\text{sp}} = N_A S_{\text{sp}} \Delta\nu_f = n_{\text{sp}} h\nu_0 N_A (G-1) \Delta\nu_f. \tag{7.1.7}$$

Clearly, ASE power can become quite large for large values of G and N_A. A side effect of high ASE levels is that at some point ASE begins to saturate amplifiers. Then, signal power begins to decrease while, at the same time, noise power keeps on increasing, resulting in severe degradation of the SNR. The ASE power can be controlled by reducing the amplifier spacing L_A. At first sight, this approach may appear counterintuitive since it increases N_A. However, noting that $N_A = L/L_A = \alpha L/\ln G$, we find that P_{sp} scales with G as $(G-1)/\ln G$ and can be reduced by lowering the gain of each amplifier. The limit $L_A \to 0$ corresponds to the technique of distributed amplification. In practice, the amplifier spacing L_A cannot be made too small. Typically, L_A is below 50 km for undersea applications but can be increased to 80 km or so for terrestrial systems with link lengths under 3000 km.

7.1.2 Dispersion Management

In Section A.3.5 we discussed the limitations imposed on system performance by dispersion-induced pulse broadening. As shown in Fig. A.3.9, the GVD effects can be minimized by using a narrow-linewidth laser and operating the system close to the zero-dispersion wavelength λ_{ZD} of the fiber. However, it is not always practical to match the operating wavelength λ with λ_{ZD}. An example is provided by terrestrial lightwave systems operating near 1.55 μm and using optical transmitters containing a DFB laser. Such systems often use the existing fiber network made of "standard" telecommunication fibers for which $\lambda_{ZD} \approx 1.31$ μm. Since the GVD parameter $\beta_2 \approx -20$ ps^2/km in the 1.55-μm region of such fibers, dispersion-induced pulse broadening limits the system performance severely. In the case of directly modulated DFB lasers, we can use Eq. (A.3.5.2) for estimating the limiting transmission distance L and find that L is limited as

$$L < (4B|D|\sigma_\lambda)^{-1}, \tag{7.1.8}$$

where σ_λ is the root-mean-square (RMS) spectral width, with a typical value around 0.15 nm for directly modulated DFB lasers. Using $D = 16$ ps/(km-nm) in Eq. (7.1.8), lightwave systems operating at 2.5 Gb/s are limited to $L \approx$ 42 km. Indeed, such systems use electronic regenerators, spaced apart by about 40 km, and cannot make use of optical amplifiers. Furthermore, their bit rate cannot be increased beyond 2.5 Gb/s because the repeater spacing becomes too small to be practical.

System performance can be improved considerably using external modulators. The transmission distance is now limited by Eq. (A.3.5.4) as

$$L < (16|\beta_2|B^2)^{-1}. \tag{7.1.9}$$

Using $\beta_2 = -20$ ps^2/km at 1.55 μm, the system length is limited to below 500 km at 2.5 Gb/s. Although improved considerably compared with the case of directly modulated DFB lasers, this dispersion limit becomes of concern when optical amplifiers are used for loss compensation. Moreover, if the bit rate is increased to 10 Gb/s, the GVD-limited transmission distance drops to 30 km, a value so low that optical amplifiers cannot be used in designing such lightwave systems. It is evident from Eq. (7.1.9) that the relatively large GVD of standard telecommunication fibers severely limits the performance of 1.55-μm systems designed to use the existing telecommunication network at a bit rate of 10 Gb/s or more.

The dispersion-management scheme is aimed at solving this practical problem. The basic idea behind dispersion management is quite simple and can be understood using the pulse-propagation equation of Section A.2.3. If nonlinear effects and fiber losses are ignored, this equation can be written as

$$\frac{\partial A}{\partial z} + \frac{i\beta_2}{2}\frac{\partial^2 A}{\partial t^2} - \frac{\beta_3}{6}\frac{\partial^3 A}{\partial t^3} = 0, \tag{7.1.10}$$

where the effect of third-order dispersion (TOD) is included by the β_3 term. In practice, this term can be neglected as long as $|\beta_2|$ is not close to zero. Equation (7.1.10) can be solved using the Fourier-transform method. In the specific case of $\beta_3 = 0$, the solution is given by

$$A(L,t) = \frac{1}{2\pi}\int_{-\infty}^{\infty} \tilde{A}(0,\omega)\exp\left(\frac{i}{2}\beta_2 L\omega^2 - i\omega t\right) d\omega, \tag{7.1.11}$$

where $\tilde{A}(0,\omega)$ is the Fourier transform of $A(0,T)$ and L is the length of a fiber with uniform GVD β_2.

Dispersion-induced degradation of optical signals is caused by different phase shifts ($\phi_s = \beta_2 L\omega^2/2$) acquired by different spectral components as a pulse propagates down the fiber. All dispersion-management schemes attempt to cancel this phase shift so that the input signal can be restored. In the simplest approach, the optical signal is propagated over multiple fiber segments with different dispersion characteristics. The basic idea can be understood by considering just two segments whose GVD parameters are chosen such that

$$\beta_{21}L_1 + \beta_{22}L_2 = 0, \tag{7.1.12}$$

where $L = L_1 + L_2$ and β_{2j} is the GVD of the fiber segment of length L_j ($j = 1, 2$). If we apply Eq. (7.1.11) to each fiber section and use the condition (7.1.12), it is easy to verify that $A(L,t) = A(0,T)$. As a result, the pulse shape is restored to its input form after traversing the two segments. The second segment is made of dispersion-compensating fiber (DCF) designed to have normal GVD near 1.55 μm ($\beta_{22} > 0$). Its length should be chosen such that $L_2 = -(\beta_{21}/\beta_{22})L_1$. For practical reasons, L_2 should be as small as possible. Commercial DCFs have values of β_{22} in excess of 100 ps^2/km and are designed with a relatively small value of the V parameter (see Section A.2.2).

Modern long-haul systems employ the loss- and dispersion-management schemes simultaneously, using a periodic dispersion map such that each sec-

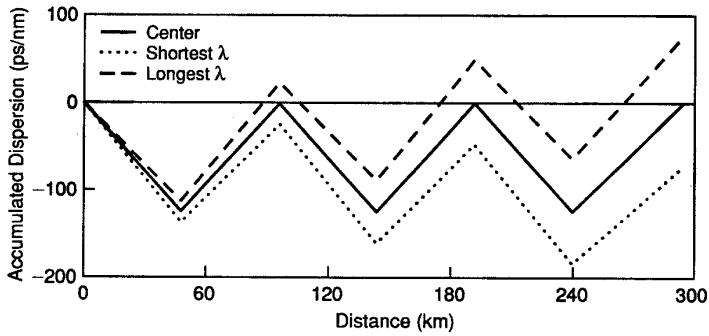

Figure 7.2 Dispersion map for center, shortest-, and longest-wavelength channels of a WDM system. (After Ref. [5], ©Lucent Technologies)

tion between two amplifiers (see Fig. 7.1) consists of two (or more) fiber segments chosen such that the average value of the GVD parameter,

$$\bar{\beta}_2 = \frac{\beta_{21}L_1 + \beta_{22}L_2}{L_1 + L_2}, \tag{7.1.13}$$

is relatively small. If the numerical value of $\bar{\beta}_2$ is close to zero, the effects of TOD become important and should be included, especially for RZ-format systems for which pulse width is a small fraction of the bit slot. The nonlinear parameter γ is larger by a factor of 3 to 4 for a DCF because of its small effective core area (about 20 μm^2). As a result, nonlinear effects in DCFs are enhanced considerably. Losses in such fibers are also large. Chirped fiber gratings provide an alternative to DCF for dispersion compensation. The main disadvantage of chirped gratings is their limited spectral range—large GVD occurs only within the stop band. As a result, multiple gratings are needed for WDM systems.

WDM systems benefit from dispersion management enormously [12] since its use avoids interchannel crosstalk induced by FWM (discussed in Section 7.6). However, the GVD cannot be compensated fully for all channels because of the wavelength dependence of β_2 and because β_3 is generally positive for all fibers. The plot of the accumulated value of dispersion, $\int_0^z D(z)\,dz$, along the fiber link for the shortest- and longest-wavelength channels in Figure 7.2 shows the typical situation for WDM systems. The average GVD can be reduced to zero for the central channel but has finite values for all other channels. The total dispersion may exceed 1000 ps/nm for the boundary channels in long-

haul WDM systems. Pre- or postcompensation techniques are sometimes used by adding different DCF lengths for different channels at the transmitter or receiver end. New types of fibers with negative values of β_3 have also been developed for this purpose. Their use permits in-line GVD compensation for all channels simultaneously.

7.2 Stimulated Brillouin Scattering

Rayleigh scattering, a major source of fiber losses, is an example of elastic scattering in which the frequency of scattered light remains unchanged. In contrast, the frequency is shifted downward during inelastic scattering. Two examples of inelastic scattering are Raman and Brillouin processes. Both of them can be understood as the conversion of a photon to a lower-energy photon such that the energy difference appears in the form of a phonon. The main difference between the two is that optical phonons (related to vibrations of silica molecules) participate in Raman scattering, whereas acoustic phonons participate in Brillouin scattering. The two processes are harmless at low powers because their scattering cross sections are relatively small. However, they become stimulated at high power levels, resulting in the nonlinear phenomena of SBS and SRS that can affect the performance of lightwave systems considerably. This section focuses on SBS from a system point of view.

7.2.1 Brillouin Threshold

SBS in optical fibers was first observed in 1972 and has been studied extensively since then because of its implications for lightwave systems [13]–[19]. As discussed in Chapter A.9, SBS generates a Stokes wave propagating in the backward direction. The frequency of the Stokes wave is down-shifted by an amount that depends on the wavelength of incident signal. This shift is known as the *Brillouin shift* and is about 11 GHz in the wavelength region near 1.55 μm. The intensity of the Stokes wave grows exponentially once the input power exceeds a threshold value. For narrowband, continuous-wave (CW) signals, the threshold power P_{th} can be estimated using [14]

$$g_B P_{\text{th}} L_{\text{eff}} / A_{\text{eff}} \approx 21, \tag{7.2.1}$$

where g_B is the Brillouin gain coefficient and A_{eff} is the effective core area. The effective interaction length is smaller than the actual fiber length because

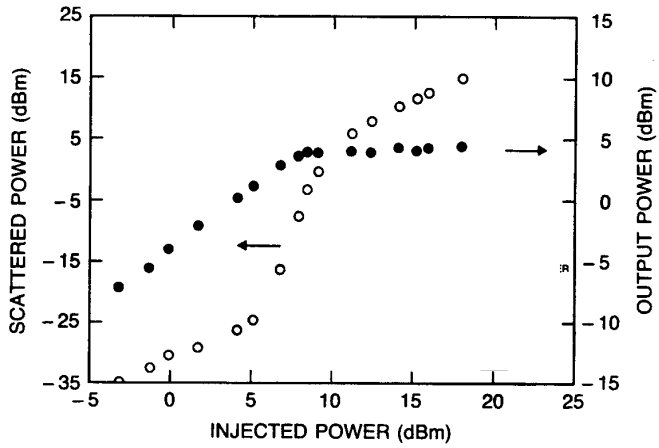

Figure 7.3 Output signal power (solid circles) and reflected SBS power (empty circles) as a function of power injected into a 13-km-long fiber. (After Ref. [17], ©1992 IEEE)

of fiber losses and is given by

$$L_{\text{eff}} = \int_0^L e^{-\alpha z}\, dz = \frac{1 - \exp(-\alpha L)}{\alpha}, \tag{7.2.2}$$

for a fiber with loss coefficient α and length L. For long fibers such that $\alpha L \gg 1$, one can use $L_{\text{eff}} \approx 1/\alpha \approx 21.74$ km when $\alpha = 0.2$ dB/km. Using $g_B \approx 5 \times 10^{-11}$ m/W and $A_{\text{eff}} = 50\ \mu\text{m}^2$ as typical values, P_{th} can be as low as 1 mW for CW signals in the wavelength region near 1.55 μm [15]. Figure 7.3 shows variations in the transmitted reflected power (through SBS) for a 13-km-long dispersion-shifted fiber as the injected CW power is increased from 0.5 to 50 mW. No more than 3 mW could be transmitted through the fiber in this experiment after the onset of SBS.

The SBS threshold increases for CW beams whose spectral width $\Delta\nu_p$ is larger than the Brillouin-gain line width ($\Delta\nu_B \sim 20$ MHz). It also increases when short optical pulses propagate through the fiber because of their relatively wide bandwidth. In lightwave systems, the optical signal is in the form of a time-dependent signal composed of an arbitrary sequence of 1 and 0 bits. One would expect the Brillouin threshold of such a signal to be higher than that of a CW pump. Considerable attention has been paid to estimating the Brillouin threshold and quantifying the SBS limitations for practical lightwave

systems [20]–[28]. The amount by which the threshold power increases depends on the modulation format used for data transmission. In the case of a coherent transmission scheme, the SBS threshold also depends on whether the amplitude, phase, or frequency of the optical carrier is modulated for information coding. Most lightwave systems modulate amplitude of the optical carrier and use the so-called on–off keying scheme.

Calculation of the Brillouin threshold is quite involved as it requires a time-dependent analysis [20]. Considerable simplification occurs if the bit rate B is assumed to be much larger than the Brillouin-gain line width $\Delta\nu_B$. Even with this assumption, the analysis is complicated by the fact that the 1 and 0 bits do not follow a fixed pattern in realistic communication systems. A simple approach assumes that the situation is equivalent to that of a CW pump whose spectrum corresponds to that caused by a random bit pattern. This is justified by noting that the backward nature of SBS would tend to average out time-dependent fluctuations. An interesting result of such an approximate analysis is that the Brillouin threshold increases by about a factor of 2 irrespective of the actual bit rate. As a result, input powers of about 6 mW can be injected into a fiber without performance degradation resulting from SBS.

In modern WDM systems, fiber losses are compensated periodically using optical amplifiers. An important question is how amplifiers affect the SBS process. If the Stokes wave were amplified by amplifiers, it would accumulate over the entire link and grow enormously. Fortunately, periodically amplified lightwave systems typically employ an optical isolator within each amplifier that blocks the passage of the Stokes wave. However, the SBS growth between two amplifiers is still undesirable for two reasons. First, it removes power from the signal once the signal power exceeds the threshold level. Second, it induces large fluctuations in the remaining signal, resulting in degradation of both the SNR and the bit-error rate [18]. For these reasons, single-channel powers are invariably kept below the SBS threshold and are limited in practice to below 10 mW.

7.2.2 Control of SBS

The issue of interchannel crosstalk is of primary concern for WDM lightwave systems. SBS leads to interchannel crosstalk only if a fiber link transmits data in counterpropagating directions simultaneously and if the channel spacing between two counterpropagating channels happens to match the Brillouin shift of about 11 GHz precisely. Crosstalk results in amplification of the lower-

frequency channel at the expense of the power carried by the counterpropagating channel. In a 1985 experiment [21], a 10% increase in the signal power of one channel was observed at a power level of only 0.3 mW in the counterpropagating channel. In a 1994 experiment [26], SBS-induced power penalties were measured in a bidirectional coherent system at power levels far below the SBS threshold (< 0.1 mW). However, the Brillouin-induced crosstalk can be easily avoided by selecting the channel spacing appropriately. Most long-haul systems use different fibers for counterpropagating channels and are thus immune to Brillouin-induced crosstalk. The situation is somewhat different in the case of analog transmission of video channels using subcarrier multiplexing [7]. In that case, SBS degrades the system performance because the SBS-induced losses in the optical-carrier power can distort the analog signal and reduce the carrier-to-noise ratio [29].

Some applications require launch powers in excess of 10 mW. An example is provided by the shore-to-island fiber links designed to transmit information over several hundred kilometers without using in-line amplifiers or repeaters [30]–[32]. Input power levels in excess of 50 mW are needed for distances > 300 km. One way to increase the input power is to raise the Brillouin threshold; several schemes have been proposed for this purpose [33]–[40]. These schemes rely on increasing either the Brillouin-gain line width $\Delta\nu_B$ or the effective spectral width of optical carrier. The former has a value of about 20 MHz for silica fibers, while the latter is typically < 10 MHz for DFB lasers used commonly for systems operating at bit rates above 2 Gb/s. The bandwidth of an optical carrier can be increased without affecting the system performance by modulating its phase at a frequency much lower than the bit rate. Typically, the modulation frequency $\Delta\nu_m$ is in the range of 200 to 400 MHz. Since the effective Brillouin gain is reduced by a factor of $(1 + \Delta\nu_m/\Delta\nu_B)$ in Eq. (7.2.1), the SBS threshold increases by the same factor. As $\Delta\nu_B \sim 20$ MHz, the launched power can be increased by more than a factor of 10 by this technique.

If the Brillouin-gain bandwidth $\Delta\nu_B$ of the fiber itself can be increased from its nominal value of 20 MHz to more than 200 MHz, the SBS threshold can be increased without requiring a phase modulator. One technique uses sinusoidal strain along the fiber length for this purpose. The applied strain changes the Brillouin shift ν_B by a few percent in a periodic manner. The resulting Brillouin-gain spectrum is much broader than that occurring for a fixed value of ν_B. The strain can be applied during cabling of the fiber. In one fiber

cable, $\Delta\nu_B$ was found to increase from 50 MHz to 400 MHz [36]. The Brillouin shift ν_B can also be changed by making the core radius nonuniform along the fiber length since the longitudinal acoustic frequency depends on the core radius [37]. The same effect can be realized by changing the dopant concentration along the fiber length. This technique increased the SBS threshold of one fiber by 7 dB [38]. A side effect of varying the core radius or the dopant concentration is that the GVD parameter β_2 also changes along the fiber length. It is possible to vary both of them simultaneously in such a way that β_2 remains relatively uniform [40].

7.3 Stimulated Raman Scattering

As discussed in Chapter A.8, SRS differs from SBS in several ways. First, it generates a forward-propagating Stokes wave. Second, the Raman shift ν_R by which the frequency of the Stokes wave is down-shifted is close to 13 THz. Third, the Raman-gain spectrum is extremely broad (see Fig. A.8.1) and extends over a frequency range wider than 20 THz. Fourth, the peak value of the Raman gain g_R is lower by more than a factor of 100 compared with that of the Brillouin gain. SRS was first observed in optical fibers in 1972 [41]. Since then, the impact of SRS on the performance of lightwave systems has been studied extensively [42]–[61].

7.3.1 Raman Crosstalk

The Raman threshold, the power level at which the Raman process becomes stimulated and transfers most of the signal power to the Stokes wave, is estimated using a relation similar to Eq. (7.2.1). It can be written as [14]

$$P_{\text{th}} \approx 16A_{\text{eff}}/(g_R L_{\text{eff}}). \tag{7.3.1}$$

As before, we can replace L_{eff} with $1/\alpha$ for long fiber lengths used in lightwave systems. Using $g_R \approx 1\times 10^{-13}$ m/W, P_{th} is about 500 mW in the spectral region near 1.55 μm. Since input powers are limited to below 10 mW because of SBS, SRS is typically not of concern for single-channel systems.

The situation is quite different for WDM systems, which simultaneously transmit multiple channels spaced 100 GHz or so apart. The same fiber in which channels propagate acts as a Raman amplifier such that the long-wavelength channels are amplified by the short-wavelength channels as long as

the wavelength difference is within the Raman-gain bandwidth. The shortest-wavelength channel is depleted most as it can pump all other channels simultaneously. Such an energy transfer among channels can be detrimental for system performance since it depends on the bit pattern—it occurs only when 1 bits are present in both channels simultaneously. The signal-dependent amplification leads to power fluctuations, which add to receiver noise and degrade the receiver performance.

The Raman crosstalk can be avoided if channel powers are made so small that Raman amplification is negligible over the fiber length. It is thus important to estimate the limiting value of the channel power. A simple model considers depletion of the highest-frequency channel in the worst case, in which all channels transmit 1 bits simultaneously [43]. The amplification factor for the mth channel is $G_m = \exp(g_m L_{\text{eff}})$, where L_{eff} is given by Eq. (7.2.2) and $g_m = g_R(\Omega_m)P_{\text{ch}}/A_{\text{eff}}$ is the Raman gain at $\Omega_m = \omega_1 - \omega_m$ provided by the shortest-wavelength channel at the frequency ω_1. For $g_m L_{\text{eff}} \ll 1$, the shortest-wavelength channel is depleted by a fraction $g_m L_{\text{eff}}$ due to SRS-induced amplification of mth channel. The total depletion for a M-channel WDM system is given by

$$D_R = \sum_{m=2}^{M} g_R(\Omega_m)P_{\text{ch}}L_{\text{eff}}/A_{\text{eff}}. \tag{7.3.2}$$

The summation in Eq. (7.3.2) can be carried out analytically if the Raman gain spectrum (see Fig. A.8.1) is approximated by a triangular profile such that g_R increases linearly for frequencies up to 15 THz with a slope $S_R = dg_R/d\nu$ and then drops to zero. The fractional power loss for the shortest-wavelength channel becomes [43]

$$D_R = \tfrac{1}{2}M(M-1)C_R P_{\text{ch}} L_{\text{eff}}, \tag{7.3.3}$$

where $C_R = S_R \Delta\nu_{\text{ch}}/(2A_{\text{eff}})$. In deriving this equation, channels were assumed to have a constant spacing $\Delta\nu_{\text{ch}}$ and the Raman gain for each channel was reduced by a factor of 2 to account for polarization scrambling.

A more accurate analysis should consider not only depletion of each channel because of power transfer to longer-wavelength channels but also its own amplification by shorter-wavelength channels. If all other nonlinear effects are neglected along with GVD, evolution of the power P_n associated with the nth channel is governed by the following equation (see Chapter A.8):

$$\frac{dP_n}{dz} + \alpha P_n = C_R P_n \sum_{m=1}^{M} (n-m)P_m, \tag{7.3.4}$$

where α is assumed to be the same for all channels. This set of M coupled nonlinear equations can be solved analytically. For a fiber of length L, the result is given by [56]

$$P_n(L) = P_n(0)e^{-\alpha L}\frac{P_t \exp[(n-1)C_R P_t L_{\text{eff}}]}{\sum_{m=1}^{M} P_m(0)\exp[(m-1)C_R P_t L_{\text{eff}}]}, \tag{7.3.5}$$

where $P_t = \sum_{m=1}^{M} P_m(0)$ is the total input power in all channels. This equation shows that channel powers follow an exponential distribution because of Raman-induced coupling among all channels.

The depletion factor D_R for the shorter-wavelength channel ($n = 1$) is obtained using $D_R = (P_{10} - P_1)/P_{10}$, where $P_{10} = P_1(0)\exp(-\alpha L)$ is the channel power expected in the absence of SRS. In the case of equal input powers in all channels, $P_t = MP_{\text{ch}}$ in Eq. (7.3.5) and D_R is given by

$$D_R = 1 - \exp\left[-\frac{1}{2}M(M-1)C_R P_{\text{ch}} L_{\text{eff}}\right]\frac{M\sinh(\frac{1}{2}MC_R P_{\text{ch}} L_{\text{eff}})}{\sinh(\frac{1}{2}M^2 C_R P_{\text{ch}} L_{\text{eff}})}. \tag{7.3.6}$$

In the limit $M^2 C_R P_{\text{ch}} L_{\text{eff}} \ll 1$, this complicated expression reduces to the simple result in Eq. (7.3.3). In general, Eq. (7.3.3) overestimates the Raman crosstalk since it does not take into account pump depletion.

7.3.2 Power Penalty

The Raman-induced power penalty is obtained using $\delta_R = -10\log(1 - D_R)$ since the input channel power must be increased by a factor of $(1 - D_R)^{-1}$ to maintain the same system performance. Figure 7.4 shows how the power penalty increases with an increase in the channel power and the number of channels. The channel spacing is assumed to be 100 GHz. The slope of the Raman gain is estimated from the gain spectrum to be $S_R = 4.9 \times 10^{-18}$ m/(W-GHz) while $A_{\text{eff}} = 50\ \mu\text{m}^2$ and $L_{\text{eff}} \approx 1/\alpha$ = 21.74 km. As seen from Fig. 7.4, the power penalty becomes quite large for WDM systems with a large number of channels. In practice, the Raman-induced power penalty should be kept small. If a value of at most 1 dB is considered acceptable, the limiting channel power P_{ch} exceeds 10 mW for 20 channels, but its value is reduced to below 1 mW when the number of WDM channels is larger than 70.

Equation (7.3.6) overestimates the Raman crosstalk since it ignores the fact that signals in each channel consist of a random sequence of 0 and 1 bits. A statistical analysis shows that Raman crosstalk is lower by about a factor of

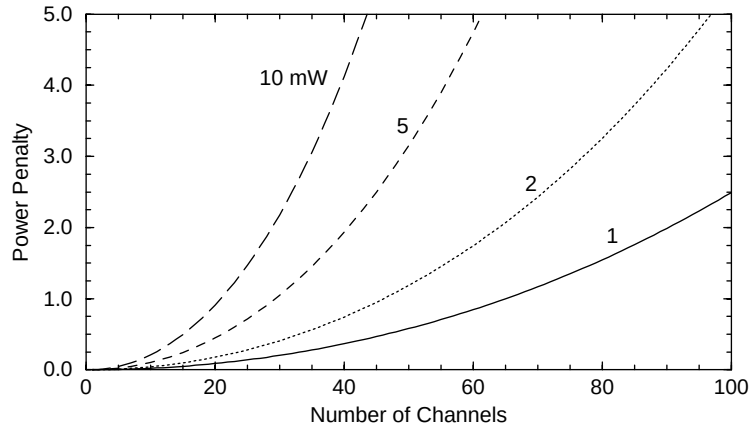

Figure 7.4 Raman-induced power penalty as a function of channel number for several values of P_{ch}. Channels are 100-GHz apart and launched with equal powers.

2 when signal modulation is taken into account [52]. The inclusion of GVD effects that were neglected in the above analysis also reduces Raman crosstalk since pulses in different channels travel at different speeds because of the group-velocity mismatch [57]. Figure 7.5 shows the the Raman-induced power penalty for a 100-km-long WDM system with 1-nm channel spacing after including the effects of both GVD and modulation statistics. Each channel operates at 10 Gb/s and is launched with same input peak power of 10 mW. The shortest-wavelength channel is assumed to be located at 1530 nm. The power penalty is smaller by a factor of 2 for standard fibers with $D = 16$ ps/(km-nm) compared with the $D = 0$ case. It exceeds 1 dB when the number of channels becomes more than 25 for $D = 2$ ps/(km-nm).

The effects of Raman crosstalk in a WDM system were quantified in a 1999 experiment by transmitting 32 channels, with 100-GHz spacing, over 100 km [60]. At low input powers ($P_{ch} = 0.1$ mW), SRS effects were relatively small and channel powers differed by only a few percent after 100 km. However, when the input power for each channel was increased to 3.6 mW, the longest-wavelength channel had 70% more power than the shortest-wavelength channel. Moreover, the channel powers were distributed in an exponential fashion as predicted by Eq. (7.3.5).

In long-haul lightwave systems, the crosstalk is also affected by the use of loss- and dispersion-management schemes. Dispersion management per-

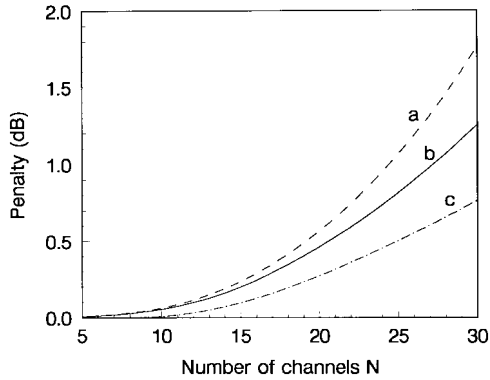

Figure 7.5 Raman-induced power penalty for a 100-km-long WDM system with 1-nm channel spacing. Dispersion parameter is 0, 2, and 16 ps/(km-nm) for curves (a)–(c), respectively. (After Ref. [57], ©1998 IEEE)

mits high values of GVD locally while reducing it globally. Since the group-velocity mismatch among different channels is quite large in such systems, the Raman crosstalk should be reduced in a dispersion-managed system. In contrast, the use of optical amplifiers for loss management magnifies the impact of SRS-induced degradation. The reason is that in-line amplifiers add broadband noise, which can seed the SRS process. As a result, noise is amplified along the link and results in degradation of the SNR. The SNR can be maintained if the channel power is increased as the number of amplifiers increases. The Raman-limited capacity of long-haul WDM systems depends on a large number of design parameters such as amplifier spacing, optical-filter bandwidth, bit rate, channel spacing, and total transmission distance [51].

Can Raman crosstalk be avoided by a proper system design? Clearly, reducing the channel power is the simplest solution but it may not always be practical. An alternative scheme lets SRS occur over the whole link but cancels the Raman crosstalk by using the technique of spectral inversion [51]. As the name suggests, if the spectrum of the WDM signal were inverted at some appropriate distance, short-wavelength channels would become long-wavelength channels and vice versa. As a result, the direction of Raman-induced power transfer will be reversed such that channel powers become nearly equal at the end of the fiber link. Complete cancellation of Raman crosstalk for a two-channel system requires spectral inversion at mid-span if GVD effects are negligible or compensated [59]. Equation (7.3.4) can be used to show that

the spectral-inversion technique should work for an arbitrary number of channels [61]. The location of spectral inversion is not necessarily in the middle of the fiber span but changes depending on gain–loss variations. Spectral inversion can be accomplished through FWM inside a fiber to realize phase conjugation; the same technique is also useful for dispersion compensation [7].

7.4 Self-Phase Modulation

As discussed in Chapter A.4, the intensity dependence of the refractive index leads to SPM-induced nonlinear phase shift, resulting in chirping and spectral broadening of optical pulses. Clearly, SPM can affect the performance of lightwave system considerably. When SPM is included, the propagation of an optical bit stream inside optical fibers is governed by the following nonlinear Schrödinger (NLS) equation [given earlier as Eq. (3.1.10)]:

$$i\frac{\partial A}{\partial z} - \frac{\beta_2}{2}\frac{\partial^2 A}{\partial T^2} + \gamma|A|^2 A = \frac{i\alpha}{2}A, \tag{7.4.1}$$

where fiber losses are included through the parameter α. The parameters β_2 and γ govern the effects of GVD and SPM, respectively. All three parameters become functions of z when loss- and dispersion-management schemes are employed for long-haul lightwave systems.

7.4.1 SPM-Induced Frequency Chirp

It is useful to eliminate the last term in Eq. (7.4.1) with the transformation

$$A(z,T) = \sqrt{P_0}\, e^{-\alpha z/2} U(z,T), \tag{7.4.2}$$

where P_0 is the peak power of input pulses. Equation (7.4.1) then takes the form

$$i\frac{\partial U}{\partial z} - \frac{\beta_2(z)}{2}\frac{\partial^2 U}{\partial T^2} + \gamma P_0 p(z)|U|^2 U = 0, \tag{7.4.3}$$

where power variations along a loss-managed fiber link are included through the periodic function $p(z)$ defined such that $p(z) = e^{-\alpha z}$ between two amplifiers but becomes 1 at the location of each lumped amplifier.

It is not easy to solve Eq. (7.4.3) analytically except in some simple cases. In the specific case of $p = 1$ and β_2 constant but negative, this equation reduces

to the standard NLS equation and has solutions in the form of solitons. This case is discussed in Chapter 8. Another special case is that of a square-shaped pulse propagating in a fiber with constant β_2. Using the transformation

$$U(z,T) = \sqrt{\rho(z,T)}\,\exp\left[i\int_0^T v(z,T)\,dT\right] \tag{7.4.4}$$

in Eq. (7.4.3), the pulse-propagation problem reduces to a fluid-dynamics problem in which the variables ρ and v play respectively the role of local density and velocity of a fluid [62]. In the optical case, these variables represent the local intensity and chirp of the pulse. For a square-shaped pulse, the pulse-propagation problem becomes identical to that of "breaking a dam" and can be solved analytically in the limit of small dispersion (the WKB approximation). This solution is useful for lightwave systems using the NRZ format and provides considerable physical insight [63]–[65].

From a practical standpoint, the effect of SPM is to chirp the pulse and broaden its spectrum. In the absence of dispersion ($\beta_2 = 0$), Eq. (7.4.3) can be solved analytically to study the extent of frequency chirping and spectral broadening (see Section A.4.1). The solution is of the form $U(z,T) = U(0,T)\exp(i\phi_{\rm NL})$, where the SPM-induced phase shift is given by

$$\phi_{\rm NL} = \gamma P_0 L_{\rm eff}|U(0,T)|^2. \tag{7.4.5}$$

The maximum phase shift, $\phi_{\max} = \gamma P_0 L_{\rm eff}$, determines the amount of frequency chirp. As a rough design guideline, the SPM effects are negligible when $\phi_{\max} < 1$ or $P_0 < \alpha/\gamma$, where we used $L_{\rm eff} \approx 1/\alpha$. For typical values of α and γ, SPM becomes important at peak power levels above 25 mW. Since SBS limits power levels to below 10 mW, SPM is of little concern for loss-limited lightwave systems. The situation changes when fiber losses are compensated using optical amplifiers. The SPM effects can then accumulate over the entire link. If N_A amplifiers are used, the maximum phase shift becomes $\phi_{\max} = \gamma P_0 N_A L_{\rm eff}$. As a result, the peak power is limited to $P_0 < \alpha/\gamma N_A$ or to below 3 mW for links with only 10 amplifiers. Clearly, SPM can be a major limiting factor for long-haul lightwave systems.

The important question is how the SPM-induced chirp affects broadening of optical pulses in the presence of dispersion. The broadening factor can be estimated, without requiring a complete solution of Eq. (7.4.3), using various approximations [66]–[72]. A variational approach was used as early as 1983 [66]. A split-step approach, in which the effects of SPM and GVD are

considered separately, also provides a reasonable estimate of pulse broadening [67]. In an extension of this technique, the SPM-induced chirp is treated as an effective chirp parameter at the input end [70]. A perturbation approach, in which the nonlinear term in Eq. (7.4.3) is treated as being relatively small, is also quite useful [72]. We focus on this approach since it can be used for systems with loss and dispersion management.

As discussed in Section A.3.3, the root-mean-square (RMS) value of the pulse width can be calculated using $\sigma = [\langle T^2 \rangle - \langle T \rangle^2]^{1/2}$, where

$$\langle T^m \rangle = \frac{\int_{-\infty}^{\infty} T^m |U(z,T)|^2 \, dT}{\int_{-\infty}^{\infty} |U(z,T)|^2 \, dT}. \tag{7.4.6}$$

For a symmetric pulse, $\langle T \rangle = 0$ and σ^2 is approximately given by

$$\sigma^2(z) = \sigma_L^2(z) + \gamma P_0 f_s \int_0^z \beta_2(z_1) \left[\int_0^{z_1} p(z_2) \, dz_2 \right] dz_1, \tag{7.4.7}$$

where σ_L^2 is the RMS width expected in the linear case ($\gamma = 0$). The shape of the input pulse enters through the parameter f_s, defined as

$$f_s = \frac{\int_{-\infty}^{\infty} |U(0,T)|^4 \, dT}{\int_{-\infty}^{\infty} |U(0,T)|^2 \, dT}. \tag{7.4.8}$$

For a Gaussian pulse with $U(0,T) = \exp[-\frac{1}{2}(T/T_0)^2]$, $f_s = 1/\sqrt{2} \approx 0.7$. For a square pulse, $f_s = 1$.

As an example, consider the case of a uniform-GVD fiber with distributed amplification such that the pulse energy remains nearly constant. Using $p(z) = 1$ with constant β_2 in Eq. (7.4.8), we obtain the simple expression

$$\sigma^2(z) = \sigma_L^2(z) + \tfrac{1}{2} f_s \gamma P_0 \beta_2 z^2. \tag{7.4.9}$$

This equation shows that the SPM enhances pulse broadening in the normal-GVD regime but leads to pulse compression in the anomalous-GVD regime. This behavior can be understood by noting that the SPM-induced chirp is positive in nature ($C > 0$). As a result, the pulse goes through a contraction phase when $\beta_2 < 0$. This is the origin of the existence of solitons in the anomalous-GVD regime. Equation (7.4.7) shows that the soliton effects are beneficial for all pulse shapes and can improve the performance of even NRZ-format systems using nearly square-shaped pulses. This improvement was predicted in the 1980s [73] and has been seen in several experiments.

7.4.2 Loss and Dispersion Management

Consider long-haul lightwave systems in which lumped amplifiers are used periodically for compensation of fiber losses. If dispersion management is also used, σ_L returns to its input value σ_0 at the end of each fiber section in between two amplifiers. It is evident from Eq. (7.4.7) that such a dispersion-compensation scheme will not work perfectly when SPM effects are significant. Even though the second term in this equation changes sign when β_2 changes sign, power variations in the two sections are different. As a result, the contribution of SPM does not cancel perfectly. Indeed, it has been noticed experimentally that system performance is better when GVD is undercompensated [74]–[76]. Equation (7.4.7) provides a simple explanation of this behavior. By optimizing the amount of GVD in the DCF, one can adjust the two terms in this equation and minimize the pulse width.

Equation (7.4.7) remains accurate as long as the second term is small compared with the first since the SPM-induced reduction in pulse width for $\beta_2 < 0$ cannot be expected to be larger than σ_L. As a rough estimate of the validity of this equation, we can use Eq. (7.4.9) to conclude that the simple analysis is valid as long as $z < (L_D L_{\rm NL})^{1/2}$, where $L_D = T_0^2/|\beta_2|$ is the dispersion length and $L_{\rm NL} = (\gamma P_0)^{-1}$ is the nonlinear length. Numerical simulations show that, at a fixed power level, the pulse width reaches a minimum value at some distance and then begins to increase. We show this behavior in Fig. 7.6 by solving Eq. (7.4.3) for a super-Gaussian input $U(0,T) = \exp[-\frac{1}{2}(T/T_0)^{2m}]$ with $m = 2$ and $p = 1$. The fiber was assumed to have uniform GVD (no dispersion management). A similar behavior is observed as a function of input peak power when the distance z is kept fixed. As the peak power increases, the pulse initially contracts because of the SPM effects, attains a minimum value at a certain value of the peak power, and then begins to increase rapidly. In practical terms, the input power should be optimized properly if we want to take advantage of the soliton-like effects for NRZ systems [73].

Another SPM-induced limitation results from the phenomenon of modulation instability occurring when the signal travels in the anomalous-GVD regime of the transmission fiber. At first sight, it may appear that modulation instability is not likely to occur for a signal in the form of a pulse train. In fact, it affects the performance of periodically amplified lightwave systems considerably. This can be understood by noting that optical pulses in an NRZ-format system occupy the entire time slot and can be several bits long depending on the bit pattern. As a result, the situation is quasi-CW-like. As early as 1990,

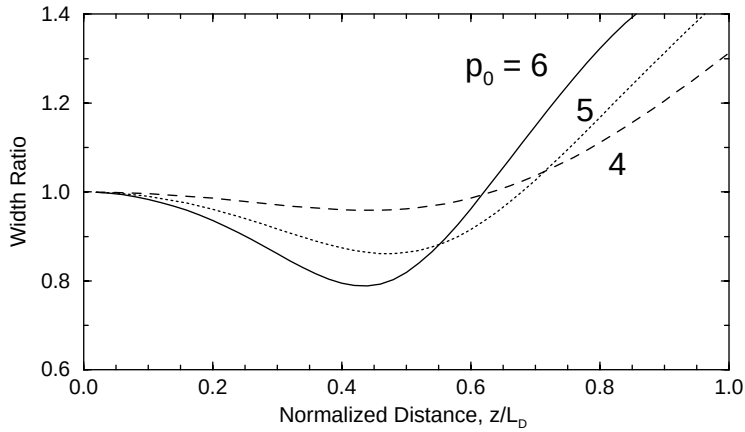

Figure 7.6 Width ratio σ/σ_0 as a function of propagation distance for a super-Gaussian pulse ($m = 2$) at three input peak powers labeled using $p_0 = \gamma P_0 L_D$.

numerical simulations indicated that system performance of a 6000-km fiber link, operating at bit rates > 1 Gb/s with 100-km amplifier spacing, would be severely affected by modulation instability if the signal propagates in the anomalous-GVD regime and is launched with peak power levels in excess of a few milliwatts [77].

SPM can lead to the degradation of SNR when optical amplifiers are used for loss compensation [78]–[89]. Such amplifiers add to a signal broadband noise that extends over the entire bandwidth of amplifiers (or optical filters when they are used to reduce noise). Even close to the zero-dispersion wavelength, amplifier noise is enhanced considerably by SPM [78], [83]. In the case of anomalous GVD, spectral components of noise falling within the gain spectrum of modulation instability will be enhanced by this nonlinear process, resulting in further degradation of the SNR [86]. Moreover, periodic power variations occurring in long-haul systems create a nonlinear index grating that can lead to modulation instability even in the normal-GVD regime [82]. Both of these effects were discussed in Section 4.3. They have also been observed experimentally. In a 10-Gb/s system, considerable degradation in system performance was noticed after a transmission distance of only 455 km [87]. In general, long-haul systems perform better when the average GVD of the fiber link is kept positive ($\bar{\beta}_2 > 0$).

7.5 Cross-Phase Modulation

As discussed in Chapter A.7, when two pulses of different wavelengths propagate simultaneously inside optical fibers, their optical phases are affected not only by SPM but also by XPM. The XPM effects are quite important for WDM lightwave systems since the phase of each optical channel is affected by both the average power and the bit pattern of all other channels [2]–[5]. Fiber dispersion converts phase variations into amplitude fluctuations, affecting the SNR considerably. A proper understanding of the interplay between XPM and GVD is of considerable importance for WDM systems [90]–[109].

7.5.1 XPM-Induced Phase Shift

Consider the case of an M-channel WDM system. The total optical field can be written as

$$A(z,T) = \sum_{m=1}^{M} A_m(z,T)\exp[i(\omega_m - \omega_0)T], \tag{7.5.1}$$

where ω_m is the carrier frequency of the mth channel and ω_0 is a reference frequency chosen, in practice, to coincide with one of the channel frequencies. Following the method of Section A.7.1, we obtain a set of M coupled NLS equations:

$$i\frac{\partial A_j}{\partial z} + \frac{i}{v_{gj}}\frac{\partial A_j}{\partial z} - \frac{\beta_{2j}}{2}\frac{\partial^2 A_j}{\partial T^2} + \gamma\left(|A_j|^2 + 2\sum_{m\neq j}^{M}|A_m|^2\right)A_j = \frac{i\alpha}{2}A_j, \tag{7.5.2}$$

where $j = 1$ to M, v_{gj} is the group velocity, and β_{2j} is the GVD parameter. The loss parameter α and the nonlinear parameter γ are assumed to be the same for all channels. The contribution of FWM is neglected in these equations, assuming that GVD is too large for FWM to become phase matched. The effects of FWM are considered in the next section.

In general, the set of M equations should be solved numerically. It can be solved analytically in the CW case with the result $A_j(L) = \sqrt{P_j}\exp(i\phi_j)$, where P_j is the input power and the nonlinear phase shift resulting from a combination of SPM and XPM is given by

$$\phi_j = \gamma L_{\text{eff}}(P_j + 2\sum_{m\neq j} P_m). \tag{7.5.3}$$

The CW solution can be applied approximately for NRZ-format systems operating at relatively low bit rates. The phase ϕ_j of a specific channel would vary

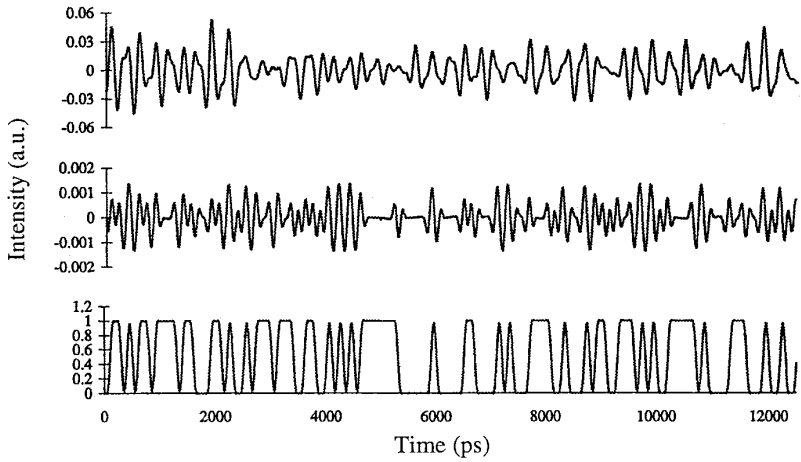

Figure 7.7 XPM-induced power fluctuations on a CW probe for a 130-km link (middle) and a 320-km link (top) with dispersion management. An NRZ bit stream in the pump channel is shown at the bottom. (After Ref. [102], ©1999 IEEE)

from bit to bit depending on the bit patterns of neighboring channels. In the worst case in which all channels have 1 bits in their time slots simultaneously, the XPM-induced phase shift is largest. If the input power is assumed to be the same for each channel, this maximum value is given by

$$\phi_{\max} = (\gamma/\alpha)(2M-1)P_{\text{ch}}, \tag{7.5.4}$$

where L_{eff} was replaced by $1/\alpha$ assuming $\alpha L \gg 1$. The XPM-induced phase shift increases linearly with M and can become quite large. It was measured in 1984 for the two-channel case [90]. Light from two semiconductor lasers operating near 1.3 and 1.5 μm was injected into a 15-km-long fiber. The phase shift at 1.5 μm, induced by the copropagating 1.3-μm wave, was measured using an interferometer. A value of $\phi_{\max} = 0.024$ was found for $P_{\text{ch}} = 1$ mW. This value is in good agreement with the predicted value of 0.022 from Eq. (7.5.4).

Strictly speaking, the XPM-induced phase shift should not affect system performance if the GVD effects were negligible. However, any dispersion in fiber converts pattern-dependent phase shifts to power fluctuations, reducing the SNR at the receiver. This conversion can be understood by noting that time-dependent phase changes lead to frequency chirping that affects dispersion-induced broadening of the signal. Figure 7.7 shows XPM-induced fluctuations

for a CW probe launched with a 10-Gb/s pump channel modulated using the NRZ format. The probe power fluctuates by as much as 6% after 320 km of dispersive fiber. The RMS value of fluctuations depends on the channel power and can be reduced by lowering it. As a rough estimate, if we use the condition $\phi_{\max} < 1$ in Eq. (7.5.4), the channel power is restricted to

$$P_{\text{ch}} < \alpha/[\gamma(2M-1)]. \tag{7.5.5}$$

For typical values of α and γ, P_{ch} should be below 10 mW even for five channels and reduces to below 1 mW for more than 50 channels.

7.5.2 Power Penalty

The above analysis ignores the effects of group-velocity mismatch. In reality, pulses belonging to different channels travel at different speeds and walk through each other at a rate that depends on their wavelength difference. Since XPM can occur only when pulses overlap in the time domain, its impact is reduced considerably by the walk-off effects. We can use the results of Section A.7.4 to gain a qualitative understanding of the walk-off process. As a faster-moving pulse belonging to one channel collides with and passes through a specific pulse in another channel, the XPM-induced chirp shifts the pulse spectrum first toward red and then toward blue. In a lossless fiber, collisions of two pulses are perfectly symmetric, resulting in no net spectral shift at the end of the collision. In a loss-managed system, with lumped amplifiers placed periodically along the link, power variations make collisions between pulses of different channels asymmetric, resulting in a net frequency shift that depends on the channel spacing. Such frequency shifts lead to timing jitter (the speed of a channel depends on its frequency because of GVD) since their magnitude depends on the bit pattern as well as on channel wavelengths. The combination of amplitude and timing jitter degrades the SNR at the receiver considerably, especially for closely spaced channels, and leads to XPM-induced power penalty [92].

Figure 7.8 shows how the power penalty depends on channel spacing and fiber dispersion at a bit-error rate of 10^{-10}. These results were obtained by launching two 10-Gb/s channels into a 200-km fiber link with one amplifier located midway [103]. Four different types of fibers were used to change the GVD. The pump-channel power was 8 dBm (6.3 mW) while the signal-channel power was kept at 2 dBm. The penalty depends on the relative pump–signal delay and the state of polarizations; thin and thick lines in Fig. 7.8 show

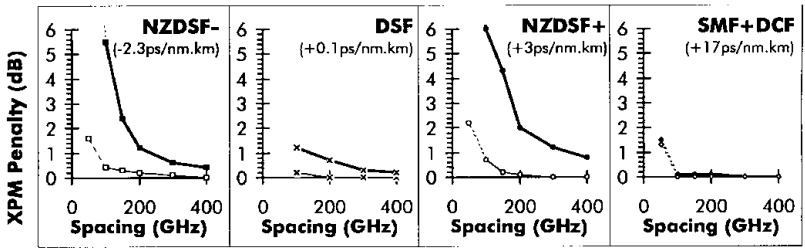

Figure 7.8 XPM-induced power penalty as a function of channel spacing for four fiber links with different dispersion. Thin and thick lines correspond to best and worst cases, respectively. (After Ref. [103], ©1999 IEEE)

the best and worst cases. The XPM-induced penalty becomes quite large for large-GVD links and small channel spacing, as expected. It can be reduced to negligible levels for fiber links with small average GVD and relatively large channel spacing (> 50 GHz). Negligible penalty occurs for the dispersion-managed link in which GVD is compensated using a DCF.

In periodically amplified lightwave systems, power variations along the fiber link affect the XPM interaction among channels. If two channels are spaced such that the relative propagation delay ΔT between them over each amplifier span is equal to a multiple of the bit slot T_B, the pulse trains in the two channels will become synchronized after each amplifier, resulting in the enhancement of the XPM-induced phase shift. Mathematically, this condition can be written as

$$\Delta T = \Delta\lambda \int_0^{L_A} D(z)\, dz = mT_B \tag{7.5.6}$$

where $\Delta\lambda$ is the channel spacing, L_A is the amplifier spacing, $D(z)$ is related to the dispersion map used between two amplifiers, and m is an integer. In the case of constant-dispersion fibers, this condition becomes $BDL_A\Delta\lambda = m$, where $B = 1/T_B$. System performance is expected to degrade whenever channel spacing $\Delta\lambda$ satisfies Eq. (7.5.6). This was indeed observed in the experiment in which the bit-error rate of a weak probe channel exhibited resonances (it increased significantly) whenever wavelength spacing of the pump channel responsible for XPM satisfied the resonance condition [106].

The XPM effects occurring within a fiber amplifier are normally negligible because of a small length of doped fiber used. The situation changes for the L-band amplifiers, which operate in the 1570- to 1610-nm wavelength region and require fiber lengths in excess of 100 m. The effective core area of doped

fibers used in such amplifiers is relatively small, resulting in larger values of the nonlinear parameter γ and enhanced XPM-induced phase shifts. As a result, the XPM can lead to considerable power fluctuations within an *L*-band amplifier [107]–[109]. A new feature is that such XPM effects are independent of the channel spacing and can occur over the entire bandwidth of the amplifier [108]. The reason for this behavior is that all XPM effects occur before pulses walk off because of group-velocity mismatch.

The XPM effects become much worse for coherent WDM systems because of the phase-sensitive nature of signal detection. In the case of amplitude-shift keying (ASK), large phase fluctuations induced by rapid power variations degrade system performance at channel powers as low as 1 mW. The impact of XPM becomes less severe when frequency- or phase-shift keying (FSK and PSK) is used since channel powers are then constant in time. In fact, XPM would be harmless if the channel powers were really constant, as a constant phase shift does not affect the system performance. In practice, channel powers fluctuate because of intensity noise associated with the transmitter or amplified spontaneous emission added by lumped amplifiers. XPM converts intensity fluctuations into phase fluctuations, which degrade the performance of a coherent receiver. In a two-channel homodyne experiment in which each channel transmitted a 10-Gb/s signal over 100 km, the XPM-induced power penalty was 7 dB when the channel power was 15 mW [110]. XPM led to degradation of the system performance for channel powers as low as 4 mW.

7.6 Four-Wave Mixing

Four-wave mixing (FWM) is a major source of nonlinear crosstalk for WDM lightwave systems [111]–[123]. The physical origin of FWM-induced crosstalk, and the resulting system degradation, can be understood by noting that FWM can generate a new wave at the frequency $\omega_F = \omega_i + \omega_j - \omega_k$, whenever three waves of frequencies ω_i, ω_j, and ω_k copropagate inside the fiber. For an *M*-channel system, *i*, *j*, and *k* vary from 1 to *M*, resulting in a large combination of new frequencies generated by FWM. In the case of equally spaced channels, most new frequencies coincide with the existing channel frequencies and interfere coherently with the signals in those channels. This interference depends on the bit pattern and leads to considerable fluctuations in the detected signal at the receiver. When channels are not equally spaced, most FWM components fall in between the channels and add to overall noise. In both cases, system

performance is affected by the loss in channel powers, but the degradation is much more severe for equally spaced channels because of the coherent nature of crosstalk.

7.6.1 FWM Efficiency

As discussed in Chapter A.10, the FWM process in optical fibers is governed by a set of four coupled equations whose general solution requires a numerical approach. If we neglect the phase shifts induced by SPM and XPM, assume that the three channels participating in the FWM process remain nearly undepleted, and include fiber losses, the amplitude A_F of the FWM component at the frequency ω_F is governed by

$$\frac{dA_F}{dz} = -\frac{\alpha}{2}A_F + d_F\gamma A_i A_j A_k^* \exp(-i\Delta k z), \tag{7.6.1}$$

where $A_m(z) = A_m(0)\exp(-\alpha z/2)$ for $m = i, j, k$ and $d_F = 2 - \delta_{ij}$ is the degeneracy factor defined such that its value is 1 when $i = j$ but doubles when $i \neq j$. This equation can be easily integrated to obtain $A_f(z)$. The power transferred to the FWM component in a fiber of length L is given by [111]

$$P_F = |A_F(L)|^2 = \eta_F (d_F\gamma L)^2 P_i P_j P_k e^{-\alpha L}, \tag{7.6.2}$$

where $P_m = |A_m(0)|^2$ is the launched power in mth channel and η_F is a measure of the FWM efficiency defined as

$$\eta_F = \left| \frac{1 - \exp[-(\alpha + i\Delta k)L]}{(\alpha + i\Delta k)L} \right|^2. \tag{7.6.3}$$

The FWM efficiency η_F depends on the channel spacing through the phase mismatch governed by

$$\Delta k = \beta_F + \beta_k - \beta_i - \beta_j \approx \beta_2(\omega_i - \omega_k)(\omega_j - \omega_k), \tag{7.6.4}$$

where the propagation constants were expanded in a Taylor series around $\omega_c = (\omega_i + \omega_j)/2$ and β_2 is the GVD parameter at that frequency. If the GVD of the transmission fiber is relatively large, ($|\beta_2| > 5$ ps^2/km), η_F nearly vanishes for typical channel spacings of 50 GHz or more. In contrast, $\eta_F \approx 1$ close to the zero-dispersion wavelength of the fiber, resulting in considerable power in the FWM component, especially at high channel powers. In the case of

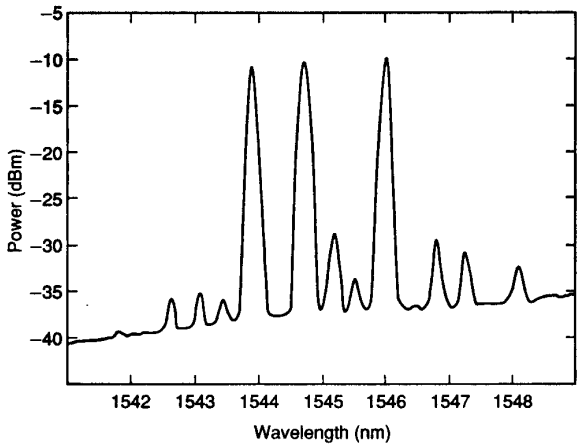

Figure 7.9 Optical spectrum measured at the output of a 25-km-long fiber when three 3-mW channels are launched into it. (After Ref. [5], ©Lucent Technologies)

equal channel powers, P_F increases as P_{ch}^3. This cubic dependence of the FWM component limits the channel powers to below 1 mW if FWM is nearly phase matched. Since the number of FWM components for an M-channel WDM system increases as $M^2(M-1)/2$, the total power in all FWM components can be quite large. Figure 7.9 shows, as an example, the optical spectrum measured at the output of a 25-km-long dispersion-shifted fiber [$D = -0.2$ ps/(km-nm) for the central channel] when three 3-mW channels are launched into it. The nine FWM components can be seen clearly. None of them coincides with the channel wavelengths because of the unequal channel spacing used in this experiment.

7.6.2 FWM-Induced Crosstalk

In the case of equal channel spacing, most FWM components fall within the channel spectra and cannot be seen as clearly as in Fig. 7.9 in the spectral domain. However, their presence is easily noticed in the time domain as they interfere with the signal coherently. Since the FWM power depends on the bit patterns of three channels, the signal power fluctuates considerably. Figure 7.10 shows the bit patterns observed for the central channel using three fibers with different GVD values. The central channel in this case is located exactly in the middle (see Fig. 7.9) such that the channel spacing is constant and equal

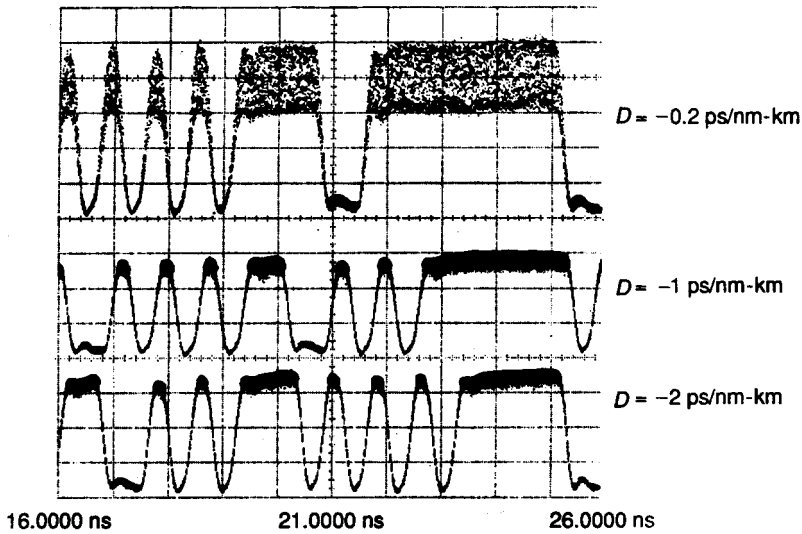

Figure 7.10 Effect of fiber dispersion on the central channel when three 3-mW channels are launched with equal channel spacing. (After Ref. [5], ©Lucent Technologies)

to 1 nm. The FWM-induced noise is quite large for low GVD values because of the quasi-phase-matched nature of the FWM process.

Modulation instability can enhance the effects of FWM for certain specific values of channel spacing [120]. The reason can be understood by noting that SPM and XPM, ignored in deriving Eq. (7.6.2), can produce phase matching even when $\beta_2 \neq 0$. We can follow the analysis of Section A.10.2 to include the SPM and XPM phase shifts. It turns out that Eq. (7.6.2) can still be used but the phase-mismatch factor Δk in Eq. (7.6.4) is replaced with [122]

$$\Delta k \approx \beta_2(\omega_i - \omega_k)(\omega_j - \omega_k) + \gamma(P_i + P_j - P_k)[1 - \exp(-\alpha L_{\text{eff}})]/(\alpha L_{\text{eff}}). \tag{7.6.5}$$

Clearly, Δk may become close to zero for some FWM terms, depending on the channel powers and spacings, when β_2 is in the anomalous-GVD regime of the fiber. The corresponding FWM process will then become phase-matched, resulting in significant power-conversion efficiency. Physically speaking, if the frequency at which the gain peak of modulation instability nearly coincides with the channel spacing in a WDM system, modulation-instability sidebands will overlap with the channel wavelengths. As a result, the FWM process will become enhanced resonantly in spite of the GVD. We can estimate the channel

spacing $\delta\nu_{\rm ch}$ for which such resonant FWM is expected to occur using Eq. (A.10.3.10) to find that

$$\Omega_s = 2\pi\delta\nu_{\rm ch} = (2\gamma P_{\rm ch}/|\beta_2|)^{1/2}. \tag{7.6.6}$$

As a rough estimate, $\delta\nu_{\rm ch} \approx 50$ GHz when $P_{\rm ch} = 5$ mW, $\beta_2 = -0.2$ ps^2/km, and $\gamma = 2$ W^{-1}/km. Since channel spacing in modern WDM systems is typically 100 GHz or less, resonance enhancement of FWM can easily occur.

A simple scheme for reducing the FWM-induced degradation consists of designing WDM systems with unequal channel spacings [116]. The main impact of FWM in this case is to reduce the channel power. This power depletion results in a power penalty at the receiver whose magnitude can be controlled by varying the launched power and fiber dispersion. Experimental measurements on a WDM system, in which eight 10-Gb/s channels were transmitted over 137 km of dispersion-shifted fiber, confirm the advantage of unequal channel spacings. In a 1999 experiment, this technique was used to transmit 22 channels, each operating at 10 Gb/s, over 320 km of dispersion-shifted fiber with 80-km amplifier spacing [123]. Channel spacings ranged from 125 to 275 GHz in the 1532- to 1562-nm wavelength region and were determined using a periodic allocation scheme [124]. The zero-dispersion wavelength of the fiber was close to 1548 nm, resulting in near phase matching of many FWM components. Nonetheless, the system performed quite well (because of unequal channel spacings) with less than 1.5-dB power penalty for all channels.

The use of a nonuniform channel spacing is not always practical since many WDM components, such as Fabry–Perot filters and waveguide-grating routers, require equal channel spacings [7]. Also, this scheme is spectrally inefficient since the bandwidth of the resulting WDM signal is considerably larger compared with the case of equally spaced channels [116]. An alternative is offered by the dispersion-management technique discussed earlier. In this case, fibers with normal and anomalous GVD are combined to form a periodic dispersion map such that GVD is locally high all along the fiber even though its average value is quite low. As a result, the FWM efficiency η_F is negligible throughout the fiber, resulting in little FWM-induced crosstalk. As early as 1993, eight channels at 10 Gb/s could be transmitted over 280 km by using dispersion management [125]. By 1996, the use of dispersion management had become quite common for FWM suppression in WDM systems because of its practical simplicity. FWM can also be suppressed by using fibers whose GVD varies along the fiber length [126].

7.7 System Design

In modern long-haul lightwave systems, the dispersive and nonlinear effects accumulate over long lengths exceeding several thousand kilometers. The design of such WDM systems requires consideration of not only the dispersive and nonlinear effects but also the spontaneous-emission noise added by fiber amplifiers. Interplay among various nonlinear effects, and its dependence on a large number of design parameters, make adoption of a numerical approach almost essential for optimization of system performance before the system is actually built. For this reason, computer modeling of lightwave systems attracted considerable attention during the 1990s [127]–[139]. In fact, several simulation packages were available commercially by 2000.

7.7.1 Numerical Modeling

What is the most appropriate numerical model for simulating the performance of WDM systems? In one approach, the total optical field is split into individual channel fields, as shown in Eq. (7.5.1), to obtain a set of M coupled NLS equations, similar to that given in Eq. (7.5.2), where M is the number of WDM channels. This equation includes GVD, SPM, and XPM effects only. It should be generalized by adding the terms representing channel coupling through FWM and SRS. The resulting set of equations may be useful for a small number of channels but becomes too complicated to be practical when M becomes large.

A simpler approach solves a single NLS equation given as in Eq. (7.4.1) by using an input field of the form

$$A(0,T) = \sum_{m=1}^{M} A_m(0,T)\exp[i(\omega_m - \omega_0)T], \tag{7.7.1}$$

where $A_m(0,T)$ is the input signal belonging to the mth channel. This technique includes the SPM, XPM, and FWM effects for all channels automatically but ignores the Raman crosstalk. The Raman-induced channel coupling can be included by using the generalized NLS equation of Section A.2.3. If we ignore the shock term because of its negligible contribution, the resulting equation becomes

$$\frac{\partial A}{\partial z} + \frac{\alpha}{2}A + \frac{i\beta_2}{2}\frac{\partial^2 A}{\partial T^2} - \frac{\beta_3}{6}\frac{\partial^3 A}{\partial T^3} = i\gamma\left(|A|^2 A - T_R A\frac{\partial A^2}{\partial T}\right), \tag{7.7.2}$$

where T_R is the Raman parameter and β_3 includes the effects of third-order dispersion (TOD). This equation is quite useful for modeling loss- and dispersion-managed WDM systems.

For realistic modeling of lightwave systems, one must consider a random sequence of 0 and 1 bits in each channel to include the pattern effects. For this reason, Eq. (7.7.2) is solved with the following input:

$$A(0,T) = \sum_{m=1}^{M} \sqrt{P_m} \left[\sum_{k=1}^{K} b_k U_m (T - kT_B) \right] \exp[i(\omega_m - \omega_0)T], \tag{7.7.3}$$

where P_m is the power and U_m is the pulse shape for the mth channel, $T_B = 1/B$ is the bit slot at the bit rate B, K represents the number of bits included in the numerical model, and $b_k = 0$ or 1 depending on whether the kth time slot contains a 0 or 1 bit. A random sequence of at least 32 bits is used in numerical simulations [127]. It should be chosen to ensure that it contains isolated as well as long sequences of 0 or 1 bits. An example of such a 32-bit sequence is 01011000101111011010100000101110. The pulse shape U_m depends on the modulation format. A Gaussian or "sech" pulse shape is used in the case of an RZ format. The full width at half maximum (FWHM) of the pulse depends on the duty cycle, a typical value being 50% of the bit slot T_B. In the case of an NRZ format, the pulse occupies the entire bit slot. A super-Gaussian shape is often used with a rise and fall time of about $0.1T_B$.

Equation (7.7.2) can be solved using the split-step Fourier method of Section A.2.4. In the case of dispersion management, the three fiber parameters—α, β_2, and γ—become z dependent since they are different for different fibers. It is easy to include their variations numerically. Signal amplification and noise added at the location of lumped amplifiers can be included through Eq. (7.1.3). It is more practical to use this equation in the frequency domain such that each spectral component of the field is modified as

$$\tilde{A}_{\text{out}}(\nu) = \sqrt{G}\tilde{A}_{\text{in}}(\nu) + \tilde{a}_n(\nu), \tag{7.7.4}$$

where $G = \exp(\alpha L_A)$ is the amplifier gain needed to compensate fiber losses, L_A is the amplifier spacing, and $\tilde{a}_n$ is a complex Gaussian random variable whose real and imaginary parts have the same variance

$$\sigma^2 = \tfrac{1}{2} n_{\text{sp}} h\nu_0 (G-1)\delta\nu, \tag{7.7.5}$$

where $\delta\nu$ is the bandwidth occupied by each spectral component (related inversely to the width of the temporal window used for numerical simulations).

The noise figure of an amplifier is related to n_{sp} as $F_n = 2n_{sp}$. An optical filter is often placed after each amplifier to reduce the broadband noise added by the amplifiers. Its effect can be included by making $\tilde{a}_n(\nu) = 0$ outside the filter bandwidth.

At the receiver end, the system performance is characterized through the bit-error rate (BER). If the total noise is assumed to follow Gaussian statistics, the BER is given by the simple expression (see Appendix A)

$$\text{BER} = \frac{1}{2}\text{erfc}\left(\frac{Q}{\sqrt{2}}\right) \approx \frac{\exp(-Q^2/2)}{Q\sqrt{2\pi}}, \tag{7.7.6}$$

where the parameter Q is defined as

$$Q = \frac{I_1 - I_0}{\sigma_1 + \sigma_0}, \tag{7.7.7}$$

and I_1 and σ_1 represent the average and RMS values of the signal for 1 bits; I_0 and σ_0 are the corresponding quantities for 0 bits. A value of $Q > 6$ ensures BER $< 10^{-9}$, a typical requirement for lightwave systems. If BER $< 10^{-12}$ is required, $Q > 7$ is needed.

The Q parameter is often used to characterize the performance of lightwave systems. In numerical simulations, it is calculated by filtering $A(L,t)$ optically to select a fixed channel, converting the bit stream to the electrical domain using $I(T) = R_d|A(L,t)|^2$, where R_d is the responsivity of the photodetector, and then filtering the electric signal with a filter whose bandwidth B_e is smaller than the bit rate B and is typically in the range of 0.6 to 0.8B. Reference [127] contains further details.

An alternative approach for characterizing system performance makes use of the eye-closure penalty [129]–[134]. Eye diagramsare commonly used for lightwave systems [7]. If each set of two successive bits are displayed repetitively in the same two-bit-wide time window, the resulting pattern looks like an open eye (in the case of the NRZ format) and is referred to as an *eye diagram*. The eye begins to close as fiber length increases because of degradation in the SNR ratio and the increase in timing jitter introduced by amplifier noise, GVD, and nonlinear effects. The eye-closure penalty is a measure of the change in the opening of the eye, quantified through the minimum value of I_1 and maximum value of I_0 at the bit center of a noisy bit stream [8].

7.7.2 Design Issues

The design of a lightwave system requires consideration of a large number of factors. Often one needs to take into account cost issues as well. An example is provided by the spacing L_A between amplifiers. Typically, system performance can be improved by reducing L_A but cost considerations dictate that L_A cannot be reduced indiscriminately. Typically, amplifier spacing should exceed 75 km to keep the overall cost low. Often, the objective of computer simulations is to design the system such that it meets the specifications with minimum cost.

The issue of modulation format (RZ versus NRZ) has attracted considerable attention [129]–[134]. Most lightwave systems up to 1999 have used NRZ, the format of choice for historical reasons. Optical pulses in an NRZ system occupy the entire bit slot and their width is nonuniform depending on the bit pattern. In contrast, all pulses are identical when the RZ format is used and their width is smaller than the bit slot. It is not obvious *a priori* which format is best when dispersive and nonlinear effects work together. Shorter pulses in the RZ case have room for broadening, but at the same time shorter pulses broaden more than longer ones because of a smaller dispersion length. Shorter pulses also have higher peak powers for a given average power and may be effected more by nonlinearity, but at the same time they can benefit from soliton-like effects. Clearly, numerical simulations should be used to compare the two formats.

An important design objective during the late 1990s was to increase the system capacity using the standard single-mode fiber (SMF) already installed in the ground. This fiber has high dispersion near 1.55 μm with $D \approx 16$ ps/(km-nm). A suitable dispersion map for such a link consists of 10 km of DCF with $D \approx -80$ ps/(km-nm) for every 50 km of SMF, resulting in a 60-km amplifier spacing. Numerical simulations for a single-channel 40-Gb/s system showed that such a system can operate over a distance of 1200 km when an RZ format is used but is limited to below 500 km in the case of NRZ format [130]. The situation is different for WDM systems because of the crosstalk induced by XPM, SRS, and FWM. Numerical simulations for a 16-channel system showed that the RZ format is more suitable at bit rates of 10 and 20 Gb/s but the NRZ format works better at 40 Gb/s [134]. Figure 7.11 shows calculated eye-closure penalties for the worst channel as a function of the launched channel power P_{ch} for a 16-channel WDM system. At low input powers, system performance is limited by amplified spontaneous emission (ASE). However, the nonlinear effects begin to degrade the WDM system for $P_{\text{ch}} > 0.5$ mW.

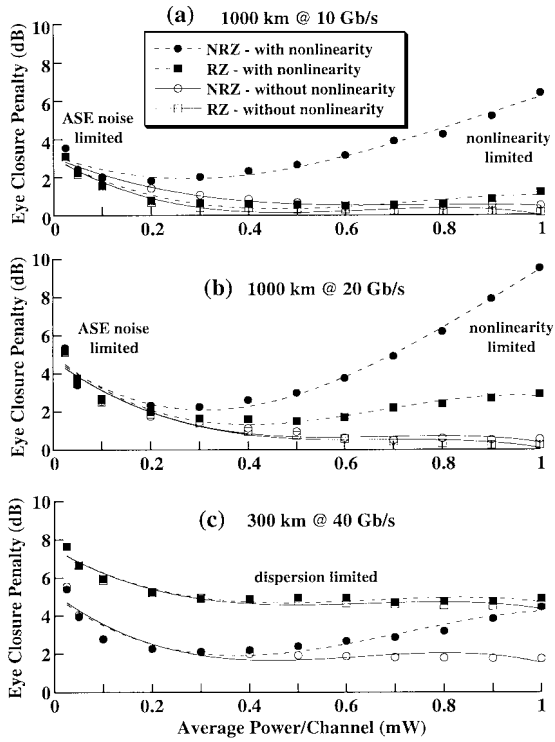

Figure 7.11 Eye-closure penalties for the worst channel as a function of channel power for a 16-channel WDM system operating at 10, 20, and 40 Gb/s. System performance is compared for RZ and NRZ formats. (After Ref. [134], ©1999 IEEE)

The transmission distance can be more than 3000 km for RZ systems operating at 10 and 20 Gb/s but is limited to below 400 km even when the NRZ format is used. It was important to use a DCF with negative GVD slope for the system to work properly. On the experimental side, 320-Gb/s transmission (32 channels at 10 Gb/s) was realized successfully over 500 km with an amplifier spacing of 125 km [132].

Design issues for undersea lightwave systems are somewhat different since the transmission distance for most such systems exceeds 6000 km. Numerical simulations have been used to design 10,000-km-long WDM systems that maximize the total capacity by optimizing the dispersion map [137]. The bit rate per channel is limited to around 10 Gb/s for such long-haul systems. Thus, high capacity should be realized by maximizing the number of WDM channels.

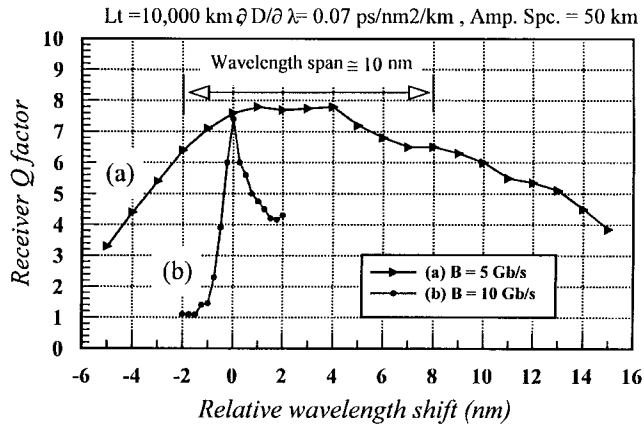

Figure 7.12 Q factor as a function of $\lambda - \lambda_{ZD}$ after 10,000 km at 5 and 10 Gb/s. (After Ref. [137], ©1999 IEEE)

Since the amplifier-gain bandwidth limits the total spectral range of a WDM signal, channel spacing becomes an important design criterion. Another important factor is the dispersion-slope compensation [140]. As mentioned before, the dispersion parameter D is different for different channels because of its wavelength dependence. The dispersion slope $dD/d\lambda$ is related to the TOD parameter β_3. If the dispersion slope is positive for both fibers used in a dispersion map, GVD cannot be compensated for all channels simultaneously. Figure 7.12 shows how the Q factor of a channel degrades after 10,000 km as its operating wavelength is shifted in the vicinity of the zero-dispersion wavelength λ_{ZD} of the fiber. The usable wavelength range with $Q > 6$ exceeds 10 nm at 5 Gb/s but is reduced to below 1 nm at 10 Gb/s. The results show that dispersion-slope compensation is essential for 10-Gb/s systems.

The spectral efficiency of WDM systems is determined by the ratio $\eta_s = B/\Delta\nu_{ch}$, where $\Delta\nu_{ch}$ is the channel spacing and B is the single-channel bit rate. The ideal value $\eta_s = 1$ is known as the *Nyquist limit*. In practice, the channel spacing is often 100 GHz for 10-Gb/s channels, resulting in a spectral efficiency of only 10%. It can be increased by optimizing the system design through numerical simulations. Figure 7.13 shows channel spacing as a function of N_{ch} for a WDM system designed to operate over 10,000 km at 5-Gb/s per channel with 50-km amplifier spacing. The spectral efficiency can be improved considerably by using low-noise amplifiers, large core-area fibers, and optimizing the duty cycle of RZ pulses. A combination of all of these can

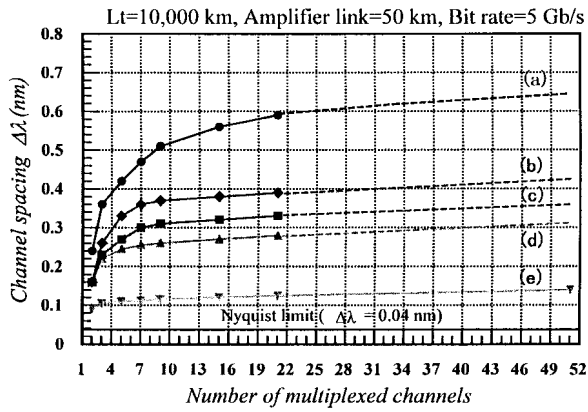

Figure 7.13 Channel spacing as a function of N_{ch} for a WDM system designed to operate over 10,000 km at 5-Gb/s per channel. (a) Conventional design; (b) 4-dB noise-figure amplifiers; (c) large core-area fibers; (d) optimum RZ format; and (e) combination of all. (After Ref. [137], ©1999 IEEE)

provide $>$ 50% spectral efficiency. Moreover, the Q parameter can exceed 6 over a wavelength range as large as 40 nm using the pre- and postcompensation techniques for individual channels, resulting in $N_{ch} > 100$ at 5-Gb/s per channel [137].

7.7.3 System Performance

Transmission experiments fall in two different categories, depending on whether they are intended for terrestrial or undersea applications. In the case of undersea lightwave systems, transmission distances are about 10,000 km, whereas they can be shorter by a factor of 10 or more for terrestrial applications. Another important difference is that undersea systems can take advantage of new fiber designs whereas terrestrial systems often need to be upgraded using the existing high-GVD fiber in the ground. The dispersion-management technique provides an ideal solution for this "upgrade" problem.

Before the advent of loss- and dispersion-management schemes, lightwave systems operated at a maximum bit rate of 10 Gb/s and required electronic regeneration at a distance of under 80 km. The situation changed after 1990 when fiber amplifiers began to be used for transmitting optical signals over distances of more than 1000 km [141]. As early as 1993, dispersion management permitted transmission of eight 10-Gb/s channels over 280 km [125]. This ex-

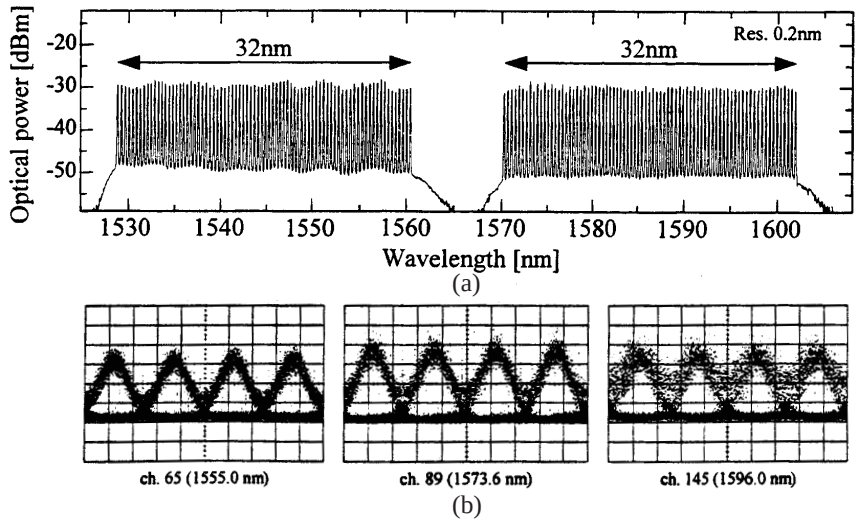

Figure 7.14 (a) Optical spectrum and (b) selected eye diagrams at 1500 km for the 160-channel WDM experiment with 3.2 Tb/s capacity. (After Ref. [148])

periment led to a march toward the demonstration of WDM systems capable of operating at 1 Tb/s. This symbolic milestone was achieved in 1996 when three different research groups reported experimental results for 1-Tb/s lightwave systems [142]–[144]. Within a year, the capacity increased to 2.6 Tb/s [145]. By 2000, the total capacity of WDM systems exceeded 3 Tb/s in several laboratory experiments [146]–[149]; the maximum capacity realized at the end of 2000 was 6.4 Tb/s.

Such a rapid advance in the system capacity required a number of key advances. In the 3.28-Tb/s experiment, 82 channels, each operating at 40 Gb/s, were transmitted over 3000 km [147]. In the 3.20-Tb/s experiment, 160 channels, each operating at 20 Gb/s, were transmitted over 1500 km [148]. Both experiments used the C and L bands simultaneously and required special hybrid amplifiers capable of amplifying signals over a 64-nm wavelength range with nearly flat gain over the entire signal bandwidth. The optical spectrum of the 160-channel WDM signal, shown in Fig. 7.14 after 1500 km of transmission (40 amplification stages), exhibits power deviations under 3 dB over the entire wavelength range. Received eye diagrams for three specific channels show that SNR degradation was different for different channels. It was, however, small enough that all channels had a BER below 10^{-9}. Such high-capacity

experiments require control of the dispersion slope to ensure dispersion compensation for all channels. They also often interleave channels such that two neighboring channels are always orthogonally polarized.

Another approach to high-capacity lightwave systems uses optical time-division multiplexing (OTDM) in combination with WDM [146]. In OTDM, several channels are first multiplexed in the time domain to obtain a bit stream at a bit rate of 100 Gb/s or more using only one laser wavelength. Then several such bit streams at different carrier wavelengths are multiplexed using the WDM technique. The OTDM technology requires quite different multiplexing and demultiplexing techniques than those used for WDM [150]. In a 1999 experiment, 3.04-Tb/s capacity was realized in a 19-channel WDM system in which each OTDM channel had a 160-Gb/s bit rate. The highest single-channel bit rate was realized in an OTDM experiment in which a 640-Gb/s signal was transmitted over 92 km [151]. The bit slot at 640 Gb/s is only 1.6-ps wide. As a result, pulses used in the experiment had an FWHM of only 1.1 ps. The higher-order dispersive and nonlinear effects become important for such short pulses and limit the transmission distance. In fact, both GVD and TOD need to be compensated along the link such that dispersion nearly vanishes over the entire spectral width of the pulse. A reverse-dispersion fiber with negative β_3 was used to accomplish this feature in the experiment.

The single-channel bit rate of undersea WDM systems is typically 10 Gb/s or less because of the degradation caused by accumulation of nonlinear effects over transoceanic distances. In fact, two transatlantic and transpacific systems (TAT-12 and TPC-5) installed in 1995 were single-channel systems operating at 5 Gb/s. Since then, both WDM and dispersion-management techniques have been used in designing such systems [152]–[163]. Most of the laboratory experiments use a fiber loop through which a WDM signal is recirculated many times to realize large transmission distances effectively. Figure 7.15 shows the design of a recirculating fiber loop schematically. Typically, the loop length is close to 500 km, and the signal is circulated 20 times or so. The loop contains multiple fiber amplifiers. It also employs DCFs periodically for dispersion compensation and gain equalizers for flattening the gain of the amplifiers.

Transmission of 32 channels, each operating at 5.3 Gb/s, was realized in 1997 using the RZ format for signal modulation [153]. Within a year, 20 WDM channels at 10.6 Gb/s were transmitted over 9000 km [154]. It was necessary to compensate the dispersion slope in this experiment. This technique also permitted transmission of a single 40-Gb/s channel over 8600 km [157]. In a

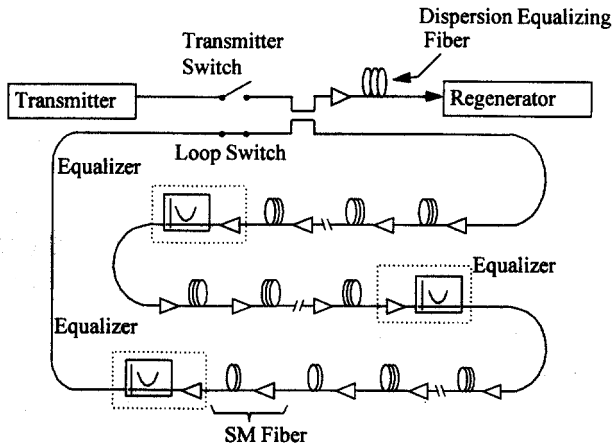

Figure 7.15 Schematic of circulating fiber loop used for long-haul transmission experiments. The transmission and loop switches control how long a bit stream circulates in the loop. (After Ref. [152], ©Lucent Technologies)

1999 experiment, management of higher-order dispersion led to an undersea WDM system capable of transmitting 25 RZ-format channels at 10 Gb/s over 9000 km [158]. Within a year, the total capacity was increased to 1 Tb/s using 100 channels, although the transmission distance was under 7750 km [161]. In a record-breaking 180-channel experiment, 1.8-Tb/s WDM data was transmitted over 7000 km [163]. The 43-nm bandwidth occupied the entire C band ranging from 1526 to 1569 nm. Channel spacing was only 0.21 nm (about 25 GHz) for most of the channels, resulting in a high spectral efficiency. The BER for most channels was quite large (about 10^{-3}), but the use of forward error-correcting codes (23% overhead) resulted in error-free operation.

How has the WDM technique benefited the commercial scene? Figure 7.16 shows the increase in the capacity of commercial lightwave systems since 1988, the year in which the first fiber-optic cable operating at 0.28 Gb/s was laid in the Atlantic Ocean. The WDM technique was used starting in 1996. As a result, the capacity of commercial terrestrial systems increased from 10 Gb/s in 1995 to 1.6 Tb/s by 2000 (fueled mainly by the growth in the Internet). A lightwave system with the total capacity of 6.4 Tb/s has also been announced. Undersea systems are designed less aggressively in general as they must operate reliably over their entire lifetime (because of the cost associated with their repair). Optical amplifiers were used in 1995 for a single-channel system op-

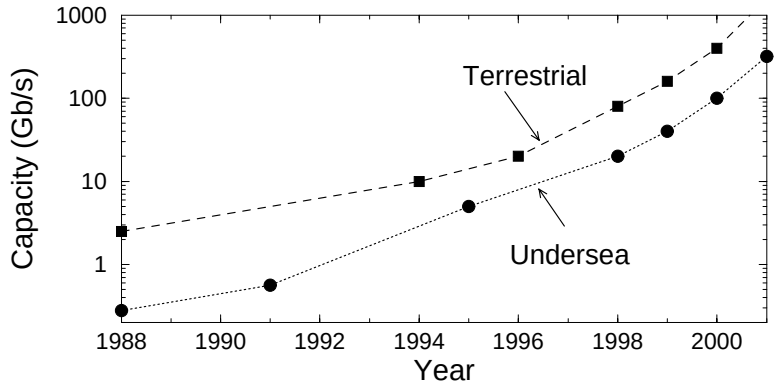

Figure 7.16 Increase in capacity of commercial lightwave systems since 1988. Dashed and dotted lines show the trend for terrestrial and undersea systems, respectively.

erating at 5 Gb/s. With the advent of WDM in 1996, 40-Gb/s systems were in oceans by 1998, and systems operating at bit rates of up to 320 Gb/s have been planned. Such systems can transmit millions of telephone calls simultaneously. One can expect transoceanic systems with a total capacity exceeding 1 Tb/s if the surge in demand continues in the 21st century.

Problems

7.1 How does spontaneous emission occurring inside optical amplifiers impact the performance of a long-haul lightwave system?

7.2 What is the total noise figure of a chain of N amplifiers spaced apart equally when all amplifiers have the same noise figure F_A?

7.3 Explain the basic idea behind dispersion management. Prove that the input pulse shape is recovered at the end of a fiber link whose average GVD is zero when the nonlinear and third-order dispersive effects are negligible.

7.4 Describe two techniques that can increase the Brillouin threshold above 10-mW level.

7.5 How does SRS lead to crosstalk in a WDM system? How can it be reduced in practice?

7.6 Show that the solution of Eq. (7.3.4) is indeed given by Eq. (7.3.5). Use this solution to calculate the Raman-induced depletion of the highest-frequency channel.

7.7 Calculate the SPM-induced phase shift at the end of a fiber of length L, neglecting GVD but including fiber losses. Estimate the power level for a π phase shift when $\alpha = 0.2$ dB/km, $\gamma = 2$ W^{-1}/km, and $L = 20$ km.

7.8 Explain why XPM-induced crosstalk is enhanced for certain values of channel spacings.

7.9 Solve Eq. (7.6.1) and find the power generated through FWM. Show that the solution is given by Eq. (7.6.2).

7.10 Develop a computer program for solving Eq. (7.7.2). Use it with input of the form in Eq. (7.7.3) for a three-channel WDM system using a 32-bit pattern in the NRZ format. Assume a 10-Gb/s bit rate for each channel, 50-GHz channel spacing, and 50-km amplifier spacing. Make the eye diagram and estimate the Q parameter after $2, 4, 6$, and 8 Mm. Use $\alpha = 0.2$ dB/km, $\beta_2 = -1$ ps^2/km, $\beta_3 = 0$, $T_R = 0$, $\gamma = 2$ W^{-1}/km, 5-dB noise figure for amplifiers, and 5-mW average channel power. What nonlinear effect is the most critical for this system?

References

[1] R. H. Stolen, *Proc. IEEE* **68**, 1232 (1980).

[2] A. R. Chraplyvy, *J. Lightwave Technol.* **8**, 1548 (1990).

[3] R. G. Waarts, A. A. Friesem, E. Lichtman, H. H. Yaffe, and R. P. Braun, *Proc. IEEE* **78**, 1344 (1990).

[4] K. H. Kim, H. K. Lee, S. Y. Park, and E. H. Lee, *J. Lightwave Technol.* **13**, 1597 (1995).

[5] F. Forghieri, R. W. Tkach, and A. R. Chraplyvy, in *Optical Fiber Telecommunications*, Vol. IIIA (Academic Press, San Diego, CA, 1997), Chap. 8.

[6] M. R. Phillips and D. M. Ott, *J. Lightwave Technol.* **17**, 1782 (1999).

[7] G. P. Agrawal, *Fiber-Optic Communication Systems*, 2nd ed. (Wiley, New York, 1997).

[8] E. Iannone, F. Matera, A. Mecozzi, and M. Settembre *Nonlinear Optical Communication Networks*, (Wiley, New York, 1998).

[9] R. Ramaswami and K. Sivarajan, *Optical Networks* (Morgan Kaufmann, Burlington, MA, 1998).

[10] G. Keiser, *Optical Fiber Communications*, 3rd ed. (McGraw-Hill, New York, 2000).

[11] P. C. Becker, N. A. Olsson, and J. R. Simpson, *Erbium-Doped Fiber Amplifiers: Fundamentals and Technology* (Academic Press, San Diego, CA, 1999).

[12] C. Kurtzke, *IEEE Photon. Technol. Lett.* **6**, 1250 (1993).

[13] E. P. Ippen and R. H. Stolen, *Appl. Phys. Lett.* **21**, 539 (1972).

[14] R. G. Smith, *Appl. Opt.* **11**, 2489 (1972).

[15] D. Cotter, *Electron. Lett.* **18**, 495 (1982); *J. Opt. Commun.* **4**, 10 (1983).

[16] T. Sugie, *J. Lightwave Technol.* **9**, 1145 (1991); *IEEE Photon. Technol. Lett.* **5**, 102 (1992).

[17] X. P. Mao, R. W. Tkach, A. R. Chraplyvy, R. M. Jopson, and R. M. Derosier, *IEEE Photon. Technol. Lett.* **4**, 66 (1992).

[18] D. A. Fishman and J. A. Nagel, *J. Lightwave Technol.* **11**, 1721 (1993).

[19] T. Sugie, *Opt. Quantum Electron.* **27**, 643 (1995).

[20] D. Cotter, *Electron. Lett.* **18**, 504 (1982).

[21] R. G. Waarts and R. P. Braun, *Electron. Lett.* **21**, 1114 (1985).

[22] Y. Aoki, K. Tajima, and I. Mito, *J. Lightwave Technol.* **6**, 710 (1988).

[23] E. Lichtman, *Electron. Lett.* **27**, 759 (1991).

[24] A. Hirose, Y. Takushima, and T. Okoshi, *J. Opt. Commun.* **12**, 82 (1991).

[25] T. Sugie, *J. Lightwave Technol.* **9**, 1145 (1991); *IEEE Photon. Technol. Lett.* **5**, 102 (1993).

[26] M. O. van Deventer, J. J. G. M. van der Tol, and A. J. Boot, *IEEE Photon. Technol. Lett.* **6**, 291 (1994).

[27] S. Rae, I. Bennion, and M. J. Carswell, *Opt. Commun.* **123**, 611 (1996).

[28] A. Djupsjöbacka, G. Jacobsen, and B. Tromborg, *J. Lightwave Technol.* **18**, 416 (2000).

[29] H. Yoshinaga, *Electron. Lett.* **2**, 1707 (1993).

[30] Y. K. Park, O. Mizuhara, L. D. Tzeng, J.-M. P. Delavaux, T. V. Nguyen, M.-L. Kao, P. D. Yeates, and J. Stone, *IEEE Photon. Technol. Lett.* **5**, 79 (1993).

[31] G. Grandpierre, O. Gautheron, L. Pierre, J.-P. Thiery, and P. Kretzmeyer, *IEEE Photon. Technol. Lett.* **5**, 531 (1993).

[32] Y. Miyamoto, T. Kataoka, A. Sano, K. Hagimoto, A. Aida, and Y. Kobayashi, *Electron. Lett.* **30**, 797 (1994).

[33] D. Cotter, *Electron. Lett.* **18**, 638 (1982).

[34] M. Tsubokawa, S. Seikai, T. Nakashima, and N. Shibata, *Electron. Lett.* **22**, 473 (1986).

[35] A. Hadjifotiou and G. A. Hill, *IEE Proc.* **133**, Pt. J, 256 (1986).

[36] N. Yoshizawa and T. Imai, *J. Lightwave Technol.* **11**, 1518 (1993).

[37] K. Shiraki, M. Ohashi, and M. Tateda, *Electron. Lett.* **31**, 668 (1995).

[38] K. Shiraki, M. Ohashi, and M. Tateda, *J. Lightwave Technol.* **14**, 50 (1996).
[39] M. M. Howerton, W. K. Burns, and G. K. Gopalakrishnan, *J. Lightwave Technol.* **14**, 417 (1996).
[40] K. Tsujikawa, K. Nakajima, Y. Miyajima, and M. Ohashi, *IEEE Photon. Technol. Lett.* **10**, 1139 (1998).
[41] R. H. Stolen, E. P. Ippen, and A. R. Tynes, *Appl. Phys. Lett.* **20**, 62 (1972).
[42] A. Tomita, *Opt. Lett.* **8**, 412 (1983).
[43] A. R. Chraplyvy, *Electron. Lett.* **20**, 58 (1984).
[44] D. Cotter and A. M. Hill, *Electron. Lett.* **20**, 185 (1984).
[45] A. M. Hill, D. Cotter, and I. Wright, *Electron. Lett.* **20**, 247 (1984).
[46] J. Hegarty, N. A. Olsson, and M. McGlashan-Powell, *Electron. Lett.* **21**, 395 (1985).
[47] M. S. Kao and J. Wu, *J. Lightwave Technol.* **7**, 1290 (1989).
[48] M. S. Kao, *Electron. Lett.* **26**, 1034 (1990).
[49] S. Chi and S. C. Wang, *Electron. Lett.* **26**, 1509 (1990).
[50] J. C. Palais, T. Y. Lin, and S. Tariq, *Fiber Integ. Opt.* **10**, 75 (1991).
[51] A. R. Chraplyvy and R. W. Tkach, *IEEE Photon. Technol. Lett.* **5**, 666 (1993).
[52] F. Forghieri, R. W. Tkach, and A. R. Chraplyvy, *IEEE Photon. Technol. Lett.* **7**, 101 (1995).
[53] Z. Wang, A. Li, C. J. Mahon, G. Jacobsen, and E. Bodtker, *IEEE Photon. Technol. Lett.* **7**, 1492 (1995).
[54] S. Tariq and J. C. Palais, *J. Lightwave Technol.* **11**, 1914 (1993); *Fiber Integ. Opt.* **15**, 335 (1996).
[55] Y. Zhao, J. S. Wang, W. Zhou, H. Y. Tam, and M. S. Demokan, *Microwave Opt. Tech. Lett.* **12**, 111 (1996).
[56] D. N. Christodoulides and R. B. Jander, *IEEE Photon. Technol. Lett.* **8**, 1722 (1996).
[57] J. Wang, X. Sun, and M. Zhang, *IEEE Photon. Technol. Lett.* **10**, 540 (1998).
[58] M. Zirngibl, *Electron. Lett.* **34**, 789 (1998).
[59] M. E. Marhic, F. S. Yang, and L. G. Kazovsky, *J. Opt. Soc. Am. B* **15**, 957 (1998).
[60] S. Bigo, S. Gauchard. A Bertaina, and J. P. Hamaide, *IEEE Photon. Technol. Lett.* **11**, 671 (1999).
[61] A. G. Grandpierre, D. N. Christodoulides, and J. Toulouse, *IEEE Photon. Technol. Lett.* **11**, 1271 (1999).
[62] Y. Kodama and S. Wabnitz, *Opt. Lett.* **20**, 2291 (1995).
[63] Y. Kodama and S. Wabnitz, *Electron. Lett.* **31**, 1761 (1995).
[64] Y. Kodama, S. Wabnitz, and K. Tanaka *Opt. Lett.* **21**, 719 (1996).
[65] A. M. Kamchatnov and H. Steudel, *Opt. Commun.* **162**, 162 (1999).

[66] D. Anderson, *Phys. Rev. A* **27**, 3135 (1983).
[67] M. J. Potasek, G. P. Agrawal, and S. C. Pinault, *J. Opt. Soc. Am. B* **3**, 205 (1986).
[68] D. Marcuse, *J. Lightwave Technol.* **10**, 17 (1992).
[69] P. A. Bélanger and N. Bélanger, *Opt. Commun.* **117**, 56 (1995).
[70] N. Kikuchi and S. Sasaki, *J. Lightwave Technol.* **13**, 868 (1995).
[71] M. Florjanczyk and R. Tremblay, *J. Lightwave Technol.* **13**, 1801 (1995).
[72] Q. Yu and C. Fan, *J. Lightwave Technol.* **15**, 444 (1997).
[73] M. J. Potasek and G. P. Agrawal, *Electron. Lett.* **22**, 759 (1986).
[74] M. Suzuki, I. Morita, N. Edagawa, S. Yamamoto, H. Taga, and S. Akiba, *Electron. Lett.* **31**, 2027 (1995).
[75] S. Wabnitz, I. Uzunov, and F. Lederer, *IEEE Photon. Technol. Lett.* **8**, 1091 (1996).
[76] A. Naka, T. Matsuda, and S. Saito, *Electron. Lett.* **32**, 1694 (1996).
[77] J. P. Hamide, P. Emplit, and J. M. Gabriagues, *Electron. Lett.* **26**, 1452 (1990).
[78] D. Mracuse, *J. Lightwave Technol.* **9**, 356 (1991).
[79] S. Ryu, *Electron. Lett.* **28**, 2212 (1992).
[80] M. Murakami and S. Saito, *IEEE Photon. Technol. Lett.* **4**, 1269 (1992).
[81] K. Kikuchi, *IEEE Photon. Technol. Lett.* **5**, 221 (1993).
[82] F. Matera, A. Mecozzi, M. Romagnoli, and M. Settembre, *Opt. Lett.* **18**, 1499 (1993).
[83] A. Mecozzi, *J. Opt. Soc. Am. B* **11**, 462 (1994).
[84] M. Yu, G. P. Agrawal, and C. J. McKinstrie, *J. Opt. Soc. Am. B* **12**, 1126 (1995).
[85] N. J. Smith and N. J. Doran, *Opt. Lett.* **21**, 570 (1996).
[86] C. Lorattanasane and K. Kikuchi, *IEEE J. Quantum Electron.* **33**, 1084 (1997).
[87] R. A. Saunders, B. A. Patel, and D. Garthe, *IEEE Photon. Technol. Lett.* **9**, 699 (1997).
[88] R. Q. Hui, M. O'Sullivan, A. Robinson, and M. Taylor, *J. Lightwave Technol.* **15**, 1071 (1997).
[89] E. Ciaramella and M. Tamburrini, *IEEE Photon. Technol. Lett.* **11**, 1608 (1999).
[90] A. R. Chraplyvy and J. Stone, *Electron. Lett.* **20**, 996 (1984).
[91] G. P. Agrawal, P. L. Baldeck, and R. R. Alfano, *Phys. Rev. A* **40**, 5063 (1989).
[92] D. Marcuse, A. R. Chraplyvy, and R. W. Tkach, *J. Lightwave Technol.* **12**, 885 (1994).
[93] T. K. Chiang, N. Kagi, M. E. Marhic, and L. G. Kazovsky, *J. Lightwave Technol.* **14**, 249 (1996).
[94] Y. Kodama, A. Murata, and S. Wabnitz, *Opt. Lett.* **21**, 1815 (1996).

[95] R. A. Saunders, B. L. Patel, H. J. Harvey, and A. Robinson, *Electron. Lett.* **32**, 2206 (1996).

[96] N. Kikuchi, K. Sekine, and S. Sasaki, *Electron. Lett.* **33**, 653 (1997).

[97] L. Rapp, *IEEE Photon. Technol. Lett.* **9**, 1592 (1997).

[98] M. Shtaif and M. Eiselt, *IEEE Photon. Technol. Lett.* **10**, 979 (1998).

[99] A. V. T. Cartaxo, *IEEE Photon. Technol. Lett.* **10**, 1268 (1998); *J. Lightwave Technol.* **17**, 178 (1999).

[100] H. J. Thiele, R. I. Killey, and P. Bayvel, *Electron. Lett.* **35**, 408 (1999).

[101] L. Rapp, *J. Opt. Commun.* **20**, 29 (1999); *J. Opt. Commun.* **20**, 144 (1999).

[102] R. Hui, K. R. Demarest, and C. T. Allen, *J. Lightwave Technol.* **17**, 1018 (1999).

[103] S. Bigo, G. Bellotti, and M. W. Chbat, *IEEE Photon. Technol. Lett.* **11**, 605 (1999).

[104] M. Eiselt, M. Shtaif, and L. D. Garettt, *IEEE Photon. Technol. Lett.* **11**, 748 (1999).

[105] M. E. Marhic, I. Morite, M. C. Ho, Y. Akasaka, and L. G. Kazovsky, *Electron. Lett.* **35**, 2045 (1999).

[106] L. E. Nelson, R. M. Jopson, A. H. Gnauck, and A. R. Chraplyvy, *IEEE Photon. Technol. Lett.* **11**, 907 (1999).

[107] M. Shtaif, M. Eiselt, R. W. Tkach, R. H. Stolen, and A. H. Gnauck, *IEEE Photon. Technol. Lett.* **10**, 1796 (1998).

[108] M. Eiselt, M. Shtaif, R. W. Tkach, F. A. Flood, S. Ten, and D. Butler, *IEEE Photon. Technol. Lett.* **11**, 1575 (1999).

[109] G. J. Pendock, S. Y. Park, A. K. Srivastava, S. Radic, J. W. Sulhoff, C. L. Wolf, K. Kantor, and Y. Sun, *IEEE Photon. Technol. Lett.* **11**, 1578 (1999).

[110] S. Norimatsu and K. Iwashita, *J. Lightwave Technol.* **11**, 795 (1993).

[111] N. Shibata, R. P. Braun, and R. G. Waarts, *IEEE J. Quantum Electron.* **23**, 1205 (1987).

[112] M. W. Maeda, W. B. Sessa, W. I. Way, A. Yi-Yan, L. Curtis, R. Spicer, and R. I. Laming, *J. Lightwave Technol.* **8**, 1402 (1990).

[113] K. Inoue, *Opt. Lett.* **17**, 801 (1992); *J. Lightwave Technol.* **10**, 1553 (1992); *J. Lightwave Technol.* **12**, 1023 (1994).

[114] K. Inoue, K. Nakanishi, K. Oda, and H. Toba, *J. Lightwave Technol.* **12**, 1423 (1994).

[115] K. Inoue and H. Toba, *J. Lightwave Technol.* **13**, 88 (1995).

[116] F. Forghieri, R. W. Tkach, and A. R. Chraplyvy, *J. Lightwave Technol.* **13**, 889 (1995).

[117] A. Yu and M. J. O'Mahony, *IEE Proc.* **142**, 190 (1995).

[118] H. Taga, *J. Lightwave Technol.* **14**, 1287 (1996).

[119] W. Zeiler, F. Di Pasquale, P. Bayvel, and J. E. Midwinter, *J. Lightwave Technol.* **14**, 1933 (1996).

[120] D. F. Grosz, C. Mazzali, S. Celaschi, A. Paradisi, and H. L. Fragnito, *IEEE Photon. Technol. Lett.* **11**, 379 (1999).

[121] M. Eiselt, *J. Lightwave Technol.* **17**, 2261 (1999).

[122] S. Song, C. T. Allen, K. R. Demarest, and R. Hui, *J. Lightwave Technol.* **17**, 2285 (1999).

[123] H. Suzuki, S. Ohteru, and N. Takachio, *IEEE Photon. Technol. Lett.* **11**, 1677 (1999).

[124] J. S. Lee, D. H. Lee, and C. S. Park, *IEEE Photon. Technol. Lett.* **10**, 825 (1998).

[125] A. R. Chraplyvy, A. H. Gnauck, R. W. Tkach, and R. M. Derosier, *IEEE Photon. Technol. Lett.* **5**, 1233 (1993).

[126] K. Nakajima, M. Ohashi, K. Shiraki, T. Horiguchi, K. Kurokawa, and Y. Miyajima, *J. Lightwave Technol.* **17**, 1814 (1999).

[127] F. Matera and M. Settembre, *J. Lightwave Technol.* **14**, 1 (1996); *Fiber Integ. Opt.* **15**, 89 (1996); *J. Opt. Commun.* **17**, 1 (1996); *Opt. Fiber Technol.* **4**, 34 (1998).

[128] X. Y. Zou, M. I. Hayee, S. M. Hwang, and A. E. Willner, *J. Lightwave Technol.* **14**, 1144 (1996).

[129] K. Inser and K. Petermann, *IEEE Photon. Technol. Lett.* **8**, 443 (1996).

[130] D. Breuer and K. Petermann, *IEEE Photon. Technol. Lett.* **9**, 398 (1997).

[131] F. Forghieri, P. R. Prucnal, R. W. Tkach, and A. R. Chraplyvy, *IEEE Photon. Technol. Lett.* **9**, 1035 (1997).

[132] S. Bigo, A. Bertaina, M. W. Chbat et al., *IEEE Photon. Technol. Lett.* **10**, 1045 (1998).

[133] D. Breuer, K. Obermann, and K. Petermann, *IEEE Photon. Technol. Lett.* **10**, 1793 (1998).

[134] M. I. Hayee and A. E. Willner, *IEEE Photon. Technol. Lett.* **11**, 991 (1999).

[135] A. Sahara, H. Kubota, and M. Nakazawa, *Opt. Commun.* **160**, 139 (1999).

[136] R. Lebref, A. Ciani, F. Matera, and M. Tamburrini, *Fiber Integ. Opt.* **18**, 245 (1999).

[137] F. M. Madani and K. Kikuchi, *J. Lightwave Technol.* **17**, 1326 (1999).

[138] J. Kani, M. Jinno, T. Sakamoto, S. Aisawa, M. Fukui, K. Hattori, and K. Oguchi, *J. Lightwave Technol.* **17**, 2249 (1999).

[139] C. M. Weinert, R. Ludwig, W. Pieper, H. G. Weber, D. Breuer, K. Petermann, and F. Kuppers, *J. Lightwave Technol.* **17**, 2276 (1999).

[140] M. Murakami, T. Matsuda, H. Maeda, and T. Imai, *J. Lightwave Technol.* **18**, 1197 (2000).

[141] T. Imai, M. Murakami, Y. Fukuda, M. Aiki, and T. Ito, *Electron. Lett.* **28**, 1484 (1992).

[142] A. R. Chraplyvy, A. H. Gnauck, R. W. Tkach et al., *IEEE Photon. Technol. Lett.* **8**, 1264 (1996).

[143] H. Onaka, H. Miyata, G. Ishikawa et al., Optical Fiber Commun. Conf., San Jose, CA, 1996, paper PD19.

[144] T. Morioka, H. Takara, S. Kawanishi et al., *Electron. Lett.* **32**, 906 (1996).

[145] Y. Yano, T. Ono, T. Ito, H. Yamazaki, M. Yamaguchi, and K. Emura, Eur. Conf. Optical Commun., Oslo, Norway, 1996, paper ThB.3.1.

[146] S. Kawanishi, H. Takara, K. Uchiyama, I. Shake, and K. Mori, *Electron. Lett.* **35**, 826 (1999).

[147] T. N. Nielsen, A. J. Stentz, K. Rottwitt et al., *IEEE Photon. Technol. Lett.* **12**, 1079 (2000).

[148] T. Ito, K. Fukuchi, Y. Inada, T. Tsuzaki, M. Harumoto, M. Kakui, and K. Fujii, Optical Fiber Commun. Conf., Baltimore, MD, 2000, paper PD24.

[149] T. Ito, K. Fukuchi, K. Sekiya, D. Ogasahara, R. Ohhira, and T. Ono, Europ. Conf. on Optical Commun., Munich, 2000, paper PD1.1.

[150] S. Kawanishi, *IEEE J. Quantum Electron.* **34**, 2064 (1998).

[151] T. Yamammoto, E. Yoshida, K. R. Tamura, K. Yonenaga, and M. Nakazawa, *IEEE Photon. Technol. Lett.* **12**, 353 (2000).

[152] N. S. Bergano, in *Optical Fiber Telecommunications*, Vol. IIIA (Academic Press, San Diego, CA, 1997), Chap. 10.

[153] N. Shimojoh, T. Naito, T. Terahara, H. Deguchi, K. Tagawa, M. Suyama, and T. Chikama, *Electron. Lett.* **33**, 877 (1997).

[154] H. Taga, M. Suzuki, N. Edagawa, N. Takeda , K. Imai, S. Yamamoto, and S. Akiba, *Electron. Lett.* **34**, 476 (1998).

[155] H. Taga, M. Suzuki, N. Edagawa, S. Yamamoto, and S. Akiba, *IEEE J. Quantum Electron.* **34**, 2055 (1998).

[156] S. Akiba and S. Yamamoto, *Opt. Fiber Technol*. **4**, 19 (1998).

[157] I. Morita, K. Tanaka, N. Edagawa, S. Yamamoto, and M. Suzuki, *Electron. Lett.* **34**, 1863 (1998).

[158] M. Murakami, T. Matsuda, and T. Imai, *Electron. Lett.* **35**, 488 (1999).

[159] Y. Yamada, S. Nakagawa, K. Takashina, T. Kawazawa, H. Taga, and K. Goto, *Electron. Lett.* **35**, 2212 (1999).

[160] T. Matsuda, M. Murakami, and T. Imai, *Electron. Lett.* **36**, 55 (2000).

[161] T. Tsuritani, Y. Yamada, A. Agata, N. Takeda, N. Edagawa, and M. Suzuki, *Electron. Lett.* **36**, 1566 (2000).

[162] J. M. Beaufils, *Opt. Fiber Technol*. **6**, 15 (2000).

[163] C. R. Davidson, C. J. Chen, M. Nissov et al., Optical Fiber Commun. Conf., Baltimore, MD, 2000, paper PD25.

Chapter 8

Soliton Lightwave Systems

As discussed in Chapter A.5, under certain conditions optical pulses can propagate inside fibers in the form of solitons—pulses that remain undistorted in spite of the nonlinear and dispersive effects. Clearly, solitons are useful for representing bits in a lightwave system since such pulses would remain confined to their assigned bit slot. This chapter focuses on soliton communication systems with emphasis on the physics and design of such systems. The basic concepts related to solitons are introduced in Section 8.1, which also discusses how solitons can be used for designing lightwave systems. Section 8.2 is devoted to loss-managed solitons, which result when fiber losses are compensated using optical amplifiers. Noise and timing-jitter issues for such solitons are discussed in Section 8.3. In Section 8.4 the focus is on dispersion-managed solitons and the advantages offered by them. The use of solitons for WDM lightwave systems is discussed in Section 8.5 with emphasis on timing jitter induced by interchannel collisions.

8.1 Basic Concepts

The use of solitons for optical communications was first suggested in 1973 [1], and by 1980s solitons had been observed experimentally [2]. The potential of solitons for signal transmission over long distances was first demonstrated in a 1988 experiment in which fiber losses were compensated using Raman amplification [3]. Remarkable progress made during the 1990s has converted optical solitons into a practical candidate for lightwave communication systems [4]–[8].

Solitons result from a balance between group-velocity dispersion (GVD) and self-phase modulation (SPM), both of which (as discussed in Chapter 7) can limit the performance of fiber-optic communication systems. To understand how such a balance is possible, note that GVD broadens optical pulses during their propagation inside a fiber except when the pulse is initially chirped in the right way. More specifically, a chirped pulse is compressed in optical fibers, even without SPM, whenever the GVD parameter β_2 and the chirp parameter C happen to have opposite signs (see Chapter 6). SPM, by itself, chirps an optical pulse such that $C > 0$. Since $\beta_2 < 0$ in the 1.55-μm wavelength region, the condition $\beta_2 C < 0$ is readily satisfied. Moreover, since the SPM-induced chirp is power dependent, it is not difficult to imagine that under certain conditions, SPM and GVD may cooperate in such a way that the SPM-induced chirp is just right to cancel the GVD-induced broadening of the pulse. The optical pulse would then propagate undistorted in the form of a soliton.

8.1.1 Properties of Solitons

The mathematical description of fiber solitons is based on the nonlinear Schrödinger (NLS) equation given earlier as Eq. (7.3.1). In this section, we neglect fiber losses by setting $\alpha = 0$ and assume that both β_2 and γ are constants along the whole length of fiber. These assumptions will be relaxed in later sections. In its normalized form, the NLS equation takes the form:

$$i\frac{\partial u}{\partial \xi} - \frac{s}{2}\frac{\partial^2 u}{\partial \tau^2} + |u|^2 u = 0, \tag{8.1.1}$$

where $s = \mathrm{sgn}(\beta_2) = \pm 1$ and

$$\xi = z/L_D, \quad \tau = T/T_0, \quad u = (\gamma L_D)^{1/2} A. \tag{8.1.2}$$

The dispersion length L_D is related to the pulse width T_0 as $L_D = T_0^2/|\beta_2|$. The NLS equation can be solved exactly by using a mathematical technique known as the inverse scattering method [9]. Although Eq. (8.1.1) has soliton-like solutions for both normal and anomalous GVD (known as *dark* and *bright solitons*, respectively), pulse-like solitons occur only in the case of anomalous dispersion. For this reason, we assume $\beta_2 < 0$ and choose $s = -1$ in Eq. (8.1.1).

The soliton solution of the NLS equation, obtained by the inverse scattering method, can be summarized as follows. When an input pulse having a "sech"

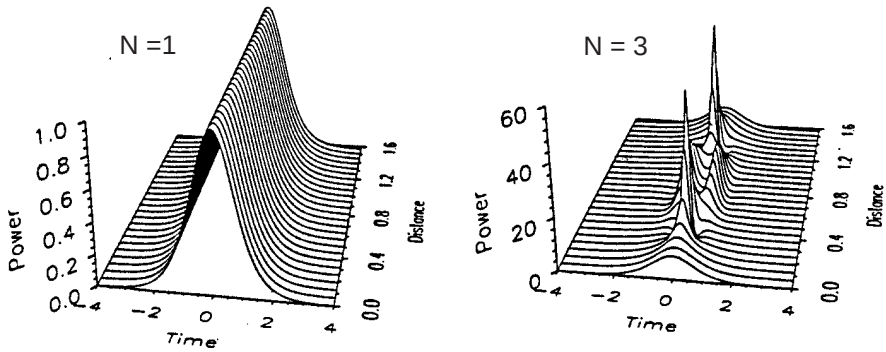

Figure 8.1 Evolution of (a) first-order and (b) third-order solitons over one soliton period.

shape such that

$$u(0,\tau) = N\,\mathrm{sech}(\tau) \tag{8.1.3}$$

is launched into a fiber, its shape remains unchanged during propagation when $N = 1$ but follows a periodic pattern for integer values of $N > 1$ such that the input shape is recovered at $\xi = m\pi/2$, where m is an integer. The optical pulse corresponding to $N = 1$ is called the *fundamental soliton*. Pulses corresponding to other integer values of N are known as *higher-order solitons*. The parameter N represents the order of a soliton. Noting that $\xi = z/L_D$, the soliton period z_0, defined as the distance over which higher-order solitons recover their original shape, is given by $z_0 = (\pi/2)L_D$. The soliton period z_0 and soliton order N play an important role in the theory of optical solitons.

The plot of the pulse shape $|u(\xi,\tau)|^2$ along the fiber length in Fig. 8.1 shows how the first-order ($N = 1$) and third-order ($N = 3$) solitons evolve over one soliton period. Only the fundamental soliton maintains its shape. In its most general form, the analytic solution of Eq. (8.1.1) in the $N = 1$ case can be written as [5]

$$u(\xi,\tau) = \eta\,\mathrm{sech}[\eta(\tau + \delta\xi - q)]\exp[-i\delta\tau + i(\eta^2 - \delta^2)\xi/2 + i\phi], \tag{8.1.4}$$

where the parameters η, q, δ, and ϕ represent the amplitude, position, frequency, and phase of the input pulse at $\xi = 0$, respectively. This solution shows clearly that the amplitude and width of a soliton are inversely related. It also shows that a frequency shift δ changes the soliton speed since the group velocity depends on the carrier frequency for an optical pulse.

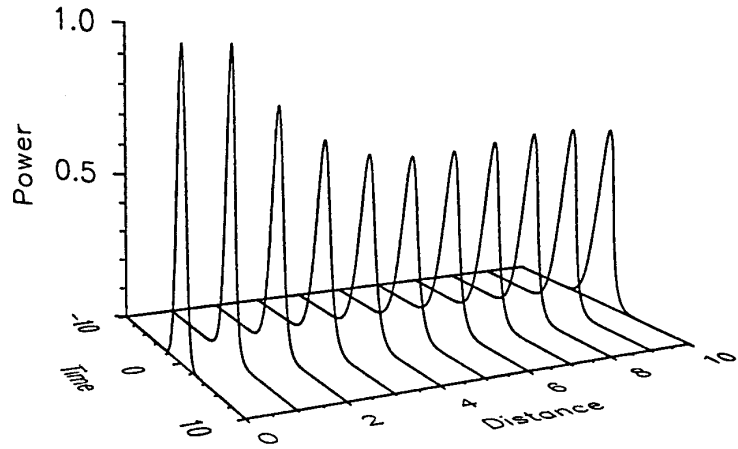

Figure 8.2 Evolution of a Gaussian pulse with $N = 1$ over the range $\xi = 0$ to 10. The pulse evolves toward a fundamental soliton by changing its shape and width.

Choosing $\eta = 1$, $q = 0$, $\delta = 0$, and $\phi = 0$ in Eq. (8.1.4), we obtain the canonical form of a fundamental soliton:

$$u(\xi, \tau) = \text{sech}(\tau) \exp(i\xi/2). \tag{8.1.5}$$

This equation shows that the optical pulse acquires a phase shift $\xi/2$ that is time independent (unchirped pulse) as it propagates inside the fiber, but its amplitude remains unchanged. It is this property of a fundamental soliton that makes it an ideal candidate for optical communications. In essence, the effects of fiber dispersion are exactly compensated by the fiber nonlinearity when the input pulse has a "sech" shape and its width and peak power are related such that

$$N = \gamma P_0 L_D = \gamma P_0 T_0^2 / |\beta_2| = 1. \tag{8.1.6}$$

An important property of optical solitons is that they are remarkably stable against perturbations. Thus, even though the fundamental soliton requires a specific shape and a certain peak power such that $N = 1$, it can be generated even when the pulse shape and the peak power deviate from the ideal conditions. Figure 8.2 shows the numerically simulated evolution of a Gaussian input pulse for which $N = 1$ but $u(0, \tau) = \exp(-\tau^2/2)$. As seen there, the pulse adjusts its shape and width in an attempt to become a fundamental soliton and attains a "sech" profile for $\xi \gg 1$. A similar behavior is observed

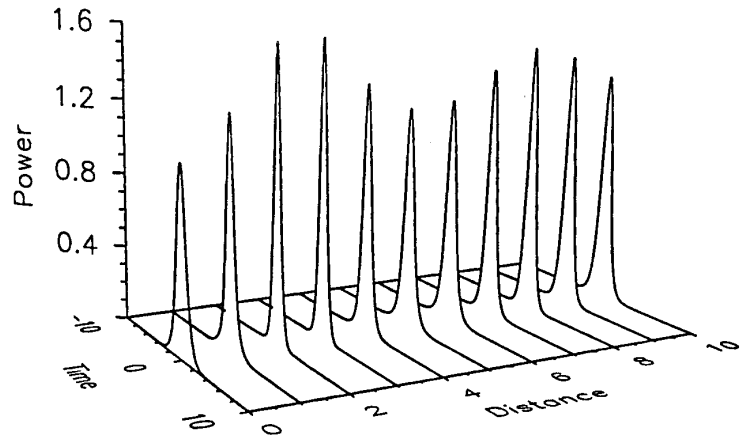

Figure 8.3 Evolution of a "sech" pulse with $N = 1.2$ over the range $\xi = 0$ to 10. The pulse evolves toward a fundamental soliton by adjusting its width and peak power.

when N deviates from 1. It turns out that the Nth-order soliton can be formed when the input value of N is in the range $N - 1/2$ to $N + 1/2$ [10]. In particular, a fundamental soliton can be excited for values of N in the range from 0.5 to 1.5. Figure 8.3 shows the evolution for $N = 1.2$ over the range $\xi = 0$ to 10 when the NLS equation is solved numerically with the initial condition $u(0, \tau) = 1.2\,\mathrm{sech}(\tau)$. Both pulse width and peak power oscillate initially but eventually become constant after the pulse has adjusted itself to satisfy the condition $N = 1$ of Eq. (8.1.5).

In general, small deviations from the ideal conditions are not detrimental for soliton propagation since the input pulse is able to adjust its parameters to form a fundamental soliton. Some pulse energy is lost during the dynamic adaptation phase in the form of dispersive waves known as *continuum radiation*. It will be seen later that such dispersive waves affect system performance and should be minimized by matching the input conditions as close to the ideal requirements as possible.

8.1.2 Soliton Bit Stream

The NRZ format cannot be used for lightwave systems when solitons are used as information bits. The reason is easily understood by noting that the soliton solution (8.1.4) extends to $|\tau| \to \infty$. It remains approximately valid for a train of solitons only when individual solitons are well isolated. For this reason, the

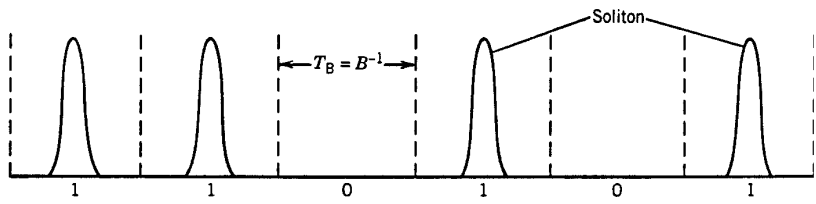

Figure 8.4 Soliton bit stream in an RZ format. Each soliton occupies a small fraction of the bit slot so that neighboring solitons are spaced far apart.

soliton width must be a small fraction of the bit slot. Figure 8.4 shows a soliton bit stream in the RZ format. The soliton width T_0 is related to the bit rate B as

$$B = \frac{1}{T_B} = \frac{1}{2q_0 T_0}, \tag{8.1.7}$$

where T_B is the duration of the bit slot and $2q_0 = T_B/T_0$ is the normalized spacing between neighboring solitons.

The input pulse characteristics needed to launch a fundamental soliton can be obtained by setting $\xi = 0$ in Eq. (8.1.5). In physical units, the amplitude of the pulse is given by

$$A(0,t) = \sqrt{P_0}\,\mathrm{sech}(t/T_0). \tag{8.1.8}$$

The peak power P_0 is obtained from Eq. (8.1.6) and is related to the pulse width T_0 and the fiber parameters as

$$P_0 = |\beta_2|/\gamma T_0^2. \tag{8.1.9}$$

The width parameter T_0 used for normalization is related to the full width at half maximum (FWHM) of the soliton as

$$T_s = 2T_0 \ln(1+\sqrt{2}) \simeq 1.763 T_0. \tag{8.1.10}$$

The pulse energy for a fundamental soliton is given by

$$E_s = \int_{-\infty}^{\infty} |A(0,t)|^2\, dt = 2P_0 T_0. \tag{8.1.11}$$

Assuming that 1 and 0 bits are equally likely to occur, the average power of the RZ signal becomes $\bar{P}_s = E_s(B/2) = P_0/2q_0$. As a simple example, $T_0 = 10$ ps for a 10-Gb/s soliton system if we choose $q_0 = 5$. The FWHM of the pulse is

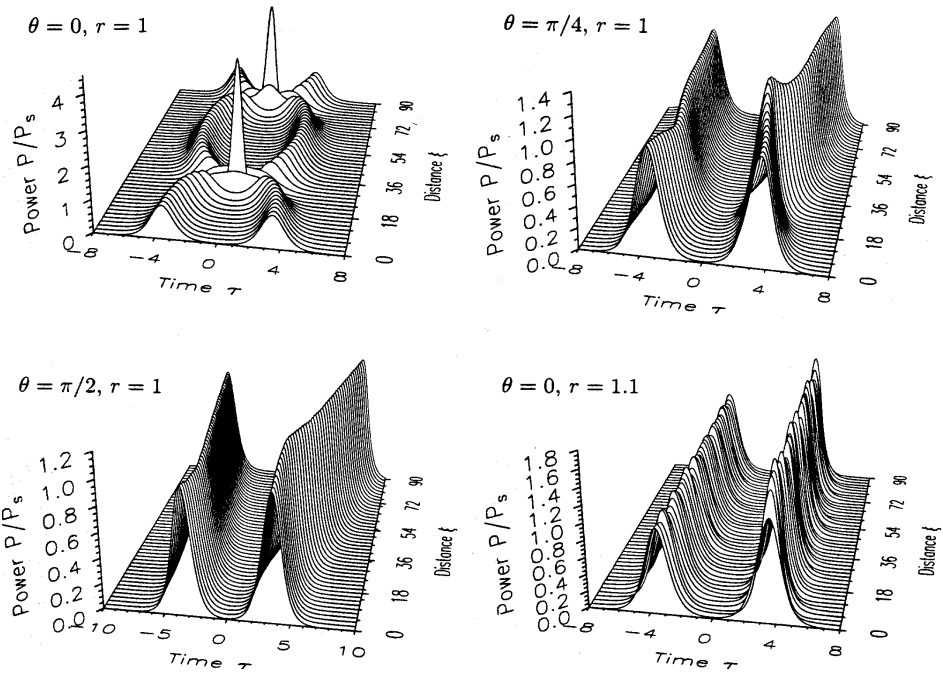

Figure 8.5 Evolution of a soliton pair over 90 dispersion lengths showing the effects of soliton interaction for four different choices of amplitude ratio r and relative phase θ. Initial spacing $q_0 = 3.5$ in all four cases.

about 17.6 ps for such solitons. The peak power of the input pulse is 5 mW using $\beta_2 = -1$ ps^2/km and $\gamma = 2$ W^{-1}/km as typical values for dispersion-shifted fibers. This value of the peak power corresponds to a pulse energy of 0.1 pJ and an average power level of only 0.5 mW.

8.1.3 Soliton Interaction

For practical reasons, one would like to pack solitons as tightly as possible. However, the presence of pulses in the neighboring bits perturbs each soliton simply because the combined optical field is not a solution of the NLS equation. This phenomenon is referred to as *soliton interaction* and has been studied extensively [11]–[15]. Section A.5.4 contains a complete discussion of soliton interaction. Here we focus on details relevant to system design.

One can understand the implications of soliton interaction by solving the

NLS equation numerically with the input corresponding to a soliton pair such that

$$u(0,\tau) = \operatorname{sech}(\tau - q_0) + r\operatorname{sech}[r(\tau + q_0)]\exp(i\theta), \tag{8.1.12}$$

where r is the relative amplitude, θ is the relative phase, and $2q_0$ is the initial separation between the two solitons. Figure 8.5 shows the evolution of such a soliton pair for several values of r and θ using $q_0 = 3.5$. Clearly, interaction between two solitons depends strongly both on the relative phase θ and on the amplitude ratio r.

Consider first the case of equal-amplitude solitons ($r = 1$). The two solitons attract each other in the in-phase case ($\theta = 0$) such that they collide periodically along the fiber length. However, for $\theta = \pi/4$, the solitons separate from each other after an initial attraction stage. For $\theta = \pi/2$, the solitons repel each other even more strongly, and their spacing increases with distance. From the standpoint of system design, this behavior is not acceptable. It leads to jitter in the arrival time of solitons since the relative phase of neighboring solitons is not likely to remain constant. One way to avoid soliton interaction is to increase q_0. For sufficiently large q_0, deviations in the soliton position are expected to be small enough that each soliton remains within its assigned bit slot throughout the fiber length.

The dependence of soliton separation on q_0 can be studied analytically by using the inverse scattering method. A perturbative approach was used in Section A.5.4 assuming $q_0 \gg 1$. In the specific case of $r = 1$ and $\theta = 0$, the soliton separation changes with distance as [12]

$$q(\xi) = q_0 + \ln|\cos(2\xi e^{-q_0})|. \tag{8.1.13}$$

This relation shows that spacing between two in-phase solitons oscillates with the period

$$\xi_p = (\pi/2)\exp(q_0). \tag{8.1.14}$$

The distance $L_{\text{coll}} = \xi_p L_D$ is called the *collision length*.

Equation (8.1.14) is quite accurate for $q_0 > 3$. Its predictions are in agreement with Fig. 8.5 where $q_0 = 3.5$. It can be used for system design as follows. If L_{coll} is much larger than the total transmission distance L_T, soliton interaction can be neglected since soliton spacing would deviate little from its initial value. As an estimate, when $q_0 = 6$, $\xi_p \approx 634$. If the dispersion length exceeds 100 km, $L_T \ll L_{\text{coll}}$ can be realized even for transoceanic distances. Using

$L_D = T_0^2/|\beta_2|$ and $T_0 = (2Bq_0)^{-1}$ from Eq. (8.1.7), the condition $L_T \ll L_{\text{coll}}$ can be written in the form of the following design criterion:

$$B^2 L_T \ll \frac{\pi \exp(q_0)}{8q_0^2|\beta_2|}. \tag{8.1.15}$$

As an example, $B^2 L_T \ll 4.4$ (Tb/s)^2-km if we use $q_0 = 6$ and $\beta_2 = -1$ ps^2/km.

A relatively large soliton spacing, necessary to avoid soliton interaction, limits the bit rate of soliton communication systems. The spacing can be reduced by up to a factor of 2 using unequal amplitudes for the neighboring solitons. As seen in Fig. 8.5, the separation for two in-phase solitons does not change by more than 10% for q_0 as small as 3.5 if their amplitudes differ by 10% initially ($r = 1.1$). Another scheme for reducing soliton interaction alternates the state of polarization such that two neighboring solitons are orthogonally polarized [16], [17]. Chapter A.6 contains a discussion of the polarization effects.

8.1.4 Effect of Fiber Loss

As discussed earlier, solitons use fiber nonlinearity to maintain their width even in the presence of fiber dispersion. However, this property holds only when fiber losses are negligible. It is not difficult to see that a decrease in the soliton energy because of fiber losses would lead to soliton broadening simply because the reduced peak power weakens the nonlinear effect necessary to counteract the GVD.

Fiber losses are included by the last term in Eq. (7.3.1), resulting in the following modified NLS equation:

$$i\frac{\partial u}{\partial \xi} + \frac{1}{2}\frac{\partial^2 u}{\partial \tau^2} + |u|^2 u = -\frac{i}{2}\Gamma u, \tag{8.1.16}$$

where we chose $s = -1$ in Eq. (8.1.1) and

$$\Gamma = \alpha L_D = \alpha T_0^2/|\beta_2| \tag{8.1.17}$$

represents fiber losses over one dispersion length. When $\Gamma \ll 1$, the last term in Eq. (8.1.16) can be treated as a small perturbation. As shown in Section A.5.4.2, Eq. (8.1.16) then has the following solution [18]:

$$u(\xi,\tau) \approx e^{-\Gamma\xi}\operatorname{sech}(\tau e^{-\Gamma\xi})\exp[i(1-e^{-2\Gamma\xi})/4\Gamma]. \tag{8.1.18}$$

The solution (8.1.18) shows that the soliton width increases exponentially because of fiber losses as

$$T_1(\xi) = T_0 \exp(\Gamma\xi) = T_0 \exp(\alpha z). \tag{8.1.19}$$

Such an exponential increase cannot be expected to continue for arbitrarily long distances. Numerical solutions of Eq. (8.1.16) indeed show a slower width increase for $\xi \gg 1$ [19]. The important point is that soliton broadening is much smaller compared with the linear case. Thus, the nonlinear effects can be beneficial for optical communication systems even when solitons cannot be maintained perfectly because of fiber losses. In a 1986 study [20], an increase in the repeater spacing by more than a factor of 2 was predicted when higher-order solitons were used as information bits.

In modern long-haul lightwave systems, pulses are transmitted over long fiber lengths without using electronic repeaters. To overcome the effect of fiber losses, solitons should be amplified periodically using either lumped or distributed amplification [21]–[24]. The simplest scheme makes use of erbium-doped fiber amplifiers in a configuration identical to that used for nonsoliton systems (see Fig. 7.1). An optical amplifier is placed periodically along the fiber link, and its gain is adjusted such that fiber losses between two amplifiers are exactly compensated by the amplifier gain. The next section considers the design issues related to such loss-managed solitons.

8.2 Loss-Managed Solitons

Consider a long-haul soliton link in which fiber losses are compensated periodically using a suitable amplification scheme. In general, losses cannot be compensated fully at every point along the fiber, and soliton energy will vary along the fiber link. The way a soliton reacts to energy losses depends strongly on the relative magnitudes of dispersion length L_D and amplifier spacing L_A. If energy variations are relatively small over each dispersion length (a few percent or less), soliton parameters can evolve adiabatically. This regime is referred to as the *quasi-adiabatic regime*. On the other hand, if soliton energy varies rapidly, a soliton can maintain its identity only if amplifier spacing L_A is kept much smaller than L_D. The reason for this restriction is that L_D (or the soliton period) sets the length scale over which a soliton reacts to energy losses. Hence, when $L_A \ll L_D$, a soliton is not distorted despite energy losses. In such lightwave systems, solitons can be amplified hundreds of times while

preserving their shape and width. We refer to such solitons as *loss-managed solitons*. They are also called path-averaged or guiding-center solitons. In this section, we discuss the issues that need attention when loss-managed solitons are used for designing lightwave systems.

8.2.1 Lumped Amplification

Periodic amplification of solitons can be accounted for by adding a gain term to Eq. (8.1.16) and writing it as

$$i\frac{\partial u}{\partial \xi}+\frac{1}{2}\frac{\partial^2 u}{\partial \tau^2}+|u|^2u=-\frac{i}{2}\Gamma u+\frac{i}{2}g(\xi)L_D u, \tag{8.2.1}$$

where the form of $g(\xi)$ depends on whether lumped or distributed amplification is used. In the case of lumped amplifiers, it can be written as

$$g(\xi)=\sum_{m=1}^{N_A} g_m \delta(\xi-\xi_m), \tag{8.2.2}$$

where N_A is the total number of amplifiers and g_m is the gain of the amplifier located at ξ_m, chosen such that lumped amplifiers compensate for all losses along the link. In the following analysis, we assume that amplifiers are spaced uniformly such that $\xi_m = m\xi_A$, where $\xi_A = L_A/L_D$ is the normalized amplifier spacing.

Because of rapid variations in the soliton energy introduced by periodic gain–loss changes, it is useful to make the transformation

$$u(\xi,\tau)=\sqrt{p(\xi)}\,v(\xi,\tau), \tag{8.2.3}$$

where $p(\xi)$ is a rapidly varying and $v(\xi,\tau)$ is a slowly varying function of ξ. By substituting Eq. (8.2.3) in Eq. (8.2.1), $v(\xi,\tau)$ is found to satisfy

$$i\frac{\partial v}{\partial \xi}+\frac{1}{2}\frac{\partial^2 v}{\partial \tau^2}+p(\xi)|v|^2v=0, \tag{8.2.4}$$

where $p(\xi)$ is obtained by solving the ordinary differential equation

$$\frac{dp}{d\xi}=[g(\xi)L_D-\Gamma]p. \tag{8.2.5}$$

The functional form of $p(\xi)$ depends on the amplification scheme used for solitons. In the case of lumped amplifiers, $p(\xi)$ decreases exponentially in

each period as $p(\xi) = \exp(-\Gamma\xi)$, with a jump to its initial value $p(0) = 1$ at the end of each period. Physically, $p(\xi)$ governs variations in the peak power (or the energy) of a soliton between two amplifiers. For a fiber with losses of 0.2 dB/km, $p(\xi)$ varies by a factor of 100 when $L_A = 100$ km.

In general, changes in the soliton amplitude are accompanied by changes in the soliton width. As a result, large rapid variations in $p(\xi)$ can destroy a soliton if its width changes rapidly since they are accompanied by emission of dispersive waves (continuum radiation). The concept of the path-averaged or guiding-center soliton makes use of the fact that solitons evolve little over a distance that is short compared with the dispersion length (or soliton period). Thus, when $\xi_A \ll 1$, the soliton width remains virtually unchanged even though its peak power $p(\xi)$ varies considerably in each section between two neighboring amplifiers. In effect, one can replace $p(\xi)$ by its average value when $\xi_A \ll 1$. This approximation can be justified by assuming a solution of Eq. (8.2.4) in the form $v = \bar{v} + \delta v$, where δv is a perturbation and $\bar{v}$ satisfies the path-averaged NLS equation

$$i\frac{\partial \bar{v}}{\partial \xi} + \frac{1}{2}\frac{\partial^2 \bar{v}}{\partial \tau^2} + \bar{p}|\bar{v}|^2\bar{v} = 0, \tag{8.2.6}$$

with $\bar{p} = \frac{1}{\xi_A}\int_0^{\xi_A} p(\xi)\,d\xi$. The perturbation δv turns out to be relatively small when $\xi_A \ll 1$ [25]. In practice, the path-averaged description is valid even for $\xi_A = 1/4$.

From a practical viewpoint, a fundamental soliton can be excited if the input peak power P_s or energy of the path-averaged soliton is chosen to be larger by a factor $1/\bar{p}$. Introducing the amplifier gain as $G = \exp(\Gamma\xi_A)$, the energy enhancement factor for loss-managed solitons is given by

$$f_{\mathrm{LM}} = \frac{P_s}{P_0} = \frac{1}{\bar{p}} = \frac{\Gamma\xi_A}{1-\exp(-\Gamma\xi_A)} = \frac{G\ln G}{G-1}, \tag{8.2.7}$$

where P_0 is the peak power in lossless fibers. Thus, soliton evolution in lossy fibers with periodic lumped amplification is identical to that in lossless fibers provided (i) amplifiers are spaced such that $L_A \ll L_D$ and (ii) the launched peak power is larger by a factor f_{LM}. As an example, $G = 10$ and $f_{\mathrm{LM}} \approx 2.56$ for 50-km amplifier spacing and fiber losses of 0.2 dB/km.

Figure 8.6 shows the evolution of a loss-managed soliton over a distance of 10,000 km for the case in which solitons are amplified every 50 km. When

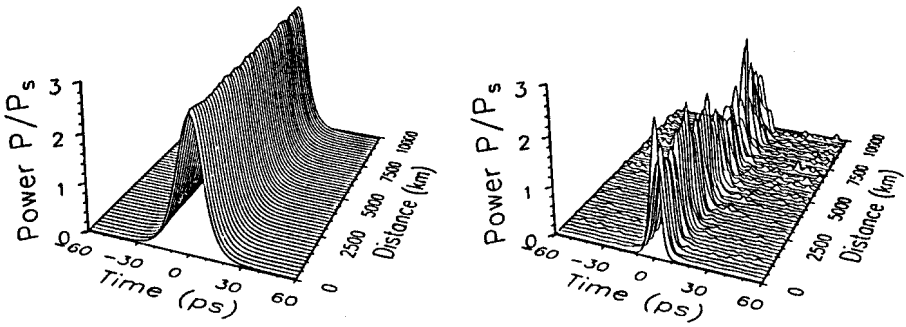

Figure 8.6 Evolution of loss-managed solitons over 10,000 km for (a) $L_D = 200$ km and (b) 25 km with $L_A = 50$ km, $\alpha = 0.22$ dB/km, and $\beta_2 = -0.5$ ps^2/km.

the input pulse width corresponds to a dispersion length of 200 km, the soliton is preserved quite well even after 10,000 km since the condition $\xi_A \ll 1$ is reasonably well satisfied. However, if the dispersion length is reduced to 25 km, the soliton is unable to sustain itself because of excessive emission of dispersive waves for $\xi_A = 2$. The condition $\xi_A \ll 1$ or $L_A \ll L_D$, required to operate in the loss-managed regime, can be related to the width T_0 by using $L_D = T_0^2/|\beta_2|$. The resulting condition is

$$T_0 \gg \sqrt{|\beta_2| L_A}. \tag{8.2.8}$$

Since the bit rate B is related to T_0 through Eq. (8.1.7), this condition can be written in the form of the following design criterion:

$$B^2 L_A \ll (4q_0^2|\beta_2|)^{-1}. \tag{8.2.9}$$

Choosing typical values, $\beta_2 = -0.5$ ps^2/km, $L_A = 50$ km, and $q_0 = 5$, we obtain $T_0 \gg 5$ ps and $B \ll 20$ Gb/s. Clearly, the use of path-averaged solitons imposes a severe limitation on both the bit rate and the amplifier spacing for soliton communication systems.

8.2.2 Distributed Amplification

The condition $L_A \ll L_D$, imposed on loss-managed solitons when lumped amplifiers are used, becomes increasingly difficult to satisfy in practice as bit rates exceed 10 Gb/s. This condition can be relaxed considerably when distributed

amplification is used. The distributed-amplification scheme is inherently superior to lumped amplification since its use provides a nearly lossless fiber by compensating losses locally at every point along the fiber link. In fact, this scheme was used as early as 1985 using the distributed gain provided by Raman amplification when the fiber carrying the signal was pumped at a wavelength of about 1.46 μm using a color-center laser [23]. Alternatively, the transmission fiber can be doped lightly with erbium ions and pumped periodically to provide distributed gain. Several experiments have demonstrated that solitons can be propagated in such active fibers over relatively long distances [26]–[30].

Mathematically, the advantage of distributed amplification can be seen from Eq. (8.2.5), which can be written in physical units as

$$\frac{dp}{dz} = [g(z) - \alpha]p. \tag{8.2.10}$$

If $g(z)$ is constant and equal to α for all z, the peak power or energy of a soliton remains constant along the fiber link. This is the ideal situation in which the fiber is effectively lossless. In practice, distributed gain is realized by injecting pump power periodically into the fiber link. Since pump power does not remain constant because of fiber losses and pump depletion (e.g., absorption by dopants), $g(z)$ cannot be made constant along the fiber. However, even though fiber losses cannot be compensated locally everywhere, they can be compensated fully over a distance L_A provided that

$$\int_0^{L_A} g(z)\,dz = \alpha L_A. \tag{8.2.11}$$

A distributed-amplification scheme is designed to satisfy Eq. (8.2.11). The distance L_A is referred to as the *pump-station spacing*.

The important question is how much soliton energy varies during each gain–loss cycle. The extent of peak-power variations depends on L_A and on the pumping scheme adopted. Backward pumping is commonly used for distributed Raman amplification since such a configuration provides high gain where the signal is relatively weak. The gain coefficient $g(z)$ can be obtained following the analysis of Section A.8.1. If we ignore pump depletion, the gain coefficient in Eq. (8.2.10) is given by $g(z) = g_0 \exp[-\alpha_p(L_A - z)]$, where α_p accounts for fiber losses at the pump wavelength. The resulting equation can

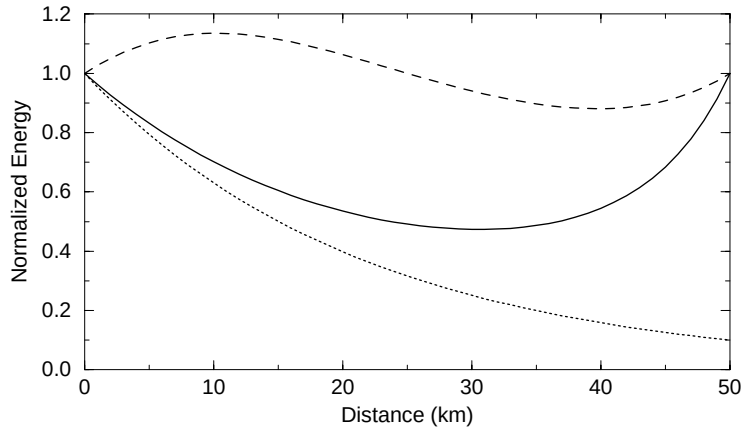

Figure 8.7 Variations in soliton energy for backward (solid line) and bidirectional (dashed line) pumping schemes with $L_A = 50$ km. The lumped-amplifier case is shown by the dotted line.

be integrated analytically to obtain

$$p(z) = \exp\left\{\alpha L_A \left[\frac{\exp(\alpha_p z) - 1}{\exp(\alpha_p L_A) - 1}\right] - \alpha z\right\}, \tag{8.2.12}$$

where g_0 was chosen to ensure that $p(L_A) = 1$. Figure 8.7 shows how $p(z)$ varies along the fiber for $L_A = 50$ km using $\alpha = 0.2$ dB/km and $\alpha_p = 0.25$ dB/km. The case of lumped amplification is also shown for comparison. Whereas soliton energy varies by a factor of 10 in the lumped case, it varies by less than a factor of 2 in the case of distributed amplification.

The range of energy variations can be reduced further using a bidirectional pumping scheme. The gain coefficient $g(z)$ in this case can be approximated (neglecting pump depletion) as

$$g(z) = g_1 \exp(-\alpha_p z) + g_2 \exp[-\alpha_p (L_A - z)]. \tag{8.2.13}$$

The constants g_1 and g_2 are related to the pump powers injected at both ends. Assuming equal pump powers and integrating Eq. (8.2.10), the soliton energy is found to vary as

$$p(z) = \exp\left[\alpha L_A \left(\frac{\sinh[\alpha_p (z - L_A/2)] + \sinh(\alpha_p L_A/2)}{2\sinh(\alpha_p L_A/2)}\right) - \alpha z\right]. \tag{8.2.14}$$

This case is shown in Fig. 8.7 by a dashed line. Clearly, a bidirectional pumping scheme is the best since it reduces energy variations to below 20%. The range over which $p(z)$ varies increases with L_A. Nevertheless, it remains much smaller than that occurring in the lumped-amplification case. As an example, soliton energy varies by a factor of 100 or more when $L_A = 100$ km if lumped amplification is used but by less than a factor of 2 when a bidirectional pumping scheme is used for distributed amplification.

The effect of energy excursion on solitons depends on the ratio $\xi_A = L_A/L_D$. When $\xi_A < 1$, little soliton reshaping occurs. For $\xi_A \gg 1$, solitons evolve adiabatically with some emission of dispersive waves (the quasi-adiabatic regime). For intermediate values of ξ_A, a more complicated behavior occurs. In particular, dispersive waves and solitons are resonantly amplified when $\xi_A \simeq 4\pi$; Such a resonance can lead to unstable and chaotic behavior [24]. For this reason, distributed amplification is used with $\xi_A < 4\pi$ in practice [26]–[30].

Modeling of soliton communication systems making use of distributed amplification requires the addition of a gain term to the NLS equation, as in Eq. (8.2.1). In the case of soliton systems operating at bit rates $B > 20$ Gb/s such that $T_0 < 5$ ps, it is also necessary to include the effects of finite gain bandwidth, third-order dispersion (TOD), and the intrapulse Raman scattering. As discussed in Section 4.6.2, Eq. (8.2.1) should then be replaced with the following equation:

$$i\frac{\partial u}{\partial \xi} + \frac{1}{2}\frac{\partial^2 u}{\partial \tau^2} + |u|^2 u = \frac{i}{2}g(\xi)L_D\left(u + \tau_2^2\frac{\partial^2 u}{\partial \tau^2}\right) - \frac{i}{2}\Gamma u + i\delta_3\frac{\partial^3 u}{\partial \tau^3} + \tau_R u\frac{\partial |u|^2}{\partial \tau}, \quad (8.2.15)$$

where τ_2 is related inversely to the gain bandwidth. The TOD parameter δ_3 and the Raman parameter τ_R are defined as in Section 4.6.2. Numerical simulations based on Eq. (8.2.15) show that the distributed-amplification scheme considerably benefits high-capacity soliton communication systems [31]. As an example, Fig. 8.8 shows the evolution of a fundamental soliton for lumped and distributed amplification (bidirectional pumping with erbium doping) for a fundamental soliton ($T_0 = 5$ ps) using $L_A = 100$ km, $L_D = 50$ km, $\tau_R = 6 \times 10^{-4}$, and $\tau_2 = \delta_3 = 0$. Since the condition $\xi_A \ll 1$ is not satisfied, lumped amplification fails to maintain the soliton even over a distance of 500 km. In

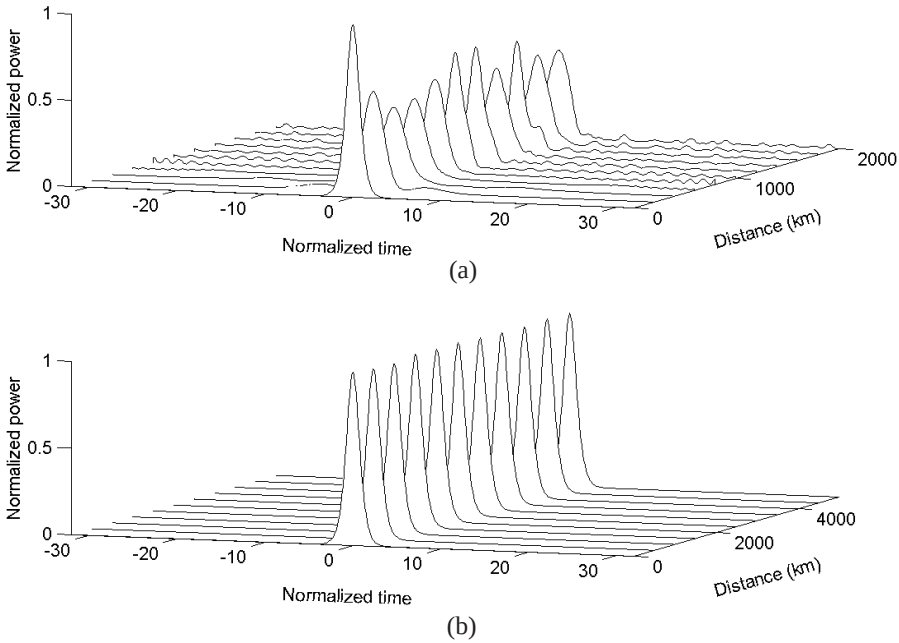

Figure 8.8 Comparison of (a) lumped and (b) distributed amplification schemes for a 20-Gb/s system designed with $L_A = 100$ km. Dispersion length is 50 km for $T_0 = 5$ ps. (After Ref. [31], ©1999 IEEE)

contrast, the soliton can propagate over a distance of more than 5000 km when distributed amplification is used.

For soliton widths below 5 ps, the Raman-induced spectral shift leads to considerable changes in soliton evolution since it modifies the gain and dispersion experienced by solitons. Fortunately, the finite gain bandwidth of amplifiers reduces the amount of spectral shift and stabilizes the soliton carrier frequency close to the gain peak [27]. Under certain conditions, the spectral shift can become so large that it cannot be compensated, and the soliton moves out of the gain window, loosing all its energy. It should be stressed that Eq. (8.2.15) approximates the gain spectrum by a parabola. Its use is justified for solitons whose spectrum is much narrower than the gain bandwidth but becomes questionable for femtosecond solitons. Equation (4.6.1) should be used for such short solitons. As seen in Fig. 4.17, the Raman-induced spectral shift drastically affects the evolution of femtosecond solitons, as also observed experimentally [28].

8.2.3 Chirped Solitons

Distributed amplification is not commonly used for practical reasons. One may ask whether it is possible to design loss-managed soliton systems using lumped amplifiers whose spacing is much larger than the dispersion length. The answer to this question is affirmative if one is willing to let the soliton parameters evolve in an adiabatic fashion. In general, any perturbation that forces changes in soliton parameters also generates continuum radiation in the form of dispersive waves. Adiabatic evolution of soliton parameters is capable of maintaining a soliton, but dispersive waves accumulated over long distances eventually affect the system performance. Several techniques have been proposed for minimizing and removing the energy lost to dispersive waves [32]–[36]. In this section, we consider the prechirping technique in which a soliton is chirped appropriately at the beginning such that both its width and chirp return to their original values in each section between two lumped amplifiers. It turns out that such prechirping can push the amplifier spacing beyond the dispersion length.

The variational method is quite useful for solving an equation such as Eq. (8.2.4) approximately. In this approach, we first note that Eq. (8.2.4) can be derived from the Euler–Lagrange equation [see Eq. (2.3.5)] using the following Lagrangian density

$$L_g = \frac{i}{2}\left(v^*\frac{\partial v}{\partial \xi} - v\frac{\partial v^*}{\partial \xi}\right) + \frac{1}{2}\left[p(\xi)|v|^4 - \left|\frac{\partial v}{\partial \tau}\right|^2\right]. \tag{8.2.16}$$

We then assume that the soliton evolves along the fiber as

$$v(\xi,\tau) = a\,\mathrm{sech}(\tau/b)\exp[i\phi - iC(\tau^2/2b^2)], \tag{8.2.17}$$

where a is the amplitude, b is the width, C is the chirp, and ϕ is the phase of the soliton. All four parameters can vary with ξ because of perturbations produced by fiber losses. Using the variational method outlined in Section 2.3.2 (see also Chapter A.5), we obtain the following set of four equations [36]:

$$\frac{da}{d\xi} = \frac{Ca}{2b^2}, \tag{8.2.18}$$

$$\frac{db}{d\xi} = -\frac{C}{b}, \tag{8.2.19}$$

$$\frac{dC}{d\xi} = \frac{4}{\pi^2}a^2 p(\xi) - (4/\pi^2 + C^2)\frac{1}{b^2}, \tag{8.2.20}$$

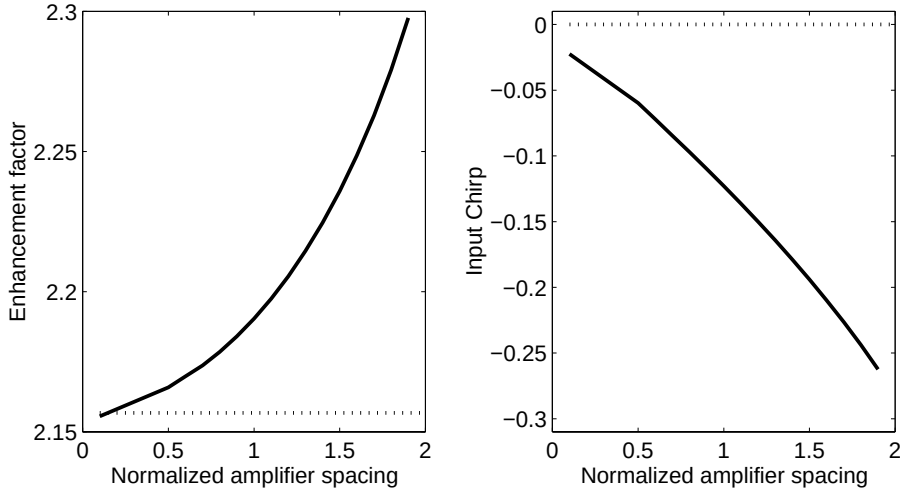

Figure 8.9 Enhancement factor f_{LM} and input chirp as a function of L_A/L_D when lumped amplifiers with 20-dB gain are placed 100 km apart. (After Ref. [36])

$$\frac{d\phi}{d\xi} = \frac{5}{6}a^2 p(\xi) - \frac{1}{3b^2}, \tag{8.2.21}$$

where $p(\xi) = \exp(-\Gamma\xi)$ in each fiber section between two optical amplifiers.

Equations (8.2.18) and (8.2.19) can be combined to show that the combination $a^2 b$ does not vary with ξ. Since the phase equation (8.2.21) is uncoupled from other equations, we only need to solve Eqs. (8.2.19) and (8.2.20) with the periodic boundary conditions

$$b(0) = b(\xi_A) \equiv 1, \qquad C(0) = C(\xi_A) \equiv C_0, \tag{8.2.22}$$

to ensure that the soliton recovers its initial state at $\xi = \xi_A$. The two boundary conditions fix the values of the soliton amplitude a_0 and the chirp C_0 at $\xi = 0$ for which the soliton can propagate from amplifier to amplifier in a periodic fashion. We can relate a_0 to the enhancement factor as $f_{\mathrm{LM}} = a_0^2$ since the soliton peak power should be increased by this factor.

Figure 8.9 shows how the energy-enhancement factor and input chirp vary with the normalized amplifier spacing, $\xi_A = L_A/L_D$, assuming that amplifiers with 20-dB gain [$G = \exp(\Gamma\xi_A) = 100$] are placed 100 km apart. When $\xi_A \ll 1$, the solution reduces to that obtained for path-averaged solitons (dotted lines) such that $C_0 \approx 0$ and f_{LM} is given by Eq. (8.2.7). As the dispersion length is

reduced and ξ_A exceeds 1, both the peak power and input chirp increase. The important point is that a properly chirped soliton can propagate through the amplifier chain in a periodic fashion. It is the prechirping of the soliton that permits the amplifier spacing to exceed the dispersion length. It should be stressed that a chirped soliton is quite different from the standard soliton [see Eq. (8.1.4)] as its width and amplitude are not inversely related.

8.3 Amplifier Noise

The use of optical amplifiers affects the evolution of solitons considerably. The reason is that amplifiers, although needed to restore the soliton energy, also add noise originating from amplified spontaneous emission (ASE). As discussed in Section 7.1, the spectral density of ASE depends on the amplifier gain G itself. This section is devoted to the effects of ASE on loss-managed solitons.

8.3.1 ASE-Induced Fluctuations

To study the impact of ASE on soliton evolution, we consider how the four soliton parameters in the NLS solution (8.1.4) are affected by amplifier noise. The effect of ASE is to change randomly the values of η, q, δ, and ϕ at the output of each amplifier. Variances of such fluctuations for the four soliton parameters can be calculated by treating ASE as a perturbation and using the approach described in Section A.5.4. As found there, in the presence of a perturbation $\varepsilon(u)$, the four soliton parameters appearing in Eq. (8.1.4) evolve as [8]

$$\frac{d\eta}{d\xi} = \mathrm{Re}\int_{-\infty}^{\infty} \varepsilon(u) F_\eta(\tau)\, d\tau, \tag{8.3.1}$$

$$\frac{d\delta}{d\xi} = \mathrm{Re}\int_{-\infty}^{\infty} \varepsilon(u) F_\delta(\tau)\, d\tau, \tag{8.3.2}$$

$$\frac{dq}{d\xi} = -\delta + \mathrm{Re}\int_{-\infty}^{\infty} \varepsilon(u) F_q(\tau)\, d\tau, \tag{8.3.3}$$

$$\frac{d\phi}{d\xi} = \frac{1}{2}(\eta^2 - \delta^2) + q\frac{d\delta}{d\xi} + \mathrm{Re}\int_{-\infty}^{\infty} \varepsilon(u) F_\phi(\tau)\, d\tau, \tag{8.3.4}$$

where Re stands for the real part and

$$F_\eta = u^*, \quad F_\delta = i\tanh[\eta(\tau - q)]u^*, \quad F_q = (\tau - q)u^*/\eta^2, \tag{8.3.5}$$

$$F_\phi = i\{(\tau - q)\tanh[\eta(\tau - q)] - 1/\eta\}u^*. \tag{8.3.6}$$

In the case of lumped amplification, solitons are perturbed by ASE in a discrete fashion at the location of the amplifiers. However, since the amplifier spacing satisfies $\xi_A \ll 1$, we assume that noise is distributed all along the fiber length. Such an approach is useful since it can be applied to the case of distributed amplification as well with only minor changes. Assuming fiber losses are fully compensated by amplifiers, adding noise, and introducing $u = \sqrt{p}\,\overline{v}$, the NLS equation (8.2.6) can be written as

$$i\frac{\partial u}{\partial \xi} + \frac{1}{2}\frac{\partial^2 u}{\partial \tau^2} + |u|^2 u = in(\xi, \tau), \tag{8.3.7}$$

where the noise term vanishes on average as $\langle n(\xi, \tau)\rangle = 0$. When $n(\xi, \tau)$ is a Markovian stochastic process with Gaussian statistics, its correlation function takes the form

$$\langle n(\xi, \tau) n^*(\xi', \tau')\rangle = S_n \delta(\tau - \tau')\delta(\xi - \xi'), \tag{8.3.8}$$

where S_n is the ASE spectral density. Following the analysis of Section 7.1, S_n is related to $S_{\rm sp} = n_{\rm sp} h\nu_0 (G-1)$ but it should be properly scaled and distributed over amplifier spacing. In soliton units,

$$S_n = n_{\rm sp} h\nu_0 (G-1)\frac{\gamma L_D^2}{L_A T_0} = \frac{F_n F_G}{N_{\rm ph}\xi_A}, \tag{8.3.9}$$

where $F_n = 2n_{\rm sp}$ is the amplifier noise figure and $F_G = (G-1)^2/(G\ln G)$ is related to the amplifier gain. This specific form of F_G results when we use the condition $N = \gamma L_D P_s = 1$ with Eq. (8.2.7). In Eq. (8.3.9), $N_{\rm ph} = 2P_0 T_0/h\nu_0$ is the average number of photons in the pulse propagating as a fundamental soliton.

Using $\varepsilon(u) = n(\xi, \tau)$ in Eqs. (8.3.1)–(8.3.4), we can find how the four soliton parameters fluctuate because of amplifier noise. It is useful to define four new noise variables using [8]

$$n_i(\xi) = \mathrm{Re}\int_{-\infty}^{\infty} n(\xi, \tau) F_i(\tau)\, d\tau, \tag{8.3.10}$$

where $i = \eta, \delta, q$, and ϕ. Their correlation functions are calculated using Eqs. (8.3.5)–(8.3.8), and the result is

$$\langle n_i(\xi) n_j(\xi')\rangle = S_i \delta_{ij}\delta(\xi - \xi'). \tag{8.3.11}$$

Assuming $\langle \eta \rangle = 1$, the spectral densities for $i = \eta, \delta, q$, and ϕ are given as [8]

$$S_\eta = S_n, \quad S_\delta = \frac{S_n}{3}, \quad S_q = \frac{\pi^2}{12} S_n, \quad S_\phi = (1 + \pi^2/12)\frac{S_n}{3}. \tag{8.3.12}$$

As a simple example, we calculate the amplitude and frequency fluctuations induced by ASE. Integrating Eqs. (8.3.1) and (8.3.2), we find

$$\eta(\xi) = 1 + \int_0^\xi n_\eta(\xi)\, d\xi, \qquad \delta(\xi) = \int_0^\xi n_\delta(\xi)\, d\xi, \tag{8.3.13}$$

where $\eta(0) = 1$ and $\delta(0) = 0$ are assumed for the fundamental soliton launched at $\xi = 0$. The variance of fluctuations is found to be

$$\sigma_\eta^2 = S_n \xi, \qquad \sigma_\delta^2 = S_n \xi / 3. \tag{8.3.14}$$

This result shows that variances of both amplitude and frequency fluctuations increase linearly along the fiber link because of the cumulative effects of ASE. Amplitude fluctuations degrade the SNR of the soliton bit stream. The SNR degradation, although undesirable, is not the most limiting factor. In fact, frequency fluctuations affect system performance much more drastically by inducing the timing jitter. We turn to this issue next.

8.3.2 Timing Jitter

A soliton communication system can operate reliably only if all solitons arrive at the receiver within their assigned bit slot. Several physical mechanisms induce deviations in the soliton position from its original location at the bit center. Among them, ASE-induced timing jitter is often dominant in practice. The origin of such jitter can be understood by noting from Eq. (8.1.4) that a change in the soliton frequency by δ affects the speed at which a soliton propagates through the fiber. If δ fluctuates because of amplifier noise, soliton transit time through the fiber link also becomes random. ASE-induced fluctuations in the arrival time of a soliton are referred to as the *Gordon–Haus timing jitter* [37]–[40].

Fluctuations in the soliton position are obtained by integrating Eq. (8.3.3) and calculating the variance of $q(\xi)$. Following the procedure outlined previously, the variance is found to be

$$\sigma_q^2 = \frac{1}{9} S_n \xi^3 + \frac{\pi^2}{12} S_n \xi, \tag{8.3.15}$$

where both δ and q were assumed to be zero at $\xi = 0$. The second term shows the direct impact of ASE on the soliton position. The first term is due to jitter induced by frequency fluctuations and dominates in practice because of its cubic dependence on the propagation distance. Keeping only the first term, the timing jitter is approximately given by

$$\sigma_q^2 \approx \frac{S_n}{9}\xi^3 = \frac{F_n F_G}{9N_{\rm ph}\xi_A}\xi^3, \tag{8.3.16}$$

where we used Eqs. (8.3.9) and (8.3.14). Using $\sigma_q = \sigma_t/T_0$, $\xi = L_T/L_D$, $N_{\rm ph} = 2P_0T_0/h\nu_0$, $P_0 = (\gamma L_D)^{-1}$, $F_n = 2n_{\rm sp}$, and $F_G = (G-1)/f_{\rm LM}$, the timing-jitter variance in physical units can be written as [38]

$$\sigma_t^2 = \frac{n_{\rm sp}h\nu_0\gamma|\beta_2|(G-1)L_T^3}{9T_0L_A f_{\rm LM}}. \tag{8.3.17}$$

Since a soliton should arrive within its allocated bit slot for its correct identification at the receiver, timing jitter should be a small fraction of the bit slot T_B. This requirement can be written as $\sigma_t/T_B < f_b$, where f_b is the fraction of the bit slot by which a soliton can move without affecting system performance adversely. Using this condition and introducing the bit rate through $B = 1/T_B = (2q_0T_0)^{-1}$, Eq. (8.3.17) can be written as a design rule:

$$BL_T < \left[\frac{9f_b^2L_A f_{\rm LM}}{h\nu_0F_n(G-1)q_0\gamma|\beta_2|}\right]^{1/3}. \tag{8.3.18}$$

The tolerable value of f_b depends on the acceptable bit-error rate and on details of receiver design; typically, $f_b < 0.1$. To see how amplifier noise limits the total transmission distance, consider a specific soliton communication system operating at 1.55 μm. Using typical parameter values, $q_0 = 5$, $\gamma = 3$ W^{-1}/km, $\beta_2 = -1$ ps^2/km, $F_n = 3$, $L_A = 50$ km, $G = 10$, and $f_b = 0.1$, BL_T must be below 80 (Tb/s)-km. For a 10-Gb/s system, the transmission distance is limited to 8000 km.

In deriving Eq. (8.3.17), solitons were assumed to be sufficiently far apart to avoid their mutual interaction. However, solitons are often packed closely together to maximize the bit rate. Since interaction between two solitons depends strongly on their separation and relative phase, both of which fluctuate due to amplifier noise, it modifies the timing jitter considerably. Considering noise-induced fluctuations of the relative phase of neighboring solitons, timing jitter of interacting solitons is generally enhanced by amplifier noise [40].

However, for a large input phase difference close to π between neighboring solitons, phase randomization leads to reduction in the timing jitter.

An important consequence of soliton interaction is that the statistics of the timing jitter deviate considerably from the Gaussian statistics expected in the absence of soliton interaction [41]–[43]. Such non-Gaussian corrections can occur even when soliton interaction is relatively weak ($q_0 > 5$). They manifest through an enhancement of the bit-error rate and must be accounted for an accurate estimate of the system performance [42]. When solitons are packed so tightly that soliton interaction becomes quite significant, the probability density function of the timing jitter develops a five-peak structure [43]. Equation (8.3.16) cannot be used for evaluating timing jitter in that case. The use of numerical simulations is essential to study the impact of ASE-induced timing jitter on a bit stream composed of interacting solitons.

Propagation of acoustic waves transverse to the fiber core can also induce timing jitter [44]–[48]. Physically speaking, confinement of the optical field within the fiber core creates a field gradient in the radial direction. This gradient of electric field generates acoustic waves through *electrostriction*, a phenomenon that creates density variations in response to variations in the electric field. Since the refractive index of fused silica is related to the material density, such acoustic waves change the refractive index (and hence the soliton velocity). Index changes last for about 2 ns, roughly the time required by the acoustic wave to traverse the fiber core. Since solitons follow one another on a much shorter timescale (0.1 ns for $B = 10$ Gb/s), the acoustic wave generated by one soliton affects tens, or even hundreds, of the following solitons. Such acoustic-wave-assisted interaction among solitons has been observed experimentally [45].

If a bit stream were composed of only 1 bits such that a soliton occupied each bit slot, all solitons would be shifted in time by the same amount by acoustic waves, creating a uniform shift of the soliton train with no impact on the timing jitter. However, since a realistic bit stream consists of a random string of 1 and 0 bits, changes in the speed of a specific soliton depend on the presence or absence of solitons in the preceding tens of bit slots. As a result, different solitons acquire slightly different speeds, resulting in timing jitter. Such *acoustic jitter* has a deterministic origin, in contrast with the Gordon–Haus jitter, which is stochastic in nature. The deterministic nature of acoustic jitter makes it possible to reduce its impact in practice by moving the detection window at the receiver through an automatic tracking circuit [46] or using a

suitable coding scheme [47].

Polarization-mode dispersion (PMD) can also induce timing jitter [49]–[51]. As solitons are periodically amplified, their state of polarization becomes random because of ASE added at every amplifier. Such polarization fluctuations lead to timing jitter through fiber birefringence since the two orthogonally polarized components travel with slightly different speeds. The effects of PMD are quantified through the PMD parameter D_p (see Chapter A.6). The timing jitter introduced by the combination of ASE and PMD can be written as [49]

$$\sigma_{\text{pol}}^2 = \frac{\pi n_{\text{sp}} F_G}{16 N_{\text{ph}}} \frac{D_p^2 L_T^2}{L_A}. \tag{8.3.19}$$

Note that σ_{pol} increases linearly with transmission distance L_T. As an estimate, $\sigma_{\text{pol}} = 0.38$ ps when $\alpha = 0.2$ dB/km, $L_A = 50$ km, $n_{\text{sp}} = 2$, $N_{\text{ph}} = 5 \times 10^5$, $D_p = 0.1$ ps/$\sqrt{\text{km}}$, and $L_T = 10$ Mm. Such a low value of σ_{pol} is unlikely to affect 10-Gb/s soliton systems with a 100-ps bit slot. However, the PMD-induced timing jitter becomes important at high bit rates, especially for fibers with large values of the PMD parameter ($D_p > 1$ ps/$\sqrt{\text{km}}$).

8.3.3 Control of Timing Jitter

It should be clear from the preceding discussion that the timing jitter ultimately limits the performance of soliton communication systems. It is essential to find a solution to the timing-jitter problem before the use of solitons can become practical. Several techniques were developed during the 1990s for controlling the timing jitter [52]–[80]. This section focuses on them with emphasis on optical filtering and modulation.

Optical Filters and Modulators

Optical filters have been used since 1991 to realize soliton transmission beyond the Gordon–Haus limit [52]–[60]. This approach makes use of the fact that the ASE spectrum is much broader than the soliton spectrum. The bandwidth of optical filters is chosen such that they let the soliton pass but block most of the ASE. Some soliton energy is lost during the filtering process. The gain of each amplifier is increased slightly to offset filter-induced losses. Unfortunately, noise within the soliton bandwidth increases rapidly because of the excess gain of amplifiers.

The filtering technique can be improved considerably by allowing the center frequency of successive filters to slide (increase or decrease) along the fiber link at a constant rate [55]. Such sliding-frequency filters avoid accumulation of ASE since soliton spectrum can shift with filters while the ASE spectrum does not. As a result, filters near the end of the fiber link block the ASE accumulated over earlier stages. Sliding-frequency filters also reduce the growth of dispersive waves that are generated by strongly perturbed solitons [57].

Solitons can also be controlled in the time domain by using amplitude modulators. The technique works by introducing additional losses for solitons that have shifted from their original position (center of the bit slot). The modulator forces solitons to move toward its transmission peak where the loss is minimum.

Soliton perturbation theory can be used to study how optical filters and modulators benefit a soliton communication system. The effect of a bandpass filter is to modify the soliton spectrum such that

$$\tilde{u}(\xi_f, \omega) \rightarrow H_f(\omega - \omega_f)\tilde{u}(\xi_f, \omega), \tag{8.3.20}$$

where $\tilde{u}(\xi_f, \omega)$ is the soliton spectral amplitude obtained by taking the Fourier transform of Eq. (8.1.4) and $H_f(\omega - \omega_f)$ is the transfer function of the optical filter located at $\xi_f = L_f/L_D$. In contrast, an amplitude modulator changes the soliton amplitude in the time domain as

$$u(\xi_m, \tau) \rightarrow T_m(\tau - \tau_m)u_s(\xi_m, \tau), \tag{8.3.21}$$

where $T_m(\tau)$ is the transmission coefficient of the modulator located at $\xi = \xi_m$. Both $H_f(\omega - \omega_f)$ and $T_m(\tau - \tau_m)$ can be approximated by a parabolic shape in the vicinity of a soliton.

If losses introduced by filters and modulators are assumed to be distributed over the entire link, their effects can be included by adding two loss terms to Eq. (8.3.7). A third term representing excess amplifier gain should also be added to offset the additional losses. The resulting perturbed NLS equation can be written as [8]

$$i\frac{\partial u}{\partial \xi} + \frac{1}{2}\frac{\partial^2 u}{\partial \tau^2} + |u|^2 u = i\varepsilon(u), \tag{8.3.22}$$

where the perturbation term is of the form

$$\varepsilon(u) = n(\xi, \tau) + \frac{\mu}{2}u - \frac{b_f}{2}\left(i\frac{\partial}{\partial \tau} - f_s\xi\right)^2 u - \frac{b_m}{2}\tau^2 u. \tag{8.3.23}$$

Here, μ is the excess gain required for compensating losses introduced by filters and modulators. The parameter b_f is related to the curvature of the filter spectrum $H_f(\omega)$. For Fabry–Perot filters spaced apart by L_f, b_f is given by

$$b_f = \frac{F_R^2}{\pi|\beta_2|L_f\Delta\nu_f^2}, \tag{8.3.24}$$

where $\Delta\nu_f$ is the free spectral range and F_R is the finesse of the filter. The normalized sliding rate is related to the actual rate ν_s as $f_s = 2\pi\nu_s T_0 L_D$. For modulators spaced apart by a distance L_m, the parameter b_m can be written as

$$b_m = a_m(\Omega_m T_0)^2(L_D/2L_m), \tag{8.3.25}$$

where a_m is the modulation index and Ω_m is the modulation frequency.

The use of $\varepsilon(u)$ from Eq. (8.3.23) in Eqs. (8.3.1)–(8.3.4) shows how the four soliton parameters evolve in the presence of optical filters and modulators. Ignoring the phase, we see that the amplitude η, the frequency δ, and the position q of each soliton evolve as [8]

$$\frac{d\eta}{d\xi} = \mu\eta - b_f[(\delta - f_s\xi)^2 + \eta^2/3]\eta - b_m[q^2 + \pi^2/(12\eta^2)]\eta + n_\eta(\xi), \tag{8.3.26}$$

$$\frac{d\delta}{d\xi} = -\frac{2}{3}b_f(\delta - f_s\xi)\eta^2 + n_\delta(\xi), \tag{8.3.27}$$

$$\frac{dq}{d\xi} = -\delta - (\pi^2 b_m/6\eta^2)q + n_q(\xi). \tag{8.3.28}$$

Consider first the case of fixed-frequency filters by setting $f_s = 0$. If we ignore ASE, assume $\eta = 1$, $\delta = 0$, and $q = 0$ initially at $\xi = 0$, the above equations show that all three soliton parameters can be maintained at their original values provided the excess gain is chosen according to

$$\mu = b_f/3 + \pi^2 b_m/12. \tag{8.3.29}$$

The effects of ASE can be included by considering fluctuations around this steady-state solution. Linearizing Eqs. (8.3.26)–(8.3.28) around $\eta = 1$, $\delta = 0$, and $q = 0$, we obtain

$$\frac{d\eta'}{d\xi} = -(c_f - c_m)\eta' + n_\eta(\xi), \tag{8.3.30}$$

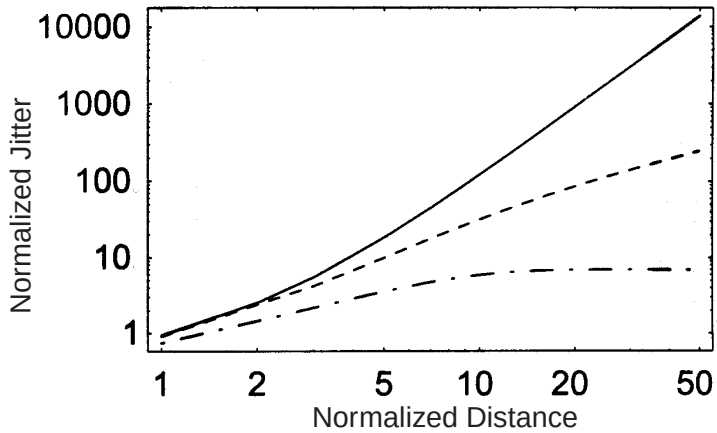

Figure 8.10 σ_q^2/S_n as a function of ξ without any control (solid line), with filters alone (dashed line, $b_f = 0.4$), and with filters and modulators (dot-dashed line, $b_m = 0.1$). (After Ref. [8], ©1998, reprinted by permission of John Wiley & Sons)

$$\frac{d\delta}{d\xi} = -c_f\delta + n_\delta(\xi), \tag{8.3.31}$$

$$\frac{dq}{d\xi} = -\delta - c_m q + n_q(\xi), \tag{8.3.32}$$

where $\eta' = \eta - 1$ and two new parameters were introduced as

$$c_f = 2b_f/3, \qquad c_m = \pi^2 b_m/6. \tag{8.3.33}$$

Equation (8.3.30) points to an important issue related to the use of modulators. If filers are not employed ($c_f = 0$), amplitude fluctuations grow exponentially, indicating that the steady state is unstable. In contrast, filters by themselves have a stabilizing effect. When both filters and modulators are used, the filtering action should be strong enough to ensure $c_f > c_m$ to avoid the instability.

Timing jitter is obtained by integrating Eq. (8.3.32) and then calculating the variance of $q(\xi)$. After some algebra, the result is found to be [8]

$$\sigma_q^2(\xi) = \frac{S_n}{3}\left\{\frac{1}{4c_f c_m(c_f+c_m)} - \frac{\exp(-2c_f\xi)}{4c_f(c_f-c_m)^2} - \frac{\exp(-2c_m\xi)}{4c_m(c_f-c_m)^2} + \frac{\exp[-(c_f+c_m)\xi]}{(c_f-c_m)^2(c_f+c_m)}\right\} + \frac{\pi^2 S_n}{12}\left[\frac{1-\exp(-2c_m\xi)}{2c_m}\right], \tag{8.3.34}$$

where S_n is given by Eq. (8.3.9). This result reduces to Eq. (8.3.15) in the limit $c_f = c_m = 0$. Figure 8.10 shows how much jitter is reduced using filters and modulators. When only filters or modulators are used, σ_q^2 grows linearly with distance, resulting in considerable improvement compared with the cubic growth occurring in their absence. When both of them are used simultaneously, the situation is even better since timing jitter becomes constant for $\xi \gg 1$. The limiting value is found from Eq. (8.3.34) to be

$$\sigma_q^2 = \frac{S_n}{12c_m}\left[\frac{1}{c_f(c_f+c_m)} + \frac{\pi^2}{2}\right]. \tag{8.3.35}$$

As seen in Fig. 8.10, the combination of filters or modulators can reduce timing jitter by several orders of magnitude for long-haul lightwave systems.

A phase modulator can also be used to control the timing jitter [70]–[72]. One can understand the effect of periodic phase modulation by recalling that a frequency shift [$\delta\omega = -\partial\phi(t)/\partial t$] is associated with any phase variation $\phi(t)$. Since a shift in soliton frequency changes the group velocity, phase modulation induces a temporal displacement. The frequency is shifted in such a way that the soliton always moves toward the center of the bit slot, thereby confining it to its original position despite timing jitter induced by ASE and other sources. Amplitude and phase modulations can be combined to further improve the system performance [72]. Optical filters and modulators help a soliton system in several other ways. Among other things, they reduce soliton interaction, clamp the level of amplifier noise, and inhibit the growth of dispersive waves [73].

Sliding-Frequency Filters

Both fixed-frequency filters and amplitude modulators reduce the SNR at the receiver. The SNR degradation arises from the μ term in Eq. (8.3.23). In time slots containing 0 bits, the field u is small enough that we can neglect the nonlinear term. The resulting linear equation can be solved to find that the noise in 0 bits grows exponentially because of the excess gain required to offset losses. Sliding-frequency filters solve this problem. To show their impact clearly, we solve Eqs. (8.3.26)–(8.3.28) with $f_s \neq 0$ but set $b_m = 0$ (no modulators) to simplify the discussion. A steady-state (ξ-independent) solution no longer exists since both the frequency and position of a soliton evolve with ξ as

$$\delta_s(\xi) = f_s\xi - 3f_s/2b_f, \qquad q_s(\xi) = -\tfrac{1}{2}f_s\xi^2 + (3f_s/2b_f)\xi. \tag{8.3.36}$$

However, the soliton amplitude can be maintained at $\eta = 1$ if the excess gain is chosen according to

$$\mu = b_f/3 + 9f_s^2/(4b_f). \tag{8.3.37}$$

Equation (8.3.36) shows that soliton frequency slides with filters. The soliton position also changes since the speed of a soliton changes with its frequency. This position shift is deterministic in nature, affects all solitons in the same way, and is not harmful to a soliton system since it keeps the pulse train intact. At the same time, the sliding-frequency filters reduce the ASE for the following reason. Initially, the noise accumulates over multiple amplifiers since the signal and noise spectra overlap. However, as the soliton spectrum shifts gradually, the accumulated ASE is filtered out later when the soliton spectrum has shifted by more than its own width.

ASE-induced fluctuations in the soliton parameters can be calculated by linearizing Eqs. (8.3.26)–(8.3.28) around the solution (8.3.36). Introducing small fluctuations as

$$\eta' = \eta - 1, \quad \delta' = \delta - \delta_s, \quad q' = q - q_s, \tag{8.3.38}$$

we obtain the following set of equations:

$$\frac{d\eta'}{d\xi} = -\frac{2}{3}b_f\eta' + 3f_s\delta' + n_\eta(\xi), \tag{8.3.39}$$

$$\frac{d\delta'}{d\xi} = -\frac{2}{3}b_f\delta' + 2f_s\eta' + n_\delta(\xi), \tag{8.3.40}$$

$$\frac{dq'}{d\xi} = -\delta' + n_q(\xi). \tag{8.3.41}$$

The stability of solitons can be analyzed by ignoring ASE and investigating whether fluctuations η' and δ' grow or damp with propagation. The solution of Eqs. (8.3.39) and (8.3.40) shows that fluctuations damp as $e^{-\lambda\xi}$ with $\lambda = 2b_f/3 \pm \sqrt{6}\,f_s$. Solitons remain stable as long as the sliding rate f_s is below a critical value given by

$$f_{\rm cr} = \sqrt{2/27}\,b_f \approx 0.272b_f. \tag{8.3.42}$$

For $f_s < f_{\rm cr}$, timing jitter only grows linearly with ξ for $\xi \gg 1$ and is approximately given by [8]

$$\sigma_q^2 = \frac{(1+2f_{\rm cr}^2)}{(1-f_{\rm cr}^2)^2}\frac{3S_n}{4b_f^2}\xi. \tag{8.3.43}$$

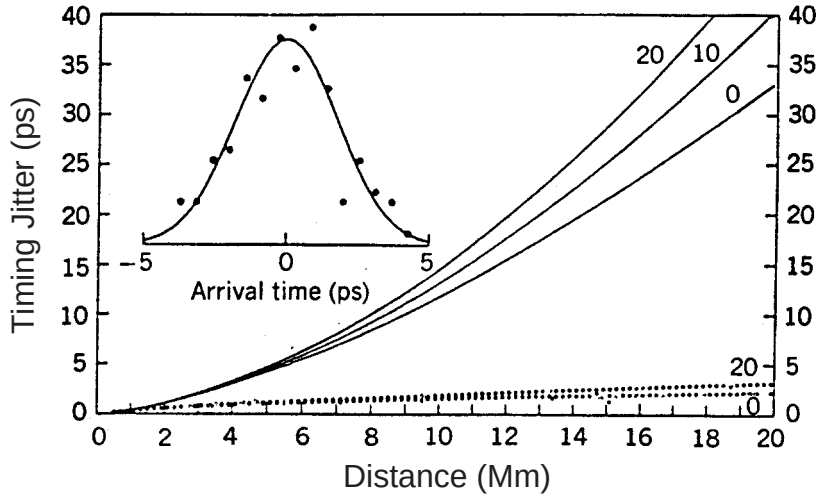

Figure 8.11 Timing jitter with (dotted lines) and without (solid lines) sliding-frequency filters as a function of distance at several bit rates. Inset shows a Gaussian fit to the jitter at 10 Mm for a 10-Gb/s system. (After Ref. [55])

For fixed-frequency filters, $f_{cr} = 0$ in the above equation. Thus, the timing jitter is enhanced because of frequency sliding but is still much lower compared with the no-filter case.

Figure 8.11 shows the reduction observed in timing jitter by using sliding-frequency filters for soliton systems at several bit rates. The bit-rate dependence is solely due to the acoustic jitter; the $B = 0$ curves show the contribution of the Gordon–Haus jitter alone. Optical filters help in reducing both types of timing jitter and permit transmission of 10-Gb/s solitons over more than 20,000 km. In the absence of filters, the timing jitter becomes so large that a 10-Gb/s soliton system cannot be operated for distances beyond 8000 km. The inset in Fig. 8.11 shows a Gaussian fit to the timing jitter of 10-Gb/s solitons at a distance of 10,000 km, obtained by solving the NLS equation numerically after including the effects of both the ASE and sliding-frequency filters [55]. The timing-jitter distribution is approximately Gaussian with a standard deviation of about 1.76 ps. In the absence of filters, the jitter exceeds 10 ps under the same conditions.

Sliding-frequency filters benefit a soliton communication system in several ways. Their use reduces not only timing jitter but also soliton interaction [64], making it possible to pack solitons more closely. The physical mechanism be-

hind reduced interaction is related to changes in the soliton phase at each filter. Rapid variations in the relative phase between neighboring solitons, occurring as a result of filtering, average out the jitter by alternating the nature of interaction from attractive to repulsive. Soliton interaction is reduced even more effectively if filter frequency is alternately shifted up and down in a zigzag pattern [65]. Equations (8.3.39)–(8.3.41) predict the same behavior irrespective of whether the center frequency of filters increases (up-sliding) or decreases (down-sliding) along the fiber link. However, this is a consequence of approximating the transfer function of filters with a parabola over the soliton spectrum. When the cubic term in the Taylor expansion of the transfer function is included, up-sliding is found to provide better performance [58].

Sliding-frequency filters may be difficult to implement in practice because of the need to maintain a precise frequency control. Several schemes have been proposed to solve this practical problem [61]–[69]. For example, an optical filter can be designed such that it automatically offsets its peak-transmission frequency from the carrier frequency of the incident soliton [61]. In another approach, significant reduction of the timing jitter was realized by periodically sliding the signal frequency while using fixed-frequency filters [62]. The spectral response of optical filters can also be tailored to improve system performance. In particular, optical filters having a relatively flat transmission passband (top-hat-like) are of interest since they minimize energy loss. Butterworth filters have attracted attention since they can reduce the accumulation of ASE without requiring sliding of their central frequency along the fiber link [68]. They can also be more effective in reducing the soliton interaction [69]. Butterworth filters were used in a 1994 experiment and allowed transmission of 20-Gb/s signals (single channel) over 11 Mm [66].

Other Techniques

Numerous ways through which solitons interact with each other and with other optical fields lead to many diverse techniques for controlling solitons. In one approach that is helpful in reducing soliton interaction, the amplitude of neighboring solitons is alternated between two values differing typically by 10%. Such a difference in amplitudes results in different rates of phase accumulation for two types of solitons. As a result, the phase difference θ between neighboring solitons changes with propagation, resulting in an averaging of soliton interaction. Recall from Section 8.1.3 that the interaction between two

neighboring solitons depends on their relative phase difference and changes from attractive to repulsive with changes in θ. Such a technique has been used successfully for transmitting solitons at a bit rate of 20 Gb/s over 11,500 km, a distance larger than the distance over which two solitons would collide in the absence of amplitude alternation [74]. In a variation of this technique, soliton frequency is altered to reduce interaction among two neighboring solitons [67]. Relatively small frequency shifts ($\sim$ 100 MHz), imposed on specific solitons in a bit stream, can double the transmission distance because of reduced soliton interaction.

Another approach to soliton control consists of inserting fast-responding saturable absorbers periodically along the fiber link. Such a device absorbs low-intensity light, such as dispersive waves, but leaves solitons intact because of their high intensities. To be effective, it should respond on a timescale shorter than the soliton width. It is difficult to find an absorber that can respond at such short timescales. However, one can use nonlinear interferometric devices that act like fast saturable absorbers (see Section 5.4). For example, a nonlinear fiber-loop mirror can reduce the timing jitter at 10,000 km [75]–[77]. The same device can also stabilize the soliton amplitude.

A soliton train can also be retimed by using the phenomenon of cross-phase modulation (XPM) in optical fibers [78]. The technique overlaps the soliton data stream with another pulse train composed of only 1 bits (generated through clock recovery, for example) in a few-kilometer fiber where XPM induces a phase shift on the soliton data stream whose magnitude can be controlled. Such a phase modulation of the soliton translates into a net frequency shift only when a soliton does not lie in the middle of its bit slot. Similar to the case of synchronous phase modulation, the direction of the frequency shift is such that the soliton is confined to the center of the bit slot.

Other nonlinear effects occurring in optical fibers can also be exploited for controlling the soliton parameters. In one study, stimulated Raman scattering was proposed for this purpose [79]. If a pump beam, modulated at the signal bit rate and up-shifted in frequency by the Raman shift (about 13 THz), is copropagated with the soliton bit stream, it simultaneously provides gain (through Raman amplification) and phase modulation (through XPM) to each soliton. Such a technique results in both phase and intensity modulations of the soliton stream and can reduce the timing jitter. Another approach makes use of four-wave mixing (FWM) for soliton reshaping and for controlling the soliton parameters [80].

8.3.4 Experimental Results

The 1988 experiment that first demonstrated the possibility of soliton transmission over long distances used a recirculating fiber loop whose loss was compensated through distributed Raman amplification [3]. The main drawback from a practical standpoint was that the experiment used two color-center lasers for generation and amplification of solitons. Diode-pumped, erbium-doped fiber amplifiers (EDFAs) became available in 1989 and were used for loss-managed solitons as lumped amplifiers almost immediately. Several 1990 experiments demonstrated soliton transmission over fiber lengths of about 100 km at bit rates of up to 5 Gb/s [81]–[83]. Input pulses in these experiments were generated using gain-switched or mode-locked semiconductor lasers. A $LiNbO_3$ modulator was used to block pulses in time slots of 0 bits. The resulting coded soliton bit stream was transmitted through several fiber sections. The amplifier spacing was chosen to satisfy the criterion $L_A \ll L_D$ and was typically in the 25- to 40-km range. In a 1991 experiment, solitons were transmitted over 1000 km at 10 Gb/s [84]. The use of 45-ps-wide solitons permitted an amplifier spacing of 50 km in this experiment.

Since 1991, most soliton transmission experiments have used a recirculating fiber loop, similar to that shown in Fig. 7.15. In one experiment, 2.5-Gb/s solitons were transmitted over 12 Mm using a 75-km fiber loop containing three EDFAs, spaced apart by 25 km [85]. In this experiment, the bit rate–distance product, $BL = 30$ (Tb/s)-km, was limited mainly by the timing jitter. In a later experiment, the 2.5-Gb/s signal could be transmitted over 14 Mm when fixed-frequency filters were placed inside the fiber loop [52]. Soon afterward, the use of sliding-frequency filters resulted in the transmission of a 5-Gb/s signal over 15 Mm [86]. Moreover, when the bit rate was doubled using the WDM technique, the resulting 10-Gb/s signal could still be transmitted over 11 Mm. In a 1993 experiment, timing-jitter reduction provided by sliding-frequency filters permitted soliton transmission over 20 Mm at 10 Gb/s and over 13 Mm at 20 Gb/s in a two-channel experiment [87]. Further improvements resulted in transmission of solitons over 35 Mm at 10 Gb/s and over 24 Mm at 15 Gb/s [88].

Several experiments used modulators for controlling timing jitter. In a 1991 experiment, solitons at 10 Gb/s could be maintained over long distances when a $LiNbO_3$ modulator was used within the 510-km loop incorporating EDFAs with 50-km spacing [89]. An experiment in 1993 indicated the possibility of ultralong transmission distances ($> 10^6$ km) by combining filters and

modulators [90]. Modulators also allow the use of a relatively large amplifier spacing [91]. This property of modulators has been exploited to transmit a 20-Gb/s soliton train over 150 Mm with an amplifier spacing of 105 km [92]. In another experiment, a single synchronous modulator, inserted just after the transmitter, allowed transmission of a 20-Gb/s signal over 3000 km [93], well beyond the Gordon–Haus limit of 2300 km. In this experiment, the clock signal for modulator was the same as that used for the transmitter. In contrast, when modulators are used along the transmission line, the clock signal must be regenerated locally.

The use of soliton systems in the 1.3-μm wavelength region using semiconductor optical amplifiers is attractive for transmission distances ~ 1000 km [94]–[96]. The motivation for such systems stems from the need to update the existing terrestrial fiber links to bit rates 10 Gb/s and beyond. Standard telecommunication fibers used in such preinstalled links have relatively high dispersion in the 1.55-μm region ($\beta_2 \approx -21$ ps^2/km), resulting in $L_D \sim 10$ km for 10-Gb/s soliton systems. Since the practical amplifier spacing exceeds 30 km, it is not possible to satisfy the condition $L_A \ll L_D$ in the 1.55-μm wavelength regime. However, if the operating wavelength is chosen near 1.3 μm, L_D exceeds 200 km and the condition $L_A \ll L_D$ is easily satisfied. Alternatively, one can use the technique of dispersion management, discussed next, to lower the average GVD in the 1.55-μm region.

8.4 Dispersion-Managed Solitons

In the loss-managed soliton systems discussed so far, the GVD of the fiber is assumed to remain constant along the entire fiber link. However, this need not be the case. It turns out that soliton systems benefit considerably if the GVD parameter β_2 varies along the link length. This section is devoted to such dispersion-managed solitons. We first consider dispersion-decreasing fibers and then focus on dispersion maps that consist of multiple sections of constant-dispersion fibers whose length and GVD are judiciously chosen.

8.4.1 Dispersion-Decreasing Fibers

An interesting scheme proposed in 1987 relaxes completely the restriction $L_A \ll L_D$, normally imposed on loss-managed solitons, by decreasing the GVD along the fiber length [97]. Such fibers are called dispersion-decreasing fibers

(DDFs) because their GVD must decrease such that it accounts for the reduced SPM experienced by solitons weakened from fiber losses.

Optimum Dispersion Profile

Since dispersion management is used in combination with loss management, soliton evolution in a DDF is governed by Eq. (8.2.4) except that the second-derivative term has a new parameter d that is a function of ξ because of GVD variations along the fiber length. The modified NLS equation takes the form

$$i\frac{\partial v}{\partial \xi} + \frac{1}{2}d(\xi)\frac{\partial^2 v}{\partial \tau^2} + p(\xi)|v|^2 v = 0, \tag{8.4.1}$$

where $v = u/\sqrt{p}$, $d(\xi) = \beta_2(\xi)/\beta_2(0)$, and $p(\xi)$ takes into account peak-power variations introduced by loss management. The distance ξ is normalized to the dispersion length, $L_D = T_0^2/|\beta_2(0)|$, defined using the GVD value at the fiber input.

Because of the ξ dependence of the second and third terms, Eq. (8.4.1) is not a standard NLS equation. However, it can be reduced to one if we introduce a new propagation variable as

$$\xi' = \int_0^{\xi} d(\xi)\, d\xi. \tag{8.4.2}$$

This transformation renormalizes the distance scale to the local value of GVD. In terms of ξ', Eq. (8.4.1) becomes

$$i\frac{\partial v}{\partial \xi'} + \frac{1}{2}\frac{\partial^2 v}{\partial \tau^2} + \frac{p(\xi)}{d(\xi)}|v|^2 v = 0. \tag{8.4.3}$$

If the GVD profile is chosen such that $d(\xi) = p(\xi) \equiv \exp(-\Gamma\xi)$, this equation becomes the standard NLS equation, and fiber losses have no effect on a soliton in spite of its reduced energy. As a result, lumped amplifiers can be placed at any distance and are not limited by the condition $L_A \ll L_D$.

The above analysis shows that fundamental solitons can be maintained in a lossy fiber provided its GVD decreases exponentially as

$$|\beta_2(z)| = |\beta_2(0)|\exp(-\alpha z). \tag{8.4.4}$$

This result can be understood qualitatively by noting that the soliton peak power P_0 decreases exponentially in a lossy fiber in exactly the same fashion. Since the soliton order N is defined as $N = \gamma P_0 T_0^2/|\beta_2|$, the requirement

$N = 1$ can be maintained, in spite of power losses, provided GVD decreases exponentially as well. For such a dispersion profile, a fundamental soliton keeps its shape and width constant even in a lossy fiber.

Fibers with a nearly exponential GVD profile have been fabricated [98]. A practical technique for making such DDFs consists of reducing the core diameter along the fiber length in a controlled manner during the fiber-drawing process. Variations in the fiber diameter change the waveguide contribution to β_2 and reduce its magnitude. Typically, GVD can be varied by a factor of 10 over a length of 20 to 40 km. The accuracy realized by the use of this technique is estimated to be better than 0.1 ps^2/km [99]. Propagation of solitons in DDFs has been demonstrated in several experiments [99]–[101]. In a 40-km DDF, solitons preserved their width and shape in spite of energy losses of more than 8 dB [100]. In a recirculating loop made using DDFs, a 6.5-ps soliton train at 10 Gb/s was transmitted over 300 km [101].

For long-haul links, DDFs can be cascaded periodically such that an amplifier placed at the end of each DDF restores the soliton energy to its value at the beginning of the DDF. Such a link can be used at high bit rates since the amplifier spacing L_A is not restricted to be smaller than L_D. However, the soliton width at high bit rates ($B > 10$ Gb/s) decreases as $T_0 = (2q_0B)^{-1}$, and T_0 becomes smaller than 5 ps when B exceeds 20 Gb/s. Propagation of ultrashort solitons through DDFs requires consideration of TOD and the Raman-induced frequency shift. Using Eq. (8.2.15) with $g = 0$ and Eq. (8.4.2), we obtain

$$i\frac{\partial v}{\partial \xi'} + \frac{1}{2}\frac{\partial^2 v}{\partial \tau^2} + |v|^2 v = i\frac{\delta_3}{d}\frac{\partial^3 v}{\partial \tau^3} + \frac{\tau_R}{d} v \frac{\partial |v|^2}{\partial \tau}, \tag{8.4.5}$$

where $\delta_3 = \beta_3/(6|\beta_2(0)|T_0)$ is the TOD parameter and $\tau_R = T_R/T_0$ governs the effects of intrapulse Raman scattering ($T_R \approx 5$ fs).

Fibers with continuously varying GVD are not readily available. As an alternative, the exponential GVD profile of a DDF can be approximated with a staircase profile by splicing together several constant-dispersion fibers with different β_2 values. This approach was studied during the 1990s, and it was found that most of the benefits of DDFs can be realized using as few as four fiber segments [102]–[106]. How should one select the length and the GVD of each fiber used for emulating a DDF? The answer is not obvious, and several methods have been proposed. In one approach, power deviations are minimized in each section [102]. In another approach, fibers of different GVD values D_m and different lengths L_m are chosen such that the product $D_m L_m$

is the same for each section. In a third approach, D_m and L_m are selected to minimize shading of dispersive waves [103].

Timing Jitter

An important question is how the last two terms in Eq. (8.4.5) affect the timing jitter of solitons [107]–[109]. Since the left side of this equation corresponds to the standard NLS equation, we can apply soliton perturbation theory. Using Eq. (8.3.1)–(8.3.4) with $i\varepsilon(u)$ given by the last two terms of Eq. (8.4.3), the timing jitter is found to be approximately given by [108]

$$\sigma_{\mathrm{DDF}}^2 = \left(\frac{4}{5}N_A^5\tau_R^2 d_R^2 + 2N_A^4\tau_R\delta_3 d_R\xi_A + \frac{4}{3}N_A^3\delta_3^2\xi_A^2\right)\xi_A S_\eta + \frac{1}{3}N_A^3 d_{GH}^2\xi_A S_\delta + N_A\xi_A S_q, \tag{8.4.6}$$

where S_η, S_δ, and S_q are given in Eq. (8.3.12) and $N_A = L_T/L_A$ represents the number of amplifiers. The parameters d_{GH} and d_R depend on the amplifier spacing and are defined as

$$d_{GH} = [1-\exp(-\Gamma\xi_A)]/\Gamma, \tag{8.4.7}$$

$$d_R = \frac{8}{15\Gamma^2}\left[\frac{1}{2} - \exp(-\Gamma\xi_A) + \exp(-2\Gamma\xi_A)\right]. \tag{8.4.8}$$

In Eq. (8.4.6) the term with S_δ represents the Gordon–Haus jitter and is a generalization of Eq. (8.3.16) for DDFs. The last term comes from the direct effect of ASE on soliton position and is negligible in practice. The three terms in parentheses have their origin in amplitude fluctuations. Both TOD and intrapulse Raman scattering convert amplitude fluctuations into timing jitter. The origin of Raman-induced timing jitter can be understood as follows. Fluctuations in the soliton amplitude produced by amplifier noise result in width fluctuations since the two are inversely related for a soliton. Width fluctuations are converted to frequency fluctuations by intrapulse Raman scattering, which are in turn translated into position fluctuations by GVD. The Raman term proportional to N_A^5 in Eq. (8.4.6) generally dominates for solitons shorter than 5 ps. The TOD contribution to timing jitter becomes important if the minimum dispersion of DDFs falls below 0.1 ps/(km-nm).

Figure 8.12 shows individual contributions of amplitude, frequency, and position fluctuations, together with the total timing jitter, as a function of transmission distance for soliton widths in the range of 1 to 40 ps by choosing

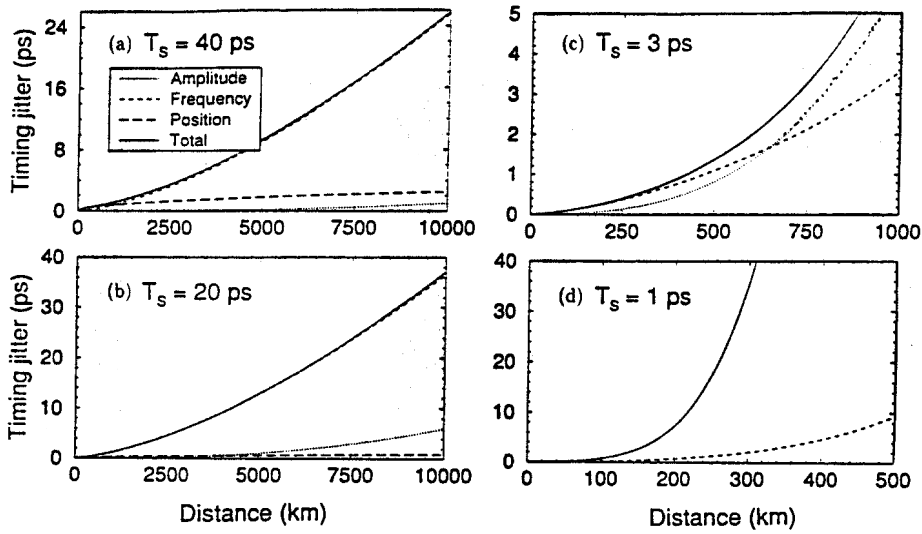

Figure 8.12 Relative contributions of frequency, amplitude, and position fluctuations to the timing jitter in dispersion-decreasing fibers for several soliton widths. Total timing jitter is shown by a solid line. (After Ref. [108])

$\beta_2^{\min} = -0.1$ ps^2/km and $L_A = 80$ km. For $T_s > 10$ ps, timing jitter originates mostly from frequency fluctuations (the Gordon–Haus jitter) since the contributions of Raman and TOD effects are small for such relatively broad solitons. When shorter solitons are used, the contribution of higher-order effects, especially the Raman effect, increases rapidly with transmission distance. For 3-ps or shorter solitons, the contribution of amplitude fluctuations to the timing jitter (mediated through the Raman effect) becomes so important that the total transmission distance is limited to only a few hundred kilometers in the absence of a soliton-control mechanism. For a transoceanic distance of 10,000 km, amplitude fluctuations dominate for soliton widths below 7 ps. For 1-ps solitons, amplitude fluctuations totally dominate the timing jitter at all distances.

The increase in timing jitter brought by the Raman and TOD effects, and a shorter bit slot at higher bit rates (10 ps at $B = 100$ Gb/s), make the control of timing jitter essential before such systems can become practical. Both optical filters and modulators should help in reducing the timing jitter even when DDFs are used. The phase-conjugation technique is also quite useful for soliton systems [110]. Its use requires either parametric amplifiers in place of EDFAs or the insertion of a nonlinear optical device before each amplifier that

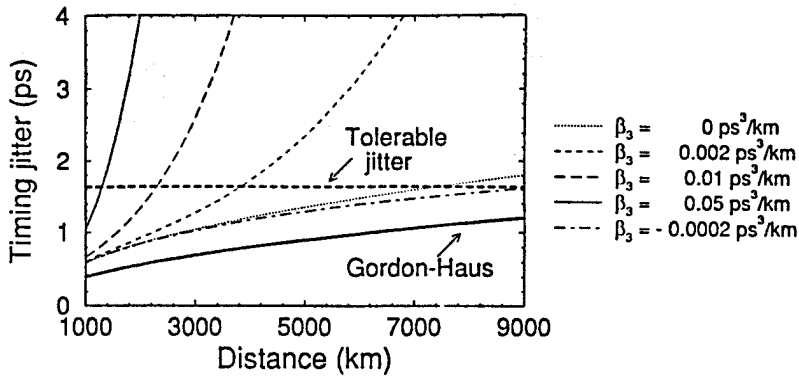

Figure 8.13 Effect of third-order dispersion on timing jitter in a DDF-based soliton communication system making use of phase conjugation. Thick solid curve shows the contribution of Gordon–Haus jitter. (After Ref. [7], ©1997, reprinted by permission of John Wiley & Sons)

changes the soliton amplitude from u to u^* while preserving all other features of the bit stream. Such a change is equivalent to inverting the soliton spectrum. FWM inside an optical fiber, fabricated with suitable dispersion characteristics, can be used for spectral inversion.

Timing jitter changes considerably when parametric amplifiers are used. Following the procedure outlined above, it is found to be [109]

$$\sigma^2_{\rm OPC} = (8N_A\tau_R^2 d_R^2 + 4N_A^2\tau_R d_R\delta_3\xi_A + \tfrac{4}{3}N_A^3\delta_3^2\xi_A^2)\xi_A S_\eta + \tfrac{1}{2}N_A d_{GH}^2\xi_A S_\delta + N_A\xi_A S_q. \tag{8.4.9}$$

This equation should be compared with Eq. (8.4.6). The Raman-induced jitter increases only linearly with N_A (compared with N_A^5 dependence) and is much smaller when phase conjugation is used. Physically, the reason for jitter reduction is related to spectral inversion, which nearly cancels the effects of the Raman-induced spectral shift over each pair of amplifiers.

Phase conjugation does not compensate for the timing jitter induced by TOD. The effects of TOD are shown in Fig. 8.13 for 2-ps solitons. The dashed horizontal line represents the tolerable value of timing jitter. For comparison, the Gordon–Haus timing jitter alone is shown by the thick solid line. Other curves correspond to different values of the TOD parameter. For $\beta_3 = 0.05$ ps^3/km—a typical value for dispersion-shifted fibers—transmission distance is limited by TOD to below 1500 km. Considerable improvement occurs when

β_3 is reduced. Transmission over 7500 km is possible for $\beta_3 = 0$ (dotted line). The distance can be increased further for slightly negative values of β_3 (dot-dashed line). Such values of β_3 are possible in fibers known as reverse-dispersion (or negative-slope) fibers.

Collision-induced timing jitter can also be reduced considerably in DDF-based soliton systems [111]. Even when the exponential GVD profile of a DDF is approximated by several constant-GVD fibers, the system performance improves as the number of fiber sections is increased. This feature is quite useful for WDM soliton systems.

8.4.2 Periodic Dispersion Maps

A disadvantage of the DDF is that the average dispersion along the link is often relatively large. Generally speaking, operation of a soliton system at a wavelength where the average GVD is low should improve system performance since it reduces the timing jitter as well as the Raman-induced spectral shift. However, for constant-GVD fiber links, as the operating wavelength approaches the zero-dispersion wavelength, several factors affect the system performance considerably [112]. For example, the TOD can induce severe pulse distortion through shading of dispersive waves when $|\beta_2| < 0.1$ ps^2/km. Moreover, as discussed in Section 7.6, FWM leads to considerable crosstalk when GVD is low. Dispersion maps consisting of alternating-GVD fibers provide a solution to these problems since their use lowers the average GVD of the entire link while keeping the GVD of each section large enough that the FWM and TOD effects remain negligible.

The use of dispersion management forces each soliton to propagate in the normal-dispersion regime of a fiber during each map period. At first sight, such a scheme should not even work, since normal-GVD fibers do not support bright solitons and lead to considerable broadening and chirping of the pulse. So, why should solitons survive in a dispersion-managed fiber link? A considerable theoretical effort devoted to this issue since 1996 has yielded an answer with a few surprises [113]–[173]. Physically speaking, if the map period is a fraction of the nonlinear length, the nonlinear effects are relatively small and the pulse evolves in a linear fashion over one map period. On a longer length scale, solitons can still form if the SPM effects are balanced by the average dispersion. As a result, solitons can survive in an average sense, even though not only the peak power but also the width and shape of such solitons oscil-

late periodically. This section describes the properties of dispersion-managed (DM) solitons and the advantages offered by them.

Soliton Characteristics

We focus on a simple dispersion map consisting of two fibers with positive and negative values of the GVD parameter β_2. Soliton evolution is governed by same equation (8.4.1) used earlier for DDFs. However, we need to scale ξ and τ differently since the pulse width and GVD both vary with ξ. One possibility is to use the minimum width $T_{\min}$ of the soliton occurring in the anomalous-GVD section for scaling so that

$$\tau = T/T_{\min}, \qquad \xi = z/L_D = z|\beta_{2a}|/T_{\min}^2, \tag{8.4.10}$$

where β_{2a} is the value of β_2 in the anomalous-GVD section of length l_a. With this normalization, $d = 1$ in that section but has a negative value ($d = \beta_{2n}/\beta_{2a}$) in the normal-GVD section of length l_n. The section lengths l_a and l_n are arbitrary. The map period $L_{\text{map}} = l_a + l_n$ can also be different than the amplifier spacing L_A. Clearly, the properties of DM solitons depend on three map parameters even when only two types of fibers are used in each map period.

Equation (8.4.1) can be solved numerically using the split-step Fourier method. Numerical simulations show that a nearly periodic solution can often be found by adjusting input pulse parameters (width, chirp, and peak power) even though these parameters vary considerably in each map period. The shape of such DM solitons is typically closer to a Gaussian profile than the "sech" shape associated with standard solitons [114]–[116]. This surprising feature can be understood from the theory of mode-locked lasers by noting that a periodically amplified fiber link is similar to a laser cavity as far as pulse evolution is concerned. More specifically, SPM-induced frequency chirping is equivalent to periodic frequency modulation (FM), resulting in FM mode locking. It is well known that such lasers produce Gaussian pulses [174].

Numerical solutions, although essential, do not lead to much physical insight. Several techniques have been used to solve the NLS equation (8.4.1) approximately. A common approach makes use of the variational method [117]–[125]. Another approach expands $v(\xi,\tau)$ in terms of a complete set of the Hermite–Gauss functions that are solutions of the linear problem [126]–[130]. A third approach solves an integral equation, derived in the spectral domain using perturbation theory [131]–[133]. To simplify the following discussion, we focus on the variational method. The Lagrangian corresponding

to the NLS equation (8.4.1) is obtained from Eq. (8.2.16) after multiplying the time-derivative term with $d(\xi)$. Since the shape of the DM soliton is close to Gaussian, the soliton is assumed to evolve as

$$v(\xi,\tau) = a\exp[-(1+iC)\tau^2/2b^2 + i\phi], \tag{8.4.11}$$

where a is the amplitude, b is the width, C is the chirp, and ϕ is the phase of the soliton. All four parameters vary with ξ because of perturbations produced by $d(\xi)$ and $p(\xi)$.

Using the variational method, we can obtain four ordinary differential equations for the four soliton parameters. The amplitude equation can be eliminated since a^2b is independent of ξ with a constant value related to pulse energy. The phase equation can also be dropped since b and C do not depend on ϕ. The DM soliton then corresponds to a periodic solution of the following two equations:

$$\frac{db}{d\xi} = -d(\xi)\frac{C}{b}, \tag{8.4.12}$$

$$\frac{dC}{d\xi} = \frac{p(\xi)}{\sqrt{2}\,b} - (1+C^2)\frac{d(\xi)}{b^2}. \tag{8.4.13}$$

These equations should be solved with the periodic boundary conditions

$$b(0) = b(\xi_{\text{map}}), \qquad C(0) = C(\xi_{\text{map}}) \tag{8.4.14}$$

to ensure that the soliton recovers its initial state after each map period $\xi_{\text{map}} = L_{\text{map}}/L_D$. The periodic boundary conditions fix the values of the initial width b_0 and the chirp C_0 at $\xi = 0$ for which a soliton can propagate in a periodic fashion in spite of dispersion management. The choice of origin where $\xi = 0$ is arbitrary. It is useful to choose it at the location where the pulse width is minimum in the anomalous-GVD section since $b_0 = 1$ and $C_0 = 0$ at that point. The amplitude a_0 is found by solving Eqs. (8.4.12)–(8.4.14) and determines the peak power of the input pulse required to excite the DM soliton.

Consider first the ideal case of lossless fibers so that $p(\xi) = 1$ in Eq. (8.4.13). This case occurs in practice when distributed amplification is used so that fiber losses are nearly compensated by the local gain all along the fiber, resulting in $p(\xi) \approx 1$. Figure 8.14(a) shows an example of the periodic solution by plotting variations of b and C over one map period. The dispersion map in this case has $d = -1$ in the normal-GVD section with $l_n < l_a$ so that the average GVD is in the anomalous region for the entire link. The results obtained

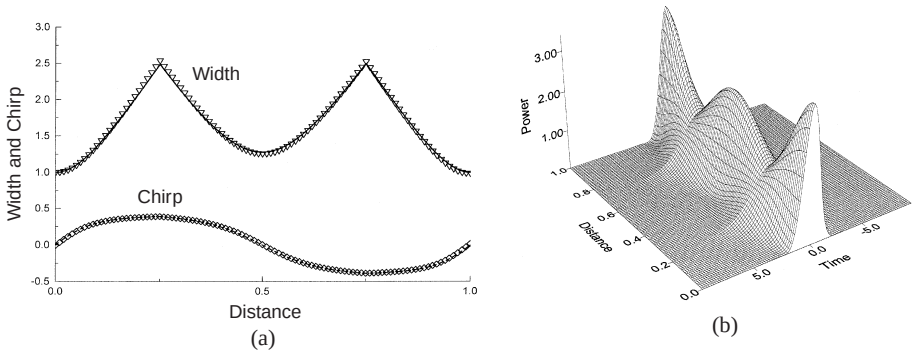

Figure 8.14 (a) Variations of the pulse width b and chirp C over one map period. The results of variational analysis (solid lines) are compared with numerics (triangles and diamonds) for the same map. (b) Variations of the pulse shape. (After Ref. [125], ©1998, reprinted with permission from Elsevier Science)

by solving Eq. (8.4.1) numerically are also shown for comparison. An example of variations in the pulse shape is shown in Fig. 8.14(b). Both pulse width and peak power vary rapidly in each map period. The pulse width becomes minimum at the center of each fiber where frequency chirp vanishes. However, the shortest pulse occurs in the middle of the anomalous-GVD section. Surprisingly, the spectral width of the pulse is smaller in the normal-GVD region. The DM soliton seen in Fig. 8.14 is quite different than a standard fundamental soliton since it does not maintain its shape, width, or peak power. Nevertheless, its parameters repeat from period to period at any location within the map. For this reason, DM solitons can be used for optical communications in spite of oscillations in the pulse width. Moreover, such solitons perform better from a system standpoint.

One can find periodic solutions of Eqs. (8.4.12)–(8.4.14) for a wide variety of dispersion maps as long as the input peak power is properly chosen. To see how the peak power depends on the map parameters, it is useful to present the results using two dimensionless parameters defined as [121]

$$\bar{d} = \frac{\beta_{2n} l_n + \beta_{2a} l_a}{\beta_{2a}(l_n + l_a)}, \qquad S = \frac{\beta_{2n} l_n - \beta_{2a} l_a}{T_{\rm FWHM}^2}, \tag{8.4.15}$$

where $T_{\rm FWHM} \approx 1.76 T_0$ is the FWHM of the soliton at the location where pulse width is minimum in the anomalous-GVD section. Physically, $\bar{d} = \bar{\beta}_2/\beta_{2a}$ is related to the average GVD of the fiber link, while the map strength S is a

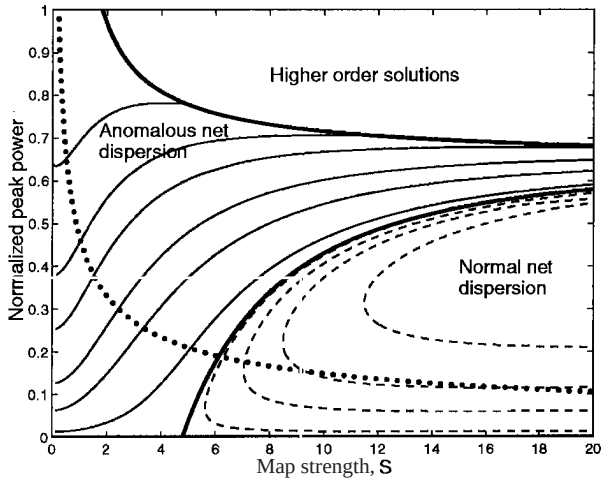

Figure 8.15 Peak power of DM solitons as a function of map strength S for several values of $\bar{d}$. The thick solid line in the middle corresponds to $\bar{d} = 0$. Solid curves on the left have average anomalous GVD ($\bar{d} = 0.01$, 0.05, 0.1, 0.2, 0.3, and 0.5). Dashed curves on the right have average normal GVD ($\bar{d} = -0.001, -0.005, -0.01$, and -0.02). The soliton energy is constant along the dotted line. (After Ref. [121])

measure of how much GVD varies between two fibers in each map period. We can also define the normalized peak power of the soliton at the input as $p_s = P_s/P_0$, where $P_0 = (\gamma L_D)^{-1}$ is the peak power required when the entire link consists of only anomalous-GVD fiber. Notice, however, that the peak power required to launch the soliton in a fiber with average GVD is smaller by a factor of $|\beta_{2a}/\bar{\beta}_2|$.

Figure 8.15 shows the peak power p_s as a function of map strength S for several values of $\bar{d}$ obtained by solving Eqs. (8.4.12)–(8.4.14). In the region marked "higher-order solitons," l_a is longer than the soliton period. The thick solid line in the middle corresponds to $\bar{d} = 0$. A surprising result is that DM solitons can exist even when the average GVD is normal (dashed curves) provided the map strength exceeds a critical value S_{cr}. Moreover, for values of $S > S_{cr}$ and $\bar{d} < 0$, there are two possible values of p_s for which a periodic solution exists. Numerical solutions of Eqs. (8.4.1) confirm these predictions [121] but the critical value of the map strength is found to be only 3.9 instead of 4.8.

The existence of DM solitons in maps with normal average GVD is quite intriguing [136]–[140] as one can envisage dispersion maps in which a soli-

ton propagates in the normal-GVD regime most of the time. An example is provided by a dispersion map in which a short section of standard fiber ($\beta_{2a} \approx -20$ ps^2/km) is used with a long section of dispersion-shifted fiber ($\beta_{2n} \approx 1$ ps^2/km) such that $\bar{\beta}_2$ is close to zero but positive. How can one understand the formation of DM solitons under such conditions? The answer is provided by the observation that the effect of GVD on a pulse depends not only on the GVD parameter β_2 but also on the temporal and spectral widths of the pulse. As seen in Fig. 8.14, the temporal width of the DM soliton does not vary in the same fashion in the two sections and becomes shorter in the anomalous-GVD section. Similarly, because of chirping, spectral width is considerably larger in the anomalous-GVD section compared with the normal-GVD section. Noting that the phase shift imposed on each spectral component varies as $\beta_2 \omega^2$ locally, we can define an effective value of the average GVD as [140]

$$\bar{\beta}_2^{\text{eff}} = \langle \beta_2 \Omega^2 \rangle / \langle \Omega^2 \rangle, \tag{8.4.16}$$

where Ω is the local value of the spectral width and averaging is over the dispersion map. If $\bar{\beta}_2^{\text{eff}}$ is negative, the DM soliton can exist even if $\bar{\beta}_2$ is positive.

The situation changes somewhat when lumped amplifiers are used so that $p(\xi) \neq 1$ in Eq. (8.4.13). The main difference is that the location where pulse has minimum width and zero chirp is no longer in the middle of each fiber section. Physically, this occurs because gain–loss variations over each map period break the symmetry around the midpoint [141]. From a practical standpoint, one needs to know either the exact location of the chirp-free points within the map or the amount of chirp at the end of each fiber section so that the input pulse can be prechirped appropriately. The periodic solution of Eqs. (8.4.12)–(8.4.14) provides this information readily. If amplifier spacing is much smaller than the map period so that $L_A \ll L_{\text{map}}$, the chirp-free point is nearly in the middle of each section since gain–loss variations are averaged out. In that case, the results shown in Fig. 8.15 hold approximately.

This simple variational analysis only provides an approximate solution since it assumes a Gaussian pulse shape at every point within the dispersion map. Numerical results show that both the pulse shape and spectrum develop oscillatory tails in the wings. Figure 8.16 shows an example of such low-intensity oscillations for a map with zero average dispersion, formed using two sections of equal lengths ($d = \pm 1$). It is not easy to find truly periodic solutions of Eq. (8.4.1) since one does not know the pulse shape *a priori*. If a

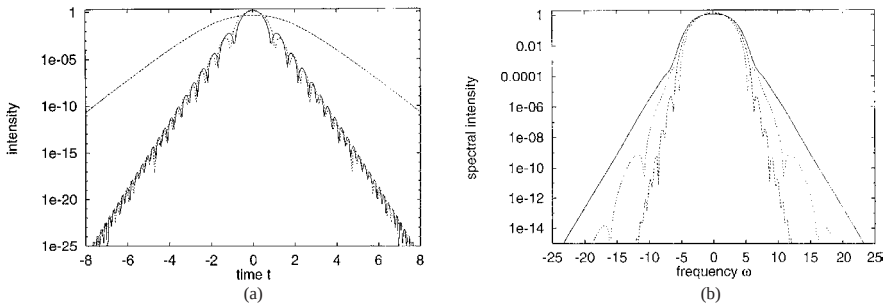

Figure 8.16 (a) Shapes and (b) spectra of a DM soliton in the middle of fiber sections with anomalous (solid line) and normal (dotted line) GVD. The dashed curve occurs at the junction of two sections. (After Ref. [169], ©2000 IEEE)

Gaussian pulse is launched with input parameters predicted by the variational analysis, the numerical solution often exhibits secondary quasi-periodic oscillations with a long period ($\sim 100\ L_{\text{map}}$). An averaging method was used for Fig. 8.16 that forced convergence toward the DM soliton that repeated precisely after each map period.

For map strengths below the critical value (about 3.9 numerically), the average GVD is anomalous for DM solitons. In that case, we are tempted to compare them with standard solitons forming in a uniform-GVD fiber link with the value $\bar{\beta}_2$. For relatively small values of S, variations in the pulse width and chirp are small enough that we can ignore them. The main difference between the average-GVD and DM solitons then stems from the higher peak power required to sustain DM solitons. The power or energy enhancement factor for a DM soliton can be defined as [113]

$$f_{\text{DM}} = P_s/P_{\text{av}} = p_s(\beta_{2a}/\bar{\beta}_2), \tag{8.4.17}$$

where P_{av} is the peak power for average-GVD solitons and $p_s = a_0^2$ is the normalized peak power shown in Fig. 8.15. The larger energy of DM solitons benefits a soliton-based lightwave system in several ways. Among other things, it improves the SNR, reduces soliton interaction, and decreases the timing jitter.

Timing Jitter

The timing jitter issue has attracted considerable attention because of its practical importance [142]–[156]. One can extend the approach of Section 8.3 to the

case of DM solitons for calculating the ASE-induced timing jitter although the analysis in general is complicated [147]. The physical origin of timing-jitter reduction can be understood from Eq. (8.3.16), applicable for weak dispersion maps with anomalous $\bar{\beta}_2$. Noting that $N_{\rm ph}$ is proportional to the soliton energy, one can expect reduction roughly by the same factor $f_{\rm DM}$ by which the energy of a DM soliton is enhanced. Of course, this argument is over simplified. In real systems, timing jitter depends on the relative location of the amplifier within the dispersion map and can be optimized by adjusting it [146].

A general theory of timing jitter for DM systems, applicable for both RZ and NRZ formats, has been developed [153]. Figure 8.17 shows the timing jitter (solid line) for a soliton system using two dispersion maps consisting of two 100-km fiber sections with GVD of -3 and 2.8 ps^2/km (a) and -3.75 and 3.55 ps^2/km (b). For $T_{\rm FWHM} = 20$ ps, the map strength S is 1.45 and 1.825 in the two cases. Lumped amplifiers are placed every 50 km to offset the 0.21-dB/km fiber losses. The dot-dashed line is the prediction of Eq. (8.3.17) with β_2 replaced by the average value $\bar{\beta}_2$. The dotted line is obtained by reducing this value by the energy enhancement factor $f_{\rm DM}$. Circles are obtained by solving Eq. (8.4.1) with ASE noise included. Clearly, dispersion management reduces timing jitter considerably compared with the value expected on the basis of average dispersion. For a 10-Gb/s system with 100-ps bit slot, jitter can be reduced to a 5-ps level without using optical filters or modulators. It can be reduced to below 1 ps at 10,000 km by reducing the average dispersion close to zero. The physical origin of jitter reduction is related to the chirped nature of a DM soliton.

Interaction between neighboring solitons also affects the timing jitter. It is easy to conclude that soliton interaction in DM systems is likely to be enhanced since the pulse width oscillates periodically and can become quite large in the normal-GVD section for strong maps. This is indeed found to be the case [147]–[149]. However, a DM soliton represents a chirped pulse (in contrast with conventional solitons), and chirping affects the interaction process considerably. It turns out that the interaction is nearly independent of the relative phase between two DM solitons. Soliton interaction also depends on the location of amplifiers within the dispersion map and can be reduced by placing them at appropriate locations [147]. For short DM solitons, one should also consider the Raman-induced frequency shift, which is reduced considerably for DM solitons [152].

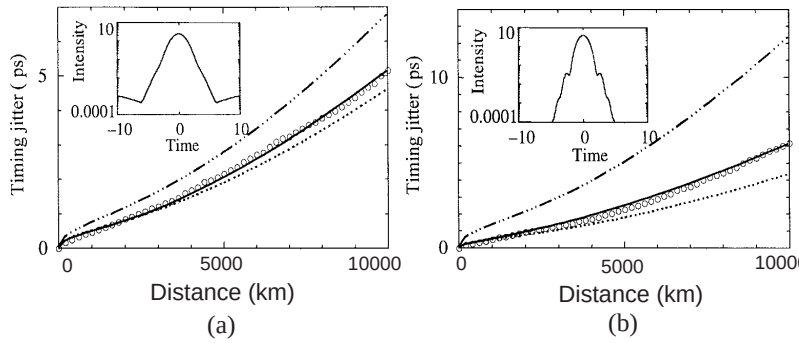

Figure 8.17 Growth of timing jitter with distance (solid line) for 10-Gb/s DM soliton systems using two different dispersion maps. Inset shows the DM soliton shape on a log scale. The dot-dashed and dotted lines represent two different approximations to timing jitter while the circles show the results of numerical simulations. (After Ref. [153], ©1999 IEEE)

Experimental Results

Dispersion-management schemes were used for solitons as early as 1992 although they were referred to by names such as partial soliton communication [175] and dispersion allocation [176]. In the simplest form of dispersion management, a relatively short segment of dispersion-compensating fiber (DCF) is added periodically to the transmission fiber, resulting in dispersion maps similar to those used for nonsoliton systems (see Section 7.1). It was found in a 1995 experiment that the use of DCFs reduced the timing jitter considerably [177]. In fact, in this 20-Gb/s experiment, the timing jitter became low enough when the average dispersion over each fiber segment was reduced to a value near -0.025 ps^2/km that the 20-Gb/s signal could be transmitted over transoceanic distances.

Since 1996, a large number of experiments have shown the benefits of DM solitons for lightwave systems [178]–[191]. In one experiment, the use of a periodic dispersion map enabled transmission of a 20-Gb/s soliton bit stream over 5520 km of a fiber link containing amplifiers at 40-km intervals [178]. In another 20-Gb/s experiment [179], solitons were transmitted over 9000 km without using any in-line optical filters since the periodic use of DCFs reduced the timing jitter by more than a factor of 3. A 1997 experiment focused on transmission of DM solitons using dispersion maps such that solitons propagated most of the time in the normal-GVD regime [180]. This 10-Gb/s experi-

ment transmitted signals over 28 Mm using a recirculating fiber loop consisting of 100 km of normal-GVD fiber and 8-km of anomalous-GVD fiber such that the average GVD was anomalous (about -0.1 ps^2/km). Periodic variations in the pulse width were also observed in such a fiber loop [181]. In a later experiment, the loop was modified to yield the average-GVD value of zero or slightly positive [182]. Stable transmission of 10-Gb/s solitons over 28 Mm was still observed. In all cases, experimental results were in excellent agreement with numerical simulations [183].

The use of dispersion management for fiber links consisting of mostly standard telecommunication fiber is of practical importance since it allows upgrading of existing fiber-optic networks [184]–[187]. A 1997 experiment used fiber gratings for dispersion compensation and realized 10-Gb/s soliton transmission over 1000 km. By 1999, 10-Gb/s DM solitons were transmitted over 16 Mm of standard fiber, reducing soliton interaction by choosing the location of amplifiers appropriately [185]. Nearly periodic propagation of DM solitons has also been observed using a recirculating fiber loop [186] consisting of 102 km of standard fiber with anomalous GVD ($\beta_2 \approx -21$ ps^2/km) and 17.3 km of DCF with normal GVD ($\beta_2 \approx 160$ ps^2/km). The map strength S was quite large in this experiment when 30-ps (FWHM) pulses were launched into the loop. Pulses were prechirped using the results of variational analysis as discussed above. A similar experiment was used to transmit 20-Gb/s solitons over 1100 km [187]. Experimental results were found to be in good agreement with DM-soliton theory.

Transmission of soliton systems at bit rates beyond 40 Gb/s or more is of considerable practical interest. Numerical simulations show the possibility of transmitting 40-Gb/s DM solitons over 2000 km of standard fiber with an appropriate dispersion map [188]. Longer distances are feasible using dispersion-shifted fibers and a weaker dispersion map. In a 1998 experiment, 40-Gb/s solitons were transmitted over 8600 km using a 140-km-long fiber loop with an average dispersion of only -0.03 ps^2/km [189]. Except for a 5-nm-bandwidth fixed-frequency filter, nothing was used inside the loop to control the timing jitter of solitons. Interaction between solitons may become an important factor at such high bit rates. It can be reduced by alternating the polarization of neighboring bits [190]. Indeed, the use of this technique permitted transmission of 40-Gb/s solitons over more than 10 Mm [191].

Higher-order effects such as TOD and the intrapulse Raman scattering become quite important at high bit rates and must be included [192]–[194].

Numerical simulations show that 80-Gb/s solitons can propagate stably over 9000 km in the presence of higher-order effects if (i) TOD is compensated within the map, (ii) optical filters are used to reduce soliton interaction, timing jitter, and the Raman-induced frequency shift, and (iii) the map period L_{map} is reduced to a fraction of amplifier spacing [192]. The bit rate can even be increased to 160 Gb/s by controlling the GVD slope and PMD, but the distance is limited to about 2000 km [193]. In practice, high-capacity soliton systems are designed using the WDM technique.

8.5 WDM Soliton Systems

As discussed in Chapter 7, the capacity of a lightwave system can be increased considerably by using the WDM technique. A WDM soliton system transmits over the same fiber several soliton bit streams, distinguishable through their different carrier frequencies. In this section we focus on several issues involved in the design of WDM soliton systems [195].

8.5.1 Interchannel Collisions

A new feature that becomes important for WDM systems is the possibility of collisions among solitons belonging to different channels because of their different group velocities. To understand the importance of such collisions, we use Eq. (8.4.3) since it includes the effects of both loss and dispersion variations. Dropping prime over ξ for notational convenience, we obtain

$$i\frac{\partial v}{\partial \xi} + \frac{1}{2}\frac{\partial^2 v}{\partial \tau^2} + b(\xi)|v|^2 v = 0, \tag{8.5.1}$$

where $b(\xi) = p(\xi)/d(\xi)$. The functional form of $b(\xi)$ depends on the details of the loss- and dispersion-management schemes.

The effects of interchannel collisions on the performance of WDM systems can be best understood by considering the simplest case of two WDM channels separated by f_{ch}. In normalized units, solitons are separated in frequency by $\Omega_{\text{ch}} = 2\pi f_{\text{ch}} T_0$. Replacing v by $u_1 + u_2$ in Eq. (8.5.1) and neglecting the FWM terms, solitons in each channel evolve according to the following two coupled equations [196]:

$$i\frac{\partial u_1}{\partial \xi} + \frac{1}{2}\frac{\partial^2 u_1}{\partial \tau^2} + b(\xi)(|u_1|^2 + 2|u_2|^2)u_1 = 0, \tag{8.5.2}$$

$$i\frac{\partial u_2}{\partial \xi} + \frac{1}{2}\frac{\partial^2 u_2}{\partial \tau^2} + b(\xi)(|u_2|^2 + 2|u_1|^2)u_2 = 0. \tag{8.5.3}$$

These equations appear identical with the coupled NLS equations obtained in Chapter A.7 for two copropagating pulses interacting through cross-phase modulation (XPM). Note, however, that the two solitons in the WDM case are propagating at different speeds because of their different frequencies. As a result, the XPM term is important only when solitons belonging to different channels overlap temporally during a collision.

It is useful to define the *collision length* L_{coll} as the distance over which two solitons interact (overlap) before separating. It is difficult to precisely determine the instant at which a collision begins or ends. A common convention uses $2T_s$ for the duration of the collision, assuming that a collision begins and ends when the two solitons overlap at their half-power points [196]. Since the relative speed of two solitons is $\Delta V = (|\beta_2|\Omega_{\text{ch}}/T_0)^{-1}$, the collision length is given by $L_{\text{coll}} = (\Delta V)(2T_s)$ or

$$L_{\text{coll}} = \frac{2T_s T_0}{|\beta_2|\Omega_{\text{ch}}} \approx \frac{0.28}{q_0|\beta_2|Bf_{\text{ch}}}, \tag{8.5.4}$$

where the relations $T_s = 1.763T_0$ and $B = (2q_0T_0)^{-1}$ were used. As an example, for $B = 10$ Gb/s, $q_0 = 5$, and $\beta_2 = -0.5$ ps^2/km, $L_{\text{coll}} \sim 100$ km for a channel spacing of 100 GHz but reduces to below 10 km when channels are separated by more than 1 THz.

Since XPM induces a time-dependent phase shift on each soliton, it leads to a shift in soliton frequency during a collision. The perturbation theory of Section 8.3.1 is often used to calculate this frequency shift. At first sight, this approach appears unsound since the XPM term is comparable in magnitude to the SPM term in Eq. (8.5.2). However, the relative phase of two solitons changes many times over the pulse width, resulting in a weak interaction on average. As a result, the XPM term can be treated as a small perturbation.

We use Eq. (8.1.4) for both u_1 and u_2 and assume that two solitons are identical before they collide. With $\eta = 1$ and $q = 0$, u_1 and u_2 are given by

$$u_m(\xi,\tau) = \text{sech}(\tau + \delta_m\xi)\exp[-i\delta_m\tau + i(1-\delta_m^2)\xi/2 + i\phi_m], \tag{8.5.5}$$

where $\delta_m = \pm\frac{1}{2}\Omega_{\text{ch}}$ for $m = 1$ and 2 because of different channel frequencies. Using $\varepsilon(u) = 2ib|u_2|^2u_1$ (the XPM term), Eq. (8.3.2) becomes

$$\frac{d\delta_1}{d\xi} = b(\xi)\int_{-\infty}^{\infty}\frac{\partial|u_1|^2}{\partial\tau}|u_2|^2\,d\tau. \tag{8.5.6}$$

The equation for δ_2 is obtained by interchanging the subscripts 1 and 2. Noting from Eq. (8.5.5) that

$$\frac{\partial |u_1|^2}{\partial \tau} = \frac{1}{\delta_1}\frac{\partial |u_1|^2}{\partial \xi}, \tag{8.5.7}$$

and using $\delta_m = \pm\frac{1}{2}\Omega_{\rm ch}$ in Eq. (8.5.6), the collision-induced frequency shift for the slower moving soliton is governed by [196]

$$\frac{d\delta_1}{d\xi} = \frac{b(\xi)}{\Omega_{\rm ch}}\frac{d}{d\xi}\left[\int_{-\infty}^{\infty} \operatorname{sech}^2(\tau - \Omega_{\rm ch}\xi/2)\operatorname{sech}^2(\tau + \Omega_{\rm ch}\xi/2)\,d\tau\right]. \tag{8.5.8}$$

The change in δ_2 occurs by the same amount but in the opposite direction. The integral over τ can performed analytically to obtain

$$\frac{d\delta_1}{dZ} = \frac{4b(Z)}{\Omega_{\rm ch}}\frac{d}{dZ}\left(\frac{Z\cosh Z - \sinh Z}{\sinh^3 Z}\right), \tag{8.5.9}$$

where $Z = \Omega_{\rm ch}\xi$. This equation provides changes in soliton frequency during interchannel collisions under quite general conditions.

Consider first the ideal case of constant-dispersion lossless fibers so that $b = 1$ in Eq. (8.5.9). In that case, integration in Eq. (8.5.9) is trivial, and the frequency shift is given by

$$\Delta\delta_1(Z) = 4(Z\cosh Z - \sinh Z)/(\Omega_{\rm ch}\sinh^3 Z). \tag{8.5.10}$$

Figure 8.18 shows how the soliton frequency changes for the slower-moving soliton during the collision of two 50-ps solitons with a channel spacing of 75 GHz. The frequency shifts up over one collision length as two solitons approach each other, reaches a peak value of about 0.6 GHz at the point of maximum overlap, and then decreases back to zero as the two solitons separate. The maximum frequency shift depends on the channel spacing. It occurs at $Z = 0$ in Eq. (8.5.10) and is found to be $4/(3\Omega_{\rm ch})$. In physical units, the maximum frequency shift becomes

$$\Delta f_{\max} = (3\pi^2 T_0^2 f_{\rm ch})^{-1}. \tag{8.5.11}$$

Since the velocity of a soliton changes with its frequency, collisions speed up or slow down a soliton, depending on whether its frequency increases or decreases. At the end of the collision, each soliton recovers the frequency and speed it had before the collision, but its position within the bit slot changes.

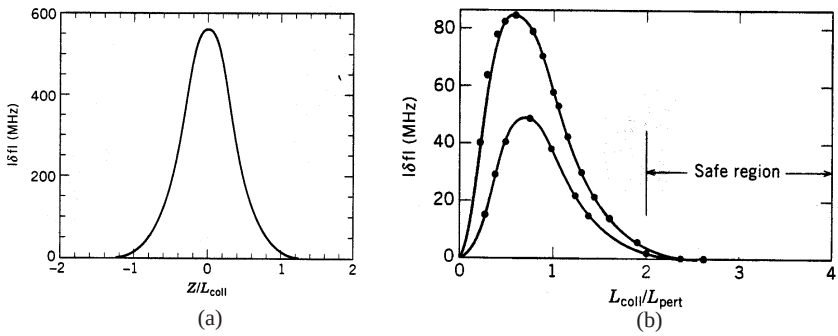

Figure 8.18 (a) Frequency shift during collision of two 50-ps solitons with 75-GHz channel spacing in a lossless fiber. (b) Residual frequency shift after a collision because of lumped amplifiers (L_A = 20 and 40 km for lower and upper curves, respectively). Numerical results are shown by solid dots. (After Ref. [196], ©1991 IEEE)

The temporal shift can be calculated by integrating Eq. (8.3.3). In physical units, it is given by

$$\Delta t = -T_0 \int_{-\infty}^{\infty} \Delta\delta_1(\xi)\, d\xi = \frac{4T_0}{\Omega_{\rm ch}^2} = \frac{1}{\pi^2 T_0 f_{\rm ch}^2}. \tag{8.5.12}$$

If all bit slots were occupied, such collision-induced temporal shifts would be of no consequence since all solitons of a channel would be shifted by the same amount. However, 1 and 0 bits occur randomly in real bit streams. Since different solitons of a channel shift by different amounts, interchannel collisions induce some timing jitter even in lossless fibers.

8.5.2 Effect of Lumped Amplification

The situation is worse in loss-managed soliton systems in which fiber loss is compensated periodically through lumped amplifiers. The reason is that soliton collisions are affected adversely by variations in soliton energy. Physically, large energy variations occurring over a collision length destroy the symmetric nature of the collision. Mathematically, the ξ dependence of $b(\xi)$ in Eq. (8.5.8) changes the frequency shift. As a result, solitons do not recover their original frequency and velocity after the collision is over. Equation (8.5.9) can be used to calculate the *residual* frequency shift for a given form of $b(\xi)$. Figure 8.18(b) shows the residual shift as a function of the ratio $L_{\rm coll}/L_{\rm pert}$, where $L_{\rm pert}$ is equal to the amplifier spacing L_A [196]. Numerical simulations (circles)

agree with the prediction of Eq. (8.5.9). The residual frequency shift increases rapidly as L_{coll} approaches L_A and can become ~ 0.1 GHz. Such shifts are not acceptable in practice since they accumulate over multiple collisions and produce velocity changes large enough to move the soliton out of the bit slot.

When L_{coll} is large enough that a collision lasts over several amplifier spacings, effects of gain–loss variations begin to average out and the residual frequency shift decreases. As seen in Fig. 8.18, it virtually vanishes for $L_{\text{coll}} > 2L_A$ (safe region). Since L_{coll} is inversely related to the channel spacing Ω_{ch}, this condition sets a limit on the maximum separation between the two outermost channels of a WDM system. The shortest collision length is obtained by replacing Ω_{ch} in Eq. (8.5.4) with $N_{\text{ch}}\Omega_{\text{ch}}$. Using $L_{\text{coll}} > 2L_A$, the number of WDM channels is limited to

$$N_{\text{ch}} < \frac{T_s L_D}{T_0 \Omega_{\text{ch}} L_A}. \tag{8.5.13}$$

One may think that the number of channels can be increased by reducing Ω_{ch}. However, its minimum value is limited to about $\Omega_{\text{ch}} = 5\Delta\omega_s$, where $\Delta\omega_s$ is the spectral width (FWHM) of solitons, because of interchannel crosstalk [197]. Using this condition in Eq. (8.5.13), the number of WDM channels is limited such that $N_{\text{ch}} < L_D/3L_A$. Using $L_D = T_0^2/|\beta_2|$ and $B = (2q_0T_0)^{-1}$, this condition can be written as a simple design rule:

$$N_{\text{ch}} B^2 L_A < (12 q_0^2 |\beta_2|)^{-1}. \tag{8.5.14}$$

For the typical values $q_0 = 5$, $|\beta_2| = 0.8$ ps^2/km, and $L_A = 40$ km, the condition becomes $B\sqrt{N_{\text{ch}}} < 10$ Gb/s. The number of channels can be as large as 16 at a relatively low bit rate of 2.5 Gb/s but only a single channel is allowed at 10 Gb/s. Clearly, interchannel collisions limit the usefulness of the WDM technique severely.

8.5.3 Timing Jitter

In addition to the sources of timing jitter discussed in Section 8.3.2 for a single isolated channel, several other sources of jitter become important for WDM systems [198]–[203]. First, each interchannel collision generates a temporal shift [see Eq. (8.5.12)] of the same magnitude for both solitons but in opposite directions. Even though the temporal shift scales as Ω_{ch}^{-2} and decreases rapidly with increasing Ω_{ch}, the number of collisions increases linearly with Ω_{ch}. As a

result, the total time shift scales as Ω_{ch}^{-1}. Second, the number of collisions that two neighboring solitons in a given channel undergo is slightly different. This difference arises because adjacent solitons in a given channel interact with two different bit groups, shifted by one bit period. Since 1 and 0 bits occur in a random fashion, different solitons of the same channel are shifted by different amounts. This source of timing jitter is unique to WDM systems because of its dependence on the bit patterns of neighboring channels [201]. Third, collisions involving more than two solitons can occur and should be considered. In the limit of a large channel spacing (negligible overlap of soliton spectra), multisoliton interactions are well described by pairwise collisions [200].

Two other mechanisms of timing jitter should be considered for realistic WDM systems. As discussed earlier, energy variations due to gain–loss cycles make collisions asymmetric when L_{coll} becomes shorter than or comparable to the amplifier spacing L_A. Asymmetric collisions leave residual frequency shifts that affect a soliton all along the fiber link because of a change in its group velocity. This mechanism can be made ineffective by ensuring that L_{coll} exceeds $2L_A$. The second mechanism produces a residual frequency shift when solitons from different channels overlap at the input of the transmission link, resulting in an incomplete collision [198]. This situation occurs in all WDM solitons for some bits. For instance, two solitons overlapping completely at the input end of a fiber link will acquire a net frequency shift of $4/(3\Omega_{\text{ch}})$ since the first half of the collision is absent. Such residual frequency shifts are generated only over the first few amplification stages but pertain over the whole transmission length and become an important source of timing jitter [199].

Similar to the case of single-channel systems, sliding-frequency filters can reduce timing jitter in WDM systems [204]–[208]. Typically, Fabry–Perot filters are used since their periodic transmission windows allow a filtering of all channels simultaneously. For best operation, the mirror reflectivities are kept low (below 25%) to reduce the finesse. Such low-contrast filters remove less energy from solitons but are as effective as filters with higher contrast. Their use allows channel spacing to be as little as five times the spectral width of the solitons [208]. The physical mechanism remains the same as for single-channel systems (see Section 8.3.3). More specifically, collision-induced frequency shifts are reduced because the filter forces the soliton frequency to move toward its transmission peak. The net result is that filters reduce the timing jitter considerably even for WDM systems [205]. Filtering can also relax the condition in Eq. (8.5.13), allowing L_{coll} to approach L_A, and thus helps to

increase the number of channels in a WDM system [207].

The technique of synchronous modulation can also be applied to WDM systems for controlling timing jitter [209]. In a 1996 experiment involving four channels, each operating at 10 Gb/s, transmission over transoceanic distances was achieved by using modulators every 500 km [210]. When modulators were inserted every 250 km, three channels, each operating at 20 Gb/s, could be transmitted over transoceanic distances [114]. The main disadvantage of modulators is that demultiplexing of individual channels is necessary.

8.5.4 Dispersion Management

As discussed in Section 7.5, FWM is the most limiting factor for WDM systems when GVD is kept constant along the fiber link. The FWM problem virtually disappears when the dispersion-management technique is used. In fact, dispersion management is essential if a WDM soliton system is designed to transmit more than two or three channels. Starting in 1996, dispersion management was used for WDM soliton systems almost exclusively.

Dispersion-Decreasing Fibers

It is intuitively clear that DDFs with a continuously varying GVD profile should help a WDM system. We can use Eq. (8.5.1) for finding the optimum GVD profile. By tailoring the fiber dispersion as $p(\xi) = \exp(-\Gamma\xi)$—the same exponential profile encountered in Section 8.4.1—the parameter b becomes 1 all along the fiber link, resulting in an unperturbed NLS equation. As a result, soliton collisions become symmetric despite fiber losses, irrespective of the ratio L_{coll}/L_A. Consequently, no residual frequency shifts occur after a soliton collision for WDM systems making use of DDFs with an exponentially decreasing GVD.

Lumped amplifiers introduce a new mechanism of FWM in WDM systems. As discussed earlier, soliton energy varies in a periodic fashion because of the loss–amplification cycle. Such periodic variations in the peak power of solitons create a nonlinear-index grating that can nearly phase-match the FWM process [212]. The phase-matching condition can be written as (see Section 4.4.2)

$$|\beta_2|(\Omega_{\text{ch}}/T_0)^2 = 2\pi m/L_A, \tag{8.5.15}$$

where m is an integer and the amplifier spacing L_A is the period of the index grating. As a result of such phase matching, a few percent of soliton energy can

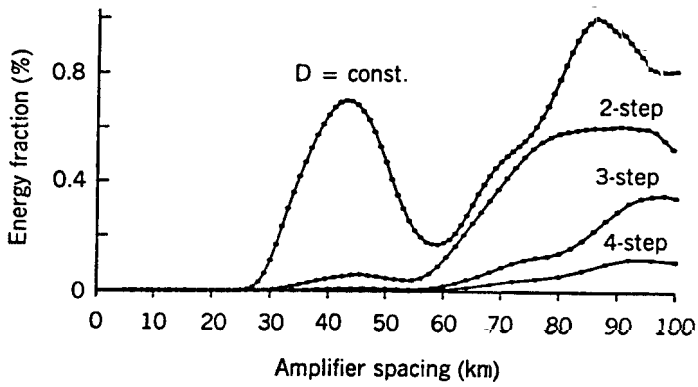

Figure 8.19 Fraction of soliton energy in an FWM sideband during a single collision when the exponential GVD profile is approximated by a staircase with two, three, and four steps. The case of constant-dispersion fibers is shown for comparison. (After Ref. [212])

be transferred to the FWM sidebands even when GVD is relatively large [212]. Moreover, FWM occurring during simultaneous collision of three solitons leads to permanent frequency shifts for the slowest- and fastest-moving solitons together with an energy exchange among all three channels [213].

FWM phase-matched by the nonlinear-index grating can also be avoided by using DDFs with an exponential GVD profile. The reason is related to the symmetric nature of soliton collisions in such systems. When collisions are symmetric, energy transferred to the FWM sidebands during the first half of a collision is returned back to the soliton during the second half of the same collision. Thus, the spectral sidebands generated through FWM do not grow with propagation of solitons. In practice, the staircase approximation for the exponential profile is used, employing multiple constant-dispersion fibers between two amplifiers.

Figure 8.19 shows the residual energy remaining in a FWM sideband as a function of amplifier length L_A when the exponential GVD profile is approximated using $m = 2$, 3, and 4 fiber sections chosen such that the product $D_m L_m$ is the same for all m [212]. Here D_m is the dispersion parameter in the mth section of length L_m. The case of constant-dispersion fibers is also shown for comparison. The average dispersion is 0.5 ps/(km-nm) in all cases. The double-peak nature of the curve in this case is due to the phase-matching condition in Eq. (8.5.15), which can be satisfied for different values of the integer

m since a peak occurs whenever $L_A = 2\pi m L_D/\Omega_{\text{ch}}^2$. Numerical simulations consider 20-ps solitons in two channels, spaced 75 GHz apart. Clearly, FWM can be nearly suppressed, with as few as three fiber sections, for an amplifier spacing below 60 km. An experiment in 1996 achieved transmission of seven 10-Gb/s channels over 9400 km using only four fiber segments in a recirculating fiber loop [214]. In a 1998 experiment, eight 20-Gb/s channels were transmitted over 10,000 km by using the same four-segment approach in combination with optical filters and modulators [215].

Periodic Dispersion Maps

Similar to the single-channel soliton systems discussed in Section 8.4.2, periodic dispersion maps consisting of two fiber segments with opposite GVD benefit the WDM soliton systems enormously. Issues such as interchannel collisions, timing jitter, and optimum dispersion maps were studied extensively during the 1990s [216]–[238]. The use of design optimization techniques has resulted in WDM soliton systems capable of operating at bit rates close to 1 Tb/s [239]–[247].

An important issue for WDM systems making use of DM solitons is how a dispersion map consisting of opposite-GVD fibers affects interchannel collisions and the timing jitter. It is easy to see that the nature of soliton collisions is changed drastically in such systems. Consider solitons in two different channels. A shorter-wavelength soliton travels faster in the anomalous-GVD section compared with the the normal-GVD section. Moreover, because of high local GVD, their relative speed is large. Also, the pulse width changes in each map period and can become quite large in some regions. The net result is that two colliding solitons move in a zigzag fashion and pass through each other many times before they separate from each other because of the much slower relative motion governed by the average value of GVD. Since the effective collision length is much larger than the map period (and the amplifier spacing), the condition $L_{\text{coll}} > 2L_A$ is satisfied even when soliton wavelengths differ by 20 nm or more. This feature makes it possible to design WDM soliton systems with a large number of high-bit-rate channels.

The residual frequency shift introduced during such a process depends on a large number of parameters including the map period, map strength, and amplifier spacing [229]–[233]. Physically speaking, residual frequency shifts occurring during complete collisions average out to zero. However, not all collisions are complete. For example, if solitons overlap initially, the incomplete

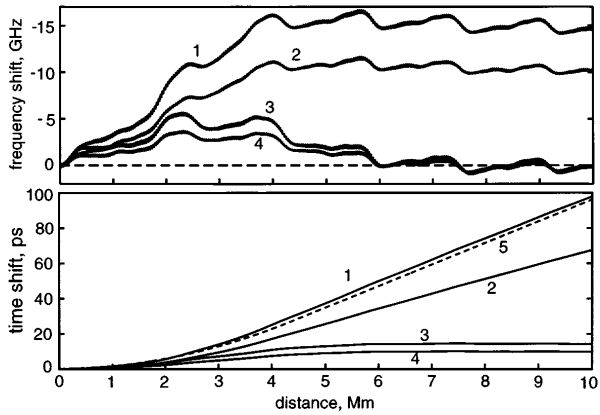

Figure 8.20 Collision-induced frequency and temporal shifts for a soliton surrounded by four channels on each side (75 GHz spacing). Curves 1 and 2 represent copolarized (1) and orthogonally polarized (2) solitons in neighboring channels. Curves 3 and 4 show the improvement with sliding-frequency filters. The dotted line is the prediction of a simple analytical model. (After Ref. [231])

nature of the collision will produce some residual frequency shift. The zigzag motion of solitons can also produce frequency shifts if the solitons approach each other near the junction of opposite-GVD fibers since they will reverse direction before crossing each other. Such partial collisions can result in large frequency shifts, which can shift solitons by a large amount within their bit slots. This behavior is unacceptable from a system standpoint.

A simple solution to this problem is provided by sliding-frequency filters [231]. Such filters reduce the frequency and temporal shifts to manageable levels in the same way they mitigate the effects of ASE-induced frequency shifts. Curve 1 in Figure 8.20 shows the frequency and temporal shifts (calculated numerically) for a central channel surrounded by four channels on each side (channel spacing 75 GHz). The soliton shifts by 100 ps (one bit slot) over 10,000 km because its frequency shifts by more than 10 GHz. The use of orthogonally polarized solitons (curve 2) improves the situation somewhat but does not solve the problem. However, if sliding-frequency filters are employed, the temporal shift is reduced to below 15 ps for copolarized solitons (curve 3) and to below 10 ps for orthogonally polarized solitons (curve 4). In these numerical simulations, the map period and amplifier spacing are equal to 40 km. The dispersion map consists of 36 km of anomalous-GVD fiber

and 4 km of DCF ($\beta_{2n} \approx 130$ ps^2/km) such that average value of dispersion is 0.1 ps/(km-nm).

On the experimental side, 16 channels at 20 Gb/s were transmitted in 1997 over 1300 km of standard fiber with a map period of 100 km using a DCF that compensated partially both GVD and its slope [239]. In a 1998 experiment, 20 channels at 20 Gb/s were transmitted over 2000 km using dispersion-flattened fiber with a channel spacing of 0.8 nm [240]. The highest capacity of 640 Gb/s was realized in a 2000 experiment in which 16 channels at 40 Gb/s were transmitted over 1000 km [245]. Many experiments focused on soliton systems for transoceanic applications. The total bit rate is lower for such systems because of long distances over which solitons must travel.

Transmission of eight channels at 10-Gb/s over transoceanic distances was realized as early as 1996 [195]. Eight 20-Gb/s channels were transmitted in a 1998 experiment but the distance was limited to 4000 km [242]. By 2000, the 160-Gb/s capacity was attained by transmitting eight 20-Gb/s channels over 10,000 km using optical filters and synchronous modulators inside a 250-km recirculating fiber loop [246]. It was necessary to use a polarization scrambler and a phase modulator at the input end. The 160-Gb/s capacity was also realized using two 80-Gb/s channels. In another experiment, up to 27 WDM channels were transmitted over 9000 km using a hybrid amplification scheme in which distributed Raman amplification (with backward pumping) compensated for nearly 70% of losses incurred over the 56-km map period [247]. These experiments show that the use of DM solitons has the potential of realizing transoceanic lightwave systems capable of operating with a capacity of 1 Tb/s or more.

Problems

8.1 A soliton communication system is operating at 1.55 μm by using fibers with $D = 2$ ps/(km-nm). The effective core area of the fiber is 50 μm^2. Calculate the peak power and the pulse energy required for fundamental solitons of 30-ps width (FWHM).

8.2 What is the soliton period for the communication system of Problem 8.1?

8.3 Verify by direct substitution that the soliton solution given in Eq. (8.1.4) indeed satisfies Eq. (8.1.1).

8.4 Solve the NLS equation numerically by using the split-step Fourier method. Any programming language, including software packages such as Mathematica and Matlab, can be used.

8.5 By propagating a fundamental soliton over 10 dispersion lengths, verify numerically that the shape of the soliton does not change on propagation. Repeat the simulation for a Gaussian input pulse shape with the same peak power and explain the results.

8.6 A 10-Gb/s soliton lightwave system is designed with $q_0 = 5$ to ensure well-separated solitons. Calculate the pulse width, peak power, energy of the pulse, and average power of the RZ signal assuming $\beta_2 = -1$ ps^2/km and $\gamma = 2$ W^{-1}/km.

8.7 A soliton communication system is designed to transmit data over 5000 km at $B = 10$ Gb/s. What should be the pulse width (FWHM) to ensure that the neighboring solitons do not interact during transmission? The dispersion parameter D is 1 ps/(km-nm) at the operating wavelength. Assume that soliton interaction is negligible when $B^2 L_T$ in Eq. (8.1.15) is 10% of its maximum allowed value.

8.8 Prove that the power-enhancement factor for loss-managed solitons is given by $G \ln G/(G-1)$, where G is the gain of lumped amplifiers.

8.9 A 10-Gb/s soliton system is designed with 50-km amplifier spacing. What should be the input peak power of a loss-managed soliton of the input pulse to ensure that a fundamental soliton is for fibers with losses of 0.2 dB/km? Assume that $T_s = 20$ ps, $\beta_2 = -0.5$ ps^2/km, and $\gamma = 2$ W^{-1}/km. What is the average launched power for such a system?

8.10 Calculate the maximum bit rate for a soliton lightwave system designed with $q_0 = 5$, $\beta_2 = -1$ ps^2/km, and $L_A = 50$ km. Assume that the condition (8.2.9) is satisfied when $B^2 L_A$ is at the 20% level. What is the soliton width at the maximum bit rate?

8.11 Derive Eq. (8.2.14) by integrating Eq. (8.2.10). Plot $p(z)$ for $L_A = 20$, 40, 60, and 80 km using $\alpha = 0.2$ dB/km and $\alpha_p = 0.25$ dB/km.

8.12 Explain in physical terms the origin of the Gordon–Haus jitter. How do optical filters and modulators reduce this source of timing jitter?

8.13 Derive Eqs. (8.3.26)–(8.3.28) using soliton perturbation theory. Find their steady-state solution when $f_s = 0$ and noise can be ignored. Under what conditions is this solution stable?

8.14 Prove that a soliton is not perturbed in a lossy fiber if dispersion decreases exponentially as $\exp(-\alpha z)$ along the fiber length.

8.15 Find the peak value of the collision-induced frequency and temporal shifts by integrating Eq. (8.5.9) with $b = 1$.

8.16 Explain how soliton collisions limit the number of channels in a WDM soliton system. Find how the maximum number of channels depends on the channel and amplifier spacings using the condition $L_{\text{coll}} > 2L_A$.

References

[1] A. Hasegawa and F. Tappert, *Appl. Phys. Lett.* **23**, 142 (1973).

[2] L. F. Mollenauer, R. H. Stolen, and J. P. Gordon, *Phys. Rev. Lett.* **45**, 1095 (1980).

[3] L. F. Mollenauer and K. Smith, *Opt. Lett.* **13**, 675 (1988).

[4] Y. Kodama and A. Hasegawa, *Progress in Optics*, Vol. 30, E. Wolf, Ed. (North-Holland, Amsterdam, 1992), Chap. 4.

[5] A. Hasegawa and Y. Kodama, *Solitons in Optical Communications* (Clarendon Press, Oxford, 1995).

[6] L. F. Mollenauer, P. V. Mamychev, and J. P. Gordon, in *Optical Fiber Telecommunications*, Vol. IIIA (Academic Press, San Diego, CA, 1997), Chap. 10.

[7] G. P. Agrawal, *Fiber-Optic Communication Systems*, 2nd ed. (Wiley, New York, 1997), Chap. 10.

[8] E. Iannone, F. Matera, A. Mecozzi, and M. Settembre, *Nonlinear Optical Communication Networks*, (Wiley, New York, 1998), Chap. 5.

[9] V. E. Zakharov and A. B. Shabat, *Sov. Phys. JETP* **34**, 62 (1972).

[10] J. Satsuma and N. Yajima, *Prog. Theor. Phys*. **55**, 284 (1974).

[11] V. I. Karpman and V. V. Solovev, *Physica* **3D**, 487 (1981).

[12] J. P. Gordon, *Opt. Lett.* **8**, 596 (1983).

[13] F. M. Mitschke and L. F. Mollenauer, *Opt. Lett.* **12**, 355 (1987).

[14] C. Desem and P. L. Chu, *IEE Proc.* **134**, 145 (1987).

[15] Y. Kodama and K. Nozaki, *Opt. Lett.* **12**, 1038 (1987).

[16] S. G. Evangelides, L. F. Mollenauer, J. P. Gordon, and N. S. Bergano, *J. Lightwave Technol.* **10**, 28 (1992).

[17] C. De Angelis and S. Wabnitz, *Opt. Commun.* **125**, 186 (1996).

[18] A. Hasegawa and Y. Kodama, *Opt. Lett.* **7**, 285 (1982).

[19] K. J. Blow and N. J . Doran, *Opt. Commun.* **52**, 367 (1985).

[20] M. J. Potasek and G. P. Agrawal, *Electron. Lett.* **22**, 759 (1986).

[21] Y. Kodama and A. Hasegawa, *Opt. Lett.* **7**, 339 (1982); **8**, 342 (1983).

[22] A. Hasegawa, *Opt. Lett.* **8**, 650 (1983); *Appl. Opt.* **23**, 3302 (1984).

[23] L. F. Mollenauer, R. H. Stolen, and M. N. Islam, *Opt. Lett.* **10**, 229 (1985).

[24] L. F. Mollenauer, J. P. Gordon, and M. N. Islam, *IEEE J. Quantum Electron.* **22**, 157 (1986).

[25] A. Hasegawa and Y. Kodama, *Phys. Rev. Lett.* **66**, 161 (1991).

[26] D. M. Spirit, I. W. Marshall, P. D. Constantine, D. L. Williams, S. T. Davey, and B. J. Ainslie, *Electron. Lett.* **27**, 222 (1991).

[27] M. Nakazawa, H. Kubota, K. Kurakawa, and E. Yamada, *J. Opt. Soc. Am. B* **8**, 1811 (1991).

[28] K. Kurokawa and M. Nakazawa, *IEEE J. Quantum Electron.* **28**, 1922 (1992).

[29] K. Rottwitt, J. H. Povlsen, S. Gundersen, and A. Bjarklev, *Opt. Lett.* **18**, 867 (1993).

[30] C. Lester, K. Bertilsson, K. Rottwitt, P. A. Andrekson, M. A. Newhouse, and A. J. Antos, *Electron. Lett.* **31**, 219 (1995).

[31] Z. M. Liao and G. P. Agrawal, *IEEE Photon. Technol. Lett.* **11**, 818 (1999).

[32] N. J. Smith and N. J. Doran, *J. Opt. Soc. Am. B* **12**, 1117 (1995).

[33] M. Matsumoto, H. Ikeda, T. Uda, and A. Hasegawa, *J. Lightwave Technol.* **13**, 658 (1995).

[34] W. Forysiak, N. J. Doran, F. M. Knox, and K. J. Blow, *Opt. Commun.* **117**, 65 (1995).

[35] R. J. Essiambre and G. P. Agrawal, *J. Opt. Soc. Am. B* **12**, 2420 (1995).

[36] Z. M. Liao, C. J. McKinstrie, and G. P. Agrawal, *J. Opt. Soc. Am. B* **17**, 514 (2000).

[37] J. P. Gordon and H. A. Haus, *Opt. Lett.* **11**, 665 (1986).

[38] D. Marcuse, *J. Lightwave Technol.* **10**, 273 (1992).

[39] T. Georges and F. Favre, *J. Opt. Soc. Am. B* **10**, 1880 (1993).

[40] T. Georges, *Opt. Fiber Technol.* **1**, 97 (1995).

[41] C. R. Menyuk, *Opt. Lett.* **20**, 285 (1995).

[42] T. Georges, *Electron. Lett.* **31**, 1174 (1995).

[43] A. N. Pinto, G. P. Agrawal, and J. F. da Rocha, *J. Lightwave Technol.* **16**, 515 (1998).

[44] E. M. Dianov, A. V. Luchnikov, A. N. Pilipetskii, and A. M. Prokhorov, *Sov. Lightwave Commun.* **1**, 235 (1991); *Appl. Phys.* **54**, 175 (1992).

[45] K. Smith and L. F. Mollenauer, *Opt. Lett.* **14**, 1284 (1989).

[46] L. F. Mollenauer, *Opt. Lett.* **21**, 384 (1996).

[47] A. N. Pilipetskii and C. R. Menyuk, *Opt. Lett.* **22**, 28 (1997).

[48] T. Adah, B. Wang, A. N. Pilipetskii, and C. R. Menyuk, *J. Lightwave Technol.* **16**, 986 (1998).

[49] L. F. Mollenauer and J. P. Gordon, *Opt. Lett.* **19**, 375 (1994).
[50] C. A. Eleftherianos, D. Syvridis, T. Sphicopoulos, and C. Caroubalos, *Opt. Commun.* **154**, 14 (1998).
[51] S. M. Baker and J. N. Elgin, *Quantum Semiclass. Opt.* **10**, 251 (1998).
[52] L. F. Mollenauer, M. J. Neubelt, M. Haner, E. Lichtman, S. G. Evangelides, and B. M. Nyman, *Electron. Lett.* **27**, 2055 (1991).
[53] A. Mecozzi, J. D. Moores, H. A. Haus, and Y. Lai, *Opt. Lett.* **16**, 1841 (1991).
[54] Y. Kodama and A. Hasegawa, *Opt. Lett.* **17**, 31 (1992).
[55] L. F. Mollenauer, J. P. Gordon, and S. G. Evangelides, *Opt. Lett.* **17**, 1575 (1992).
[56] Y. Kodama and S. Wabnitz, *Opt. Lett.* **19**, 162 (1994).
[57] M. Romagnoli, S. Wabnitz, and M. Midrio, *Opt. Commun.* **104**, 293 (1994).
[58] E. A. Golovchenko, A. N. Pilipetskii, C. R. Menyuk, J. P. Gordon, and L. F. Mollenauer, *Opt. Lett.* **20**, 539 (1995).
[59] A. Mecozzi, M. Midrio, and M. Romagnoli, *Opt. Lett.* **21**, 402 (1996).
[60] S. Kawai and K. Iwatsuki, *J. Lightwave Technol.* **16**, 2347 (1998).
[61] H. Kim, J. H. Jang, and Y. C. Chung, *IEEE Photon. Technol. Lett.* **8**, 1193 (1996).
[62] G. Aubin, T. Montalant, J. Moulu, B. Nortier, F. Pirio, and J.-B. Thomine, *Electron. Lett.* **31**, 52 (1995).
[63] H. Toda, H. Yamagishi, and A. Hasegawa, *Opt. Lett.* **20**, 1002 (1995).
[64] V. V. Afanasjev, *Opt. Lett.* **18**, 790 (1993).
[65] J. C. Dung, S. Chi, and S. Wen, *Opt. Lett.* **20**, 1862 (1995).
[66] M. Suzuki, N. Edagawa, H. Taga, H. Tanaka, S. Yamamoto, and S. Akiba, *Electron. Lett.* **30**, 1083 (1994).
[67] A. L. J. Teixeira, G. P. Agrawal, and J. R. F. da Rocha, *Electron. Lett.* **32**, 1995 (1996).
[68] A. Mecozzi, *Opt. Lett.* **20**, 1859 (1995).
[69] S. Wabnitz and E. Westin, *Opt. Lett.* **21**, 1235 (1996).
[70] S. Wabnitz, *Electron. Lett.* **29**, 1711 (1993).
[71] N. J. Smith, W. J. Firth, K. J. Blow, and K. Smith, *Opt. Lett.* **19**, 16 (1994).
[72] S. Bigo, O. Audouin, and E. Desurvire, *Electron. Lett.* **31**, 2191 (1995).
[73] N. J. Smith, K. J. Blow, W. J. Firth, and K. Smith, *Opt. Commun.* **102**, 324 (1993).
[74] M. Suzuki, N. Edagawa, H. Taga, H. Tanaka, S. Yamamoto, and S. Akiba, *Electron. Lett.* **30**, 1083 (1994).
[75] M. Matsumoto, H. Ikeda, and A. Hasegawa, *Opt. Lett.* **19**, 183 (1994).
[76] E. Yamada and M. Nakazawa, *IEEE J. Quantum Electron.* **30**, 1842 (1994).
[77] A. Takada and W. Imajuku, *Electron. Lett.* **32**, 677 (1996).

[78] T. Widdowson, D. J. Malyon, A. D. Ellis, K. Smith, and K. J. Blow, *Electron. Lett.* **30**, 990 (1994).

[79] S. Kumar and A. Hasegawa, *Opt. Lett.* **20**, 1856 (1995).

[80] V. S. Grigoryan, A. Hasegawa, and A. Maruta, *Opt. Lett.* **20**, 857 (1995).

[81] M. Nakazawa, K. Suzuki, and Y. Kimura, *IEEE Photon. Technol. Lett.* **2**, 216 (1990).

[82] N. A. Olsson, P. A. Andrekson, P. C. Becker, J. R. Simpson, T. Tanbun-Ek, R. A. Logan, H. Presby, and K. Wecht, *IEEE Photon. Technol. Lett.* **2**, 358 (1990).

[83] K. Iwatsuki, S. Nishi, and K. Nakagawa, *IEEE Photon. Technol. Lett.* **2**, 355 (1990).

[84] E. Yamada, K. Suzuki, and M. Nakazawa, *Electron. Lett.* **27**, 1289 (1991).

[85] L. F. Mollenauer, B. M. Nyman, M. J. Neubelt, G. Raybon, and S. G. Evangelides, *Electron. Lett.* **27**, 178 (1991).

[86] L. F. Mollenauer, E. Lichtman, G. T. Harvey, M. J. Neubelt, and B. M. Nyman, *Electron. Lett.* **28**, 792 (1992).

[87] L. F. Mollenauer, E. Lichtman, M. J. Neubelt, and G. T. Harvey, *Electron. Lett.* **29**, 910 (1993).

[88] L. F. Mollenauer, P. V. Mamyshev, and M. J. Neubelt, *Opt. Lett.* **19**, 704 (1994).

[89] M. Nakazawa, E. Yamada, H. Kubota, and K. Suzuki, *Electron. Lett.* **27**, 1270 (1991).

[90] M. Nakazawa, K. Suzuki, E. Yamada, H. Kubota, Y. Kimura, and M. Takaya, *Electron. Lett.* **29**, 729 (1993).

[91] H. Kubota and M. Nakazawa, *Electron. Lett.* **29**, 1780 (1993).

[92] G. Aubin, E. Jeanny, T. Montalant, J. Moulu, F. Pirio, J.-B. Thomine, and F. Devaux, *Electron. Lett.* **31**, 1079 (1995).

[93] M. Nakazawa, K. Suzuki, H. Kubota, E. Yamada, and Y. Kimura, *Electron. Lett.* **30**, 1331 (1994).

[94] G. Onishchukov, V. Lokhnygin, A. Shipulin, and P. Reidel, *Electron. Lett.* **34**, 1597 (1998).

[95] M. Golles, I. M. Uzunov, and F. Lederer, *J. Opt. Soc. Am. B* **16**, 689 (1999).

[96] Z. Bakonyi, G. Onishchukov, C. Knoll, M. Golles, F. Lederer, and R. Ludwig, *IEEE Photon. Technol. Lett.* **12**, 570 (2000).

[97] K. Tajima, *Opt. Lett.* **12**, 54 (1987).

[98] V. A. Bogatyrjov, M. M. Bubnov, E. M. Dianov, and A. A. Sysoliatin, *Pure Appl. Opt.* **4**, 345 (1995).

[99] D. J. Richardson, R. P. Chamberlin, L. Dong, and D. N. Payne, *Electron. Lett.* **31**, 1681 (1995).

[100] A. J. Stentz, R. Boyd, and A. F. Evans, *Opt. Lett.* **20**, 1770 (1995).

[101] D. J. Richardson, L. Dong, R. P. Chamberlin, A. D. Ellis, T. Widdowson, and W. A. Pender, *Electron. Lett.* **32**, 373 (1996).

[102] W. Forysiak, F. M. Knox, and N. J. Doran, *Opt. Lett.* **19**, 174 (1994).

[103] T. Georges and B. Charbonnier, *Opt. Lett.* **21**, 1232 (1996); *IEEE Photon. Technol. Lett.* **9**, 127 (1997).

[104] S. Cardianal, E. Desurvire, J. P. Hamaide, and O. Audouin, *Electron. Lett.* **33**, 77 (1997).

[105] A. Hasegawa, Y. Kodama, and A. Murata, *Opt. Fiber Technol*. **3**, 197 (1997).

[106] S. Kumar, Y. Kodama, and A. Hasegawa, *Electron. Lett.* **33**, 459 (1997).

[107] R.-J. Essiambre and G. P. Agrawal, *Opt. Commun.* **131**, 274 (1996).

[108] R.-J. Essiambre and G. P. Agrawal, *J. Opt. Soc. Am. B* **14**, 314 (1997).

[109] R.-J. Essiambre and G. P. Agrawal, *J. Opt. Soc. Am. B* **14**, 323 (1997).

[110] R.-J. Essiambre and G. P. Agrawal, *Opt. Lett.* **21**, 116 (1996).

[111] A. Hasegawa, S. Kumar, and Y. Kodama, *Opt. Lett.* **21**, 39 (1996).

[112] A. D. Ellis, T. Widdowson, and X. Shan, *Electron. Lett.* **32**, 381 (1996).

[113] N. J. Smith, F. M. Knox, N. J. Doran, K. J. Blow, and I. Bennion, *Electron. Lett.* **32**, 54 (1996).

[114] M. Nakazawa, H. Kubota, and K. Tamura, *IEEE Photon. Technol. Lett.* **8**, 452 (1996).

[115] M. Nakazawa, H. Kubota, A. Sahara, and K. Tamura, *IEEE Photon. Technol. Lett.* **8**, 1088 (1996).

[116] A. B. Grudinin and I. A. Goncharenko, *Electron. Lett.* **32**, 1602 (1996).

[117] I. R. Gabitov and S. K. Turitsyn, *Opt. Lett.* **21**, 327 (1996).

[118] M. Matsumoto and H. A. Haus, *IEEE Photon. Technol. Lett.* **9**, 785 (1997).

[119] E. Shapiro and S. K. Turitsyn, *Opt. Lett.* **22**, 1544 (1997); *Phys. Rev. E* **56**, R4951 (1997); *Opt. Lett.* **23**, 682 (1998).

[120] V. S. Grigoryan, T. Yu, E. A. Golovchenko, C. R. Menyuk, and A. N. Pilipetskii, *Opt. Lett.* **22**, 1609 (1997).

[121] A. Berntson, N. J. Doran, W. Forysiak, and J. H. B. Nijhof, *Opt. Lett.* **23**, 900 (1998).

[122] J. N. Kutz, P. Holmes, S. G. Evangelides, and J. P. Gordon, *J. Opt. Soc. Am. B* **15**, 87 (1998).

[123] T. I. Lakoba, J. Yang, D. J. Kaup, and B. A. Malomed, *Opt. Commun.* **149**, 366 (1998).

[124] S. K. Turitsyn and E. G. Shapiro, *Opt. Fiber Technol*. **4**, 151 (1998).

[125] S. K. Turitsyn, I. Gabitov, E. W. Laedke, V. K. Mezentsev, S. L. Musher, E. G. Shapiro, T. Schafer, and K. H. Spatschek, *Opt. Commun.* **151**, 117 (1998).

[126] T. I. Lakoba and D. J. Kaup, *Phys. Rev. E* **58**, 6728 (1998).

[127] S. K. Turitsyn, T. Schafer, K. H. Spatschek, and V. K. Mezentsev, *Opt. Commun.* **163**, 122 (1999).

[128] H. A. Haus and Y. Chen, *J. Opt. Soc. Am. B* **16**, 24 (1999).

[129] S. K. Turitsyn and E. G. Shapiro, *J. Opt. Soc. Am. B* **16**, 1321 (1999).

[130] T. I. Lakoba and G. P. Agrawal, *J. Opt. Soc. Am. B* **16**, 1332 (1999).

[131] I. R. Gabitov, E. G. Shapiro, and S. K. Turitsyn, *Phys. Rev. E* **55**, 3624 (1997).

[132] M. J. Ablowitz and G. Bioindini, *Opt. Lett.* **23**, 1668 (1998).

[133] C. Paré and P. A. Belangér, *Opt. Lett.* **25**, 881 (2000).

[134] S. Kumar and A. Hasegawa, *Opt. Lett.* **22**, 372 (1997).

[135] N. J. Smith, N. J. Doran, W. Forysiak, and F. M. Knox, *J. Lightwave Technol.* **15**, 1808 (1997).

[136] J. H. B. Nijhof, N. J. Doran, W. Forysiak, and F. M. Knox, *Electron. Lett.* **33**, 1726 (1997).

[137] V. S. Grigoryan and C. R. Menyuk, *Opt. Lett.* **23**, 609 (1998).

[138] J. N. Kutz and S. G. Evangelides, Jr., *Opt. Lett.* **23**, 685 (1998).

[139] Y. Chen and H. A. Haus, *Opt. Lett.* **23**, 1013 (1998).

[140] J. H. B. Nijhof, W. Forysiak, and N. J. Doran, *Opt. Lett.* **23**, 1674 (1998).

[141] S. K. Turitsyn, J. H. B. Nijhof, V. K. Mezentsev, and N. J. Doran, *Opt. Lett.* **24**, 1871 (1999).

[142] N. J. Smith, W. Forysiak, and N. J. Doran, *Electron. Lett.* **32**, 2085 (1996).

[143] G. M. Carter, J. M. Jacob, C. R. Menyuk, E. A. Golovchenko, and A. N. Pilipetskii, *Opt. Lett.* **22**, 513 (1997).

[144] S. Kumar and F. Lederer, *Opt. Lett.* **22**, 1870 (1997).

[145] R. M. Mu, V. S. Grigoryan, C. R. Menyuk, E. A. Golovchenko, and A. N. Pilipetskii, *Opt. Lett.* **23**, 930 (1998).

[146] J. N. Kutz and P. K. A. Wai, *IEEE Photon. Technol. Lett.* **10**, 702 (1998); *Electron. Lett.* **34**, 522 (1998); *Opt. Lett.* **23**, 1022 (1998).

[147] M. Matsumoto, *Opt. Lett.* **22**, 1238 (1997); *IEEE Photon. Technol. Lett.* **10**, 373 (1998); *J. Opt. Soc. Am. B* **15**, 2831 (1998).

[148] S. Kumar, M. Wald, F. Lederer, and A. Hasegawa, *Opt. Lett.* **23**, 1019 (1998).

[149] T. Georges, *J. Opt. Soc. Am. B* **15**, 1553 (1998).

[150] L. F. Mollenauer, P. V. Mamyshev, and J. P. Gordon, *Opt. Lett.* **24**, 220 (1999).

[151] A. Berntson and B. A. Malomed, *Opt. Lett.* **24**, 507 (1999).

[152] T. I. Lakoba and D. J. Kaup, *Opt. Lett.* **24**, 808 (1999).

[153] V. S. Grigoryan, C. R. Menyuk, and R. M. Mu, *J. Lightwave Technol.* **17**, 1346 (1999).

[154] S. K. Turitsyn and E. G. Shapiro, *J. Opt. Soc. Am. B* **16**, 1321 (1999).

[155] A. Tonello, A. D. Capobianco, S. Wabnitz, and S. K. Turitsyn, *Opt. Commun.* **176**, 103 (2000).

[156] G. Bento, F. Neddam, and S. Wabnitz, *Opt. Lett.* **25**, 144 (2000).

[157] J. P. Gordon and L. F. Mollenauer, *Opt. Lett.* **24**, 223 (1999).

[158] T. Yu, R. M. Mu, V. S. Grigoryan, and C. R. Menyuk, *IEEE Photon. Technol. Lett.* **11**, 75 (1999).

[159] K. Shimoura and S. Seikai, *IEEE Photon. Technol. Lett.* **11**, 200 (1999).

[160] P. A. Belangér and C. Paré, *J. Lightwave Technol.* **17**, 445 (1999).

[161] Y. J. Wen and X. L. Yang, *IEEE Photon. Technol. Lett.* **11**, 433 (1999).

[162] S. K. Turitsyn and E. G. Shapiro, *J. Opt. Soc. Am. B* **16**, 1321 (1999).

[163] S. Chi, J. C. Dung, and S. C. Lin, *IEEE Photon. Technol. Lett.* **11**, 1605 (1999).

[164] T. Hirooka and S. Wabnitz, *Opt. Fiber Technol*. **6**, 109 (2000).

[165] J. D. Ania-Castanon, P. Garcia-Fernandez, and J. M. Soto-Crespo, *Opt. Lett.* **25**, 159 (2000).

[166] N. Efremidis, K. Hizanidis, B. A. Malomed, H. E. Nistazakis, and D. J. Frantzeskakis, *J. Opt. Soc. Am. B* **17**, 952 (2000).

[167] S. K. Turitsyn, M. P. Fedourk, E. G. Shapiro, V. K. Mezentsev, and E. G. Turitsyna, *IEEE J. Sel. Topics Quantum Electron.* **6**, 263 (2000).

[168] J. Pina, B. Abueva, and C. G. Goedde, *Opt. Commun.* **176**, 397 (2000).

[169] J. H. B. Nijhof, W. Forysiak, and N. J. Doran, *IEEE J. Sel. Topics Quantum Electron.* **6**, 330 (2000).

[170] L. J. Richardson, W. Forysiak, and N. J. Doran, *Opt. Lett.* **25**, 1010 (2000).

[171] W. Xue, G. Zhou, Z. Li, and S. Guo, *J. Lightwave Technol.* **18**, 926 (2000).

[172] J. Atai and B. A. Malomed, *J. Opt. Soc. Am. B* **17**, 1134 (2000).

[173] J. Kumasako, M. Matsumoto, and S. Waiyapot, *J. Lightwave Technol.* **18**, 1064 (2000).

[174] A. E. Siegman, *Lasers* (University Science Books, Mill Valley, CA, 1986), Chap. 27.

[175] H. Kubota and M. Nakazawa, *Opt. Commun.* **87**, 15 (1992).

[176] M. Nakazawa and H. Kubota, *Electron. Lett.* **31**, 216 (1995).

[177] M. Suzuki, I. Morita, N. Edagawa, S. Yamamoto, H. Taga, and S. Akiba, *Electron. Lett.* **31**, 2027 (1995).

[178] A. Naka, T. Matsuda, and S. Saito, *Electron. Lett.* **32**, 1694 (1996).

[179] I. Morita, M. Suzuki, N. Edagawa, S. Yamamoto, H. Taga, and S. Akiba, *IEEE Photon. Technol. Lett.* **8**, 1573 (1996).

[180] J. M. Jacob, E. A. Golovchenko, A. N. Pilipetskii, G. M. Carter, and C. R. Menyuk, *IEEE Photon. Technol. Lett.* **9**, 130 (1997).

[181] G. M. Carter and J. M. Jacob, *IEEE Photon. Technol. Lett.* **10**, 546 (1998).

[182] V. S. Grigoryan, R. M. Mu, G. M. Carter, and C. R. Menyuk, *IEEE Photon. Technol. Lett.* **10**, 45 (2000).

[183] R. M. Mu, C. R. Menyuk, G. M. Carter, and J. M. Jacob, *IEEE J. Sel. Topics Quantum Electron.* **6**, 248 (2000).

[184] A. B. Grudinin, M. Durkin, M. Isben, R. I. Laming, A. Schiffini, P. Franco, E. Grandi, and M. Romagnoli, *Electron. Lett.* **33**, 1572 (1997).

[185] I. S. Penketh, P. Harper, S. B. Aleston, A. M. Niculae, I. Bennion, and N. J. Doran, *Opt. Lett.* **24**, 803 (1999).

[186] F. Favre, D. Le Guen, and T. Georges, *J. Lightwave Technol.* **17**, 1032 (1999).

[187] M. Zitelli, F. Favre, D. Le Guen, and S. Del Burgo, *IEEE Photon. Technol. Lett.* **9**, 904 (1999).

[188] D. S. Govan, W. Forysiak, and N. J. Doran, *Opt. Lett.* **23**, 1523 (1998).

[189] I. Morita, K. Tanaka, N. Edagawa, S. Yamamoto, and M. Suzuki, *Electron. Lett.* **34**, 1863 (1998).

[190] F. Matera, M. Settembre, and M. Tamburrini et al., *J. Lightwave Technol.* **17**, 2225 (1999).

[191] I. Morita, K. Tanaka, N. Edagawa, and M. Suzuki, *J. Lightwave Technol.* **17**, 2506 (1999).

[192] A. H. Liang, H. Toda, and A. Hasegawa, *Opt. Lett.* **24**, 799 (1999).

[193] T. Hirooka, T. Nakada, and A. Hasegawa, *IEEE Photon. Technol. Lett.* **6**, 633 (2000).

[194] T. Lakoba and G. P. Agrawal, *J. Lightwave Technol.* **18**, Nov. (2000).

[195] L. F. Mollenauer and P. V. Mamyshev, *IEEE J. Quantum Electron.* **34**, 2089 (1998).

[196] L. F. Mollenauer, S. G. Evangelides, and J. P. Gordon, *J. Lightwave Technol.* **9**, 362 (1991).

[197] A. F. Benner, J. R. Sauer, and M. J. Ablowitz, *J. Opt. Soc. Am. B* **10**, 2331 (1993).

[198] Y. Kodama and A. Hasegawa, *Opt. Lett.* **16**, 208 (1991).

[199] T. Aakjer, J. H. Povlsen, and K. Rottwitt, *Opt. Lett.* **18**, 1908 (1993).

[200] S. Chakravarty, M. J. Ablowitz, J. R. Sauer, and R. B. Jenkins, *Opt. Lett.* **20**, 136 (1995).

[201] R. B. Jenkins, J. R. Sauer, S. Chakravarty, and M. J. Ablowitz, *Opt. Lett.* **20**, 1964 (1995).

[202] X. Y. Tang and M. K. Chin, *Opt. Commun.* **119**, 41 (1995).

[203] P. K. A. Wai, C. R. Menyuk, and B. Raghavan, *J. Lightwave Technol.* **14**, 1449 (1996).

[204] L. F. Mollenauer, E. Lichtman, G. T. Harvey, M. J. Neubelt, and B. M. Nyman, *Electron. Lett.* **28**, 792 (1992).

[205] A. Mecozzi and H. A. Haus, *Opt. Lett.* **17**, 988 (1992).

[206] R. Ohhira, M. Matsumoto, and A. Hasegawa, *Opt. Commun.* **111**, 39 (1994).

[207] M. Midrio, P. Franco, F. Matera, M. Romagnoli, and M. Settembre, *Opt. Commun.* **112**, 283 (1994).

[208] E. A. Golovchenko, A. N. Pilipetskii, and C. R. Menyuk, *Opt. Lett.* **21**, 195 (1996).

[209] E. Desurvire, O. Leclerc, and O. Audouin, *Opt. Lett.* **21**, 1026 (1996).

[210] M. Nakazawa, K. Suzuki, H. Kubota, Y. Kimura, E. Yamada, K. Tamura, T. Komukai, and T. Imai, *Electron. Lett.* **32**, 828 (1996).

[211] M. Nakazawa, K. Suzuki, H. Kubota, and E. Yamada, *Electron. Lett.* **32**, 1686 (1996).

[212] P. V. Mamyshev and L. F. Mollenauer, *Opt. Lett.* **21**, 396 (1996).

[213] S. G. Evangelides and J. P. Gordon, *J. Lightwave Technol.* **14**, 1639 (1996).

[214] L. F. Mollenauer, P. V. Mamyshev, and M. J. Neubelt, *Electron. Lett.* **32**, 471 (1996).

[215] M. Nakazawa, K. Suzuki, H. Kubota, A. Sahara, and E. Yamada, *Electron. Lett.* **34**, 103 (1998).

[216] X. Tang, R. Mu, and P. Ye, *Opt. Quantum Electron.* **26**, 969 (1994).

[217] E. Kolltveit, J. P. Hamaide, and O. Audouin, *Electron. Lett.* **32**, 1858 (1996).

[218] S. Wabnitz, *Opt. Lett.* **21**, 638 (1996).

[219] E. A. Golovchenko, A. N. Pilipetskii, and C. R. Menyuk, *Electron. Lett.* **33**, 735 (1997); *Opt. Lett.* **22**, 1156 (1997).

[220] H. Sugahara, H. Kato, and Y. Kodama, *Electron. Lett.* **33**, 1056 (1997).

[221] Y. Kodama, A. V. Mikhailov, and S. Wabnitz, *Opt. Commun.* **143**, 53 (1997).

[222] Y. Kodama and A. Murata, *Opt. Lett.* **22**, 1692 (1997).

[223] J. F. L. Devaney, W. Forysiak, A. M. Niculae, and N. J. Doran, *Opt. Lett.* **22**, 1695 (1997).

[224] J. H. B. Nijhof, N. J. Doran, W. Forysiak, and A. Berntson, *Electron. Lett.* **34**, 481 (1998).

[225] T. S. Yang, W. L. Kath, and S. K. Turitsyn, *Opt. Lett.* **23**, 597 (1998).

[226] M. J. Ablowitz, G. Bioindini, S. Chakravarty, and R. L. Horne, *Opt. Commun.* **150**, 305 (1998).

[227] A. Mecozzi, *J. Opt. Soc. Am. B* **15**, 152 (1998).

[228] S. Kumar, *Opt. Lett.* **23**, 1450 (1998).

[229] T. Hirooka and A. Hasegawa, *Opt. Lett.* **23**, 768 (1998).

[230] A. M. Niculae, W. Forysiak, A. J. Golag, J. H. B. Nijhof, and N. J. Doran, *Opt. Lett.* **23**, 1354 (1998).

[231] P. V. Mamyshev and L. F. Mollenauer, *Opt. Lett.* **24**, 1 (1999).

[232] H. Sugahara, A. Maruta, and Y. Kodama, *Opt. Lett.* **24**, 145 (1999).

[233] Y. Chen and H. A. Haus, *Opt. Lett.* **24**, 217 (1999).

[234] H. Sugahara, H. Kato, T. Inoue, A. Maruta, and Y. Kodama, *J. Lightwave Technol.* **17**, 1547 (1999).

[235] D. J. Kaup, B. A. Malomed, and J. Yang, *Opt. Lett.* **23**, 1600 (1998); *J. Opt. Soc. Am. B* **16**, 1628 (1999).

[236] A. Hasegawa and T. Hirooka, *Electron. Lett.* **36**, 68 (2000).

[237] S. K. Turitsyn, M. Fedoruk, T. S. Yang, and W. L. Kath, *IEEE J. Quantum Electron.* **36**, 290 (2000).

[238] V. S. Grigoryan and A. Richter, *J. Lightwave Technol.* **18**, 1148 (2000).

[239] F. Favre, D. Le Guen, M. L. Moulinard, M. Henry, and T. Georges, *Electron. Lett.* **33**, 2135 (1997).

[240] K. Tanaka, I. Morita, M. Suzuki, N. Edagawa, and S. Yamamoto, *Electron. Lett.* **34**, 2257 (1998).

[241] L. F. Mollenauer, R. Bonney, J. P. Gordon, and P. V. Mamyshev, *Opt. Lett.* **24**, 285 (1999).

[242] I. Morita, M. Suzuki, N. Edagawa, K. Tanaka, and S. Yamamoto, *J. Lightwave Technol.* **17**, 80 (1999).

[243] F. Neddam, P. Le Lourec, B. Biotteau et al., *Electron. Lett.* **35**, 1093 (1999).

[244] M. L. Dennis, W. I. Kaechele, L. Goldberg, T. F. Carruthers, and I. N. Duling, *IEEE Photon. Technol. Lett.* **11**, 1680 (1999).

[245] K. Suzuki, H. Kubota, A. Sahara, and M. Nakazawa, *Electron. Lett.* **36**, 443 (2000).

[246] M. Nakazawa, H. Kubota, K. Suzuki, E. Yamada, and A. Sahara, *IEEE J. Sel. Topics Quantum Electron.* **6**, 363 (2000).

[247] L. F. Mollenauer, P. V. Mamyshev, J. Gripp, M. J. Neubelt, N. Mamysheva, L. Grüner-Nielsen, and T. Veng, *Opt. Lett.* **25**, 704 (2000).

Appendix A

Bit-Error Rate

The performance of a lightwave system is judged by the bit-error rate (BER), defined as the probability of incorrect identification of a bit by the decision circuit of the receiver. For example, a BER of 2×10^{-9} corresponds to two errors per billion bits on average. Most lightwave systems require BER to be $< 1 \times 10^{-9}$. Some modern systems are designed to operate with a BER below 10^{-12}. The BER depends on the signal-to-noise ratio (SNR) of the current generated at the receiver when a optical bit stream is converted into the electric domain. The SNR, in turn, depends on various noise mechanisms such as shot noise, thermal noise, and ASE noise associated with the received signal.

The fluctuating electric signal at the receiver is passed to the decision circuit, which samples it periodically at the bit rate to determine individual bits. The sampled value I fluctuates from bit to bit around an average value I_1 or I_0, depending on whether the bit corresponds to 1 or 0 in the bit stream. The decision circuit compares the sampled value with a threshold value I_D and calls it bit 1 if $I > I_D$ and bit 0 if $I < I_D$. An error occurs if $I < I_D$ for 1 bits because of receiver noise. An error also occurs if $I > I_D$ for 0 bits. Both sources of errors can be included through the error probability, defined as

$$\text{BER} = p(1)P(0/1) + p(0)P(1/0), \tag{A.1}$$

where $p(1)$ and $p(0)$ are the probabilities of receiving bits 1 and 0, respectively, $P(0/1)$ is the conditional probability of deciding 0 when a 1 bit is received, and $P(1/0)$ is the conditional probability of deciding 1 when a 0 bit is received. Since 1 and 0 bits are equally likely to occur in a realistic bit stream, $p(1) =$

$p(0) = 1/2$, and the BER becomes

$$\text{BER} = \tfrac{1}{2}[P(0/1) + P(1/0)]. \tag{A.2}$$

The quantities $P(0/1)$ and $P(1/0)$ depend on the probability density function $p(I)$ of the sampled value I. The functional form of $p(I)$ depends on the statistics of various noise sources responsible for current fluctuations. It is not easy to find an analytic form of $p(I)$. For this reason, it is common to assume that $I(t)$ is a Gaussian random process. However, both the average and the variance of the Gaussian distribution are taken to be different for 1 and 0 bits such that

$$p_m(I) = \frac{1}{\sigma_m\sqrt{2\pi}} \exp\left[-\frac{(I - I_m)^2}{2\sigma_m^2}\right], \tag{A.3}$$

where $m = 0$ or 1, I_1 and I_0 represent average currents for 1 and 0 bits, and σ_1^2 and σ_0^2 are the corresponding variances.

If I_D is the decision threshold, an error occurs for a 1 bit if $I < I_D$. Similarly, a 0 bit is incorrectly identified if $I > I_D$ for it. Using these conditions, the conditional probabilities can be written as

$$P(0/1) = \frac{1}{\sigma_1\sqrt{2\pi}} \int_{-\infty}^{I_D} \exp\left[-\frac{(I - I_1)^2}{2\sigma_1^2}\right] dI = \frac{1}{2}\,\text{erfc}\left(\frac{I_1 - I_D}{\sigma_1\sqrt{2}}\right), \tag{A.4}$$

$$P(1/0) = \frac{1}{\sigma_0\sqrt{2\pi}} \int_{I_D}^{\infty} \exp\left[-\frac{(I - I_0)^2}{2\sigma_0^2}\right] dI = \frac{1}{2}\,\text{erfc}\left(\frac{I_D - I_0}{\sigma_0\sqrt{2}}\right), \tag{A.5}$$

where erfc stands for the complementary error function defined as

$$\text{erfc}(x) = \frac{2}{\sqrt{\pi}} \int_x^{\infty} \exp(-y^2)\, dy. \tag{A.6}$$

Substituting Eqs. (A.4) and (A.5) in Eq. (A.2), the BER is given by

$$\text{BER} = \frac{1}{4}\left[\text{erfc}\left(\frac{I_1 - I_D}{\sigma_1\sqrt{2}}\right) + \text{erfc}\left(\frac{I_D - I_0}{\sigma_0\sqrt{2}}\right)\right]. \tag{A.7}$$

Equation (A.7) shows that the BER depends on the decision threshold I_D of the receiver. In practice, I_D is optimized to minimize the BER. The minimum occurs when I_D is chosen such that

$$(I_1 - I_D)/\sigma_1 = (I_D - I_0)/\sigma_0 \equiv Q. \tag{A.8}$$

The optimum value of I_D depends on the noise level and is given as

$$I_D = \frac{\sigma_0 I_1 + \sigma_1 I_0}{\sigma_0 + \sigma_1}. \tag{A.9}$$

When the noise level is the same for all bits, we can set $\sigma_1 = \sigma_0$ in Eq. (A.9). Since $I_D = \frac{1}{2}(I_1 + I_0)$ in that case, the decision threshold should be in the middle of the average currents for 0 and 1 bits. This is the situation for most receivers when noise is dominated by the thermal noise.

The BER with the optimum setting of the decision threshold is obtained using Eqs. (A.7) and (A.8) and is given by the following simple expression:

$$\text{BER} = \frac{1}{2}\text{erfc}\left(\frac{Q}{\sqrt{2}}\right) \approx \frac{\exp(-Q^2/2)}{Q\sqrt{2\pi}}, \tag{A.10}$$

where the approximate form is reasonably accurate for $Q > 3$. The Q parameter is found from Eqs. (A.8) and (A.9) to be

$$Q = \frac{I_1 - I_0}{\sigma_1 + \sigma_0}. \tag{A.11}$$

This parameter plays an important role in the system design. The BER improves as Q increases and is about 10^{-9} when $Q = 6$. It becomes lower than 10^{-12} for $Q > 7$.

Appendix B

Acronyms

Each scientific field has its own jargon, and the field of nonlinear fiber optics is no exception. Although an attempt was made to avoid extensive use of acronyms, many still appear throughout the book. Each acronym is defined the first time it appears in a chapter so that the reader does not have to search the entire text to find its meaning. As a further help, all acronyms are listed here in alphabetical order.

AM	amplitude modulation
ASE	amplified spontaneous emission
ASK	amplitude-shift keying
BER	bit-error rate
CW	continuous wave
DBR	distributed Bragg reflector
DCF	dispersion-compensating fiber
DDF	dispersion-decreasing fiber
DFB	distributed feedback
DM	dispersion-managed
DSF	dispersion-shifted fiber
EDFA	erbium-doped fiber amplifier
EDFL	erbium-doped fiber laser
FDM	frequency-division multiplexing
FFT	fast Fourier transform
FM	frequency modulation
FROG	frequency-resolved optical gating
FSK	frequency-shift keying

FWHM	full width at half maximum
FWM	four-wave mixing
GVD	group-velocity dispersion
LCM	liquid-crystal modulator
LEAF	large effective-area fiber
MCVD	modified chemical vapor deposition
MI	modulation instability
MQW	multiquantum well
MZI	Mach–Zehnder interferometer
NLS	nonlinear Schrödinger
NALM	nonlinear amplifying-loop mirror
NOLM	nonlinear optical-loop mirror
NRZ	nonreturn-to-zero
OOK	on–off keying
OPC	optical phase conjugation
OTDM	optical time-division multiplexing
OVD	outside-vapor deposition
PCM	pulse-code modulation
PDM	polarization-division multiplexing
PEF	polarization-evolution frequency
PLVS	polarization-locked vector soliton
PM	phase modulation
PMD	polarization-mode dispersion
PSK	phase-shift keying
RDF	reverse-dispersion fiber
RIN	relative intensity noise
RMS	root-mean-square
RZ	return-to-zero
SBS	stimulated Brillouin scattering
SCM	subcarrier multiplexing
SDH	synchronous digital hierarchy
SIT	self-induced transparency
SLA	semiconductor laser amplifier
SNR	signal-to-noise ratio
SPM	self-phase modulation
SRS	stimulated Raman scattering
TDM	time-division multiplexing

TOAD	terahertz optical asymmetric demultiplexer
TOD	third-order dispersion
TROG	time-resolved optical gating
VAD	vapor-axial deposition
VCSEL	vertical-cavity surface-emitting laser
VPE	vapor-phase epitaxy
WDM	wavelength-division multiplexing
XPM	cross-phase modulation
YAG	yttrium almunium garnet
ZDWL	zero-dispersion wavelength

Index

Optics and Photonics
(formerly Quantum Electronics)

N. S. Kapany and J. J. Burke, *Optical Waveguides*
Dietrich Marcuse, *Theory of Dielectric Optical Waveguides*
Benjamin Chu, *Laser Light Scattering*
Bruno Crosignani, Paolo DiPorto and Mario Bertolotti, *Statistical Properties of Scattered Light*
John D. Anderson, Jr., *Gasdynamic Lasers: An Introduction*
W. W. Duly, *CO_2 Lasers: Effects and Applications*
Henry Kressel and J. K. Butler, *Semiconductor Lasers and Heterojunction LEDs*
H. C. Casey and M. B. Panish, *Heterostructure Lasers: Part A. Fundamental Principles; Part B. Materials and Operating Characteristics*
Robert K. Erf, Editor, *Speckle Metrology*
Marc D. Levenson, *Introduction to Nonlinear Laser Spectroscopy*
David S. Kilger, editor, *Ultrasensitive Laser Spectroscopy*
Robert A. Fisher, editor, *Optical Phase Conjugation*
John F. Reintjes, *Nonlinear Optical Parametric Processes in Liquids and Gases*
S. H. Lin, Y. Fujimura, H. J. Neusser and E. W. Schlag, *Multiphoton Spectroscopy of Molecules*
Hyatt M. Gibbs, *Optical Bistability: Controlling Light with Light*
D. S. Chemla and J. Zyss, editors, *Nonlinear Optical Properties of Organic Molecules and Crystals, Volume 1, Volume 2*
Marc D. Levenson and Saturo Kano, *Introduction to Nonlinear Laser Spectroscopy, Revised Edition*
Govind P. Agrawal, *Nonlinear Fiber Optics*
F. J. Duarte and Lloyd W. Hillman, editors, *Dye Laser Principles: With Applications*
Dietrich Marcuse, *Theory of Dielectric Optical Waveguides, 2nd Edition*
Govind P. Agrawal and Robert W. Boyd, editors, *Contemporary Nonlinear Optics*
Peter S. Zory, Jr. editor, *Quantum Well Lasers*
Gary A. Evans and Jacob M. Hammer, editors, *Surface Emitting Semiconductor Lasers and Arrays*
John E. Midwinter, editor, *Photonics in Switching, Volume I, Background and Components*
John E. Midwinter, editor, *Photonics in Switching, Volume II, Systems*
Joseph Zyss, editor, *Molecular Nonlinear Optics: Materials, Physics, and Devices*
Mario Dagenais, Robert F. Leheny and John Crow, *Integrated Optoelectronics*
Govind P. Agrawal, *Nonlinear Fiber Optics, Second Edition*
Jean-Claude Diels and Wolfgang Rudolph, *Ultrashort Laser Pulse Phenomena: Fundamentals, Techniques, and Applications on a Femtosecond Time Scale*
Eli Kapon, editor, *Semiconductor Lasers I: Fundamentals*
Eli Kapon, editor, *Semiconductor Lasers II: Materials and Structures*
P. C. Becker, N. A. Olsson, and J. R. Simpson, *Erbium-Doped Fiber Amplifiers: Fundamentals and Technology*
Raman Kashyap, *Fiber Bragg Gratings*
Katsunari Okamoto, *Fundamentals of Optical Waveguides*
Govind P. Agrawal, *Nonlinear Fiber Optics, Third Edition*